INTERNATIONAL DOCTORAL
SCHOOL OF THE USC

Pablo
Fernández Garrido

PhD Thesis

DEVELOPMENT OF NEW ANALYSIS METHODS FOR THE STUDY OF MOLECULAR AGGREGATION AND ADSORPTION

Santiago de Compostela, 2021

Doctoral Programme in Materials Science

USC
UNIVERSIDADE
DE SANTIAGO
DE COMPOSTELA

DOCTORAL THESIS

DEVELOPMENT OF NEW ANALYSIS METHODS FOR THE STUDY OF MOLECULAR AGGREGATION AND ADSORPTION

Pablo Fernández Garrido

INTERNATIONAL PHD SCHOOL OF THE UNIVERSITY OF SANTIAGO DE COMPOSTELA

PHD PROGRAMME IN MATERIALS SCIENCE

SANTIAGO DE COMPOSTELA

2021

USC
UNIVERSIDADE
DE SANTIAGO
DE COMPOSTELA

DECLARACIÓN DO AUTOR/A DA TESE

D./Dna. **Pablo Fernández Garrido**

Título da tese: **Development of new analysis methods for the study of molecular aggregation and adsorption**

Presento a miña tese, seguindo o procedemento axeitado ao Regulamento, e declaro que:

1) A tese abarca os resultados da elaboración do meu traballo.
2) De ser o caso, na tese faise referencia ás colaboracións que tivo este traballo.
3) Confirmo que a tese non incorre en ningún tipo de plaxio doutros autores nin de traballos presentados por min para a obtención doutros títulos.
4) A tese é a versión definitiva presentada para a súa defensa e coincide a versión impresa coa presentada en formato electrónico

E comprométome a presentar o Compromiso Documental de Supervisión no caso de que o orixinal non estea na Escola.

En **Santiago de Compostela**, Seleccione a data.

Sinatura electrónica

USC
UNIVERSIDADE
DE SANTIAGO
DE COMPOSTELA

AUTORIZACIÓN DO DIRECTOR / TITOR DA TESE

Development of new analysis methods for the study of molecular aggregation and adsorption

D. Ángel Piñeiro Guillén

INFORMA:

Que a presente tese, correspóndese co traballo realizado por D. Pablo Fernández Garrido, baixo a miña dirección/titorización, e autorizo a súa presentación, considerando que reúne os requisitos esixidos no Regulamento de Estudos de Doutoramento da USC, e que como director desta non incorre nas causas de abstención establecidas na Lei 40/2015.

De acordo co indicado no Regulamento de Estudos de Doutoramento, declara tamén que a presente tese de doutoramento é idónea para ser defendida en base á modalidade de Monográfica con reprodución de publicacións, nos que a participación do doutorando foi decisiva para a súa elaboración e as publicacións se axustan ao Plan de Investigación.

En Santiago de Compostela, de de 2021

USC
UNIVERSIDADE
DE SANTIAGO
DE COMPOSTELA

A meus pais,

que teñen a responsabilidade
última sobre todo isto.

USC
UNIVERSIDADE
DE SANTIAGO
DE COMPOSTELA

'Arriba, cú de media libra!'

Jesús Fernández
Buño's last blacksmith

USC
UNIVERSIDADE
DE SANTIAGO
DE COMPOSTELA

Agradecementos

Poida que esta sexa unha das primeiras páxinas que ti, persoa que decidiu abrir este traballo a pesar do seu volume, leas, pero é sen dúbida a última que eu vou escribir. Este *non capítulo* da tese significa, dalgún xeito, que está rematada. E así é, rematou. Agora invádeme unha sensación de felicidade e de tremor, pois o que se aveciña é incerto. Mentiría se digo que quedo satisfeito co traballo desenvolto ó longo da miña etapa predoutoral, pois a miña forma de ser sempre me esixe máis. Satisfeito non, pero si contento por todo o desenvolto. Son curioso por natureza, e sempre me quedan demasiadas preguntas por resolver. Igual é por iso polo que decidín dedicarme ó que me apaixona: buscarlle respostas. Porén, se fun capaz de chegar a este momento, non foi só por min mesmo, senón por tódalas persoas que me acompañaron ó longo dos anos e que, nalgún momento, me aportaron algo e me fixeron ser quen son. A todas elas, empregando o siloxismo hipotético ($\frac{P \to Q, Q \to R}{\therefore P \to R}$), tamén lles corresponde parte deste traballo. Que persoas? Pois case con quen teño compartido algún que outro café. É dicir, moita xente. E por aí debería comezar:

Agradezo ás antigas poboacións das rexións de Etiopía e do Medio Oriente por teren producido as primeiras infusións de café, así como as súa comercialización e extensión. Sen elas, nin tería rematado a tese nin tería falado tanto coa xente.

Agora si. É o momento de comezar coa xente que me acompañou. Se non me tivese movido tanto estes anos, isto sería moito máis sinxelo. Non sei como poñe-la orde, nin a quen, nin a cantos. Así que, seguindo un pouco a temática desta tese, vou falar de certos agregados de persoas e de monómeros independentes. Síntoo moito se me deixo a alguén. De ser así, saberá de sobra que son un despistado para estas cousas.

En primeiro lugar coido que é necesario agradecer ás persoas que fixeron que acabase facendo isto que se lle chama *ciencia*. Por orde de aparición na miña vida, debo agradecer a Aurelio, a Carlos, a de la Viña e a Antonio Vidal, meus profesores de Ciencias Naturais, Física e Química, e Física dende que era cativo ata que entrei na facultade. Entre todos abrístesme un mundo cheo de descubrimentos.

Xa a nivel universitario, teño que agradecer individualmente a tres persoas, que se merecen cadanseu parágrafo:

A Alfredo Amigo, por se-la primeira persoa en confiar en min nesta universidade e por abrirme as portas do seu laboratorio. Recordo esa conversa a comezos do 2012, na que se me gustaba *cacharrear* había un laboratorio cunha morea de cousas coas que xogar á miña disposición. Se ben ó longo da miña recentemente estreada etapa investigadora descubrín que en comparación con outros sitios non había tantas, ese sempre será o meu primeiro *lab*.

A Pilar Brocos, por se-la voz do sentidiño. Soubo guiarme xunto con Alfredo ó

longo dos primeiros anos e dos Traballos Finais de X (X ∈ Grao,Máster). Aínda non sei moi ben como, pero acabamos cadrando en horarios de traballo, compartindo moitas charlas alén da ciencia.

A Ángel Piñeiro, meu director de tese. Por tratarme coma un igual dende un comezo, por axudarme cando era necesario, tanto a nivel de traballo como persoal, e por deixarme certa liberdade para andar a proba-las miñas ideas felices. A pesar de serche eu difícil de entender e manexar, coido que ao final conseguimos pechar algunha das moreas de cousas que tiñamos entre mans.

Seguindo un pouco dentro deste mundo académico, gustaríame menciona-lo grupo dos Seminarios de Investigación MD Física-Química e dos Beertings, quen nos vemos tódalas semanas para falar e debater sobre os nosos proxectos (e outras cousas que xorden) mais ós que, polos tempos que corren, dá a casualidade de que aínda non nos coñecemos en persoa! Todas esas reunións a última hora da tarde pagaron a pena. Sempre queda algo novo por aprender e algunha liña por poñer máis recta e centrada nas presentacións. Dentro deste agregado si que me gustaría destaca-la figura dos monómeros Rebeca e Martín, con quen teño o pracer de traballar dende que decidín meter a cabeza no mundo das Simulacións de Dinámica Molecular e das ciclodextrinas. Teño que recordarvos que quedaron experimentos pendentes sobre o encapsulamento da quinina por medio de ciclodextrinas en disolucións auga/etanol. Esperemos que pronto se poidan levar a cabo.

I would also like to thank Margarida Bastos, Adrián Velázquez-Campoy and Philippe Dumas for their support during these years working with the calorimeters. Their ideas and discussions made this project to be possible.

En este párrafo me gustaría agradecer a toda la gente con la que he tenido el placer de encontrarme en Zaragoza. Entre las personas del BIFI y los BIFIsaurios me habéis hecho estar como en casa desde el primer juepincho. Con la variedad de formas de ser y de pensar que aquí me he encontrado hace que de cada persona tenga algo positivo pero distinto que destacar. Nombraros de uno en uno haría este *no capítulo* mucho más largo de lo que ya es. Prefiero que vuestra imagen se quede como un agregado estable, unido por las interacciones de monte-cerveza y las BIFI excursiones.

Outro dos agregados fundamentais co que interaccionei nesta etapa é grupo dos cafés en Mates e Psicoloxía, e maila súa extensión ó grupo do Cocido, ás marchas ciclistas a Fisterra e mais ás escapadas para comer, aínda que haxa que ir a Asturias. Dentro deste complexo, sobresaen Ramón, Tuco e Mateo, con quen teño compartido máis vivencias e dos que teño recibido maior soporte. A pesar de que nesta última tempada ande demasiado desaparecido, volverei.

Entramos xa nese grupo de monómeros libres. A cadaquén podería dedicarlle o seu parágrafo independente, pero non me quero poñer moito máis sentimental. Alberto, Sara, Pablo Villar, Paula, Gonzalo, Marta, Juan e Yass. Todos vós fostes esenciais dende antes incluso de que entrase no doutoramento. Sempre puiden contar con vós e agradezo o voso apoio ó longo de tantos anos, especialmente cando as cousas deixaron de ser sinxelas. Grazas por estardes aí.

Sonia, quería aproveitar tamén este recuncho para agradecerche o teu apoio nesta etapa final. A túa ledicia é contaxiosa. Apareciches no peor momento e, aínda así, fas que todo pague a pena. Grazas por ser (ti) e por estar (aquí).

Para rematar, non podería pasar por alto o apoio da familia. De meus avós, de Cris, da tía Ana, de Nacho, de Jorge e especialmente de meu pai e miña nai, por me apoiar dende antes incluso de que eu fose consciente de que estaban aí. Grazas

USC UNIVERSIDADE DE SANTIAGO DE COMPOSTELA

por fomenta-la miña curiosidade dende pequeno e por pasar frío todas esas noites cando comezaba a formarme como científico intentando ver como funcionaba o meu primeiro telescopio.

Esta tesis ha sido posible gracias al programa de *Ayudas para contratos predoctorales para la formación de doctores 2016*, convocado por el Ministerio de Economía y Competitividad y cofinanciado por el Fondo Social Europeo, cuya referencia de la ayuda es BES-2016-076761. El trabajo ha estado vinculado a los proyectos MAT2015-71826-P (Ministerio de Economía y Competitividad) y PID2019-111327GB-I00 (Agencia Estatal de Investigación y el Fondo Europeo de Desarrollo Regional). Parte de los resultados obtenidos y publicados en esta tesis han sido desarrollados gracias a las colaboraciones en el Instituto de Biocomputación y Física de Sistemas Complejos (BIFI) de Zaragoza, en el Institut de Génétique et de Biologie Moléculaire et Cellulaire (IGBMC) de Estrasburgo, en la Faculdade de Ciências da Universidade do Porto, y en el Centro de Supercomputación de Galicia (CESGA). También se han desarrollado pruebas en el laboratorio de TA Instruments/Waters en Sollentuna, Suecia, aunque los resultados y conclusiones no han sido concluyentes y, por lo tanto, no han sido publicados. El formato escrito de esta tesis está basado en la plantilla TEXIS.

USC
UNIVERSIDADE DE SANTIAGO DE COMPOSTELA

USC
UNIVERSIDADE
DE SANTIAGO
DE COMPOSTELA

About this dissertation

This dissertation corresponds to a *Monographic thesis with total reproduction of publications*. In compliance with the requirements needed for this kind of thesis, according to the Doctoral Programme in Materials Science (RD 99/2011) and the International PhD School of the University of Santiago de Compostela (EDIUS) regulation, the structure of this dissertation contains:

- Summary (Expanded in Galician, shorter in English)
- Introduction (Part I)
- Objectives (Part I)
- Methodology (Part II)
- Results (Part III)
- Conclusions (Part IV)
- Bibliography (Part IV)

Additionally, the list of publications included in this thesis is presented in the Appendix (Part V).

All the figures included in this thesis are of my authorship, with the exception of some of the figures in the publications. With respect to the latter, the rights to be used are included with the total reproduction of each publication.

USC
UNIVERSIDADE DE SANTIAGO DE COMPOSTELA

USC
UNIVERSIDADE
DE SANTIAGO
DE COMPOSTELA

Resumo

Os procesos de agregación e adsorción molecular a interfases entre medios de diferente polaridade son necesarios en innumerables fenómenos da natureza e aplicacións industriais. Dende a formación de membranas celulares ata a constitución de materiais autoensamblados, pasando pola encapsulación de partículas en produtos de limpeza, son fenómenos baseados na agregación organizada de moléculas. Existe unha clara conexión entre os procesos de agregación e adsorción, de tal maneira que son moi difíciles de separar: polo xeral, as moléculas con alta afinidade a interfases entre medios de diferente polaridade presentan tamén unha alta capacidade de se organizaren en fase líquida. Dada a importancia destes dous procesos, existe un gran número de técnicas experimentais (espectroscopia de absorción/emisión en distintas frecuencias, dispersión de luz ou partículas, propiedades eléctricas, magnéticas, químicas, ópticas ou mecánicas, medidas calorimétricas, e un amplo rango de técnicas de microscopia) e computacionais para abordalos. Non existe porén unha técnica que avalíe simultaneamente ámbolos dous fenómenos no mesmo experimento. Por outro lado, o comportamento das moléculas en ámbalas fases é con frecuencia completamente diferente. Disolucións de moitas substancias a concentracións case desprezables na fase líquida producen unha saturación na superficie.

O obxectivo desta tese consiste en proporcionar novos métodos de análise para o estudo de procesos de agregación e adsorción molecular que establezan unha diferenza cualitativa con respecto aos métodos actualmente dispoñibles. En particular, desenvolveuse unha nova técnica para a determinación da calor de procesos en interfases de fluídos. O seu desenvolvemento produciuse tanto a nivel de establecemento do procedemento experimental como da análise dos seus resultados. Esta técnica, que denominamos Calorimetría de Interfases Fluídas, amosouse que é sensible a diferentes líquidos puros e mesturas, así como á adsorción de moléculas na interfase. Ademais, no eido da calorimetría, traballouse na elaboración de modelos de unións moleculares e, en particular, de agregacións moleculares, que permiten extraer unha importante cantidade de información a partir dun simple experimento. De xeito complementario, desenvolvéronse diferentes métodos computacionais, tanto na elaboración de programas de axuste ós modelos termodinámicos antes citados como en simulacións de dinámica molecular. O obxectivo destes últimos estudos, ademais do propio interese dos sistemas analizados, consistiu en buscar os límites dos métodos experimentais desenvoltos. As metodoloxías desenvoltas e o resultados do traballo están recollidos na presente tese, a cal está organizada en catro partes diferenciadas: Introdución e obxectivos, Metodoloxía, Resultados, e Conclusións.

Na Parte I realízase a introdución ós conceptos chave sobre os que se constrúe a tese. Está composta por tres capítulos, que se sintetizan a continuación:

O Capítulo 1 contén unha achega ás interfases e á relación entre a adsorción

e a agregación molecular. Comeza por unha descrición das interfases dende o punto de vista clásico, correspondente á aproximación mecánica para dar pé, logo, á súa descrición termodinámica. Dende esta segunda aproximación, defínense as relacións termodinámicas fundamentais na descrición das interfases fluídas. Neste senso, establécese o vínculo entre a tensión superficial e maila enerxía interna, a entalpía, e os potenciais termodinámicos de Helmholtz e Gibbs, ademais de amosa-la dobre composición da tensión superficial: enerxética e entrópica. Tras esta descrición, introdúcese e descríbese o concepto de adsorción e mailo seu efecto na tensión superficial, así como os tres principais tipos de adsorbatos. Desta clasificación destácase o comportamento dos tensioactivos e das moléculas anfipáticas, aquelas que presentan na súa estrutura rexións hidrófobas e hidrófilas. É, precisamente, esta última calidade a que lles confire as súas principais características en interfase: a súa adsorción e a diminución drástica da tensión superficial do fluído. Logo afóndase na causa deste comportamento e introdúcese, a través do efecto hidrófobo, a súa relación coa autoorganización no seo do líquido e a formación de estruturas en disolución. Este capítulo remata coa numeración de diferentes métodos empregados na caracterización das interfases e dos procesos que nelas teñen lugar, destacando a ausencia de técnicas calorimétricas. Será esta a técnica experimental introducida e desenvolta nesta tese.

Unha das aplicacións dos compostos autoorganizados é a encapsulación doutras moléculas no seu interior. O exemplo máis claro é a incorporación de fármacos pouco solubles en auga a micelas. No interior destes agregados o ambiente é hidrófobo e pode incorporar compostos apolares. No Capítulo 2 preséntase un tipo de molécula con forma de cono truncado e baleirado no interior: as ciclodextrinas. O interior deste cono é hidrófobo e no seu exterior ten rexións hidrófilas que lle permiten ser soluble en auga. Debido a estas propiedades, as ciclodextrinas poden incorporar, tamén, pequenas moléculas no seu interior e servir, do mesmo xeito que as micelas, de encapsuladores de fármacos insolubles. Ó longo deste capítulo preséntanse as súas propiedades individuais e formando agregados e complexos moleculares, tanto no seo da disolución como na interfase. É nesta aproximación onde as ciclodextrinas, e sobre todo os seus complexos, se comportan tamén como moléculas anfipáticas, creando estruturas supramoleculares en disolución e na superficie de separación entre dous fluídos con diferente polaridade. Para rematar, realízase un breve repaso sobre as principais aplicacións destas moléculas e, a través do Artigo I, sobre o caso particular da súa aplicación en terapias antivirais. O capítulo volve pecharse enumerando as principais técnicas de caracterización das ciclodextrinas e os seus complexos moleculares.

A través dos dous capítulos previos faise unha introdución ós procesos de agregación e adsorción molecular, así como ás técnicas experimentais que permiten a súa caracterización. No capítulo 3 afóndase nun destes métodos en particular: a Calorimetría de Titulación Isoterma, ITC polas súas siglas en inglés. Este apartado comeza por unha introdución máis xeral da calorimetría e da súa relación con outras técnicas térmicas e calorimétricas, tralo cal se pasa á descrición do aparello de ITC. Hoxe en día existen dous fabricantes principais de calorímetros de ITC, mais o seu funcionamento está baseado nos mesmos principios. Ámbolos dous calorímetros están compostos por dúas celas que conteñen o mesmo líquido e que se atopan pechadas nunha cuberta adiabática que as illa termicamente do exterior. Esta cuberta permite, ademais, manter unha temperatura controlada do experimento. As dúas celas están en contacto entre si mediante un dispositivo Peltier que detecta

USC UNIVERSIDADE DE SANTIAGO DE COMPOSTELA

cambios de temperatura entre as celas. Sobre a cela de medida realízase a titulación dun fluído sobre o xa incorporado, o cal pode producir un efecto térmico detectado polo dispositivo Peltier. Este efecto é compensado pola electrónica do calorímetro e a potencia necesaria para mante-lo equilibrio térmico entre as dúas celas é rexistrada. A partir desta potencia determínase a calor vinculada a cada inxección da titulación. Tras unha explicación con maior detalle sobre o funcionamento do calorímetro de Microcal-Malvern, realízase unha achega ó programa de control do equipo ademais das magnitudes que se poden obter en cada experimento e o formato de ficheiro no que se atopan. Para rematar, lévase a cabo unha pequena revisión sobre as aplicacións do ITC, entre as que se destacan os procesos de unión molecular en ciclodextrinas e os procesos de autoorganización de tensioactivos. Con todo, extraemos unha conclusión, e é que son precisamente estes dous últimos sistemas os que tamén presentan un comportamento en interfase co seu conseguinte proceso térmico que, cos medios actuais, non se pode detectar.

Trala presentación do vínculo entre os procesos de adsorción e agregación, xa foi observado que non hai un único procedemento experimental que permita obter información de ámbolos dous á vez. Ademais, non só non hai unha técnica que permita o estudo dos dous procesos, senón que tampouco existe unha forma de caracteriza-los fenómenos caloríficos que acontecen na interfase de dous fluídos. Debido á alta sensibilidade da calorimetría de titulación isotérmica, xa probada para a caracterización da agregación en disolución, proponse como obxectivo principal deste traballo unha modificación sobre a mesma que permita medi-la calor asociada a fenómenos interfaciais, tales como a adsorción ou a mesma creación da interfase. Tamén se busca, como obxectivos secundarios, outras técnicas experimentais e computacionais que permitan desenvolver, entender e complementa-lo método que se propón, así como a de achegar máis información sobre os procesos de adsorción e agregación en xeral.

Neste punto chegamos á Parte II, onde se presenta a metodoloxía empregada nesta tese. Como xa se comentou, o obxectivo principal é o desenvolvemento dunha nova técnica experimental, que se presenta aquí. Esta técnica, a Calorimetría de Interfases Fluídas, emprega un calorímetro de ITC sen ningunha modificación e, en vez de titular un fluído sobre a cela de medida, inxéctase aire ou un líquido inmiscible. Esta inxección realízase de forma continua a unha velocidade baixa (inferior ós 0.22 $\mu L/s$) o que permite que, no caso da inxección de aire, se formen e se destrúan burbullas de forma ininterrompida. Isto implica a creación e destrución dunha interfase fluída (aire/auga) no interior da cela de medida, o que permite que toda a calor producida ou consumida neste proceso sexa medida. Ademais, non se crea unha única interfase, senón que por cada experimento se crean varias ducias de burbullas, cun sinal periódico, reproducible e rico en información. Esta metodoloxía foi probada en diferentes calorímetros, a diferentes velocidades de inxección de aire, con varios líquidos puros e tamén disolucións acuosas, así como a varias temperaturas ou potencias de referencia. O que se observou non é só as particularidades antes destacadas, senón que tamén se puido comproba-la sensibilidade da técnica ós diferentes líquidos probados, pois producen sinais de inxección moi diferentes. Porén, a pesar de seren diferentes, a traza de calor que deixa a formación de burbullas garda a mesma información: cambio de capacidade calorífica na cela pola inxección de aire, formación, crecemento e liberación da burbulla, evaporación/condensación do vapor, e outros aportes que aínda estamos estudando. A partir do establecemento desta técnica, obtivéronse xa resultados de medida da tensión

superficial por medio da calor de formación de burbulla e resultados preliminares da adsorción de proteínas así como da interfase líquido/líquido.

Como técnicas complementarias, preséntanse a Simulación de Dinámica Molecular (MD polas súas siglas en inglés), as medidas de tensión superficial por volume de gota e a determinación da velocidade do son e da densidade de líquidos. A MD consiste nunha técnica de simulación de resolución atomística onde se resolven as ecuacións de movemento das partículas do sistema que se estude. Estas simulacións permiten obter información tanto cinética como termodinámica das moléculas obxectivo, así como das moléculas que compoñen o seu entorno ou solvente. O principal limitador destas simulacións é o tempo de cómputo e mailo tamaño do sistema. En relación ás técnicas experimentais, explícase a determinación da tensión superficial por volume de gota, empregada para determina-la validez dos datos obtidos por medio da Calorimetría de Interfases Fluídas. Esta técnica consiste na determinación do volume máximo que unha pinga pendurada dun capilar pode chegar a ter antes de caer. Basease, polo tanto, no balance de forzas entre o peso da pinga e maila forza debido á tensión superficial que a mantén suxeita ó capilar. A última técnica descrita é a da determinación da velocidade do son e da densidade de líquidos, que se realiza co mesmo aparello de xeito automático, co cal é posible, cunha soa mostra, levar a cabo de medidas a diferentes temperaturas, o que permite unha caracterización termodinámica das propiedades no seo dos fluídos.

A Parte III contén os resultados desta tese. Está dividida pola técnica de estudo empregada, e amósanse tanto resultados para as propiedades interfaciais como para a caracterización no interior dos fluídos.

Os primeiros resultados, tanto preliminares como asentados, da Calorimetría de Interfases Fluídas amósanse no Capítulo 7. As achegas xa comprobadas son as da tensión superficial. Por medio da periodicidade do sinal de calor producido polas burbullas e a calibración dos instrumentos empregados, determináronse as isotermas de tensión superficial de disolucións de etanol en auga e de mesturas acuosas de tensioactivos, tanto iónicos como non iónicos. Esta caracterización realizouse empregando tres calorímetros distintos do mesmo modelo, traballando a diferentes velocidades de inxección e de temperatura. Para a obtención dos datos de tensión superficial, desenvolveuse un algoritmo de obtención do período de formación de burbullas, válido incluso para sinais moi ruidosos ou cunha liña base inestable. Este algoritmo non só determina o valor do período, senón que tamén realiza unha estimación da incerteza asociada á medida. Os resultados obtidos foron comparados con medidas realizadas co tensiómetro de volume de gota e con resultados xa publicados previamente tanto por nós como por outros grupos de investigación. A concordancia resulta excelente, o que abre as portas para a súa aplicación a pesar de non ter introducido ningunha modificación do equipo.

Os resultados preliminares da Calorimetría de Interfases Fluídas van, precisamente, no camiño da mellora e da adaptación do calorímetro comercial á creación de burbullas e gotas. O paso máis importante que se precisa é o do control da formación das interfases, algo que resulta moi complicado co inxector existente. É por iso polo que se probaron diferentes inxectores externos, cos cales reducir máis o fluxo de fluído cara o interior da cela ou cos que sermos capaces de dete-la inxección na mentres se está creando a burbulla ou, incluso, recolle-lo aire e reduci-lo tamaño da superficie xa creada. As primeiras achegas neste sentido son xa prometedoras, pois conseguiuse reproduci-los resultados xa conseguidos ata o de agora, pero cun inxector externo que permite reducir aínda máis a velocidade de inxección. De forma

USC UNIVERSIDADE DE SANTIAGO DE COMPOSTELA

paralela ó traballo no control da formación de burbullas, continuáronse probando novos sistemas. Os resultados que se amosan son os correspondentes á adsorción de proteínas que, polo de agora, son só preliminares. Non obstante, abondan para comprobar que o calorímetro si é sensible á súa adsorción. Ademais, debido ás dificultades que implica traballar con burbullas, xa que son moi sensibles ós cambios de presións, comezáronse a realizar experimentos de inxección dun líquido inmiscible noutro (ciclohexano en auga). Estes experimentos, porén, non reportan o mesmo tipo de sinal que os de burbullas. O que acontece é que as gotas que se forman na inxección de auga en ciclohexano son tan grandes que tocan a parede da cela e forman un fluxo continuo, como unha billa. O resultado é un cambio na liña base debido ó cambio de capacidade calorífica da cela. Non obstante, non é un resultado negativo, pois conséguese, trala inxección de todo o líquido, a formación dunha interfase no fondo da cela. Isto aproveitouse para o estudo da adsorción de proteínas á superficie de separación auga/ciclohexano, cuxos resultados se amosan. Esta sección remata coa parte máis teórica da análise dos resultados da Calorimetría de Interfases Fluídas, que aínda está en desenvolvemento.

O capítulo 8 recolle dous traballos enfocados á caracterización, mediante ITC, de procesos de recoñecemento e unión molecular. O primeiro deles é a publicación das ecuacións e dos algoritmos de axuste que compoñen AFFINImeter, un programa deseñado para a análise de datos de ITC. O artigo contén, con respecto ó algoritmo de análise: a descrición do tratamento dos datos brutos obtidos do calorímetro; como se crean os modelos, deseñados para que o usuario os poida modificar con facilidade, que serán logo axustados ós datos experimentais; a corrección da concentración, xa que a titulación dun líquido noutro produce un desprazamento do volume na cela, o cal precisa ser modelado para obter resultados precisos; o algoritmo de axuste, que inclúe o procedemento de minimización, selección das sementes, e determinación das incertezas. Ademais, preséntanse o modelo de axuste de cinética en datos de calorimetría, un exemplo práctico de uso do programa, unha lista de boas prácticas para a análise de interaccións moleculares, e mais un exemplo de como empregar AFFINImeter para a simulación de resultados de calorimetría, o que resulta de utilidade para o deseño previo dun experimento.

O segundo artigo incluído no apartado de resultados de calorimetría corresponde a un modelo para a análise da agregación de tensioactivos a partir de medidas en ITC. O modelo permite determinar, entre outras magnitudes, o número de agregación micelar, a entalpía e maila enerxía libre de micelización. No artigo descríbese o modelo termodinámico e mailo procedemento de axuste e estimación de incertezas. Tamén se incorporan resultados experimentais para catro compostos a varias temperaturas, sobre os que o modelo é aplicado e comparado con resultados de fluorescencia e cos atopados na literatura.

O seguinte bloque de resultados corresponde ó desenvolvemento de programas de axuste para o estudo da agregación e da adsorción de tensioactivos por outras técnicas distintas á calorimetría. O primeiro dos aportes presentado é o rexistro e a descrición de STAND. STAND é un programa desenvolto para a análise de datos de tensión superficial de tensioactivos en disolucións acuosas e que permite obter, a partir do axuste ó modelo termodinámico do mesmo nome, os valores de: número de agregación, enerxía libre de micelización, constante de adsorción, concentración superficial de exceso, porcentaxe de superficie cuberta, e evolución das especies libre e micelada en función da concentración total de tensioactivo. O segundo dos traballos presentados neste bloque corresponde ó estudo da termodinámica de mi-

celización dun tensioactivo non iónico: o *decyl-β-D-glucopyranoside*. Para tal fin, empregáronse medidas de tensión superficial, densidade e velocidade do son. A miña aportación máis importante neste traballo é o desenvolvemento dos programas de axuste.

O último apartado de resultados corresponde ós obtidos por Simulación de Dinámica Molecular. Como se destaca ó comezo do capítulo, este contén un único artigo, mais ó longo desta tese realizáronse diferentes traballos que non están incluídos ou que se atopan aínda sen publicar. Os resultados aquí presentados corresponden ó estudo do complexo formado por dúas ciclodextrinas (α-CD) e un tensioactivo iónico, o SDS (Dodecil Sulfato de Sodio). Estudouse o comportamento do mesmo tanto en disolución como en interfase a través do uso de diferentes campos de forzas, incluídos dous campos de forzas modificados para acelera-la simulación. Os resultados entre os campos de forzas modificados e sen modificar son moi semellantes entre eles, o que de por si pode resultar de tremenda utilidade para a simulación de sistemas que precisen dun maior tempo de simulación. Porén, o resultado máis sorprendente deste traballo reside na observación das estruturas de moléculas de auga arredor do complexo. Obsérvanse unhas formas xeométricas de maior e menor densidade de auga que se manteñen incluso cando o complexo se atopa na interfase. Ademais desta estruturación destaca a organización do momento dipolar das moléculas do solvente, o que suxire a aparición dunha rotación do complexo cando este se move á interfase.

Como conclusión final, cumpriuse o obxectivo principal desta tese, que era o desenvolvemento dunha nova metodoloxía experimental que permitise medi-la calor de procesos en interfases fluídas. De forma paralela, traballouse no desenvolvemento de novos métodos de análise de resultados de agregación e adsorción a partir de medidas de calorimetría, de tensión superficial ou de velocidade do son e densidade. Finalmente, tamén se desenvolveron novas metodoloxías para o estudo destes procesos a través de Simulacións de Dinámica Molecular.

USC UNIVERSIDADE DE SANTIAGO DE COMPOSTELA

Summary

Spontaneous molecular aggregation and adsorption to interfaces between media of different polarity are ubiquitous phenomena in natural and artificially designed systems. The formation of cell membranes, the encapsulation of particles by cleaning products, and the manufacturing of functional coatings, amongst many other processes, are a consequence of these intimately connected molecular self-organization mechanisms. The existence of an interface requires the presence of a bulk subphase, and molecules with high affinity for interfaces typically exhibit a clear ability to aggregate in the liquid phase. Given the importance of both processes, there is a large number of experimental, computational and hybrid techniques to address them: absorption/emission spectroscopies, particle or light scattering, electrical, chemical, optical or mechanical properties, calorimetric measurements, a wide range of microscopy techniques, molecular dynamics and fluid dynamics simulations. Nevertheless, no experimental method is available to simultaneously assess bulk aggregation and adsorption. On the other hand, the behaviour of molecules in both phases is often completely different. For many substances, solutions at almost negligible concentrations in the liquid phase may lead to saturation at the interface.

The aim of this thesis is to provide new methods to characterize molecular aggregation and adsorption processes that establish a qualitative difference with respect to those currently available. In particular, a new technique has been developed to directly determine the heat associated to the adsorption of molecules at fluid interfaces by using commercially available isothermal titration calorimeters. Both the experimental procedure and the required computational analytical tools were developed. The new methodology, which we called Fluid Interface Calorimetry, has been shown to be sensitive to the composition of the liquid sample, as well as to the adsorption of macromolecules at fluid interfaces. Complementarily, original contributions to the analysis of molecular recognition and molecular aggregation phenomena by calorimetry experiments in the liquid phase have been developed and validated. Out of calorimetry, surfactant aggregation and adsorption studies by surface tension, sound velocity and density have been carried out. In all cases, original analytical models were proposed and implemented in automated computational codes. Finally, molecular dynamics simulations of macromolecular systems at interfaces were performed, testing the hydrogen isotope exchange method to speed up the sampling without loss of resolution. The structure of water molecules around the solute molecules was analysed in detail, finding exotic patterns that depend on the local behaviour of the different molecular groups.

Overall, this work aims to contribute to the understanding of spontaneous molecular aggregation and adsorption phenomena by providing new experimental, computational and analytical tools. Hopefully, some of these methods will be useful to understand complex systems and behaviours present in natural systems as well as to design functional materials for new applications.

USC
UNIVERSIDADE
DE SANTIAGO
DE COMPOSTELA

Contents

Agradecementos xi

About this dissertation xv

Resumo xvii

Summary xxiii

0. The not-so-scientific motivation 1

I Introduction and objectives 3

1. Interfaces, a place between two worlds 5
- 1.1. The first approach to fluid interfaces . . . 6
- 1.2. An introduction to fluid interface thermodynamics . . . 9
- 1.3. Adsorption to fluid interfaces . . . 15
- 1.4. Amphiphiles and self-assembly . . . 20
- 1.5. Interfacial characterization of amphiphiles . . . 23

2. Cyclodextrins: the sweet molecular carrier 25
- 2.1. Just cyclodextrins . . . 27
- 2.2. Self-assembly of cyclodextrins and interfacial behaviour . . . 29
- 2.3. Cyclodextrin applications . . . 30
- 2.4. Paper I . . . 33
- 2.5. Cyclodextrin and cyclodextrin complexes characterization . . . 51

3. The warm-up for new analysis and techniques by Isothermal Titration Calorimetry 53
- 3.1. Isothermal Titration Calorimetry: the ITC . . . 54
- 3.2. An ITC experiment . . . 57
- 3.3. The analysis of ITC data . . . 60
- 3.4. ITC applications . . . 65

4. Objetives 67

II Methods 69

5. ITC and interfaces 71

5.1. Paper II . . . 73
5.2. Patent registration . . . 93

6. Molecular Dynamics Simulations and other complementary techniques 97
6.1. Molecular Dynamics simulations in a nutshell . . . 98
6.2. Surface tension, sound velocity and density . . . 100
6.3. Computational tools . . . 103

III Results 105

7. Fluid Interface Calorimetry Results 107
7.1. Better bubble control . . . 107
7.2. Biomolecules adsorption . . . 108
7.3. Liquid-liquid experiments . . . 109
7.4. ITC theory . . . 111
7.5. Paper III . . . 115

8. New models in bulk ITC 127
8.1. Paper IV . . . 129
8.2. Paper V . . . 149

9. Surfactant aggregation studies 163
9.1. Software registration . . . 165
9.2. Paper VI . . . 173

10. MD simulations 189
10.1. Paper VII . . . 191

IV Conclusions and bibliography 219

11. Conclusions and future work 221
11.1. Fluid Interface Calorimetry . . . 221
11.2. Software development, modelling and analysis tools . . . 222

12. Bibliography 225

V Appendix 255

A. List of publications and scientific contributions 257
A.1. Publications included in this dissertation . . . 257
A.2. Publications not included in this dissertation . . . 261
A.3. Conferences . . . 261

B. Complementary information of Papers III and V 263

USC UNIVERSIDADE DE SANTIAGO DE COMPOSTELA

List of figures

1.1. Four quotidian interfacial phenomena . . . 6
1.2. A simple diagram of the liquid-vapour system . . . 7
1.3. Representation of the Lennard-Jones potential as a function of the distance between two spheres. . . . 9
1.4. Simple drawing representing the rectangular area that is increased in Equations 1.35 and 1.36. . . . 14
1.5. Figure illustrating the difference between absorption and adsorption. 15
1.6. Classification of the three types of adsorbates. . . . 16
1.7. Change of the Gibbs dividing plan position effect on the surface density of compoment 1. . . . 18
1.8. Representation of a surfactant. . . . 21
1.9. Water molecules liberation and micellization. . . . 22

2.1. Evolution of CDs publications since 1970 . . . 27
2.2. α-*D*-glucopyranose representations . . . 28
2.3. Representation of the three native CDs. . . . 29

3.1. ITC diagram . . . 56
3.2. Evolution of jacket and shield temperatures . . . 57
3.3. Effect on the supplied power P after the introduction of the syringe tip in the cell. . . . 58
3.4. Effect on the supplied power P after the stirring initialization. . . . 58
3.5. Effect on the supplied power P after a titration. . . . 59
3.6. Effect on the supplied power P after a full experiment. . . . 60
3.7. Different screenshots of the VP-ITC controller software. . . . 61
3.8. Correspondence between the ITC diagram and the software values. . 62
3.9. ITC *.itc* and *.dat* files structure . . . 63
3.10. Power-time and heat-concentration representation. . . . 64

5.1. Classification of the developed ITC interfacial experiments according to the sample. . . . 72

6.1. A picture representing the periodic boundary conditions in 2D. . . . 100
6.2. Diagram showing the formation of a pendant drop and force balance before the detaching. . . . 101
6.3. DSA cells schematic representation . . . 102

USC UNIVERSIDADE DE SANTIAGO DE COMPOSTELA

7.1. Bubbles emerging from the TAM cannula and 3D design of an improved tip. 108
7.2. The water/BSA solution/Cyclohexane experiment diagram 110
7.3. First results of BSA adsorption at liquid-liquid interface. 111
7.4. Preliminary results of the curve fitting of air-into-water bubble's heat signal. 112
7.5. PID simulation for ITC 113

9.1. Screenshot of the old web version of STAND. 170

USC UNIVERSIDADE DE SANTIAGO DE COMPOSTELA

List of acronyms and abbreviations

AFM ..... Atomic Force Microscopy
BSA ..... Bovine Serum Albumin
CD ..... Cyclodextrin
COVID-19 ..... COronaVirus DIsease 2019
Cryo-TEM ..... Cryogenic Transmission Electron Microscopy
DLS ..... Dynamic Light Scattering
DP ..... Differential Power (referred to ITC)
DSC ..... Differential Scanning Calorimeter
DTA ..... Differential Thermal Analysis
FF ..... Force Field
FFT ..... Fast Fourier Transform
HIE ..... Hydrogen Isotope Exchage
HP-β-CD ..... Hydroxypropyl-β-CD
ITC ..... Isothermal Titration Calorimetry
Lys ..... Lysozyme
MD ..... Molecular Dynamics
Me-β-CD ..... Methyl-β-CD
P ..... Power (referred to ITC)
PBC ..... Periodic Boundary Condition
PID ..... Proportional-Integral-Derivative
PME ..... Particle Mess Ewald
QM ..... Quantum Mechanics
RP ..... Reference Power (referred to ITC)
SARS-CoV-2 ..... Severe Acute Respiratory Syndrome COronaVirus 2
SBE-β-CD ..... Sulphobutylether-β-CD
SDS ..... Sodium Dodecyl Sulfate
SEM ..... Scanning Electron Microscopy
TAA ..... ThermoAcoustics Analysis
TEM ..... Transmission Electron Microscopy
TGA ..... ThermoGravimetric Analysis
TMA ..... ThermoMechanical Analysis
TOA ..... ThermoOptical Analysis
WM ..... Water Model

USC
UNIVERSIDADE DE SANTIAGO DE COMPOSTELA

USC
UNIVERSIDADE
DE SANTIAGO
DE COMPOSTELA

Chapter 0

The not-so-scientific motivation

Las utopías realizables merecen la pena

José Luis Rodríguez Zapatero, Spanish Prime Minister

This PhD project did not start the day I paid my first PhD enrolment fee. During the summer of 2014, before starting my Master degree, I had gotten some experience working in a wet-lab by measuring surface tension values of surfactant solutions. At that time I joined the AFFINImeter team to work on calorimetry. My aim was to learn how to develop isothermal titration calorimetry (ITC) experiments and I also had the opportunity to contribute to the development of the software by testing it with systems exhibiting non-trivial interaction mechanisms. Here is where I met cyclodexrins, as well as several technical and scientific challenges related to the connection between molecular adsorption and aggregation.

Cyclodextrins are ideal structures to test complex interactions due to their ability to self-assemble as well as to encapsulate hydrophobic or amphiphilic compounds. It has been observed that the combination of cyclodextrins and surfactants in aqueous solution leads to interesting structures ranging from simple supramolecular complexes to more exotic mesoscopic arrangements. The binding process and the transition to organized structures are expected to exhibit a heat exchange that could be measured by ITC. However, typical calorimetric experiments are performed inside the sample cell and so, all the heat that can be detected by the instrument corresponds to interactions that take place in the bulk solution. Cyclodextrin-surfactant solutions also form bidimensional films with interesting mechanical properties at interfaces that have not widely characterized. And here is where Ángel Piñeiro, who would be later my PhD supervisor, asked *the question*: Is it possible to directly measure the heat associated to molecular interaction processes that take place at fluid interfaces? or, going further: Is it possible to directly measure the heat associated to the creation/destruction of an interface, the surface tension-related heat? These questions remained in my head for years and this is why, when I completed my Master, I decided to address them during my PhD. The answers that I found, including the implementation of new methodologies required to reach them, are the core of this thesis.

Scientific methods are typically classified in three compartments: computatio-

nal, theoretical, and experimental. However, the borders between them are flexible and permeable. It is rare nowadays that any kind of research can be developed in just one single mode without the support of another or even the other two methodological branches. The need to work with different types of complementary methodologies can be extrapolated to the combination of multiple disciplines. The synergy resulting from multitechnique/multidisciplinary research facilitates the application of new discoveries and developments to different fields. It means that a step forward in the knowledge of a topic needs a walk around. It needs the understanding of further processes to realize what is still unknown and what part of the already-known can help to advance. The work presented in this thesis aims to be an example of that: it approaches the research on interfaces from the experimental, theoretical, and computational points of view at the same time.

Interfaces, cyclodextrins, calorimetry, molecular self-assembling, adsorption ... This thesis spins around all these terms. The way they are related is what gives sense to this project. Now it is time to introduce them.

USC UNIVERSIDADE DE SANTIAGO DE COMPOSTELA

Part I

Introduction and objectives

The main characters of this work: The link between interfaces and aggregation, cyclodextrins, and ITCs will be introduced in this part. Paper I is here included.

USC
UNIVERSIDADE
DE SANTIAGO
DE COMPOSTELA

USC
UNIVERSIDADE
DE SANTIAGO
DE COMPOSTELA

Chapter 1

Interfaces, a place between two worlds

Sometimes the most direct path between two points is actually a two-dimensional line!

In "The Legend of Zelda: A Link Between Worlds"

An interface is the transition region defining the shape of a solid object or the boundary between two fluids. Because of its different behaviour with respect to a bulk phase, a new branch of research emerged since the previous works of Agnes Pockels, Irving Langmuir or Katherine Blodgett (and many other researchers) at the beginning of the XX century: surface or interface science. Surface or interface are used indistinctively, though surface is more commonly used as referred to the geometrical meaning. Surface science comprises the study of solid-gas or solid-liquid interface, but also the so-called fluid interfaces: liquid-liquid or liquid-gas (Adamson and Gast, 1997). For the purpose of this work, we are going to focus on the latter.

Fluid interfaces are ubiquitous. These very thin regions prevent matter from diffusing freely between two phases. They are invisible to the human eye but are the responsible of a large series of phenomena such as the formation of liquid drops and their shape, the aggregation of material and objects at the surface of liquids, the ring-like shape of some liquids' stains, or the ability of some insects to walk over the surface of water. These phenomena (Figure 1.1) represent just four different and quotidian examples of interfacial effects (Hu and Bush, 2005; Lautrup, 2011; Mampallil and Eral, 2018; Vella and Mahadevan, 2005).

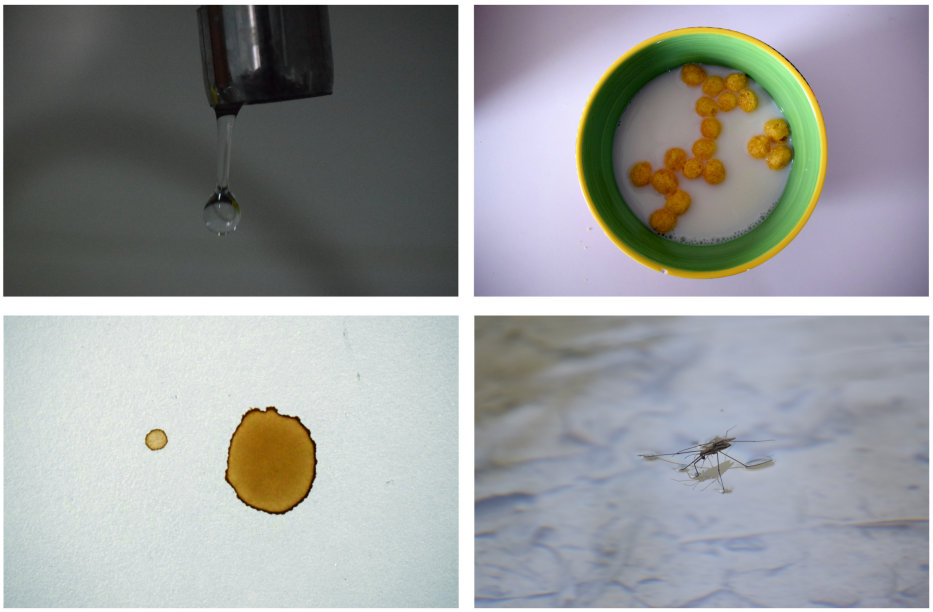


Figure 1.1: Four quotidian interfacial phenomena: a drop hanging from a tap, a bowl of cereals with aggregation on the surface of milk, a coffee stain with its characteristic ring-like pattern, and a water strider walking on fresh water.

1.1. The first approach to fluid interfaces

From the thermodynamic point of view, *interface* is the surface that divides each of the phases in a heterogeneous system (Hiemenz and Rajagopalan, 2016; Keszei, 2012). In a real system, the interface is not strictly bidimensional due to its thickness, which may not be negligible. Thus, it is more correct to talk about an *interfacial region* or, if the interface itself can be considered as a separated phase, the *interphase* (McNaught and Wilkinson, 1997). In any of these scenarios, the interface can be studied as an independent subsystem where the physical or chemical properties suffer a dramatic change when compared to the contiguous bulk phases. In this region, a force that tends to minimize the interfacial area appears. The surface tension, γ, is a magnitude directly connected to this force, arising from the existence of an interface. The explanation, following the discussion of Sychev (Sychev, 1973), can be first approached by considering a fluid in equilibrium with its vapour. A liquid molecule placed deep in the bulk (molecule I), a molecule placed in a shallow region (molecule II) and a molecule at the interface (molecule III) will illustrate the problem (Figure 1.2).

USC UNIVERSIDADE DE SANTIAGO DE COMPOSTELA

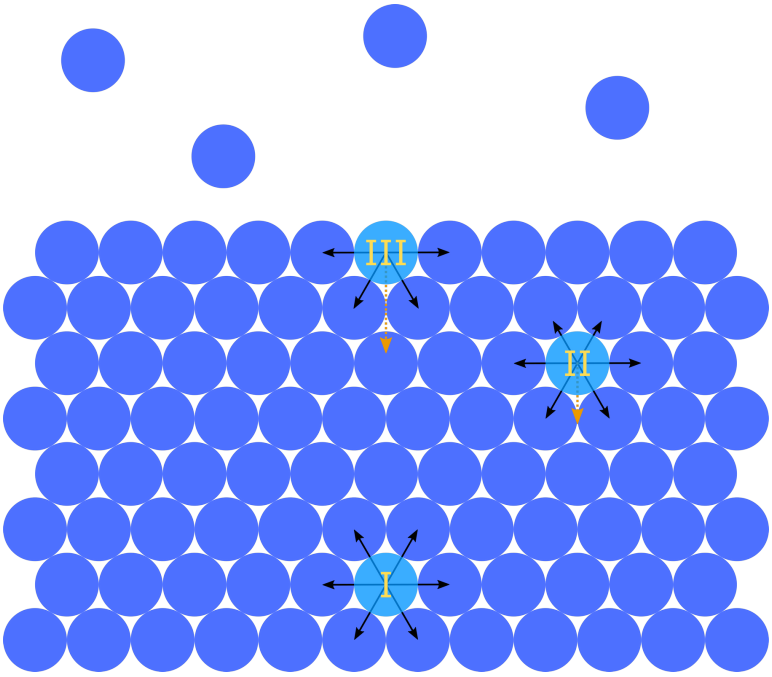


Figure 1.2: A simple diagram of the liquid-vapour system. Each circle represents a molecule/atom/ion of the liquid that may be evaporated. Three particles are highlighted to facilitate the explanation provided in the main text. Different black arrows arising from the centre of each particle represent the forces actuating on it. When the resultant force is not null, an orange dashed arrow represents the resultant.

Molecule I is surrounded by a large number of identical particles, all of them pulling with the same force (all they are of the same type). The closest the particle to molecule I, the higher the force. As molecule I is in the bulk, its environment is the same in all directions and the resulting force is null. Molecule II represents another case. Its nearest neighbours are all the same particles, but it is close to the surface. The number of molecules above is lower than the number of molecules below and so, a net force acts on molecule II. The clearest example of this lack of symmetry is molecule III, which is at the interface. At that point, the particles above molecule III are part of the vapour. These are the same kind of molecule as those in the bulk, so the attraction between them and molecule III is the equivalent. However, the density of the vapour phase is much lower than that of the liquid (except for the critical point). This means that the force towards or from molecule III is not as strong as the force between the molecules forming part of the liquid. Again, a net force, stronger than that acting on molecule II, acts on molecule III. This qualitative explanation is useful for all the molecules at the interface, including not just the first molecular layer but all the molecules experiencing a non negligible net force. This net force due to the anisotropy of the interface is perpendicular to the surface and points towards the liquid bulk. It is worth to comment that this discussion is only valid for average forces since instantaneous forces can eventually be significantly different from the average value at a given region. From this approach, the forces

acting on the interfacial molecules will cause an excess energy at the surface with respect to the molecules in bulk, the *surface energy*. Since the surface has an excess energy, the system will tend to minimize it by reducing the surface area. This implies that if a molecule is displaced from the bulk to the interface, a certain amount of work is needed. The increasing in the surface area is proportional to the number of molecules placed there and, since the number of molecules moved to an interface is, except for specific systems, much lower than respect to the bulk, the work per moved molecule is constant. The relation between the work associated to the increase of area (ΔW) and the area variation (ΔA) is a constant value characteristic of each fluid interface: the *surface tension* (Lautrup, 2011).

$$\Delta W = \gamma \Delta A \tag{1.1}$$

The previous explanation is, as it was already mentioned, a first approach. It is not accurate from the mechanical perspective (Pellicer *et al.*, 1995), but it is useful to understand the physics behind interfaces. The problem in the previous explanation is that the existence of these forces from the surface towards the liquid indicates that the system is not under equilibrium. To complete and to clarify the exposition, also repulsive forces must be considered. The Lennard-Jones (LJ) potential can be a useful intermolecular potential to illustrate the interactions between two molecules (Figure 1.3): there is a minimum of the potential at a certain distance between the molecules but, at closer positions a repulsion appears. The repulsive part corresponds to the interaction of the electronic clouds of the molecules, while the attractive is due to the van der Waals interaction (Marchand *et al.*, 2011). In more complex fluids, the LJ potential may not be enough to explain the liquid behaviour, and coulombian forces for electrolyte solutions (Markovich *et al.*, 2014) or hydrogen bond (H-bond) interactions should be also included. In any case, what arises from this approach is that, when molecules become closer, a repulsion appears in counterpart to the unbalanced attraction from the surface. A good explanation from the microscopic and mechanical point of view can be read in the works of Berry (Berry, 1971) and, more updated and based on the previous, Durand (Durand, 2020), where the problem is embraced by the pressure analysis.

The mechanical analysis is commonly used to introduce a more thermodynamical explanation and they are usually found together, despite the microscopic interactions are just looked over (Kronberg *et al.*, 2014; Lyklema, 2000; Probstein, 1994). Some recent works that combine both views can be found in the works of Snoeijer, Andreotti and co-workers (Marchand *et al.*, 2011; Snoeijer and Andreotti, 2008; Weijs *et al.*, 2014). The conclusion, from all the explanations, goes to the same point: the surface tension comes from the adhesion forces of liquid molecules that became unbalanced at the interface. This situation derives in the appearance of an excess surface energy with respect to the bulk. From a more macroscopic and energetic perspective, the thermodynamics of surface tension will be now introduced (Keszei, 2012; Lyklema, 2000; Möbius and Miller, 1998a).

USC UNIVERSIDADE DE SANTIAGO DE COMPOSTELA

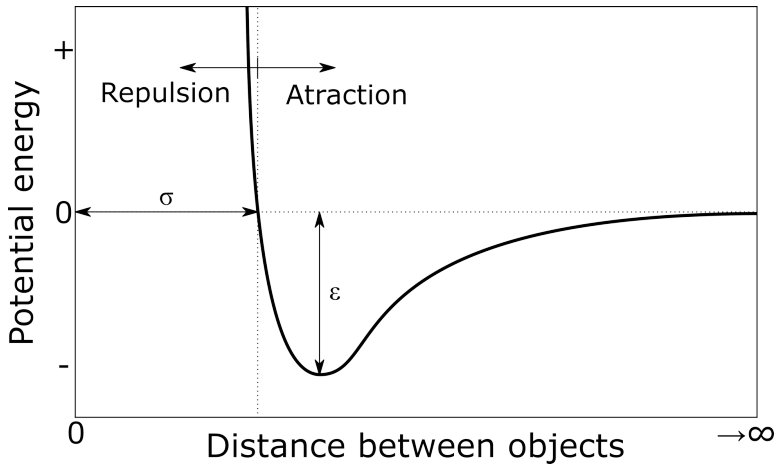


Figure 1.3: Representation of the Lennard-Jones potential as a function of the distance between two spheres. The parameters σ and ϵ are the two magnitudes needed for the definition of the potential, namely the distance between at which the potential is 0 (states the regions of attraction and repulsion) and the minimum value of the potential.

1.2. An introduction to fluid interface thermodynamics

It has just been said that the existence of the interface produces an energy excess in the studied system. Let the system be multicomponent with k different species. The internal energy U can be expressed as a function of the extensive magnitudes entropy, S; volume, V; number of moles of each species, $n_i, i = 1 \dots k$; and now, the area, A:

$$U = U(S, V, A, n_1, \dots, n_k) = U(S, V, A, \mathbf{n}) \tag{1.2}$$

And the differential fundamental equation results:

$$\begin{aligned} dU = &\left(\frac{\partial U}{\partial S}\right)_{V,A,\mathbf{n}} dS + \left(\frac{\partial U}{\partial V}\right)_{S,A,\mathbf{n}} dV \\ &+ \left(\frac{\partial U}{\partial A}\right)_{S,V,\mathbf{n}} dA + \sum_{i=1}^{k} \left(\frac{\partial U}{\partial n_i}\right)_{S,V,A,n_{j\neq i}} dn_i \end{aligned} \tag{1.3}$$

The partial derivatives of the internal energy, except for the derivative with respect to the area, are the intensive magnitudes temperature, T; pressure, p; and the chemical potentials related to each presented species, μ_i:

$$\left(\frac{\partial U}{\partial S}\right)_{V,A,\mathbf{n}} = T \tag{1.4}$$

USC DE SANTIAGO DE COMPOSTELA

$$\left(\frac{\partial U}{\partial V}\right)_{S,A,\mathbf{n}} = -p \tag{1.5}$$

$$\left(\frac{\partial U}{\partial n_i}\right)_{S,V,A,n_{j\neq i}} = \mu_i \tag{1.6}$$

Finally, the partial derivative of the internal energy with respect to the area is the surface tension. This is its thermodynamical definition.

$$\left(\frac{\partial U}{\partial A}\right)_{S,V,\mathbf{n}} = \gamma \tag{1.7}$$

And so, Equation 1.3 becomes:

$$dU = TdS - pdV + \gamma dA + \sum_{i=1}^{k} \mu_i dn_i \tag{1.8}$$

Following the same explanation, the surface tension can be included in the other thermodynamic potential energies: the enthalpy, H; the Helmholtz free energy, F; and the Gibbs free energy, G. The Legendre transformations applied to the internal energy look for a change in one or more of the independent variables of the function by their corresponding conjugate variable: S by T (Helmholtz), V by p (enthalpy) or both (Gibbs). These changes do not affect the surface tension-area relationship, and these potentials are still area dependent. The demonstration is shown for the enthalpy and extended to the other potentials:

$$H = U + pV \tag{1.9}$$

$$\begin{aligned} dH = d\left(U + pV\right) &= dU + Vdp + pdV \\ &= TdS + Vdp + \gamma dA + \sum_{i=1}^{k} \mu_i dn_i \end{aligned} \tag{1.10}$$

$$H = H(S, p, A, \mathbf{n}) \tag{1.11}$$

Using the same mathematical elaboration, the Helmholtz free energy in terms of the surface results:

$$F = F(T, V, A, \mathbf{n}) \tag{1.12}$$

$$dF = -SdT - pdV + \gamma dA + \sum_{i=1}^{k} \mu_i dn_i \tag{1.13}$$

USC UNIVERSIDADE DE SANTIAGO DE COMPOSTELA

And the Gibbs free energy:

$$G = G(T, p, A, \mathbf{n}) \tag{1.14}$$

$$dG = -SdT + Vdp + \gamma dA + \sum_{i=1}^{k} \mu_i dn_i \tag{1.15}$$

From these relations, surface tension can also be expressed as the partial derivatives of the previous thermodynamic potential energies:

$$\gamma = \left(\frac{\partial H}{\partial A}\right)_{S,p,\mathbf{n}} \tag{1.16}$$

$$\gamma = \left(\frac{\partial G}{\partial A}\right)_{T,p,\mathbf{n}} \tag{1.17}$$

$$\gamma = \left(\frac{\partial F}{\partial A}\right)_{T,V,\mathbf{n}} \tag{1.18}$$

The previous equations correspond to a multicomponent system where the effect of the area has been considered. For clearness and to focus in a more concrete example, the surface excess analysis of a two phase system is explained (Griffiths, 1980; Kang, 2005; Lyklema, 2000; Sychev, 1973). Let α and β be the two phases in contact through the interface σ. Because the internal energy is additive, the excess internal energy related to the interface can be expressed as:

$$U^\sigma = U - U^\alpha - U^\beta = U^\sigma(S^\sigma, V^\sigma, A, \mathbf{n}^\sigma) \tag{1.19}$$

In fact, any extensive thermodynamic property, Φ, can be decomposed in that way:

$$\Phi^\sigma = \Phi - \Phi^\alpha - \Phi^\beta \tag{1.20}$$

From this definition, the basic equations for the surface thermodynamics can be expressed. By order, the differential fundamental equation, the Euler equation and the Gibbs-Duhem equation are here presented:

$$dU^\sigma = TdS^\sigma - pdV^\sigma + \gamma dA + \sum_{i=1}^{k} \mu_i dn_i^\sigma \tag{1.21}$$

$$U^\sigma = TS^\sigma - pV^\sigma + \gamma A + \sum_{i=1}^{k} \mu_i n_i^\sigma \tag{1.22}$$

$$S^\sigma dT - V^\sigma dp + Ad\gamma + \sum_{i=1}^{k} n_i^\sigma d\mu_i = 0 \tag{1.23}$$

By means of these sets of equations and by the connections with the thermodynamic potentials and magnitudes, the thermodynamics of the interface can be developed. In order to not extent too much this section, only the Helmholtz free energy is going to be presented, as it is usually shown and studied in the referenced books and works, together with Equation 1.18 (Pellicer *et al.*, 1995). From the definition of the Helmholtz free energy, it can be extended to the study of the interface:

$$F^\sigma = U^\sigma - TS^\sigma = -pV^\sigma + \gamma A^\sigma + \sum_{i=1}^{k} \mu_i n_i^\sigma \tag{1.24}$$

The Gibbs approximation, for the study of large systems where the volume of the interface can be neglected, establishes that $V^\sigma = 0$, making the surface a 2D flat plane. Going back to the example of a liquid in equilibrium with its vapour, only one chemical species remains, n. The Gibbs dividing plane is set so $n^\sigma = 0$ (Griffiths, 1980; Lyklema, 2000) and, under these conventions, Equation 1.24 becomes:

$$F^\sigma = U^\sigma - TS^\sigma = \gamma A^\sigma \tag{1.25}$$

The surface density of any magnitude M^σ is represented by $m^\sigma = M^\sigma/A$, that simplifies the lasts two terms of Equation 1.25:

$$\gamma = u^\sigma - Ts^\sigma \tag{1.26}$$

Equation 1.26 indicates that the surface tension can be understood by means of an energetic and an entropic part. Now, making use of the Gibbs-Duhem equation (Equation 1.23) and the Gibbs approximation, another relation for γ can be obtained (Lyklema, 1999):

$$d\gamma = -s^\sigma dT \rightarrow s^\sigma = -\frac{d\gamma}{dT} \tag{1.27}$$

This last equation expresses that the change in surface tension with temperature (for a simple fluid it is only temperature-dependent) is fully entropic, given by a rearrangement of molecules at the interface. It also allows expressing the surface internal energy density just as a function of the surface tension and the temperature for a pure liquid in equilibrium with its vapour.

$$u^\sigma = \gamma + T\frac{d\gamma}{dT} \tag{1.28}$$

One may think that the pressure should also appear in the equation, but due to the considerations that have been used, for a simple system like this, the pressure and the temperature are linked by the Clausius-Clapeyron relation, as the curvature of the interface has been neglected because of the Gibbs approximation.

From the previous explanations it is seen that the surface tension has two contributions: the energetic and the entropic ones. They were obtained considering just one component in the system. For a more general case, it can also be derived from Equation 1.18 with the same conclusion:

$$\gamma = \left(\frac{\partial F}{\partial A}\right)_{T,V,\mathbf{n}} = \left(\frac{\partial U}{\partial A}\right)_{T,V,\mathbf{n}} + T\left(\frac{\partial S}{\partial A}\right)_{T,V,\mathbf{n}} \tag{1.29}$$

USC UNIVERSIDADE DE SANTIAGO DE COMPOSTELA

The final relationship with respect to the one component system regards the definition of the surface tension as the free energy density (Meier, 2014). From Equation 1.25,

$$F^\sigma = \gamma A^\sigma \rightarrow f^\sigma = \gamma \tag{1.30}$$

The last equation means that the surface tension of a pure liquid in equilibrium with its vapour is equivalent to the work per unit area required to expand the interface under isothermal conditions.

All the considerations until now have been proposed to give a thermodynamical sense to the surface tension. These reflections have been done assuming a two-phase system of a pure liquid in equilibrium with its vapour, although the surface tension definition does not depend on the fact that the system is mono or multicomponent. Definitions 1.7, 1.16, 1.17 and 1.18 have been made with no specific considerations about the thermodynamic system. For more species in solution, the surface tension will depend on more magnitudes and will not be as simple as 1.28 or 1.30. The interactions of more than one species at the interface will produce a change in the excess surface energy and so, in the surface tension. For a multicomponent system of two phases in contact, and regarding Equation 1.23 and the Gibbs convention, that states $V^\sigma = 0$, we obtain:

$$S^\sigma dT + Ad\gamma + \sum_{i=1}^{k} n_i^\sigma d\mu_i = 0 \tag{1.31}$$

For a simplification of the equation, the surface density, $\Gamma_i = n_i^\sigma / A$, is introduced, and the differential surface tension can be described as:

$$-d\gamma = s^\sigma dT + \sum_{i=1}^{k} \Gamma_i d\mu_i \tag{1.32}$$

Which is known as the *Gibbs adsorption equation*. This equation states that the change in the surface tension depends on the surface composition, in addition to an entropic molecular rearrangement. Another interfacial concept has just appeared: *adsorption*. It will be developed in detail in the next section.

Until now, no considerations about the shape of the interface have been taken into account. The Young-Laplace equation connects the curvature of the interface (determined by the curvature radii r_1 and r_2,), the surface tension and the pressure difference between both sides of the interface:

$$\Delta p = \gamma \left(\frac{1}{r_1} + \frac{1}{r_2} \right) \tag{1.33}$$

This equation will not be derived here, but a thermodynamic (Sychev, 1973) or mechanical approach (Adamson and Gast, 1997; Batchelor, 2000; Landau and Lifshitz, 1987) can be followed in the literature. The Young-Laplace equation sets the shape of an interface at equilibrium between two fluids by a second-order derivative equation that, in cartesian coordinates, is:

$$\Delta p = \gamma \left(\frac{\frac{d^2y}{dx^2}}{\left[1 + \left(\frac{dy}{dx}\right)^2\right]^{3/2}} + \frac{\frac{dy}{dx}}{x\left[1 + \left(\frac{dy}{dx}\right)^2\right]^{1/2}} \right) \tag{1.34}$$

USC UNIVERSIDADE DE SANTIAGO DE COMPOSTELA

This equation does not depend on whether the system is mono or multicomponent, it just relates the pressure at both sides of an interface, independently of its origins, and can be applied to any interface *at equilibrium*.

Surface tension has been introduced as a thermodynamic magnitude, but it has been historically (and it continues to be) studied as a mechanical property of the interface. Both concepts are not opposed since they emerge from the same microscopic behaviour: the surface energy excess. In the book of Keszei (Keszei, 2012), the mechanical (force per unit length) and thermodynamic (energy per unit area) views are connected by means of the Gibbs free energy (Equation 1.17 and Figure 1.4). The work required to increase the area of a rectangular surface by increasing just one of their sides at constant temperature and pressure is:

$$\Delta G = \int_{A_0}^{A_1} \gamma dA = \int_{x_0}^{x_1} \gamma b dx \tag{1.35}$$

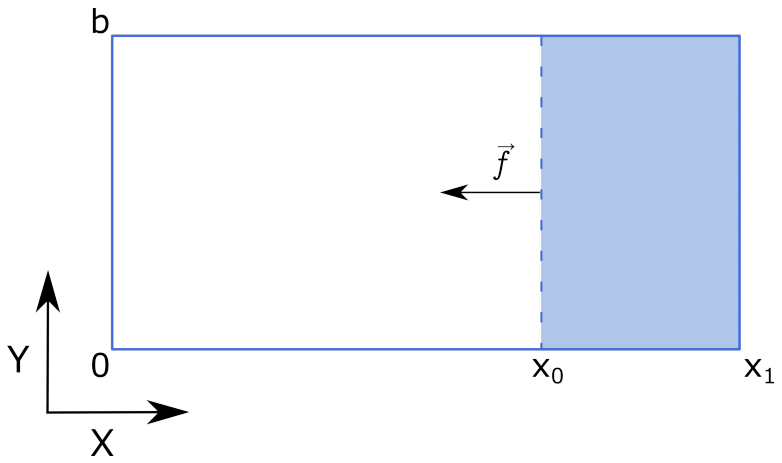


Figure 1.4: Simple drawing representing the rectangular area that is increased in Equations 1.35 and 1.36. The vertical dimension is kept constant and the horizontal dimension is increased from x_0 to x_1, what originates the force f against the surface increment.

The mechanical-thermodynamic relationship proposed by Keszei states that the work calculated in Equation 1.35 has been done against a force f that actuates along the x coordinate:

$$\Delta W = \int_{x_0}^{x_1} f dx \tag{1.36}$$

Both equations are two expressions of the same phenomenon, so they must be identical:

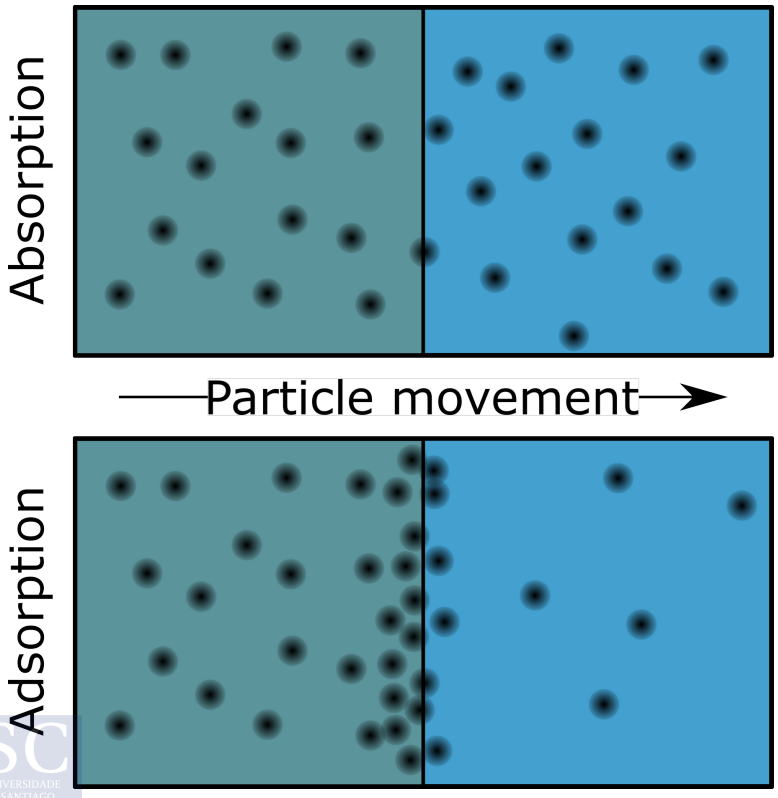
$$\Delta G = \Delta W \rightarrow \gamma b = f;\ \gamma = f/b \tag{1.37}$$

USC UNIVERSIDADE DE SANTIAGO DE COMPOSTELA

This reasoning, despite simple, is quite effective to achieve the connection between the surface tension definition and the mechanical force that appears when the area of the interface is changed. As reported by the same author: 'It is worth to note that this force is much easier to measure, and appropriate methods lead to a more accurate value of the surface tension, than measuring energy changes'.

1.3. Adsorption to fluid interfaces

Adsorption is the mechanism by which particles from a fluid (atoms, molecules, ions, colloids, nanoparticles, polymers, proteins, etc) move to the interface with another media. Despite the adsorption to solid interfaces has been widely studied for historical reasons (Langmuir proposed his adsorption model for gases on a solid surface plane in 1918 (Langmuir, 1918)) and also due to its implication in catalysis or contaminants removal (Bastos-Neto *et al.*, 2020; Cussler, 2009; Foo and Hameed, 2010; Ruthven, 2001), the discussion in this section is focused on fluid interfaces. The difference between adsorption and absorption phenomena is that in the latter the particles from the first media spread in the second, while in adsorption processes they remain at the interface. In terms of a stricter equilibrium approach, there should be particles in both phases but increasing their density close to the interface (Radke, 2015) (Figure 1.5). Depending on the forces that keep the molecules at the interface, the *chemisorption* or the *physisorption* are the two main types of adsorption processes. In chemisorption, new chemical bonds are generated between the adsorbed particles and the compounds at the interface. On the other hand, the physical adsorptions include the van der Waals forces and the rest of electrostatic interactions, hydrogen bonds or lyophobic interactions (or entropy-driven). Physical adsorption is predominant in fluid interfaces.



USC UNIVERSIDADE DE SANTIAGO DE COMPOSTELA

Figure 1.5: Figure illustrating the difference between absorption and adsorption.

The adsorption of particles at the interface typically produces a change in the surface energy. It will increase or decrease depending on the type of interactions between the adsorbed particle (the *adsorbate*) and the composition of the interface. In any of these scenarios, the adsorption of particles at the interface will take place following the surface energy difference, and so a change in the surface tension. Depending on the way that the surface tension changes as a function of the diluted particles, three different types of adsorbates can be identified (Figure 1.6). To understand their behaviour, we go back to the Gibbs adsorption equation (Equation 1.32) for isothermal conditions ($dT = 0$) and considering a two component binary system (a solution in equilibrium with its vapour, for example). Under these assumptions, Equation 1.32 becomes the *Gibbs adsorption isotherm* equation:

$$-d\gamma = \Gamma_1 d\mu_1 + \Gamma_2 d\mu_2 \tag{1.38}$$

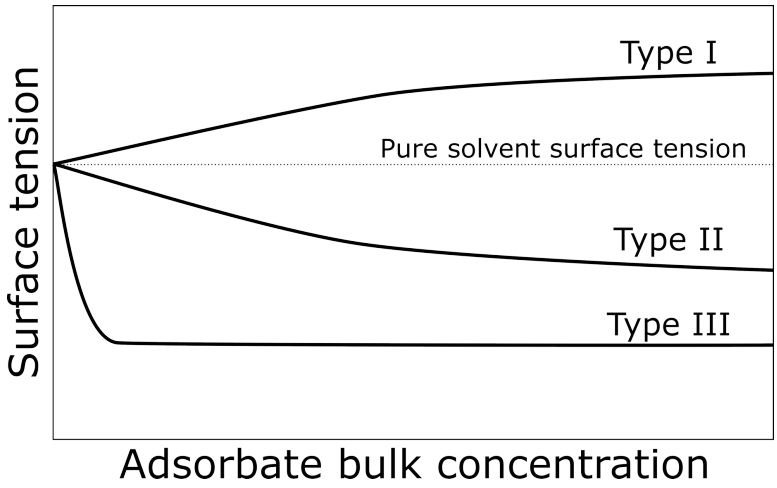


Figure 1.6: The three types of adsorbates are classified depending on of their surface tension profile as a function of their bulk concentration.

The convention of the Gibbs dividing plane is arbitrary (Adamson and Gast, 1997) and the surface excess (the surface density Γ) of each component of the system is referred to the position of the plane. This plane may be understood as a reference point and no as a physical magnitude, and so the surface concentrations of the species should be also mentioned with respect to which position of the plane they have been determined. For simplicity, we choose the reference plane where the surface concentration of component 1 (the solvent) becomes 0, reducing Equation 1.38 to a function just in terms of compound 2 (the solute and the studied adsorbent):

USC UNIVERSIDADE DE SANTIAGO DE COMPOSTELA

$$d\gamma = -\Gamma_2 d\mu_2 \tag{1.39}$$

The total chemical potential of component 2 can be expressed in terms of the standard chemical potential of the same compound μ_2^0, the temperature T, the gas constant R and the activity of compound 2 in the solution a_2:

$$\mu_2 = \mu_2^0 + RTln(a_2) \xrightarrow{dT=0} d\mu_2 = RTdln(a_2) = RT\frac{da_2}{a_2} \tag{1.40}$$

The activity contains the effects of a non-ideal mixing in the energy of the system. It is usually expressed in terms of the activity coefficient f multiplied by the mole fraction x of considered component (Brow, 1998):

$$a_2 = f_2(p, T, \{x_i\})x_2 \tag{1.41}$$

For diluted solutions, the activity coefficient is close to 1, and so the combination of Equations 1.39 and 1.40 becomes:

$$d\gamma = -\Gamma_2 RT\frac{dx_2}{x_2} \rightarrow \Gamma_2 = -\frac{x_2}{RT}\frac{d\gamma}{dx_2} \tag{1.42}$$

Equation 1.42 can be also expressed in terms of the component 2 concentration (or molarity or molality), c_2, by continuing with the assumption of diluted solution, which implies that the number of moles of the solvent (n_1) is much larger than n_2:

$$x_2 = \frac{n_2}{n_1 + n_2} \approx \frac{n_2}{n_1} = \frac{c_2 V}{M_{w_2} n_1} \tag{1.43}$$

The volume and the number of solvent molecules can be considered constant values as a function of the component 2 concentration:

$$dx_2 = \frac{V}{M_{w_2} n_1} dc_2 \rightarrow \frac{x_2}{dx_2} = \frac{c_2}{dc_2} \tag{1.44}$$

And Equation 1.42 becomes:

$$\Gamma_2 = -\frac{c_2}{RT}\frac{d\gamma}{dc_2} \tag{1.45}$$

The temperature, the gas constant and the concentration are always positive, what means that the derivative of the surface tension with respect to the concentration will determine the sign of the surface concentration of compound 2. The three types of surface tension variations represented in Figure 1.6 can be now approached. Type I correspond to a substance with negative surface concentration, while Types II and III correspond to positive surface concentration, with the special case of type III, where the surface tension suffers a dramatic reduction at low concentrations until a saturation point, where it remains mostly constant.

To understand the meaning of the surface concentration sign, we must highlight again that it has been defined with respect an arbitrary plane, which definition makes $\Gamma_1 = 0$. The extension of this definition (schematically shown in Figure 1.7) makes that the change from the real system to the 2D plane keeps the area under the curve (concentration vs interface perpendicular position) equal at both sides of the plane's position. This is true for component 1, which is our reference. Component 2 excess surface concentration will be determined with respect to the same line, so its value (and sign) will depend on the areas at both sides of the plane. A negative value represents that the surface has a deficiency of compound 2 with respect to the plane, i.e. the area below the plane is larger than above. In other words, there is less relative amount of compound 2 at the interface than in bulk. If the ratio between compound 2 and 1 is the same, the change at the interface would

be equivalent and $\Gamma_2 = 0$. The conclusion is that the increase of surface tension happens because of the tendency of compound 2 to remain in bulk. For aqueous solutions, Type I adsorbate is usually related to inorganic salts or sugar solutions, which interactions with water are ionic or hydrogen bond mediated.

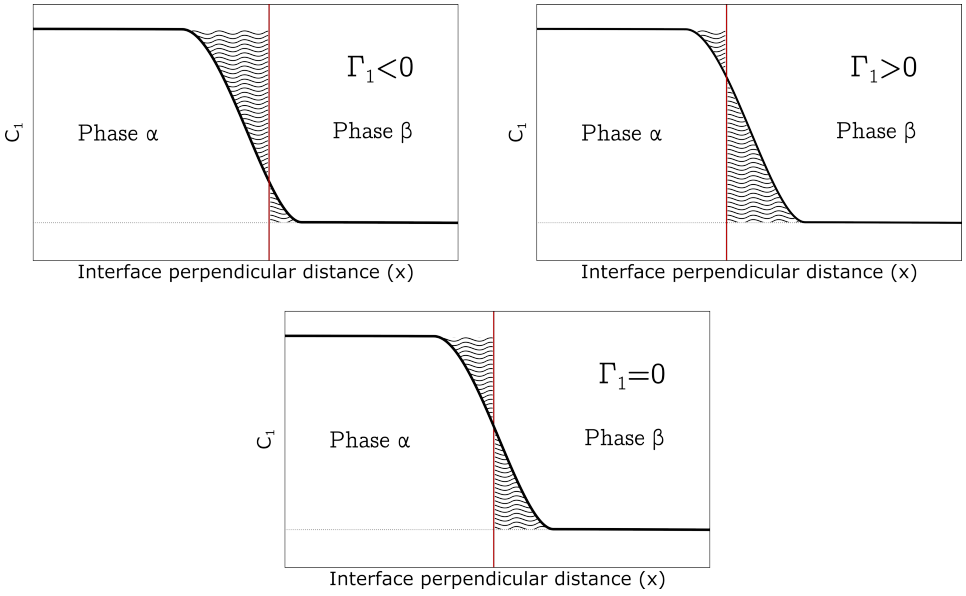


Figure 1.7: Change of the Gibbs dividing plan position effect on the surface density of compoment 1.

The negative sign of surface excess concentration has been related to the fact that the adsorbate has higher affinity for the bulk than by the interface and its concentration at the interface (or the ratio of particles) is reduced. From 1.26, the change in surface tension at constant temperature is:

$$\Delta\gamma = \Delta u^{\sigma} - T\Delta s^{\sigma} \tag{1.46}$$

The change in the surface tension with respect to the pure solvent is positive, so the surface energy density must increase, or the surface entropy density must decrease. The fact that the adsorbate tends to remain in bulk phase makes the interface to be mostly filled by the solvent, so the composition is expected to be equivalent to that in the pure liquid. On the other hand, the surface tension of a solution (γ) has been expressed in terms of the surface tension of the pure solvent (γ_s^0), the temperature T, the Boltzmann constant k, a constant A_s that reflects the cross-sectional area of the solvent molecules, and the solvent activities in bulk (a_s^b) and at the interface (a_s^σ) (Kronberg *et al.*, 2014):

USC UNIVERSIDADE DE SANTIAGO DE COMPOSTELA

$$\gamma = \gamma_s^0 + \frac{kT}{A_s} ln \frac{a_s^\sigma}{a_s^b} \tag{1.47}$$

Where the constant A_s is defined in terms of the molar volume v_s and the Avogadro number N_a:

$$A_s = \left(\frac{v_s}{N_a}\right)^{2/3} \tag{1.48}$$

The change in surface tension from pure solvent to solution is reflected in the logarithm of the activities' ratio. The increasing of the ratio of the solvent activity at the interface with respect to that in the bulk phase will also produce an increment in the surface tension. Here, concentration changes in the bulk can also affect the interface. Going back to the study of aqueous solutions, when an electrolyte is added to water, it will tend to remain in solution rather than to adsorb at the interface. The water interface does not change, but the activity of water molecules in the bulk is reduced due to the addition of the particles, thus increasing the surface tension as reflected by Equation 1.47.

Type II adsorbate is now easier to understand. It corresponds to soluble or partially soluble particles with high affinity for the interface, where they reduce the surface tension of the pure solvent, either by the decreasing the surface excess internal energy (the interactions at the interface are weaker for the solution than for the pure solvent) or by increasing the entropy (Equation 1.46). Regarding aqueous solutions, this behaviour corresponds to soluble organic compounds. Methanol, ethanol, or propanol are type II adsorbates in aqueous solution. In this case, the alcohols are completely soluble in water but the adsorption to the interface is not proportional to the bulk concentration, although it is always positive. In this scenario, the surface tension is monotonically decreasing with concentration, which means that the derivative has always the same sign, but not the same value. On the other hand, after certain concentration, the surface concentration of the adsorbate has a maximum and then it decreases, while the surface tension continues to decrease. Again, as in the previous case, this is due to the change in the bulk-interface ratio of the chemical compounds' activity (Chodzińska *et al.*, 2012).

Finally, type III adsorbates, which also decrease the surface tension of the solvent, have a tendency that differs from the other two types: the change in surface tension with concentration suffers a dramatic shift after a certain concentration. The derivative of this curve is high at low concentrations, what indicates a great preference of the adsorbate by the interface. After reaching a critical concentration, it remains almost constant, suggesting that the increasing of concentration in the bulk has no additional effects at the interface. This kind of adsorbates are typically identified as *surfactants* (*surf*ace *act*ive ag*ents*). However, most amphipathic particles can be included in this classification. Amphipathic particles (*amphiphiles*) are compounds that present, at least, one lyophilic and one lyophobic group. A lyophilic group is a part of the amphiphile that is attracted by the solvent. A lyophobic group is usually defined as the region that tends to get away from the solvent, mainly due to entropic effects: the attraction of the lyophobic part towards the solvent is so weak that it increases the mean number of interactions between solvent particles, making them more organized and stable around this group. This has the effect of increasing the local energy and entropy, so these parts seem to be repelled as a final result. In a binary system, the amphiphile particles rapidly move to the interface, keeping the lyophilic parts towards the solvent and the lyophobic groups towards the other phase (the gas or the other liquid). The adsorption of amphiphiles has the effect of decreasing the energy of the interface and, at the same time, increasing the local entropy in solution by *freeing* solvent molecules. The combination of these two processes leads to the adsorption of amphiphiles even

at very low concentrations, thus provoking a dramatic decrease of surface tension. The adsorption of these particles is not instantaneous. It depends on their size and affinity for the interface. It is more commonly approached as a kinetic equilibrium where the adsorption and desorption of particles at the interface is produced by an intermediate place between the proper interface and a region in the bulk called the *subsurface* (Dukhin *et al.*, 1995; Eastoe and Dalton, 2000; Moroi, 1992)

While type II adsorbates decrease the surface tension along the soluble range of concentration, it has already been mentioned that the surface concentration has a maximum at some point. Beyond this concentration, the surface tension changes come from the changes in the bulk-interface activity ratio. However, this is not true for amphiphilic particles. At low concentrations, they are adsorbed at the interface until a maximum surface concentration value is reached. At this concentration, the interface becomes saturated, typically creating a *monolayer*. At higher concentrations, the adsorption of more particles is not possible. Beyond this critical concentration, if the bulk concentration rises, the interactions of the lyophobic parts of the amphiphiles in contact with the solvent are highly increasing the energy and reducing the entropy of the whole system but they cannot move to the interface, so they self-assemble, creating soft structures in the bulk. Regarding the aqueous solution example, surfactants are type III adsorbates, as well as a large number of proteins, peptides, polymers, nanoparticles or, as it will be mentioned in Chapter 2, cyclodextrin complexes.

1.4. Amphiphiles and self-assembly

The action by which particles spontaneously organize in complex structures creating a configuration of minimal energy is known as *self-assembly*. The shape, size or stability of these structures depend on the particle chemical and physical properties as well as on the interactions with the solvent. This process is not restricted to microscopic agents, it is also observed in the macroscopic world and even in social behaviour of animals, but the cases here exposed are related to the *molecular self-assembly* in solution, included in the field of *soft matter* (Kalyanasundaram, 1987; Uskoković, 2008; Whitesides and Boncheva, 2002; Wolkenstein, 1983).

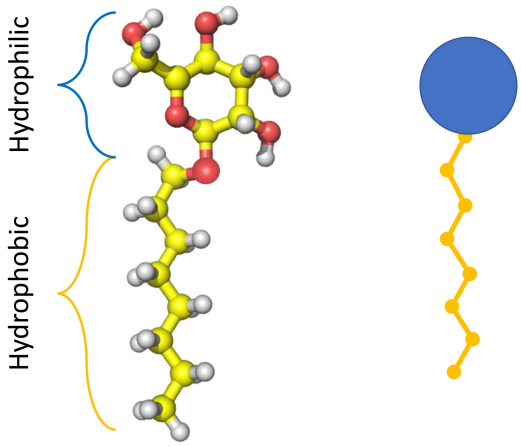
In the last part of the previous section, the behaviour of amphipathic molecules in water was described. The interest of this kind of molecules is huge, not just for their properties in solution but also for their behaviour at interfaces and the combination of both. For example, surfactants, that may be one of the simplest molecules to which the concept of self-assembly applies, are molecules schematically composed by a hydrophilic and a hydrophobic part (Figure 1.8). When they are in aqueous solution, because of their amphipathic structure, they are adsorbed at the interface and they acquire a specific orientation to keep the hydrophobic part out of the water. After reaching the critical concentration and increasing the number of molecules in water, they start to self-assemble, creating supramolecular spherical structures called *micelles*. In this configuration, the hydrophobic parts of the surfactants point inside the sphere and the hydrophilic parts compose its surface. The energy of the whole system is reduced with respect to that where all the monomers are free in solution (Abbott, 2015; Kronberg *et al.*, 2014; Moroi, 1992). Approaching this phenomenon from the entropic point of view, the increase of order of the solute is overcompensated by the much larger disorder of the water

USC UNIVERSIDADE DE SANTIAGO DE COMPOSTELA

molecules under this configuration (Figure 1.9) (de Jesus and Yin, 2017; Nash, 2017; Rocha *et al.*, 2020). To ensure, however, that a process may happen, the Gibbs free energy variation (Equation 1.49) must be negative, and even if the entropy of the whole system increases, if the enthalpy variation is too high, the process will not take place spontaneously. However, for most micellization studies, the entropic part of the Gibbs free energy is higher (in absolute value) than the enthalpic one (Majhi and Blume, 2001), what states the fact that this process is driven by the so called *hydrophobic effect* (Heintz *et al.*, 2010; Jolicoeur and Philip, 1974; Kronberg *et al.*, 2014; Tanford, 1978, 1980).

$$\Delta G = \Delta H - T\Delta S \tag{1.49}$$

Micelles are the former kind of aggregates that surfactants show when increasing their concentration in aqueous media. The critical concentration abovementioned, for this kind of compounds, is known as the *critical micelle concentration*, or *cmc*. More precisely, it is the concentration *range* around which micelles start to be detected. The cmc, for a binary solution (just water and the surfactant molecules), depends on the temperature. For a given temperature, around the cmc, micelles are formed by a variable number of surfactant molecules that oscillates around an average value, the *aggregation number* or N_{agg}. Above the cmc, the size of the micelles grows and their shape evolves from sphere to more exotic forms. As a function of concentration, temperature or the addition of other compounds, the shape, size, and structure of the self-assembled surfactants arrangements goes from spherical micelle to worm-like structures, vesicles or bicontinuous structures (Abbott, 2015; Kronberg *et al.*, 2014; Moroi, 1992). This kind of aggregates are presented in all life-forms. The lipid bilayer that constitutes the cell membrane is another kind of self-assembled structure driven by the same kind of interactions.



USC UNIVERSIDADE DE SANTIAGO DE COMPOSTELA

Figure 1.8: Left: Representation of an example surfactant: Octyl-β-*D*-glucoside. Right: general diagram of a surfactant.

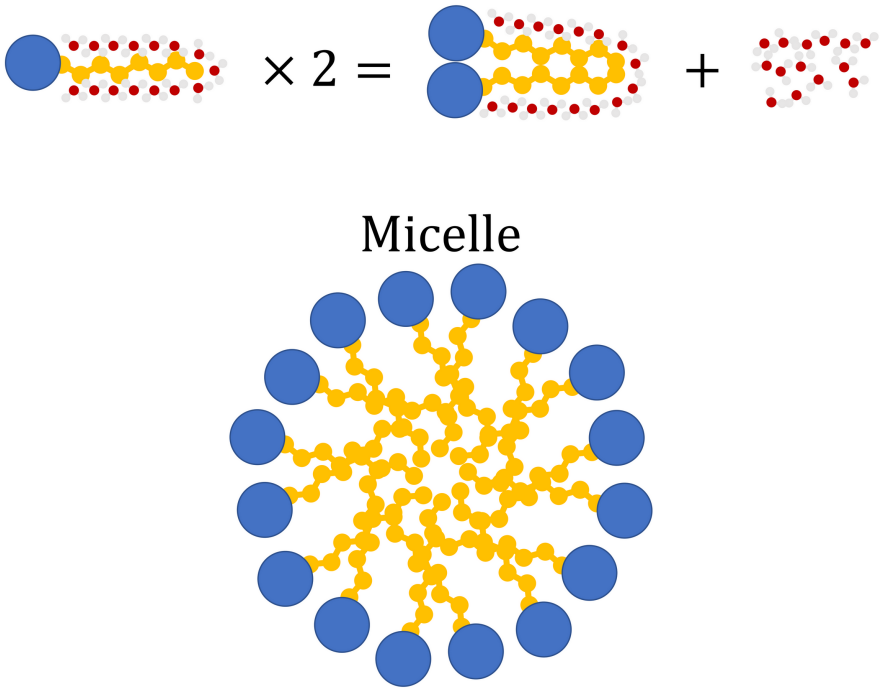


Figure 1.9: Up: Water molecules liberation after two surfactant molecules have binded. Down: The final conformation of a micelle after the aggregation of several surfactants.

Surfactants are not only relevant by their self-structures in solution. Their amphipathic behaviour at the interface and the later hydrophobic interaction in bulk enables the surfactants to be employed in many fields, including soaps, cosmetics, and drug formulation, among other industries. The amphipathic behaviour is responsible of the self-assembly, but it also allows the binding to organic nonpolar compounds, like oils. The hydrophobic part of an amphiphile is lipophilic (and the hydrophilic is lipophobic). So, when the self-assembled structures are formed, they can encapsulate hydrophobic compounds inside. This means that hydrophobic or poorly soluble compounds can be incorporated into the bulk of the solution by this encapsulation mechanism into self-assembled structures. The first example of their applications is, as it has been mentioned, soaps. Soaps in water, are used since ancient times for washing and cleaning. Basically, to remove dirt. Dirt includes a combination of many compounds, but they can be distributed schematically in water soluble and non-soluble. If dirty is water soluble, it can be easily removed just using this solvent. However, if it is non-soluble, then another organic compound should be used for washing. The problem is that organic solvents may be dangerous for the human skin if used too frequently. Another extra difficulty is that dirty is not always divided in polar/non-polar (hydrophilic/hydrophobic) and the addition of surfactants to water is the best way for the removing of both types of dirt. The surfactant has two effects: it can encapsulate organic molecules from the interface to the bulk (for later removal), but it also reduces the surface tension of the solution, what eases the process of attaching to certain surfaces and the later bulk diffusion

USC UNIVERSIDADE DE SANTIAGO DE COMPOSTELA

(Rosen and Kunjappu, 2012).

Out of cleaners, surfactants are also used as wetting enhancers in agriculture (the surface tension reduction of water droplets makes them easier to be absorbed by plants); in oil spill recoveries, used as emulsifiers; in enhanced oil recovery, in extraction, and in the later transportation (the surfactants reduce the surface tension of the oil making it easier to be extracted and it reduces the viscosity for the transportation); to increase the solubility of drugs in pharmaceutical formulations and for controlled drug release (the encapsulation of poorly soluble drugs let them to remain in bulk for later delivery); for the development of new medical treatments (in cancer treatments, for example, by the use of designed block copolymers); and many others (Al-Roomi *et al.*, 2004; Blanco *et al.*, 2011; Gogoi *et al.*, 2003; Hassan *et al.*, 2011; Jimoh and Lin, 2019; Mulligan, 2005; Schramm *et al.*, 2003; Uchegbu and Florence, 1995).

Larger amphipathic molecules, like proteins, also self-assemble forming more complex structures, which are plenty extended in all living forms (Kalyanasundaram, 1987; Kerfeld *et al.*, 2005; Kushner, 1969; Wolkenstein, 1983). Usually, the structure of these macromolecules cannot be divided into such simple parts like one-one hydrophilic-hydrophobic distribution. They have multiple interacting sites, which derives in their huge number of possible conformations in aqueous solution. Their link to life, their hierarchical structuring, their structure-dependent function or their biocompatibility make proteins the perfect target to be replicated in the development of new self-assembled materials and the reason why they are widely studied in the development of biomaterials (Ariga *et al.*, 2019; Bai *et al.*, 2016; Mendes *et al.*, 2013; Varga, 2016; Whitesides and Boncheva, 2002).

1.5. Interfacial characterization of amphiphiles

Bulk aggregation and adsorption process are linked. The study of one of these phenomena should provide information about the other because the reason why amphipathic particles adsorb at interfaces is the same that they have to self-assemble: the entropic effect (Barry and Dogic, 2010; McManus *et al.*, 2016; Nash, 2017). Interfaces should be, hereby, a reflection of what can happen in bulk. When amphiphiles move to the interface, in the presence of two phases, they can show different deportments with respect to bulk. Surfactants have already been presented but, for example, proteins in contact with two immiscible phases (oil-water) at the interface can denaturalize and display structural regions that would be hidden in solution, among other special behaviors (Alahverdjieva *et al.*, 2008a; Arooj *et al.*, 2016; Bergfreund *et al.*, 2021; Graham and Phillips, 1979; Lu *et al.*, 1998; Möbius and Miller, 1998b). Even transport properties between two phases can be mediated by molecules at interfaces (Karnes and Benjamin, 2017).

Surfactants, peptides, proteins or any other kind of amphipathic particles or supramolecular complexes have a special interest, as it has already been said, in the development of new materials, but also in the food industry, pharmaceutics, textiles or medicine (Barthelat *et al.*, 2016; Subramani and Ahmed, 2018; Zhang, 2003). The study of these compounds at interfaces is usually done by means of the surface tension, different types of scattering or spectroscopy, ellipsometry or circular dichroism (Bracco and Holst, 2013; Costa *et al.*, 2017; DÁpolito *et al.*, 2018; Javadi *et al.*, 2013; Kairaliyeva *et al.*, 2017; Schlossman, 2002). These are some

of the examples of techniques to analyse the interface, although in none of them the *heat* involved in adsorption and interfacial processes at fluid interfaces can be measured, as previously noticed by Bastos-Neto et al. (Bastos-Neto *et al.*, 2020): 'despite its importance, work on the experimental and theoretical study of multicomponent heat of adsorption on heterogeneous adsorbents is extremely limited [...] The development of mathematical models to simulate adsorption processes requires accurate knowledge of equilibrium, kinetic and heats for the system of interest over all conditions of pressure, temperature, composition, and adsorbate loading encountered in the adsorber during the separation process'.

Thus, there is a lack of methods to assess the heat associated to the spontaneous adsorption and arrangement of molecules at interfaces, as well as to the range of associated supramolecular structures formed in the bulk solution. Filling this gap is one of the motivations of this project.

USC UNIVERSIDADE DE SANTIAGO DE COMPOSTELA

Chapter 2

Cyclodextrins: the sweet molecular carrier

I will take the Ring, though I do not know the way

Frodo Baggins, in "The Lord of the Rings"

The hydrophobic effect is responsible for the self-assembly of amphiphiles in aqueous solution and for their adsorption at water/air interfaces. In the micellization processes, the encapsulation of poorly soluble agents is typically entropy-driven but the self-assembly, the adsorption or the binding to other molecules may be also mediated by electrostatic interactions or hydrogen bonds. The final system created by these processes includes a certain number of molecules attached by non-covalent bonds. *Supramolecular chemistry* is the branch of science dealing with these processes. The encapsulation of molecules is not restricted to aggregates of a relatively large number of molecules, as it happens with micelles. Single macromolecules can also enclose smaller molecular groups forming the so called inclusion complexes. The relevance of such complexes relies on their simple structure, easier to study and manipulate than those formed by tens of particles. Despite its simpler composition, the ability to encapsulate small insoluble molecules is outstanding. Its importance is such that a branch of the supramolecular chemistry is focused just on these compounds: the *host-guest chemistry*. One of the most widely used *host* molecules nowadays are cyclodextrins, which are studied in this work.

Cyclodextrins (CDs) are a family of cyclic molecules composed by the repetition of glucose units (native cyclodextrins) and their chemically modified derivatives. Their shape is usually described as toroidal or as a hollow truncated cone, although their flexibility allows these molecules to modify their structure depending on their environment. The first work related to CDs was published more than a century ago by Villiers, who reported the isolation of this kind of molecules by an enzymatic reaction from starch (Villiers, 1891). At the beginning of the XX century, Schardinger continued the work of Villiers by describing the method for the elaboration and separation of CDs. This author was the pioneer in studying the chemistry of these compounds (Crini, 2014). During the following decades until the 1970s, more

and more properties of CDs emerged from the works of Pringsheim, Freudenberg, Cramer and French, among others. In the course of these years, the links between the glucoses, the CDs cyclic behaviour and structure and their ability to form inclusion complexes were investigated (Crini, 2014; Kurkov and Loftsson, 2013; Szejtli, 1998; Del Valle, 2004). Since the 1970s, CDs have been widely exploited and their industrial applications have continuously grown (see Figure 2.1). These applications have been focused mostly on their ability to encapsulate other molecules in the pharmaceutical industry (Gu and Wheate, 2021; Wankar *et al.*, 2020), but they have also been increasingly relevant in food industry (Pais *et al.*, 2020; dos Santos *et al.*, 2017), cosmetics (Bilensoy, 2011; Kronberg *et al.*, 2014) and textiles (Bezerra *et al.*, 2020), just to mention a few of them before an extension in Section 2.3. The interest of these molecules cannot be understood without knowing them more in detail.

USC UNIVERSIDADE DE SANTIAGO DE COMPOSTELA

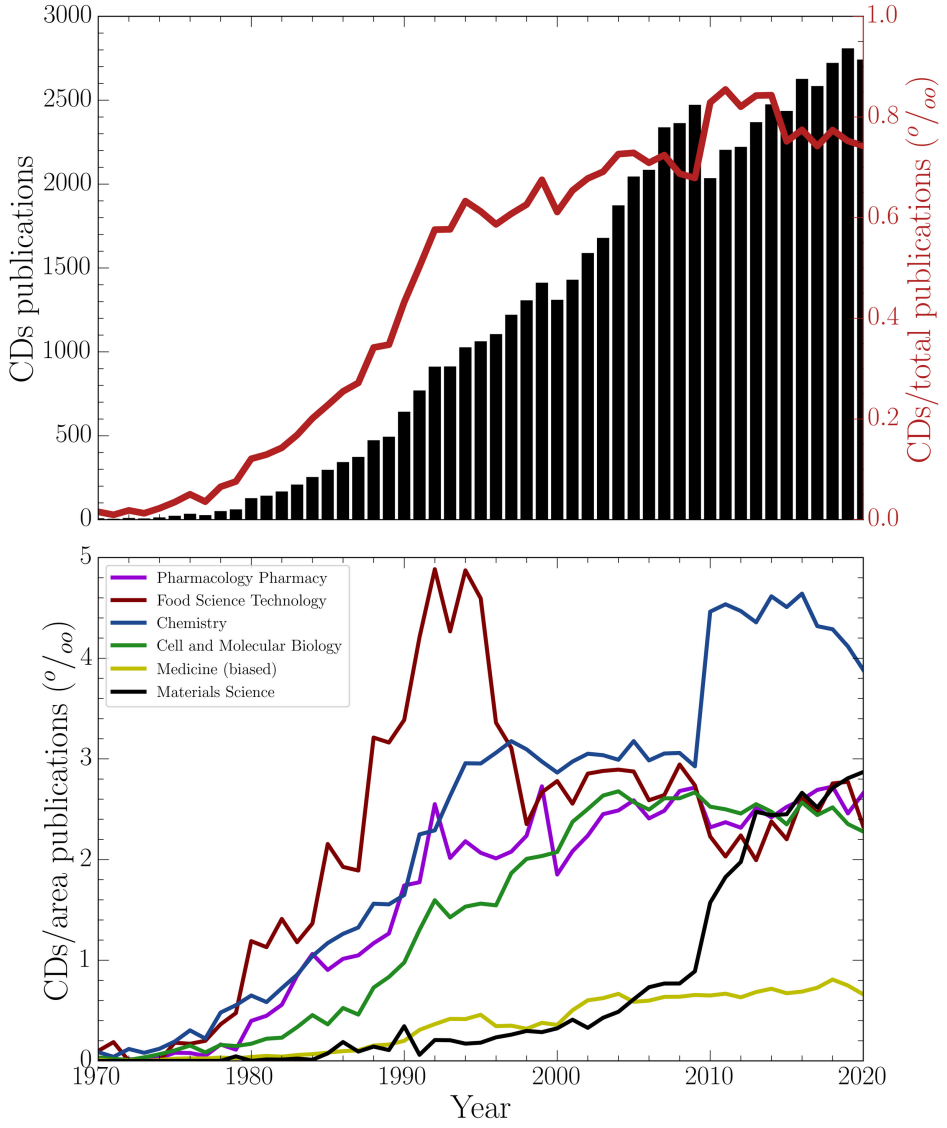


Figure 2.1: Evolution of CDs publications since 1970. Up: Total number of publications and relative number with respect to all the published works in all areas of research. Down: Relative number of CDs publications per selected research area. Data obtained from https://www.webofscience.com/.

2.1. Just cyclodextrins

The main picture of a native cyclodextrin has already been presented: a cyclic repetition of α-*D*-glucopyranose units. α-*D*-glucopyranose is one of the cyclic forms of glucose, composed of a six-membered ring (5 carbon atoms and one oxygen) with no double bonds. Each carbon is linked to a hydroxyl group, except for carbon 5

(C5), which is linked to a hydroxymethyl group (Figure 2.2-A). In native CDs, each α-*D*-glucopyranose molecule is bonded to another by an α-1,4 link, known as O-glycosidic bond. This means that, after the CD ring completion, all the hydroxyl (secondary hydroxyl) groups point to the same direction and the hydroxymethyl (primary hydroxyl) groups point in the opposite direction (Figure 2.2-B) (Bender and Komiyama, 1978; Jin, 2013; Szejtli, 1988, 1998).

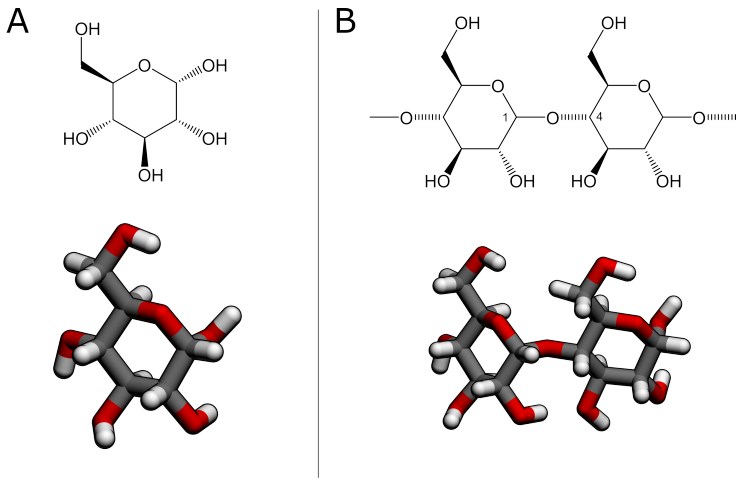


Figure 2.2: A: α-*D*-glucopyranose molecule representations. B: two α-*D*-glucopyranose bonded by means of the O-glycosidic bond

The structural configuration of CDs reveals their amphipathic behaviour: the diverse hydroxyl groups, that point outside the CD, are hydrophilic, and the inner cavity is mainly hydrophobic . We refer to natural or native CDs as those formed only by non-modified glucose units, the number of which will determine the size of the molecule and its physical properties. Depending on their number of repeated glucose units, the α-CD (6), β-CD (7) or the γ-CD (8) (Figure 2.3) are the most common native CDs. Larger structures such as δ-CD (9), ϵ-CD (10) or bigger CDs have not only been proposed but also developed (Larsen, 2002). Lower number of glucose units to form cyclic molecules were supposed not to be achieved, but 5 units-CD (Nakagawa *et al.*, 1994) and even 4 and 3 units-CD (Ikuta *et al.*, 2019) have also been synthesised. The physical properties of all these molecules, are size dependent, although all of them present amphipathic behaviour: hydrophobic cavity and hydrophilic groups outsize. This quality is what makes CDs so useful in many applications. Due to their hydrophilic part, CDs are water soluble, although their solubility varies between CDs. At the same time, the inner hydrophobic cavity allows the CDs to encapsulate small non-polar molecules. All together, these properties confer the CDs the ability to be outstanding nanocarriers of non-soluble molecules in aqueous solution. Nevertheless, their striking properties do not end just in their amphipathic-related-versatility, their biocompatibility, biodegradability, low cost and low toxicity are also really important (Davis and Brewster, 2004; Del Valle, 2004; Wankar *et al.*, 2020). And yet this only refers to native CDs. Trying to optimize some of the applications of CDs, based on their physicochemical properties,

USC UNIVERSIDADE DE SANTIAGO DE COMPOSTELA

chemical modifications on native structures have been studied and applied. Since the 1980s, when the first patent of a modified cyclodextrin was registered, many others came later (Kurkov and Loftsson, 2013; Muller and Brauns, 1985; Pitha *et al.*, 1986).

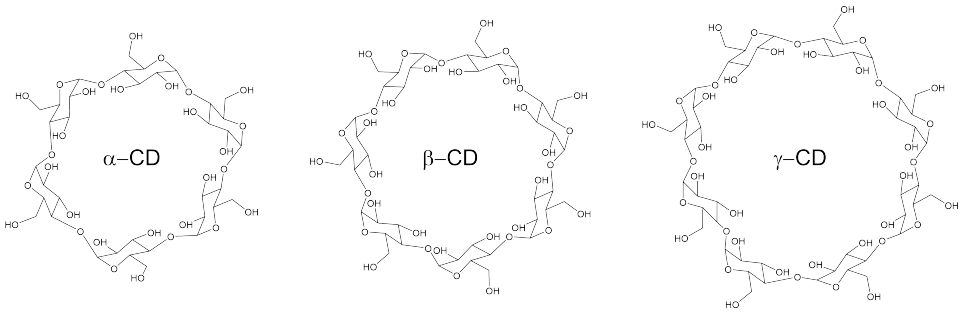


Figure 2.3: Representation of the three native CDs.

Among all the modified CDs, three of them could stand out as the most widely employed: Methyl-β-CD (Me-β-CD), Hydroxypropyl-β-CD (HP-β-CD) and Sulphobutylether-β-CD (SBE-β-CD). They have been designed to increase the solubility and the applications of the native β-CD. These modified CDs were synthetized for general purposes, but more specific designs can be found too. A clear example of that is the *sugammadex*, a modified γ-CD with specific affinity for rocuronium bromide and vecuronium bromide, two compounds used in different kinds of anaesthesia. Its specificity allows the sugammadex to be introduced in the human body to reverse the effect of the drugs by their encapsulation (Yang and Keam, 2009).

2.2. Self-assembly of cyclodextrins and interfacial behaviour

Like other amphiphiles, cyclodextrins tend to aggregate and to adsorb at interfaces. These phenomena has been observed regarding solutions composed only by CDs and also when they are forming host-guest complexes. Despite CDs can be classified as amphiphiles, their structure or their hydrophilic/hydrophobic regions distribution make their aggregation mechanism to be more complex than surfactants and more difficult to predict (Kurkov and Loftsson, 2013). The self-assembling of cyclodextrins was first observed for the native molecules (Coleman *et al.*, 1992; Szente *et al.*, 1998), but their extension to modified CDs was later seen too (Do *et al.*, 2017; González-Gaitano *et al.*, 2002). The formed structures are large aggregates (hundreds of nm), but they do not present a clear organization or structure (Bonini *et al.*, 2006; González-Gaitano *et al.*, 2002). The differences in the concentration needed for the self-assembling depend on the topology of each CD and seems to be straightly related to their solubility. The comparison between α and β CDs dynamics in water solutions and the number of H-bonds that a CD can form with the water surrounding molecules or other neighbour CD was shown to be key to understand the lower solubility of the β-CD with respect to the other native

molecules (Coleman *et al.*, 1992; Mixcoha *et al.*, 2014). Because of the main use of CDs as drug nanocarriers, the interest in their aggregation was focused to the difficulties that these complexes could origin in their ability to encapsulate poorly soluble drugs (Jansook *et al.*, 2010). However, it was shown too that the characterization of the aggregation could also be useful for the determination of their ability to form host-guest complexes (Bikádi *et al.*, 2006; Messner *et al.*, 2010; Loftsson *et al.*, 2019) and to create designed CDs self-assembled structures, like nanotubes (Polarz *et al.*, 2001; Wu *et al.*, 2006). Because of these applications, the interest in their characterization and control rapidly spread (Puskás *et al.*, 2013; Sá Couto *et al.*, 2018; Zaman *et al.*, 2017). Even if, as it was previously said in Chapter 1, the self-assembling and the adsorption at interface are linked, native CD monomers do not have high affinity for interfaces. They do not significantly affect the surface tension (Sá Couto *et al.*, 2018) as they seem to remain close to the interface, at the subsurface (Chief Elk and Benjamin, 2015; Mixcoha *et al.*, 2014). However, bulk aggregates do really have notable affinity for interfaces (Hernandez-Pascacio *et al.*, 2016). On the other hand, some modified CDs have been observed to behave like surfactants, dramatically reducing the surface tension of water even at relatively low concentrations (Ferreira *et al.*, 2012).

Notwithstanding the importance of the self-assembly of cyclodextrins, the most relevant studies right now regard CD complexes. The behaviour of CDs solutions by the incorporation of a guest dramatically changes. New aggregated structures appear, and their possibilities and applications, both in bulk and at interfaces, have only just begun. The formation of larger aggregated structures by CD-guest complexes is employed to create new drug-delivery systems with enhanced properties with respect to the single CD-guest system (Muankaew *et al.*, 2020; Wankar *et al.*, 2020). In these examples, the formation of micelle-like structures (Loftsson *et al.*, 2004; Sajomsang *et al.*, 2011) or nanoaggregations (Lucio *et al.*, 2017) could be highlighted. With respect to interfacial properties of aqueous solutions, some CD complexes have been observed to increase their surface tension and viscoelasticity with respect to pure solvent, creating structured patterns at the interface (Ferreira *et al.*, 2012; Hernández-Pascacio *et al.*, 2008; Hernandez-Pascacio *et al.*, 2007, 2016; Luviano *et al.*, 2020). However, the most outstanding results concerning CDs complexes are those related to the development of new biomaterials. It has been noticed that, like surfactants and proteins, CDs complexes can form the same kind of structures in bulk (Wang *et al.*, 2020; Yang *et al.*, 2017), included the so-named cyclodextrinosomes (Mathapa and Paunov, 2013b,a). The studies about why and how these structures can be formed, to understand and predict their future applications are still ongoing. The hydrophobic effect and the later stabilization by H-bond and other non-covalent interactions seem to play the major role in these aggregates (Messner *et al.*, 2011b,a; Ryzhakov *et al.*, 2016; Jansook *et al.*, 2018).

2.3. Cyclodextrin applications

USC UNIVERSIDADE DE SANTIAGO DE COMPOSTELA

CDs are gaining ground in more and more fields of research because of their versatility. While there exist some direct applications of these molecules, mainly of modified CDs, they are largely used together with other molecules forming supramolecular complexes. CDs are widely employed in the pharmaceutical industry as nanocarriers of poorly water-soluble drugs (Brewster and Loftsson, 2007), as

well as to improve the taste of some drugs in pharmaceutical formulations(Arima *et al.*, 2012; Chay *et al.*, 2018). Most applications of CDs in pharmacology, address drug encapsulation and delivery (Bilensoy, 2011; Davis and Brewster, 2004; Jansook *et al.*, 2018; Szejtli, 2004; Uekama, 2004). However, drug-CD complex properties present limitations, and new proposals combining three or more compounds in these complexes (forming a cross-linked cyclodextrin dimer, including a third compound as a co-complexing agent to facilitate the inclusion, or creating CD-based polymers) are being carried out (Jansook *et al.*, 2019; Khomutov and Donova, 2011; Patel and Hirlekar, 2019; Wankar *et al.*, 2020). The relationship between CDs and drugs goes beyond. CDs have also been used for target therapy and delivery (Erdoar and Bilensoy, 2018; Shen *et al.*, 2019; Uekama, 2004), to enhance drug effects (Gandhi *et al.*, 2020) or to increase their stability (Bilensoy, 2011; Matilainen *et al.*, 2008; Popielec and Loftsson, 2017; Samuelsen *et al.*, 2019).

Without neglecting biological applications but going out of the pharmaceutical industry, CDs are presented in biomedical implementations such as cholesterol removers (Anderson *et al.*, 2021; Coisne *et al.*, 2016; Kritharides *et al.*, 1996; Mahjoubin-Tehran *et al.*, 2020), genetic material carriers (Davis and Brewster, 2004; Kihara *et al.*, 2002) or bioimaging (Bartlett *et al.*, 2007; Fenyvesi *et al.*, 2014), just to name a couple among a huge number of applications (Braga, 2019; Davis and Brewster, 2004; Leclercq, 2016; Wankar *et al.*, 2020). In other areas, CDs are presented in food industry (Astray *et al.*, 2009; Fourmentin *et al.*, 2018; Pais *et al.*, 2020; dos Santos *et al.*, 2017), as pollutant removers (Flaherty *et al.*, 2013; Fliszár-Nyúl *et al.*, 2019; Liu *et al.*, 2020), in the development of new materials (Guo and D. Wilson, 2013; Hashidzume *et al.*, 2019; Yun *et al.*, 2010) or in chemical, textile or cosmetic industries (Bezerra *et al.*, 2020; Bilensoy, 2011; Gatiatulin *et al.*, 2020; Dodziuk, 2006).

It is inevitable, because of the times we are living, to talk about applications of CDs related to COVID-19. During this pandemic crisis, biomedical research focused on the fight against the virus, and CDs also play an important role here. The following chapter section corresponds to Paper I: a review about the applications of CDs against the SARS-CoV-2.

USC UNIVERSIDADE DE SANTIAGO DE COMPOSTELA

USC
UNIVERSIDADE
DE SANTIAGO
DE COMPOSTELA

2.4. Paper I

"The Lord of the NanoRings: Cyclodextrins and the battle against SARS-CoV-2", published in *International Journal of Pharmaceutics* (2020), is a review about the applications of CDs in antiviral therapies that could be close to the SARS-CoV-2: CDs as excipients in antivirals, as stabilizers, modified CDs as antivirals, CDs in antivirals vaccines, or other more general applications. This work has been developed in collaboration with people from: (1) Departamento de Física Aplicada, Facultade de Física, Universidade de Santiago de Compostela; (2) Departamento de Química Orgánica, Center for Research in Biological Chemistry and Molecular Materials, Universidade de Santiago de Compostela. The list of authors is presented below, by order and with their corresponding affiliations. The corresponding authors are marked with a *:

Pablo F. Garrido (1), Martín Calvelo (2), Alexandre Blanco-González (2), Uxía Veleiro (1), Fabián Suárez (1), Daniel Conde (2), Alfonso Cabezón (2), Ángel Piñeiro (1)*, Rebeca Garcia-Fandino (2)*.

According to the CRediT authorship contribution statement (Brand *et al.*, 2015), my contributions to this publication are: Writing - Review & Editing.

Garrido PF, Calvelo M, Blanco-González A, Veleiro U, Suárez F, Conde D, Cabezón A, Piñeiro Á, Garcia-Fandino R (2020a). The Lord of the NanoRings: Cyclodextrins and the battle against SARS-CoV-2. *Int. J. Pharm.*, **588**, 119689. ISSN 03785173. doi: 10.1016/j.ijpharm.2020.119689. URL https://www.doi.org/10.1016/j.ijpharm.2020.119689

USC UNIVERSIDADE DE SANTIAGO DE COMPOSTELA

USC
UNIVERSIDADE
DE SANTIAGO
DE COMPOSTELA

International Journal of Pharmaceutics 588 (2020) 119689

Contents lists available at ScienceDirect

International Journal of Pharmaceutics

journal homepage: www.elsevier.com/locate/ijpharm

The Lord of the NanoRings: Cyclodextrins and the battle against SARS-CoV-2

Pablo F. Garrido[a], Martín Calvelo[b], Alexandre Blanco-González[b], Uxía Veleiro[a], Fabián Suárez[a], Daniel Conde[b], Alfonso Cabezón[b], Ángel Piñeiro[a,*], Rebeca Garcia-Fandino[b,*]

[a] Departamento de Física Aplicada, Facultade de Física, Universidade de Santiago de Compostela, E-15782 Santiago de Compostela, Spain
[b] Departamento de Química Orgánica, Center for Research in Biological Chemistry and Molecular Materials, Universidade de Santiago de Compostela, Campus Vida s/n, E-15782 Santiago de Compostela, Spain

ARTICLE INFO

Dedicated to Prof. Thorsteinn Loftsson, one of the greatest Nanoring Lords, in his 70th birthday.

Keywords:
Cyclodextrins
Coronavirus
SARS-CoV-2
COVID-19
Rings

ABSTRACT

A handful of singular structures and laws can be observed in nature. They are not always evident but, once discovered, it seems obvious how to take advantage of them. In chemistry, the discovery of reproducible patterns stimulates the imagination to develop new functional materials and technological or medical applications. Two clear examples are helical structures at different levels in biological polymers as well as ring and spherical structures of different size and composition. Rings are intuitively observed as holes able to thread elongated structures. A large number of real and fictional stories have rings as inanimate protagonists. The design, development or just discovering of a special ring has often been taken as a symbol of power or success. Several examples are the Piscatory Ring wore by the Pope of the Catholic Church, the NBA Championship ring and the One Ring created by the Dark Lord Sauron in the epic story The Lord of the Rings. In this work, we reveal the power of another extremely powerful kind of rings to fight against the pandemic which is currently affecting the whole world. These rings are as small as ~1 nm of diameter and so versatile that they are able to participate in the attack of viruses, and specifically SARS-CoV-2, in a large range of different ways. This includes the encapsulation and transport of specific drugs, as adjuvants to stabilize proteins, vaccines or other molecules involved in the infection, as cholesterol trappers to destabilize the virus envelope, as carriers for RNA therapies, as direct antiviral drugs and even to rescue blood coagulation upon heparin treatment.

"*One ring to rule them all. One ring to find them. One ring to bring them all and in the darkness bind them.*" J. R. R. Tolkien.

1. Introduction

Cyclodextrins (CDs) are within the most powerful and versatile ring structures ever known. They could be considered as the molecular level equivalent of the mythical One Ring created in Middle-earth. In this analogy, Villiers played the role of the Dark Lord Sauron, by isolating these cyclic oligosaccharides from the reaction of the enzyme cyclodextrin glycosyltransferase with starch (Crini, 2014; Szente et al., 2016; Villiers, 1891). Later on, Schardinger, pioneer of CD chemistry, gave a detailed description on their preparation and separation (French, 1957). More recently, Kurkov and Loftsson (Kurkov and Loftsson, 2013) made relevant contributions to the Ring Community. Despite having been known for more than 120 years, CDs only really took off in the 1980s, when the industrial scale production led to their first applications in the pharmaceutical and food industries. Since then, these rings are amongst the most versatile/multi-functional molecules used in molecular research and chemical applications, playing a relevant role in different fields such as pharmacy, medicine, chemistry, materials design, food or agricultural science (Ain et al., 2015; Braga, 2019; Martin et al., 2018).

CD molecules are known to crystallize as truncated cones (Khan and Durakshan, 2013; Saokham and Loftsson, 2017), whose cavity size is determined by the number of glucopyranoside groups (GPUs): 6 (α-CD), 7 (β-CD) or 8 (γ-CD) (Fig. 1, top). In this conformation, all the secondary hydroxyl groups (attached to the C2 and C3 carbon atoms of the glucose units) are oriented toward the wide edge of the cavity (known as the head of the CD structure), whereas the primary hydroxyls form the narrow entry of the cavity. Such distribution of polar groups determines the specific physicochemical properties of these molecules, including their solubility and their ability to encapsulate hydrophobic groups in their cavity (Koźbiał and Gierycz, 2013). As a result, CDs are widely used to increase the solubility, to protect or to reduce the toxicity of a large variety of different molecules including drugs, dyes and surfactant agents. In order to optimize the applications of CDs, their

* Corresponding authors.
E-mail addresses: Angel.Pineiro@usc.es (Á. Piñeiro), rebeca.garcia.fandino@usc.es (R. Garcia-Fandino).

https://doi.org/10.1016/j.ijpharm.2020.119689
Received 29 May 2020; Received in revised form 19 July 2020; Accepted 21 July 2020
Available online 25 July 2020
0378-5173/ © 2020 Elsevier B.V. All rights reserved.

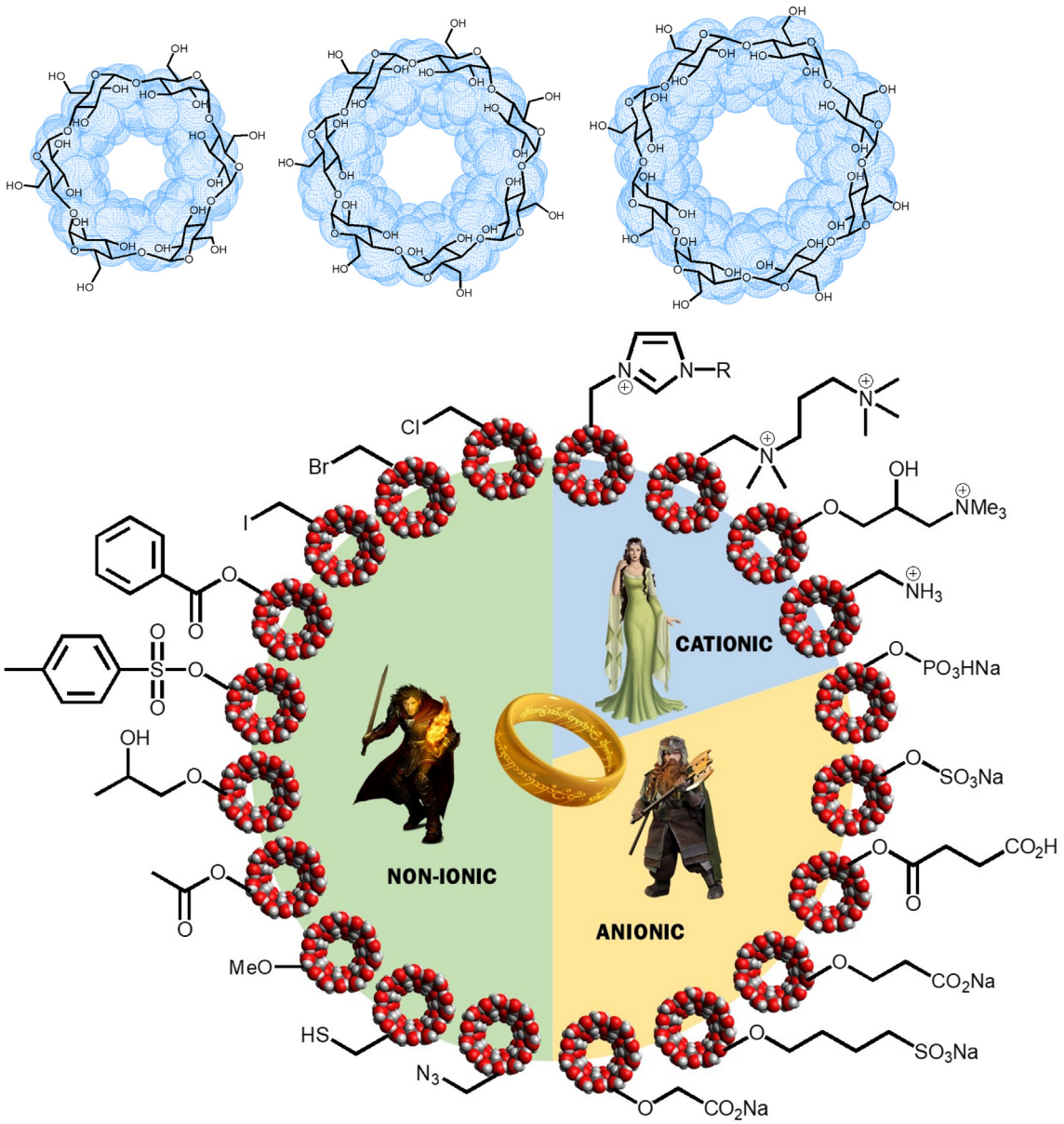


Fig. 1. Top: 2D and 3D structures of native α-, β- and γ-CDs. Bottom: General classification of the most common CD derivatives and a visual comparative with the three rings of power for the Elven-kings, the seven for the Dwarf-lords and the nine rings for Mortal Men, from Tolkien's novel.

hydroxyl groups are commonly substituted, leading to synthetic derivatives that can be divided in three main groups (Fig. 1, bottom): non-ionic, such as 2-hydroxypropyl-β-CD (HP-β-CD) or randomly methylated-β-cyclodextrin (RM-β-CD), cationic, such as permethylated propylenediamine-β-CD (PEMPDA-β-CD) and ionic, such as sulfobutylether-β-CD (SBE-β-CD) (Davis and Brewster, 2004).

CDs are biocompatible, they do not generate immune response and they also have low toxicity. Their successful use in inclusion complexes with bioactive compounds has allowed the development of commercially available formulations for oral, parenteral, nasal, pulmonary, and skin delivery of drugs (Adeoye and Cabral-Marques, 2017; Conceição et al., 2018; Lakkakula and Maçedo Krause, 2014; Loftsson, 2002; Loftsson and Brewster, 1996; Zhang and Ma, 2013). These features reveal the power of these versatile ring structures, and enable them, like the Hobbit Frodo Baggins' neck pendant, to be used as very powerful weapons in the crudest of battles, where viruses become enemies.

Severe acute respiratory syndrome coronavirus 2 (SARS-CoV-2) is a novel coronavirus that emerged towards the end of 2019 in Wuhan, Hubei Province (People's Republic of China) and is responsible for the coronavirus disease 2019 (COVID-19) global pandemic (Coelho Paraguassu et al., 2020). Coronaviruses are spherical-like capsules with a diameter of 80–120 nm enclosed by a lipid membrane with encrusted proteins –including the receptors employed to anchor target cells – that contain basically a single-stranded RNA chain (Fig. 2). They have been classified in 4 different lineages that are associated to different species: α-coronavirus, β-coronavirus, δ-coronavirus and γ-coronavirus (Chan et al., 2013). Prior to SARS-CoV-2, six coronaviruses were known to cause diseases in humans, including SARS-CoV and MERS-CoV (Zhu et al., 2020). Like them, SARS-CoV-2 is a β-coronavirus.

Coronaviruses recognize specific receptors in target cells through S proteins on their surface. In the case of SARS-CoV-2 and SARS-CoV the natural receptor is human angiotension-converting enzyme 2 (ACE2). Once the virus enters the cell, an acute infection takes place (Fig. 2). It has been reported, however, that some attack routes include host cells where the expression level of ACE2 is very low under normal conditions, like for example in the central nervous system (CNS), where they could induce neuronal injury (Baig et al., 2020; Li et al., 2020). This has been recently connected with the possible ability of the virus to use the

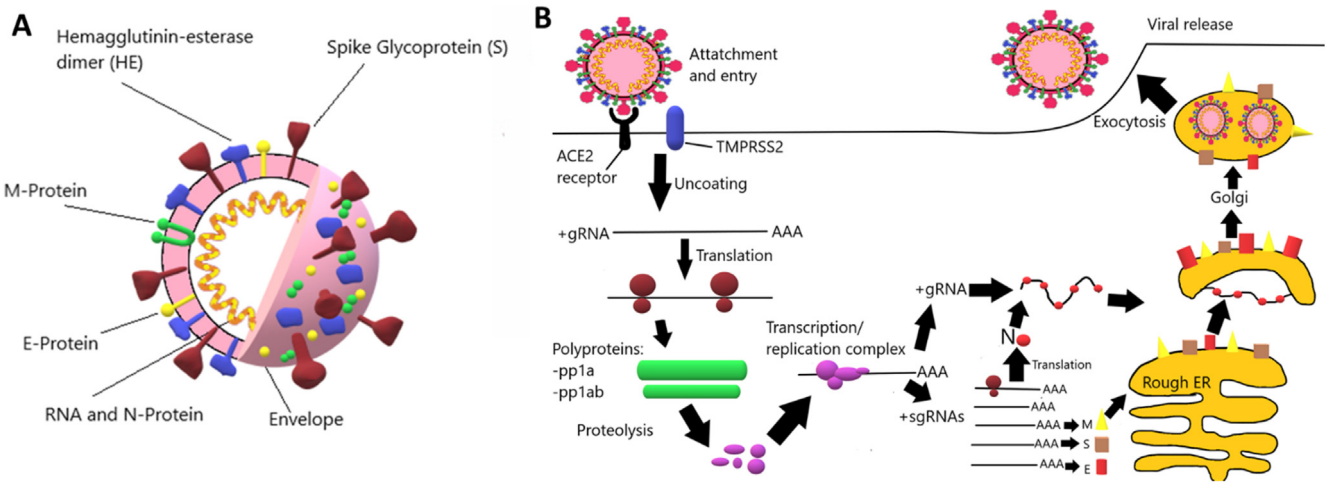


Fig. 2. A. Representative structure of SARS-COV-2. B. Proposed mode of action of SARS-COV-2 towards human cells.

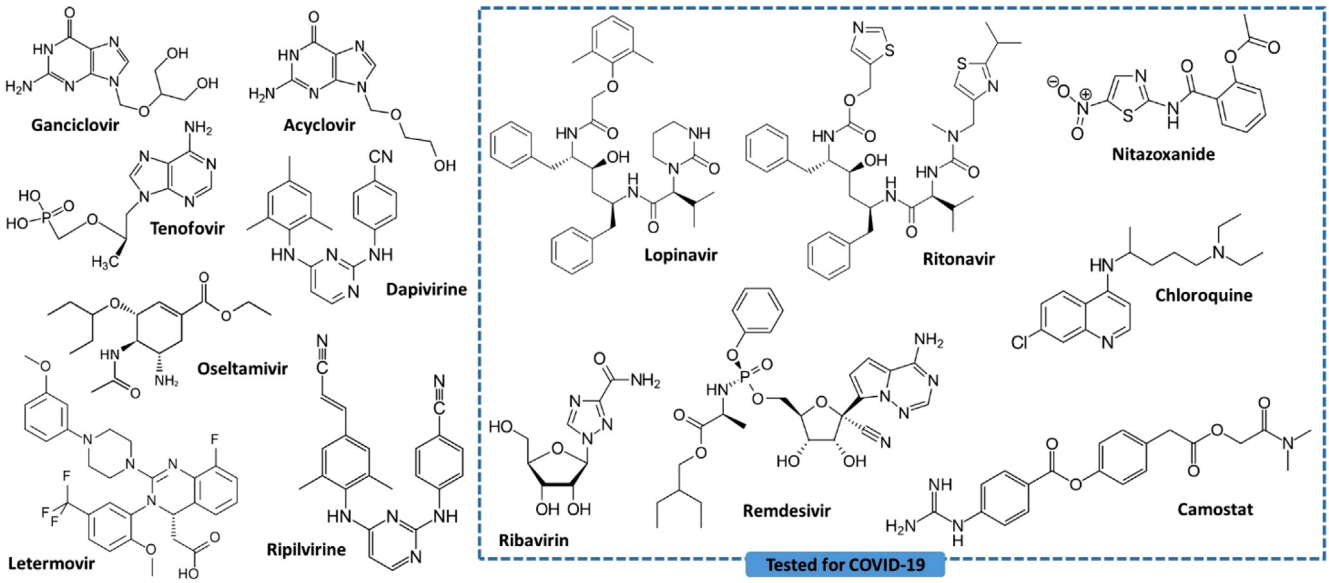


Fig. 3. 2D-structures of some antivirals that have been used in treatments for virus infections administrated with CDs as encapsulation agents. The molecules marked in the square have been tested in the treatment of COVID-19.

nicotinic acetylcholine receptor (nAChR) as an alternative anchor port to infect cells (Changeux et al., 2020). The most common symptoms of COVID-19 are similar to other coronavirus infections: fever (87.9%), cough (67.7%), fatigue (38.1%) and, to a less extent, diarrhea (3.7%) and vomiting (5.0%) (Guan et al., 2020). To date, no effective and specific therapeutic method can be used to treat patients suffering from SARS-CoV-2 infection. However, due to the high rate of infection and to the global reach of this pandemic, a number of new treatments arising from intensive research in many labs and companies along the world has emerged (Liu et al., 2020; Sanders et al., 2020).

Although it might appear, *a priori*, that in a war of such magnitude against highly-lethal-to-humans viral enemies, small cyclic and sugary molecules could be of little use, they are revealed as extremely powerful and versatile. In this review, we will analyze the different approaches that have been carried out using CDs till the end of May 2020, both in treatments for COVID-19 and in its containment and prevention. Since hundreds of research labs over the world are focused in this problem it is difficult not to miss some significant contributions, although we hope to include at least some of the most important. Additionally, it is expected that more applications of CDs related to this pandemic will arise at the short term.

1.1. The encapsulating Army: Cyclodextrins as excipients for antiviral drugs

Antivirals are drugs used to treat viral infections. Most antivirals are focused on the inhibition of the viral replication mechanism inside the organism, so they need to be both safe and effective to avoid damaging the host and get rid of the infection. While some antivirals are effective against many different viruses –the so called broad-spectrum antivirals– others only target specific viruses. Overall, antiviral administration is conditioned by their physicochemical properties, such as solubility, stability and permeability. The distribution and bioavailability of the drug can be optimized by using excipients, which can also be employed to reduce the dose of the antiviral needed to achieve an effective therapy. In this scenario, CDs can act as Trojan horses by hiding, protecting and slowly releasing pharmaceutical active principles in a hostile environment. Their cavity allows the encapsulation of hydrophobic groups forming inclusion complexes, without modifying the structure and the chemical properties of the guest. Alternative interaction mechanisms such as the formation of non-inclusion complexes or the solubilization through aggregates can also be present in CD solutions. The use of CDs as a drug-delivery platform for antivirals has been studied by many groups. In the present section, we will summarize the

role of native and modified CDs in formulations of heterogeneous antiviral treatments and then how they are used specifically in treatments of SARS-CoV-2.

1.1.1. Native Cyclodextrins in general antiviral formulations

Nicolazzi et al. reported the formation of inclusion complexes between **Ganciclovir** (GCV), an antiviral used specifically against human cytomegalovirus (HCMV), and β-CD (Fig. 3). In this case, the CD is employed to increase the poor solubility of the drug, as well as to facilitate its penetration in the organism. The comparison between CDs with rings of different diameter revealed that the middle-size structure (β-CD) is more appropriate for the encapsulation of this drug than the narrower α-CD and the wider γ-CD (Nicolazzi et al., 2001). GCV:β-CD inclusion complex provides an enhanced antiviral effect in different HCMV strains, even in those that developed a GCV resistance (Nicolazzi et al., 2002). The enhanced bioavailability of these inclusion complexes allows a reduction on the dose of GCV and, consequently, a reduction in the drug's toxicity. Another example is **Ribavirin** (RBV) (Fig. 3), an antiviral used in the treatment of human respiratory syncytial virus, also employed as an oral drug against hepatitis C, hemorrhagic fever virus infections or measles virus (MEV). The use of this drug is limited by its toxicity (Grancher et al., 2004), but its complexation with α-CD or β-CD lead to a five-fold or a two-fold decrease, respectively, in the 50% inhibitory concentration (IC_{50}) against both MEV strains. The antiviral activity of the complex RBV:α-CD was also demonstrated to be stronger than free ribavirin, in an *in vivo* model of measles virus (MV) encephalitis in mice, finding also a benefit of α-CD for drug delivery to the brain (Jeulin et al., 2009). Even when the action mechanism still needs to be elucidated, this animal model revealed the virological and pharmacological potential of α-CD as a drug carrier for central nervous system disorders. RBV has been tested as a therapeutic treatment for SARS-CoV and MERS-CoV patients, since it has been reported to inhibit the viral 3-chymotrypsin like protease, but no significant effect was observed (Zumla et al., 2016). CDs have occasionally been used to mask the bitter taste of some antivirals, such as **Oseltamivir** phosphate (an active ingredient of Tamiflu®) (Fig. 3), which is a neuraminidase inhibitor approved for the treatment of influenza virus (Sevukarajan et al., 2010). *In vitro* activity of this drug against SARS-CoV-2 has not been documented.

1.1.2. Modified Cyclodextrins in general antiviral formulations

Not only native CDs but also CD derivates have been studied as potential drug-delivery platforms to treat several viral diseases. For instance, HP-β-CD has been proved to be an effective excipient in the intravenous administration of **Letermovir**, an antiviral developed to deal with cytomegalovirus (CMV) in immunocompromised patients, such as transplant recipients or seropositive individuals (Fig. 3) (Erb-Zohar et al., 2017). The effectiveness of this formulation in phase III essays, without significant adverse events (Marty et al., 2017), lead to the approval of the treatment, now available as Prevymis™ Injection. HP-β-CD has also been reported as an effective platform for **Acyclovir** (ACV) oral delivery, a broad-spectrum antiviral used, for example, in herpes simplex (HSV) or varicella infections (Fig. 3). Nair et al. reported the formation of ACV:HP-β-CD inclusion complexes that increased the solubility of the antiviral, ensuring the dissolution of the drug in the aqueous media and its later absorption by the mucosal surface (Nair et al., 2014). Other CD-derivate platforms have been reported to enhance the solubility and bioavailability of ACV: Piperno et al. designed a platform based on β-CD/multiwalled carbon nanotubes (β-CD-MWCNT) that showed a sustained delivery of ACV and good results interfering with herpes simplex virus 1 (HSV-1) replication, higher than with the free drug (Iannazzo et al., 2014; Mazzaglia et al., 2018). Cavalli and her team characterized β-CD/poly(amidoamine) copolymers (Bencini et al., 2008), βCD-poly(4-acryloylmorpholine) nanoparticles (Cavalli et al., 2009) and carboxylated nanosponges (Lembo et al., 2013), as well as the effect of their use as ACV excipients. *In vitro* results were promising due to the absence of toxicity of both ACV and the CD-derivatives and to the enhanced antiviral effect shown. CD-based nanosponges have been also developed for the delivery of **Ripilvirine** (RPV), an antiretroviral drug used on the treatment of HIV (Fig. 3) (Rao et al., 2018). Nanosponges provided an enhanced bioavailability of RPV *in vitro* and *in vivo*, compared with the administration of free antiviral and RPV:β-CD and RPV:HP-β-CD complexes. Besides that, nanosponges' high zeta potential prevents the aggregation of the nanoparticles in aqueous solution, allowing the formation of stable dispersions in the media. CD-based nanosponges are a promising drug-delivery platform because of their ability to encapsulate both hydrophilic and lipophilic drugs. On the other hand, Notario-Pérez et al. (Notario-Pérez et al., 2020) synthesized mucoadhesive vaginal discs for the controlled release of HIV antiretroviral drugs, **Tenofovir** and **Dapivirine** (Fig. 3). The presence of CDs in freeze-dried hydroxypropylmethyl cellulose gels, allowed the controlled release of the drugs and also modified the mechanical properties of the formulation by improving its resistance as well as the adherence to the vaginal mucosa during enough time to the complete liberation of the antiviral drug.

1.1.3. Cyclodextrins in formulations against SARS-CoV-2

CDs have also been used to encapsulate possible antivirals attacking at different stages on viral lifecycle in the battle against COVID-19. **Nitazoxanide** (Fig. 3), traditionally an antiparasitic drug, has also demonstrated *in vitro* antiviral activity against MERS and SARS-CoV-2 (Padmanabhan, 2020). Its interaction with β-CD has been studied by different physicochemical methods, showing that it forms inclusion complexes with 1:1 stoichiometry (Radi et al., 2014). **Camostat mesylate** (Fig. 3), a pancreatitis agent approved in Japan, has shown to prevent nCoV cell entry *in vitro* through inhibition of the host serine protease (Hoffmann et al., 2020). Conflicting *in vitro* data are not able to determine if this drug has a detrimental or protective effect in the treatment for COVID-19. Supramolecular interactions studies with α-, β-, and γ-CD revealed a 1:1 stoichiometry for all the complexes formed (Kwon et al., 2009). The results also suggested that the cavity size of γ-CD, rather than those of a α- or β-CD, is required to accommodate the guanidine group. This study also showed a multimodal molecular encapsulation with this larger CD. The combination of **Lopinavir (LPV)/Ritonavir (RTV)**, approved for treating HIV, demonstrated *in vitro* activity against other novel coronaviruses via inhibition of 3-chymotrypsin-like protease (Fig. 3) (Sanders et al., 2020). The combination of CDs with these compounds is expected to handle their adverse effects. Based on phase solubility diagrams, Goyal and Vavia (Goyal and Vavia, 2012) found that γ-CD and HP-β-CD form 1:1 complexes with these drugs, so both CDs are expected to be well suited to work as excipients for them. This study also suggested that the presence of non-inclusion complexes could contribute to the considerable solubilisation enhancing of LPV. Recently, γ-CD with a high degree of 2-hydroxypropyl substitutions (HP17-γ-CD) proved to considerably increase the solubility of LPV (Adeoye et al., 2020). The preparation method of the complex has also been discussed, showing higher solubility improvement by supercritical assisted spray drying (SASD) compared with co-evaporation (CoEva). Very recently, a third active compound, interferon β-1b, was added to this cocktail with promising results (Hung et al., 2020). **Remdesivir (GS-5734)** (Fig. 3) has been brought up as a hopeful antiviral for treating Covid-19 (Wang et al., 2020a,b). This compound is relatively insoluble and chemically unstable in aqueous media. In order to increase its solubility, Gilead Inc. patented last 2019 a method for comprising Remdesivir, jointly dispensed with CDs (Larson, 2019). Remdesivir was first described to specifically treat the Ebola Virus Disease, but simultaneously presented as a broad spectrum antiviral (with potential to act *in vitro* against other pathogenic RNA viruses, including filoviruses, arenaviruses, and coronaviruses) (Warren et al., 2016). In this first study, the vehicle used for carrying the drug consisted already in a solution of 12% SBE-CD. Other clinical trials for SARS-CoV and MERS-CoV virus have explicitly mentioned the usage of

CDs as vehicle for Remdesivir (at the same percentage) (de Wit et al., 2020; Sheahan et al., 2020, 2017). They found that indeed this CD derivate is useful for an intravenous solution and showed how to prepare it. In this study, it was assumed a 1:1 complex, in agreement with the experimental observation that the drug solubility and the amount of CD are linearly dependent. It should also be remarked that upon addition of NaOH, the complex did not break, which was surprising, in their own words, as *increasing the pH can result in weakened or broken complexation.* SBE-β-CD can be used for parenteral administration of the drug, but it has been reported to exhibit physiological adverse effects on kidney. The antimalarial drug, **chloroquine** (Fig. 3) and its derivate, **hydroxychloroquine**, have been also been tested in the treatment of patients infected by SARS-CoV-2 (Gao et al., 2020; Touret and de Lamballerie, 2020). The enantioseparation of this racemic drug has been studied by several groups using CDs as chiral selectors, suggesting that the presence of carboxyl or sulphate functional groups on CD derivatives is advantageous for the resolution of chloroquine enantiomers (Németh et al., 2011). Despite being a hydrophilic drug, it was shown that both solubility and bioavailability of chloroquine diphosphate could be enhanced and some of its side effects reduced after encapsulation with CDs, in a 1:1 stoichiometry (ASHP, 2020; Roy et al., 2020). However, recent studies have suggested a limited efficacy of both drugs against COVID-19 (Geleris et al., 2020; Vinetz, 2020).

1.2. Collaborative weapons: Cyclodextrins as stabilizers or co-drugs

As it was shown with the Last Alliance of Elves and Men in response to the threat of conquest by the Dark Lord Sauron, unity makes strength, and that should be considered in any battle. Synergy between different combined compounds often results to be much more powerful than additive effect of different separate compounds. It has been shown that CDs can strengthen the effect of other molecules, including monoclonal antibodies as well as other proteins, peptides or even nucleotides, to enhance their activity in the combat against pathogenic agents (Fig. 4A). Therapeutic proteins are often combined with CDs in pharmaceutical formulations to stabilize their structure against denaturation and aggregation during storage and shipment (Castellanos et al., 2006; Fernández et al., 2004; Serno et al., 2011, 2010; Tavornvipas et al., 2004). Monoclonal antibodies directed against key inflammatory cytokines or other aspects of the immune response represent another potential class of adjunctive therapies for COVID-19. The rationale for their use is that the underlying pathophysiology of significant organ damage in the lungs and other organs is caused by an amplified immune response and cytokine release, or “cytokine storm”. (Mehta et al., 2020). More than 130 monoclonal antibodies have already been approved for clinical use. Moreover, a broad range of therapeutic antibodies are also undergoing clinical trials (Lu et al., 2020; Marichal-Gallardo and Álvarez, 2012). The main part of these formulations is administered parenterally. However, pulmonary route is a potential alternative for local and/or systemic delivery of proteins/peptides (Bodier-Montagutelli et al., 2018; Kane et al., 2013). There are several obstacles in the formulation of inhalable proteins or peptides including intrinsic instability and drug permeation across the nasal membrane (Bajracharya et al., 2019; Schüle et al., 2008). It has been demonstrated that HP-β-CD and β-CD have a marked effect in the stability and particle properties of spray-dried IgG. The type of excipients as well as its concentration in antibody formulation influenced yield, particle size, aerodynamic behavior and antibody stability. In particular, HP-β-CD not only enhanced aerosol performance of the powder, but also contributed to preserve the secondary structure of the protein and inhibited its aggregation during spray drying. Optimal particle property and antibody stability was obtained with proper combination of CDs and simple sugars, such as trehalose (Ramezani et al., 2017). Recent findings have also suggested that polypseudorotaxane hydrogels consisting of α- or γ-CD and PEG (mw 20,000 Da) markedly improved stabilities of human IgG against heating and shaking (Higashi et al., 2015), suggesting them as stabilizers for antibody drugs without changing their pharmacokinetics (Fig. 4B) (Higashi, 2019).

Based on early case series from China, it has been reported that interleukin 6 (IL-6) could be a key driver in the dysregulated inflammation caused by COVID-19 (Zhou et al., 2020). Thus, monoclonal antibodies against IL-6 could theoretically dampen this process and improve clinical outcomes. Some of the monoclonal antibody IL-6 receptor antagonists employed in COVID-19 treatments are **Tocilizumab** (Lauder et al., 2013; Xu et al., 2020) and **Sarilumab** (Sanofi, 2020). Other monoclonal antibody or immunomodulatory agents in clinical trials in China or available for expanded access in the US include **Bevacizumab** (anti–vascular endothelial growth factor medication; NCT04275414), **Eculizumab** (antibody inhibiting terminal complement; NCT04288713) and **Fingolimod** (immunomodulator approved for multiple sclerosis; NCT04280588). It was found that low amounts of Fingolimod in a free form, as a salt, or as a phosphate derivative could be stabilized for long periods of time, using CDs, for oral administration. The use of the CD in the formulation process permits the blending of the different ingredients (active substance and excipients) in such a way that a mixture of uniform particle size is obtained and thus an even distribution of the drug content in the final composition is ensured (Rane, 2017). Several companies such as Regeneron, Wuxi Biologics, CytoDyn and Vir Biotechnology are trying to speed up the development of neutralizing antibodies against coronavirus (Bloomberg, 2020; CytoDyn, 2020; Pharma Advancement, 2020; Regeneron, 2020), based on previous successful treatments that include monoclonal antibodies to specifically target other viruses. An advantage of this strategy is the associated long-term effects of the resulting treatment.

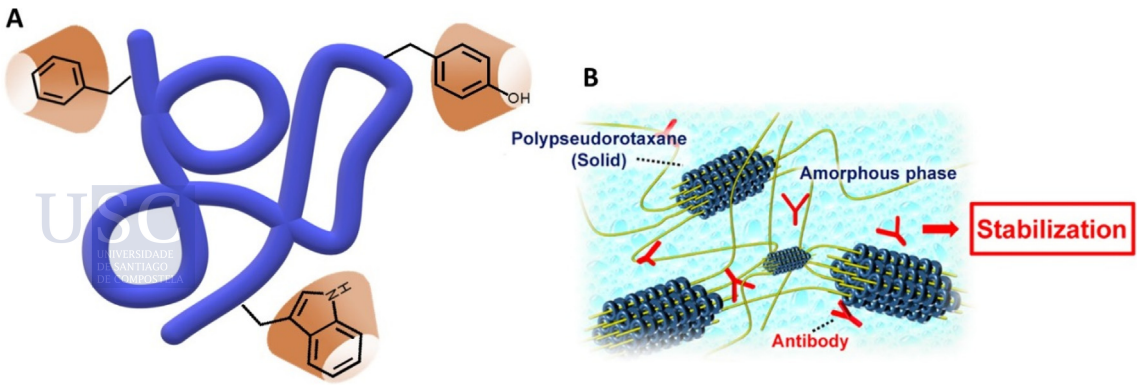


Fig. 4. A. Representation of CDs interacting with a protein; the classical inclusion involves aromatic aminoacids. B. Stabilization of Antibodies by Polypseudorotaxane Hydrogels (reproduced with permission from Yakugaku Zasshi, 139, 175–183. Copyright 2019. The Pharmaceutical Society of Japan) (Higashi et al., 2019).

On the other hand, interferons (IFNs) are a group of signaling proteins (De Andrea et al., 2002) made and released by host cells in response to the presence of different viruses. In a typical scenario, a virus-infected cell releases interferons causing nearby cells to heighten their anti-viral defenses. IFNs belong to the large class of proteins known as cytokines, molecules used for communication between cells to trigger the protective defenses of the immune system that help eradicate pathogens (Parkin and Cohen, 2001). Their name comes from their ability to "interfere" with viral replication by protecting cells from virus infections. IFN-α and IFN-β have been studied for nCoVs. IFN-β demonstrated significant activity against MERS (Morra et al., 2018; Stockman et al., 2006). β-CD (Miertus et al., 1999) and HP-β-CD (Del Curto, 2010) has been suggested to play a role in the stabilization of this protein. The eventual protection of IFNs, based on patients of COVID-19 taking them for other indications (Totura and Bavari, 2019), is not clear and some conflicts between *in vitro* and *in vivo* with animal data were found. As it was mentioned in the previous section, very recently, the combination of IFN-β with Lopinavir (LPV) and Ritonavir (RTV) showed promising results (Hung et al., 2020).

CDs are also proving to be extremely valuable in prevention against viral attacks on the mucous membranes in the mouth, throat and nose, which are the major source of SARS-CoV-2 exchange through expectorations and inhalation of particles from air. Some new generation mouth rinses could contribute to lower the viral load, thus preventing oral transmission. In particular, CDs have been combined with Citrox and then tested as therapeutic oral and/or nasal rinses with the aim to reduce viral load of saliva and nasopharyngeal microbiota, including potential SARS-CoV-2 carriage. Taking advantage of the vulnerability of the virus to oxidation, the use of oxidative amphiphilic CDs has also been proposed as a complementary strategy to reduce viral load in mucous membranes (Carrouel et al., 2020a,b).

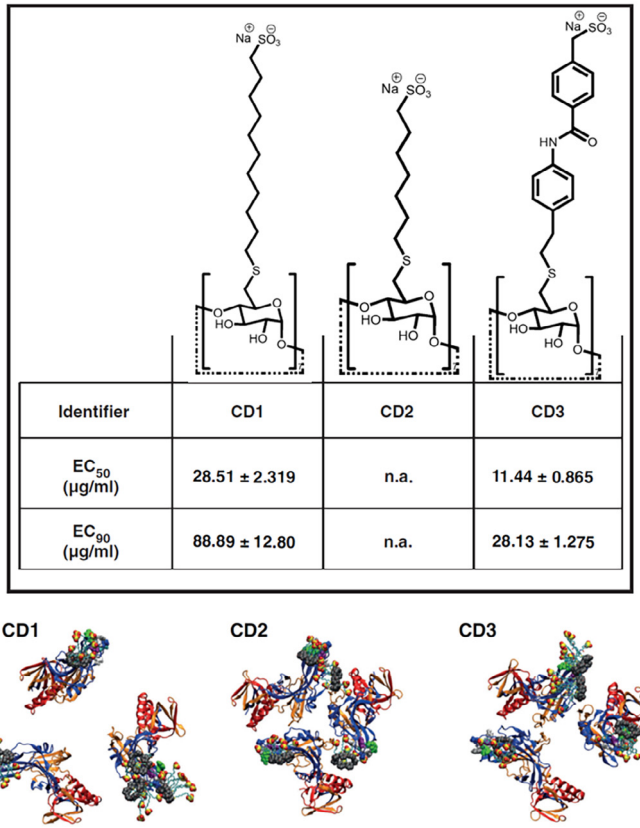
Recently, Sun et al. (2020) discussed the mechanism and production of CD-soluble angiotensin-converting enzyme 2 (CD-sACE2) inclusion compounds in the treatment of SARS-CoV-2 infections by blocking S-proteins. sACE2, the extracellular region of ACE2 retains the enzyme activity of ACE2 and can bind to the S-protein of SARS-CoV, being able to inhibit SARS-CoV infected cells. Since the infection mechanism of SARS-CoV and SARS-CoV-2 is basically the same, sACE2 could also inhibit the infection of SARS-CoV-2. The formation of a complex of CD and sACE2 could effectively improve the water solubility of sACE2 so it meets the requirements for drug atomization inhalation. The inclusion conjugates release sACE2 after entering the body via atomization or other drug delivery means, and the released sACE2 would combine with SARS-CoV-2 S-proteins to block the virus's ability to infect and destroy human cells.

1.3. Using the ring as a direct weapon: Modified cyclodextrins as antiviral drugs

Like the Ring coveted by the deranged bipolar Gollum, each CD is unique and has properties that make it different from the others. A given CD sequence, *i.e.* the type of substitution in every glucopyranoside unit and the number of such units, endows the entire structure with specific properties. Actually, the versatility of CDs relies on the possibility to introduce different chemical substitutions in the primary or secondary hydroxyl groups, as well as to control the ratio of substituted groups. It is possible to take advantage of this feature to transform CDs in powerful weapons against a variety of targets. It has been demonstrated that modified CDs can directly act as effective broad-spectrum antivirals. Thus, they can be potent weapons to fight multiple viral infections. S. T. Jones et al, synthesized very recently (Jones et al., 2020) several biocompatible sulfonated CDs that proved to be active against a large number of herpes simplex HS-dependent viruses (Fig. 5). These CDs are broad-spectrum virucidal, *i.e.*, they definitely destroy the virus, in contrast to virustatic agents that just block some of their action mechanisms. Additionally, they present a high barrier to viral resistance, they are biocompatible at μM concentrations and not cytotoxic. Several linkers were tested to join the sulfonic unit to the CD (Fig. 5) showing that its length and flexibility is key to provide virucidal activity. The known ability of CDs to extract cholesterol from membranes has also been proposed as an alternative viricidal action mechanism (*vide infra*). However, essays in a cholesterol rich medium highlighted that β-CD with a sulfonic group linked by an aliphatic chain of 11 carbon atoms (CD1) is antiviral in a cholesterol-independent manner. Molecular Dynamics simulations were carried out in order to determine the action mechanism of these modified CDs in the presence of glycoprotein B (gB) from HSV-2, suggesting that the CDs interacts with the binding loop of gB, producing a conformational change in the protein and thus rendering it unable to attack the host cell. The molecule has been patented and a spin-out company is being set up to continue pushing this new antiviral towards real-world use, but as far as we know it has not been tested towards SARS-CoV-2.

Another study, published prior to the COVID-19 pandemic, had already suggested different modified CDs as good antiviral candidates (Pan et al., 2015). Adenovirus was chosen as a model system due to its known resistance to a broad spectrum of antiviral drugs. Here, novel polycationic star polymers with polyhexamethylene guanidine hydrochloride (PHMG) have been demonstrated to possess excellent antimicrobial and virucidal activity, which can be modulated by modifications in the topological structure (*i.e.*, the arm number and the monomer ratio) of the composing copolymers (Fig. 6A). Plaque assay demonstrated that the star polymer inhibits the binding of adenovirus to its cellular receptor, then blocking the cell entry, with a virucidal efficiency of 96.3% at 50 ppm. Other action mechanisms, such as cholesterol depletion, were discarded since adenovirus lacks a lipid envelope. Cytotoxicity of these structures was assessed and found to be negligible under 50 ppm concentration. Other CD derivatives with antiviral activity include conjugate compounds of γ-CD with fullerenes –showing significant antiviral activity for influenza and twice as much for OSV (Zhu et al., 2018) or terpene derivatives (Tian et al., 2017; Xiao et al., 2016) On the side of the terpene derivatives, Sulong Xiao et al. studied a series of multivalent pentacyclic triterpene-CD conjugates displaying strong anti-influenza virus activity comparable and even higher than that of Oseltamivir with a low cytotoxicity (Fig. 6B) (Xiao et al., 2016). Multiple pentacyclic triterpenes were grafted to the primary face of α-, β- and γ-CD scaffolds. They show high affinity to influenza HA protein, disrupting the interaction of hemagglutinin (a protein of the virus surface) with the sialic acid receptor and thus the attachment of viruses to host cells. A strong correlation between both the nature of the CD and the terpene and the virucidal properties was found. Too large or too small CD ring cavities were found to cause an important decrease on activity, playing the number of ligands also an important role. The structures that proved to be the most effective against influenza virus were those based on β-CD with seven pentacyclic terpenes tethered to it, with a promising IC_{50} of 1.60 μM, whereas virucidal activty of the isolated ligand was only detected at concentrations above 100 μM. Cytotoxic assays showed that the range of concentrations for virucidal activity is far below the concentration that must be reached before any harmful effects start to take place in the cells (> 100 μM). This group also essayed a similar strategy but using per-O-methylated β-CD (Fig. 6B) (Tian et al., 2017) and, more recently, they also investigated β-CD-GA conjugates, in which a major constituent of the herb *Glycyrrhiza glabra* (Glycyrrhetinic acid), was covalently coupled to the primary face of β-CD using 1,2,3-triazole moiety along with varying lengths of linker. These structures provided promising results to be used as potential anti-influenza virus agents (Liang et al., 2019). All these new CDs are non-toxic against host cells and they show significant antiviral activity, but the data is still limited to *in vitro* studies and more research on these molecules is required to fully understand their practical utility.

Recently, we discuss the mechanism and production of cyclodextrin-soluble angiotensin-converting enzyme 2 (CD-sACE2) inclusion



Identifier	CD1	CD2	CD3
EC_{50} (μg/ml)	28.51 ± 2.319	n.a.	11.44 ± 0.865
EC_{90} (μg/ml)	88.89 ± 12.80	n.a.	28.13 ± 1.275

Table 1. Inhibitory activity of CD1 on different viruses. Results are mean of two independent experiments. n.a., not assessable.

	Virus	EC_{50} (μg/ml)	EC_{50} (μM)	CC_{50} (μg/ml)	SI
CD1	HSV-1	46.9	15.3	>300	>6.39
	HSV-2	26.4	8.61	>300	>11.4
	HSV-2 R ACV^R	19.8	6.46	>300	>15.2
	HSV-2 clinical	34.3	11.2	>300	>8.74
	RSV-A	9.11	2.99	>300	>32.9
	RSV-B	5.48	1.79	>300	>54.7
	HMPV	0.613	0.201	>300	>489
	PIV3	1.198	0.394	>300	>250
	HIV	10.19*	3.35	>300	>29.4
	DENV-2	14.1	4.63	>300	>21.3
	ZIKV	0.61	0.200	>300	>492
	HCV	3.88	1.27	>300	>77.3
	HCV Y93H	6.26	2.04	>300	>47.9
	HCV D168A	2.87	0.939	>300	>105
	EV-D68	n.a.	n.a.	>300	>n.a.
	H3N2	n.a.	n.a.	>300	>n.a.
Captisol	All viruses	n.a.	n.a.	>300	>n.a.

*The experiment was conducted on a surrogate model of infection.

Fig. 5. Structures of modified CDs and relative effective concentrations of inhibition of HSV-2 growth. Representative snapshots of the modified CDs interacting with HSV-2 gB proteins after 50 ns of Molecular Dynamics simulations. Reproduced (with corrections over the original) with permission from Science Advances, 6, 5, eaax9318. © The Authors, some rights reserved; exclusive licensee American Association for the Advancement of Science. Distributed under a Creative Commons Attribution NonCommercial License 4.0 (CC BY-NC) http://creativecommons.org/licenses/by-nc/4.0/ (Jones et al., 2020).

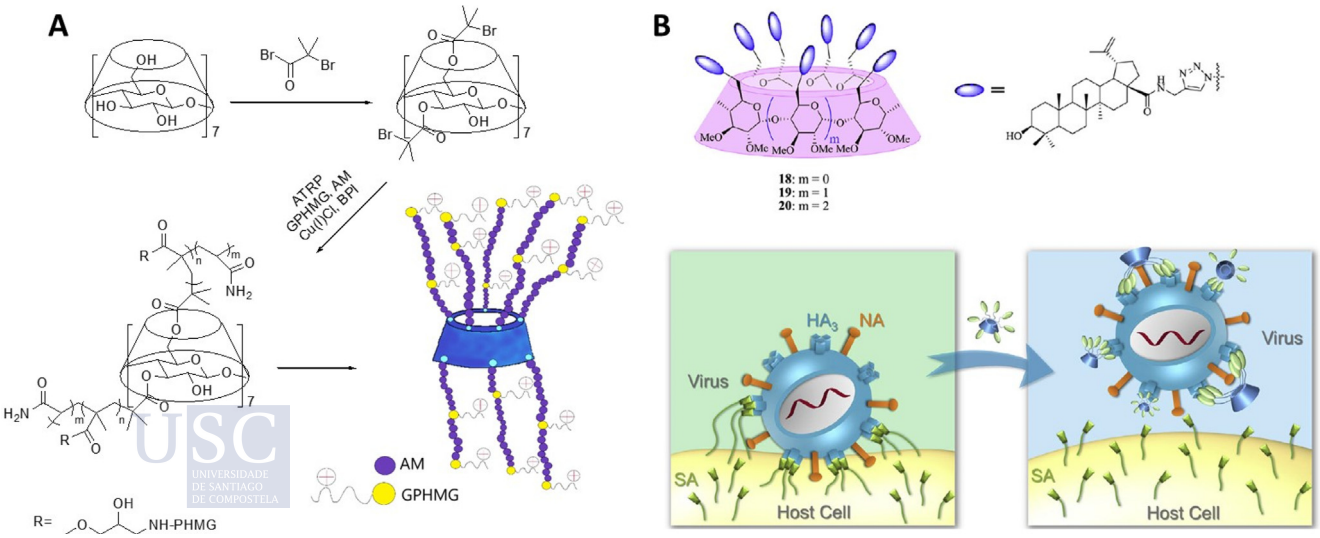


Fig. 6. A. Novel star-like polymers used for deactivating bacteria and viruses. Adapted from (Pan et al., 2015). B. Top: Multivalent pentacyclic triterpene-CD conjugates (using per-O-methylated β-CD) displaying strong anti-influenza virus activity. Reproduced with permission from European Journal of Medicinal Chemistry, 134, 133-139. Copyright 2017. Elsevier. (Tian et al., 2017). Down: Proposed mechanism for multivalent pentacyclic triterpene-functionalized per-O-methylated CD conjugates mediated blocking of influenza virus entry, wherein the multivalent pentacyclic-triterpenes tightly bind to viral homotrimeric HA protein, thus disrupting the attachment of viruses to host cells. Reproduced with permission from European Journal of Medicinal Chemistry, 134, 133-139. Copyright 2017. Elsevier. (Tian et al., 2017).

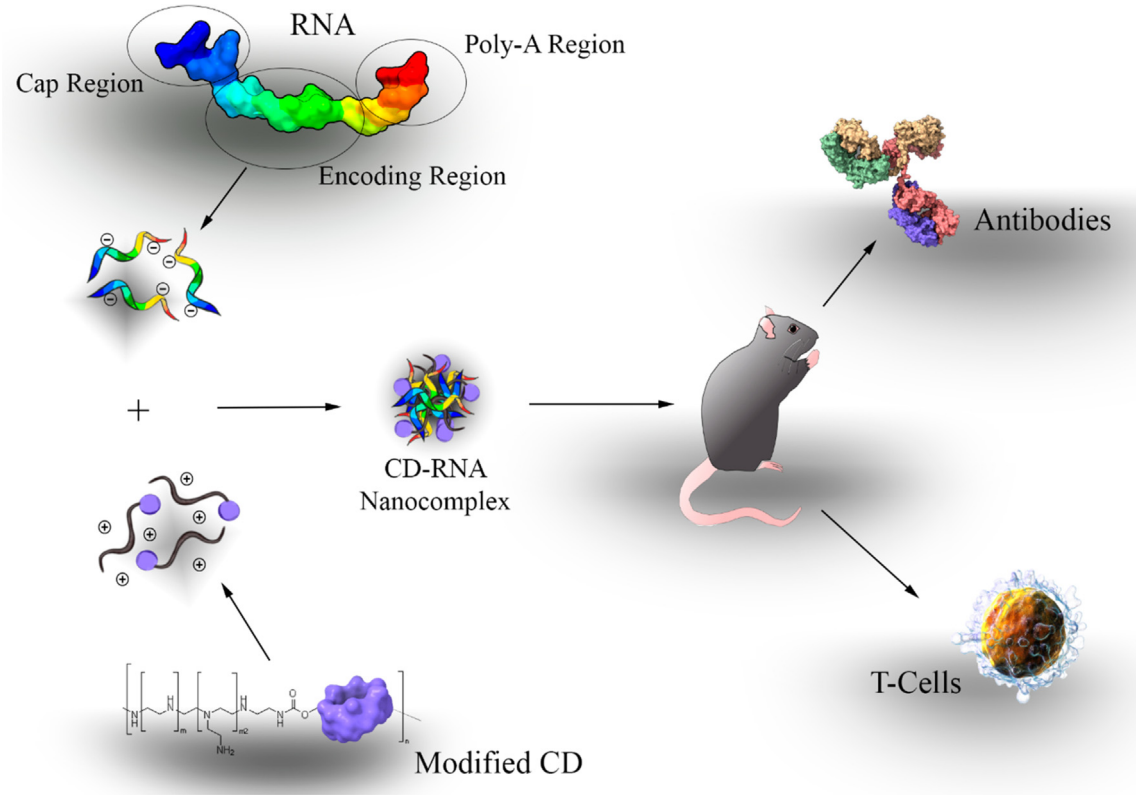


Fig. 7. Scheme of a CD-based mRNA vaccine platform, with an optimized mRNA structure and administrated in a most appropriate route. Adapted from (Tan et al., 2020).

compounds in the treatment of SARS-CoV-2 infections by blocking S-proteins. On the basis of the current research evidence, we believe that CD-sACE2 inclusion compounds have the potential to treat COVID-19.

1.4. Sentinels to prevent invasions: Cyclodextrins in antiviral vaccines

The production of stable vaccines for COVID-19 is a global urgency, with a large number of initiatives in progress since the release of the 2019-nCoV genetic sequence in early January 2020. Most projects are based on non-living subunits and mRNA technologies, which require efficient, stable and safe adjuvant components to stimulate immunity (Fig. 7). Intranasal vaccination with inactivated viral antigens is an attractive and valid alternative to currently available influenza (flu) vaccines. T. Kusakabe et al. examined whether HP-β-CD could act as a mucosal adjuvant for this treatment (Kusakabe et al., 2016). HP-β-CD seems to prevent the production of active immunoglobulins E (IgE), which can lead to autoimmunity; in contrast to classical adjuvants such as alum, which is well known to cause this problem. Thus, the use of HP-β-CD reduces the risk of inducing allergic IgE responses. Nevertheless, injection of HP-β-CD can also provoke some acute inflammation in lymphatic nodes but no systemic cytokine response was observed after injection in mice (Onishi et al., 2015). HP-β-CD also induced dendritic cells maturation and its subsequent activation of the T cells. It augmented the antigen-specific IgG in the blood. HP-β-CD predominantly induced IgG1 but not IgG2, indicating preferential enhancement of Th2 responses rather than Th1 responses. Type 2 T-helper (Th2) cell response, enhances antigen (vaccine)-specific antibody titers, maintains a longer immune response and induces the maturation of dendritic cells vital for a long lasting effective immune response (Kim et al., 2016; Onishi et al., 2015). HP-β-CD was selected because it has proved to be highly biocompatible. A common influenza vaccine containing 30% of HP-β-CD as adjuvant increased in the production of antibodies and produced a 100% survival rate in mice challenged with a lethal dose of influenza virus. The response produced by the vaccine takes place in every part of the body and does not remain localised at the administration site (Kim et al., 2016). It was also found that intranasal or subcutaneous administration of HP-β-CD increased the immunogenicity of influenza vaccines. HP-β-CD seems to be appropriate as a mucosal adjuvant because it induces antigen-specific IgA and IgG in the airway mucosal tissues as well as in the blood.

Vaccine compositions comprising inactivated poliovirus in combination with CDs, both natural and derivatized, wherein the CDs thereof protects and preserves the antigenicity and/or immunogenicity of inactivated poliovirus, especially in presence of thiomersal has also been patented (Chacornac et al., 2016). The authors have unexpectedly found that CDs are capable of minimizing the degradation of IPV (Inactivated Polio Vaccine or Virus) in presence of thiomersal, in particular in the situations described above. Whereas CDs have a wide range of applications in different areas of drug delivery and pharmaceutical industry, they have never been reported as protectant of IPV antigenicity and/or immunogenicity. More particularly, the inventors observed that CDs are capable of minimizing the loss of D-antigen titer of IPV blended to a composition comprising thiomersal and alum. The composition comprises at least one type of CD, preferably γ-CD or β-CD and hydroxypropyl, hydroxyethyl, glucosyl, maltosyl or maltotriosyl CD derivatives.

Based on this precedents, some researchers suggest the potential application of HP-β-CD as an adjuvant in developing successful vaccines for 2019-nCoV prevention (Roquette, 2020). Daiichi Sankyo is already conducting a Phase I clinical trial in Japan for their HP-β-CD adjuvanted influenza split vaccine Cyclodextrin News, 2018), which started in October 2017 and it can be the first CD-adjuvated vaccine.

1.5. Trying to break the enemy's borders: Cyclodextrins as cholesterol trappers to damage the viral capsid membrane

Lipid membranes are key structural part of many viruses, including SARS-CoV-2. Their main functions are to encapsulate the genetic material and also to interact with the environment through a number of partially-embedded partially-protruding proteins. The disruption of this membrane definitely destroys the virus. The presence of lipid rafts in such membranes is also though to play an important role in the virus life cycle (Li et al., 2007; Lorizate and Kräusslich, 2011; Mazzon and Mercer, 2014; Nayak and Hui, 2004; Ono and Freed, 2005; Schmitt and Lamb, 2005). Cholesterol, which is known to participate in the integrity and fluidity of bilayers, is one of the main components of these lipids rafts (Krause and Regen, 2014). Several diseases, such as Alzheimer, cancer, and atherosclerosis, have been related to the presence of cholesterol and other sterol derivatives in biological membranes (Anderson et al., 2020; Taylor and Hooper, 2007). The fluidity of membranes is a key point in the interaction between viruses and cells (Yang et al., 2016). Zawada et al. found that Influenza virions are enriched in cholesterol with respect to healthy cell membranes (Zawada et al., 2016). Additionally, they proposed that whereas this process is sensitive to concentration, it is not dependent on sterol identity for any of the sterols that they tested. Other studies revealed the requirement for cholesterol in liposomes for the fusion of Influenza virus (Nussbaum et al., 1992), as well as the clear effect of such molecule in the kinetics of this process (Domanska et al., 2013).

CDs have shown to be able to effectively extract and encapsulate cholesterol from lipid membranes (Crini, 2014; Leclercq, 2016; Mahammad and Parmryd, 2015; Nishijo et al., 2003; Zidovetzki and Levitan, 2007). A large evidence and quantitative analysis of cholesterol trapping by different CD derivatives has been carried out during the last two decades by different experimental and theoretical methods. It was concluded that β-CDs are more prone to encapsulate sterol molecules than α-CD and γ-CD (Ohtani et al., 1989; Ohvo and Slotte, 1996). Although this selectivity has been attributed to the differences in the cavity size, it is important to note that the inner cavity of a single β-CD is too narrow (diameter of ~8 Å) for totally host a cholesterol molecule (~18 Å wide). This fact, together with a quantitative thermodynamic analysis, suggests that two stacked β-CDs are required to encapsulate this molecule (Tsamaloukas et al., 2005). Another important parameter to take into account for an effective trapping is the water solubility of the CD itself (Davis and Brewster, 2004). The solubility of native β-CD is relatively low (about one order of magnitude lower than that of α-CD and β-CD). In order to increase it, a number of β-CD derivatives have been synthesized introducing different chemical modifications in the hydroxyl groups at positions 2, 3 and 6 or the glucopyranoside units. HP-β-CD and Me-β-CDs are probably the most used in cell biology studies (Uekama, 2004). Me-β-CDs has shown to be more efficient than HP and tetradecasulfated-β-CDs to encapsulate cholesterol (Atger et al., 1997; Christian et al., 1999, 1997; Kilsdonk et al., 1995). The extraction of cholesterol from lipid bilayers has also been simulated by Coarse-Grained Molecular Dynamics simulations using a constrained Me-β-CD dimer (Lopez et al., 2013; López et al., 2011) (Fig. 8B).

Taking advantage of such cholesterol trapping capabilities and considering the excess of cholesterol in viral envelopes with respect to healthy cells, the use of β-CD derivatives to treat viral infections has been suggested (Braga, 2019). It has been recently demonstrated that randomly methylated β-CDs (RAMEB) are able to reduce the infectivity of viral particles of influenza A (H1N1 strain) by cholesterol depletion (Sun and Whittaker, 2003; Verma et al., 2018). The proposed mechanism (Fig. 8A) is that the extraction of cholesterol by CDs from the lipid rafts lead to the structural deformation of the viral membrane, being even possible to form holes (Barman and Nayak, 2007).

Me-β-CDs have also been used to inhibit the attachment of coronaviruses to host cells, again via cholesterol depletion (Guo et al., 2017). Moreover, Choi et al. have shown that this CD provides good activity in the treatment of murine coronavirus (Choi et al., 2005). In this case, the use of the CD does not affect the virus binding, but it is able to reduce the virus entry and the cell–cell fusion by reducing the amount of cholesterol present in the membrane. The efficiency of Me-β-CDs against coronavirus, influenza A, and canine coronavirus infections have been also probed in Vero E6 cell lines following the same mechanism (Lorizate and Kräusslich, 2011; Lu et al., 2008). Furthermore, Tang et al. have highlighted the role of the cholesterol in the Parainfluenza Virus Type 3, observing a markedly reduction in the infectivity of this virus again via the elimination of cholesterol by Me-β-CDs (Tang et al., 2019).

The importance of the cholesterol in the initial steps of SARS-CoV infection has already been proved (Glende et al., 2008; Meher et al., 2019). Additionally, very recently it has been found an abnormally low cholesterol concentration in serum among patients with COVID-19 infection, claiming again that it is playing a significant role (Hu et al., 2020). The use of CDs for the treatment of viral infections, trying to use their cholesterol depletion capabilities in order to inhibit the virus contagion, is becoming increasingly popular (Baglivo et al., 2020). HIV and hepatitis C have been successfully treated in this way already for a long time, reaching almost complete abolishment of infectivity by HIV-1 virions (Graham et al., 2003; Guyader et al., 2002; Sagan et al., 2006; Tang et al., 2012). The ability of these CDs to reduce viral infectivity has also been demonstrated against human metapneumovirus (HMPV) (Chen et al., 2019), herpes simplex virus 1 (HSV-1) (Wudiri et al., 2017; Wudiri and Nicola, 2017), varicella-zooster virus (VZV) (Hambleton et al., 2007) and a less common one, the Newcastle disease virus (NDV) (Cantín et al., 2007; Martín et al., 2012).

Other formulations have also been proposed, as the one developed recently by ASDERA (Advanced Statistics for Drug and Diet Exploration, Repurposing, and Approval). They suggest the use of an intestinally absorbed oral α-CDs against SARS-CoV-2, reducing the serum phospholipids by "intermittent fasting mimetic" (ASDERA, 2020).

In summary, given the significant influence of cholesterol in virus infections, the use of molecules able to specifically target it represent promising weapons against pandemic diseases like COVID-19. Under this panorama, CDs have been confirmed as well suited candidates for this challenge.

1.6. Intercepting messages of the enemy: Cyclodextrins in RNA therapies

RNA interference (RNAi) was proposed in the late 1990s as a method to silence pathogenic gene targets, including viral RNA. This technique consists in using small complementary RNA duplexes to target and neutralize specific mRNA molecules with identical sequence to specifically inhibit gene expression or genetic translation. Preliminary studies with SARS-CoV demonstrated the feasibility of developing siRNAs as effective anti-SARS drugs (Chang and Hu, 2006; Shi et al., 2005; Wang et al., 2004; Zhang et al., 2004). More than thirty patents describing the use of RNAi for therapeutic treatment of SARS can be found in the CAS content collection, including siRNA molecules, antisense oligonucleotides, RNA aptamers, microRNA inhibitors and even ribozyme (Liu et al., 2020). Some of these patents propose siRNAs Targeting Coronavirus Proteins M, N, or E, or the Replicase and RNA Polymerase Region.

The most important limitation in the use of this technology is the delivery of the RNA-drug to reach the cytoplasm of the target cell maintaining its integrity, since siRNA is highly unstable (half-life $<$ 1 h in human plasma). CDs are well suited to help in this task due to their very low toxicity and versatility to include different chemical modifications (Chaturvedi et al., 2011; Evenou et al., 2018; O'Mahony et al., 2013). CDs have been specifically grafted to self-assemble in the presence of nucleotides thus encapsulating and so protecting them from degradation (Mellet et al., 2011; Sallas and Darcy, 2008). For this aim,

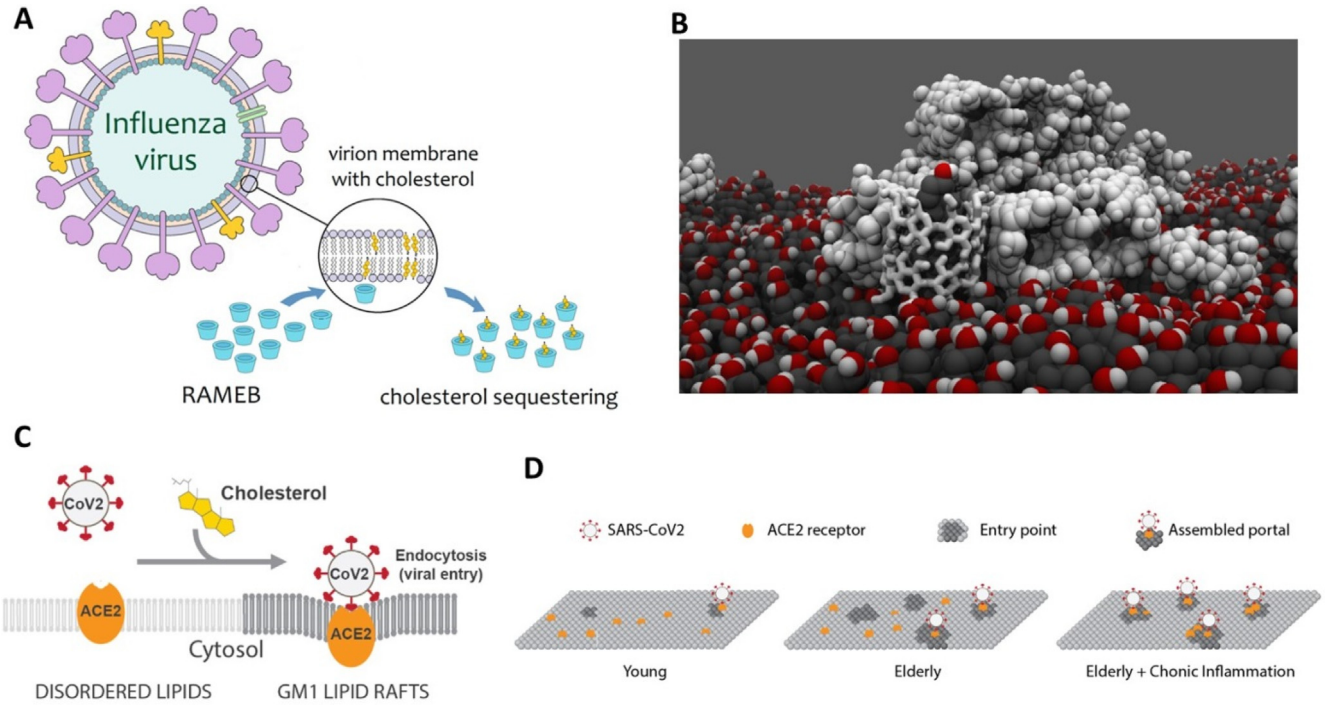


Fig. 8. A. Schematic representation of the mode of action proposed for the RAMEB against influenza viral particles. RAMEB sequesters membrane cholesterol, resulting in damage to the integrity of the viral envelope. Reproduced from (Braga, 2019) under Creative Common CC BY license. B. Proposed model for CD-mediated cholesterol extraction from lipid model membranes, based on Molecular Dynamics simulations: Reproduced from (López et al., 2011) under Creative Commons Attribution License. C. Proposed model for infectivity in SARS-CoV-2 in presence of cholesterol (lipid rafts) and with age and chronic disease (D). When cholesterol is low there are very few entry points and their diameter is small (similar to children). With age, average cholesterol levels in the tissue increase, thereby increasing the number and size of viral entry points (similar to adults). Reproduced from (Wang et al., 2020a), under CC-BY-NC-ND 4.0 International license.

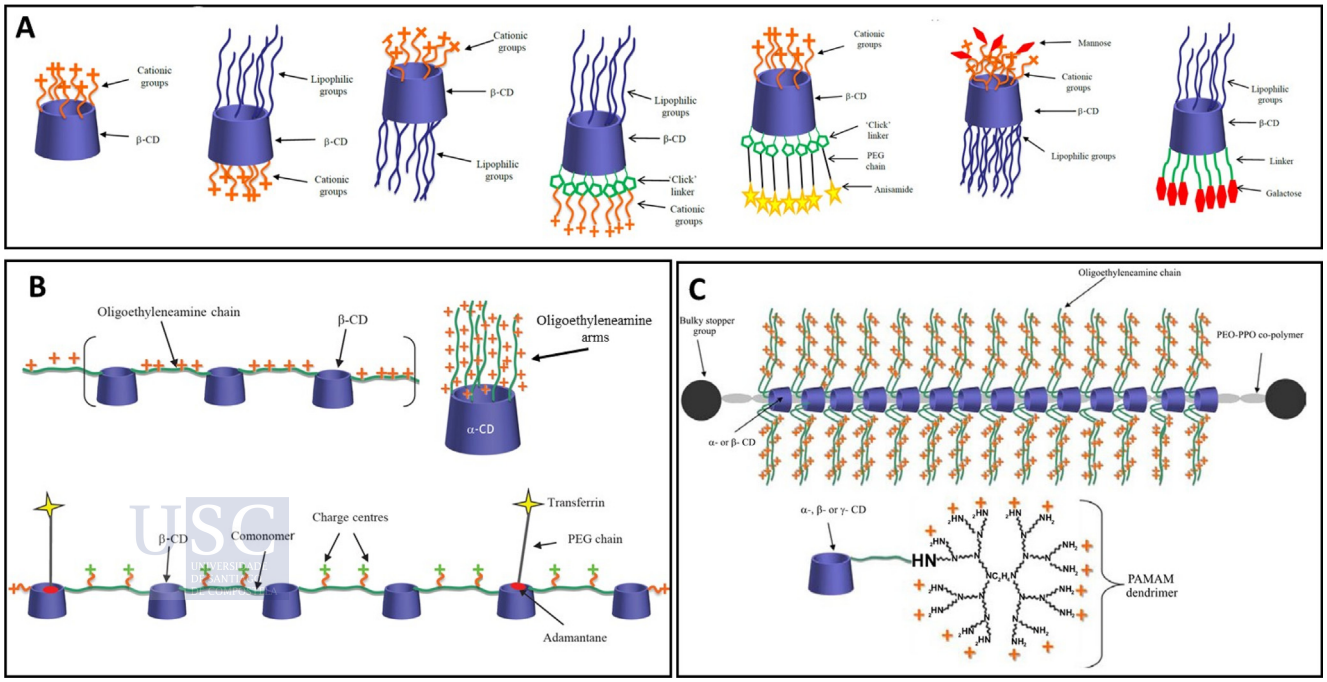


Fig. 9. A. Examples of functionalised CD gene and siRNA delivery vectors. B. Schematic representations of various CD-containing polymers. C. Cationic polyrotaxanes consisting of oligoethylenimine-conjugated CDs threaded onto co-polymers of poly(propylene oxide) (PPO) and poly(ethylene oxide) (PEO). CDs conjugated to PAMAM dendrimers. Figures reproduced with permission from Pharmaceutical Nanotechnology, 1, 6–14. Copyright 2013. Bentham Science Publishers Ltd. (M. O'Mahony et al., 2013).

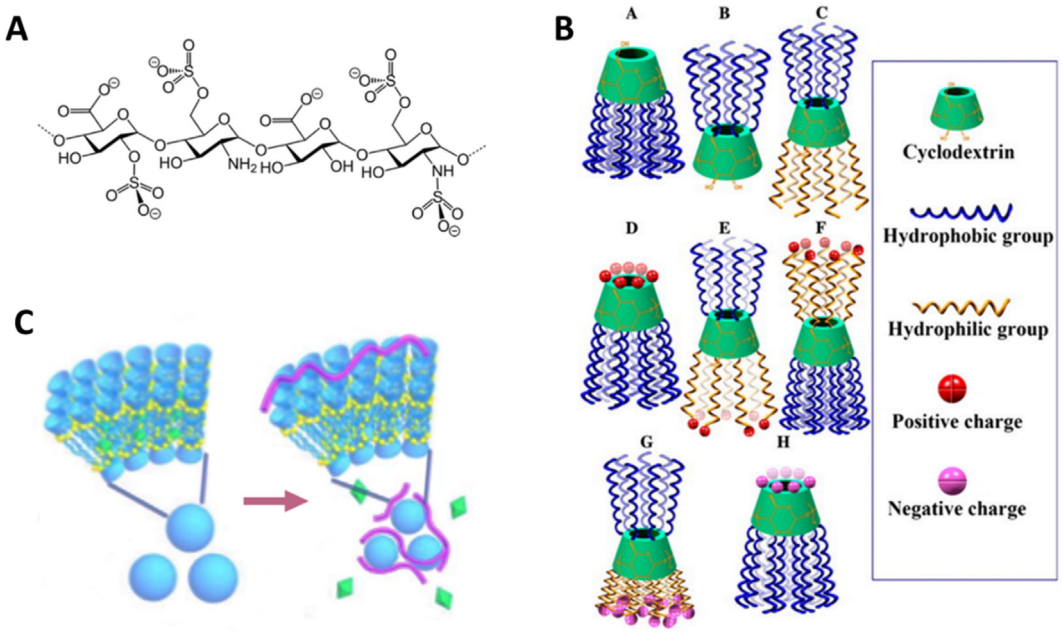


Fig. 10. A. Heparin 2D structure. B. Examples of various amphiphilic CDs. Neutral (A,B,C), positively (D,E,F) and negatively (G,H) charged, reproduced with permission from Advanced Drug Delivery Reviews, 65, 1215–1233. Copyright 2013. Elsevier (Zhang and Ma, 2013). C. Representation of a co-assembly of amphiphilic multi-charged CDs and vitamin K (represented as green octahedrons). After de arrow, heparin (pink wires) capture and vitamin K releasing process, reproduced with permission from Chemical Communications, 55, 11790–11793. Copyright 2019. Royal Society of Chemistry (Li et al., 2019).

cationic modifications in CDs showed to be well suited since DNA and siRNA are negatively charged, so the predominant interaction is through complementary electrostatic charges (Guo et al., 2010). (Fig. 9A) The additional introduction of hydrophobic groups lead to liquid-crystalline structures which can also be used as gene delivery vectors (Cryan et al., 2004). CDs can also be part of the delivery system to modify its properties. For instance, they have been incorporated to the backbone of polymers (Davis, 2009), appended to pre-existing polymeric or dendrimeric vectors (Fig. 9B) (Arima and Motoyama, 2009; Ping et al., 2011), or in polyrotaxane systems (Fig. 9C) (Li et al., 2006; Yang et al., 2009).

Antisense oligonucleotides are promising agents to treat viral infections due to their high specificity against particular species or strains (Agrawal, 1996). However, their therapeutic use is limited by their susceptibility to be degraded by nucleases before reaching their target, although this can be partially avoided by modifying their saccharide backbone. By incorporating β-CD as encapsulating agent in the formulation, a system containing a phosphodiester oligo directed toward the initiation region of the mRNA coding for the spike protein and containing the intergenic consensus sequence of an enteric coronavirus was designed (Abdou et al., 1997). CDs proved to increase the stability of the oligo, by protecting it from degradation. Antisense oligonucleotides have been developed not only for treatment and/or prevention of SARS virus but also for diagnosis purposes. Hybrid DNA/RNA antisense oligonucleotides have been designed to disrupt the pseudoknot in the frameshift site of the SARS coronavirus RNA (Crooke et al., 2008). Other antisense oligonucleotides have been proposed to target proteins involved in inflammatory processes caused by viruses (Liu et al., 2020).

1.7. Blood on the battlefield: Cyclodextrins as anticoagulant agents

A large range of symptoms have been reported for COVID-19. Coagulopathy and disseminated intravascular coagulation were reported to appear in most of deaths (Tang et al., 2020). Anticoagulant or blood thinner factors such as heparin, have been recommended for critically ill patients, although their efficacy has not been validated yet (Song et al., 2020). Low molecular weight heparins (LMWHs) (Fig. 10) are considered to be as effective as unfractionated heparin (UFH) to treat deep vein thrombosis and pulmonary embolism, and it is safer since they provoke a lower immune sensitization (Shulman, 2000). In the same line as other antiviral drugs and vaccines, nasal delivery of these anticoagulant factors has been proposed. In general, this method proved to act quicker than standard subcutaneous administration but in the case of LMWHs, their structural and physicochemical properties (still relatively high molecular weight of ~5000 Da, hydrophilicity and strong negative surface charge) require the assistance of an absorption promoter (Arnold et al., 2002). As stated above, CDs are well suited for this end. In particular, dimethyl-beta-cyclodextrin (DM-β–CD) proved to be highly efficient to enhance absorption of LMWHs both *in vitro* and *in vivo*. The action mechanism seems to be the opening of the tight junctions between cells (Yang et al., 2004).

Controversially, CDs have been proposed and tested as heparin antidotes in a recent patent (Meijers et al., 2019). The employed CD includes at least one -S-(Cn-alkylene)-R substituent and it is intended to reverse the effect of anticoagulant agents. These CDs have also been proposed as sensors to detect heparin levels or as heparin traps to reverse surgical procedures, in a similar way Sugammadex (a modified CD that includes eight carboxyl thio ether substituted groups in a γ-CD scaffold) is widely employed to reverse neuromuscular blockade induced by several drugs in general anesthesia (Cyclolab, n.d.). Alveron Pharma is currently running a clinical study with modified CDs that promote blood coagulation by reversing the effect of blood thinners. The advantage of these CDs is that they restore coagulation independently of the type of anticoagulant used, so they are considered as universal coagulants (Thuja Capital, 2019).

New amphiphilic multi-charged CDs (AMCD) have recently been developed to work as anti-heparin coagulants (Fig. 10). Their action mechanism seems to be the assembly around UFH or LMWHs to neutralize their blood-thinner effect. A formulation consisting of AMCD and vitamin K (VK) has also been proposed to simultaneously correct VK deficiency in hemodialysis patients at the same time that heparin is neutralized by the CDs (Li et al., 2019).

In summary, several modified CDs are well suited as highly efficient coagulation restoring factors. A number of proposals have already been developed to this aim and more research is in progress in this field.

2. Conclusions

Making a comparison between CDs and the unique Ring of the legendary novel of *The Lord of the Rings*, J. R. R. Tolkien, the presence of these molecules in different treatments of COVID-19 have been reviewed. Their applications as encapsulating agents for antiviral drugs, as adjuvants to stabilize proteins or other molecules involved in the infection, adjuvants in vaccines, as cholesterol trappers to destabilize the virus capsid, as carriers for RNA therapies, as antivirals themselves, and even useful in anticoagulant therapies, highlight the great power of this sweet molecules. More than ever, we are in the situation to subscribe the words a thousand times pronounced by the dual character Gollum-Sméagol: “My precious”.

CRediT authorship contribution statement

Pablo F. Garrido: Writing - review & editing. **Martín Calvelo:** Writing - review & editing. **Alexandre Blanco-González:** Writing - review & editing. **Uxía Veleiro:** Writing - review & editing. **Fabián Suárez:** Writing - review & editing. **Daniel Conde:** Writing - review & editing. **Alfonso Cabezón:** Writing - review & editing. **Ángel Piñeiro:** Conceptualization, Writing - review & editing, Supervision. **Rebeca Garcia-Fandino:** Conceptualization, Writing - review & editing, Supervision.

Declaration of Competing Interest

The authors declare that they have no known competing financial interests or personal relationships that could have appeared to influence the work reported in this paper.

Acknowledgments

This work was supported by the Spanish Agencia Estatal de Investigación (AEI) and the ERDF (CTQ2016-78423-R and RTI2018-098795-A-I00), and by the Xunta de Galicia and the ERDF (ED431G 2019/03 and Centro singular de investigación de Galicia accreditation 2016-2019, ED431G/09). R.G.-F. thanks to Ministerio de Ciencia, Innovación y Universidades for a “Ramón y Cajal” contract (RYC-2016-20335). M.C. thanks to Xunta de Galicia for a predoctoral fellowship (ED481A-2017/068). P. F. G. thanks the Spanish Ministry of Economy and Competitiveness and the European Social Fund for his predoctoral research grant, reference BES-2016-076761.

References

Abdou, S., Collomb, J., Sallas, F., Marsura, A., Finance, C., 1997. Beta-cyclodextrin derivatives as carriers to enhance the antiviral activity of an antisense oligonucleotide directed toward a coronavirus intergenic consensus sequence. Arch. Virol. 142, 1585–1602. https://doi.org/10.1007/s007050050182.

Adeoye, O., Cabral-Marques, H., 2017. Cyclodextrin nanosystems in oral drug delivery: a mini review. Int. J. Pharm. 531, 521–531. https://doi.org/10.1016/j.ijpharm.2017.04.050.

Adeoye, O., Conceição, J., Serra, P.A., Bento da Silva, A., Duarte, N., Guedes, R.C., Corvo, M.C., Aguiar-Ricardo, A., Jicsinszky, L., Casimiro, T., Cabral-Marques, H., 2020. Cyclodextrin solubilization and complexation of antiretroviral drug lopinavir: in silico prediction; Effects of derivatization, molar ratio and preparation method. Carbohydr. Polym. 227, 115287. https://doi.org/10.1016/j.carbpol.2019.115287.

Agrawal, S., 1996. Antisense oligonucleotides: towards clinical trials. Trends Biotechnol. 14, 376–387. https://doi.org/10.1016/0167-7799(96)10053-6.

Ain, S., Kumar, B., Pathak, K., 2015. Cyclodextrins: versatile carrier in drug formulations and delivery systems. Int. J. Pharm. Chem. Biol. Sci. 5.

Anderson, A., Campo, A., Fulton, E., Corwin, A., Jerome, W.G., O’Connor, M.S., 2020. 7-Ketocholesterol in disease and aging. Redox Biol. 29, 101380. https://doi.org/10.1016/j.redox.2019.101380.

Arima, H., Motoyama, K., 2009. Recent findings concerning PAMAM dendrimer conjugates with cyclodextrins as carriers of DNA and RNA. Sensors 9, 6346–6361. https://doi.org/10.3390/s90806346.

Arnold, J., Ahsan, F., Meezan, E., Pillion, D.J., 2002. Nasal administration of low molecular weight heparin. J. Pharm. Sci. 91, 1707–1714. https://doi.org/10.1002/jps.10171.

ASDERA, 2020. ASDERA alpha-cyclodextrin against coronavirus [WWW Document]. URL < http://www.asdera.com/sars-nutrition.html > (accessed 5.20.20).

ASHP, 2020. Assessment of Evidence for COVID-19-Related Treatments [WWW Document]. URL < https://www.ashp.org/-/media/assets/pharmacy-practice/resource-centers/Coronavirus/docs/ASHP-COVID-19-Evidence-Table.ashx > (accessed 5.18.20).

Atger, V.M., De La Llera Moya, M., Stoudt, G.W., Rodrigueza, W.V., Phillips, M.C., Rothblat, G.H., 1997. Cyclodextrins as catalysts for the removal of cholesterol from macrophage foam cells. J. Clin. Invest. 99, 773–780. https://doi.org/10.1172/JCI119223.

Baglivo, M., Baronio, M., Natalini, G., Beccari, T., Chiurazzi, P., Fulcheri, E., Petralia, P., Michelini, S., Fiorentini, G., Miggiano, G.A., Morresi, A., Tonini, G., Bertelli, M., 2020. Natural small molecules as inhibitors of coronavirus lipid-dependent attachment to host cells: a possible strategy for reducing SARS-COV-2 infectivity? Acta Biomed. 91, 161–164. https://doi.org/10.23750/abm.v91i1.9402.

Baig, A.M., Khaleeq, A., Ali, U., Syeda, H., 2020. Evidence of the COVID-19 virus targeting the CNS: tissue distribution, host-virus Interaction, and proposed neurotropic mechanisms. ACS Chem. Neurosci. 11, 995–998. https://doi.org/10.1021/acschemneuro.0c00122.

Bajracharya, R., Song, J.G., Back, S.Y., Han, H.-K., 2019. Recent advancements in non-invasive formulations for protein drug delivery. Comput. Struct. Biotechnol. J. 17, 1290–1308. https://doi.org/10.1016/j.csbj.2019.09.004.

Barman, S., Nayak, D.P., 2007. Lipid raft disruption by cholesterol depletion enhances influenza a virus budding from MDCK cells. J. Virol. 81, 12169–12178. https://doi.org/10.1128/jvi.00835-07.

Bencini, M., Ranucci, E., Ferruti, P., Trotta, F., Donalisio, M., Cornaglia, M., Lembo, D., Cavalli, R., 2008. Preparation and in vitro evaluation of the antiviral activity of the Acyclovir complex of a β-cyclodextrin/poly(amidoamine) copolymer. J. Control. Release 126, 17–25. https://doi.org/10.1016/j.jconrel.2007.11.004.

Bloomberg, 2020. Vir Biotechnology CEO on Finding a Coronavirus Antibody – Bloomberg [WWW Document]. URL < https://www.bloomberg.com/news/videos/2020-01-29/vir-biotechnology-ceo-confident-coronavirus-vaccine-will-be-found-video > (accessed 5.18.20).

Bodier-Montagutelli, E., Mayor, A., Vecellio, L., Respaud, R., Heuzé-Vourc’h, N., 2018. Designing inhaled protein therapeutics for topical lung delivery: what are the next steps? Expert Opin. Drug Deliv. 15, 729–736. https://doi.org/10.1080/17425247.2018.1503251.

Braga, S.S., 2019. Cyclodextrins: emerging medicines of the new millennium. Biomolecules 9, 801. https://doi.org/10.3390/biom9120801.

Cantín, C., Holguera, J., Ferrerira, L., Villar, E., Muñoz-Barroso, I., 2007. Newcastle disease virus may enter cells by caveolae-mediated endocytosis. J. Gen. Virol. 88, 559–569. https://doi.org/10.1099/vir.0.82150-0.

Carrouel, F., Conte, M.P., Fisher, J., Gonçalves, L.S., Dussart, C., Llodra, J.C., Bourgeois, D., 2020a. COVID-19: a recommendation to examine the effect of mouthrinses with β-cyclodextrin combined with citrox in preventing infection and progression. J. Clin. Med. 9, 1126. https://doi.org/10.3390/jcm9041126.

Carrouel, F., Viennot, S., Ottolenghi, L., Gaillard, C., Bourgeois, D., 2020b. Nanoparticles as anti-microbial, anti-inflammatory, and remineralizing agents in oral care cosmetics: a review of the current situation. Nanomaterials 10, 140. https://doi.org/10.3390/nano10010140.

Castellanos, I.J., Flores, G., Griebenow, K., 2006. Effect of cyclodextrins on α-chymotrypsin stability and loading in PLGA microspheres upon s/o/w encapsulation. J. Pharm. Sci. 95, 849–858. https://doi.org/10.1002/jps.20512.

Cavalli, R., Donalisio, M., Civra, A., Ferruti, P., Ranucci, E., Trotta, F., Lembo, D., 2009. Enhanced antiviral activity of Acyclovir loaded into β-cyclodextrin-poly(4-acryloylmorpholine) conjugate nanoparticles. J. Control. Release 137, 116–122. https://doi.org/10.1016/j.jconrel.2009.04.004.

Chacornac, I., Francon, A., Vacus, P., 2016. Vaccine composition comprising ipv and cyclodextrins. WO2016012385A1.

Chan, J.F.W., To, K.K.W., Tse, H., Jin, D.Y., Yuen, K.Y., 2013. Interspecies transmission and emergence of novel viruses: lessons from bats and birds. Trends Microbiol. 21, 544–555. https://doi.org/10.1016/j.tim.2013.05.005.

Chang, Z., Hu, J., 2006. RNAi therapeutics: can siRNAs conquer SARS? Gene Ther. 13, 871–872. https://doi.org/10.1038/sj.gt.3302682.

Changeux, J.-P., Amoura, Z., Rey, F., Miyara, M., 2020. A nicotinic hypothesis for Covid-19 with preventive and therapeutic implications. Qeios (Preprint).

Chaturvedi, K., Ganguly, K., Kulkarni, A.R., Kulkarni, V.H., Nadagouda, M.N., Rudzinski, W.E., Aminabhavi, T.M., 2011. Cyclodextrin-based siRNA delivery nanocarriers: a state-of-the-art review. Expert Opin. Drug Deliv. 8, 1455–1468. https://doi.org/10.1517/17425247.2011.610790.

Chen, S., He, H., Yang, H., Tan, B., Liu, E., Zhao, X., Zhao, Y., 2019. The role of lipid rafts in cell entry of human metapneumovirus. J. Med. Virol. 91, 949–957. https://doi.org/10.1002/jmv.25414.

Choi, K.S., Aizaki, H., Lai, M.M.C., 2005. Murine coronavirus requires lipid rafts for virus entry and cell-cell fusion but not for virus release. J. Virol. 79, 9862–9871. https://doi.org/10.1128/jvi.79.15.9862-9871.2005.

Christian, A.E., Haynes, M.P., Phillips, M.C., Rothblat, G.H., 1997. Use of cyclodextrins for manipulating cellular cholesterol content. J. Lipid Res. 38, 2264–2272.

Christian, A.E., Byun, H.S., Zhong, N., Wanunu, M., Marti, T., Fürer, A., Diederich, F., Bittman, R., Rothblat, G.H., 1999. Comparison of the capacity of β-cyclodextrin derivatives and cyclophanes to shuttle cholesterol between cells and serum lipoproteins. J. Lipid Res. 40, 1475–1482.

Coelho Paraguassu, E., Chen, H., Zhou, F., Xu, Z., Wang, M., 2020. Coronavirus and COVID-19: the latest news and views from the scientific community about the new coronavirus and COVID-19. Braz. J. Implantol. Health Sci. 2, 96–109. https://doi.org/10.36557/2674-8169.2020v2n3p96-109.

Conceição, J., Adeoye, O., Cabral-Marques, H.M., Lobo, J.M.S., 2018. Cyclodextrins as excipients in tablet formulations. Drug Discov. Today 23, 1274–1284. https://doi.org/10.1016/j.drudis.2018.04.009.
Crini, G., 2014. Review: a history of cyclodextrins. Chem. Rev. 114, 10940–10975. https://doi.org/10.1021/cr500081p.
Crooke, S.T., Ecker, D.J., Sampath, R., Freier, S.M., Massire, C., Hofstadler, S.A., Lowery, K.S., Swayze, E.E., Baker, B.F., Bennett, C.F., 2008. Compositions and methods for the treatment of severe acute respiratory syndrome (SARS). WO2005023083A2.
Cryan, S.A., Donohue, R., Ravoo, B.J., Darcy, R., O'Driscoll, C.M., 2004. Cationic cyclodextrin amphiphi]es as gene delivery vectors. J. Drug Deliv. Sci. Technol. 14, 57–62. https://doi.org/10.1016/s1773-2247(04)50006-0.
Cyclodextrin News, 2018. Cyclodextrin News [WWW Document]. URL < https://cyclodextrinnews.com/2018/09/25/a-clinical-phase1-study-of-hydroxypropyl-beta-cyclodextrin-hpbcd-adjuvanted-influenza-split-vaccine/ > (accessed 5.18.20).
Cyclolab, n.d. Cyclodextrins as APIs [WWW Document]. URL < https://cyclolab.hu/userfiles/LMWH antidote.pdf > (accessed 5.18.20).
CytoDyn, 2020. Leronlimab Under Evaluation for Potential Treatment of Coronavirus :: CytoDyn Inc. (CYDY) [WWW Document]. URL < https://www.cytodyn.com/newsroom/press-releases/detail/379/leronlimab-under-evaluation-for-potential-treatment-of > (accessed 5.18.20).
Davis, M.E., 2009. The first targeted delivery of siRNA in humans via a self-assembling, cyclodextrin polymer-based nanoparticle: from concept to clinic. Mol. Pharm. 6, 659–668. https://doi.org/10.1021/mp900015y.
Davis, M.E., Brewster, M.E., 2004. Cyclodextrin-based pharmaceutics: past, present and future. Nat. Rev. Drug Discov. 3, 1023–1035. https://doi.org/10.1038/nrd1576.
De Andrea, M., Ravera, R., Gioia, D., Gariglio, M., Landolfo, S., 2002. The interferon system: an overview. Eur. J. Paediatr. Neurol. 6, A41–A46. https://doi.org/10.1053/ejpn.2002.0573.
de Wit, E., Feldmann, F., Cronin, J., Jordan, R., Okumura, A., Thomas, T., Scott, D., Cihlar, T., Feldmann, H., 2020. Prophylactic and therapeutic remdesivir (GS-5734) treatment in the rhesus macaque model of MERS-CoV infection. Proc. Natl. Acad. Sci. U. S. A. 117, 6771–6776. https://doi.org/10.1073/pnas.1922083117.
Del Curto, M.D., 2010. Stabilized interferon liquid formulations. WO2005058346A1.
Domanska, M.K., Wrona, D., Kasson, P.M., 2013. Multiphasic effects of cholesterol on influenza fusion kinetics reflect multiple mechanistic roles. Biophys. J. 105, 1383–1387. https://doi.org/10.1016/j.bpj.2013.08.003.
Erb-Zohar, K., Kropeit, D., Scheuenpflug, J., Stobernack, H., Hulskotte, E., van Schanke, A., Zimmermann, H., Rübsamen-Schaeff, H., 2017. Intravenous hydroxypropyl β-cyclodextrin formulation of letermovir: a phase I, randomized, single-ascending, and multiple-dose trial. Clin. Transl. Sci. 10, 487–495. https://doi.org/10.1111/cts.12483.
Evenou, P., Rossignol, J., Pembouong, G., Gothland, A., Colesnic, D., Barbeyron, R., Rudiuk, S., Marcelin, A.-G., Ménand, M., Baigl, D., Calvez, V., Bouteiller, L., Sollogoub, M., 2018. Bridging β-cyclodextrin prevents self-inclusion, promotes supramolecular polymerization, and promotes cooperative interaction with nucleic acids. Angew. Chem. Int. Ed. 57, 7753–7758. https://doi.org/10.1002/anie.201802550.
Fernández, M., Villalonga, M.L., Fragoso, A., Cao, R., Villalonga, R., 2004. Effect of β-cyclodextrin-polysucrose polymer on the stability properties of soluble trypsin. Enzyme Microb. Technol. 34, 78–82. https://doi.org/10.1016/j.enzmictec.2003.09.003.
French, D., 1957. The schardinger dextrins. Adv. Carbohydr. Chem. 12, 189–260. https://doi.org/10.1016/S0096-5332(08)60209-X.
Gao, J., Tian, Z., Yang, X., 2020. Breakthrough: chloroquine phosphate has shown apparent efficacy in treatment of COVID-19 associated pneumonia in clinical studies. Biosci. Trends 14 (2020), 01047. https://doi.org/10.5582/BST.2020.01047.
Geleris, J., Sun, Y., Platt, J., Zucker, J., Baldwin, M., Hripcsak, G., Labella, A., Manson, D.K., Kubin, C., Barr, R.G., Sobieszczyk, M.E., Schluger, N.W., 2020. Observational study of hydroxychloroquine in hospitalized patients with Covid-19. N. Engl. J. Med. 382, 2411–2418. https://doi.org/10.1056/NEJMoa2012410.
Glende, J.H., Pfefferle, S., Drosten, C., Schwegmann-Weßels, C., Herrler, G., 2008. Lipid microdomains are important for the entry process of SARS coronavirus to target cells. FASEB J. 22, 282. https://doi.org/10.1096/fasebj.22.2_supplement.282.
Goyal, G., Vavia, P.R., 2012. Complexation approach for fixed dose tablet formulation of lopinavir and ritonavir: an anomalous relationship between stability constant, dissolution rate and saturation solubility. J. Incl. Phenom. Macrocycl. Chem. 73, 75–85. https://doi.org/10.1007/s10847-011-0022-7.
Graham, D.R.M., Chertova, E., Hilburn, J.M., Arthur, L.O., Hildreth, J.E.K., 2003. Cholesterol depletion of human immunodeficiency virus type 1 and simian immunodeficiency virus with β-cyclodextrin inactivates and permeabilizes the virions: evidence for virion-associated lipid rafts. J. Virol. 77, 8237–8248. https://doi.org/10.1128/jvi.77.15.8237-8248.2003.
Grancher, N., Venard, V., Kedzierewicz, F., Ammerlaan, W., Finance, C., Muller, C.P., Le Faou, A., 2004. Improved antiviral activity in vitro of ribavirin against measles virus after complexation with cyclodextrins. Antiviral Res. 62, 135–137. https://doi.org/10.1016/j.antiviral.2004.01.003.
Guan, W., Ni, Z., Hu, Yu., Liang, W., Ou, C., He, J., Liu, L., Shan, H., Lei, C., Hui, D.S.C., Du, B., Li, L., Zeng, G., Yuen, K.-Y., Chen, R., Tang, C., Wang, T., Chen, P., Xiang, J., Li, S., Wang, Jin-lin, Liang, Z., Peng, Y., Wei, L., Liu, Y., Hu, Ya.-hua., Peng, P., Wang, Jian-ming, Liu, J., Chen, Z., Li, G., Zheng, Z., Qiu, S., Luo, J., Ye, C., Zhu, S., Zhong, N., 2020. Clinical characteristics of coronavirus disease 2019 in China. N. Engl. J. Med. 382, 1708–1720. https://doi.org/10.1056/NEJMoa2002032.
Guo, J., Fisher, K.A., Darcy, R., Cryan, J.F., O'Driscoll, C., 2010. Therapeutic targeting in the silent era: advances in non-viral siRNA delivery. Mol. BioSyst. 6, 1143–1161. https://doi.org/10.1039/c001050m.
Guo, H., Huang, M., Yuan, Q., Wei, Y., Gao, Y., Mao, L., Gu, L., Tan, Y.W., Zhong, Y., Liu, D., Sun, S., 2017. The important role of lipid raft-mediated attachment in the infection of cultured cells by coronavirus infectious bronchitis virus beaudette strain. PLoS ONE 12, e0170123. https://doi.org/10.1371/journal.pone.0170123.
Guyader, M., Kiyokawa, E., Abrami, L., Turelli, P., Trono, D., 2002. Role for human immunodeficiency virus Type 1 membrane cholesterol in viral internalization. J. Virol. 76, 10356–10364. https://doi.org/10.1128/jvi.76.20.10356-10364.2002.
Hambleton, S., Steinberg, S.P., Gershon, M.D., Gershon, A.A., 2007. Cholesterol dependence of varicella-zoster virion entry into target cells. J. Virol. 81, 7548–7558. https://doi.org/10.1128/jvi.00486-07.
Higashi, T., 2019. Cyclodextrin-based molecular accessories for drug discovery and drug delivery. Chem. Pharm. Bull. 67, 289–298. https://doi.org/10.1248/cpb.c18-00735.
Higashi, T., Tajima, A., Ohshita, N., Hirotsu, T., Hashim, I.I.A., Motoyama, K., Koyama, S., Iibuchi, R., Mieda, S., Handa, K., Kimoto, T., Arima, H., 2015. Design and evaluation of the highly concentrated human IgG formulation using cyclodextrin polypseudorotaxane hydrogels. AAPS PharmSciTech 16, 1290–1298. https://doi.org/10.1208/s12249-015-0309-x.
Higashi, T., Motoyama, K., Arima, H., 2019. Supramolecular pharmaceutical sciences: a novel concept for future pharmaceutical sciences. Yakugaku Zasshi 139, 175–183. https://doi.org/10.1248/yakushi.18-00168-4.
Hoffmann, M., Kleine-Weber, H., Schroeder, S., Krüger, N., Herrler, T., Erichsen, S., Schiergens, T.S., Herrler, G., Wu, N.H., Nitsche, A., Müller, M.A., Drosten, C., Pöhlmann, S., 2020. SARS-CoV-2 cell entry depends on ACE2 and TMPRSS2 and is blocked by a clinically proven protease inhibitor. Cell 181, 271–280.e8. https://doi.org/10.1016/j.cell.2020.02.052.
Hu, X., Chen, D., Wu, L., He, G., Ye, W., 2020. Low serum cholesterol level among patients with COVID-19 infection in Wenzhou, China. SSRN Electron. J. https://doi.org/10.2139/ssrn.3544826.
Hung, I.F.-N., Lung, K.-C., Tso, E.Y.-K., Liu, R., Chung, T.W.-H., Chu, M.-Y., Ng, Y.-Y., Lo, J., Chan, J.W.-M.J.J.F.-W., Tam, A.R., Shum, H.-P., Chan, V., Wu, A.K.-L., Sin, K.-M., Leung, W.-S., Law, W.-L., Lung, D.C., Sin, S., Yeung, P., Yip, C.C.-Y., Zhang, R.R., Fung, A.Y.-F., Yan, E.Y.-W., Leung, K.-H., Ip, J.D., Chu, A.W.-H., Chan, W.-M.W.-M., Ng, A.C.-K., Lee, R., Fung, K., Yeung, A., Wu, T.-C., Chan, J.W.-M.J.J.F.-W., Yan, W.-W., Chan, W.-M.W.-M., Chan, J.W.-M.J.J.F.-W., Lie, A.K.-W., Tsang, O.T.-Y., Cheng, V.C.-C., Que, T.-L., Lau, C.-S., Chan, K.-H., To, K.K.-W., Yuen, K.-Y., 2020. Triple combination of interferon beta-1b, lopinavir–ritonavir, and ribavirin in the treatment of patients admitted to hospital with COVID-19: an open-label, randomised, phase 2 trial. Lancet. https://doi.org/10.1016/S0140-6736(20)31042-4.
Iannazzo, D., Mazzaglia, A., Scala, A., Pistone, A., Galvagno, S., Lanza, M., Riccucci, C., Ingo, G.M., Colao, I., Sciortino, M.T., Valle, F., Piperno, A., Grassi, G., 2014. β-Cyclodextrin-grafted on multiwalled carbon nanotubes as versatile nanoplatform for entrapment of guanine-based drugs. Colloids Surfaces B Biointerfaces 123, 264–270. https://doi.org/10.1016/j.colsurfb.2014.09.025.
Jeulin, H., Venard, V., Carapito, D., Finance, C., Kedzierewicz, F., 2009. Effective ribavirin concentration in mice brain using cyclodextrin as a drug carrier: evaluation in a measles encephalitis model. Antiviral Res. 81, 261–266. https://doi.org/10.1016/j.antiviral.2008.12.006.
Jones, S.T., Cagno, V., Janeček, M., Ortiz, D., Gasilova, N., Piret, J., Gasbarri, M., Constant, D.A., Han, Y., Vuković, L., Král, P., Kaiser, L., Huang, S., Constant, S., Kirkegaard, K., Boivin, G., Stellacci, F., Tapparel, C., 2020. Modified cyclodextrins as broad-spectrum antivirals. Sci. Adv. 6, eaax9318. https://doi.org/10.1126/sciadv.aax9318.
Kane, C., O'Neil, K., Conk, M., Picha, K., 2013. Inhalation delivery of protein therapeutics. Inflamm. Allergy - Drug Targets 12, 81–87. https://doi.org/10.2174/1871528111312020002.
Khan, N.A., Durakshan, M., 2013. Cyclodextrin: an overview. Int J Bioassays 2, 858–865.
Kilsdonk, E.P.C., Yancey, P.G., Stoudt, G.W., Bangerter, F.W., Johnson, W.J., Phillips, M.C., Rothblat, G.H., 1995. Cellular cholesterol efflux mediated by cyclodextrins. J. Biol. Chem. 270, 17250–17256. https://doi.org/10.1074/jbc.270.29.17250.
Kim, S.K., Yun, C.-H., Han, S.H., 2016. Induction of dendritic cell maturation and activation by a potential adjuvant, 2-hydroxypropyl-β-cyclodextrin. Front. Immunol. 7, 435. https://doi.org/10.3389/fimmu.2016.00435.
Koźbiał, M., Gierycz, P., 2013. Comparison of aqueous and 1-octanol solubility as well as liquid-liquid distribution of acyclovir derivatives and their complexes with hydroxypropyl-β-cyclodextrin. J. Solution Chem. 42, 866–881. https://doi.org/10.1007/s10953-013-9995-8.
Krause, M.R., Regen, S.L., 2014. The structural role of cholesterol in cell membranes: from condensed bilayers to lipid rafts. Acc. Chem. Res. 47, 3512–3521. https://doi.org/10.1021/ar500260t.
Kurkov, S.V., Loftsson, T., 2013. Cyclodextrins. Int. J. Pharm. 453, 167–180. https://doi.org/10.1016/j.ijpharm.2012.06.055.
Kusakabe, T., Ozasa, K., Kobari, S., Momota, M., Kishishita, N., Kobiyama, K., Kuroda, E., Ishii, K.J., 2016. Intranasal hydroxypropyl-β-cyclodextrin-adjuvanted influenza vaccine protects against sub-heterologous virus infection. Vaccine 34, 3191–3198. https://doi.org/10.1016/j.vaccine.2016.04.001.
Kwon, S., Lee, W., Shin, H.J., Yoon, S. il, Kim, Y. Tae, Kim, Y.J., Lee, K., Lee, S., 2009. Characterization of cyclodextrin complexes of camostat mesylate by ESI mass spectrometry and NMR spectroscopy. J. Mol. Struct. 938, 192–197. https://doi.org/10.1016/j.molstruc.2009.09.025.
Lakkakula, J.R., Maçedo Krause, R.W., 2014. A vision for cyclodextrin nanoparticles in drug delivery systems and pharmaceutical applications. Nanomedicine 9, 877–894. https://doi.org/10.2217/nnm.14.41.
Larson, N., 2019. Compositions comprising an rna polymerase inhibitor and cyclodextrin for treating viral infections. US20190083525A1.
Lauder, S.N., Jones, E., Smart, K., Bloom, A., Williams, A.S., Hindley, J.P., Ondondo, B., Taylor, P.R., Clement, M., Fielding, C., Godkin, A.J., Jones, S.A., Gallimore, A.M., 2013. Interleukin-6 limits influenza-induced inflammation and protects against fatal

lung pathology. Eur. J. Immunol. 43, 2613–2625. https://doi.org/10.1002/eji.201243018.
Leclercq, L., 2016. Interactions between cyclodextrins and cellular components: towards greener medical applications? Beilstein J. Org. Chem. 12, 2644–2662. https://doi.org/10.3762/bjoc.12.261.
Lembo, D., Swaminathan, S., Donalisio, M., Civra, A., Pastero, L., Aquilano, D., Vavia, P., Trotta, F., Cavalli, R., 2013. Encapsulation of Acyclovir in new carboxylated cyclodextrin-based nanosponges improves the agent's antiviral efficacy. Int. J. Pharm. 443, 262–272. https://doi.org/10.1016/j.ijpharm.2012.12.031.
Li, Y., Bai, W., Hashikawa, T., 2020. The neuroinvasive potential of SARS-CoV2 may play a role in the respiratory failure of COVID-19 patients. J. Med. Virol. 92, 552–555. https://doi.org/10.1002/jmv.25728.
Li, P.Y., Chen, Y., Chen, C.H., Liu, Y., 2019. Amphiphilic multi-charged cyclodextrins and vitamin K co-assembly as a synergistic coagulant. Chem. Commun. 55, 11790–11793. https://doi.org/10.1039/c9cc06545h.
Li, G.M., Li, Y.G., Yamate, M., Li, S.M., Ikuta, K., 2007. Lipid rafts play an important role in the early stage of severe acute respiratory syndrome-coronavirus life cycle. Microbes Infect. 9, 96–102. https://doi.org/10.1016/j.micinf.2006.10.015.
Li, J., Yang, C., Li, H., Wang, X., Goh, S.H., Ding, J.L., Wang, D.Y., Leong, K.W., 2006. Cationic supramolecules composed of multiple oligoethylenimine-grafted β-cyclodextrins threaded on a polymer chain for efficient gene delivery. Adv. Mater. 18, 2969–2974. https://doi.org/10.1002/adma.200600812.
Liang, S., Li, M., Yu, X., Jin, H., Zhang, Y., Zhang, L., Zhou, D., Xiao, S., 2019. Synthesis and structure-activity relationship studies of water-soluble β-cyclodextrin-glycyrrhetinic acid conjugates as potential anti-influenza virus agents. Eur. J. Med. Chem. 166, 328–338. https://doi.org/10.1016/j.ejmech.2019.01.074.
Liu, C., Zhou, Q., Li, Y., Garner, L.V., Watkins, S.P., Carter, L.J., Smoot, J., Gregg, A.C., Daniels, A.D., Jervey, S., Albaiu, D., 2020. Research and development on therapeutic agents and vaccines for COVID-19 and related human coronavirus diseases. ACS Cent. Sci. 6, 315–331. https://doi.org/10.1021/acscentsci.0c00272.
Loftsson, T., 2002. Cyclodextrins and the biopharmaceutics classification system of drugs. J. Incl. Phenom. Macrocycl. Chem. 44, 63–67. https://doi.org/10.1023/A:1023088423667.
Loftsson, T., Brewster, M.E., 1996. Pharmaceutical applications of cyclodextrins. 1. Drug solubilization and stabilization. J. Pharm. Sci. 85, 1017–1025. https://doi.org/10.1021/js950534b.
López, C.A., de Vries, A.H., Marrink, S.J., 2011. Molecular mechanism of cyclodextrin mediated cholesterol extraction. PLoS Comput. Biol. 7, e1002020. https://doi.org/10.1371/journal.pcbi.1002020.
Lopez, C.A., De Vries, A.H., Marrink, S.J., 2013. Computational microscopy of cyclodextrin mediated cholesterol extraction from lipid model membranes. Sci. Rep. 3, 1–6. https://doi.org/10.1038/srep02071.
Lorizate, M., Kräusslich, H.G., 2011. Role of lipids in virus replication. Cold Spring Harb. Perspect. Biol. 3, 1–20. https://doi.org/10.1101/cshperspect.a004820.
Lu, R.M., Hwang, Y.C., Liu, I.J., Lee, C.C., Tsai, H.Z., Li, H.J., Wu, H.C., 2020. Development of therapeutic antibodies for the treatment of diseases. J. Biomed. Sci. 27, 1–30. https://doi.org/10.1186/s12929-019-0592-z.
Lu, Y., Liu, D.X., Tam, J.P., 2008. Lipid rafts are involved in SARS-CoV entry into Vero E6 cells. Biochem. Biophys. Res. Commun. 369, 344–349. https://doi.org/10.1016/j.bbrc.2008.02.023.
Mahammad, S., Parmryd, I., 2015. Cholesterol depletion using methyl-β-cyclodextrin. Methods Mol. Biol. 1232, 91–102. https://doi.org/10.1007/978-1-4939-1752-5_8.
Marichal-Gallardo, P.A., Álvarez, M.M., 2012. State-of-the-art in downstream processing of monoclonal antibodies: process trends in design and validation. Biotechnol. Prog. 28, 899–916. https://doi.org/10.1002/btpr.1567.
Martin, J., Díaz-Montaña, E.J., Asuero, A.G., 2018. Cyclodextrins: past and present. In: Cyclodextrin - A Versatile Ingredient. InTech. https://doi.org/10.5772/intechopen.72736.
Martín, J.J., Holguera, J., Sánchez-Felipe, L., Villar, E., Muñoz-Barroso, I., 2012. Cholesterol dependence of Newcastle Disease Virus entry. Biochim. Biophys. Acta - Biomembr. 1818, 753–761. https://doi.org/10.1016/j.bbamem.2011.12.004.
Marty, F.M., Ljungman, P., Chemaly, R.F., Maertens, J., Dadwal, S.S., Duarte, R.F., Haider, S., Ullmann, A.J., Katayama, Y., Brown, J., Mullane, K.M., Boeckh, M., Blumberg, E.A., Einsele, H., Snydman, D.R., Kanda, Y., DiNubile, M.J., Teal, V.L., Wan, H., Murata, Y., Kartsonis, N.A., Leavitt, R.Y., Badshah, C., 2017. Letermovir prophylaxis for cytomegalovirus in hematopoietic-cell transplantation. N. Engl. J. Med. 377, 2433–2444. https://doi.org/10.1056/NEJMoa1706640.
Mazzaglia, A., Scala, A., Sortino, G., Zagami, R., Zhu, Y., Sciortino, M.T., Pennisi, R., Pizzo, M.M., Neri, G., Grassi, G., Piperno, A., 2018. Intracellular trafficking and therapeutic outcome of multiwalled carbon nanotubes modified with cyclodextrins and polyethylenimine. Colloids Surfaces B Biointerfaces 163, 55–63. https://doi.org/10.1016/j.colsurfb.2017.12.028.
Mazzon, M., Mercer, J., 2014. Lipid interactions during virus entry and infection. Cell. Microbiol. 16, 1493–1502. https://doi.org/10.1111/cmi.12340.
Meher, G., Bhattacharjya, S., Chakraborty, H., 2019. Membrane cholesterol modulates oligomeric status and peptide-membrane interaction of severe acute respiratory syndrome coronavirus fusion peptide. J. Phys. Chem. B 123, 10654–10662. https://doi.org/10.1021/acs.jpcb.9b08455.
Mehta, P., McAuley, D.F., Brown, M., Sanchez, E., Tattersall, R.S., Manson, J.J., 2020. COVID-19: consider cytokine storm syndromes and immunosuppression. Lancet 395, 1033–1034. https://doi.org/10.1016/S0140-6736(20)30628-0.
Meijers, J.C.M., Bakhtiari, K., Peters, S.L.M., Zollinger, D.P., 2019. Cyclodextrins as procoagulants. WO2017188820A1.
Mellet, C.O., Fernández, J.M.G., Benito, J.M., 2011. Cyclodextrin-based gene delivery systems. Chem. Soc. Rev. 40, 1586–1608. https://doi.org/10.1039/c0cs00019a.
Miertus, S., Chiellini, E., Chiellini, F., Kona, J., Tomasi, J., Solaro, R., 1999. Modelling of molecular interactions and inclusion phenomena in substituted β-cyclodextrin: from simple probes to proteins. Macromol. Symp. 138, 41–55. https://doi.org/10.1002/masy.19991380106.
Morra, M.E., Van Thanh, L., Kamel, M.G., Ghazy, A.A., Altibi, A.M.A., Dat, L.M., Thy, T.N.X., Vuong, N.L., Mostafa, M.R., Ahmed, S.I., Elabd, S.S., Fathima, S., Le Huy Vu, T., Omrani, A.S., Memish, Z.A., Hirayama, K., Huy, N.T., 2018. Clinical outcomes of current medical approaches for Middle East respiratory syndrome: a systematic review and meta-analysis. Rev. Med. Virol. 28. https://doi.org/10.1002/rmv.1977.
Nair, A.B., Attimarad, M., Al-Dhubiab, B.E., Wadhwa, J., Harsha, S., Ahmed, M., 2014. Enhanced oral bioavailability of acyclovir by inclusion complex using hydroxypropyl-β-cyclodextrin. Drug Deliv. 21, 540–547. https://doi.org/10.3109/10717544.2013.853213.
Nayak, D.P., Hui, E.K.W., 2004. The role of lipid microdomains in virus biology. Subcell. Biochem. 37, 443–491. https://doi.org/10.1007/978-1-4757-5806-1_14.
Németh, K., Tárkányi, G., Varga, E., Imre, T., Mizsei, R., Iványi, R., Visy, J., Szemán, J., Jicsinszky, L., Szente, L., Simonyi, M., 2011. Enantiomeric separation of antimalarial drugs by capillary electrophoresis using neutral and negatively charged cyclodextrins. J. Pharm. Biomed. Anal. 54, 475–481. https://doi.org/10.1016/j.jpba.2010.09.020.
Nicolazzi, C., Abdou, S., Collomb, J., Marsura, A., Finance, C., 2001. Effect of the complexation with cyclodextrins on the in vitro antiviral activity of ganciclovir against human cytomegalovirus. Bioorg. Med. Chem. 9, 275–282. https://doi.org/10.1016/S0968-0896(00)00247-9.
Nicolazzi, C., Venard, V., Le Faou, A., Finance, C., 2002. In vitro antiviral efficacy of the ganciclovir complexed with β-cyclodextrin on human cytomegalovirus clinical strains. Antiviral Res. 54, 121–127. https://doi.org/10.1016/S0166-3542(01)00218-2.
Nishijo, J., Moriyama, S., Shiota, S., 2003. Interactions of cholesterol with cyclodextrins in aqueous solution. Chem. Pharm. Bull. (Tokyo) 51, 1253–1257. https://doi.org/10.1248/cpb.51.1253.
Notario-Pérez, F., Martín-Illana, A., Cazorla-Luna, R., Ruiz-Caro, R., Tamayo, A., Rubio, J., María-Dolores, V., 2020. Mucoadhesive vaginal discs based on cyclodextrin and surfactants for the controlled release of antiretroviral drugs to prevent the sexual transmission of HIV. Pharmaceutics 12, 321. https://doi.org/10.3390/pharmaceutics12040321.
Nussbaum, O., Rott, R., Loyter, A., 1992. Fusion of influenza virus particles with liposomes: requirement for cholesterol and virus receptors to allow fusion with and lysis of neutral but not of negatively charged liposomes. J. Gen. Virol. 73, 2831–2837. https://doi.org/10.1099/0022-1317-73-11-2831.
O'Mahony, A.M., O'Neill, J.M., Godinho, B.M.D.C., Darcy, R., Cryan, J.F., O'Driscoll, C.M., 2013. Cyclodextrins for non-viral gene and siRNA delivery. Pharm. Nanotechnol. 1, 6–14. https://doi.org/10.2174/2211738511301010006.
Ohtani, Y., Irie, T., Uekama, K., Fukunaga, K., Pitha, J., 1989. Differential effects of alpha-, beta- and gamma-cyclodextrins on human erythrocytes. Eur. J. Biochem. 186, 17–22. https://doi.org/10.1111/j.1432-1033.1989.tb15171.x.
Ohvo, H., Slotte, J.P., 1996. Cyclodextrin-mediated removal of sterols from monolayers: effects of sterol structure and phospholipids on desorption rate. Biochemistry 35, 8018–8024. https://doi.org/10.1021/bi9528816.
Onishi, M., Ozasa, K., Kobiyama, K., Ohata, K., Kitano, M., Taniguchi, K., Homma, T., Kobayashi, M., Sato, A., Katakai, Y., Yasutomi, Y., Wijaya, E., Igarashi, Y., Nakatsu, N., Ise, W., Inoue, T., Yamada, H., Vandenbon, A., Standley, D.M., Kurosaki, T., Coban, C., Aoshi, T., Kuroda, E., Ishii, K.J., 2015. Hydroxypropyl-β-cyclodextrin spikes local inflammation that induces Th2 cell and T follicular helper cell responses to the coadministered antigen. J. Immunol. 194, 2673–2682. https://doi.org/10.4049/jimmunol.1402027.
Ono, A., Freed, E.O., 2005. Role of lipid rafts in virus replication. Adv. Virus Res. 64, 311–358. https://doi.org/10.1016/S0065-3527(05)64010-9.
Padmanabhan, S., 2020. Potential dual therapeutic approach against SARS-CoV-2/COVID-19 with Nitazoxanide and Hydroxychloroquine. (Preprint). < https://doi.org/10.13140/RG.2.2.28124.74882 > .
Pan, Y., Xue, Y., Snow, J., Xiao, H., 2015. Tailor-made antimicrobial/antiviral star polymer via ATRP of cyclodextrin and guanidine-based macromonomer. Macromol. Chem. Phys. 216, 511–518. https://doi.org/10.1002/macp.201400525.
Parkin, J., Cohen, B., 2001. An overview of the immune system. Lancet 357, 1777–1789. https://doi.org/10.1016/S0140-6736(00)04904-7.
Pharma Advancement, 2020. WuXi Biologics Enables Development of Multiple Neutralizing Antibodies for Novel Coronavirus [WWW Document]. URL < https://www.pharmaadvancement.com/manufacturing/wuxi-biologics-enables-development-of-multiple-neutralizing-antibodies-for-novel-coronavirus/ > (accessed 5.18.20).
Ping, Y., Liu, C., Zhang, Z., Liu, K.L., Chen, J., Li, J., 2011. Chitosan-graft-(PEI-β-cyclodextrin) copolymers and their supramolecular PEGylation for DNA and siRNA delivery. Biomaterials 32, 8328–8341. https://doi.org/10.1016/j.biomaterials.2011.07.038.
Radi, A.E., Nassef, H.M., El-Naggar, A.E., 2014. Electrochemical and spectral characterization of the host-guest inclusion complex of the antiparasitic drug nitazoxanide with β-cyclodextrin. Monatsh. Chem. 145, 421–426. https://doi.org/10.1007/s00706-013-1109-1.
Ramezani, V., Vatanara, A., Seyedabadi, M., Nabi Meibodi, M., Fanaei, H., 2017. Application of cyclodextrins in antibody microparticles: potentials for antibody protection in spray drying. Drug Dev. Ind. Pharm. 43, 1103–1111. https://doi.org/10.1080/03639045.2017.1293679.
Rane, S., 2017. Formulations comprising 2-amino-2-[2-(4-octylphenyl) ethyl] propane-1, 3-diol. WO2012135561A1.
Rao, M.R.P., Chaudhari, J., Trotta, F., Caldera, F., 2018. Investigation of cyclodextrin-based nanosponges for solubility and bioavailability enhancement of rilpivirine.

AAPS PharmSciTech 19, 2358–2369. https://doi.org/10.1208/s12249-018-1064-6.
Regeneron, 2020. Regeneron Announces Expanded Collaboration with HHS to Develop Antibody Treatments for New Coronavirus | Regeneron Pharmaceuticals Inc. [WWW Document]. URL < https://newsroom.regeneron.com/news-releases/news-release-details/regeneron-announces-expanded-collaboration-hhs-develop-antibody > (accessed 5.18.20).
Roquette, 2020. Combating Coronavirus: Key Role of Cyclodextrins in Treatment and Prevention [WWW Document]. URL < https://www.roquette.com/-/media/media-centre/press-releases/2020/2020-02-11-combating-viruses/position-paper—coronavirus-combatment-via-cyclodextrins.pdf?la=en > (accessed 5.18.20).
Roy, A., Saha, S., Roy, D., Bhattacharyya, S., Roy, M.N., 2020. Formation & specification of host–guest inclusion complexes of an anti-malarial drug inside into cyclic oligosaccharides for enhancing bioavailability. J. Incl. Phenom. Macrocycl. Chem. 97, 65–76. https://doi.org/10.1007/s10847-020-00984-1.
Sagan, S.M., Rouleau, Y., Leggiadro, C., Supekova, L., Schultz, P.G., Su, A.I., Pezacki, J.P., 2006. The influence of cholesterol and lipid metabolism on host cell structure and hepatitis C virus replication. Biochem. Cell Biol. 84, 67–79. https://doi.org/10.1139/o05-149.
Sallas, F., Darcy, R., 2008. Amphiphilic cyclodextrins – advances in synthesis and supramolecular chemistry. Euro. J. Org. Chem. 2008, 957–969. https://doi.org/10.1002/ejoc.200700933.
Sanders, J.M., Monogue, M.L., Jodlowski, T.Z., Cutrell, J.B., 2020. Pharmacologic treatments for coronavirus disease 2019 (COVID-19): a review. JAMA - J. Am. Med. Assoc. 323, 1824–1836. https://doi.org/10.1001/jama.2020.6019.
Sanofi, 2020. Sanofi and Regeneron begin global Kevzara® (sarilumab) clinical trial program in patients with severe COVID-19 - Mar 16, 2020 [WWW Document]. URL < http://www.news.sanofi.us/2020-03-16-Sanofi-and-Regeneron-begin-global-Kevzara-R-sarilumab-clinical-trial-program-in-patients-with-severe-COVID-19 > (accessed 5.18.20).
Saokham, P., Loftsson, T., 2017. γ-Cyclodextrin. Int. J. Pharm. 516, 278–292. https://doi.org/10.1016/j.ijpharm.2016.10.062.
Schmitt, A.P., Lamb, R.A., 2005. Influenza virus assembly and budding at the viral budozone. Adv. Virus Res. 64, 383–416. https://doi.org/10.1016/S0065-3527(05)64012-2.
Schüle, S., Schulz-Fademrecht, T., Garidel, P., Bechtold-Peters, K., Frieß, W., 2008. Stabilization of IgG1 in spray-dried powders for inhalation. Eur. J. Pharm. Biopharm. 69, 793–807. https://doi.org/10.1016/j.ejpb.2008.02.010.
Serno, T., Carpenter, J.F., Randolph, T.W., Winter, G., 2010. Inhibition of agitation-induced aggregation of an IgG-antibody by hydroxypropyl-β-cyclodextrin. J. Pharm. Sci. 99, 1193–1206. https://doi.org/10.1002/jps.21931.
Serno, T., Geidobler, R., Winter, G., 2011. Protein stabilization by cyclodextrins in the liquid and dried state. Adv. Drug Deliv. Rev. 63, 1086–1106. https://doi.org/10.1016/j.addr.2011.08.003.
Sevukarajan, M., Bachala, T., Nair, R., 2010. Novel Inclusion complexs of oseltamivir phosphate-with [beta] cyclodextrin: physico-chemical characterization. J. Pharm. Sci. Res. 2, 583.
Sheahan, T.P., Sims, A.C., Graham, R.L., Menachery, V.D., Gralinski, L.E., Case, J.B., Leist, S.R., Pyrc, K., Feng, J.Y., Trantcheva, I., Bannister, R., Park, Y., Babusis, D., Clarke, M.O., MacKman, R.L., Spahn, J.E., Palmiotti, C.A., Siegel, D., Ray, A.S., Cihlar, T., Jordan, R., Denison, M.R., Baric, R.S., 2017. Broad-spectrum antiviral GS-5734 inhibits both epidemic and zoonotic coronaviruses. Sci. Transl. Med. 9. https://doi.org/10.1126/scitranslmed.aal3653.
Sheahan, T.P., Sims, A.C., Leist, S.R., Schäfer, A., Won, J., Brown, A.J., Montgomery, S.A., Hogg, A., Babusis, D., Clarke, M.O., Spahn, J.E., Bauer, L., Sellers, S., Porter, D., Feng, J.Y., Cihlar, T., Jordan, R., Denison, M.R., Baric, R.S., 2020. Comparative therapeutic efficacy of remdesivir and combination lopinavir, ritonavir, and interferon beta against MERS-CoV. Nat. Commun. 11, 1–14. https://doi.org/10.1038/s41467-019-13940-6.
Shi, Y., Yang, D.H., Xiong, J., Jia, J., Huang, B., Jin, Y.X., 2005. Inhibition of genes expression of SARS coronavirus by synthetic small interfering RNAs. Cell Res. 15, 193–200. https://doi.org/10.1038/sj.cr.7290286.
Shulman, R.I., 2000. Assessment of low-molecular-weight heparin trials in cardiology. Pharmacol. Ther. 87, 1–9. https://doi.org/10.1016/S0163-7258(00)00060-7.
Song, J.C., Wang, G., Zhang, W., Zhang, Y., Li, W.Q., Zhou, Z., 2020. Chinese expert consensus on diagnosis and treatment of coagulation dysfunction in COVID-19. Mil. Med. Res. 7, 19. https://doi.org/10.1186/s40779-020-00247-7.
Stockman, L.J., Bellamy, R., Garner, P., 2006. SARS: systematic review of treatment effects. PLoS Med. 3, 1525–1531. https://doi.org/10.1371/journal.pmed.0030343.
Sun, P., Lu, X., Xu, C., Wang, Y., Sun, W., Xi, J., 2020. CD-sACE2 inclusion compounds: an effective treatment for coronavirus disease 2019 (COVID-19). J. Med. Virol. jmv.25804. https://doi.org/10.1002/jmv.25804.
Sun, X., Whittaker, G.R., 2003. Role for influenza virus envelope cholesterol in virus entry and infection. J. Virol. 77, 12543–12551. https://doi.org/10.1128/jvi.77.23.12543-12551.2003.
Szente, L., Szemán, J., Sohajda, T., 2016. Analytical characterization of cyclodextrins: history, official methods and recommended new techniques. J. Pharm. Biomed. Anal. 130, 347–365. https://doi.org/10.1016/j.jpba.2016.05.009.
Tan, L., Zheng, T., Li, M., Zhong, X., Tang, Y., Qin, M., Sun, X., 2020. Optimization of an mRNA vaccine assisted with cyclodextrin-polyethyleneimine conjugates. Drug Deliv. Transl. Res. 10, 678–689. https://doi.org/10.1007/s13346-020-00725-4.
Tang, N., Bai, H., Chen, X., Gong, J., Li, D., Sun, Z., 2020. Anticoagulant treatment is associated with decreased mortality in severe coronavirus disease 2019 patients with coagulopathy. J. Thromb. Haemost. 18, 1094–1099. https://doi.org/10.1111/jth.14817.
Tang, Y., George, A., Taylor, T., Hildreth, J.E.K., 2012. Cholesterol depletion inactivates XMRV and leads to viral envelope protein release from virions: evidence for role of cholesterol in XMRV infection. PLoS ONE 7, e48013. https://doi.org/10.1371/journal.pone.0048013.
Tang, Q., Liu, P., Chen, M., Qin, Y., 2019. Virion-associated cholesterol regulates the infection of human parainfluenza virus type 3. Viruses 11, 438. https://doi.org/10.3390/v11050438.
Tavornvipas, S., Tajiri, S., Hirayama, F., Arima, H., Uekama, K., 2004. Effects of hydrophilic cyclodextrins on aggregation of recombinant human growth hormone. Pharm. Res. 21, 2369–2376. https://doi.org/10.1007/s11095-004-7691-5.
Taylor, D.R., Hooper, N.M., 2007. Role of lipid rafts in the processing of the pathogenic prion and Alzheimer's amyloid-β proteins. Semin. Cell Dev. Biol. 18, 638–648. https://doi.org/10.1016/j.semcdb.2007.07.008.
Thuja Capital, 2019. Alveron Pharma closes series A round to advance a cyclodextrin based procoagulant medicine into the clinic — Thuja [WWW Document]. URL < https://www.thujacapital.com/news/2019/5/16/alveron-pharma-closes-series-a-round-to-advance-a-cyclodextrin-based-procoagulant-medicine-into-the-clinic > (accessed 5.18.20).
Tian, Z., Si, L., Meng, K., Zhou, X., Zhang, Y., Zhou, D., Xiao, S., 2017. Inhibition of influenza virus infection by multivalent pentacyclic triterpene-functionalized per-O-methylated cyclodextrin conjugates. Eur. J. Med. Chem. 134, 133–139. https://doi.org/10.1016/j.ejmech.2017.03.087.
Totura, A.L., Bavari, S., 2019. Broad-spectrum coronavirus antiviral drug discovery. Expert Opin. Drug Discov. 14, 397–412. https://doi.org/10.1080/17460441.2019.1581171.
Touret, F., de Lamballerie, X., 2020. Of chloroquine and COVID-19. Antiviral Res. 177, 104762. https://doi.org/10.1016/j.antiviral.2020.104762.
Tsamaloukas, A., Szadkowska, H., Slotte, P.J., Heerklotz, H., 2005. Interactions of cholesterol with lipid membranes and cyclodextrin characterized by calorimetry. Biophys. J. 89, 1109–1119. https://doi.org/10.1529/biophysj.105.061846.
Uekama, K., 2004. Design and evaluation of cyclodextrin-based drug formulation. Chem. Pharm. Bull. (Tokyo) 52, 900–915. https://doi.org/10.1248/cpb.52.900.
Verma, D., Gupta, D., Lal, S., 2018. Host lipid rafts play a major role in binding and endocytosis of influenza a virus. Viruses 10, 650. https://doi.org/10.3390/v10110650.
Villiers, A., 1891. Sur la fermentation de la fécule par l'action du ferment butyrique. Compt. Rend. Acad. Sci 112, 536–538.
Vinetz, J.M., 2020. Lack of efficacy of hydroxychloroquine in covid-19. BMJ 369. https://doi.org/10.1136/bmj.m2018.
Wang, M., Cao, R., Zhang, L., Yang, X., Liu, J., Xu, M., Shi, Z., Hu, Z., Zhong, W., Xiao, G., 2020b. Remdesivir and chloroquine effectively inhibit the recently emerged novel coronavirus (2019-nCoV) in vitro. Cell Res. 30, 269–271. https://doi.org/10.1038/s41422-020-0282-0.
Wang, H., Yuan, Z., Pavel, M.A., Hansen, S.B., 2020. The role of high cholesterol in age-related COVID19 lethality. bioRxiv 2020.05.09.086249. < https://doi.org/10.1101/2020.05.09.086249 > .
Wang, Z., Ren, L., Zhao, X., Hung, T., Meng, A., Wang, J., Chen, Y.-G., 2004. Inhibition of severe acute respiratory syndrome virus replication by small interfering RNAs in mammalian cells. J. Virol. 78, 7523–7527. https://doi.org/10.1128/jvi.78.14.7523-7527.2004.
Warren, T.K., Jordan, R., Lo, M.K., Ray, A.S., Mackman, R.L., Soloveva, V., Siegel, D., Perron, M., Bannister, R., Hui, H.C., Larson, N., Strickley, R., Wells, J., Stuthman, K.S., Van Tongeren, S.A., Garza, N.L., Donnelly, G., Shurtleff, A.C., Retterer, C.J., Gharaibeh, D., Zamani, R., Kenny, T., Eaton, B.P., Grimes, E., Welch, L.S., Gomba, L., Wilhelmsen, C.L., Nichols, D.K., Nuss, J.E., Nagle, E.R., Kugelman, J.R., Palacios, G., Doerffler, E., Neville, S., Carra, E., Clarke, M.O., Zhang, L., Lew, W., Ross, B., Wang, Q., Chun, K., Wolfe, L., Babusis, D., Park, Y., Stray, K.M., Trancheva, I., Feng, J.Y., Barauskas, O., Xu, Y., Wong, P., Braun, M.R., Flint, M., McMullan, L.K., Chen, S.S., Fearns, R., Swaminathan, S., Mayers, D.L., Spiropoulou, C.F., Lee, W.A., Nichol, S.T., Cihlar, T., Bavari, S., 2016. Therapeutic efficacy of the small molecule GS-5734 against Ebola virus in rhesus monkeys. Nature 531, 381–385. https://doi.org/10.1038/nature17180.
Wudiri, G.A., Nicola, A.V., 2017. Cellular cholesterol facilitates the postentry replication cycle of herpes simplex virus 1. J. Virol. 91. https://doi.org/10.1128/jvi.00445-17.
Wudiri, G.A., Schneider, S.M., Nicola, A.V., 2017. Herpes simplex virus 1 envelope cholesterol facilitates membrane fusion. Front. Microbiol. 8, 2383. https://doi.org/10.3389/fmicb.2017.02383.
Xiao, S., Si, L., Tian, Z., Jiao, P., Fan, Z., Meng, K., Zhou, X., Wang, H., Xu, R., Han, X., Fu, G., Zhang, Y., Zhang, L., Zhou, D., 2016. Pentacyclic triterpenes grafted on CD cores to interfere with influenza virus entry: a dramatic multivalent effect. Biomaterials 78, 74–85. https://doi.org/10.1016/j.biomaterials.2015.11.034.
Xu, X., Han, M., Li, T., Sun, W., Wang, D., Fu, B., Zhou, Y., Zheng, X., Yang, Y., Li, X., Zhang, X., Pan, A., Wei, H., 2020. Effective treatment of severe COVID-19 patients with tocilizumab. Proc. Natl. Acad. Sci. https://doi.org/10.1073/pnas.2005615117.
Yang, T., Hussain, A., Paulson, J., Abbruscato, T.J., Ahsan, F., 2004. Cyclodextrins in nasal delivery of low-molecular-weight heparins: in vivo and in vitro studies. Pharm. Res. 21, 1127–1136. https://doi.org/10.1023/B:PHAM.0000032998.84488.7a.
Yang, S.T., Kreutzberger, A.J.B., Lee, J., Kiessling, V., Tamm, L.K., 2016. The role of cholesterol in membrane fusion. Chem. Phys. Lipids 199, 136–143. https://doi.org/10.1016/j.chemphyslip.2016.05.003.
Yang, C., Wang, X., Li, H., Ling Ding, J., Yun Wang, D., Li, J., 2009. A supramolecular gene carrier composed of multiple cationic α-cyclodextrins threaded on a PPO-PEO-PPO triblock polymer. Polymer (Guildf). 50, 1378–1388. https://doi.org/10.1016/j.polymer.2009.01.010.
Zawada, K.E., Wrona, D., Rawle, R.J., Kasson, P.M., 2016. Influenza viral membrane fusion is sensitive to sterol concentration but surprisingly robust to sterol chemical identity. Sci. Rep. 6, 1–10. https://doi.org/10.1038/srep29842.
Zhang, Y., Li, T., Fu, L., Yu, C., Li, Y., Xu, X., Wang, Y., Ning, H., Zhang, S., Chen, W.,

Babiuk, L.A., Chang, Z., 2004. Silencing SARS-CoV Spike protein expression in cultured cells by RNA interference. FEBS Lett. 560, 141–146. https://doi.org/10.1016/S0014-5793(04)00087-0.

Zhang, J., Ma, P.X., 2013. Cyclodextrin-based supramolecular systems for drug delivery: recent progress and future perspective. Adv. Drug Deliv. Rev. 65, 1215–1233. https://doi.org/10.1016/j.addr.2013.05.001.

Zhou, F., Yu, T., Du, R., Fan, G., Liu, Y., Liu, Z., Xiang, J., Wang, Y., Song, B., Gu, X., Guan, L., Wei, Y., Li, H., Wu, X., Xu, J., Tu, S., Zhang, Y., Chen, H., Cao, B., 2020. Clinical course and risk factors for mortality of adult inpatients with COVID-19 in Wuhan, China: a retrospective cohort study. Lancet 395, 1054–1062. https://doi.org/10.1016/S0140-6736(20)30566-3.

Zhu, X., Xiao, S., Zhou, D., Sollogoub, M., Zhang, Y., 2018. Design, synthesis and biological evaluation of water-soluble per-O-methylated cyclodextrin-C60 conjugates as anti-influenza virus agents. Eur. J. Med. Chem. 146, 194–205. https://doi.org/10.1016/j.ejmech.2018.01.040.

Zhu, N., Zhang, D., Wang, W., Li, X., Yang, B., Song, J., Zhao, X., Huang, B., Shi, W., Lu, R., Niu, P., Zhan, F., Ma, X., Wang, D., Xu, W., Wu, G., Gao, G.F., Tan, W., 2020. A novel coronavirus from patients with pneumonia in China, 2019. N. Engl. J. Med. 382, 727–733. https://doi.org/10.1056/NEJMoa2001017.

Zidovetzki, R., Levitan, I., 2007. Use of cyclodextrins to manipulate plasma membrane cholesterol content: evidence, misconceptions and control strategies. Biochim. Biophys. Acta - Biomembr. 1768, 1311–1324. https://doi.org/10.1016/j.bbamem.2007.03.026.

Zumla, A., Chan, J.F.W., Azhar, E.I., Hui, D.S.C., Yuen, K.Y., 2016. Coronaviruses-drug discovery and therapeutic options. Nat. Rev. Drug Discov. 15, 327–347. https://doi.org/10.1038/nrd.2015.37.

USC UNIVERSIDADE DE SANTIAGO DE COMPOSTELA

2.5. Cyclodextrin and cyclodextrin complexes characterization

The characterization of CD complexes and CD-based aggregates is not simple. The physicochemical properties of these structures are not easy to predict. A battery of theoretical and experimental methods has been employed for this aim, with different level of success. The main experimental methods aimed to determine the physicochemical properties of cyclodextrin complexes and their aggregates are introduced in this section.

A variety of microscopy methods has demonstrated to be useful to characterize CD-based assemblies at different size scales. Atomic Force Microscopy (AFM) has been used for the characterization of the α-CD/SDS (Sodium Dodecyl Sulfate) self-assembled nanotubes at the air/water interface (Hernandez-Pascacio *et al.*, 2007), SBE-β-CD-mediated nanoparticles (Liu *et al.*, 2016), or vesicles formed by the aggregation of dimers composed by β-CD and dodecane (Zhou *et al.*, 2014); Scanning Electron Microscopy (SEM) has been applied on the determination of cyclodextrin-modifed morphology of red blood cells (Ishiguro *et al.*, 2011) or the study of the encapsulation of oil from the oil/water interface by α-CD and β-CD, and the later formation of emulsions and cyclodextrinosomes (Mathapa and Paunov, 2013b,a); Transmission Electron Microscopy (TEM) was employed for the find out the morphology of β-CD/prophyrin-based networks (Zhou *et al.*, 2019); or Cryo-TEM, which has been used for the characterization of self-assembled β-CD (Bonini *et al.*, 2006) or modified β-CD (Gèze *et al.*, 2004) aggregates in water. For the two latest works, also Dynamic Light Scattering (DLS) was used to provide the size of CD aggregates.

The solubility, the stoichiometry of supramolecular complexes and the association constant corresponding to each chemical species are other important properties that should be taken into account in the design and optimization of applications using CDs. For the determination of these magnitudes, several spectroscopic, chromatographic or even interface techniques, like surface tension measurements, have been used (Czapkiewicz and Tutaj, 1993; Dharmawardana *et al.*, 1993; Jansook *et al.*, 2018; Marques, 2010; Dodziuk, 2006). Calorimetry is one of the most useful methods to provide information on these systems. In contrast to some spectroscopy methods, it commonly allows quantifying the affinity between a given CD and a potential cavity-guest without any chemical label, doing the experiments more reliable and less invasive. It has been said that 'Calorimetry is the only direct method for determination of the reaction enthalpy'(Rekharsky and Inoue, 1998) and so, a more direct way to determine the complexation thermodynamics of CDs. The sensitivity of microcalorimetry, and more specifically of Isothermal Titration Calorimetry, has improved during the last years while the amount of sample required to perform an experiment was significantly reduced (Bouchemal and Mazzaferro, 2012; Hazra and Kumar, 2015; Saha *et al.*, 2016; Thanassoulas and Nounesis, 2019). A detailed description of ITC is provided in Chapter 3.

USC UNIVERSIDADE DE SANTIAGO DE COMPOSTELA

USC
UNIVERSIDADE
DE SANTIAGO
DE COMPOSTELA

Chapter 3

The warm-up for new analysis and techniques by Isothermal Titration Calorimetry

In this house we obey the laws of thermodynamics

Homer J. Simpson, fictional character

Calorimetry is a collection of experimental techniques that, not so long ago, were previously included as a branch of thermal analysis (Brow, 1998).It has been independently studied during the last decades as its applications become more relevant. Additionally, the instruments required for these measurements left specialised laboratories thus allowing the democratization of their use (Bastos, 2016; Wilhelm and Letcher, 2017). The differentiation relies on the definition. While thermal analysis regards the study of a sample magnitude (mass, volume, conductivity, ...) as a function on the temperature, calorimetry involves all the techniques that measure heat or heat flow rates. Depending on the magnitude to be measured, there exist different thermoanalytical methods: Differential Thermal Analysis (DTA) measures the temperature difference between a sample and a reference as a function of temperature; ThermoGravimetric Analysis (TGA) assesses the change in mass; ThermoMechanical Analysis (TMA) quantifies the change in a dimension or in a mechanical property of a sample under the action of static, dynamic or negligible forces; ThermoOptical (TOA), ThermoAcoustics (TAA), and many others (Brow, 1998; Warrington and Höhne, 2008) are also considered within thermal analysis. There is, however, a method that is both thermoanalytical and calorimetric: Differential Scanning Calorimeter (DSC), that measures the heat involved during the temperature change of a sample.

Out of the thermal analysis, calorimetry is linked to the measurement of heat exchange of a physical, chemical, or biological process. The first documented calorimetric study was made by Lavoisier and Laplace, at the end of the XVIII century, to determine the heat produced by a living guinea pig. Several milestones in calorimetry appeared during the following decades: work-heat equivalent determined

by experimentation and the bases for the modern thermodynamics by Joule, the definition of the concept of enthalpy by Hess, or the definition of endothermic and exothermic reaction and the development of the first bomb calorimeter by Berthelot. Together with the evolution of electric circuits, electronics and the discovery of the thermo-electrical phenomena, the scope of calorimetry exploded during the XX century and, as in the case of thermal analysis, many different techniques emerged depending on the process to be studied (Meschel, 2020). Several ways to classify these calorimeters have appeared, regarding the way of determining the heat, their operation mode, the controlled parameter for which the heat is measured, or the construction principle (Lee *et al.*, 2012; Marison *et al.*, 1998; Brow, 1998; Warrington and Höhne, 2008; Zielenkiewicz, 2008). For the specific field of clinical and metabolic studies in living beings, indirect and direct calorimetry is also defined (Kenny *et al.*, 2017; Mtaweh *et al.*, 2018). The purpose of this thesis is to extend the analysis of adsorption and aggregation that, as many other biological, chemical, or physical processes, takes place in fluid systems. Despite the application of the calorimeters using fluids is wider, they are usually included in the branch of biocalorimetry, in part due to their development, that was mainly focused on biochemical or biological systems, and also due to the fact that their uses are derived from this research (Marison *et al.*, 1998). The set of calorimeters employed nowadays in biocalorimetry are mainly Differential Scanning Calorimeters (DSC), and Isothermal Titration Calorimeters (ITC) (Bastos, 2016). In this thesis, we will focus on ITC.

3.1. Isothermal Titration Calorimetry: the ITC

This chapter section is based in a literature selection (Archer and Schulz, 2020; Bastos, 2016; Blandamer *et al.*, 1998; Freire *et al.*, 1990; Grolier and Del Río, 2012; Ladbury, 2004; Ladbury and Chowdhry, 1996; Lewis and Murphy, 2005; Quinn *et al.*, 2016; del Río and Grolier, 2017; Takeda and Matsuo, 2014; Thomson and Ladbury, 2005; Velázquez-Campoy *et al.*, 2004; Wiseman *et al.*, 1989), the different instrument user manuals, some discussions with researchers from the two main manufacturers (Microcal and TA), a short research stay in the laboratories of TA-Waters in Sollentuna (Sweden), several discussion with many other researchers from different labs and the experience of working during the last years with several ITC instruments. Because of this mixture of information, all the main references are located at the beginning of the section and are only going to be cited again when necessary.

Isothermal Titration Calorimetry (ITC) is a calorimetric technique that typically measures the heat exchange after one or more injections of a liquid solution into another at constant temperature. In the present work, we introduce an innovation in this technique, by injection of air into a solution, aiming to create an interface during the process. Thus, in general, we will make reference to fluids instead of liquids, in order to consider the possible injection of air or any other gas into the sample cell. There are two main manufacturers of ITC nowadays: Microcal from Malvern Panalytical and TA Instruments, from Waters. VP-ITC, iTC200 and PEAQ-ITC from Microcal-Malvern, and TAM isothermal calorimeter, Nano ITC and Affinity ITC from to TA-Waters (and their respective automated versions) are the currently commercially available and more used isothermal titration calorimeters at present. Experiments shown in this work were performed using calorimeters

USC UNIVERSIDADE DE SANTIAGO DE COMPOSTELA

from both companies, mainly from VP-ITC instruments. This choice was motivated by the availability of ITCs both in our university and in the lab of several collaborators and also by the fact that this is the instrument with the highest signal-to-noise ratio for our experiments.

The fundamental principles of functioning of ITC designs from the two main manufacturing companies are very similar. Following the definition given by Zielenkiewicz (Zielenkiewicz, 2008), these are twin-designed calorimeters, that correspond to instruments with two identical cells placed inside, where the thermal reaction only happens in one of them whereas the other one works as a reference. The second classification of these calorimeters refers to the way of measuring the heat, that is the power compensation principle: 'The principle of the power compensation calorimeter is to keep the temperature of the system, or the temperature difference between sample and reference, constant'(Suurkuusk *et al.*, 2016). The reason to highlight this sentence is that the ITCs are not strictly isothermal in all cases. As it was observed in the performed experiments and will be shown later, the experimental temperature could change around 0.1 K during an experiment of more than a couple of hours, which does not affect most of the ITC measurements. In power compensation instruments, a constant power is applied on both cells (sample and reference) and when a heat exchange happens in the sample cell (which would modify its temperature), the power actuating on it changes, so that the temperature difference between the cells will remain constant (a more detailed explanation is later exposed). All the mentioned calorimeters follow this principle, except the TAM, in which the measurement unit is submerged in a huge thermostatic bath, and it can also operate in flow mode.

The main differences between ITC instruments from both designs relies on: the cell shape (coin/lollipop-shaped for Microcal-Malvern, cylindrical for TA-Waters), the feedback system, and the shield that keeps the temperature or the temperature difference constant. The schematic representation of a Microcal-Malvern ITC is illustrated in Figure 3.1. All the following considerations along this manuscript are referred to this schema, as this instrument was, by far, the most employed during all the experiments performed for this project.

The Microcal-Malvern design (Figure 3.1) consists in two identical cells (*reference* and *sample* cells) located in a vessel inside the calorimeter, the so-called twin design. This vessel is surrounded by two jackets or shields. The inner one, the *adiabatic jacket* (represented in orange with T_1 its temperature), keeps the experimentally selected temperature. The outer jacket, called *outer shield* (represented in blue with T_2 its temperature), enclose the adiabatic jacket and has two functions: to prevent external heat perturbations and to allow the passive cooling of the adiabatic jacket (and so, the cells). Outer shield is always at a temperature around 1 K below the temperature of the adiabatic jacket.

Reference and sample cells are linked by a thermopile (an electronic device that transforms a temperature difference into an electric potential difference) and connected to their corresponding heaters (power suppliers). A constant power, the *Reference Power* or *RP*, is applied on the reference cell during the whole experiment. This power (*heat power*) is very low (a maximum value of 30 μcal/s can be used in the VP-ITC) and it does not significantly affect any ITC experiment. However, it slightly increases the reference cell temperature (T_R). For 1.4 ml of water, the highest RP value will suppose an increment of less than 0.08 K after 1 hour, around 20 μK /s. Although this temperature change seems to be small, it is significant for a

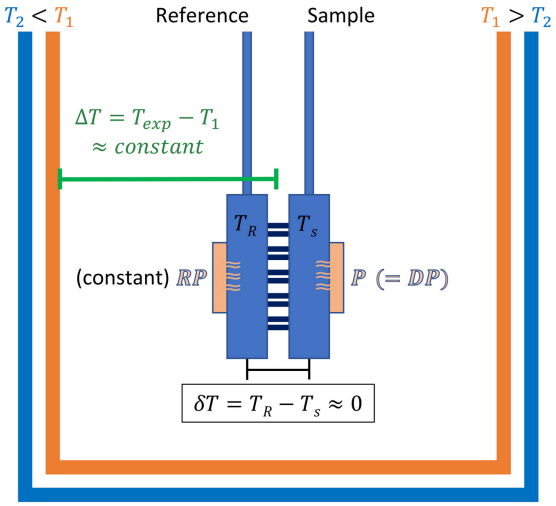


Figure 3.1: ITC diagram

microcalorimetric experiment. The temperature change in the reference cell due to the application of the RP induces a voltage in the thermopile that is collected by a feedback system. The feedback is connected to the sample cell heater and activates it, so the power supplied to the sample cell (we will name it P, despite it is widely and wrongly spread the term DP) will compensate the change in the temperature difference between cells and will bias the temperature of the sample cell (T_S), to reach T_R. We will denote the temperature difference between cells δT, which will be forced by the feedback system to remain close to 0 during any experiment. From now on, for δT being almost 0, we can define an experimental temperature as the mean value between cells: $T_{exp} = \frac{T_R+T_S}{2} \approx T_R \approx T_S$. If nothing happens and the cells are filled with the same fluid, P=RP.

The last part of the calorimeter to be explained is the adiabatic jacketcells relation. It was mentioned before that the purpose of the adiabatic jacket was to keep the temperature selected for the experiment. However, due to the continuous power supply to the cells, the experimental temperature increases. To avoid a heat flux from the surroundings of the cells to them, the adiabatic jacket is set to their temperature, meaning that if the experimental temperature increases, the jacket temperature should also increase in the same manner (Figure 3.2). To do so, the adiabatic jacket is connected to a heater that is linked to the cells by another feedback system. This second feedback aims to keep the temperature difference between the cells and the adiabatic jacket, ΔT, constant. The reason to keep ΔT constant but greater than zero is unclear in the available documentation of the instrument but it could be related to specific electronic considerations. Although this temperature difference is not null, it is very low (less than 1 mK) and it can be registered during any experiment. The reason to apply a constant RP is also unclear, but it may be related to the sensitivity of the heat sensor.

USC UNIVERSIDADE DE SANTIAGO DE COMPOSTELA

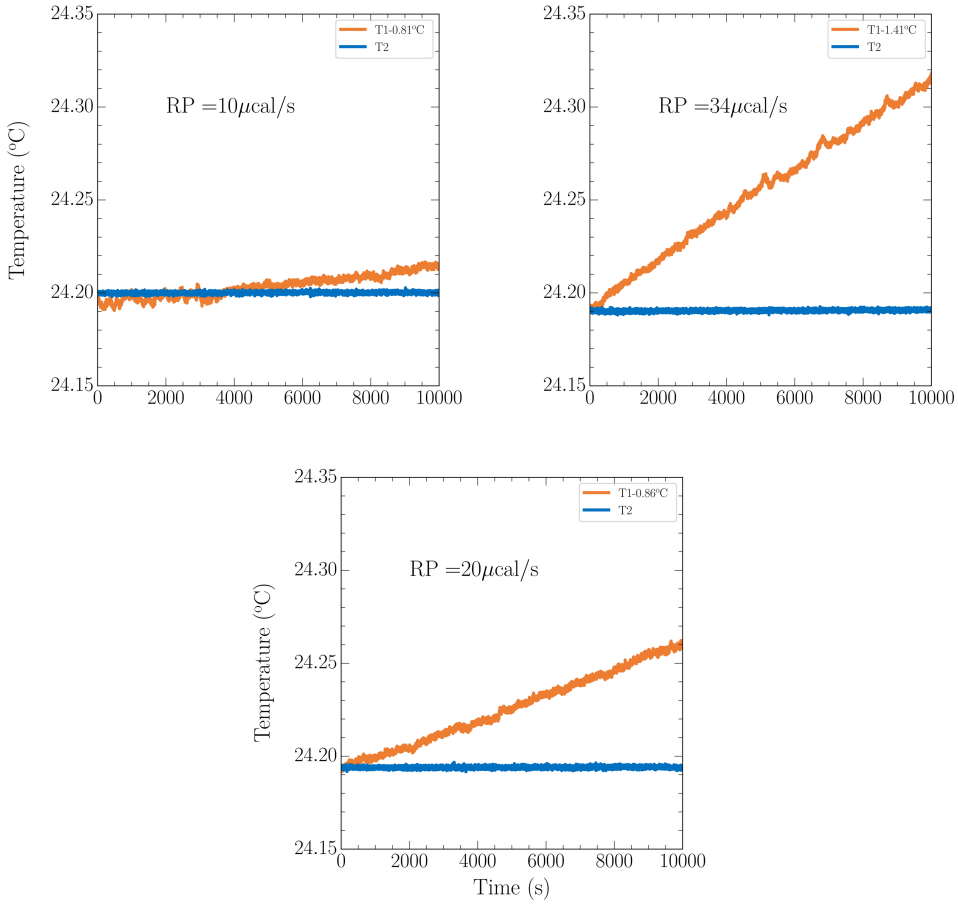


Figure 3.2: Evolution of the adiabatic jacket temperature (T_1, orange) and outer shield temperature (T_2, blue) using three different values of RP during 10000 s. It can be appreciated that the jacket temperature has just increased 0.1 K in the worst scenario, while the shield temperature remains constant. The initial difference value of T_1 and T_2 is substracted so both temperatures can be plotted in the same graph. Temperature and time scales have been set identically between the three cases so they can be compared. Temperature is represented in ^{o}C in the plot, according to the outcoming magnitude from the calorimeter.

3.2. An ITC experiment

In a typical ITC experiment, the syringe is introduced in the sample cell. This fact, even if the fluid in both cells is the same, will change the value of P with respect to the RP. The sample cell is no longer exactly the same as the reference cell while it has the tip of the syringe inside. This does not affect the measurements and it is necessary to have it, but it should be mentioned anyway. The result of this is that P<RP (Figure 3.3).

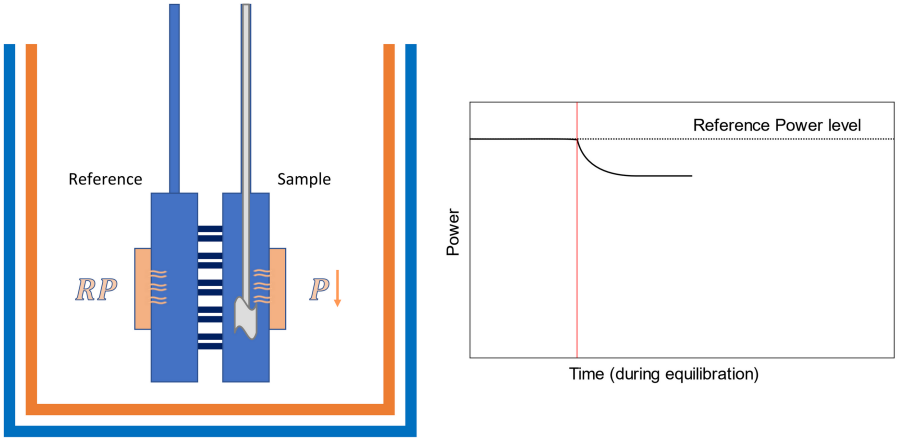
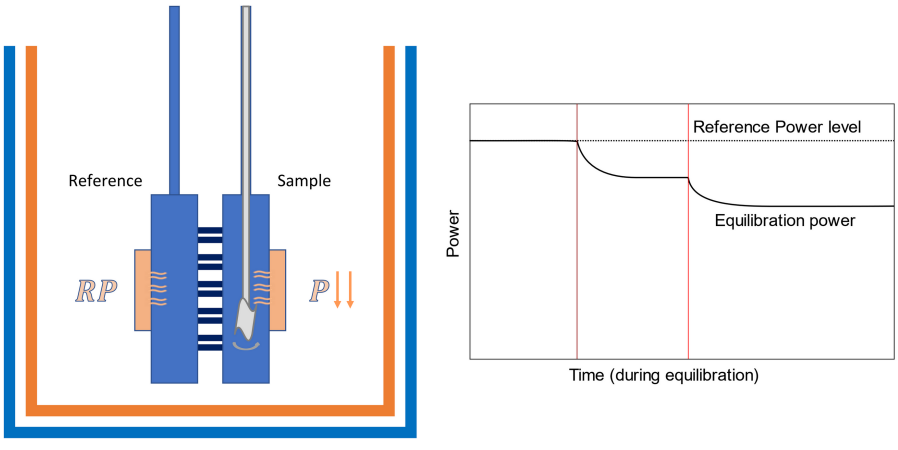


Figure 3.3: Effect on the supplied power P after the introduction of the syringe tip in the cell.

After the introduction of the capillary, the stirring is initialized. In typical ITC instruments, a stirrer is incorporated for the proper mixture of the fluid in the cell and the injected one. This stirring leads to an exothermic heat signal, so it will increase the temperature of the sample cell with respect to the reference. By means of the feedback system, the stirring heat supply is compensated by decreasing P. The advantage of the stirring heat is that it is a continuous contribution once the equilibrium is reached and so, the value of P will decrease by a constant amount with respect to RP. Then, the equilibration power, the *baseline* for our experiment, is reached (Figure 3.4).



USC UNIVERSIDADE DE SANTIAGO DE COMPOSTELA

Figure 3.4: Effect on the supplied power P after the stirring initialization.

Finally, the injection starts. Independently of the number of injections, their duration, recovering time, or other considerations, the injection of a fluid into another

is expected to occur with a thermal process. A chemical reaction, a dilution, the binding/unbinding of molecules or, as it will be our study, the creation of an interface, will consume or release heat, with their corresponding feedback actuation to compensate the effect by increasing or decreasing P. If the process is exothermic, the power is decreased. If the process is endothermic, the power is increased. The power associated to these effects is not constant, as in the case of the stirring. The duration of the power change and its value will depend on the thermal process inside the sample cell. If it is short in time, the change in power will be seen as a pulse. If, after the injection, the reaction takes place during a considerable amount of time, like an enzymatic reaction, the change in P will be larger in time. After the power compensation of an injection, the value of P is expected to recover the value before the injection, the *baseline* (Figure 3.5). In a real experiment, this only happens when the thermal properties of the system contained in the sample cell, like the conductivity or heat capacity, do not significantly change upon the injection and the system is stable. The time to recover the baseline is called the *response time,* τ, although it is still under study and may not be just defined by a simple parameter.

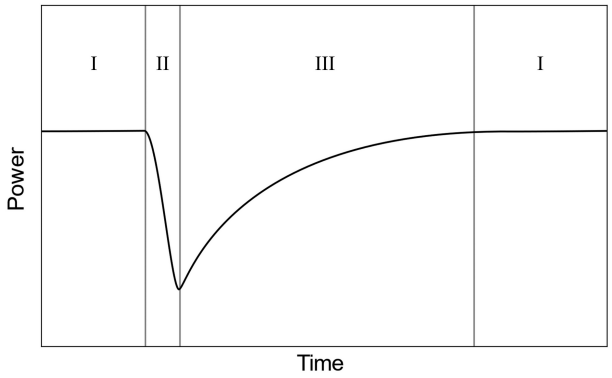


Figure 3.5: Effect on the supplied power P of after a titration. Region I corresponds to the baseline. Region II represents the change of power immediately after the titration (exothermic in this representation). Region III shows the final recovery of the baseline. The integration of the power heat curve between regions II and III corresponds to the total heat involved in the titration process and the reaction that it may initiate in the sample cell.

USC UNIVERSIDADE DE SANTIAGO DE COMPOSTELA

Once the experiment is completed, and the values of P have been recorded as a function of time (Figure 3.6). The injections can be identified by the initial time of the injection and their duration and so, the power related to the injection can be identified. It is time to translate these results into heat.

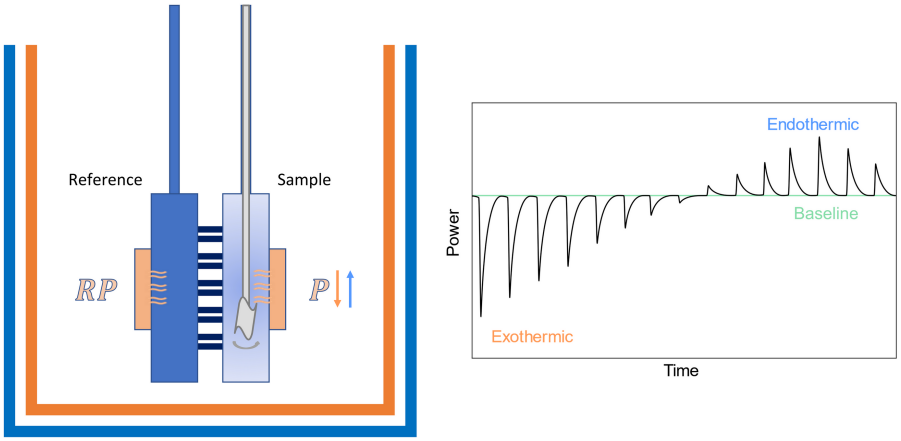


Figure 3.6: Effect on the supplied power P after a full experiment composed of several titrations, both exothermic or endothermic.

3.3. The analysis of ITC data

From an ITC experiment using a Microcal-Malvern instrument and its control software, two files can be obtained with the values of different magnitudes as a function of time. If the *extended data mode* is selected (Figure 3.7), a *.dat* file with the values of time, P, T_1, ΔT and T_2, together other two magnitudes that are not considered due to the lack of information about them, is created. By selecting this mode, the same parameters will be saved in the *.itc* file. Additionally, these magnitudes can be displayed in the upper part of the software main window by double-clicking in the DT parameter. The correspondence between the displayed magnitudes and the previously defined are shown in Figure 3.8.

USC
UNIVERSIDADE DE SANTIAGO DE COMPOSTELA

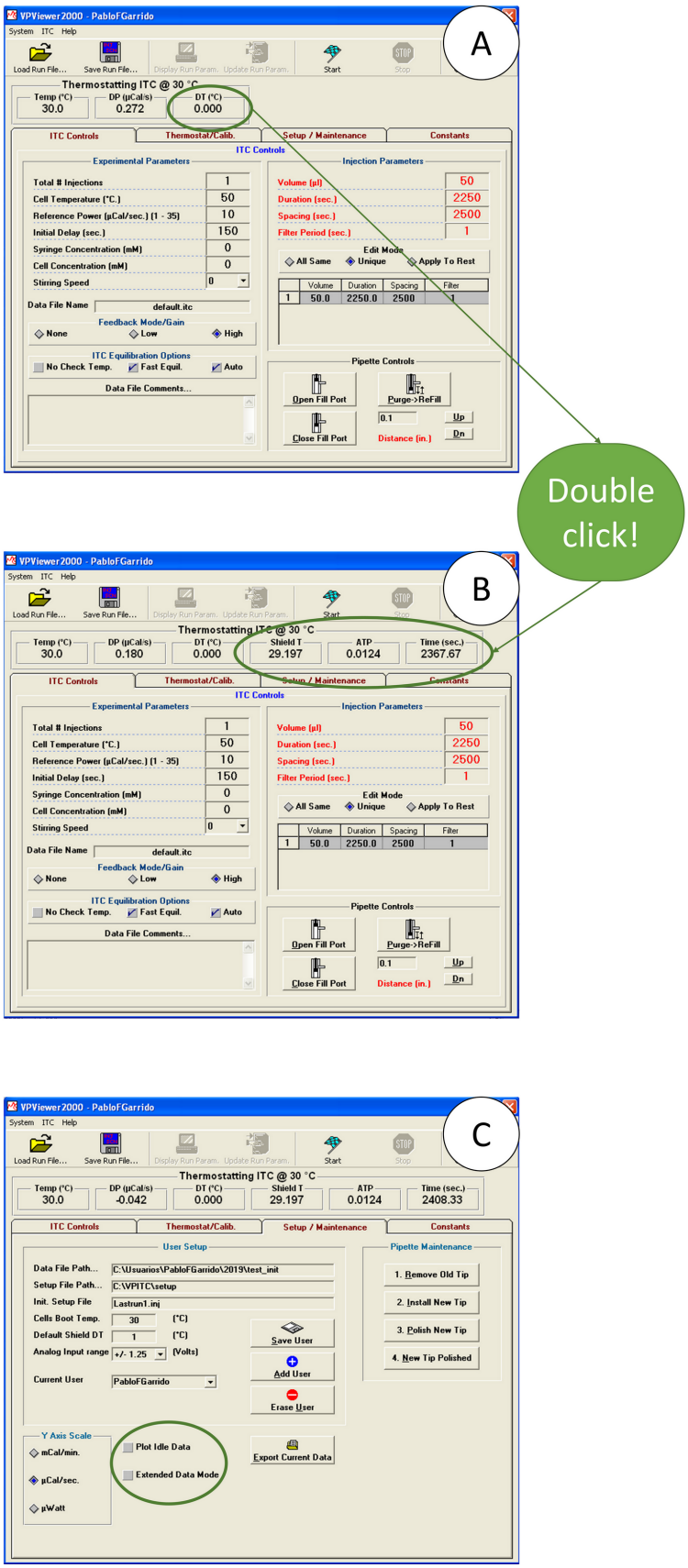


Figure 3.7: Different screenshots of the VP-ITC controller software. A and B: main window before and after the extension of the shown magnitudes. C: tab where the *extended data mode* is located

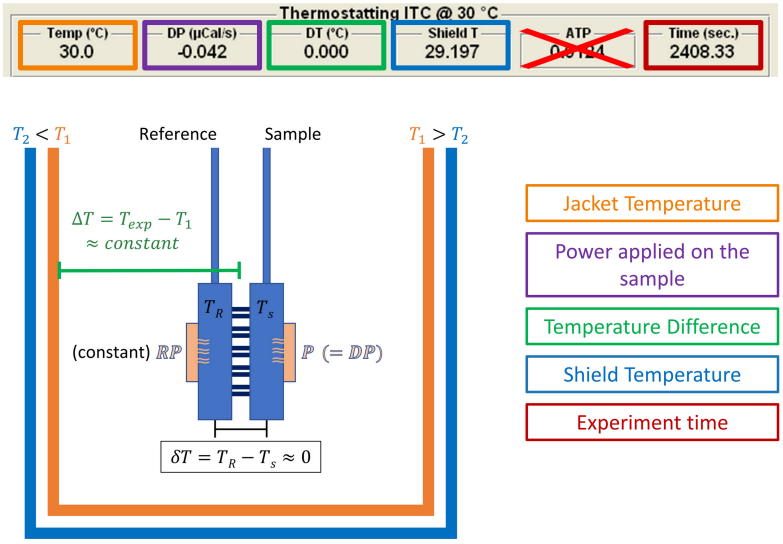


Figure 3.8: Correspondence between the names and locations of Figure 3.1 magnitudes in the software. The colours are kept to help the understanding throughout the text

The *.dat* file contains data collected from the start of the equilibration to the beginning of the experiment (the titration). After the equilibration, the value of the same magnitudes is saved in the *.itc* file, although with the columns in a different order. This latter file also contains information about the design of the experiment and about the instrument (Figure 3.9). The basic information needed for the data analysis is kept in the *.itc* file. If the *extended data mode* available in the instrument control software is not activated, the file will only contain the values of time, power and jacket temperature, together with the metadata of the experiment. This is enough for an ITC standard analysis. From the time, power and the injections information, all the thermodynamic information can be obtained.

USC UNIVERSIDADE DE SANTIAGO DE COMPOSTELA

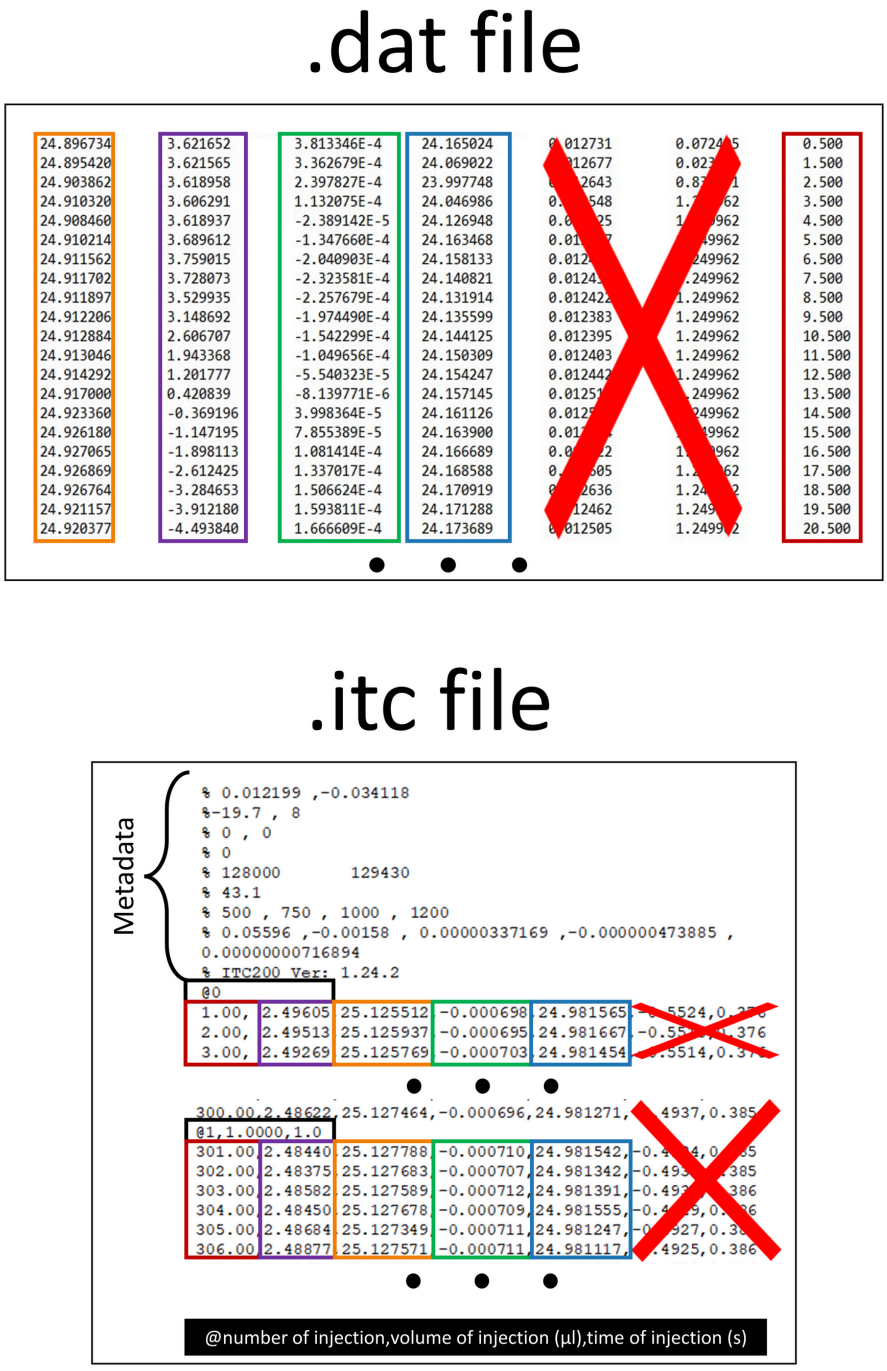


Figure 3.9: Overview of the two files that can be obtained. The colours surrounding the values represent the magnitude that is stored in each column.

The value of the power saved in the *.itc* file corresponds to the heat power supplied to the sample cell to maintain δT=0 . This heat power has previously been calibrated (the correspondence between electric and heat power), but it does not provide thermodynamic information yet. To do so, this power needs to be integrated as a function of time, thus being transformed into heat. The easiest way to do that is by considering the beginning of each injection and integrating the heat power signal from one injection to the next one (3.10). By this way, the heat corresponded to each injection, including that corresponding to any possible intermolecular interaction, is obtained. It is really important to properly design the experiment before the measurements because if the time between injections is not long enough, the perturbed signal will not reach again the baseline and the heat obtained by integration will not be accurate. It is in this point were the misunderstanding about naming P or DP appears. By using the raw data, the magnitude from the *.itc* file is the heat power, P. However, when the data is pre-processed, it is usually shown as a *differential power*, or DP: the difference between a common origin (RP or P at time 0) and the measured power or the difference between the baseline and the measured power. For the power integration, this does not affect the calculations, but it is convenient to highlight the differences between these magnitudes and to clearly set that for all the measurements presented in this work, the values of P and not those of DP are shown.

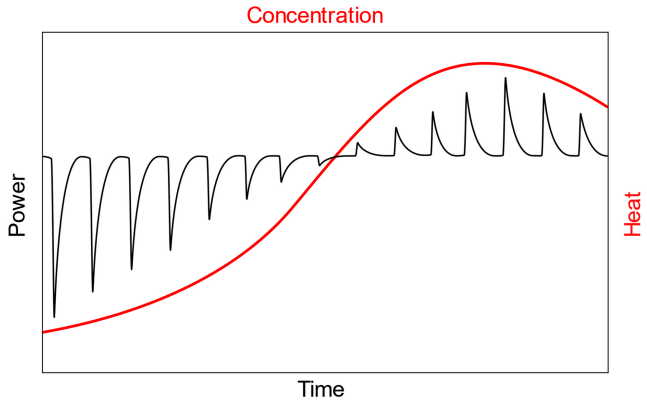


Figure 3.10: Representation of the power-time result of a titration experiment (black) and the heat-concentration curve resulting from the integration (red).

The concentration in the sample cell of the solutes involved in an ITC experiment can be determined from the volume per injection, the initial concentrations of each molecule in the cell and the concentration of the solute(s) in the syringe. From this information, the analysis of heat exchanged during the experiment as a function of the molar ratio will provide the basic thermodynamic profile of the studied molecular interaction: the variation of enthalpy ΔH corresponding to the studied process, the binding constant K_a, the reaction stoichiometry n and the entropy variation ΔS. To obtain this information from the heat (or enthalpy because it is delivered under isobaric conditions) isotherm, a model is needed. There are many

USC UNIVERSIDADE DE SANTIAGO DE COMPOSTELA

proposals, most of them are focused on simple bindings. In Paper IV, a software for ITC data analysis in more complex systems is presented.

3.4. ITC applications

The ability of the ITC to determine thermodynamic properties of titration-induced changes in a system and the fact that the method does not imply any modification on the target molecules have helped up ITC to be a versatile technique for the characterizations of biological binding processes. The number of published works using ITC is large. A general overview can be obtained joining the works of Professors John E. Ladbury (University of Leeds) and Robert J. Falconer (University of Adelaide) (Ababou and Ladbury, 2006, 2007; Cliff *et al.*, 2004; Cliff and Ladbury, 2003; Falconer, 2016; Falconer and Collins, 2011; Falconer *et al.*, 2010, 2021; Ghai *et al.*, 2012; Ladbury, 2001, 2004, 2010; Ladbury and Chowdhry, 1996; Ladbury *et al.*, 2009; Thomson and Ladbury, 2005), who have published several reviews selecting the applications of the ITC for time intervals of a year to a lustrum, from the 2000s up to now. There exist two years of gap between the publications of Ladbury to Falconer, which have been filled with the compilations of Okhrimenko and Jelesarov (Okhrimenko and Jelesarov, 2008) and Bjelič and Jelesarov (Bjelić and Jelesarov, 2008). From these reviews, it is clear that ITC is widely used in macromolecule-ligand characterization, enzymatic reactions studies, drug design or general binding and complexation. In connection with the present work, I would like to introduce some particular applications: cyclodextrins, micellization and the determination of the binding kinetics by ITC.

It was mentioned in the previous chapter that ITC is commonly used for cyclodextrin-based complexes characterization. Most of these systems are drugs encapsulated in cyclodextrins, and the aim is to determine the binding constant to investigate the stability of the supramolecular structure and also its stoichiometry (Bouchemal, 2008; Callies *et al.*, 2016; DÁria *et al.*, 2021; Gal *et al.*, 2018; Saha *et al.*, 2016; Stensgaard Diget *et al.*, 2019) and to explore their properties to better understand their behaviour in aqueous solutions by the complexation with model molecules (Kellett *et al.*, 2021; Schönbeck and Holm, 2019; Tomeček *et al.*, 2021; Wszelaka-Rylik and Gierycz, 2015; Xavier-Júnior *et al.*, 2019), among which surfactants have excel (Araujo Marques *et al.*, 2021; Benkő *et al.*, 2014; Bouchemal and Mazzaferro, 2012; Brocos *et al.*, 2011; Concha-Santos *et al.*, 2013; Luviano *et al.*, 2020; Meira *et al.*, 2018; Ondo and Costas, 2017; dos Santos Silva Araújo *et al.*, 2021; Dodziuk, 2006; Vargas *et al.*, 2018).

Surfactants are amphipathic molecules that have their own relevance out of the cyclodextrins connection, as they have already been mentioned in Chapter 1. In solution, these molecules form self-assembly structures, ranging from small micelles to larger and more complex structures. These configurations are in equilibrium with different species and aggregates and they depend on the molecular structure, concentration and temperature. Because of this dependence, surfactants are ideal to be studied by ITC (Archer and Schulz, 2020; Basílio and Garcia-Rio, 2012; Dai and Tam, 2003; Heintz *et al.*, 2010; Kessler *et al.*, 2012; Loh *et al.*, 2016; Majhi and Blume, 2001; Marsh, 2012; Medeiros *et al.*, 2018; Medoš *et al.*, 2020; Medoš and Bešter-Rogač, 2017; Olesen *et al.*, 2014; Perspicace *et al.*, 2013; Šarac *et al.*, 2017; Vázquez-Tato *et al.*, 2018).

The last specific application of ITC to be mentioned is kinITC: the obtention of kinetic parameters from ITC experiments (Burnouf *et al.*, 2012; Dumas *et al.*, 2016). This new application is based on the direct analysis of the power heat obtained from the experiments and not just of the heat after the integration. It has been implemented in the AFFINImeter software (Paper IV) to make it more reachable (Piñeiro *et al.*, 2019) and its applications are continuously growing (Beckwith *et al.*, 2021; Erlekam *et al.*, 2019; Glöckner and Klebe, 2021; Glöckner *et al.*, 2020; Igde *et al.*, 2017; Li *et al.*, 2017; Muñoz *et al.*, 2019; Zihlmann *et al.*, 2018)

All these applications of ITC refer to bulk solution properties or reactions. However, it is well known that the interface is highly sensitive to the concentration of species in the bulk solution. The combination of interfacial and bulk properties is ideal to characterize a specific binding or aggregation phenomenon and also to better understand the connection between self-assembling and adsorption processes. As it was mentioned before, ITC allows a direct determination of thermodynamic properties in solution. Here we will show that this instrument is also useful to characterize interfaces.

USC
UNIVERSIDADE DE SANTIAGO DE COMPOSTELA

Chapter 4

Objetives

Quien me ha impedido cumplir mi programa electoral es la realidad

Mariano Rajoy Brey, Spanish Prime Minister

The main objective of this thesis is to develop a new experimental technique to directly measure the heat associated to the creation-disruption of interfacial area. The new method, that will be named *Fluid Interface Calorimetry* aims to be able to simultaneously assess aggregation and the adsorption processes of the same system, taking advantage of the design and sensitivity of modern ITC instruments.

Several secondary objectives are proposed to complement the main one, namely:

- To compare the structure of water obtained around complex structures in the bulk solution and at air-water interfaces. This will be addressed by Molecular Dynamics simulations.
- To contribute to the analysis of ITC measurements, mainly for the characterization of self-assembled systems. New measurements, models and analysis methods were proposed to this end.
- To perform interfacial and aggregation analysis by means of other techniques, in parallel to the calorimetric analysis, to validate the proposed new methods and to understand the limitations of the Fluid Interface Calorimetry.
- To develop and validate the code and analysis software that allows using the new models and methodologies.

USC
UNIVERSIDADE DE SANTIAGO DE COMPOSTELA

USC
UNIVERSIDADE
DE SANTIAGO
DE COMPOSTELA

Part II

Methods

Part II introduces the use of ITC as a technique to determine interfacial properties, which represents the main innovation of this thesis. Molecular Dynamics simulations are also employed to provide structural information with atomic resolution, able to shed light on the driving forces responsible for specific aggregation/adsorption processes. Some other experimental and computational methods, used to a lesser extent, are also presented. Paper II and the Patent registration are here included.

USC
UNIVERSIDADE
DE SANTIAGO
DE COMPOSTELA

USC
UNIVERSIDADE
DE SANTIAGO
DE COMPOSTELA

Chapter 5

ITC and interfaces

A mellor leña está onde non entra o carro

Galician proverb

In the Objetives section, it was mentioned that the main goal of this thesis is to develop a new technique able to assess fluid interface thermal phenomena. For the determination of interfacial magnitudes, many different techniques are typically applied, but none of them, to our knowledge, can directly determine the heat associated to the adsorption processes. Based on the power sensitivity of modern ITCs and on the wide range of applications related to molecular association already tested with these instruments, the isothermal titration calorimeters currently available in the market are exceptional candidates to address our primary goal. These instruments have never been used in fluid interface characterization, so our work is pioneer in this sense. The development and optimization of the method are presented in this chapter.

Along this thesis project, more than 1000 fluid interface experiments (Figure 5.1) have been carried out, testing different injection rates, temperatures, fluids, and environmental conditions. These include new ways of controlling the injection by external pumps as well as by stopped injections to follow the evolution of the baseline in processes showing slow kinetics. Also, different ITCs have been tested, although most of the measurements were obtained using VP-ITC instruments. The most important results corresponding to this development, how to use and how to analyse the results are collected in Paper II, the Patent registration and Paper III.

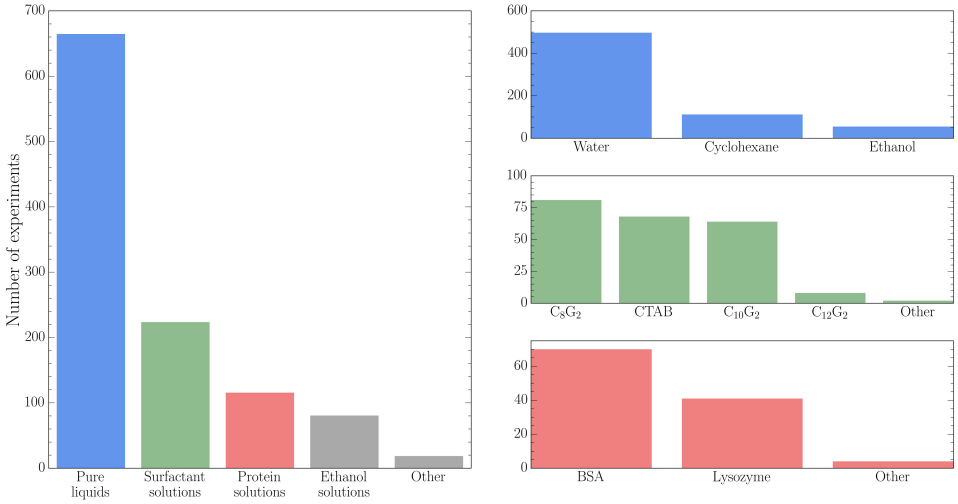


Figure 5.1: Classification of the developed ITC interfacial experiments according to the sample. It can be appreciated that more than half of the experiments have been carried out using pure liquids as they were mainly used for the development and optimization.

USC UNIVERSIDADE DE SANTIAGO DE COMPOSTELA

5.1. Paper II

"Fluid interface calorimetry", published in *Journal of Colloid and Interface Science* (2021), is a regular article where a new methodology is presented. Making use of already developed ITCs, the first measurements of heat (power) related to fluid interfacial processes are here presented: bubble formation in different liquids, protein adsorption and determination of surface tension. The technique is also explained, emphasizing in the injection rate dependence, the reproducibility or the influence of temperature. This work has been developed in collaboration with people from: (1) Departamento de Física Aplicada, Facultade de Física, Universidade de Santiago de Compostela; (2) CIQ-UP, Departamento de Química e Bioquímica, Faculdade de Ciências da Universidade do Porto; (3) Institute of Biocomputation and Physics of Complex Systems (BIFI), Joint Units IQFR-CSIC-BIFI, and GBsC-CSIC-BIFI, Universidad de Zaragoza; Department of Biochemistry and Molecular and Cell Biology, Universidad de Zaragoza; Aragón Institute for Health Research (IIS Aragón); Biomedical Research Networking Centre for Liver and Digestive Diseases (CIBERehd); Fundacion ARAID, Government of Aragón; (4) IGBMC, Dept of Integrative Biology, Strasbourg University. The list of authors is presented below, by order and with their corresponding affiliations. The corresponding authors are marked with a *:

Pablo F. Garrido (1)*, Margarida Bastos (2), Adrián Velázquez-Campoy (3), Philippe Dumas (4), Ángel Piñeiro (1)*.

According to the CRediT authorship contribution statement (Brand *et al.*, 2015), my contributions to this publication are: Conceptualization; Methodology; Software; Validation; Formal analysis; Investigation; Writing - Original Draft; Writing - Review & Editing; Visualization

Garrido PF, Bastos M, Velázquez-Campoy A, Dumas P, Piñeiro Á (2021). Fluid interface calorimetry. *J. Colloid Interface Sci.*, **596**, 119–129. ISSN 00219797. doi: 10.1016/j.jcis.2021.03.098. URL https://www.doi.org/10.1016/j.jcis.2021.03.098

USC UNIVERSIDADE DE SANTIAGO DE COMPOSTELA

USC
UNIVERSIDADE
DE SANTIAGO
DE COMPOSTELA

Journal of Colloid and Interface Science 596 (2021) 119–129

Contents lists available at ScienceDirect

Journal of Colloid and Interface Science

journal homepage: www.elsevier.com/locate/jcis

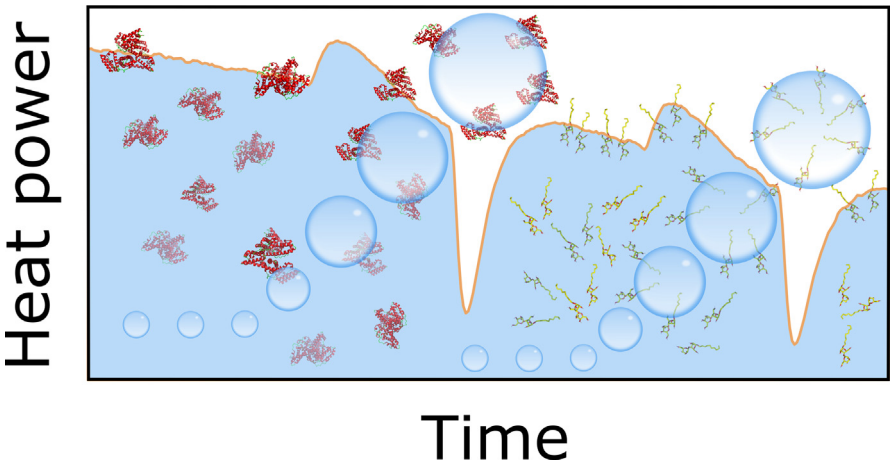
Regular Article

Fluid interface calorimetry

Pablo F. Garrido [a,*], Margarida Bastos [b], Adrián Velázquez-Campoy [c,d,e,f,g], Philippe Dumas [h], Ángel Piñeiro [a,*]

[a] Departamento de Fisica Aplicada, Facultade de Fisica, Universidade de Santiago de Compostela, E-15782 Santiago de Compostela, Spain
[b] CIQ-UP, Departamento de Quimica e Bioquimica, Faculdade de Ciencias da Universidade do Porto, R. Campo Alegre 687, P-4169-007 Porto, Portugal
[c] Institute of Biocomputation and Physics of Complex Systems (BIFI), Joint Units IQFR-CSIC-BIFI, and GBsC-CSIC-BIFI, Universidad de Zaragoza, Zaragoza 50018, Spain
[d] Department of Biochemistry and Molecular and Cell Biology, Universidad de Zaragoza, 50009 Zaragoza, Spain
[e] Aragon Institute for Health Research (IIS Aragon), 50009 Zaragoza, Spain
[f] Biomedical Research Networking Centre for Liver and Digestive Diseases (CIBERehd), 28029 Madrid, Spain
[g] Fundacion ARAID, Government of Aragon, 50018 Zaragoza, Spain
[h] IGBMC, Dept of Integrative Biology, Strasbourg University, F67404 Illkirch CEDEX, France

GRAPHICAL ABSTRACT



ARTICLE INFO

Article history:
Received 17 February 2021
Revised 15 March 2021
Accepted 16 March 2021
Available online 22 March 2021

Keywords:
Interfaces
Calorimetry
Adsorption
Isothermal Titration Calorimetry
Surface Tension

ABSTRACT

Hypothesis: Amphiphilic molecules spontaneously adsorb to fluid polar-nonpolar interfaces. The time-scale of such adsorption depends on the molecular size and structure of the solute. This process should be accompanied by a power heat exchange that could be detected by commercial isothermal calorimeters.

Experiments: Air is injected in the bulk of different aqueous solutions contained in the sample cell of an isothermal titration calorimeter. The formation of the resulting bubbles leads to a liquid/air interface to which the solute molecules spontaneously adsorb. Continuous injection experiments to produce multiple bubbles as well as experiments with static bubbles stand from the capillary tip, aiming to observe slow adsorption processes, were performed.

Findings: The power associated with the formation, growth and release of air bubbles in different liquids was measured. Different independent contributions that can be associated to the pressure change in the

* Corresponding authors.
E-mail addresses: Pablo.Fernandez@usc.es (P.F. Garrido), Angel.Pineiro@usc.es (Ángel Piñeiro).

https://doi.org/10.1016/j.jcis.2021.03.098
0021-9797/© 2021 Elsevier Inc. All rights reserved.

gas phase, the evaporation-condensation of the solvent, the increase of interfacial area, the change in the heat capacity of the sample cell content, and the release of the bubble were observed. The periodic pattern produced by the continuous injection of air at a constant rate is used to determine the surface tension of different liquids, including solutions of different molecules and (bio)macromolecules.
© 2021 Elsevier Inc. All rights reserved.

1. Introduction

Isothermal titration calorimetry (ITC) is a highly sensitive and versatile technique aimed for the characterization of molecular interactions. No labelled or chemically modified compounds are required to perform the measurements, the molecules do not need to be fixed to any artificial substrate, and the experiments are directly performed in solution, mimicking the conditions where the target molecules are typically expected to carry out their native function [1]. Well-designed ITC experiments can provide thermodynamic information on systems that interact in complex ways, including molecular recognition processes coupled to aggregation and/or dissociation events. The variety of systems that can be characterized by calorimetric methods is not restricted by the size or the structure of the involved molecules or molecular aggregates. Competitive multivalent interactions, dissociation-aggregation mechanisms, protein or polymer conformational changes induced by the binding of small molecules, and the interaction between vesicles, liposomes or artificial nanoparticles with proteins, peptides and other molecules have been characterized by calorimetric methods [2–4]. Simpler mechanisms like the dissociation of dimeric proteins or the aggregation of small molecules giving micelles have also been studied by ITC [5,6]. Typically, thermodynamic parameters such as the enthalpy and the association (dissociation) constants are obtained from the analysis of ITC experiments, from which the Gibbs energy and the entropy contributions to the studied process can be calculated. Further, a method to obtain kinetic information, taking advantage of the analysis of the raw data provided by ITC, has been published [7] and made easy to use [8,9]. Advanced computational tools designed to analyze a large variety of calorimetric experiments, and aimed to the characterization of interaction mechanisms, including also kinetic parameters for one-step interactions, are publicly available [10–13].

The use of ITC in the study of intermolecular interactions has been somewhat hindered by the amount of sample required for each measurement, typically larger than in the case of other techniques such as Surface Plasmon Resonance (SPR) or MicroScale Thermophoresis (MST). However, the important reduction of cell volume in the last generation instruments, together with the abovementioned features of ITC, and the fact that it is the only technique that can provide full thermodynamic characterization of the process under study from a single experiment, has positioned ITC as the best alternative for the characterization of a large variety of inter- and intra- molecular interactions. As such, calorimetric studies of physicochemical events provide fundamental information for their full characterization. Noteworthy, specific experimental and theoretical calorimetric methods have been developed to assess the heat of adsorption of gases and liquids onto solids [14,15]. Despite the wide range of calorimetric applications, to the best of our knowledge, no attempts have yet been made to measure the heat of molecular adsorption or surface formation at fluid interfaces. Such measurements would require to follow the formation of new surface in real time. The thermodynamic and kinetic characterization of the interaction between different fluid phases would facilitate the understanding of a number of applications, mainly those related with foams, interfacial (bio)-films, adsorption mechanisms and the characterization of liquid/-vapor or liquid/liquid interfaces.

Several techniques are available to assess thermodynamic, structural and kinetic properties of molecules at interfaces, such as surface tension, ellipsometry and different microscopy and spectroscopy approaches [16–19]. Surface tension (γ) is the most basic of these properties and different methods are available to determine its value for a given liquid sample. The correlation between the surface tension and the maximum pressure of a bubble attached to the tip of a capillary while it is growing in a liquid upon air injection is one of the most classical approaches, the so called "maximum bubble pressure method" [16]. This method is well suited to be implemented in typical isothermal titration calorimeters with none or just slight modifications in the instruments. The injection of air into the calorimeter measurement cell at controlled pressure and/or flow rate is expected to allow quantitative surface tension measurements of liquid samples, while simultaneously determining the corresponding power exchange upon air injection. No other experimental method can directly obtain the dependence of the measured heat of adsorption to fluid interfaces on the molecular composition of the studied solution. In the present paper we show that: i) the power corresponding to the injection of air and consequent formation of bubbles in a liquid sample can be easily assessed by using standard ITC instruments; ii) these experiments clearly distinguish different liquids; and iii) if water is the solvent, different concentrations of cosolvents, surfactants and even proteins can be differentiated. The experimental procedure required to create and analyze air/liquid bubbles in a calorimetric cell, with no modifications in the instrument, as well as the main variables that can affect the measurements, are described in detail. Further to this, several potential applications of this method and some modifications in the experimental setup are proposed, to improve the results at the quantitative level.

2. Materials and methods

2.1. Materials

Ultrapure water (Elix 3 purification system, Milipore Corp.), ethanol (99.8% min. purity from Panreac) and cyclohexane (99.7% min. purity from Honeywell) were used in the experiments. All liquids were degassed trough vacuum prior to the ITC measurements. Decyl-β-D-maltopyranoside ($C_{10}G_2$) was purchased from Anatrace, Bovine Serum Albumin (BSA) was purchased from Sigma and Ethylammonium Nitrate (EAN) was purchased from Iolitec. All the compounds were used as received, without further purification.

2.2. Selection of the instrument

We aimed at measuring the thermal power accompanying the formation, growing and releasing of air bubbles. The power signal involved in these experiments is expected to be weak and to change quickly, so we need an instrument with high sensitivity and short response time. In this work, the injection system of current ITC instruments was employed to achieve our aim. The shape and volume of the sample cell and the radius of the capillary used for the injection are key parameters for these measurements since

the bubble should be large enough to be detectable and not too large to avoid contact with the cell walls. A range of apparently suitable ITC instruments are commercially available. Nowadays, two main companies manufacture ITCs: TA-Instruments and MicroCal/Malvern Panalytical. The former uses cylindrical-shaped cells while the later uses coin-shaped cells, whereas the range of available volumes are similar (for volumes up to 1400 μL). Nevertheless, fundamental differences between these branches exist as regarding the way the power is measured, the feedback and the stirring systems. These differences have an impact in the detected power signal that should be taken into account when interpreting and analyzing the raw data. Since we are interested in the kinetics of the bubble formation process, for our experiments the power sensitivity is more relevant than the minimum power detection. However, even though ITC instruments are well suited to monitor kinetic signals [7,20,21], they usually aim at the thermodynamic characterization of the studied process, and therefore the latter parameter is typically considered more important than the former. Fortunately, the short-term noise (STN), which is an estimation of the power fluctuations when the sample is thermally stabilized before the start of the titration experiment, is typically provided by the manufacturers in the technical specification sheet of the instrument and can be taken as an estimation of the power sensitivity. In present work we tested seven different titration calorimeters (see Table 1).

During our preliminary tests, all the instruments described in Table 1, except the commercial version of the TAM III, were able to detect the signal corresponding to the air injection/bubble formation. As stated above, the volume of the bubble, which depends directly on the diameter of the capillary of the injection system, should be large enough to produce a detectable power signal (larger than the STN) and the cell volume should also be not too large to ensure no contact between the bubble and the cell wall. Note that the power due to bubble formation could be magnified by optimizing the air injection rate and the diameter of the capillary. The injection rate is normally accessible from the control software. It should be slow enough so that the characteristic response time of the instrument allows observing the kinetic signal but also fast enough to produce a measurable power distinguishable from the baseline. Thus, the instrumental response time is also a key feature for these experiments. It is worth commenting that the response time depends on the sample solution due to the change in the heat conductivity and heat capacity arising from the different compositions and interactions with the sample cell [23]. So special care should be taken to keep the cell extremely clean to prevent changes in the response time.

ITC instruments usually contain a stirring system to guarantee that the solution in the sample cell is homogeneous in a short time. In our experiments the stirrer had to be disconnected or even removed to allow the formation of the bubble. In all experiments reported in this work, the standard injection system of the corresponding instrument was employed to introduce the bubbles in the sample cell. We just connected the clean and dry syringe, filled with air at atmospheric pressure, to the ITC and injected the air at a controlled rate. It is important to stress that the pressure of the air contained in the syringe will not be constant through these experiments, as it will be discussed below. Finally, we would call the attention to the fact that using this method a large number of bubbles can be spontaneously formed during a single experiment.

The signal in the VP-ITC in our preliminary tests was clearer and more reproducible than that from the other instruments, probably due to its higher specific sensitivity (lower STN to cell-volume ratio). Therefore, we decided to focus on the VP-ITC for the experiments production and analysis. This is due to the combination of its geometrical features, specific sensitivity and also to the fact that we have access to three different versions of this instrument (see Table 1) and we can assess the reproducibility of the data using them. No modification at all in the instruments was performed for any of the measurements reported in the present work.

3. Bubble formation in VP-ITC

As explained above, the bubbles were created in the ITC sample cell using the own injection system of the instrument. Special care was taken with the cleaning and with the connections of the syringe (plunger and positioning of the syringe in the instrument for the experiment and connection for the installation of the home-made manometer as will be explained later) to prevent air leakages. Once a specific injection rate is set in the control software, the bubbles are spontaneously created in the sample cell. Depending on the composition of the solution in the sample cell, between 10 and 60 bubbles are typically created in an experiment using a syringe of 200 μL.

Standard ITC experiments consist in sequential small injections of one liquid solution into another of different composition. In the calorimeter used, the power supplied to the reference cell triggers the feedback power on the sample cell, aimed at minimizing the difference in temperature between the sample and the reference cells, and thus the feedback power on the sample cell is registered, and the integral of the signal perturbation upon each injection is plotted as a function of the concentration ratio of the involved compounds in order to perform a thermodynamic analysis. The recovering of a stable baseline is important to get a reasonable estimation of the heat exchanged during each injection. Ideally, the signal corresponding to the injection of bubbles should be performed in a similar way, *i.e.* the volume of air required to form a single bubble should be injected and then we should wait for the recovering of the baseline before pumping more air in the sample cell. However, the compressibility of the injected fluid in our case is much higher than that of standard liquid solutions, and the pressure is significantly changed during the experiment. This, together with the time delay between the event that takes place in the sam-

Table 1
Main features of the ITC instruments employed in the present work. The information of this table was obtained from the corresponding specification sheets provided by the manufacturing companies. For the TA calorimeters, the range of response time and noise arises from the standard volume (maximum) and low volume (minimum) experiments.

Company	ITC	Cell geometry	Cell volume (μL)	Syringe volume (μL)	Short term noise level (nW)	Response time (s)
TA Instruments/Waters	TAM prototype*	Cylindrical	1000–20000	100–2500	–	–
	TAM III	Cylindrical	4000–20000	100–2500	10	–
	Nano ITC	Cylindrical	190–1000	100–250	1.4–2.5	11.0–18.0
	Affinity ITC	Cylindrical	190–1000	up to 250	1.3–2.5	3.3–18.0
MicroCal/Malvern Panalytical	VP-ITC**	Coin shaped	1400	295	2.0	20
	ITC-200	Coin shaped	200	40	0.84***	10
	PEAQ-ITC	Coin shaped	200	40	0.63	8

* This is a non-commercial version of the TAM III, available at MB's Laboratory, University of Porto.
** Three types of VP-ITC (versions 06.05.673, 08.01.255 and 11.10.994) were used in the present work.
*** [22].

ple cell and the registered signal, makes difficult to decide the precise time required for the creation of single bubbles as well as the time required for the injection and for the recovering of the baseline. In all experiments done initially in this way there were indeed uncertainties on what was really happening in the sample cell during what was being considered a single-bubble event: (*i*) creation, growing and release of a bubble; (*ii*) same as (*i*) but followed by the creation of a second bubble in the same injection; (*iii*) release of a bubble that was already created during the previous injection; or (*iv*) release of a mature bubble followed by the formation of another one. For this reason we decided to follow a different strategy, based on a relatively slow but continuous injection, producing sequential bubbles. The main disadvantage of this method is that a stable baseline is not completely reached before the creation of a new bubble. However, if the injection rate is slow enough, a rich kinetic signal can be obtained without much interference from successive bubbles. It is well known that the formation, growing and release of a bubble in the tip of the capillary depends on the air pressure in the syringe, as well as on the surface tension and hydrostatic pressure of the liquid (Fig. 1). Additionally, when introducing the syringe in the instrument to initiate a new experiment, some liquid raises through the needle due to capillarity, what slightly increases the pressure inside the syringe. The balance between these contributions is expected to change with time since the air is continuously being injected and the bubble changes in volume and shape as a response to this pumping.

The injection rate in a VP-ITC can be set by selecting a single injection of a large volume with a specific injection time in the control software. In the present work, a waiting period of 150–300 s was used before starting the air-titration experiments. The total volume of a 200 μL syringe was injected during 9000 s for the slowest experiments and 900 s for the fastest ones. Faster experiments should not be performed as they result in overlapped signal contributions. The baseline was again registered at the end of the titration for at least 300 s.

The formation, growth and release of the bubble depend on the size and shape of the tip of the capillary used to inject the air. In the case of the VP-ITC instruments the capillary used to inject the solution from the syringe in the sample cell has helical-shaped tip, since it is also employed as a propeller to guarantee the homogeneity of the liquid in a typical experiment (Fig. 1). In principle, this geometry would not be ideal for our aims, but as it will be shown later, our results using it were highly reproducible. It is known that a gas bubble reaches its maximum internal pressure when it becomes a hemi-sphere of diameter equal to that of the inner part of the capillary from which it emerges. Beyond this size, as the volume increases the pressure decreases following the Laplace-Young equation ($\Delta P = P_{int} - P_{ext} = 2\gamma/r$ with γ the surface tension and r the radius of the bubble), until the bubble is released [24]. In the case of the VP-ITC, the bubble remains attached to the capillary for a time longer than expected if the needle walls are thinner than its inner diameter, so finally its 'exotic' geometry seems to help to stabilize the bubbles. This is interesting since it contributes to a clearer signal in the instrument.

4. Results for air-water bubbles

Water was chosen as the reference pure liquid to test and optimize the experimental setup. Beyond its immediate availability, its high surface tension gives rise to the formation of large bubbles. In this section, we show how different parameters affect the bubble formation and detection.

4.1. Injection rate dependence

Since two different phases coexist during bubble formation, several events are expected to contribute to the power signal, namely the compression/decompression of the air, vaporization/-condensation effects at the interface, surface creation/destruction, and mechanical perturbations. Another important contribution to

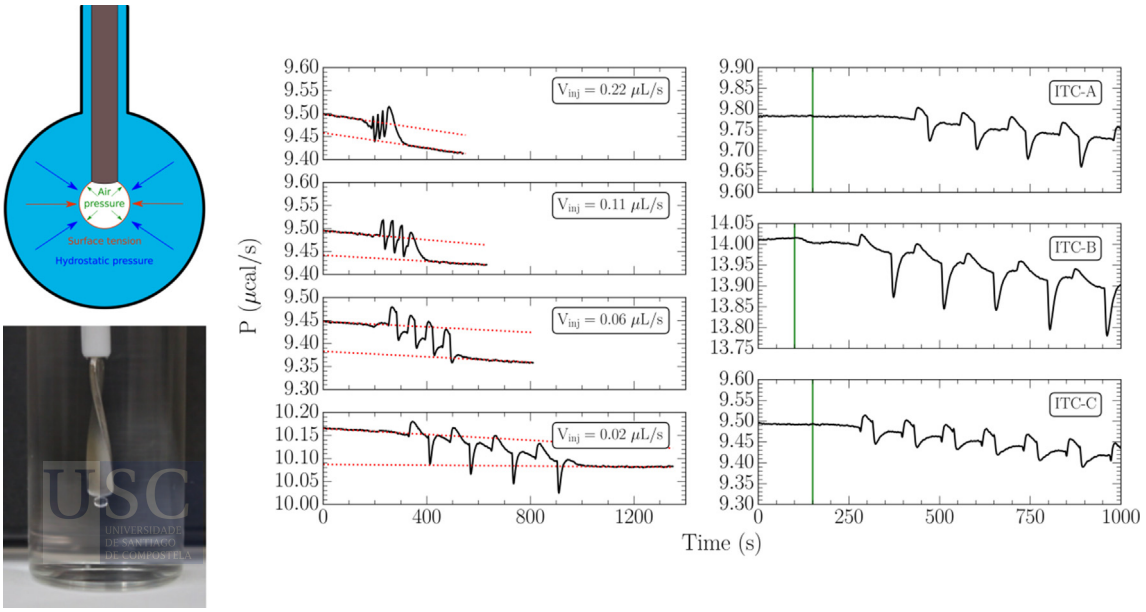


Fig. 1. Left-up: Representation of a bubble inside a calorimetric cell. The arrows indicate the direction of the force due to air pressure (from inside the bubble, pointing outwards) as well as surface tension and hydrostatic pressure (from outside the bubble, pointing inwards). Left-down: picture of the helical-shaped capillary needle of the syringe used with the VP-ITC, immersed in water with a bubble formed and still attached to the tip. Middle: Raw power signal obtained for the injection of air into water at 298 K for four different injection rates: 0.22, 0.11, 0.06 and 0.02 μL/s; corresponding to the injection of 20 μL of air during 90, 180, 360 and 900 s respectively. Red dotted lines represent the baseline linear extrapolation before and after the titration experiment. Right: Comparison of experiments with the same setup (air into water at 0.02 μL/s injection rate and 298 K) using the ITC instruments A, B and C, as indicated by the labels. The green vertical lines indicate the beginning of the injection. (For interpretation of the references to colour in this figure legend, the reader is referred to the web version of this article.)

the signal is the pumping in/out of heat to the cell due to the temperature difference between the environment and the measurement cell. For reasonably slow injections, the heat power contributions of thermodynamic nature associated to the bubble formation should not depend on the injection rate, in contrast to those related to mechanical or external effects. So, the injection rate is expected to affect the time evolution of the thermodynamic contributions to the power signal but not the corresponding areas. Our experiments of air bubbles in pure water revealed that the signal is very clear and reproducible at injection rates lower than 0.06 μL/s, while for faster injection rates different contributions overlap to each other, including those coming from different bubbles (Fig. 1). They also show that the number of bubble formation events that can be observed in the power profile for a given total volume does not depend on the injection rate, as expected, and that the signal is richer in information at slower injection rates.

4.2. Reproducibility of the power profile

The signal is periodic, regardless the injection rate. Independent experiments performed at the same injection rate with the same liquid using the same ITC instrument were practically indistinguishable (Fig. S1). At most, slight differences were visible for the initial power and the slope of the baseline. Less obvious is the tiny difference in the period of the signal between experiments. All together, these differences determine the statistical variability between different measurements using the same instrument.

The same experiment was replicated with three different VP-ITC instruments: 06.05.673, 08.01.255 and 11.10.994 in Table 1; that will be named A, B and C, respectively, from now on. The size of the positive and negative contributions to the power profile is significantly different in each experiment (Fig. 1), producing thus a signal of different shape. However, the number of contributions, as well as the corresponding signs, are the same in all experiments. As expected, the three signals are periodic, but the periods are also significantly different. These differences are similar to those observed when changing the injection rate: the different contributions are more separate from each other in ITC-B than in ITC-A and ITC-C (Fig. 1), which results from a modification of the profile of the signal due to variable overlapping of positive and negative peaks. Also, even when the same injection rate and solvent are employed, the number of bubbles generated within the same time interval was different in each case, assuming that each repeat of the periodic signal corresponds to a bubble. This can only be due to instrument variability, likely at the level of the injection systems and/or the capillaries, since ITC-A and ITC-C were located in the same laboratory and both experiments were performed at the same time using the same sample. Additionally, two other significant differences are observed in ITC-B with respect to ITC-A and ITC-C: a larger negative peak and a higher measured equilibrium power, although the same reference power was used for the three calorimeters, 10 μcal/s. The way that these magnitudes can affect the measurement will be analyzed in the following sections.

4.3. Baseline

USC UNIVERSIDADE DE SANTIAGO

For all the data presented in this work there is a systematic negative drift in the baseline during the air-titration experiments. Additionally, in some experiments there is an initial slope in the pre-titration equilibration period, although this is often very small or even negligible (Fig. 1). Repeats of experiments using different initial slopes in the baseline always exhibit a negative drift during the air-titration experiment, with almost identical power profile for each bubble (Fig. S2) This indicates that the initial slope does not significantly affect the results of these experiments and that both contributions to the baseline drift (the initial one and that coming from the air-titration) are independent from each other.

4.4. Reference power

The reference power (RP) is the constant electrical power applied to the reference cell so that the heat absorbed or released in the sample cell (where the bubbles are formed) can be measured through the change in power needed to minimize the difference of temperature between the two cells, through a feedback compensation system. The RP introduces an offset to the baseline and so it changes the maximum power that can be measured without saturation of the instrument. RP significantly affects the slope in the power profile throughout the air-titration experiment (Fig. 2) as well as the shape of the signal corresponding to each bubble, although no clear trends were identified in the variation of such shape. Notably, the period of the signal, and so the bubble size, remains unchanged.

4.5. Temperature dependence

In order to check the impact of the temperature, air-titration experiments with the ITC cells at 283, 293, 298, 310 and 323 K and the lab temperature between 293 and 296 K, were performed (Fig. 2). The temperature is expected to affect the volume of the bubbles by changing the internal air pressure and the surface tension of the liquid-air interface, consequently changing the power signal. Again, a periodic signal with different contributions for each bubble was observed. The main contributions to the signal in the previous experiments at 298 K were a positive peak followed by a negative one (Fig. 1). Notably, the amplitude and even the sign of the first peak clearly changes with temperature, while the second peak remains always negative (exothermic) without a clear trend in amplitude. The evolution of the first peak is clear: it is slightly negative at 283 K, then it becomes slightly positive at 293 K, and the maximum grows in a proportional way to the temperature. This is basically the result of the influence of room temperature on the measurements, as there is no perfect shielding of the calorimetric cell from the surroundings. Repeats of these experiments reproduced the same behavior. On a side note, it is worth to comment that the baseline showed to be less stable at the higher working temperatures.

5. Analysis of air-titration experiments

Our reference experiments are performed using a reference power of 20 μcal/s, an injection rate of 0.02 μL/s (100 μL injected in 4500 s), and an initial and final delays of 300 s. Additionally, the equilibration signal before and after the titration experiment were typically registered for a minimum of 1000 s. A representative experiment is shown in Fig. 3, with the equilibrated signal followed by the periodic profile corresponding to 24 consecutive bubbles and finally the recovery of a constant baseline. The systematic drop of baseline as the air is pumped into the sample cell, together with the clear reproducibility of the power profile corresponding to each bubble are clear in this experiment. The baseline drift during the titration experiment is due to the feedback system used by the employed instrument (VP-ITC from MicroCal), keeping constant the difference of temperature between the reference cell and the sample cell when the temperature of the latter changes due to an exothermic or endothermic process. To detect such temperature fluctuations, a constant power is applied on the reference cell (RP). When both cells contain exactly the same type and amount of liquid, and no stirring is used, the power to be applied to the sample cell to cancel the temperature difference, in the

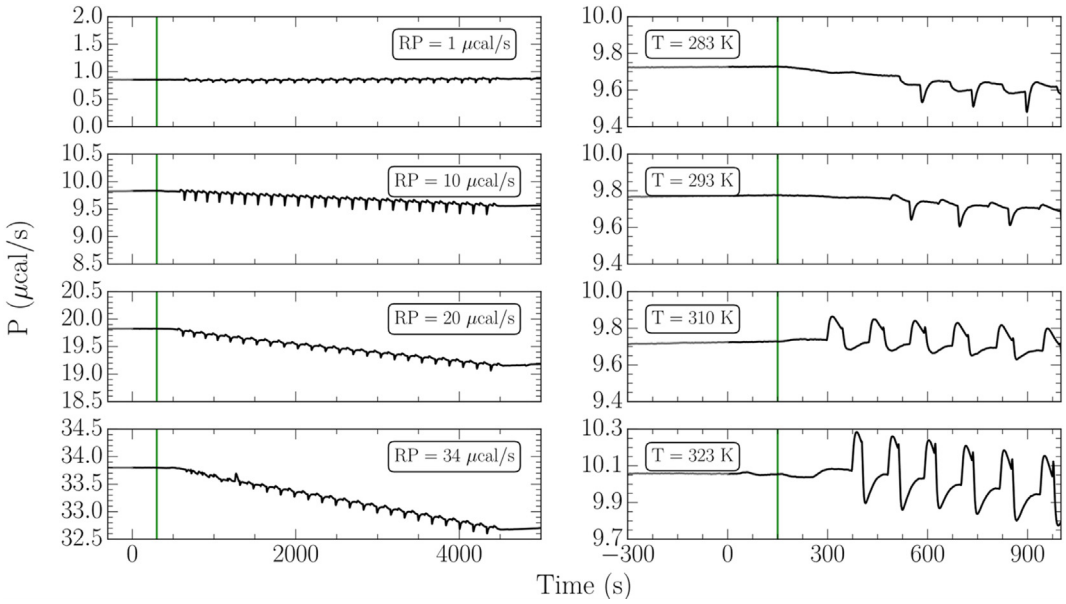


Fig. 2. Left: Power vs time profiles for the injection of air into water at 298 K and 0.02 μL/s, as a function of the reference power (indicated in each plot). Right: Power vs time profile of air-titration experiments for the temperatures indicated in each plot. In all cases, the green vertical lines indicate the beginning of the injection.

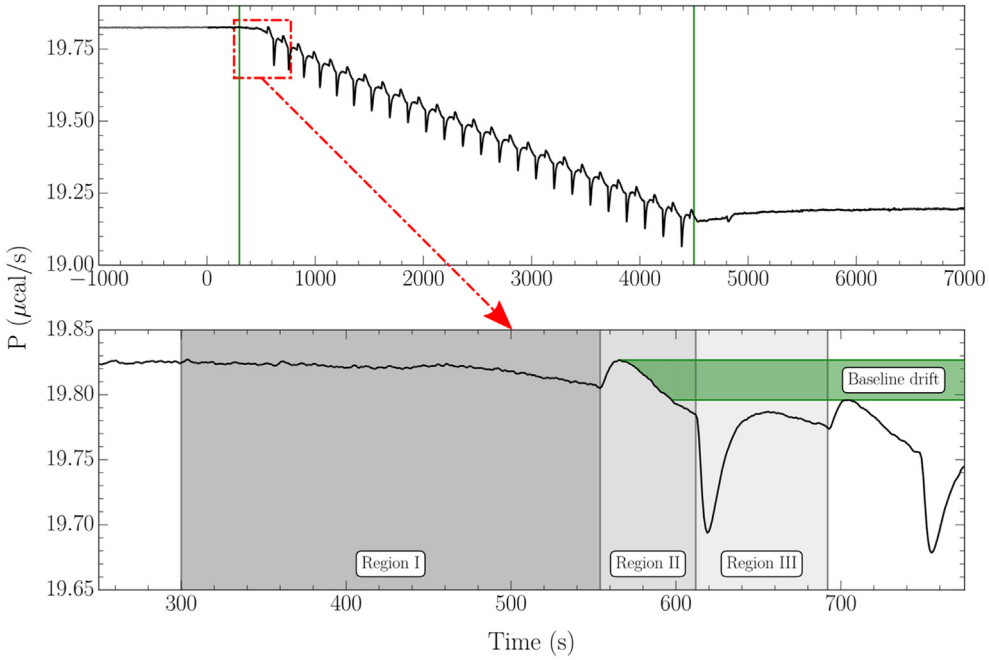


Fig. 3. Experiment corresponding to the injection of air into water using a reference power of 20 μcal/s, an injection rate of 0.022 μL/s (100 μL injected in 4500 s), and an initial and final delays of 300 s. The equilibration signal before and after the titration experiment was registered for 1000 and 2200 s, respectively. The whole titration is shown in the upper plot while the lower one shows the initial amplified region including the profile described by the first two bubbles. The green vertical lines indicate the beginning and end of the air-injection. (For interpretation of the references to colour in this figure legend, the reader is referred to the web version of this article.)

absence of thermal reactions, should be equal to the RP (Fig. 3 during the equilibration period prior to the air-titration). Assuming that the air injected in the sample cell during our experiments remains trapped, and an equivalent volume of liquid is therefore displaced outside the coin-shaped container, the amount of water and thus the total heat capacity of the sample cell decreases upon each injection. This means that the power required to keep constant the difference of temperature with respect to the reference cell decreases as the amount of injected air increases. The addition of a compound in the sample cell with higher heat capacity than that in the reference cell would result in a positive drift in the baseline. This was tested by experiments injecting water into cyclohexane (not shown). It is possible to take advantage of the baseline drift observed in our experiments to estimate the volume of air contained in the sample cell (see example in the Supplementary Material). This change in the baseline is not observed in the TA Instruments ITCs, most likely as the results of the different design of the sample cell, that being cylindrical will probably allow the release of air out of the measurement region during the titration experiment, at odds with what happens in the lollipop cells' shape in the MicroCal instrument.

To better understand the source of the different contributions to the power signal, we connected an analogic manometer to the injection system. This allowed us to observe on the flight the strong pressure changes due to the different stages in the bubble production: appearance at the tip of the capillary, growth, and releasing. This device does not form part of the standard design of the ITC instrument and the readings for the pressure change were not recorded but just used to identify the events that take place in the measurement cell at real time. The complementary information coming from ITC and pressure changes allowed us to identify three different regions in the raw power signal (Fig. 3). Region I was only detected at the beginning of the experiment. The corresponding power signal is weak, hardly distinguishable from the baseline, but it is present in all our experiments. During this stage, no bubble was formed and the manometer did not detect a significant pressure change, so it should correspond to a slow increase in pressure of the air contained in the syringe accompanied by a decrease in the level of liquid in the capillary and probably to some condensation at the small water/air interface of the meniscus. The initial height level of the solvent in the needle could be higher than that in the sample cell due to the capillary rise of the liquid. This explains why this contribution is detected only before the appearance of the first bubble. In contrast to region I, regions II and III were completely reproducible along the rest of the periodic profile. Our joint analysis of the pressure change and the calorimetric signal, complemented with the reproduction of the experiment outside of the ITC cell, in a transparent flask (Fig. 1) allowed us to identify the region II with the appearance and growth of the bubble at the tip of the capillary (see video in the Supplementary Material). Once the bubble appears, a quick expansion of the gas phase, accompanied by the increase of the liquid vapor interface area, takes place. Finally, Region III begins by the sharp peak associated with the delivery of the bubble, which is accompanied by the re-compression of the air (the pressure inside the syringe decreases when the bubble goes out) and the condensation of the vapor, as in region I. After this release, the cycle starts again but with a higher pressure than in the initial bubble, so the processes associated to region I are not appreciated for the rest of the bubbles. Additionally, there is a power contribution due to the bubble release strong perturbation. As stated above, the released bubble remains inside the sample cell displacing the corresponding volume of liquid, thus changing the total heat capacity of the sample cell. This provokes the baseline drift, as shown in the Supplementary Material.

6. Direct applications of the method

In the previous sections it has been shown that ITC instruments are able to detect a rich and highly reproducible power profile for the injection of air into water. In the present section we will show how it is possible to take advantage of this kind of experiments for different aims. The most obvious utility of the method is its use to extract thermodynamic, kinetic and mechanic information from the power profile. Next, we will show how that profile depends on the pure liquids located in the sample cell, how the period can be used to get accurate surface tension values for different liquids and samples, including biomacromolecules, and also how to use it in liquid-liquid interfaces.

6.1. Pure liquids and simple solutions

Water has an unusually high surface tension, so the volume of the bubbles formed in this liquid is abnormally high compared to that in other liquids with more ordinary surface tension values. In addition to water, the power profile for the continuous injection of air in ethanol, cyclohexane and EAN were registered (Fig. 4). As expected, the power profile is similar for all the compounds. The same contributions described above can be observed, although their magnitudes are different in each case. The correlation with the surface tension is clear not only in the period of the signal profile but also in the size (area or total heat) of some contributions, particularly in the negative peak associated to the release of the bubble from the capillary tip. Plainly, the periodic profile corresponding to each bubble contains a lot of useful information that deserves to be analyzed in detail. Although there are several phenomena involved in these experiments that lead to a significant heat exchange, they are not strongly coupled to each other and this facilitates the modeling of the signal. Ideally, we should be able to decouple the kinetic contribution of the molecular adsorption to the interface. From that contribution the surface tension could be directly obtained based on thermodynamic considerations, using a surface equation of state. The development of a model able to address this aim is currently in progress. Meanwhile, we focused on the period of the signal, that is expected to be clearly correlated to the bubble volume and therefore with the surface tension of the liquid in the sample cell. Beyond the pure liquid experiments, solutions with low concentration ethanol in water were also tested (Fig. 4). The addition of ethanol alters the bubble signal profile of water and the period decreases in a way that is proportional to the surface tension of the mixture, as expected.

6.2. Determination of surface tension

A number of different methods are commercially available to determine surface tension of liquids and liquid mixtures. Maximum drop volume tensiometers are based on a correlation between the maximum volume of a drop pending from a capillary and the surface tension, while maximum bubble pressure tensiometers use the maximum pressure of a bubble created in the bulk of a liquid phase for the same aim [25]. In our case, we get a periodic signal that can be exploited in a similar way. We propose to use the period as a direct observable to correlate with the surface tension of the studied liquid. The employed protocol has been described in detail in a recently registered patent [26]. This hypothesis was tested using different systems. First, we got the period for different pure liquids (see previous section) and then we got the period for a mixture of ethanol and $C_{10}G_2$ in water. High quality surface tension data obtained from a standard tensiometer are available in the literature, so the period as a function of the surface tension was plotted for all the studied concentrations at different injection rates. The behavior was completely linear, confirming our hypothesis (Fig. 5). Then we used just two pure compounds with extreme surface tension values (water for highest and ethanol or cyclohexane for lowest) as a reference and got the scaling factor to transform periods into surface tension values. The results are in excellent agreement with those obtained using standard surface tension instruments. The advantages of using ITC are clear: (*i*) isothermal calorimeters provide much more information than a standard tensiometer,; (*ii*) the required amount of sample is very low and it can be recovered at the end of the experiment since the injection of air do not contaminate it; (*iii*) the implementation of an additional injection system would allow changing the concentration of the sample cell with no need to open and clean it. This would also contribute to a considerable saving in time and sample. Additionally, ITC allows measuring properties for exactly the same solution both in the bulk and at the interface. Note that most experimental methods employed to characterize interfaces require specific setups and sample preparation, but it is not common to use exactly the same sample to perform measurements at both phases.

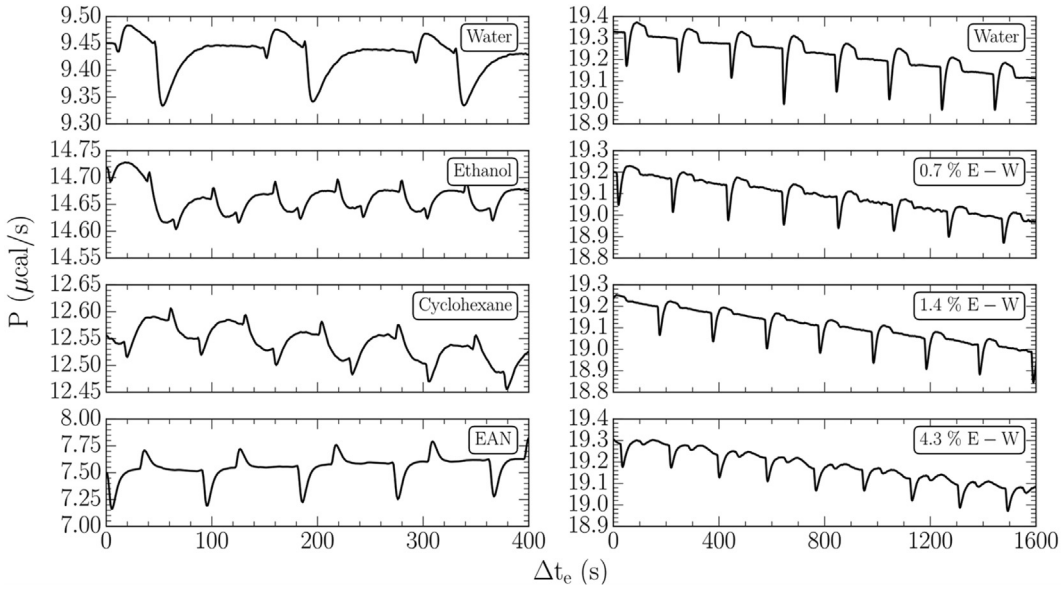


Fig. 4. Left: Experiments corresponding to the injection of air into water, ethanol, cyclohexane and ethylammonium nitrate using a reference power of 10, 20, 20 and 10 μcal/s, respectively, and an injection rate of 0.02 μL/s (100 μL injected in 4500 s). In all cases, a representative period of 400 s containing a minimum of 3 bubbles was selected. The power scale (ordinate axis) is the same for water, ethanol and cyclohexane (0.2 μcal/s), but not for EAN (1 μcal/s). Right: ITC experiments corresponding to the injection of air into different concentrations of ethanol in water using a reference power of 20 μcal/s and an injection rate of 0.02 μL/s (200 μL injected in 9000 s). Δt_e represents the elapsed time from the first point selected to plot along the titration experiments.

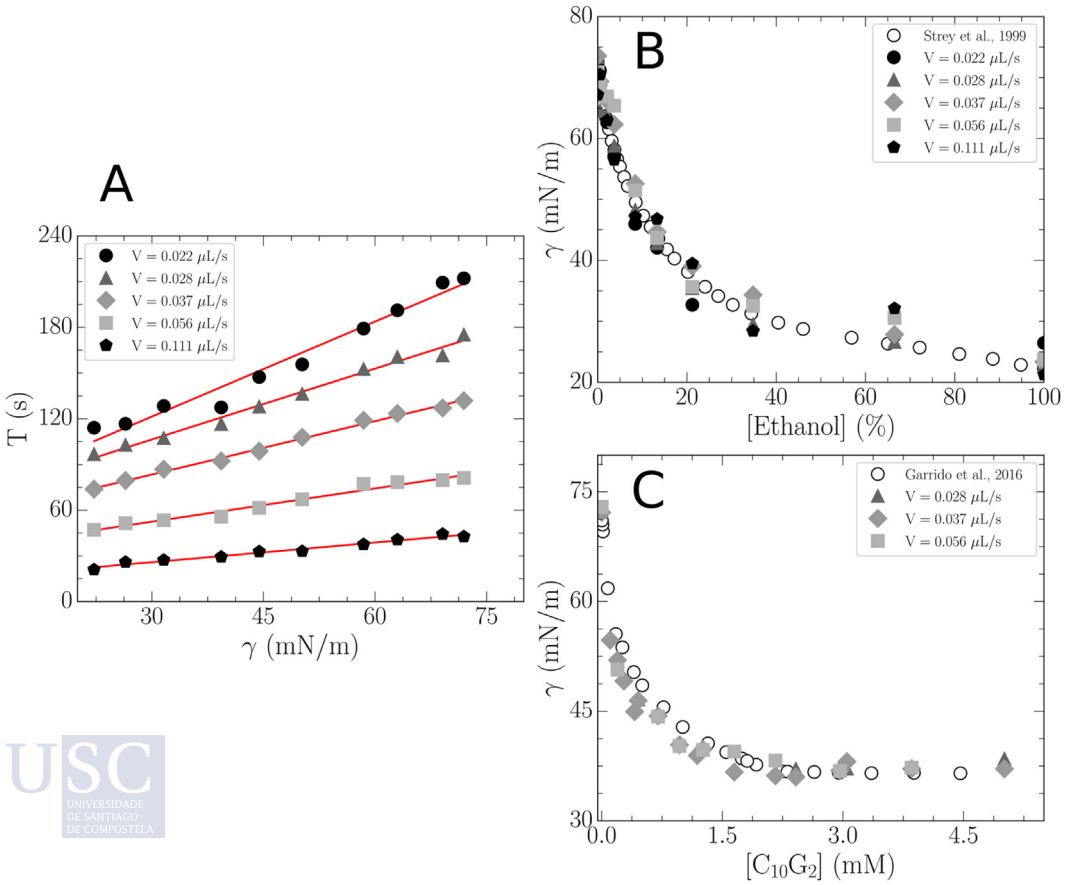


Fig. 5. Left: correlation between surface tension (γ) and period of bubble formation obtained for different concentrations of ethanol in water at different injection rates. Right: Surface tension values as a function of the concentration obtained for mixtures of ethanol and $C_{10}G_2$ in water, for different injection rates, compared with literature [27,28].

Similar experiments were performed using different concentrations of BSA in water. BSA is a globular protein with recognized surface activity [29]. It was observed that the period for bubble release clearly depends on the protein concentration (Fig. 6). However, since the adsorption of proteins is known to be relatively slow (in the time scale of tens of minutes or hours) due to its slow dif-

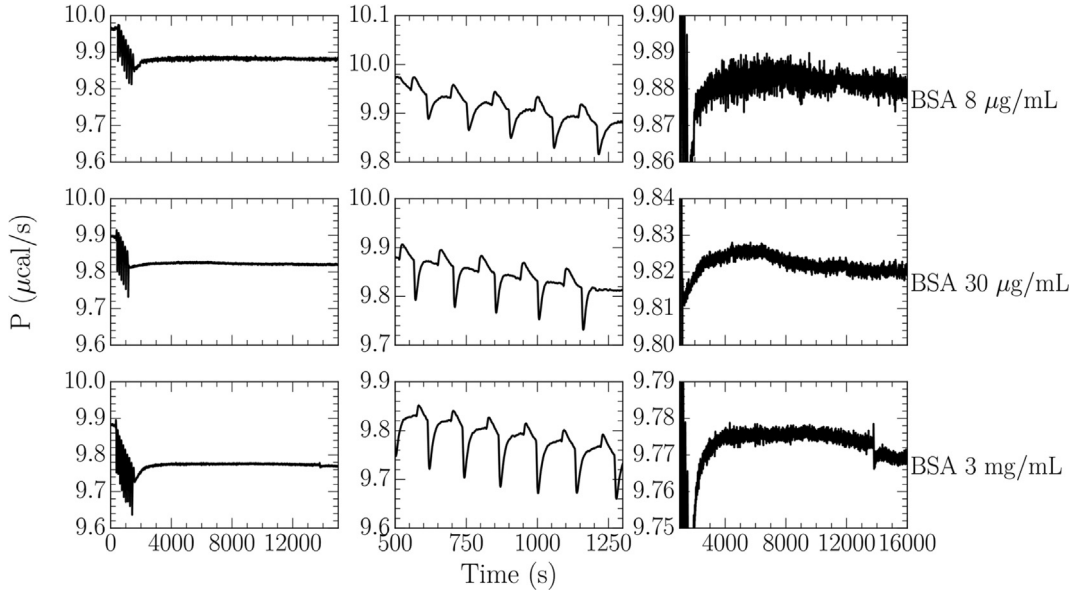


Fig. 6. Left: ITC experiments corresponding to the injection of 10 bubbles of air into different concentrations of BSA in water (see labels on the right of the plots), followed by 14,000 s of equilibration time to follow the signal corresponding to the potential adsorption of protein and to the recovering of the baseline. Middle and right: amplification on the titration and equilibration regions, respectively.

fusion, some additional experiments were performed by trying to stop the injection at a point where the bubble remains in the tip of the capillary. In this way, it should be possible to follow the kinetic signal of the protein adsorption process. These experiments present two main difficulties: (*i*) the injection should stop when the size of the bubble is significant in order to have enough surface area accessible for the adsorption of the protein to the liquid surface; (*ii*) the power exchanged is probably very low since we would measure the power associated to a slow process corresponding to the adsorption of large molecules to a relatively small area; and (*iii*) the dependence on the concentration should be carefully considered since the surface is expected to be quickly saturated at high concentrations of the macromolecule, so the kinetic signal should be negligible under those conditions, and (*iv*) the same point is expected to be slowly reached at too low concentrations due to the slow diffusion. The kinetic signal corresponding to these experiments at three different concentrations of BSA are shown in Fig. 6. Although the profile seems to depend on the protein concentration, the differences do not exhibit a clear trend. Altogether, our results for the experiments with proteins indicate that the method is definitely sensitive to the concentration, as revealed by the period (152 s for water or 149, 144 and 130 s for the 8 μg/mL, 30 μg/mL and 3 mg/mL BSA solutions, respectively), but some optimization in the instrument is still required to measure the adsorption kinetics.

6.3. Liquid-liquid interfaces

The previous method can be extrapolated to the characterization of liquid-liquid interfaces. Such interfaces only exist when using two immiscible liquids. The signal corresponding to the injection of water in cyclohexane was registered (Fig. S3). The liquid injected from the capillary forms a second phase which volume continuously grows in the sample cell. In this case no drops are formed and the water phase is always connected to the capillary. The signal raised linearly as a function of the amount of injected water. This behavior has been associated to the heat capacity change in the sample cell (see Supplementary Material). Additional experiments using different aqueous solutions of BSA instead of pure water completely saturated the signal, revealing that the instrument is really sensitive to the presence of protein. These experiments are promising, but they need to be optimized before producing useful information.

7. Conclusions and perspectives

In the present work it is conclusively shown that the heat corresponding to the formation of bubbles in a liquid solution can be detected by ITC and that the kinetic profile is perfectly reproducible between independent experiments and among different bubbles within the same experiment. The heat power signal showed to be extraordinarily rich in information, with contributions associated to different thermodynamic and dynamic processes, such as the creation of interfacial area, evaporation-condensation processes, pressure changes in the gas phases, heat exchange with the environment, bubble release and change in the heat capacity of the sample cell. It is also shown that the periodic heat power signal can be used as a new method to determine the surface tension of different liquids as well as for a given liquid as a function of the concentration of a solute. Moreover, the heat power associated to protein adsorption is registered for the first time, showing the versatility of our proposal. It is also shown that thermodynamics governs the signal, since the drop in the baseline upon air-injection was quantitatively connected to the change in heat capacity of the cell. This analysis was also useful to determine the amount of air contained in the cell at any point of the titration experiment. Overall, the new methodology presented in this work is based on the close connection between bulk solution and interfacial properties. Surface tension measurements have been used in the past to get the aggregation number of micelles in the bulk solution [6,27,30] and even association constants for the formation of supramolecular complexes [31]. No similar measurements are available for comparison since this is the first time that heat power corresponding to the formation of bubbles, and in general fluid-fluid interfacial experiments, are reported. However, the pressure profile of bubbles is well known and widely employed to measure surface tension of a variety of solutions [16]. Our results are in perfect agreement with typical maximum bubble pressure experi-

ments but it exhibits clear advantages and it has a lot of room for improvement. We are currently working on developing advanced kinetic and thermodynamic models to characterize these measurements. Although the experimental results shown in present work were obtained using unmodified instruments, we suggest that some modifications could greatly improve the quality and versatility of the measurements. For instance, by using the same model of calorimeter but different instruments, it is shown that small variations in the capillary shape and size have a large impact in the registered signal. Also, the introduction of complementary devices, such as pressure and optical sensors, would definitely help to understand the information provided by the heat power profile and so to design better experiments. There are also various possibilities for optimization in the injection system, not only in the geometry and size of the needle, but also in the introduction of an extra capillary to change the composition of the liquid in real time, or in the control of the injection rate with different patterns that could even depend on the real time pressure by a feedback system. The possibility to change the concentration of the liquid phase by using a second injection system would allow to efficiently measure the heat power associated to the surface adsorption of biomacromolecules as a function of their concentration, opening new possibilities in the characterization of protein conformational changes or protein association induced by interaction with interfaces, or even the spontaneous formation of biofilms. This is something of outstanding interest that has already been addressed by alternative computational and experimental methods [32–35].

Overall, in this work we present the first measurements of interfacial calorimetry. To our knowledge, the kinetic (power signal) and thermodynamic (heat associated to each contribution to the power profile) information provided by this method cannot be obtained by any other experimental technique. More practical applications are expected to arise from the proposed methodology.

CRediT authorship contribution statement

Pablo F. Garrido: Formal analysis, Investigation, Methodology, Validation, Writing. **Margarida Bastos:** Investigation, Methodology, Writing. **Adrián Velázquez-Campoy:** Investigation, Methodology, Writing. **Philippe Dumas:** Investigation, Methodology, Writing. **Ángel Piñeiro:** Conceptualization, Funding adquisition, Investigation, Methodology, Project administration, Writing.

Declaration of Competing Interest

The authors declare that they have no known competing financial interests or personal relationships that could have appeared to influence the work reported in this paper.

Acknowledgements

We would like to gratefully thank the help and support from Mike Brandts, from Malvern/Microcal, for the information provided on the basic properties of VP-ITC instruments, as well as from Malin Suurkuusk and Peter Vikegard, from Waters/TA Instruments, for allowing us to use the calorimeters available in their lab. The authors thank the financial support of the Spanish Ministry of Economy and Competitiveness (projects MAT2015-71826-P to Á. P. and BFU2016-78232-P to A.V.C.), the Agencia Estatal de Investigación (AEI) (project PID2019-111327GB-I00 to Á. P.) and Fundação para a Ciência e Tecnologia (FCT), Portugal, for CIQUP (project UIDB/00081/2020 to M.B.). P. F. G. thanks the Spanish Ministry of Economy and Competitiveness and the European Social Fund for his predoctoral research grant, reference BES-2016-076761. These research projects were partially supported by European ERDF Funds (MCIU/AEI/FEDER, EU). Facilities provided by the Galician Supercomputing Centre (CESGA) are also acknowledged.

Appendix A. Supplementary data

Supplementary data to this article can be found online at https://doi.org/10.1016/j.jcis.2021.03.098.

References

[1] J.E. Ladbury, M.L. Doyle, Biocalorimetry 2: Applications of Calorimetry in the Biological Sciences, John Wiley & Sons, Ltd, Chichester, UK, 2004. doi: 10.1002/0470011122.
[2] M. Textor, S. Keller, Calorimetric Quantification of Cyclodextrin-Mediated Detergent Extraction for Membrane-Protein Reconstitution, in: A.L. Feig (Ed.), Methods Enzymol., Elsevier, 2016, pp. 129–156. doi: 10.1016/bs.mie.2015.07.033.
[3] R.J. Falconer, Applications of isothermal titration calorimetry - the research and technical developments from, 2011 to 2015, J. Mol. Recognit. 29 (2016) 504–515, https://doi.org/10.1002/jmr.2550.
[4] T. Silva, B. Claro, B.F.B. Silva, N. Vale, P. Gomes, M.S. Gomes, S.S. Funari, J. Teixeira, D. Uhríková, M. Bastos, Unravelling a Mechanism of Action for a Cecropin A-Melittin Hybrid Antimicrobial Peptide: The Induced Formation of Multilamellar Lipid Stacks, Langmuir 34 (2018) 2158–2170, https://doi.org/10.1021/acs.langmuir.7b03639.
[5] A. Velazquez-Campoy, S.A. Leavitt, E. Freire, Characterization of Protein-Protein Interactions by Isothermal Titration Calorimetry, in: H. Fu (Ed.), Protein-Protein Interact. Methods Appl., Humana Press, Totowa, NJ, 2004, pp. 35–54. doi: 10.1385/1-59259-762-9:035.
[6] W. Loh, C. Brinatti, K.C. Tam, Use of isothermal titration calorimetry to study surfactant aggregation in colloidal systems, Biochim. Biophys. Acta - Gen. Subj. 2016 (1860) 999–1016, https://doi.org/10.1016/j.bbagen.2015.10.003.
[7] D. Burnouf, E. Ennifar, S. Guedich, B. Puffer, G. Hoffmann, G. Bec, F.F.F. Disdier, M. Baltzinger, P. Dumas, kinITC: A new method for obtaining joint thermodynamic and kinetic data by isothermal titration calorimetry, J. Am. Chem. Soc. 134 (2011) 559–565, https://doi.org/10.1021/ja209057d.
[8] P. Dumas, Joining thermodynamics and kinetics by kinITC, in: M. Bastos (Ed.), Biocalorimetry Found. Contemp. Approaches, CRC Press, 2016, pp. 281–300. doi: 10.1201/b20161.
[9] P. Dumas, E. Ennifar, C. Da Veiga, G. Bec, W. Palau, C. Di Primo, A. Piñeiro, J. Sabin, E. Muñoz, J. Rial, Extending ITC to Kinetics with kinITC, in: Methods Enzymol., Academic Press Inc., 2016, pp. 157–180. doi: 10.1016/bs.mie.2015.08.026.
[10] E. Muñoz, A. Piñeiro, AFFINImeter Software: from its Beginnings to Future Trends- A Literature review, J. Appl. Bioanal. 4 (2018) 124–139, https://doi.org/10.17145/jab.18.017.
[11] Á. Piñeiro, E. Muñoz, J. Sabín, M. Costas, M. Bastos, A. Velázquez-Campoy, P.F. Garrido, P. Dumas, E. Ennifar, L. García-Río, J. Rial, D. Pérez, P. Fraga, A. Rodríguez, C. Cotelo, AFFINImeter: A software to analyze molecular recognition processes from experimental data, Anal. Biochem. 577 (2019) 117–134, https://doi.org/10.1016/j.ab.2019.02.031.
[12] H. Zhao, G. Piszczek, P. Schuck, SEDPHAT - A platform for global ITC analysis and global multi-method analysis of molecular interactions, Methods 76 (2015) 137–148, https://doi.org/10.1016/j.ymeth.2014.11.012.
[13] S. Keller, C. Vargas, H. Zhao, G. Piszczek, C.A. Brautigam, P. Schuck, High-precision isothermal titration calorimetry with automated peak-shape analysis, Anal. Chem. 84 (2012) 5066–5073, https://doi.org/10.1021/ac3007522.
[14] S. Builes, S.I. Sandler, R. Xiong, Isosteric Heats of Gas and Liquid Adsorption, Langmuir 29 (2013) 10416–10422, https://doi.org/10.1021/la401035p.
[15] J. Jukič, Differential heats of adsorption, Chem. Pap. 29 (1975) 653–659.
[16] A. Javadi, N. Mucic, M. Karbaschi, J.Y. Won, M. Lotfi, A. Dan, V. Ulaganathan, G. Gochev, A.V. Makievski, V.I. Kovalchuk, N.M. Kovalchuk, J. Krägel, R. Miller, Characterization methods for liquid interfacial layers, Eur. Phys. J. Spec. Top. 222 (2013) 7–29, https://doi.org/10.1140/epjst/e2013-01822-3.
[17] S.S. Dukhin, G. Kretzschmar, R. Miller, Dynamics of adsorption at liquid interfaces: theory, experiment, application, Elsevier, Amsterdam, 1995.
[18] G. Bracco, B. Holst, Surface science techniques, Springer, Berlin, Heidelberg, 2013. doi: 10.1007/978-3-642-34243-1.
[19] J.M. Ruso, Á. Piñeiro (Eds.), Proteins in solution and at interfaces: methods and applications in biotechnology and materials science, John Wiley & Sons, Hoboken, New Jersey, 2013.
[20] M.K. Transtrum, L.D. Hansen, C. Quinn, Enzyme kinetics determined by single-injection isothermal titration calorimetry, Methods 76 (2015) 194–200, https://doi.org/10.1016/j.ymeth.2014.12.003.
[21] K.A. Vander Meulen, S.E. Butcher, Characterization of the kinetic and thermodynamic landscape of RNA folding using a novel application of isothermal titration calorimetry, Nucleic Acids Res. 40 (2012) 2140–2151, https://doi.org/10.1093/nar/gkr894.
[22] N.H. Yennawar, J.A. Fecko, S.A. Showalter, P.C. Bevilacqua, A High-Throughput Biological Calorimetry Core: Steps to Startup, Run, and Maintain a Multiuser Facility, in: Methods Enzymol., Academic Press Inc., 2016, pp. 435–460. doi: 10.1016/bs.mie.2015.07.024.

[23] C. Jesús, F. Socorro, M.R. De Rivera, New approach to Tian's equation applied to heat conduction and liquid injection calorimeters, J. Therm. Anal. Calorim. 110 (2012) 1523–1532, https://doi.org/10.1007/s10973-011-2117-1.
[24] K.J. Mysels, The maximum bubble pressure method of measuring surface tension, revisited, Colloids Surfaces 43 (1990) 241–262, https://doi.org/10.1016/0166-6622(90)80291-B.
[25] A.W. Adamson, A.P. Gast, Physical chemistry of surfaces, sixth ed., John Wiley & Sons, New York, 1997.
[26] P.F. Garrido, M. Bastos, Á. Piñeiro, Method for determining interfacial tension, WO2020043792A1, 2020. https://worldwide.espacenet.com/patent/search/family/067777338/publication/WO2020043792A1?q=pn%3DWO2020043792A1.
[27] P.F. Garrido, P. Brocos, A. Amigo, L. García-Río, J. Gracia-Fadrique, Á. Piñeiro, STAND: Surface Tension for Aggregation Number Determination, Langmuir 32 (2016) 3917–3925, https://doi.org/10.1021/acs.langmuir.6b00477.
[28] R. Strey, Y. Viisanen, M. Aratono, J.P. Kratohvil, Q. Yin, S.E. Friberg, On the Necessity of Using Activities in the Gibbs Equation, J. Phys. Chem. B. 103 (1999) 9112–9116, https://doi.org/10.1021/jp990306w.
[29] A. Berthold, H. Schubert, N. Brandes, L. Kroh, R. Miller, Behaviour of BSA and of BSA-derivatives at the air/water interface, Colloids Surfaces A Physicochem. Eng. Asp. 301 (2007) 16–22, https://doi.org/10.1016/j.colsurfa.2006.11.054.
[30] N.E. Olesen, R. Holm, P. Westh, Determination of the aggregation number for micelles by isothermal titration calorimetry, Thermochim. Acta 588 (2014) 28–37, https://doi.org/10.1016/j.tca.2014.04.028.
[31] Á. Piñeiro, X. Banquy, S. Pérez-Casas, E. Tovar, A. García, A. Villa, A. Amigo, A.E. Mark, M. Costas, S. Perez-Casas, E. Tovar, A. García, A. Villa, A. Amigo, A.E. Mark, M. Costas, On the characterization of host-guest complexes: Surface tension, calorimetry, and molecular dynamics, of cyclodextrins with a non-ionic surfactant, J. Phys. Chem. B 111 (2007) 4383–4392, https://doi.org/10.1021/jp0688815.
[32] C. Postel, O. Abillon, B. Desbat, Structure and denaturation of adsorbed lysozyme at the air-water interface, J. Colloid Interface Sci. 266 (2003) 74–81, https://doi.org/10.1016/S0021-9797(03)00571-X.
[33] M. Arooj, N.S. Gandhi, C.A. Kreck, D.W.M. Arrigan, R.L. Mancera, Adsorption and Unfolding of Lysozyme at a Polarized Aqueous-Organic Liquid Interface, J. Phys. Chem. B 120 (2016) 3100–3112, https://doi.org/10.1021/acs.jpcb.6b00536.
[34] Q. Kou, Z. Wu, N. Hu, Thermodynamic adsorption properties of bovine serum albumin and lysozyme on the bubble surface from the binary solution, Chem. Eng. Res. Des. 102 (2015) 26–33, https://doi.org/10.1016/j.cherd.2015.06.013.
[35] B.A. Noskov, A.A. Mikhailovskaya, S. Lin, G. Loglio, R. Miller, Bovine Serum Albumin Unfolding at the Air / Water Interface as Studied by Dilational Surface Rheology, Langmuir 26 (2010) 17225–17231, https://doi.org/10.1021/la103360h.

USC UNIVERSIDADE DE SANTIAGO DE COMPOSTELA

USC
UNIVERSIDADE
DE SANTIAGO
DE COMPOSTELA

Supplementary Material for

Fluid interface calorimetry

Pablo F. Garrido[1*], Margarida Bastos[2], Adrián Velázquez-Campoy[3,4,5,6,7], Philippe Dumas[8], Ángel Piñeiro[1*]

[1]Departamento de Fisica de Aplicada, Facultade de Fisica, Universidade de Santiago de Compostela, E-15782, Santiago de Compostela, Spain. [2]CIQ-UP, Departamento de Quimica e Bioquimica, Faculdade de Ciencias da Universidade do Porto, R. Campo Alegre 687, P-4169-007, Porto, Portugal. [3]Institute of Biocomputation and Physics of Complex Systems (BIFI), Joint Units IQFR-CSIC-BIFI, and GBsC-CSIC-BIFI, Universidad de Zaragoza, Zaragoza, 50018, Spain. [4]Department of Biochemistry and Molecular and Cell Biology, Universidad de Zaragoza, 50009, Zaragoza, Spain. [5]Aragon Institute for Health Research (IIS Aragon), 50009, Zaragoza, Spain. [6]Biomedical Research Networking Centre for Liver and Digestive Diseases (CIBERehd), 28029, Madrid, Spain. [7]Fundacion ARAID, Government of Aragon, 50018, Zaragoza, Spain. [8]IGBMC, Dept of Integrative Biology, Strasbourg University, F67404, Illkirch CEDEX, France.

E-mail: Pablo.Fernandez@usc.es, Angel.Pineiro@usc.es

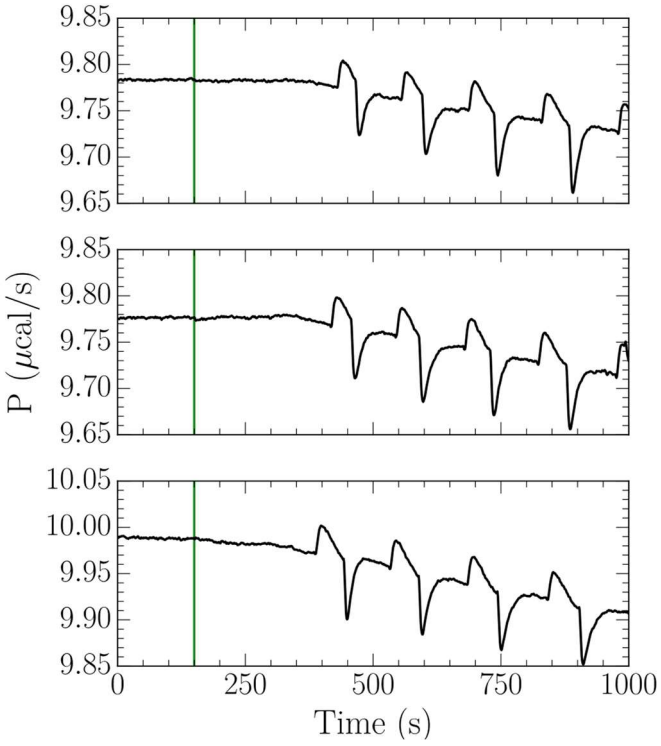


Figure S1.- Three independent injections using ITC-A at 298 K and 0.02 µL/s injection rate. The plots are restricted to the initial 1000 s to better distinguish the different contributions to the power signal. The vertical green lines indicate the beginning of the injection after the initial delay.

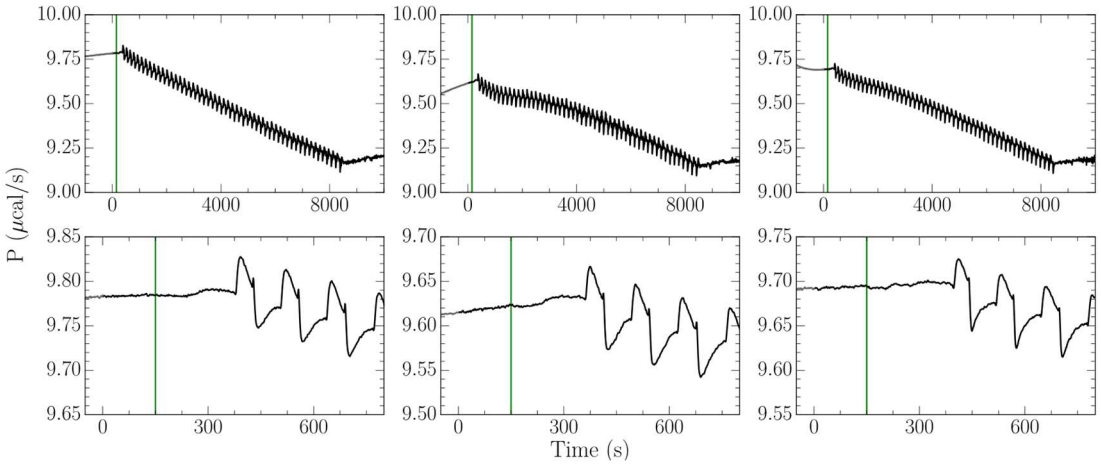


Figure S2.- Power vs time profile for the injection of air into water at 298 K with a reference power of 10 µcal/s and an injection rate of 0.02 µL/s (200 µL in 9000 s). Top: complete experiments, together with 1000 s of equilibration time. Bottom: zoom on the first 800 s together with the last 50 s of equilibration. The green vertical lines indicate the beginning of the air injection.

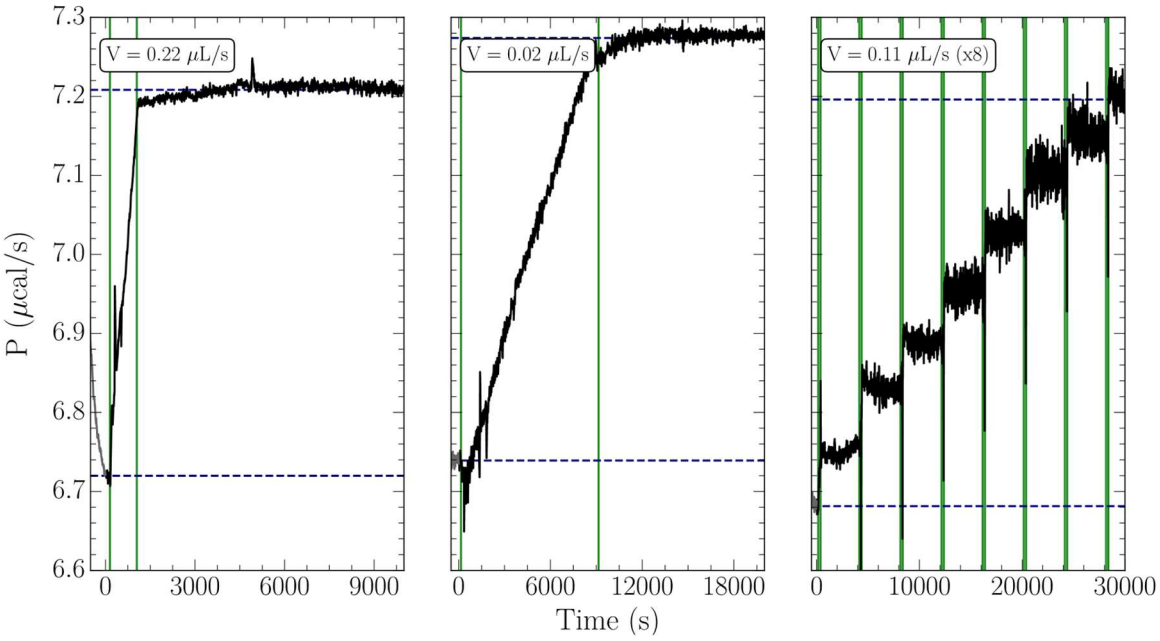


Figure S3.- Power signal corresponding to the injection of water into cyclohexane at 0.22 µL/s (left), 0.02 µL /s (middle) and to the injection of 8 x 25 µL during 225 s (0.11 µL /s), using 4000 s between injections (right). In all the cases, a reference power of 10 µcal/s was applied. The ordinate axis is common for the three plots so that the experiments can be easily compared. Green vertical lines indicate the beginning and the end of each injection. Horizontal blue dashed lines indicate the power mean values at the beginning and at the end of the measurements.

USC
UNIVERSIDADE DE SANTIAGO DE COMPOSTELA

Calculation of the volume of air contained in the sample cell based on the baseline drift

As indicated in the main text, the baseline drift is due to the change of composition in the sample cell upon the introduction of air. The heat capacity of air is very different from that of aqueous solutions so, when introducing it in the cell its total heat capacity is expected to markedly decrease. When this happens, the power required to keep the sample and reference cells at the same temperature are significantly different, thus leading to a change in the baseline. From the definition of heat capacity Cp:

$$Cp = \left(\frac{dQ}{dT}\right)_P = \left(\frac{dQ}{dt}\right)\left(\frac{dt}{dT}\right) = P(t)\left(\frac{dt}{dT}\right) \tag{1}$$

where Q is the heat required to change the temperature (T) of the system per temperature unit, t represents the elapsed time and $P(t)$ is the power associated to the heat change, which is a function of time. By applying this to both the reference (R) and the sample (S) cells:

$$Cp^R = RP\left(\frac{dt}{dT_R}\right) \Rightarrow \frac{RP}{Cp^R} = \frac{dT_R}{dt} \tag{2}$$

$$Cp^S(t) = P(t)\left(\frac{dt}{dT_S}\right) \Rightarrow \frac{P(t)}{Cp^S(t)} = \frac{dT_S}{dt} \tag{3}$$

since both cells are expected to be under thermodynamical equilibrium with each other and, because both RP and Cp^R are constant

$$\frac{dT_R}{dt} = \frac{dT_S}{dt} \Rightarrow \frac{RP}{Cp^R} = \frac{P(t)}{Cp^S(t)} \tag{4}$$

Thus, the ratio $P(t)/Cp^S(t)$ is a constant

$$\frac{P(0)}{Cp^S(0)} = \frac{P(t)}{Cp^S(t)} = \frac{P(t_{max})}{Cp^S(t_{max})} \tag{5}$$

where t_{max} is the time at the end of the experiment. Thus:

$$\frac{P(0)}{P(t_{max})} = \frac{Cp^S(0)}{Cp^S(t_{max})} \Rightarrow \frac{P(0)}{P(t_{max})} - 1 = \frac{Cp^S(0)}{Cp^S(t_{max})} - 1 \Rightarrow \frac{\Delta P}{P(t_{max})} = \frac{\Delta Cp^S}{Cp^S(t_{max})} \Rightarrow \frac{P(t_{max})}{\Delta P} = \frac{Cp^S(t_{max})}{\Delta Cp^S} \tag{6}$$

with $\Delta P = P(0) - P(t_{max})$ and $\Delta Cp^S = Cp^S(0) - Cp^S(t_{max})$.

The heat capacity change upon the injection of a volume of air (V_{inj}), thus displacing the same amount of the liquid contained in the sample cell, is given by:

$$\Delta Cp^S = -V_{inj}\,\rho_{sol} cp^{sol} \tag{7}$$

where ρ_{sol} and cp^{sol} are the density and the specific heat capacity per mass unit of solution, respectively.

The absolute heat capacity of the sample cell includes contributions of the injection needle, of the cell itself as well as of all the compounds, sensors and actuators, in contact with it. Such contributions can be easily estimated from specific measurements, as we will see next. Going back to equation (1), for an equilibrated baseline, with no injections:

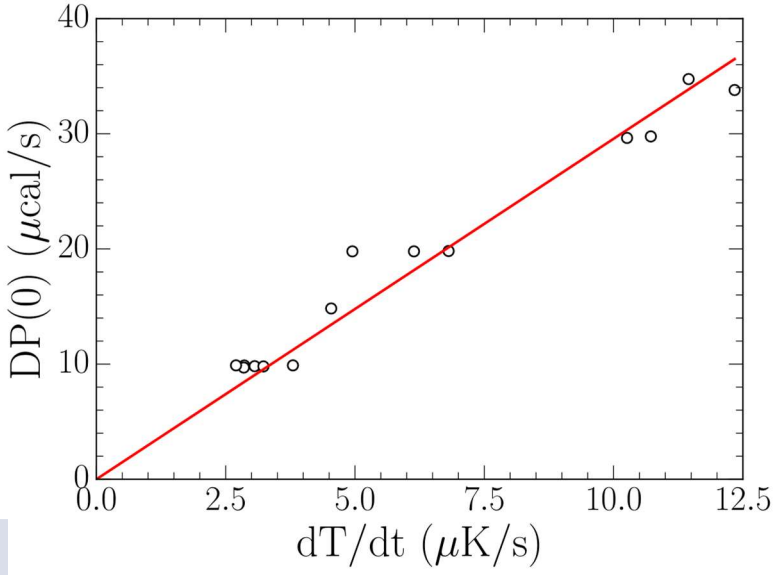
$$Cp(0) = P(0)\left(\frac{dt}{dT}\right) \Rightarrow Cp^{S}(0) = \frac{P(0)}{dT_S/dt} \tag{8}$$

Thus, we just need the slope of the $T_S(t)$ and the initial power applied to the sample cell to get the heat capacity of the whole sample cell. Note that the temperature of the sample cell slightly increases during the experiment in the microcal ITCs employed in this work. This increase depends on the reference power used for the experiment but a representative value is 0.05 K/h. This value is not registered by the software of the instrument but the raw output file contains the temperature of the adiabatic jacket (T_J), which differs from the temperature of the reference cell by a constant value (ΔT_2). This difference is maintained by a feedback system. Simultaneously, the reference cell also differs from the sample cell by another constant (ΔT_1). Thus,

$$T_S = T_R + \Delta T_1 = T_J + \Delta T_2 + \Delta T_1 \tag{9}$$

$$\frac{dT_S}{dt} = \frac{dT_J}{dt} + \frac{d\Delta T_2}{dt} + \frac{d\Delta T_1}{dt} = \frac{dT_J}{dt} \tag{10}$$

Even if the temperatures T_S and T_J are slightly different, their derivatives should be identical because ΔT_1 and ΔT_2 are kept constant. Making use of some of the experiments already shown in the main text, using the same ITC (ITC-A) and solution (water), *Figure* S4 shows the initial DP as a function of the time derivative of T_J. By using equation (8) to fit these results we get the heat capacity of the whole sample cell: $Cp(0) = 2.96 \pm 0.15\ cal/K$.



USC
UNIVERSIDADE DE SANTIAGO DE COMPOSTELA

Figure S4.- DP before starting the air injection (DP(0)) as a function of the slope of T(t) for 15 air into water experiments at different RP values (o). The red line is the linear fitting to equation (8).

Using this result, the volume of air injected can be determined using the equations (6) and (7):

$$\Delta Cp^S = \frac{Cp^S(0)}{\frac{P(t_{max})}{\Delta P} - 1} \Rightarrow V_{inj} = -\frac{Cp^S(0)}{\frac{P(t_{max})}{\Delta P} - 1}\frac{1}{\rho_{sol} cp^{sol}} \tag{11}$$

This equation can be used to determine the volume of air contained in the sample cell just from the change in the baseline even for a relatively long experiment where several bubbles are created. For instance, for the data corresponding to the *Figure* 3 of the main text: $Cp(0) = 2.96 \pm 0.15\ cal/K$, $P(t_{max}) = 19.195\ \mu cal/s$, $\Delta P = 0.630\ \mu cal/s$, $\rho_{sol} = 0.997\ g/mL$ and $cp^{sol} = 1\ cal/(g \cdot K) \Rightarrow V_{inj} = 93.5 \pm 4.9\ \mu L$. This value agrees very well with the total injected volume requested in the experiment ($100\ \mu L$). The small difference could be partially due to the compressibility of the air as well as to possible errors in the injection system: syringe and motor.

USC
UNIVERSIDADE DE SANTIAGO DE COMPOSTELA

USC
UNIVERSIDADE
DE SANTIAGO
DE COMPOSTELA

5.2. Patent registration

"Method for determining interfacial tension", is an international patent application about the use of the ITC for the determination of surface tension. The patent has been just granted in Spain (on 24 August, 2021; number ES2745339B2). The language is more technical and less scientific than an article and so, as the work is partially explained in Paper II and Paper III, only the front pages are included in this dissertation. The patent protects the idea for commercial purposes but it does not prevent its application in academia. This work has been developed in collaboration with people from: (1) Departamento de Física Aplicada, Facultade de Física, Universidade de Santiago de Compostela; (2) CIQ-UP, Departamento de Química e Bioquímica, Faculdade de Ciências da Universidade do Porto. The list of authors is presented below with their corresponding affiliations. The rights are equally distributed.

Ángel Piñeiro (1), **Pablo F. Garrido** (1), Margarida Bastos (2).

According to the CRediT authorship contribution statement (Brand *et al.*, 2015), my contributions to this publication are: Conceptualization; Methodology; Software; Validation; Formal analysis; Investigation; Visualization

https://worldwide.espacenet.com/patent/search/family/067777338/publication/WO2020043792A1?q=pn%3DWO2020043792A1

USC UNIVERSIDADE DE SANTIAGO DE COMPOSTELA

USC
UNIVERSIDADE
DE SANTIAGO
DE COMPOSTELA

(12) INTERNATIONAL APPLICATION PUBLISHED UNDER THE PATENT COOPERATION TREATY (PCT)

(19) World Intellectual Property Organization
International Bureau

(43) International Publication Date
05 March 2020 (05.03.2020)

WIPO | PCT

(10) International Publication Number
WO 2020/043792 A1

(51) International Patent Classification:
G01N 13/02 (2006.01) *G01N 25/20* (2006.01)

(21) International Application Number:
PCT/EP2019/073001

(22) International Filing Date:
28 August 2019 (28.08.2019)

(25) Filing Language: English

(26) Publication Language: English

(30) Priority Data:
P201830848 28 August 2018 (28.08.2018) ES
115752 26 August 2019 (26.08.2019) PT

(71) Applicants: **UNIVERSIDADE DE SANTIAGO DE COMPOSTELA** [ES/ES]; Reitorado da Universidade de Santiago de Compostela, Colexio de San Xerome, Pza. do Obradoiro, s/n, E-15782 Santiago de Compostela, A Coruña (ES). **UNIVERSIDADE DO PORTO** [PT/PT]; Gabinete UPIN Praça Gomes Teixeira 4º andar Sala 419, 4099-002 Porto (PT).

(72) Inventors: **PIÑEIRO GUILLÉN, Angel**; Área de Valorización, Transferencia y Emprendimiento, Edificio EMPRENDIA - Campus Vida, 15782 Santiago de Compostela - A Coruña (ES). **FERNÁNDEZ GARRIDO, Pablo**; Área de Valorización, Transferencia y Emprendimiento, Edificio EMPRENDIA - Campus Vida, 15782 Santiago de Compostela - A Coruña (ES). **HENRIQUES MESQUITA BASTOS, Margarida Maria**; CIQUP, Department of Chemistry and Biochemistry, Faculty of Sciences, University of Porto, R. Campo Alegre, 687, P-4169-007 Porto (PT).

(54) Title: METHOD FOR DETERMINING INTERFACIAL TENSION

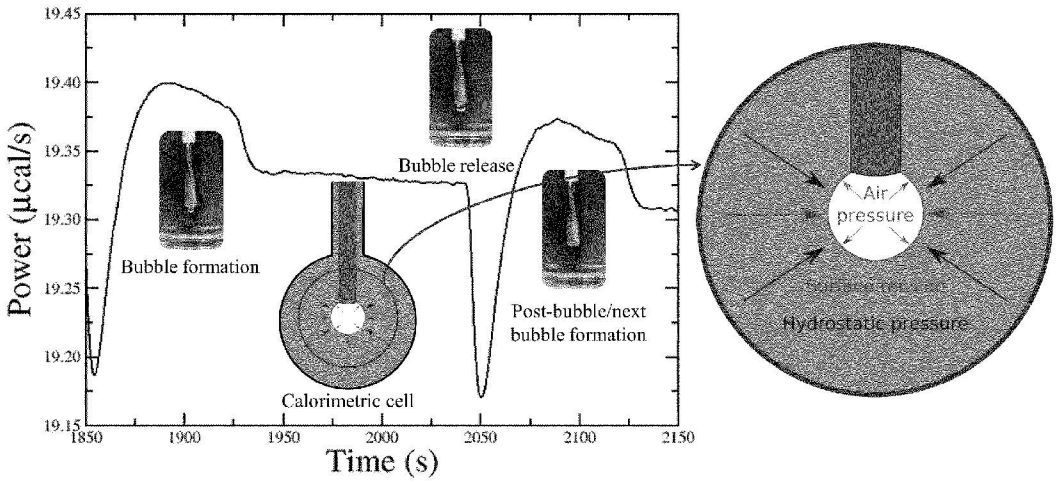


Figure 1

(57) Abstract: The present invention relates generally to methods for characterization of fluids, and, particularly, to methods of determining an interfacial tension between a first liquid and a second fluid, the method comprising the steps of: (a) introducing the second fluid into the first liquid at a constant flow-rate so as to cause the second fluid to periodically form successive droplets or bubbles; (b) recording a heat change of step (a) as a function of time, obtaining a periodic heat versus time profile; (c) obtaining the period of the heat change recorded in step (b); (d) providing a calibrated relationship of the interfacial tension as a function of period for said constant flow-rate and said second fluid; and (e) correlating the period obtained in step (c) with the calibrated relationship, and determining the interfacial tension between the first liquid and the second fluid for said constant flow-rate.

WO 2020/043792 A1

[Continued on next page]

(74) **Agent: ABG INTELLECTUAL PROPERTY LAW, S.L.**; Avenida de Burgos,16D, Edificio Euromor, E-28036 Madrid (ES).

(81) **Designated States** *(unless otherwise indicated, for every kind of national protection available)*: AE, AG, AL, AM, AO, AT, AU, AZ, BA, BB, BG, BH, BN, BR, BW, BY, BZ, CA, CH, CL, CN, CO, CR, CU, CZ, DE, DJ, DK, DM, DO, DZ, EC, EE, EG, ES, FI, GB, GD, GE, GH, GM, GT, HN, HR, HU, ID, IL, IN, IR, IS, JO, JP, KE, KG, KH, KN, KP, KR, KW, KZ, LA, LC, LK, LR, LS, LU, LY, MA, MD, ME, MG, MK, MN, MW, MX, MY, MZ, NA, NG, NI, NO, NZ, OM, PA, PE, PG, PH, PL, PT, QA, RO, RS, RU, RW, SA, SC, SD, SE, SG, SK, SL, SM, ST, SV, SY, TH, TJ, TM, TN, TR, TT, TZ, UA, UG, US, UZ, VC, VN, ZA, ZM, ZW.

(84) **Designated States** *(unless otherwise indicated, for every kind of regional protection available)*: ARIPO (BW, GH, GM, KE, LR, LS, MW, MZ, NA, RW, SD, SL, ST, SZ, TZ, UG, ZM, ZW), Eurasian (AM, AZ, BY, KG, KZ, RU, TJ, TM), European (AL, AT, BE, BG, CH, CY, CZ, DE, DK, EE, ES, FI, FR, GB, GR, HR, HU, IE, IS, IT, LT, LU, LV, MC, MK, MT, NL, NO, PL, PT, RO, RS, SE, SI, SK, SM, TR), OAPI (BF, BJ, CF, CG, CI, CM, GA, GN, GQ, GW, KM, ML, MR, NE, SN, TD, TG).

Published:

— *with international search report (Art. 21(3))*

USC UNIVERSIDADE DE SANTIAGO DE COMPOSTELA

Chapter 6

Molecular Dynamics Simulations and other complementary techniques

Cuanto más sepáis de todo, mejor. Por saber muchísimo no os va a pasar nada malo, luego ya veremos.

Mariano Rajoy Brey, Spanish Prime Minister

To better understand interfacial and aggregation processes and to support the Fluid Interface Calorimetry development, other techniques have been used. The most exploited one was Molecular Dynamics simulations (MD), a computational method to study the evolution of a system with atomic resolution by solving the equations of motion of its components: atoms, ions, solvent molecules, and any other component of the target solution. MD was included in this project to try to shed some light on the forces driving aggregation and adsorption processes. A method to accelerate the computational simulations has also been explored. Just the results that have been already published are here included. Additional results have been produced and they are expected to be published soon.

Other three experimental methods have been used to determine the aggregation and the adsorption of molecules: surface tension measurements, sound velocity and density determination and, as mentioned, standard ITC measurements for bulk phenomena. ITC has already been described in Chapter 3. Sound velocity and density will be briefly described in this Chapter.

Finally, an important part of the work carried out during this project is the development and implementation in computational codes of the algorithms required to analyse the experimental data. The development of these codes was possible thanks to the availability of a large number of public libraries, from which I took advantage. Thus, a section to recognize the previous work of other people as well as to roughly describe the new developed code will be included.

6.1. Molecular Dynamics simulations in a nutshell

MD simulations are, overall, a kind of computational simulation based on the physical laws describing the behaviour of molecular systems. The resolution of this methodology is typically atomistic, and the evolution of the particles is determined by classical mechanics (Allen and Tildesley, 2017; Haile, 1997; Rapaport, 2004). A proper parametrization of the simulated molecules leads to excellent results, with the limitations of the employed classical approach, to describe many molecular processes. Quantum mechanics (QM) can explain processes that cannot be afforded by classical MD, such as the formation/disruption of covalent bonds, but this approach is currently too slow to study molecular systems involving more than a few tens of atoms. MD simulations are currently used for the study of biophysical systems composed by hundreds of thousands of atoms where their main features are expected to be characterized just by their structure and charge distributions. The denaturalization of a protein in solution, a number of aggregation/dissociation adsorption/desorption processes and even molecular recognition events can be reasonably well approached by MD simulations. The main limitations are the accuracy of the required force fields and algorithms employed to determine the interactions that drive the evolution of the simulated system and the availability of computational resources that limit the time and size scale of the trajectories. Several methods have been developed to overcome these issues, such as the implementation of multiscale simulations as well as the so called steered molecular dynamics.

To perform a classical MD simulation, the Hamilton's equations of motion are numerically solved from an initial predefined state. The Hamilton's equations are a set of differential equations that determine the evolution in time of the position and the momenta of all the particles consisting a target system, by means of an operator called the *Hamiltonian*. The Hamiltonian H is defined as the sum of the kinetic, T, and the potential, V, energy of the system:

$$H = T + V \tag{6.1}$$

The general application of the MD simulation is the integration of the Hamilton's equations for the atoms that compose the system. If there are N atoms, each of them with coordinates $\mathbf{q_i}$ and momenta $\mathbf{p_i}$, where $i = 1 \dots N$ denotes the label of each atom, their Hamilton's equations are:

$$\frac{d\mathbf{q_i}}{dt} = \frac{\partial H}{\partial \mathbf{p_i}} \qquad \frac{d\mathbf{p_i}}{dt} = -\frac{\partial H}{\partial \mathbf{q_i}} \tag{6.2}$$

These are first order differential equations, which need one initial condition to be solved. This classical formulation of the problem is equivalent to the application of the Newtonian law of motion, which is second order derivative, and it describes the same phenomena. In any case, these equations should be numerically solved by the selection of the considered integration algorithm and its corresponding *time step*, which determines the sampling of the integration. The result of the integration is the *trajectory*, which contains the values of the position and velocity of each particle at every time interval from the beginning of the simulation.

USC UNIVERSIDADE DE SANTIAGO DE COMPOSTELA

The time step controls both the stability and convergence of the equations' resolution. It also determines the computational time required to reach a given length for the whole trajectory: larger time steps will allow longer trajectories with

the same computational cost, but it will considerably affect the stability of the simulation. The time step is conditioned by the lightest atoms (hydrogens), whose movements are faster than those of heavier atoms. It should be small enough to reproduce these movements, but not too much so the final trajectory represents a too short period of time. Several multi time step strategies as well as methods to increase this parameter, thus doing the simulations significantly faster, have been developed (Abreu and Tuckerman, 2020; Kim, 2014; Pechlaner *et al.*, 2021; Reißer *et al.*, 2017).

The results of a MD simulation depend critically on the Hamiltonian. The kinetic contribution to this function is directly obtained from the velocities of the individual particles composing the system. The potential function includes a number of parameters associated to each bond, angle, or dihedral contribution, and to the non-bonded contributions such as the van der Waals radius and the partial charge associated to each atom. It must take into account everything that should be relevant in the evolution of the system. The set of parametrizations included in the definition of the potential energy are refered as the *Force Field* (FF).

In addition to the previous considerations, the environment in which the solute is studied should also be modelled. This includes the simulation of the solvent and also the boundaries of the system. Typical macromolecules require several thousand water molecules to solvate them even at very low concentrations. To speed up the simulations, a simplification in these solvent molecules, smaller than the main one, is taken. This simplification is called the *solvent model*, or *Water Model* (WM) for aqueous solutions. There exist a large variety of WM, each of one optimized for determined systems.

The boundaries of the simulated system are also important. Normally, they are modelled by building a unit cell that is replicated in the three dimensions, thus filling all the space and leading to a virtually infinite system. In this scenario, the simulation of a single reference cell is reproduced in the replicas without real borders, so when the a particle leaves a cell traversing one of its walls, a replica of this particle enters the same cell by traversing the opposite wall exactly with the same velocity (Figure 6.1). This is the so called periodic boundary conditions (PBCs) algorithm. The combination of a reliable solvent model with suitable PBCs is another of the key factors on which the performance of the simulations critically depends.

USC UNIVERSIDADE DE SANTIAGO DE COMPOSTELA

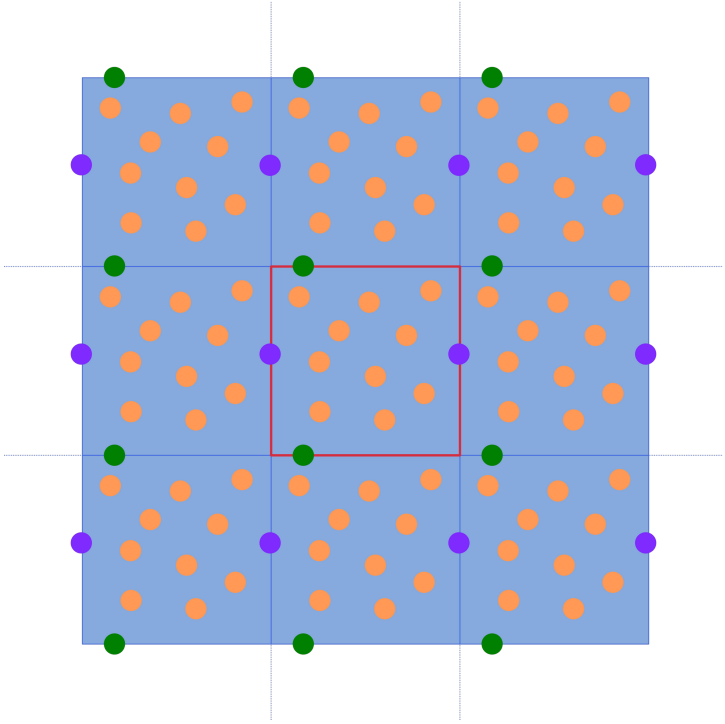


Figure 6.1: A picture representing the periodic boundary conditions in 2D. The red central box represents the main simulation cell. The purple and the green particles illustrate the effect of the periodic boundary conditions in the border.

Other complementary algorithms are also important for both the reliability and the computational cost of MD simulations. For instance, the long-range interactions are typically approached by the so-called Particle Mess Ewald (PME) method, which distributes the partial charges of the system in a grid that is then Fourier transformed with a three-dimensional Fast Fourier Transform (FFT). The control of pressure and temperature also require specific algorithms. Additionally, reasonable initial coordinates for all the involved atoms should be proposed before starting the simulation. Once all these compounds have been selected, the numerical integration of the motion equation is iteratively solved, thus allowing the system to evolve for the time required to study some event. For this work we used the GROMACS engine (Spoel *et al.*, 2005) to perform all the calculations, which were executed in the Supercomputing Centre of Galicia.

6.2. Surface tension, sound velocity and density

USC
UNIVERSIDADE DE SANTIAGO DE COMPOSTELA

The characterization of surfactant aggregation processes using different experimental methods have also been performed in order to complement or to validate the results obtained from ITC analysis or to get more insight on specific systems. The behaviour at interfaces of surfactant systems has been analysed by surface tension

measurements, from which also bulk properties like the aggregation number can be determined (Garrido *et al.*, 2016). For bulk studies, the sound velocity, and the density as a function of concentration and temperature have been used.

The surface tension measurements were carried out in a drop volume tensiometer, the TVT2 from Lauda. The drop volume method is based on the Tate's law (Möbius and Miller, 1998a), which states that when a pendant drop is pending of a capillary tube, at the moment just before it is detached, the drop's weight is equal to the surface tension force that keeps the drop attached along the perimeter of the tip (Figure 6.2). However, neither the weight nor the surface tension force are exactly the forces acting on the drop. The weight that is considered is the *apparent weight*, which results from subtracting the buoyancy effect to the actual weight. This is almost negligible when the drop is surrounded by air, but significant when a drop of al liquid is injected in another immiscible liquid. The surface tension force is proportional to the surface tension and to the contact line perimeter, because at the detaching instant, the drop shows a narrower neck that slightly decreases the vertical action of the surface tension. Let r_{cap} be the radius of the capillary, γ the surface tension, f a correction factor for the surface tension force, V the volume of the drop, $\Delta\rho$ the density difference between the drop and its surroundings, and g the gravity. The equation describing this force balance is given by:

$$2\pi r_{cap}\gamma f = V\Delta\rho g \tag{6.3}$$

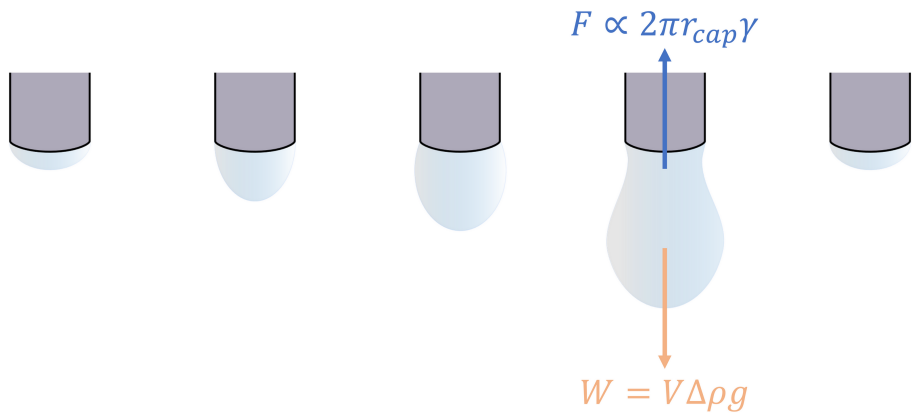


Figure 6.2: Diagram showing the formation of a pendant drop and force balance before the detaching.

USC UNIVERSIDADE DE SANTIAGO DE COMPOSTELA

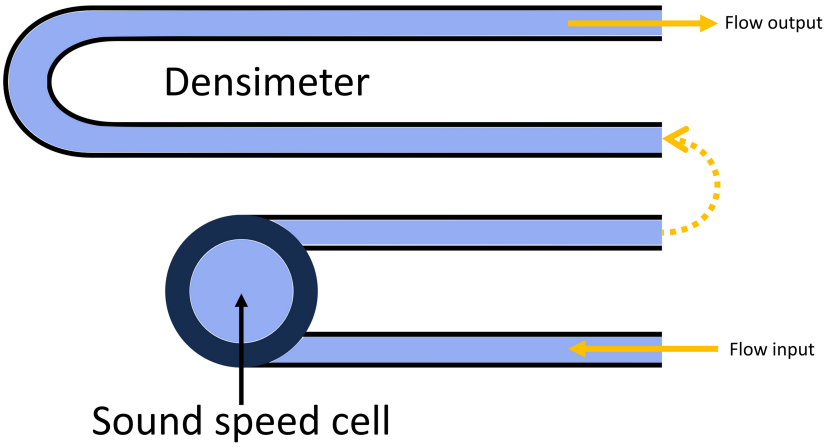
And so, the surface tension can be obtained if all the other magnitudes are known:

$$\gamma = \frac{V\Delta\rho g}{2\pi r_{cap} f} \tag{6.4}$$

The drop volume is directly measured by the tensiometer, the density (density difference) has to be previously determined and the capillary radius is provided by the manufacturer. The only remained magnitude is f, which is calibrated and given by the tensiometer manufacturer in the software that controls the instrument. As specified in the user's manual, this factor is a function of the capillary radius and the volume of the drop. The TVT2 allows a surface tension determination with a resolution up to 0.01 mN/m.

In this project, two different modes to determine the surface tension have been used: the standard and the quasi-static. In the standard mode, the drops are continuously created. To prevent hydrodynamic effects that could disturb the drop, the plunger speed is reduced four times from the beginning of the formation to the end. The volume of each drop is measured and their corresponding surface tension is determined. Finally, the surface tension of the solution is obtained from the average value from all the drops. The quasi-static mode is employed for slow adsorption speed solutes. In this mode a drop with a certain volume is formed and left attached to the end of the syringe tip. The drop detaches when a sufficient amount of adsorbant arrives at the interface, reducing the surface tension. The time the drop is pending from the tip is measured, and another drop, with a reduced volume, is now created. The method is repeated until the final drop remains attached to the tip. The surface tension of the solution is obtained form the drop volume vs time relation.

The sound velocity and density measurements were determined using the same instrument: the Anton Paar DSA 5000. The instrument is composed by two independent measurement sites (Figure 6.3) but it is loaded with a unique filling, so both the sound velocity and the density can be measured using the same sample, around 3 ml of solution, and at a temperature range from 273 K to 343 K, that can be varied without refilling (Fortin *et al.*, 2013).



USC
UNIVERSIDADE DE SANTIAGO DE COMPOSTELA

Figure 6.3: DSA cells schematic representation

The sound velocity cell is cylindrical-like and has two piezoelectrical transdu-

cers, one at each base of the cylinder. One of the transducers produce ultrasound oscillations (3 MHz) and the other receives them. From a simple relation, the velocity is determined as the distance between both transducers and the time lapse between the emission and reception of the wave. However, this simple relationship is corrected from electronic or temperature contributions by the software of the instrument. For an accurate determination of these factors, a calibration using pure water at 293 K, 313 K, and 333 K is needed, ideally before every set of measurements.

The density cell is based on the vibrating tube method. The cell is a U-shaped tube filled with the sample liquid and it is exited to its characteristic frequency. From the differences on the oscillating mode of the tube with or without the sample, its density can be determined, again, by an in-software parametrization.

6.3. Computational tools

Data treatment and analysis has been performed with own-developed codes, mostly developed in *Python* language (Hunt, 2019; Lee, 2014; Lee and Hubbard, 2015), except for standard ITC experiments, that have been processed with *AFFINImeter* (Muñoz and Piñeiro, 2018; Piñeiro *et al.*, 2019), and other analysis in different collaborations, where *C* (Press *et al.*, 1992) or *R* (Hilfiger, 2015) languages, or other specific programs have been used.

Regarding the own Python-developed codes, the main libraries employed are: *Numpy* for numerical operations (Harris *et al.*, 2020), *Matplotlib* for graphical representations (Hunter, 2007), *Pandas* for data files manipulation (Reback *et al.*, 2020), *SciPy* for advanced mathematical calculations (Virtanen *et al.*, 2020), and *Spyder* as the default IDE (Integrated Development Environment) (Spyder collective, 2021), all provided and supported by the *Anaconda* scientific distribution (Anaconda Inc., 2019). Other secondary libraries are: *Sympy* for symbolic calculations (used in ITC simulations) (Meurer *et al.*, 2017), *scikit-image* for image processing and analysis (results not yet published) (Van Der Walt *et al.*, 2014) or *MDAnalysis* for MD simulations data treatment (Gowers *et al.*, 2016; Michaud-Agrawal *et al.*, 2011).

It should be mentioned that Paper II, the Patent registration, and Paper III are based on ITC data analysis performed by own-developed codes in Python language. The analysis of the MD simulations results in Paper VII and the fitting in Paper V and Paper VI has also been carried out by own-developed codes in Python. Additionally, one of the codes developed during this thesis has been registered (section Software registration) and part of the rest is expected to be implemented in the AFFINImeter platform (`https://www.affinimeter.com/`).

USC UNIVERSIDADE DE SANTIAGO DE COMPOSTELA

USC
UNIVERSIDADE
DE SANTIAGO
DE COMPOSTELA

Part III

Results

Part III presents the results of the ITC for interfacial properties determination, new models concerning bulk processes in ITC, the computational studies about cyclodextrin complexes at interfaces and in bulk, and two surfactants aggregation studies. Paper III, Paper IV,Paper V,Paper VI,Paper VII are here included together with the Software registration and explanation.

USC
UNIVERSIDADE
DE SANTIAGO
DE COMPOSTELA

USC
UNIVERSIDADE
DE SANTIAGO
DE COMPOSTELA

Chapter 7

Fluid Interface Calorimetry Results

Estoy en una situación muy positiva, con un optimismo contenido

Pedro Sánchez Pérez-Castejón, Spanish Prime Minister

Fluid Interface Calorimetry has been already applied to the determination of surface tension of different compounds in aqueous solution, what is presented in Paper III. Some ongoing developments and preliminary results, part of them roughly described in Paper II, deserve more space in this Chapter. The better control of the bubble formation, the adsorption of biomolecules, experiments at liquid-liquid interfaces, and the theoretical developments are some representative examples.

7.1. Better bubble control

Commercial ITC instruments are not optimized for fluid interface experiments, so some improvements had to be applied for our purposes. In this thesis, an external micropump, new tip designs, a handmade manometer, and an external injector have been tried. The first approach to get a greater control in bubble formation was to use a micropump with pressure and injection rate control. The required combination of both small pressure changes lower than 100 Pa and steady flow control for rates not higher than 0.2 $\mu L/s$ was almost impossible with the instrumentation at our disposal. After testing several devices, we concluded that the best injection system should be a micropump with flow control able to measure (not necessary to control) those pressure changes. With such device, all the heat processes that are detected in the calorimeter can be linked to a pressure change, which in addition to increase the accuracy of the measurements, it would provide a complementary thermodynamic magnitude. A handmade manometer was attached to the ITC injector to approach the final idea. From this test, the main heat events detected in the calorimeter have been identified.

Parallel tests were performed with an external injector connected to the ITC syringe. The native ITC engine was disconnected for this test, but the syringe is placed as usual. The air is pumped into the cell by the external injector, connected to the upper orifice of the syringe, allowing rates slower than those obtained by the original ITC engine. Using this external injector, the results using the native engine have been reproduced.

Finally, a slight widening of the cannula tip was tested, thus allowing larger bubbles. This modification was implemented just in a TAM microcalorimeter since the cannula in this instrument is easy to replace and also because the corresponding cell is more suitable for this end, in contrast with the thin coin-shaped cells of Microcal instruments. The problem with the TAM calorimeter was its long response time and low sensitivity, so we used it just for these small tests.

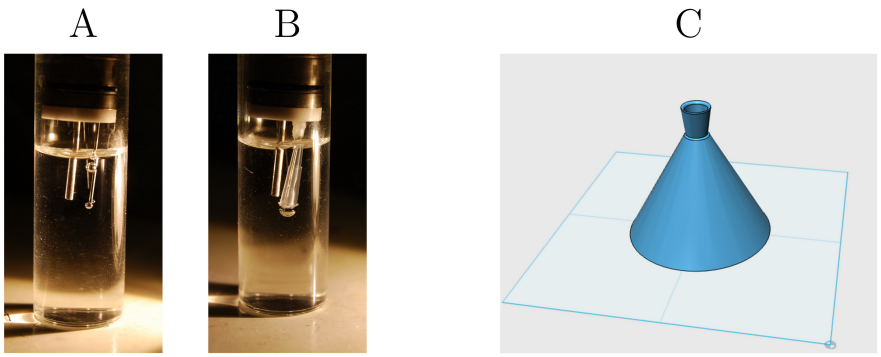


Figure 7.1: A: bubbles emerging from the TAM cannula. B: a greater bubble emerging from a modified cannula tip. C: 3D design of a new improved tip.

7.2. Biomolecules adsorption

Once the bubble formation inside the ITC was understood and the main heat contributions identified, we started to use the method aiming to get the heat corresponding to adsorption and interfacial phenomena. Initially, only pure liquids (water, ethanol or cyclohexane) were essayed. Next, surfactant solutions were introduced, what derived in the surface tension application of Fluid Interface Calorimetry (Paper III). However, the adsorption rate can be a limitation of the method to follow the corresponding signal for small molecules such as surfactants, which is much faster than the response time of the instrument. Larger molecules, such as proteins, are not affected by this limitation since the corresponding adsorption can take place in a time scale of several hours.

Bovine Serum Albumin (BSA) and Lysozyme (Lys) were selected to test whether Fluid Interface Calorimetry is able to detect the signal corresponding to their adsor-

USC UNIVERSIDADE DE SANTIAGO DE COMPOSTELA

ption. These proteins have been previously studied by other interfacial techniques and, considering also their low cost and high stability, they represent the ideal targets for these tests (Alahverdjieva *et al.*, 2008b; Berthold *et al.*, 2007; Kou *et al.*, 2015; Lad *et al.*, 2006; Lu *et al.*, 1998; Rodríguez Niño and Rodríguez Patino, 1998; Tihonov *et al.*, 2015; Wen and Franses, 2001; Zhou *et al.*, 2013). However, because of the lack of technical support on the development of the bubble control system, both the time needed to adapt the ITC to these experiments, to control, measure and standardize the procedure, and the resources needed for its proper development exceeded the limits of this thesis project. Nonetheless, some preliminary results could be achieved, which are reflected in Paper II. These tests indicate that the method should be optimized before considering Fluid Interface Calorimetry as an standard for the characterization of adsorption processes of these systems. We propose the use of medium size molecules such as certain proteins or peptides, which should be ideal to test as well as to drive the optimization of this method. Such molecules have not been tested yet but it is planed to work with them at the short term. Another advantage of such systems is that they can be studied by alternative methods such as MD simulations, which would allow us to understand well the main mechanisms behind the adsorption process.

7.3. Liquid-liquid experiments

In the absence of an optimized method to control the air bubbles created in a liquid sample, we tested the Fluid Interface Calorimetry method using immiscible liquids. In these experiments, a liquid is injected from the ITC syringe, as usual, into another immiscible liquid thus creating a drop with a clear interface between the two liquids. Some results for the injection of water into cyclohexane are shown in Paper II, but more tests have been developed, even if no final conclusions can be obtained. The most complete experiment in this branch of the Fluid Interface Calorimetry is the water/BSA solution/Cyclohexane experiment. In this experiment, different blanks were analysed (water into water, water into cyclohexane, water into a cell filled half by water and half by cyclohexane) to study the system of interest: BSA solution towards water/cyclohexane interface. The objective of this experiment was to determine the heat of adsorption of BSA at the interface, but the results were not clear. A new problem emerged: the reference cell. The reference cell was always filled with water, as it is suggested for most of the aqueous solutions experiments. However, when the composition of the cell changes so dramatically, the feedback system starts working deficiently. If the experiments are not taken carefully, the signal may saturate, making the results useless. Again, like in the previous section, the lack of time pushed us to just approach the liquid-liquid interface experiments. However, great expectations are linked to this branch. The good control of the drop formation (much better than that for bubbles) and the less sensitiveness to pressure changes makes this kind of experiments very well suited to extend the implementation of the method.

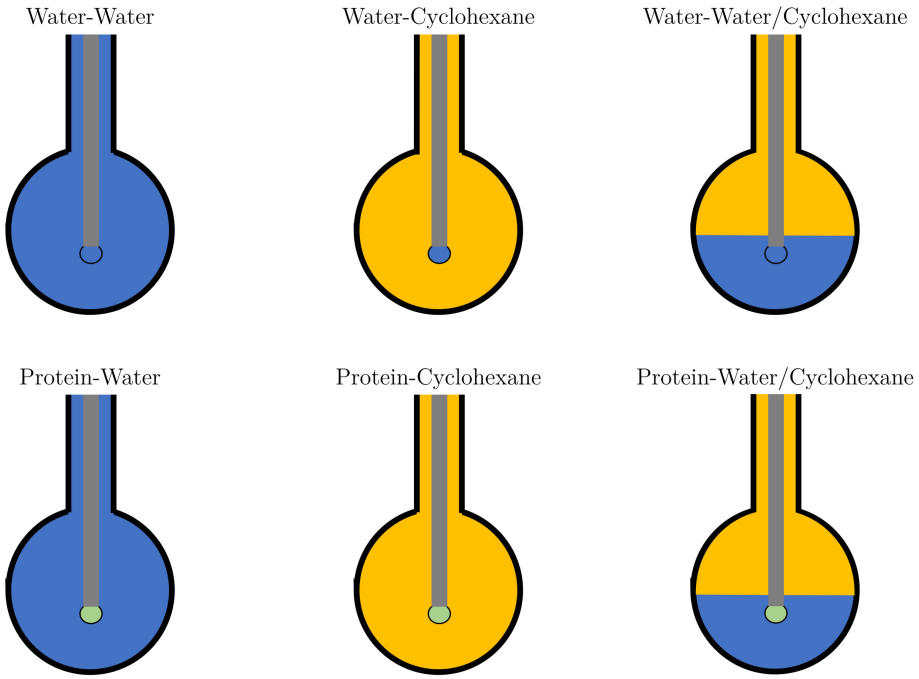


Figure 7.2: The water/BSA solution/Cyclohexane experiment diagram

USC UNIVERSIDADE DE SANTIAGO DE COMPOSTELA

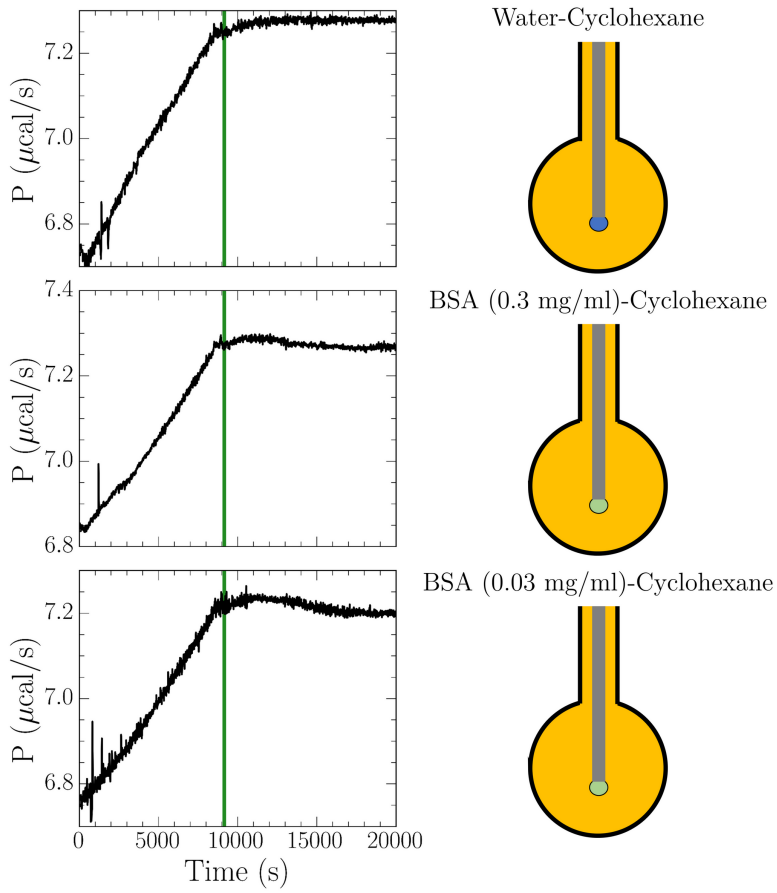


Figure 7.3: First results of BSA adsorption. The first plot corresponds to water into cyclohexane injection, while the other two correspond to the injection of BSA solution into cyclohexane. The green vertical lines indicate the end of the injections. After those injections, a new interface (water or solution/cyclohexane) is created in the cell, as the liquids are immiscible. A heat event is observed in the interfaces with BSA that would suggest adsorption to that new interface.

7.4. ITC theory

The results presented in Paper II are qualitative and mainly focused on the explanation of the technique and its possibilities. In Paper III, the algorithm developed to analyse the Fluid Interface Calorimetry row data for the determination of surface tension is presented. The implemented analytical method showed to be useful to provide reasonably accurate surface tension values of liquid solutions. Preliminary results from a complementary physical model able to describe the whole ITC raw signal are shown in Figure 7.4). This model includes the description of the

thermal effect of compression/expansion of air, the heat capacity change due to the injection of air into the cell, the thermal perturbation of the bubble delivery and other heat effects that are just approached by a mathematical parameterization. It also takes into account the response time of the instrument by means of the Tian's equation (Bastos, 2016; Jesús *et al.*, 2012).

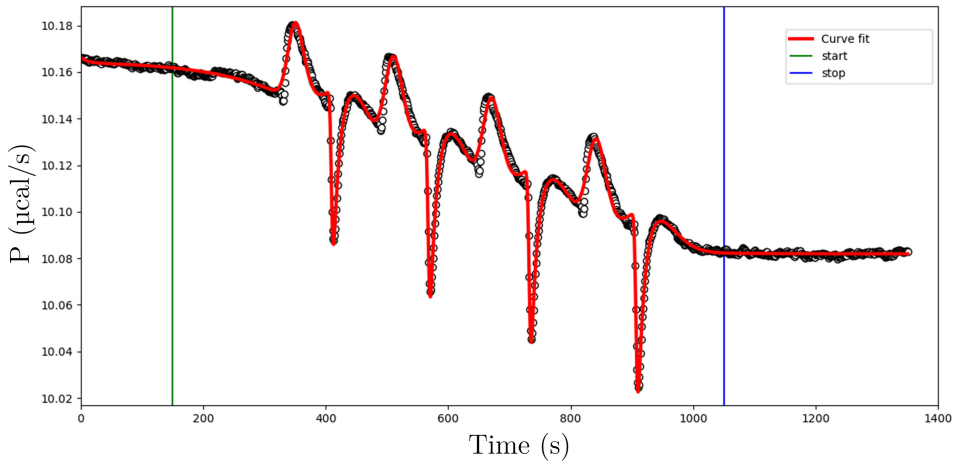
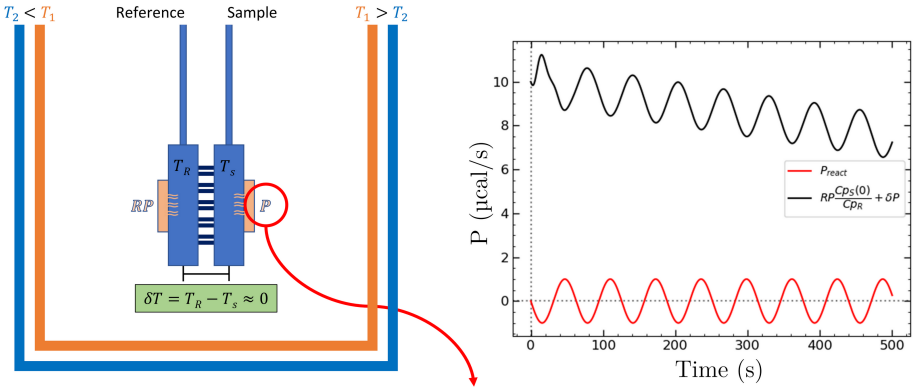


Figure 7.4: Preliminary results of the curve fitting of air-into-water bubble's heat signal.

USC UNIVERSIDADE DE SANTIAGO DE COMPOSTELA

The ITC's electronic influence on raw data and the reference cell effect is also being studied. The ITC's electronics is approached by solving and fitting the PID (Proportional-Integral-Derivative) controller equation (Figure 7.5). Experiments alternating ethanol, cyclohexane and water are being carried out to investigate the effect of the reference cell content on the row data.



$$P(t) = P(0) + \delta P(t)$$

$$\delta P(t) = K_P \delta T(t) + K_I \int_0^t \delta T(t)dt + K_D \dot{\delta T}(t)$$

Figure 7.5: Diagram showing the PID equation for the power P and first result of simulation (black line, right plot) of a sinusoidal heat (red line, right plot) produced in the cell, inducing a heat capacity change (like the injection of bubbles).

USC UNIVERSIDADE DE SANTIAGO DE COMPOSTELA

USC
UNIVERSIDADE
DE SANTIAGO
DE COMPOSTELA

7.5. Paper III

"Unsupervised bubble calorimetry analysis: Surface tension from isothermal titration calorimetry", published in *Journal of Colloid and Interface Science* (2022, online 2021), is a regular article where the previously presented Fluid interface calorimetry is used for the determination of the surface tension of surfactants or ethanol aqueous solutions. The algorithm for the data analysis and the obtention of the surface tension from the power heat detected by the ITC is here presented. This work has been developed in collaboration with people from: (1) Departamento de Física Aplicada, Facultade de Física, Universidade de Santiago de Compostela; (2) CIQ-UP, Departamento de Química e Bioquímica, Faculdade de Ciências da Universidade do Porto; (3) Institute of Biocomputation and Physics of Complex Systems (BIFI), Joint Units IQFR-CSIC-BIFI, and GBsC-CSIC-BIFI, Universidad de Zaragoza; Department of Biochemistry and Molecular and Cell Biology, Universidad de Zaragoza; Aragón Institute for Health Research (IIS Aragón); Biomedical Research Networking Centre for Liver and Digestive Diseases (CIBERehd); Fundacion ARAID, Government of Aragón; (4) IGBMC, Dept of Integrative Biology, Strasbourg University. The list of authors is presented below, by order and with their corresponding affiliations. The corresponding authors are marked with a *:

Pablo F. Garrido (1)*, Margarida Bastos (2), Adrián Velázquez-Campoy (3), Alfredo Amigo (1), Philippe Dumas (4), Ángel Piñeiro (1)*.

According to the CRediT authorship contribution statement (Brand *et al.*, 2015), my contributions to this publication are: Conceptualization; Methodology; Software; Validation; Formal analysis; Investigation; Writing - Original Draft; Writing - Review & Editing; Visualization

Garrido PF, Bastos M, Velázquez-Campoy A, Amigo A, Dumas P, Piñeiro Á (2022). Unsupervised bubble calorimetry analysis: Surface tension from isothermal titration calorimetry. *J. Colloid Interface Sci.*, **606**, 1823–1832. ISSN 00219797. doi: 10.1016/j.jcis.2021.08.115. URL https://www.doi.org/10.1016/j.jcis.2021.08.115

Supplementary Material is included in the Appendix B

USC UNIVERSIDADE DE SANTIAGO DE COMPOSTELA

USC
UNIVERSIDADE
DE SANTIAGO
DE COMPOSTELA

Journal of Colloid and Interface Science 606 (2022) 1823–1832

Contents lists available at ScienceDirect

Journal of Colloid and Interface Science

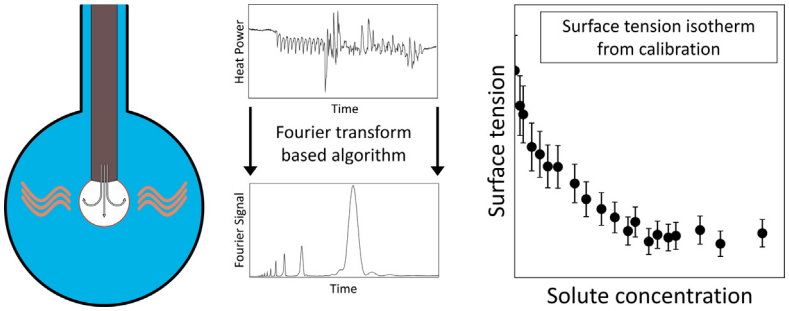
journal homepage: www.elsevier.com/locate/jcis

Unsupervised bubble calorimetry analysis: Surface tension from isothermal titration calorimetry

Pablo F. Garrido [a,*], Margarida Bastos [b], Adrián Velázquez-Campoy [c,d,e,f,g], Alfredo Amigo [a], Philippe Dumas [h], Ángel Piñeiro [a,*]

[a] Departamento de Fisica de Aplicada, Facultade de Fisica, Universidade de Santiago de Compostela, E-15782 Santiago de Compostela, Spain
[b] CIQ-UP, Departamento de Quimica e Bioquimica, Faculdade de Ciencias da Universidade do Porto, R. Campo Alegre 687, P-4169-007 Porto, Portugal
[c] Institute of Biocomputation and Physics of Complex Systems (BIFI), Joint Units IQFR-CSIC-BIFI, and GBsC-CSIC-BIFI, Universidad de Zaragoza, Zaragoza 50018, Spain
[d] Department of Biochemistry and Molecular and Cell Biology, Universidad de Zaragoza, 50009 Zaragoza, Spain
[e] Aragon Institute for Health Research (IIS Aragon), 50009 Zaragoza, Spain
[f] Biomedical Research Networking Centre for Liver and Digestive Diseases (CIBERehd), 28029 Madrid, Spain
[g] Fundacion ARAID, Government of Aragon, 50018 Zaragoza, Spain
[h] IGBMC, Dept of Integrative Biology, Strasbourg University, F67404 Illkirch CEDEX, France

GRAPHICAL ABSTRACT



ARTICLE INFO

Article history:
Received 5 July 2021
Revised 13 August 2021
Accepted 14 August 2021
Available online 20 August 2021

Keywords:
Interfaces
Adsorption
Isothermal Titration Calorimetry
Surface Tension
Data analysis

ABSTRACT

Hypothesis: The injection of air into the sample cell of an isothermal titration calorimeter containing a liquid provides a rich-in-information signal, with a periodic contribution arising from the creation, growing and release of bubbles. The identification and analysis of such contributions allow the accurate determination of the surface tension of the target liquid.
Experiments: Air is introduced at a constant rate into the sample cell of the calorimeter containing either a pure liquid or a solution. The resulting calorimetric signal is analyzed by a new algorithm, which is implemented into a computational code.
Findings: The thermal power generated by our experiments is often noisy, thus hiding the periodic signal arising from the bubbles' formation and release. The new algorithm was tested with a range of different types of calorimetric raw data, some of them apparently being just noise. In all cases, the contribution of the bubbles to the signal was isolated and the corresponding period was successfully determined in an automated way. It is also shown that two reference measurements suffice to calibrate the instrument at a given temperature, regardless the injection rate, allowing the direct determination of surface tension values for the liquid contained in the sample cell.

© 2021 The Author(s). Published by Elsevier Inc. This is an open access article under the CC BY license (http://creativecommons.org/licenses/by/4.0/).

* Corresponding authors.
E-mail addresses: Pablo.Fernandez@usc.es (P.F. Garrido), Angel.Pineiro@usc.es (Á. Piñeiro).

https://doi.org/10.1016/j.jcis.2021.08.115
0021-9797/© 2021 The Author(s). Published by Elsevier Inc.
This is an open access article under the CC BY license (http://creativecommons.org/licenses/by/4.0/).

1. Introduction

Molecular self-organization in the bulk of a liquid solution is intimately connected to the adsorption at the corresponding liquid-air interface. The surface tension is a property that depends directly on the composition of such interface. Thus, for a solution where the solute molecules do not adsorb , the corresponding surface tension should be undistinguishable from that of the pure solvent. However, the experimental evidence shows that the concentration of a given solute at the border region between a liquid and air can be several orders of magnitude larger than that in the bulk of the denser phase [1]. So, the surface tension can be considered as a highly efficient concentration sensor of a liquid solution. This becomes evident when dissolving hydrophobic or amphiphilic molecules in water as these solutes prefer the air-water interface to the bulk solution, thus leading to a significant decrease of the surface tension until the interface is saturated. At higher concentrations the surface tension becomes practically constant. The onset of this region is known as critical micelle concentration (cmc) or critical aggregation concentration (cac), because micelles of different size and shape, vesicles or other types of aggregates are spontaneously formed in the bulk solution beyond it. The kinetics of these processes plays an important role in how they can be characterized. Small molecules, like typical surfactants, diffuse very quickly and their adsorption can be considered as instantaneous for the observer, while the adsorption of large molecules such as proteins can take several hours [2]. A battery of different methods are available to determine the surface tension of liquid solutions: drop volume, drop profile, capillary rise, maximum bubble pressure or du Noüy ring, among others [3,4], since this is considered a basic property of amphiphilic molecules, with a large number of applications in many industries [5–11].

We have recently proposed a new method to determine surface tension values from Isothermal Titration Calorimetry (ITC) [12] that exhibits clear advantages with respect to other classical alternatives: very low sample consumption, easy automation of the experiments, a rich kinetic signal with meaningful physical information, usefulness for a large range of different solute and solvent molecules, and the possibility of performing experiments for the same system both in the bulk solution and at the interface. This method is based on the injection of air at a constant rate into the sample cell of an ITC instrument, and it can be considered as the first direct application of bubble calorimetry.

The eventual appearance of bubbles in calorimetric cells has traditionally been avoided since they typically introduce significant noise in the measurements. Thus, liquid solutions are often subjected to treatments aimed to remove traces of dissolved air that might perturb the experiments. Here we take advantage of the high sensitivity of modern ITC instruments to register the thermal power resulting from the creation, growing and delivery of relatively small bubbles in different solutions when air is injected in the liquid bulk at a constant rate. The obtained signals have a clear periodic contribution since the size of the bubbles is limited by the surface tension of the liquid contained in the measurement cell. This contribution is often hidden by other significant and more-difficult-to-predict sources of heat such as the coalescence of previously released bubbles in the bulk of the liquid solution, the interaction with the cell walls, temperature fluctuation of the environment, baseline drift due to change of composition in the sample cell, etc. For the experiments using pure water the raw data is extremely clean. The periodic contribution to the signal associated to the formation and delivery of bubbles into the solution, is easy to identify. Additional heat contributions due to the condensation/evaporation of solvent molecules and to the change in heat capacity of the sample cell due liquid displacement upon air injection can also be easily identified in these experiments.

It has been demonstrated that there is a linear correlation between the period of the signal obtained in bubble calorimetry experiments and the surface tension of the liquid contained in the sample cell of the instrument [12]. Thus, upon a suitable calibration, the period can be directly used for surface tension determinations by ITC. For solvents with significant vapor pressure and also for liquid solutions with relatively low surface tension, the signal is especially noisy, and often it is not even possible to identify by eye the periodic contribution arising from the bubbles. This represented a strong barrier for the wide use of this new method. The aim of the present work is to address this issue by developing a protocol able to identify the contribution of the bubbles to the ITC signal for a variety of solvent conditions, as well as to effectively determine the corresponding period in a fully automated way, from which the surface tension can be obtained. Our algorithm was implemented into a computational code and tested using a large variety of thermal power profiles corresponding to measurements of three surfactants in aqueous solution at different concentrations and temperatures, as well as measurements for pure water, ethanol and cyclohexane at the same temperatures. Complementarily, we have optimized our previous protocol for the calibration of the instrument, which is required to provide accurate surface tension values. As a result, it is demonstrated that two single reference measurements suffice to get a transformation factor from the period of the calorimetric bubble signal to the surface tension, regardless the injection rate.

2. Materials and methods

2.1. Materials and sample preparation

Ultrapure water (conductivity of 18.2 MΩ·m, Elix 3 purification system, Milipore Corp.), ethanol (99.8% min. purity from Panreac) and cyclohexane (99.7 % min. purity from Honeywell) were used in the experiments. Octyl-β-D-maltopyranoside (C_8G_2), decyl-β-D-maltopyranoside ($C_{10}G_2$) were purchased from Anatrace, and cetyltrimethylammonium bromide (CTAB) from Sigma-Aldrich. These compounds were used as received, without further purification. All the solutions were degassed trough vacuum prior the ITC measurements. Ethanol, $C_{10}G_2$ and CTAB solutions were prepared directly at their final concentrations. The same process was performed for C_8G_2 except for concentrations below 6 mM, which were prepared by diluting a stock solution at 7.20 mM.

2.2. Surface tension measurements

The surface tension of pure ethanol and $C_{10}G_2$ aqueous solutions at 298 ± 0.1 K, as well as that of water, cyclohexane and C_8G_2 aqueous solutions at 283 ± 0.1 K, 298 ± 0.1 K, 310 ± 0.1 K and 323 ± 0.1 K were measured by using a Lauda drop volume tensiometer (TVT 2 model, Germany) with the measurement cell connected to an external temperature bath. A capillary with inner radius of 1.70 mm and a 2.5 mL syringe were employed in all cases. The measurements were performed using the *standard mode* as programmed in the LAUDA software. In this operation mode, the injection rate is sequentially halved 4 times, registering the maximum volume of the drop when it detaches from the capillary. The initial rates were 0.81 μL/s for water and for the surfactant solutions, and 0.40 μL/s for ethanol and cyclohexane.

2.3. Calorimetric experiments

Three different VP-ITC instruments from MicroCal were employed: ITC-A (version 06.05.673), ITC-B (version 08.01.255)

and ITC-C (version 11.10.994). ITCs A and C are located in the same room while ITC B is in a different laboratory. The experimental procedure was described in our previous work [12]. The employed injection rates (v) range from 0.111 μL/s to 0.022 μL/s and the temperature of both laboratories was 296 ± 2 K. No modifications were applied in any of the ITC commercial instruments. The measurements employed in our previous article on Fluid Interface Calorimetry [12] (ethanol and $C_{10}G_2$ in water solution, both at 298 K and at different injection rates) were recycled here. The rest of the measurements were specifically carried out for the present work.

3. ITC data analysis

Because the raw data corresponding to the injection of air at a constant rate into the sample cell of an ITC instrument is often very noisy, a robust protocol able to effectively analyze a large variety of signals is required. In the present work, air injection measurements were collected for three surfactants in aqueous solution at different concentrations and temperatures, as well as for pure water, ethanol and cyclohexane at the same temperatures. As explained in our previous work, the surface tension of a liquid can be obtained from the period of the signal corresponding to the creation, growing and spontaneous release of bubbles during the air injection experiments [12]. This signal represents one contribution to the thermal power profile in our experiments, but other significant contributions are also present, including the drift in the baseline caused by the change in heat capacity of the sample cell, electrical, mechanical or thermal noise, thermal power caused by the coalescence of bubbles in the sample cell, heat exchange with the environment due to the difference of temperature, amongst other unexpected and/or difficult-to-control phenomena. A selection of raw calorimetric profiles corresponding to different air-injection measurements will be employed to illustrate the different steps of our algorithm. These include a non-trivial but reasonably well-behaved experiment with water (Fig. 1-a, black line), a less ideal experiment with a $C_{10}G_2$ solution (Fig. 1-b, black line), a noisy power profile for a different concentration of the same solution (Fig. 1-c, black line), and a very dirty signal obtained for ethanol (Fig. 1-d, black line). At this point we will ignore the specific sources of the radically different behaviors. The algorithm proposed to get the period of the bubble contribution from the thermal power profile consists in several steps that will be described in detail.

3.1. Baseline correction

There are different methods to obtain characteristic frequencies from a time dependent function with different periodic contributions. The most typical is the application of a Fourier transform. This mapping from the time to the frequency space can be automated in a fully unsupervised way. However, all our measurements contain a drift in the baseline caused by the change in composition of the sample cell upon injection of air into a liquid solution. Approaching this drift, ideally linear, by a series of sinusoidal functions introduces artificial peaks in the resulting Fourier transform. To avoid this problem, a baseline correction is applied to the experimental raw data. A general correction that will be able to address a variety of different behaviors should not be limited to a single function or type of functions. In our case, a series of four sequential filters will be applied to the original signal to get a reasonable baseline. It should be stressed that we are not looking for an accurate baseline that would be required to integrate quantitatively signal perturbations, but for a smooth baseline that prevents the appearance of artificial contributions to the Fourier transform in a subsequent analysis. The filters applied to the raw thermal power profile to reach this aim are: (i) a resolution downgrade; (ii) a Savitzky-Golay filtering protocol; (iii) a moving average; and (iv) an additional Savitzky-Golay filtering for low frequency noise. Finally, the resulting baseline is subtracted from the original data for further analysis.

3.1.1. Resolution downgrade (RD)

The peaks corresponding to the bubble release represent the largest contribution to the periodic signal that we aim to characterize, but they should be ignored for the identification of the baseline. Thus, as a first approach towards this goal, the whole profile is replaced by the average values determined over windows of $\sqrt{10N}$ length, where N is the total number of data points considered. This means that a hypothetical signal described by 1000 points would be distributed in 100 windows, and the whole profile would be replaced by the average of each of these trajectory seg-

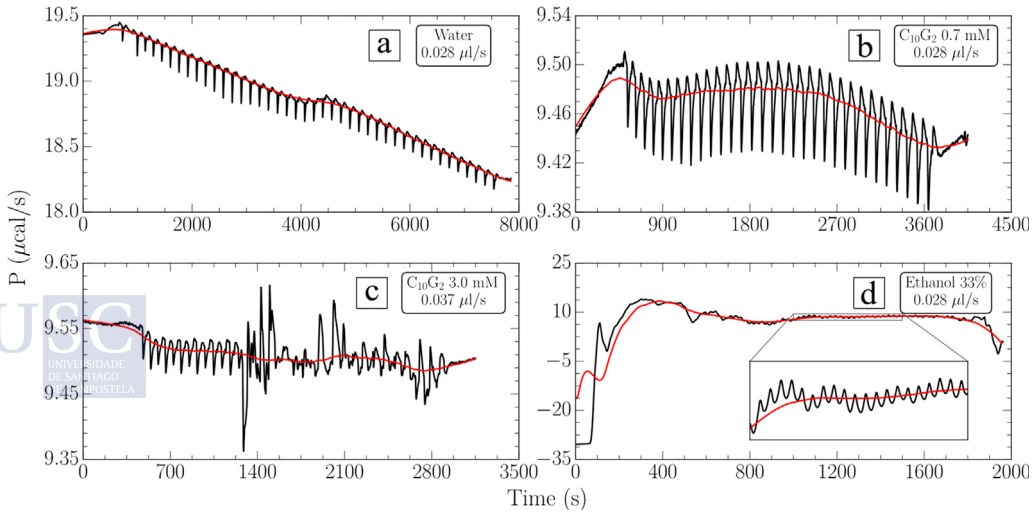


Fig. 1. Black lines: Calorimetric raw data measurements corresponding to four different types of air-injection profiles. In all the cases, air with no specific treatment was injected into the corresponded liquid. The liquid and injection rate of each thermal power profile is indicated in each plot. The inset in the plot corresponding to the ethanol contains a close-up of the signal in the region where the contribution of the bubbles is clearer. Red lines: estimated baselines after the RD followed by SG filtering protocol. (For interpretation of the references to color in this figure legend, the reader is referred to the web version of this article.)

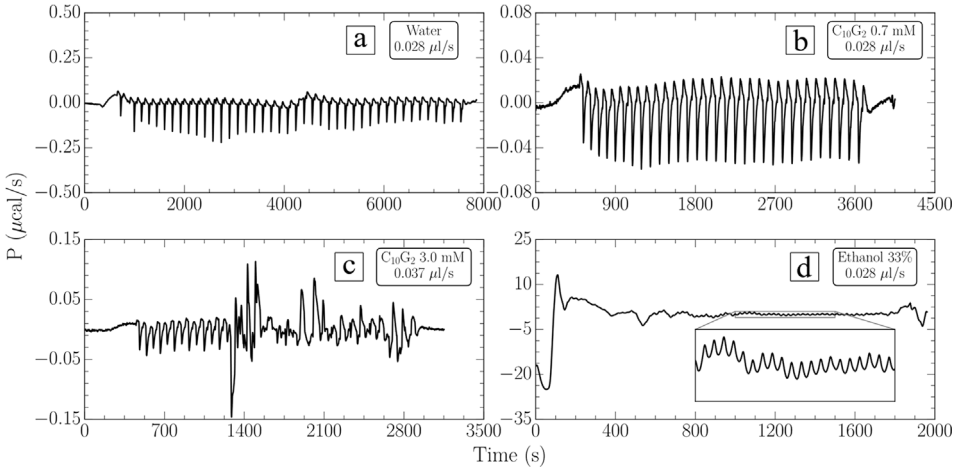


Fig. 2. Same data as in Fig. 1 after baseline subtraction.

ments. The length of the windows was chosen after several trials, considering an adequate result for this filter and taking as a reference the typical criteria used to set the number of bins in histograms. The resulting profile is closer to an ideal baseline than the original raw data, even for the signals with sharp perturbations (Figs. S1 and S2 in the SM).

3.1.2. Savitzky-Golay (SG) filtering

The output of the resolution downgrade is smoothed by applying a SG filtering protocol [13–15] with a second degree fitting polynomial. Due to the heterogeneity of the ITC profiles, we decided to apply four different SG filters using as a window size 10%, 20%, 30% and 40% the length of the downgraded signal in each of them. The average trend obtained from those filters is then filled with the same number of points as the original signal by cubic splines interpolation (Fig. 1).

3.1.3. Moving average (MA)

In order to smooth the high-frequency fluctuations that eventually remain after the previous SG protocol, a moving average was performed, using 10% of the trajectory length as a window size. The impact of this filter is often not significant, but it leads to a less artificial baseline in some cases.

3.1.4. Savitzky-Golay (SG) filter for low frequencies

A single SG filter is finally applied again with a second-degree fitting polynomial and using 50% of the trajectory as a window size. The aim of this filter is to correct low frequency fluctuations. The result of this last filter is only accepted when the difference between the resulting signal and the original data is significantly reduced. An F-test was applied to decide whether or not this filter is applied.

3.1.5. Baseline subtraction

Once the baseline is obtained following the above-described protocol, it is subtracted from the raw data for further analysis (Fig. 2). As it will be shown later, this treatment suffices to prevent the appearance of artificial contributions to the Fast Fourier transform (FFT) caused by the baseline drift.

3.2. Fourier analysis

After removal of the baseline, a Fast Fourier transform (FFT) is applied to get the characteristic frequencies of the signal. The loss of resolution associated to the use of FFT was amended by adding zeros at the end of the trajectory, thus increasing the length of the data array by a factor of 10. This method has been described in detail by Comisarow and Melka [16]. As expected, the application of FFT to the raw data does not provide useful information (Fig. 3, top row). In contrast, the result of the FFT on the baseline-corrected data provides a clear peak that can be associated to the period of the main contribution to the total signal coming from the bubbles, at least for the experiments with less noise and less perturbations in the thermal power profile. This result illustrates the need for the baseline correction on the raw data. However, the application of this filter to the less ideal measurements still shows many peaks, corresponding to artificial contributions of different period (Fig. 3, second row). Thus, we decided to perform a moving FFT (MFFT), similar to a wavelet analysis [17], on the baseline-corrected data in order to isolate the impact of strong perturbations that only affect specific regions of the thermal power profile (Fig. 3, third row). Using this methodology with a window size of 20% of the whole data array, the appearance of local noise along the experiment can be clearly identified. Further to this, an increase in the period for the beginning of the titration experiment is appreciated. However, in some signals the noise or the size of the perturbations is too high and still masks the useful information (Fig. 3, third row). This is due to the different size of the peaks obtained by the FFT in the different regions of the thermal power profile. A local normalization of the area of the spectra obtained from the MFFT was performed to overcome this problem. This strategy clearly improves the signal because the distribution of the spectrum over many peaks, at least for the noisy regions upon normalization of the corresponding area, significantly reduces the height of each peak compared to regions where a single peak results from the local MFFT (Fig. 3, fourth row). This method provides a period that slightly changes along the titration experiment. The final spectrum from which the periods can be directly determined, is obtained from the average of the normalized MFFT (Fig. 3, last row). The whole process, from raw data to final spectrum, is shown in the Supplementary Material (Figs. S1-S10) for 40 different bubble injection experiments.

3.3. Estimation of the period uncertainty

The resolution of the FFT and the uncertainty in the determination of the period are considered the major sources of error. The contribution to the uncertainty coming from the resolution of the FFT, $s_r(T)$, is given by the following equation:

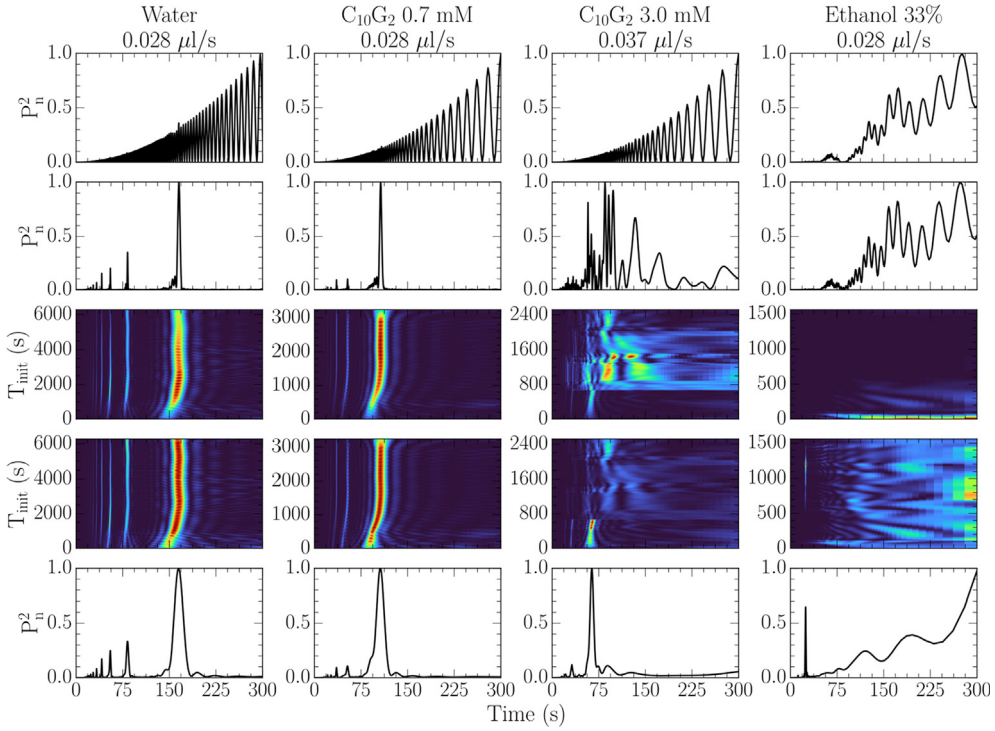


Fig. 3. Illustration of the sequential FFT analyses performed on the thermal power profile obtained from the air titration experiments in the systems indicated on the top of each column. They include: the FFT applied on the raw data (first row), the FFT applied on the baseline-corrected data (second row), the MFFT applied on the baseline-corrected data (third row), the normalized MFFT applied also on the baseline corrected data (fourth row), and the average of the previous normalized MFFT (fifth row). The x-axis is shared for all the plots. The y-axis depends on the plot: for the first, second and fifth rows, it represents the FFT density normalized by the highest peak; for the third and fourth rows, the normalized FFT density is shown with a color gradient (dark blue for lowest values and dark red for highest) and the initial time for each MFFT is represented in the y-axis. (For interpretation of the references to color in this figure legend, the reader is referred to the web version of this article.)

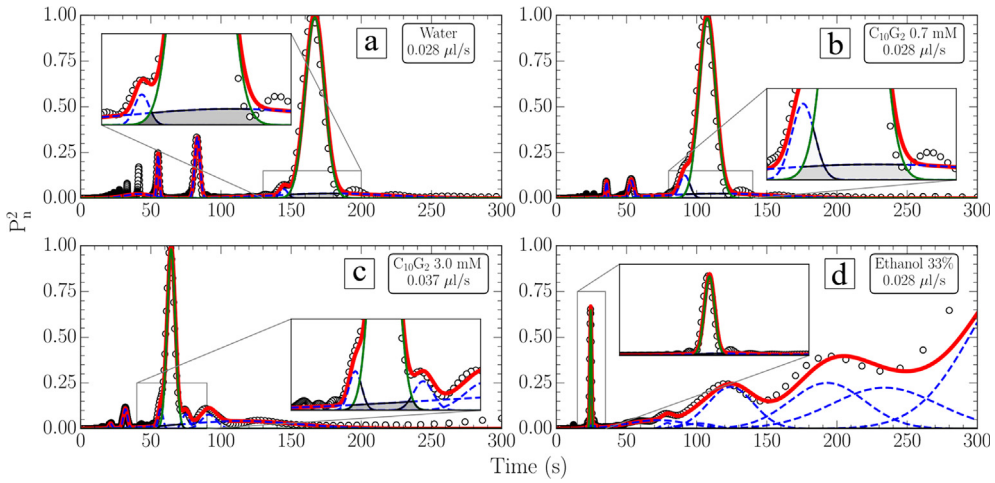


Fig. 4. Fitting of the averaged normalized MFFT spectra corresponding to the same experiments of Fig. 1 to a series of Gaussian functions (red lines) together with the individual Gaussian contributions (blue dashed lines). The green line corresponds to the main peak while the overlapped area is highlighted in grey. For each plot, an inset with a zoom around the overlapping area is shown. (For interpretation of the references to color in this figure legend, the reader is referred to the web version of this article.)

$$s_r(T) = \sqrt{\left(\frac{\partial T}{\partial f}\right)^2 s^2(f)} = \sqrt{T^4 \frac{(\Delta f)^2}{12}} = \frac{1}{\sqrt{12}} T^2 \Delta f \qquad (1)$$

where f is the frequency, $s(f)$ its uncertainty, Δf is the frequency resolution in the transformed space, and T is the period. Eq. (1) is obtained from the standard application of the propagation of uncertainties, considering a square distribution for the frequencies.

The second contribution to the uncertainty comes from the determination of the peak corresponding to the period. The final spectrum, obtained from the average of the normalized MFFT functions, still contains several contributions that were fitted to a series of normal distributions. Gaussian functions were selected for these fittings since they provide a suitable description of the different peaks. The peaks were detected by using the Peakutils Python package [18]. One Gaussian function per peak was employed for the fitting of the spectrum and two additional functions were taken to fit the background. The value of the period can be directly determined from these fittings and the corresponding uncertainty is

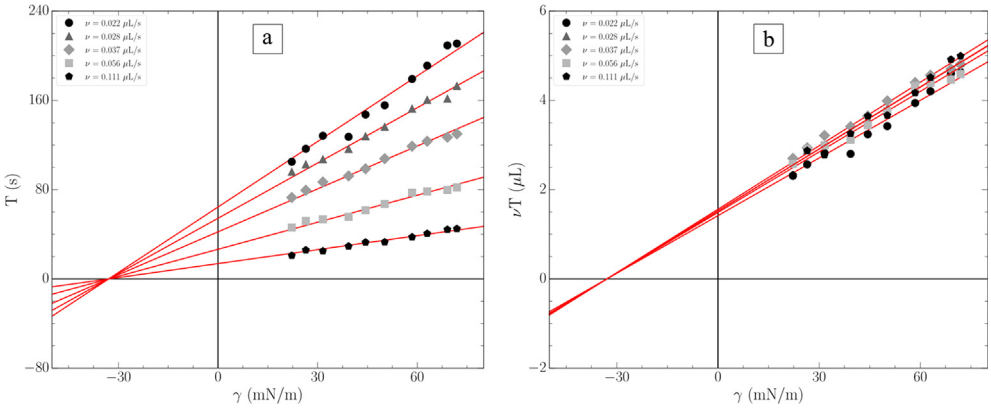


Fig. 5. a: Period obtained from air injection titration experiments by ITC using the protocol described above for different injection rates (see legends), as a function of the experimental surface tension obtained from the literature [19]. b: Bubble volume obtained as the product of the period by the injection rate, as a function of the surface tension for the same systems represented in a. The red lines in both plots represent the linear fittings of the experimental points restrained to share a common point at $\gamma = \gamma_0 = -34.9$ mM/m and T = 0 s. The common value of $p = \nu\, dT/d\gamma$ for all lines is 0.0444 (s(p) = 0.0015). (For interpretation of the references to color in this figure legend, the reader is referred to the web version of this article.)

Table 1
Summary of the experiments performed in the present work, where the employed ITC instruments, injection rates and temperatures are shown.

System	ITC			Injection rate (μl/s)					Temperature (K)			
	A	B	C	0.022	0.028	0.037	0.056	0.111	283	298	310	323
Ethanol-water (1)		x		x	x		x	x		x		
Ethanol-water (2)		x		x	x	x	x	x		x		
$C_{10}G_2$	x		x		x	x	x			x		
C_8G_2	x			x					x	x	x	x
CTAB	x		x		x	x	x			x		

*Ethanol-water solutions were independently prepared and tested twice.

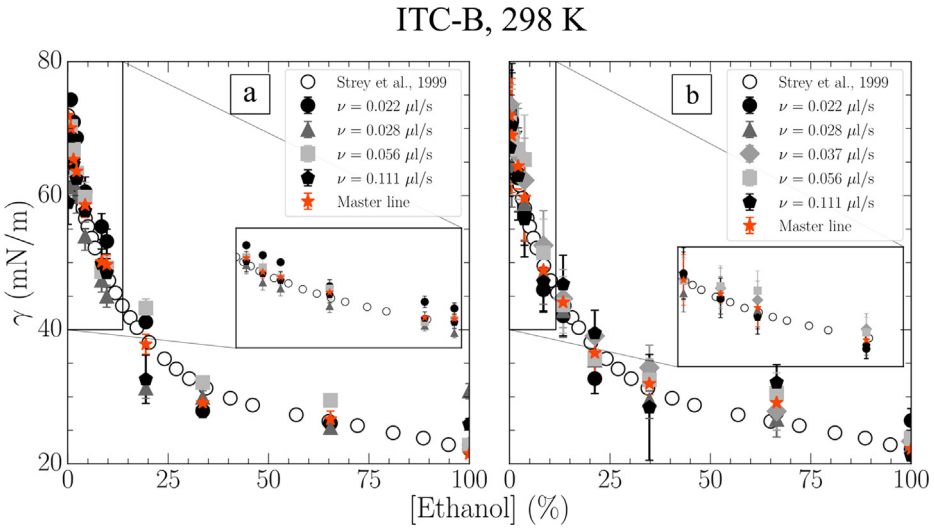


Fig. 6. Comparison between experimental surface tension values of ethanol in water solutions taken from the literature (empty circles) and those obtained following our ITC protocol. Both isotherms have been determined using the same ITC (ITC-B) at the same temperature (298 K). The solutions used for the determination of the isotherms in both plots were independently prepared. Black and grey solid symbols represent the surface tension values obtained from bubble-periods at different concentrations, and calibrations using just pure water and ethanol, at each injection rate. Red symbols represent the surface tension values obtained from the average of all the periods for different injection rates, at each concentration, and using the linear fitting of bubble volume vs surface tension for pure water and ethanol, regardless the injection rate, for the calibration (equivalent to the master line in Fig. 5-b). (For interpretation of the references to color in this figure legend, the reader is referred to the web version of this article.)

obtained from the covariance matrix. For noisy spectra, where more than one curve can be overlapped, the period is obtained from the mean value of all the peaks, weighted by the overlapped area with the main peak, normalized by its own area. This means that the weight for the main peak is 1. The value of the final period (T), its contribution to the uncertainty coming from the fitting and peak overlapping ($s_f(T)$), and the combined total uncertainty ($s_c(T)$) are:

$$T = \frac{\sum_i \tau_i A_i}{\sum_i A_i} \tag{2}$$

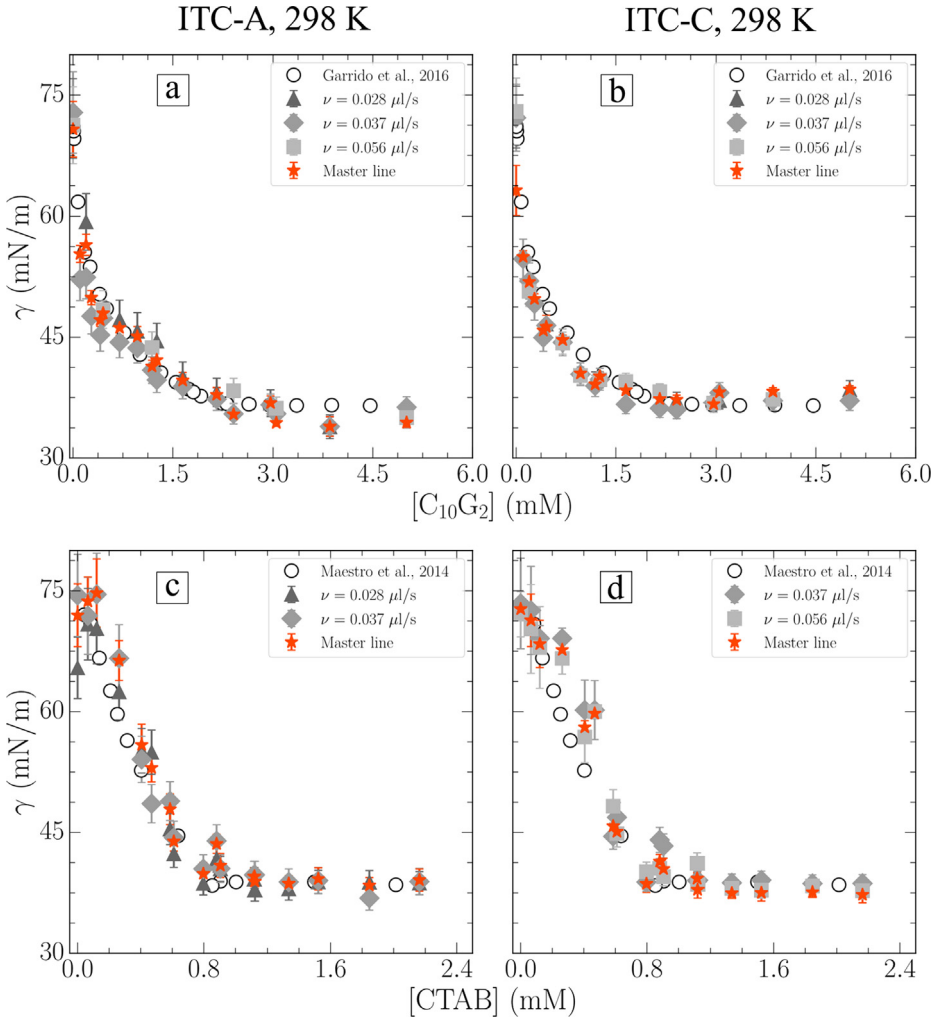


Fig. 7. Comparison between experimental surface tension values of non-ionic surfactant ($C_{10}G_2$) or ionic surfactant (CTAB) aqueous solutions taken from the literature (empty circles) and those obtained following our ITC protocol. For each system, the solutions were prepared once and measured in two different ITCs (ITC-A and ITC-C) at 298 K. Grey solid symbols represent the surface tension values obtained from bubble-periods at different concentrations, and calibrations using just pure water and cyclohexane, at each injection rate. Red symbols represent the surface tension values obtained from the average of all the periods for different injection rates, at each concentration, and using the linear fitting of bubble volume vs surface tension for pure water and cyclohexane, regardless the injection rate, for the calibration (equivalent to the master line in Fig. 5-b). (For interpretation of the references to color in this figure legend, the reader is referred to the web version of this article.)

$$s_f^2(T) = \frac{\sum_i s^2(\tau_i) A_i^2}{\sum_i A_i^2} \tag{3}$$

$$s_c(T) = \sqrt{s_r^2(T) + s_f^2(T)} \tag{4}$$

where τ_i the time value of each fitted peak, $s(\tau_i)$ its uncertainty and A_i the overlapped area normalized with the main peak. The whole process is illustrated in Fig. 4.

3.4. Calibration of the ITC instrument

The volume of a liquid drop pending from a capillary or the maximum pressure of an air bubble injected into a liquid are the observable magnitudes from which the surface tension is typically determined. Quantitative results require a calibration of the corresponding instruments throughout a correlation curve between the measurement and the target property. In our previous work we have observed a linear correlation between the period obtained from air titration experiments and the surface tension of the liquid sample contained in the calorimetric cell. Thus, two different reference compounds suffice to get a calibration curve for a given instrument at each injection rate. Interestingly, we observed that, in all conditions, the extrapolation of the linear correlations between the period and the surface tension at different injection rates converge to a common point with coordinates (γ_0, T = 0) (Fig. 5 and Figs. S11-S12 in the SM). Another observation is that the product p = ν dT/dγ is constant whatever the value of ν within a given experiment, thus leading to a master line in a representation of the bubble volume vs the surface tension that depends mainly on the instrument and on the temperature of the sample cell (Fig. 5 and Figs. S11-S12 in the SM). This means that dV/dγ = p = constant with V = νT is the volume of the bubble reached after the time T. As a result, the two parameters γ_0 and p suffice to characterize completely an experiment like that of Fig. 5. The observed linearity V = V_0 + p γ between the bubble volume and the surface tension is not immediately explained in full from first principles. However, the balance between buoyancy and surface tension when a bubble is about to detach is strictly analogous to the balance between weight and surface tension when a drop of liquid is about to fall in a "drop volume tensiometer". As it is well known the same linearity is observed in the latter situation [3]. Overall, this means that measuring two reference liquids is enough to calibrate the instrument in order to get accurate surface tension measurements

at any injection rate, although the calibration should be periodically repeated if the environmental conditions are not stable.

4. Surface tension validation and reproducibility

Surface tension values for all the systems indicated in the Methods section were measured by ITC, and compared to the values obtained in the present work using a drop volume tensiometer or taken from the literature [19–21]. Surface tension values of water and cyclohexane at different temperatures (Table S1, SM) and ethanol at 298 K (for the ethanol–water system) were employed to calibrate the instruments. These compounds were used for the calibration because they represent extreme cases of well characterized substances with high (water) and low (cyclohexane and ethanol) surface tension values, respectively. Air titration experiments were performed for four different systems as a function of their concentration, for different injection rates and temperatures, using three different ITC instruments, in order to check for instrument reproducibility (see Table 1). The analysis protocol for the determination of the period and the corresponding uncertainty described in the previous section was implemented in a Python code, which was employed to process all the titration thermal power profiles obtained from ITC. Together with the abovementioned libraries, this code is also based on some features from Numpy and Matplotlib [22,23]. These analyses are illustrated for 40 different measurements in the SM (Figs. S1-S10) showing that the algorithm works well for the wide range of trajectories collected for this work. As shown in Figs. 6–8, the surface tension values obtained by ITC agree very well with those obtained from alternative methods. Further to this, the reproducibility when using different injection rates as well as different instruments is good, with discrepancies being in most cases within the calculated uncertainties. Additionally, the effect of the location of the instrument was considered to see if some other parameter such as the external pressure, moisture or different temperature control, could significantly affect the results. Although the noise in the signal or the profile of the raw data can be affected by these external factors, the resulting surface tension values after the previously described analytical treatment are not significantly different.

5. Conclusions and perspectives

Surface tension is one of the most basic properties of liquids and liquid solutions. It is an extraordinary composition sensor, able to detect even nanomolar concentrations of amphiphilic compounds in aqueous solution. Its decrease in the presence of amphiphilic compounds is related to their ability to form aggregates in the bulk [20,24–26]. Equilibrium constants for the formation of complexes between molecules of different surface affinity have even been calculated from surface tension measurements [27]. Many industrial and technological applications are based on the use of amphiphilic compounds with high surface activity. The knowledge of the value

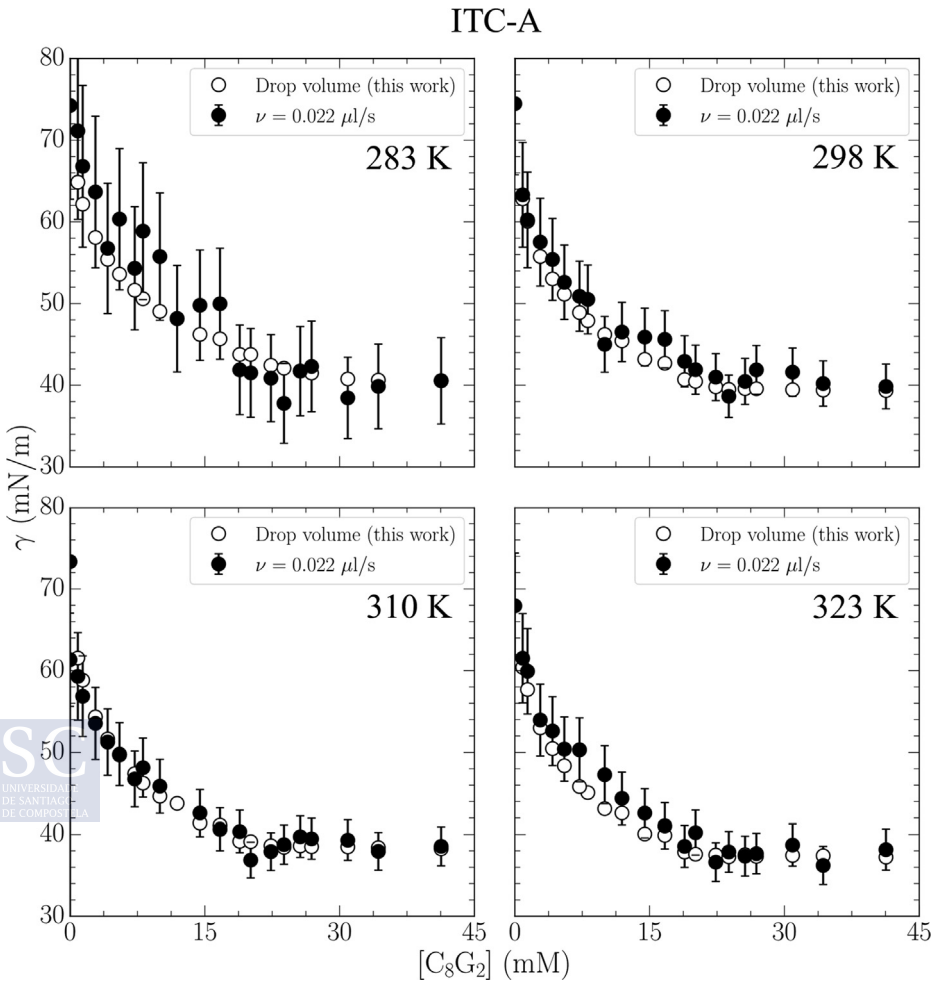


Fig. 8. Comparison between experimental surface tension values of non-ionic surfactant (C_8G_2) aqueous solutions obtained by using a drop volume TVT-2 tensiometer (Lauda) and those obtained following our ITC protocol. All the solutions were prepared once and measured in the same ITC (ITC-A) at 283, 298, 310 and 323 K.

for this property in different conditions and/or concentrations of amphiphiles is key to predict and understand their behavior at molecular level, as well as to optimize or develop new applications. Due to this, a battery of experimental methods is commercially available to measure surface tension of pure liquids and liquid mixtures, such as drop volume, drop profile, capillary rise, maximum bubble pressure, or du Noüy ring, among others [3,4]. Notably, none of these methods is able to simultaneously provide information on the behavior of the studied system in the bulk solution and at the interface. We have recently proposed a new protocol based on the injection of air at a constant rate into the sample cell of an isothermal titration calorimeter that exhibits many advantages with respect to other classical methods of surface tension determination. Bubble calorimetry is the only method that allows measurements of the thermal power associated to different association/dissociation processes both in the bulk and the interface for the same solution, using a small amount of sample, which concentration can be easily changed in a controlled way. This represents a significant saving of time and material. Nevertheless, a problem with these measurements is that they challenge the sensitivity of ITC instruments and so the useful information is often hidden within signal perturbations and noise. The significant breakthrough of the present work is that we propose a general protocol that is able to analyze even the most difficult thermal power profiles in an effective way to assess accurately the periodic nature of the thermal power signal associated with bubble formation and release, which is directly connected to the surface tension of the liquid. This protocol has been implemented into a computational code to allow a fully automated and unsupervised analysis that directly provides surface tension values and the corresponding uncertainties from air titration experiments in an ITC instrument. This computational code is available under request and it is currently being implemented in a freely accessible web application.

6. Contributions

P.F.G. and A.A. performed and analyzed the experiments. Á.P. conceived and supervised the project. P.F.G., M.B., A.V-C., A.A., P. D. and Á.P. analyzed the results and wrote the manuscript.

Declaration of Competing Interest

The authors declare that they have no known competing financial interests or personal relationships that could have appeared to influence the work reported in this paper.

Acknowledgements

The authors thank the financial support of the Spanish Ministry of Economy and Competitiveness (projects MAT2015-71826-P to Á. P. and BFU2016-78232-P to A.V.C.), the Agencia Estatal de Investigación (AEI) (project PID2019-111327GB-I00 to Á. P.) and Fundação para a Ciência e Tecnologia (FCT), Portugal, for CIQUP (project UIDB/00081/2020 to M.B.). P. F. G. thanks the Spanish Ministry of Economy and Competitiveness and the European Social Fund for his predoctoral research grant, reference BES-2016-076761. These research projects were partially supported by European ERDF Funds (MCIU/AEI/FEDER, EU). Facilities provided by the Galician Supercomputing Centre (CESGA) are also acknowledged.

Appendix A. Supplementary material

Supplementary data to this article can be found online at https://doi.org/10.1016/j.jcis.2021.08.115.

References

[1] S.S. Dukhin, G. Kretzschmar, R. Miller, Dynamics of Adsorption at Liquid Interfaces: Theory, Experiment, Application, Elsevier, Amsterdam, 1995.
[2] R. Miller, E.V. Aksenenko, V.S. Alahverdjieva, V.B. Fainerman, C.S. Kotsmar, J. Krägel, M.E. Leser, J. Maldonado-Valderrama, V. Pradines, C. Stefaniu, A. Stocco, R. Wüstneck, Thermodynamics and Kinetics of Mixed Protein/Surfactant Adsorption Layers at Liquid Interfaces, in: J.M. Ruso, Á. Piñeiro (Eds.), Proteins Solut. Interfaces, John Wiley & Sons Inc, Hoboken, NJ, USA, 2013, pp. 389–427, https://doi.org/10.1002/9781118523063.ch20.
[3] H.Y. Erbil, Experimental Determination of Surface Tension at Pure Liquid and Solution Surfaces/Interfaces, in: Surf. Chem. Solid Liq. Interfaces, Blackwell Publishing Ltd., Oxford, UK, 2006: pp. 223–249. https://doi.org/10.1002/9781444305401.ch6.
[4] A.W. Adamson, A.P. Gast, Physical chemistry of surfaces, 6th ed., John Wiley & Sons, New York, 1997.
[5] L.L. Schramm, ed., Surfactants, Cambridge University Press, 2000. https://doi.org/10.1017/CBO9780511524844.
[6] T. Karbowiak, F. Debeaufort, A. Voilley, Importance of surface tension characterization for food, pharmaceutical and packaging products: A review, Crit. Rev. Food Sci. Nutr. 46 (5) (2006) 391–407, https://doi.org/10.1080/10408390591000884.
[7] P. Ragesh, V. Anand Ganesh, S.V. Nair, A.S. Nair, A review on "self-cleaning and multifunctional materials", J. Mater. Chem. A. 2 (36) (2014) 14773–14797, https://doi.org/10.1039/C4TA02542C.
[8] S.B.G.M. O'Brien, Some surface tension and contact angle problems in industry, J. Adhes. Sci. Technol. 6 (9) (1992) 1037–1051, https://doi.org/10.1163/156856192X00926.
[9] N. Mukherjee, B. Bansal, X.D. Chen, Measurement of Surface Tension of Homogenised Milks, Int. J. Food Eng. 1 (2005), https://doi.org/10.2202/1556-3758.1013.
[10] J.M. Luna, R.D. Rufino, L.A. Sarubbo, G.M. Campos-Takaki, Characterisation, surface properties and biological activity of a biosurfactant produced from industrial waste by Candida sphaerica UCP0995 for application in the petroleum industry, Colloids Surfaces B Biointerfaces. 102 (2013) 202–209, https://doi.org/10.1016/j.colsurfb.2012.08.008.
[11] C. Hill, J. Eastoe, Foams: From nature to industry, Adv. Colloid Interface Sci. 247 (2017) 496–513, https://doi.org/10.1016/j.cis.2017.05.013.
[12] P.F. Garrido, M. Bastos, A. Velázquez-Campoy, P. Dumas, Á. Piñeiro, Fluid interface calorimetry, J. Colloid Interface Sci. 596 (2021) 119–129, https://doi.org/10.1016/j.jcis.2021.03.098.
[13] W.H. Press, S.A. Teukolsky, Savitzky-Golay Smoothing Filters, Cit. Comput. Phys. 4 (6) (1990) 669, https://doi.org/10.1063/1.4822961.
[14] A. Savitzky, M.J.E. Golay, Smoothing and differentiation of data by simplified least squares procedures, Anal. Chem. 36 (8) (1964) 1627–1639, https://doi.org/10.1021/ac60214a047.
[15] P. Virtanen, R. Gommers, T.E. Oliphant, M. Haberland, T. Reddy, D. Cournapeau, E. Burovski, P. Peterson, W. Weckesser, J. Bright, S.J. van der Walt, M. Brett, J. Wilson, K.J. Millman, N. Mayorov, A.R.J. Nelson, E. Jones, R. Kern, E. Larson, C.J. Carey, İ. Polat, Y.u. Feng, E.W. Moore, J. VanderPlas, D. Laxalde, J. Perktold, R. Cimrman, I. Henriksen, E.A. Quintero, C.R. Harris, A.M. Archibald, A.H. Ribeiro, F. Pedregosa, P. van Mulbregt, A. Vijaykumar, A.P. Bardelli, A. Rothberg, A. Hilboll, A. Kloeckner, A. Scopatz, A. Lee, A. Rokem, C.N. Woods, C. Fulton, C. Masson, C. Häggström, C. Fitzgerald, D.A. Nicholson, D.R. Hagen, D.V. Pasechnik, E. Olivetti, E. Martin, E. Wieser, F. Silva, F. Lenders, F. Wilhelm, G. Young, G.A. Price, G.-L. Ingold, G.E. Allen, G.R. Lee, H. Audren, I. Probst, J.P. Dietrich, J. Silterra, J.T. Webber, J. Slavič, J. Nothman, J. Buchner, J. Kulick, J.L. Schönberger, J.V. de Miranda Cardoso, J. Reimer, J. Harrington, J.L.C. Rodríguez, J. Nunez-Iglesias, J. Kuczynski, K. Tritz, M. Thoma, M. Newville, M. Kümmerer, M. Bolingbroke, M. Tartre, M. Pak, N.J. Smith, N. Nowaczyk, N. Shebanov, O. Pavlyk, P.A. Brodtkorb, P. Lee, R.T. McGibbon, R. Feldbauer, S. Lewis, S. Tygier, S. Sievert, S. Vigna, S. Peterson, S. More, T. Pudlik, T. Oshima, T.J. Pingel, T.P. Robitaille, T. Spura, T.R. Jones, T. Cera, T. Leslie, T. Zito, T. Krauss, U. Upadhyay, Y.O. Halchenko, Y. Vázquez-Baeza, SciPy 1.0: fundamental algorithms for scientific computing in Python, Nat. Methods. 17 (3) (2020) 261–272, https://doi.org/10.1038/s41592-019-0686-2.
[16] M.B. Comisarow, J.D. Melka, Error Estimates for Finite Zero-Filling in Fourier Transform Spectrometry, Anal. Chem. 51 (13) (1979) 2198–2203, https://doi.org/10.1021/ac50049a032.
[17] G. Kaiser, A Friendly Guide to Wavelets, 1st ed., Birkhäuser Boston (Original work published 1994), Boston, 2011. https://doi.org/10.1007/978-0-8176-8111-1.
[18] L.H. Negri, C. Vestri, lucashn/peakutils: v1.1.0, Zenodo. (2017). https://doi.org/10.5281/ZENODO.887917.
[19] R. Strey, Y. Viisanen, M. Aratono, J.P. Kratohvil, Q.i. Yin, S.E. Friberg, On the Necessity of Using Activities in the Gibbs Equation, J. Phys. Chem. B. 103 (43) (1999) 9112–9116, https://doi.org/10.1021/jp990306w.
[20] P.F. Garrido, P. Brocos, A. Amigo, L. García-Río, J. Gracia-Fadrique, Á. Piñeiro, STAND: Surface Tension for Aggregation Number Determination, Langmuir. 32 (16) (2016) 3917–3925, https://doi.org/10.1021/acs.langmuir.6b0047710.1021/acs.langmuir.6b00477.s001.
[21] A. Maestro, E. Rio, W. Drenckhan, D. Langevin, A. Salonen, Foams stabilised by mixtures of nanoparticles and oppositely charged surfactants: Relationship between bubble shrinkage and foam coarsening, Soft Matter. 10 (36) (2014) 6975–6983, https://doi.org/10.1039/C4SM00047A.

[22] C.R. Harris, K.J. Millman, S.J. van der Walt, R. Gommers, P. Virtanen, D. Cournapeau, E. Wieser, J. Taylor, S. Berg, N.J. Smith, R. Kern, M. Picus, S. Hoyer, M.H. van Kerkwijk, M. Brett, A. Haldane, J.F. del Río, M. Wiebe, P. Peterson, P. Gérard-Marchant, K. Sheppard, T. Reddy, W. Weckesser, H. Abbasi, C. Gohlke, T.E. Oliphant, Array programming with NumPy, Nature. 585 (7825) (2020) 357–362, https://doi.org/10.1038/s41586-020-2649-2.
[23] J.D. Hunter, Matplotlib: A 2D graphics environment, Comput. Sci. Eng. 9 (3) (2007) 90–95, https://doi.org/10.1109/MCSE.2007.55.
[24] H. Wang, H. Kong, J. Zheng, H. Peng, C. Cao, Y. Qi, K. Fang, W. Chen, Systematically exploring molecular aggregation and its impact on surface tension and viscosity in high concentration solutions, Molecules. 25 (2020) 1588, https://doi.org/10.3390/molecules25071588.
[25] C. Hill, A. Czajka, G. Hazell, I. Grillo, S.E. Rogers, M.W.A. Skoda, N. Joslin, J. Payne, J. Eastoe, Surface and bulk properties of surfactants used in fire-fighting, J. Colloid Interface Sci. 530 (2018) 686–694, https://doi.org/10.1016/j.jcis.2018.07.023.
[26] J. Gu, B. Yin, S. Fu, M. Feng, Z. Zhang, H. Dong, F. Gao, Y.S. Zhao, Surface tension driven aggregation of organic nanowires: Via lab in a droplet, Nanoscale. 10 (23) (2018) 11006–11012, https://doi.org/10.1039/C8NR02592D.
[27] Á. Piñeiro, X. Banquy, S. Pérez-Casas, E. Tovar, A. García, A. Villa, A. Amigo, A.E. Mark, M. Costas, On the Characterization of Host−Guest Complexes: Surface Tension, Calorimetry, and Molecular Dynamics of Cyclodextrins with a Non-ionic Surfactant, J. Phys. Chem. B. 111 (2007) 4383–4392, https://doi.org/10.1021/jp0688815.

USC UNIVERSIDADE DE SANTIAGO DE COMPOSTELA

Chapter 8

New models in bulk ITC

All models are wrong, but some are useful

George E. P. Box, British statistician

The core of this project spins around new experimental methods based on ITC. During this period, I had the opportunity to make significant contributions to the analysis of raw ITC signals as well as to test models already implemented in the publicly available AFFINImeter software. This collaboration with the AFFINImeter team is reflected in Paper IV. Also resulting from the joint treatment of aggregation data in the bulk and of adsorption information at interfaces, I contributed to the development of a thermodynamic model that has been published in Paper V.

USC
UNIVERSIDADE DE SANTIAGO DE COMPOSTELA

USC
UNIVERSIDADE
DE SANTIAGO
DE COMPOSTELA

8.1. Paper IV

"AFFINImeter: A software to analyze molecular recognition processes from experimental data", published in *Analytical Biochemistry* (2019), is a regular article where AFFINImeter, a software for the analysis of ITC data, is presented and where the algorithms and models that this software uses are explained. The publication is completed with the analysis of some complex experiments. This work has been developed in collaboration with people from: (1) Departamento de Física Aplicada, Facultade de Física, Universidade de Santiago de Compostela; (2) AFFINImeter Scientific & Development team, Software 4 Science Developments; (3) Laboratorio de Biofisicoquímica, Departamento de Fisicoquímica, Facultad de Química, Universidad Nacional Autónoma de México; (4) CIQ-UP, Departamento de Química e Bioquímica, Faculdade de Ciências da Universidade do Porto; (5) Institute of Biocomputation and Physics of Complex Systems (BIFI), Joint Units IQFR-CSIC-BIFI, and GBsC-CSIC-BIFI, Universidad de Zaragoza; Department of Biochemistry and Molecular and Cell Biology, Universidad de Zaragoza; Aragón Institute for Health Research (IIS Aragón); Biomedical Research Networking Centre for Liver and Digestive Diseases (CIBERehd); Fundacion ARAID, Government of Aragón; (6) IGBMC, Dept of Integrative Biology, Strasbourg University (7) CNRS, Architecture et Réactivité de lÁRN, Institut de Biologie Moléculaire et Cellulaire, Université de Strasbourg; (8) Centro de Investigación en Química Biolóxica e Materiais Moleculares (CIQUS), Departamento de Química Física, Universidade de Santiago de Compostela; (9) Fundación Pública Galega Centro Tecnolóxico de Supercomputación de Galicia (CESGA). The list of authors is presented below, by order and with their corresponding affiliations. The corresponding authors are marked with a *:

Ángel Piñeiro (1)*, Eva Muñoz (2), Juan Sabín (2), Miguel Costas (3), Margarida Bastos (4), Adrián Velázquez-Campoy (5), **Pablo F. Garrido** (1) , Philippe Dumas (6), Eric Ennifar (7), Luis García-Río (8), Javier Rial (2), Daniel Pérez (2), Patricia Fraga (2), Aurelio Rodríguez (9), Carmen Cotelo (9).

According to the CRediT authorship contribution statement (Brand *et al.*, 2015), my contributions to this publication are: Validation; Formal analysis; Investigation.

Piñeiro Á, Muñoz E, Sabín J, Costas M, Bastos M, Velázquez-Campoy A, Garrido PF, Dumas P, Ennifar E, García-Río L, Rial J, Pérez D, Fraga P, Rodríguez A, Cotelo C (2019). AFFINImeter: A software to analyze molecular recognition processes from experimental data. *Anal. Biochem.*, **577**, 117–134. ISSN 00032697. doi: 10.1016/j.ab.2019.02.031. URL https://www.doi.org/10.1016/j.ab.2019.02.031

USC UNIVERSIDADE DE SANTIAGO DE COMPOSTELA

USC
UNIVERSIDADE
DE SANTIAGO
DE COMPOSTELA

Analytical Biochemistry 577 (2019) 117–134

Contents lists available at ScienceDirect

Analytical Biochemistry

journal homepage: www.elsevier.com/locate/yabio

AFFINImeter: A software to analyze molecular recognition processes from experimental data

Ángel Piñeiro[a,*], Eva Muñoz[b], Juan Sabín[b], Miguel Costas[c], Margarida Bastos[d], Adrián Velázquez-Campoy[e,f,g,h,i], Pablo F. Garrido[a], Philippe Dumas[j], Eric Ennifar[k], Luis García-Río[l], Javier Rial[b], Daniel Pérez[b], Patricia Fraga[b], Aurelio Rodríguez[m], Carmen Cotelo[m]

[a] Departamento de Física de Aplicada, Facultade de Física, Universidade de Santiago de Compostela, E-15782, Santiago de Compostela, Spain
[b] AFFINImeter Scientific & Development team, Software 4 Science Developments, S. L. Ed. Emprendia, Santiago de Compostela, A Coruña, 15782, Spain
[c] Laboratorio de Biofisicoquímica, Departamento de Fisicoquímica, Facultad de Química, Universidad Nacional Autónoma de México, México City, 04510, Mexico
[d] CIQ-UP, Departamento de Química e Bioquímica, Faculdade de Ciências da Universidade do Porto, R. Campo Alegre 687, P-4169-007, Porto, Portugal
[e] Institute of Biocomputation and Physics of Complex Systems (BIFI), Joint Units IQFR-CSIC-BIFI, and GBsC-CSIC-BIFI, Universidad de Zaragoza, Zaragoza, 50018, Spain
[f] Department of Biochemistry and Molecular and Cell Biology, Universidad de Zaragoza, 50009, Zaragoza, Spain
[g] Aragon Institute for Health Research (IIS Aragon), 50009, Zaragoza, Spain
[h] Biomedical Research Networking Centre for Liver and Digestive Diseases (CIBERehd), 28029, Madrid, Spain
[i] Fundacion ARAID, Government of Aragon, 50018, Zaragoza, Spain
[j] IGBMC, Dept of Integrative Biology, Strasbourg University, F67404, Illkirch CEDEX, France
[k] CNRS, Architecture et Réactivité de l'ARN, Institut de Biologie Moléculaire et Cellulaire, Université de Strasbourg, UPR 9002, F-67000, Strasbourg, France
[l] Centro de Investigación en Química Biolóxica e Materiais Moleculares (CIQUS), Departamento de Química Física, Universidade de Santiago, 15782, Santiago, Spain
[m] Fundación Pública Galega Centro Tecnolóxico de Supercomputación de Galicia (CESGA), Avda. de Vigo s/n, 15705, Santiago de Compostela, Spain

ARTICLE INFO

Keywords:
Molecular recognition
Affinity
Isothermal titration calorimetry
Thermodynamics
Kinetics
Analysis software

ABSTRACT

The comprehension of molecular recognition phenomena demands the understanding of the energetic and kinetic processes involved. General equations valid for the thermodynamic analysis of any observable that is assessed as a function of the concentration of the involved compounds are described, together with their implementation in the AFFINImeter software. Here, a maximum of three different molecular species that can interact with each other to form an enormous variety of supramolecular complexes are considered. The corrections currently employed to take into account the effects of dilution, volume displacement, concentration errors and those due to external factors, especially in the case of ITC measurements, are included. The methods used to fit the model parameters to the experimental data, and to generate the uncertainties are described in detail. A simulation tool and the so called kinITC analysis to get kinetic information from calorimetric experiments are also presented. An example of how to take advantage of the AFFINImeter software for the global multi-temperature analysis of a system exhibiting cooperative 1:2 interactions is presented and the results are compared with data previously published. Some useful recommendations for the analysis of experiments aimed at studying molecular interactions are provided.

1. Introduction

The understanding of the underlying mechanisms involved in molecular recognition processes requires the knowledge of the structural, energetic and kinetic features associated with these events. This in turn allows the rational design or optimization of chemical and biochemical compounds for specific applications. Examples of processes that can be studied in solution are protein-ligand association, the dissociation/association of protein oligomers, the encapsulation of small molecules in hydrophobic cavities or in molecular aggregates formed by amphiphilic compounds, step-wise binding of small molecules to a large polymer, spontaneous aggregation of molecules into larger self-organized structures, micelle formation/dissociation, and adsorption of molecules onto solid interfaces [1,2].

For the quantitative characterization of these processes we need to apply a thermodynamic model to a set of experimentally obtained data

* Corresponding author.
E-mail address: Angel.Pineiro@usc.es (Á. Piñeiro).

https://doi.org/10.1016/j.ab.2019.02.031
Received 29 November 2018; Received in revised form 21 February 2019; Accepted 28 February 2019
Available online 05 March 2019
0003-2697/ © 2019 Published by Elsevier Inc.

of an observable property that is sensitive to the amount of free and bound species in the system [3–5]. For recognition or binding processes between any two molecules (M and A) at a given temperature and pressure, the representation of such an observable as a function of the total concentration of M or A (or, alternatively, as a function of the concentration ratio [M]/[A] or [A]/[M]) is typically referred to as "equilibrium isotherm" or "saturation binding curve". From this curve, quantitative information on the thermodynamic properties of the studied process (equilibrium constant, Gibbs energy, enthalpy, entropy, heat capacity) can be obtained. This equilibrium thermodynamic information can in turn be used to interpret the data at molecular level, together with information from other experiments and/or models (X-ray diffraction, NMR, molecular dynamics simulations, statistical thermodynamics, *etc*). Additionally, when the observable is also monitored as a function of time for different M or A concentrations, a kinetic characterization of the binding event is also possible [6].

Different experimental techniques are available to study molecular recognition. The most commonly used methods are Isothermal Titration Calorimetry (ITC), Nuclear Magnetic Resonance (NMR), Surface Plasmon Resonance (SPR), Microscale Thermophoresis (MST) and a variety of spectroscopic methods including fluorescence, circular dichroism, IR and UV—vis. The thermodynamic information obtained from any of these techniques for a given process must *in principle* be the same. However, differences are expected when the experimental setup is not identical, *e.g.* the use of different sample volume and concentrations in order to maximize the signal-to-noise ratio, the immobilization of the target compound to a substrate or the use of an external marker (*e.g.* a fluorescent tag). Particularly in the cases of immobilized or labelled reactants the system is expected to behave differently from experiments where free, unlabelled molecules are present in solution. Different techniques may also differ in the way the system is perturbed and the observed signal is measured. For instance, ITC is based on sequential perturbations of equilibrium states followed by return to equilibrium. The measured signal is the heat released or absorbed upon small concentration changes due to several factors: dilution, aggregation/dissociation or the transformation between supramolecular complexes of different stoichiometry. Therefore, the kinetics of the binding process may affect the results obtained for the thermodynamic parameters obtained from ITC, mainly for slow-binding ligands. In contrast, most of the techniques designed for the study of intermolecular interactions register an observable signal of well equilibrated samples, *i.e.*, the samples are not perturbed during the experiment. Nevertheless, even under the same conditions and techniques, different values for the thermodynamic parameters are found in the literature. There are a large number of reasons for these discrepancies to occur, ranging from uncertainties in sample concentration, incorrect instrument calibration, technical difficulties to obtain a good signal-to-noise ratio, and finally differences arising from the data fitting. A detailed discussion of the relevance of each of the factors leading to the inconsistencies between the thermodynamic parameters obtained from different techniques is indeed outside the scope of the present work. However, it should be noted that efforts are being made towards the standardization of results obtained from different biophysical techniques [7].

In order to improve the characterization of a large variety of molecular processes that are often involved in fundamental or applied research, several companies are continuously making efforts to optimize the sensitivity and performance of the instruments, as well as improving the hardware and software aimed at collecting the primary data (raw signal). Concurrently, complementary software is needed to properly analyze experimental information of different degrees of complexity and retrieve the thermodynamic constants that characterize the processes under study. For this, the selection of a proper binding model, the correct estimation of the involved parameters, avoiding local minima and over-parameterization, as well as getting a good estimation of uncertainties, are of paramount importance. AFFINImeter was designed in order to fulfil these aims. This software offers the traditional binding models, but more importantly, it makes possible to develop user-tailored models in a very simple way, a possibility not publicly available in any other analysis software. Furthermore, during the processing of the raw signal useful information is sometimes discarded, as it has been the case for ITC measurements –a technique that has been traditionally employed mainly to get thermodynamic data– where the kinetic information has remained mostly unaddressed. AFFINImeter allows users to obtain valuable kinetic information from the raw ITC data, with no additional effort nor sample consumption, using a particular development called kinITC [8]. At present, AFFINImeter can analyze binding curves from ITC, from NMR, and from spectroscopy data. These different AFFINImeter applications are referred to as AFF-ITC, AFF-NMR and AFF-Spectroscopy. In the present work, we describe the main features and technical details of this software, with special emphasis on the implementation of thermodynamic binding models that represent a large variety of binding and molecular recognition events and mechanisms.

2. Software description

The software currently available for the analysis of binding events from experimental measurements has different origins: (i) software attached to a specific instrument, typically developed and provided by the equipment manufacturers; (ii) third-party software specialized in a single technique for several instrument brands; and (iii) third-party software for a range of techniques and instrument brands. The last two are usually developed by private companies or academic groups.

AFFINImeter is currently a shareware software belonging to the last group, thus aiming at having special applications to different techniques. The AFFINImeter branch for ITC (AFF-ITC) is currently more complete than those for NMR and other spectroscopies (AFF-NMR and AFF-Spectroscopy) since the former includes the analysis of the raw data for ITC instruments commercialized by the main manufacturers. The raw data analysis for NMR measurements is externally performed by MNova (http://mestrelab.com/software/mnova/binding/), which works jointly with AFF-NMR. The analysis of raw data for other spectroscopies will be implemented in AFFINImeter in the future. Belonging to group (iii), the models, fitting engines and algorithms, as well as the treatment of uncertainties and local minima —the core of AFFINImeter— are common for AFF-ITC, AFF-NMR and AFF-Spectroscopy. In what follows, the main features of AFFINImeter are illustrated through their application to ITC data.

The main features of the AFFINImeter software are briefly described here. They are explained in detail in the following sections.

- Fully automated integration of the ITC raw data, including noise removal, baseline correction and calculation of the uncertainty for each data point of the equilibrium isotherm;
- Complete flexibility in the design of models for the thermodynamic analysis, defined by the user in a comprehensive and simple form. Examples of possible events/models are self-association, multi-site binding, competitive interactions, formation of ternary complexes (consisting of any stoichiometric combination of 3 different molecules) and coupling between several processes (*e.g.* self-association + 1:1 binding);
- Kinetic analysis using the kinITC method [9] applied to the ITC raw data corresponding to 1:1 and 1:n interactions. This method allows obtaining the rate constants (k_{on} and k_{off}) with no extra effort, using the same titration experiment data employed for the thermodynamic analysis;
- Fitting parameters that allow correction for the concentration of active (i.e. competent to form complexes) titrant (syringe) and titrate (calorimetric cell);
- No need to provide numerical starting values for the fitted parameters;

- Dynamic mathematical/logical relationships between parameters and also between their maximum/minimum boundaries. This is useful mainly when including hybrid models (see below) and also to prevent over-parameterization;
- Powerful analysis of local minima and final parameter uncertainties;
- Global analysis of several measurements, including direct + reverse experiments, repeats of the same experiment or multi-temperature experiments, by sharing fitting parameters when convenient;
- Powerful simulation tool using an unlimited number of models;
- Results supplied in detail, including species distribution plot. The automated report of the obtained results is generated in html and pdf formats. The values represented in each plot can also be downloaded in csv format for further treatment by the users. The plots can be downloaded in vectorial format to keep maximum resolution;
- In addition to standard user accounts, administrator accounts are also available to manage user accounts. Administrator accounts have access to the data of their associated users;
- Accessibility from any device with internet connection.

2.1. Treatment of raw data to obtain the equilibrium isotherm

The processing of the raw data to generate the equilibrium isotherm is a very important step in the analysis of the experimental data. AFF-NMR does not directly analyze the NMR raw data, but takes the equilibrium isotherm from the MNova Software [http://mestrelab.com/]. For AFF-Spectroscopy it is currently assumed that the raw data has been externally processed. In contrast, AFF-ITC uses the raw data from the most common ITC instruments (Malvern-MicroCal and TA Instruments) generating the equilibrium isotherm and the equilibration time curve (ETC) used to yield kinetic information from the ITC experiment (see section 2.8 for details). The basis of the raw data treatment and data management in AFF-ITC and kinITC has been reported in Refs. [10,11]. Here we describe only the relevant parts in data treatment that allow comprehension of the thermodynamic parameters' retrieval.

The raw data of a power-compensation ITC instrument consists of a two column file containing the power supplied to the sample cell to keep the temperature constant and the corresponding time. During a typical experiment, the power supplied signal changes due to small perturbations during baseline periods (stirring, small environmental temperature changes, etc.) and also due to the larger perturbation produced by the injection of small aliquots of the solution contained in the syringe into a solution located in the sample cell (injection-recovering period). After the system in the cell has returned to equilibrium, a stable baseline is recovered. Thus, the signal corresponding to the injection-recovering period is recorded as a power *vs* time peak. To perform the thermodynamic analysis, the peaks of a complete titration have to be integrated. For this, the software automatically generates a baseline for each injection, which is subtracted from the raw signal. These individual baselines are obtained by fitting a smooth function joining the first point of the signal injection −just before the perturbation begins− to the trend of the last part of the signal, i.e. excluding the perturbed region. The employed function for this fitting is a linear combination of orthogonal functions (Legendre polynomials of first, second and third order). Finally, the noise is reduced producing a corrected titration curve that can be directly visualized. The noise removal is based on analysis of local deviations to the signal trend. Several controls are available to the user in order to manipulate the level of noise to be removed as well as to choose the time period between peaks to be considered as baseline. Thereafter the peaks are integrated, generating the equilibrium isotherm, and the associated uncertainties per point, σ, are calculated. The process is fully automated by default, but the user can easily modify the integration limits. The integral of each peak represents the heat released or absorbed due to the events (binding for example) that take place in the sample cell as a result of each injection. This energy is normalized by the number of moles of the injected compound (or number of moles of reactant in the cell), leading to the molar enthalpy change. The corresponding uncertainty for each point in the isotherm is the sum of three contributions [10]: (i) that due to the signal's noise, determined as the product of its standard deviation in the baseline region times the duration of the signal perturbation upon injection; (ii) that emerging from possible outliers in the perturbed region, that is evaluated as the difference between the area obtained by numerical integration of the experimental peak and the area corresponding to the integration of a mathematical function fitted to the same data (the employed mathematical function is a truncated series expansion of peak functions, with the number of terms used being chosen by a F-test for statistical significance); and (iii) that arising from the dispersion of the points constituting the isotherm, estimated from the difference between the interpolation or extrapolation of first and second order polynomials to groups of sequential three and four points in the equilibrium isotherm. The software performs several rounds of interpolations and extrapolations taking the points from lower to higher titrant concentrations and in the opposite direction. The minimum difference between the experimental value and the extrapolated/interpolated point found among all these rounds is taken as a contribution to the final uncertainty. The calculation of this contribution is clearly described by Keller et al. [12]. Our implementation is an adaptation of the method described by these authors. The total uncertainty is determined as the square root of the sum of squares of all contributions. This allows assigning an uncertainty to every experimental point in the equilibrium isotherm. This is possible even for points where the signal abruptly changes, provided that the dispersion between the two regions (*i.e.* before and after the abrupt change) is small, as typically occurs for very strong interactions.

An example for the automatic treatment of ITC raw data is shown in Fig. 1. By default, the binding isotherm and the so called Equilibration Time Curve (the curve obtained by plotting the time required for each injection to recover the baseline vs the corresponding concentration ratio, see Fig. 1 and section 2.8) are analysed assuming a simple 1:1 interaction. An F-test is employed to decide if corrections due to the dilution of the titrant and/or to the concentration of active reactants are required. The analysis for a single experiment typically takes a few seconds and it is fully automated for the simplest interactions. A maximum of 10 experiments can be simultaneously uploaded and processed. This is useful to simultaneously process multi-temperature experiments where the software employs the van't Hoff and Eyring equations. If the interaction model is more complex, then the user can specifically design a reaction scheme using the model builder tool to analyze the experimental data (see Fig. 2 and this video: https://www.youtube.com/watch?v=dhfW-PQ-qVA).

2.2. The use of generalized equations to build interaction models

There is a wide variety of software available for the analysis of intermolecular interactions from data obtained with specific biophysical techniques/applications (*i.e.* Origin, Nanoanalyze and HypCa for ITC, Scrubber for SPR, Titan for NMR, and Sedphat for a number of techniques including AUC, ITC and DLS) as well as generic analysis software of binding curves (*i.e.* GraphPad, SigmaPlot and DynaFit). Generally, these computational programs can be classified as software that only offers a list of predefined models that are independently implemented, or as software that permits the implementation of new models. In the latter case, generation and validation of new models is not straightforward and requires a good knowledge of equilibrium thermodynamics, mathematics, and algorithms, and possibly also computational programming. Further, for some instruments it is necessary to be familiar with technical details that could affect the equations to be programmed. It is worth to mention that the validation of new models is not trivial mainly because typically no reference results are available. For these reasons, only experienced users are able to use these advanced tools to create models.

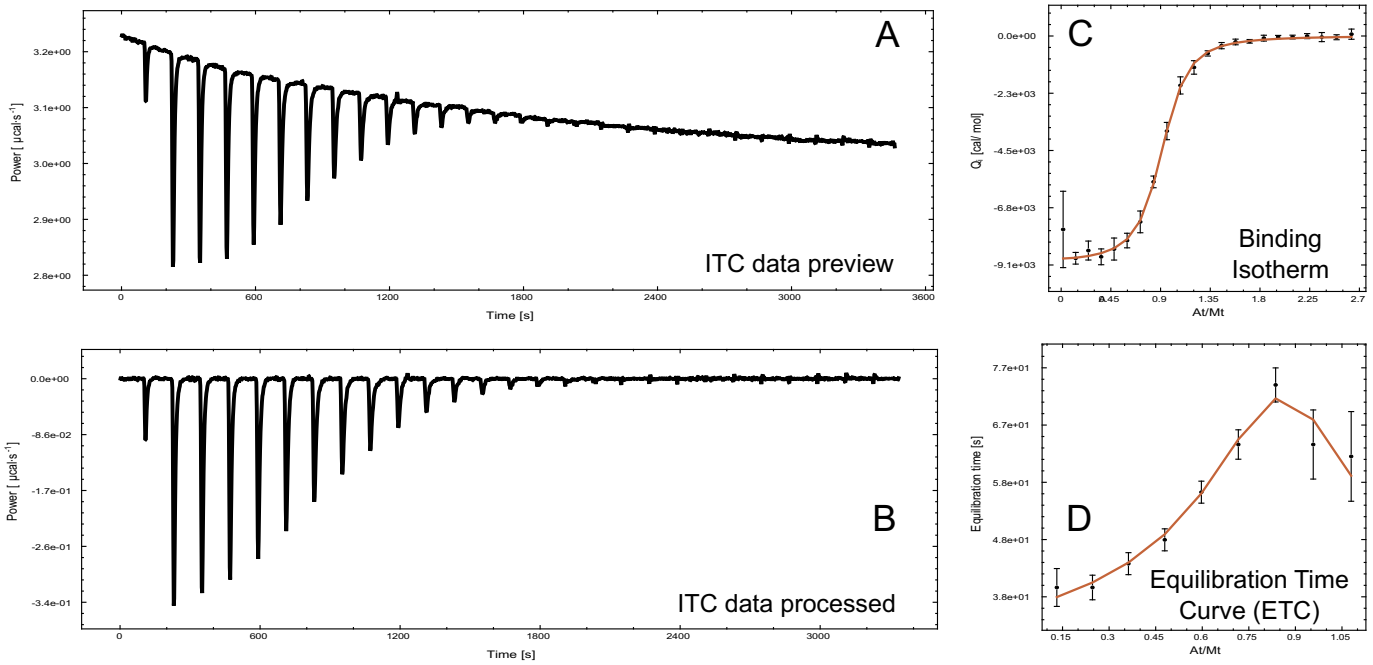


Fig. 1. Graphs automatically displayed in AFFINImeter-ITC upon raw data upload and processing. A) ITC data preview, which shows the raw thermogram; B) processed thermogram after baseline correction and noise removal; C) binding isotherm, resulting from the peak-by-peak integration of the processed thermogram as a function of At/Mt (titrant to titrate molar ratio) with the error bars determined as explained in the text; D) Equilibration time curve (ETC) resulting from the equilibration time for each injection as a function of the stoichiometric ratio At/Mt (the error bars of the ETC are determined using only the third contribution explained in the text and the time resolution of the experiment, typically 1 s). Solid red lines in C and D are the results of the fittings to a 1:1 binding model and to equation (8) in Ref. [11], respectively. (For interpretation of the references to colour in this figure legend, the reader is referred to the Web version of this article.)

AFFINImeter has solved these problems by adopting a different strategy –the use of generalized equations for the two main families of binding models, namely "stoichiometric equilibria" (SE) and "independent sites" (IS) models (see below). Since the equations are generalized, the amount of available models for each family is virtually unlimited. The validation is also much more simple and robust, since any error present in relatively simple models (easy to detect) should also be present in more complex models. Thus, the mathematical induction method can be employed to demonstrate the validity of non-trivial models (typically difficult and in many cases impossible mainly due to the lack of appropriate data) from the results obtained with simple ones. Predictions based on simulation of experiments upon variation of the different parameters can also be used to check for the consistency of the results. Note that AFFINImeter allows the simulation of experiments corresponding to any of these two model families.

The SE models are based on stoichiometric (or macroscopic) equilibrium constants and they are typically applied to low stoichiometry interactions where the different binding sites can be coupled to each other. The IS models are based on site-specific (or microscopic) equilibrium constants where the different binding sites do not interact with each other, although they can be grouped in sets where the sites have identical affinity and enthalpy of interaction with the involved species. The main features of the SE and IS models are summarized in Table 1, and both approaches are described in detail in the following sections. Standard available software for the study of intermolecular interactions includes just a few predefined SE models, as well as non-competitive IS models for one-set and two-sets of independent sites. This translates into a number of limitations, namely (i) competitive IS interactions are not implemented; (ii) no SE competitive models, other than for 1:1 interactions, are available; (iii) hybrid binding models such as coupled dissociation/binding and those that represent non-standard experiments (*e.g.* those where there is an "extra" compound or cosolute simultaneously present in both the syringe and cell in the ITC instrument) are missing; (iv) fitting parameters that account for potential deviations between nominal and true active concentration of the compounds participating in the binding event can only be considered for 1:1 interactions; and (v) the enthalpic contribution of the dilution of the titrant to the total signal in ITC instruments is not properly modelled (or not modelled at all), thus requiring complementary experiments in many cases. These five limitations have been surpassed in AFFINImeter, as described and discussed in what follows.

2.2.1. Nomenclature and experimental setups in ITC experiments

General binding models that involve the participation of 1, 2 or 3 different molecules have been implemented in AFFINImeter for both model families (SE and IS). In a standard ITC experiment there is a target molecule −typically a macromolecule located in the sample cell− to which one ligand candidate −initially located in the syringe at a higher concentration− can bind. However, several factors like the possible low solubility of the ligand or limitations in the amounts of the compound available, lead to exchange the reactants in the syringe and cell, performing the often called reverse experiment. From the thermodynamic point of view direct and reverse experiments are symmetrical, *i.e.* the thermodynamic equations and parameters describing the interaction between two molecules are the same, irrespective of the experiment's design. AFFINImeter denotes the main solute in the sample cell as M (as a reference to "macromolecule", the most typical setup) and the main solute in the syringe as A regardless the position of the reactants. A third compound participating in the interaction, B, may be present in both the sample cell and the syringe, only in the sample cell, or only in the syringe. Additionally, dilution experiments where only the compound A is initially located in the syringe and the sample cell is filled with the solvent can be convenient to test for any potential self-association/aggregation of compound A. Dilution experiments are also used to study the dissociation of protein oligomers, polymer aggregates or de-micellization. The ITC experimental setups that can be considered in AFF-ITC are depicted in Fig. 2.

2.2.2. Equilibrium constants – stoichiometric vs site models

SE models consider the equilibria between stoichiometric species

Table 1
Main features of Stoichiometric Equilibria and Independent Sites models as implemented in AFFINImeter. A detailed description of both types of models together with some examples are provided in sections 2.2.3 and 2.2.4.

Stoichiometric Equilibria models	Independent Sites models
Consist of a set of connected equilibria (reaction scheme) between stoichiometric species, written in chemical language. The stoichiometric equilibria can be established between free species (uncomplexed initial compounds) and a complex of defined stoichiometry or between two different complexes.	Consist of one or more sets of sites. Each set is characterized by a number of independent sites that are thermodynamically equivalent. Sites of the same set will bind the ligand with the same binding affinity and enthalpy change. Sites of different sets are not equivalent. All sites are independent to each other.
Allow the thermodynamic characterization of equilibria between stoichiometric species.	Allow the thermodynamic characterization of binding equilibria between the ligand and the receptor site(s) and defines the stoichiometry of the ligand-receptor complex.
Considers the possibility that binding of one ligand may influence the binding of other ligand(s), *i.e.* cooperative binding in multi-site binding events.	Assume that binding sites are independent, and therefore it is not applicable to the characterization of cooperative interactions.
Each equilibrium considered is characterized by the corresponding stoichiometric (or macroscopic) equilibrium constant and enthalpy change.	The binding sites are grouped in sets with identical site (or microscopic) equilibrium constant and enthalpy, thus allowing the interaction of a macromolecule with a large number of ligand molecules, without increasing the number of fitting parameters
Competitive ligands can be considered	Competitive ligands can be considered

regardless the location of the ligand in a specific site of the receptor, while IS models explicitly assumes binding of the ligand to specific sites. Therefore, the equilibrium constants in each model family have a different meaning, although they are in fact related.

Let's consider the interaction of a ligand (A) with a divalent macromolecule (M) as depicted in Fig. 3. Using the SE approach two stoichiometric species can be formed, M_1A_1 and M_1A_2, and the following stepwise chemical reactions can be written:

$$M + A \leftrightarrow M_1A_1$$
and
$$M_1A_1 + A \leftrightarrow M_1A_2 \quad (1)$$

with the corresponding stepwise stoichiometric equilibrium constants being:

$$K_{11} = [M_1A_1]/([M]\cdot[A])$$
and
$$K_{12} = [M_1A_2]/([M_1A_1]\cdot[A]) \quad (2)$$

where [M], [A], $[M_1A_1]$ and $[M_1A_2]$ denote the molar concentrations of free M and A species and of complexes of stoichiometry 1:1 and 1:2, respectively. K_{11} is the binding constant characterizing the formation of the complex M_1A_1 from the free species, regardless of the binding site, while K_{12} characterizes the formation of the complex M_1A_2 from M_1A_1

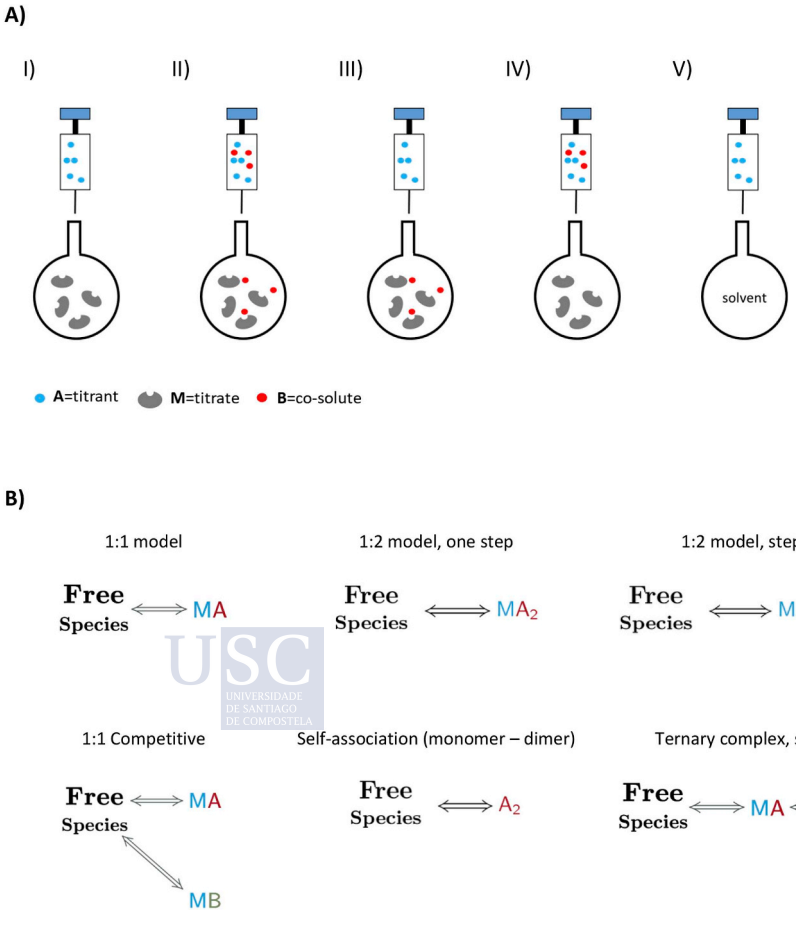


Fig. 2. A) Schematic representation of ITC experimental setups and nomenclature used in AFFINImeter showing: I) standard titration of A into M; titration of A into M in the presence of II) B in the cell and in the syringe; III) B mixed with M in the cell; IV) B mixed with A in the syringe; V) dilution experiment of A, in syringe, into solvent in the cell. B) A few illustrative examples of AFFINImeter binding models. Note that the possible presence of a co-solute (B) in the syringe, in the cell or in both locations significantly expands the variety of models that can be applied, including displacement experiments or the formation of relatively complex chemical species consisting of more than two molecules.

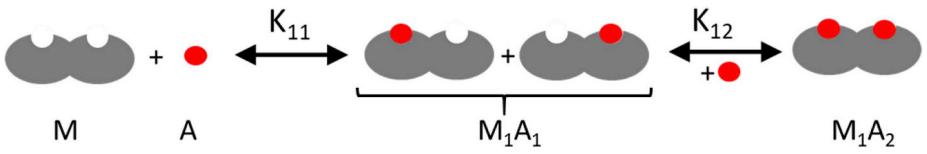


Fig. 3. Schematic diagram of binding equilibria based on stoichiometric constants, for the interaction between a bivalent receptor, M, with a monovalent ligand, A, is represented.

and a second A molecule.

The formation of the M_1A_2 complex can also be written as a single step process:

$$M + 2\,A \leftrightarrow M_1A_2 \quad (3)$$

leading to the **global** stoichiometric equilibrium constant:

$$\boldsymbol{\beta_{11}} = [M_1A_2]/([M]\cdot[A]^2) \quad (4)$$

The global and stepwise constants are related as $\boldsymbol{\beta_{11}} = K_{11}\cdot K_{12}$ and thus the units of the global and stepwise equilibrium constants are different. Note that the change in free energy for the formation of a given complex is determined as the natural logarithm of the product of the corresponding equilibrium constant by the ratio of standard state concentrations of reactants and products, raised to the appropriate powers. Thus, the argument of the logarithm is dimensionless, as required. The values of global and stepwise constants cannot be directly compared and differ, typically, by several orders of magnitude. AFFINImeter uses stepwise equilibrium constants and so they are always denoted by *K*, even though the equilibria consisting any model can skip specific stoichiometric species, i.e. the difference of the sum of the stoichiometric coefficients of a given chemical species upon a reaction can be higher than 1. For instance, for the reaction scheme $M + A \leftrightarrow M_1A_1 + 2\,A \leftrightarrow M_1A_3$ the complex M_1A_2 is not present and the difference between the stoichiometric coefficient of M_1A_1 and M_1A_3 is 2. The values of *K* for different orders of association cannot be directly compared. The best way to compare the weight of two reactions is to observe the species distribution plots (see below).

On the other hand, for the same system, i.e. for a monovalent ligand A binding to a divalent macromolecule M, the two involved sites can be considered to be distinguishable (see Fig. 4). The explicit consideration of specific binding sites involves the incorporation of four complexes and four equilibria into the model:

$$M + A \leftrightarrow M_{s1}A_1$$
$$M + A \leftrightarrow M_{s2}A_1$$
$$M_{s1}A_1 + A \leftrightarrow M_1A_2$$
$$M_{s2}A_1 + A \leftrightarrow M_1A_2$$

where $M_{s1}A_1$ is the 1:1 complex with site 1 occupied by A, while $M_{s2}A_1$ is the 1:1 complex with the site 2 occupied. This reaction scheme implies a larger number of parameters, as a different equilibrium constant is needed for each site:

$$K_{s1} = [M_{s1}A_1]/([M]\cdot[A])$$
and
$$K_{s2} = [M_{s2}A_1]/([M]\cdot[A]) \quad (5)$$

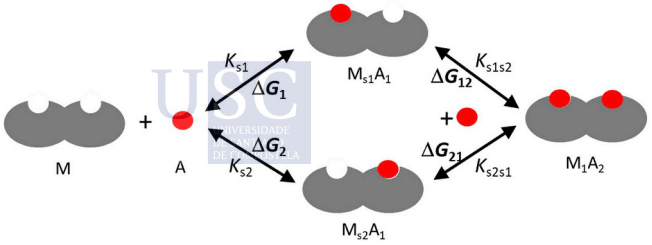


Fig. 4. Schematic diagram of binding equilibria based on site constants, for the interaction between a bivalent receptor, M, with a monovalent ligand, A. The site equilibrium constant and the change in Gibbs energy associated to each reaction is defined next to each arrow.

and two additional constants for the saturation of M, depending on which site was first occupied:

$$K_{s1s2} = [M_1A_2]/([M_{s1}A_1]\cdot[A])$$
and
$$K_{s2s1} = [M_1A_2]/([M_{s2}A_1]\cdot[A]) \quad (6)$$

Thus in this case we are dealing with the so called microscopic, or 'site specific' binding constants.

Since the stoichiometric species M_1A_1 in the SE model represents the sum of possible complexes of 1:1 stoichiometry formed between M and A, then $M_1A_1 = M_{s1}A_1 + M_{s2}A_1$. Therefore, the relationship between stoichiometric and site-specific equilibrium constants is:

$$K_{11} = K_{s1} + K_{s2}$$
and
$$K_{12} = (K_{s1s2}\cdot K_{s2s1})/(K_{s1s2} + K_{s2s1}) \quad (7)$$

From the above descriptions and definitions it is clear that site equilibrium constants are more informative than stoichiometric constants, but the number of site equilibrium constants is, in this particular case, twice that of stoichiometric constants. The problem is simplified by the fact that, in this case, the 1:2 complex is the same regardless the pathway employed to reach it, so the reactions represented in Fig. 4 are not independent: $\Delta G_1 + \Delta G_{12} = \Delta G_2 + \Delta G_{21}$. This introduces a connection between the constants given by equations (5) and (6): $K_{s1}/K_{s2} = K_{s2s1}/K_{s1s2}$. Anyway, for more complex interactions, of higher order stoichiometry, the number of required thermodynamic parameters would make the problem using site constants unapproachable. The situation can be simplified if:

$$K_{s2s1} = K_{s1}$$
and
$$K_{s1s2} = K_{s2} \quad (8)$$

This simplification means that the sites are considered independent from each other, *i.e.* binding of A to site 2 does not influence the binding of a second molecule of A to site 1, and vice-versa. The relationship between stoichiometric (macroscopic) and site-specific (microscopic) constants then becomes:

$$K_{11} = K_{s1} + K_{s2}$$
and
$$K_{12} = (K_{s1}\cdot K_{s2})/(K_{s1} + K_{s2}) \quad (9)$$

Furthermore, if sites are independent **and** equivalent, all site constants will be equal:

$$K_{s1} = K_{s2} = K_{s1s2} = K_{s2s1} \quad (10)$$

and then,

$$K_{11} = 2\cdot K_{s1}$$
and
$$K_{12} = K_{s1}/2 \quad (11)$$

Thus, finally we can write for the system under consideration

$$K_{12} = K_{11}\,/\,4 \quad (12)$$

An equivalent derivation of this equation can be found in Ref. [3]. It is worth to mention that equation (12) fulfils for a divalent interaction with two independent and equivalent sites. However, fulfilment of the previous equations does not necessarily imply that the interactions are divalent, since when dealing with an experimental data set arising from a different type of mechanism –perhaps even more complex than a

divalent interaction – the system might also be well described by those same equations. For example, apparently complex three-steps mechanisms can be described exactly by a trivial one-step mechanism. This is the case for a macromolecule exhibiting an equilibrium between two conformational states with different affinities and enthalpies for a given ligand. Such a composite mechanism requires one set of equilibrium constant and enthalpic terms for the interconversion step and two additional sets for the two association/dissociation steps. However, as far as thermodynamics is concerned, the same system can be rigorously described by a simple one-step mechanism with a single set of apparent equilibrium constant and enthalpy terms that can be expressed as functions of the original three sets of equilibrium constants and enthalpies [4].

2.2.3. Stoichiometric equilibrium (SE) models

Equations (1)–(4) can be generalized to describe the interaction between three molecules M, A and B, forming complexes of any stoichiometry. Since the reaction scheme leading to a complex of certain stoichiometry in terms of stepwise reactions is not unique, it is convenient to write the equations in terms of global equilibrium constants (it is worth to remind again that AFFINImeter uses stepwise constants and that the global and the stepwise equilibrium constants can be easily related):

$$m\cdot\mathrm{M} + a\cdot\mathrm{A} + b\cdot\mathrm{B} \leftrightarrow \mathrm{M}_m\mathrm{A}_a\mathrm{B}_b$$

and

$$\beta_{mab} = [\mathrm{M}_m\mathrm{A}_a\mathrm{B}_b]/([\mathrm{M}]^m\cdot[\mathrm{A}]^a\cdot[\mathrm{B}]^b) \tag{13}$$

Thus, if a particular observable X (e.g. molar enthalpy of complex formation) is sensitive to the presence of $\mathrm{M}_m\mathrm{A}_a\mathrm{B}_b$, the observed signal is the sum of population-weighted contributions of free and bound species, and the averaged signal contained in a volume V would be given by eq. (14). It is worth to note that some experimental observables require signal average based on different concentration units such as mole fraction (*e.g.* chemical shift) or mole fraction of total intensity (*e.g.* fluorescence anisotropy.

$$X = \sum_{s,j,k=0}^{m,a,b} X_{sjk}\cdot[M_sA_jB_k]\cdot V \tag{14}$$

where X_{sjk} is the molar contribution of $\mathrm{M}_s\mathrm{A}_j\mathrm{B}_k$ to the observable X and

$$[\mathrm{M}_s\mathrm{A}_j\mathrm{B}_k] = \boldsymbol{\beta}_{sjk}\cdot[\mathrm{M}]^s\cdot[\mathrm{A}]^j\cdot[\mathrm{B}]^k \tag{15}$$

where β_{sjk} is the global stoichiometric equilibrium constant corresponding to the formation of $\mathrm{M}_s\mathrm{A}_j\mathrm{B}_k$ and the total concentration of each compound ($[\mathrm{M}]_\mathrm{T}$, $[\mathrm{A}]_\mathrm{T}$ and $[\mathrm{B}]_\mathrm{T}$) is distributed between the existing free and complexed forms:

$$[\mathrm{M}]_\mathrm{T} = \sum_{s,j,k=0}^{m,a,b} s\cdot[M_sA_jB_k] \tag{16}$$

$$[\mathrm{A}]_\mathrm{T} = \sum_{s,j,k=0}^{m,a,b} j\cdot[M_sA_jB_k] \tag{17}$$

$$[\mathrm{B}]_\mathrm{T} = \sum_{s,j,k=0}^{m,a,b} k\cdot[M_sA_jB_k] \tag{18}$$

where the factors s, j and k in equations (16)–(18) account for the number of M, A and B molecules within each $\mathrm{M}_s\mathrm{A}_j\mathrm{B}_k$ complex, respectively. Note that Equations (16)–(18) include in the sums the possibility of self-association of a single compound (M_s, A_j, or B_k), as well as the formation of various combinations of hetero-complexes formed by two compounds ($\mathrm{M}_s\mathrm{A}_j$, $\mathrm{A}_j\mathrm{B}_k$ or $\mathrm{M}_s\mathrm{B}_k$).

Equations (14)–(18) include two parameters for each chemical species: X_{sjk} and $\boldsymbol{\beta}_{sjk}$. The values for those parameters can be numerically obtained by fitting equation (14) to the experimental data, *i.e.* to the observable X as a function of the total concentration of the involved compounds. For each set of $\{X_{sjk}, \boldsymbol{\beta}_{sjk}\}$ values used during the iterative fitting procedure, the concentration of the different chemical species can also be numerically determined using equations 16–18, provided that the total concentration of the three compounds is known. For the final values of $\{X_{sjk}, \boldsymbol{\beta}_{sjk}\}$, the concentration of each complex, as well as its contribution to the averaged signal, can be determined for every concentration of the three compounds. These equations can be directly used to obtain stoichiometric equilibrium constants from the analysis of binding curves obtained by NMR titrations and general spectrometric measurements (available in AFF-NMR and AFF-Spectroscopy). For ITC their use is not straightforward when the experiments are performed in instruments of the "filled type" (i.e., Malvern MicroCal or TA instruments) as (i) due to instrument's design, upon each injection an equivalent volume of solution is expelled from the effective cell volume, implying that the concentration of the compounds in the cell is changed after each injection in a way in which calculation might depends on various assumptions; (ii) the measured heat does not correspond to a specific concentration, but rather to the heat absorbed or delivered during the concentration change, *i.e.* the shape of the equilibrium isotherm may depend on the volume and speed of the injections, as well as on stirring speed; and (iii) the total signal may contain the contributions of the heat of dilution, mainly those of the injected compounds. Thus, for filled type ITCs it is necessary to consider the calculation of the concentration change in the cell after each injection, as well as the corresponding corrections to the detected heat. Additionally, the contribution of the dilution effect to the signal should be subtracted. This last effect can be done after the experiment if separate dilution experiments are performed, or can be included in the equations if modelled. Both options can be applied with AFFINImeter, although the last one is usually more practical and no less accurate. Including all the above mentioned terms, the final equation used in AFFINImeter for the analysis of ITC data under the stoichiometric equilibrium scheme is:

$$\Delta Q_\mathrm{i} = \{-Q_{\mathrm{syr,i}} + (Q_{\mathrm{i}+1} - Q_\mathrm{i}) + Q_{\mathrm{corr,i}} + \Delta H_{\mathrm{dil}}\cdot([\mathrm{A}_{\mathrm{syr}}] - [\mathrm{A}]_{\mathrm{T,i}}) + Q_{\mathrm{db}}\} / ([\mathrm{A}_{\mathrm{syr}}]\cdot v_{\mathrm{inj,i}}) \tag{19}$$

where ΔQ_i is the heat absorbed or delivered per mole of A added during the injection i. Note that the presence of M and B in any experiment is optional (see Fig. 2), but it is compulsory that compound A be present at some concentration in the syringe. $Q_{\mathrm{syr,i}}$ is the total heat required to form all chemical species present in the injected volume ($v_{\mathrm{inj,i}}$):

$$Q_{\mathrm{syr,i}} = \sum_{s,j,k=0}^{m,a,b} \Delta H_{sjk}\cdot[M_sA_jB_k]\cdot v_{inj,i} \tag{20}$$

with ΔH_{sjk} being the molar enthalpy change corresponding to the formation of the complex $M_sA_jB_k$ from the free species (equivalent to X_{sjk} in eq. (14)). Similarly, Q_i is the total heat required to form all chemical species present in the cell, and is given by:

$$Q_\mathrm{i} = \sum_{s,j,k=0}^{m,a,b} \Delta H_{sjk}\cdot[M_sA_jB_k]_i\cdot V_i \tag{21}$$

One should note that whereas for $Q_{\mathrm{syr,i}}$ the concentration of each chemical species does not depend on the injection since the concentration of the syringe is constant, in the case of Q_i the concentration of the complexes depends on the total concentration of each species in the cell, so it is expected to be different for each injection. In eq. (21) the index i was included for the total volume of the solution in the cell (V_i), although for Malvern MicroCal or TA ITC instruments it is a constant. In equation (19), $Q_{\mathrm{corr,i}}$ is the heat contribution associated with the sample that is displaced (removed from the section of cell where the sensors are located) during the injection. Since the concentration changes after each injection, and the contributions Q_{syr} and Q_i are calculated using the concentrations in the cell after i and i+1 injections, $Q_{\mathrm{corr,i}}$ is taken as the average between the heat delivered or absorbed corresponding to a volume $v_{\mathrm{inj,i}}$ that leaves the cell upon

injection:

$$Q_{corr,i} = [(Q_i + Q_{i+1}) / 2] \cdot v_{inj,i} / V_i \quad (22)$$

In contrast to other software for the analysis of ITC measurements, in AFFINImeter the dilution contribution is calculated as the product of the dilution molar enthalpy (ΔH_{dil}) and the difference between the concentration of A in the syringe [A_{syr}] and that in the sample cell after each injection $[A]_{T,i}$ (see eq. (19)). As expected, this term is maximum for the first injection and decreases as the concentration of A in the cell approaches that in the syringe. Finally, in Equation (19) there is an additional term (Q_{db}) that represents a constant correction for a potential baseline shift, generally due to external (not specific for the studied system) physical phenomena such as mechanical mixing of two fluid samples, temperature equilibration due to temperature gradient along the injection syringe, composition mismatches between syringe and cell solutions, electrical noise or temperature fluctuations, both in the room where the instrument is located, etc.

In summary, the generalization of the stoichiometric equilibrium equations as implemented in AFFINImeter allows an easy application of many models to the experimental ITC data, involving a maximum of three different compounds. Although in AFFINImeter all the stoichiometric equilibrium constants are considered as stepwise (and hence denoted as *K*), global stoichiometric binding constants can also be used provided all the reactions introduced by the user in the model builder (https://www.youtube.com/watch?v=dhfW-PQ-qVA) use the free species as unique reactants to form all the involved complexes. As stated at the beginning of this section, we only indicated here the equations corresponding to the global equilibrium constants because the equations based on stepwise constants depend on the specific reaction scheme or reaction pathway chosen for the studied system. However, these equations are easy to derive from the above given expressions (see previous section). The sequential equilibrium models implemented in AFFINImeter have been employed in a number of studies including proteins, DNA and other heterogeneous systems [13–17].

2.2.4. Implementation of independent sites (IS) models

General site equilibrium constants were introduced in section 2.2.2. It was shown that when the sites are independent and equivalent, all the site equilibrium constants are identical. This is a useful model for the study of many multivalent interactions where these conditions are fulfilled. In this model, the equilibrium constant and the enthalpy change for the interaction can be obtained for each site, together with the number of binding sites, considered a fitting parameter. One-set-of-independent-sites and two-sets-of-independent-sites models are available in several programs for the analysis of ITC data. In these models, all binding sites within each set are independent and equivalent to each other. The sites of different sets are also independent, but they have different affinity and enthalpy of interaction. To our knowledge, the equations for competitive IS models, *i.e.* considering two competitive ligands for each site, are not publicly available yet. AFFINImeter implemented the generalization of IS models for multiple sets of independent and equivalent sites for each set, with two possible ligands (A and B) competing with different affinity and enthalpy of interaction for all the sites. Some publications taking advantage of these functionalities have been recently reviewed in Ref. [18]. The equations of this general model are described next. From a kinetic point of view:

$$v_a^{A_s} = k_a^{A_s}(n_s - \langle A\rangle_s - \langle B\rangle_s)\cdot[A]$$
and
$$v_d^{A_s} = k_d^{A_s}\langle A\rangle_s \quad (23)$$

where $v_a^{A_s}$ and $v_d^{A_s}$ are the rate of association and dissociation of the molecule A to the set s of a given macromolecule M, $k_a^{A_s}$ and $k_d^{A_s}$ are the kinetic constants for the same process, n_s is the total number of sites for the considered set, $\langle A\rangle_s$ and $\langle B\rangle_s$ are the average number of A and B molecules per mol of M in the set s, and [A] is the concentration of free A in the solution. Under equilibrium conditions the rates of adsorption and desorption match:

$$k_a^{A_s}(n_s - \langle A\rangle_s - \langle B\rangle_s)\cdot[A] = k_d^{A_s}\langle A\rangle_s \quad (24)$$

thus,

$$K_{A_s}\cdot[A] = \theta_{A_s}/(1 - \theta_{A_s} - \theta_{B_s}) \quad (25)$$

where the microscopic equilibrium constant for the binding of A to any site of the set s in M is defined as $K_{A_s} = k_a^{A_s} / k_d^{A_s}$ and the fraction of occupied sites are defined by $\theta_{A_s} = \langle A\rangle_s / n_s$ and $\theta_{B_s} = \langle B\rangle_s / n_s$. The same equations can be written for B:

$$k_a^{B_s}(n_s - \langle A\rangle_s - \langle B\rangle_s)\cdot[B] = k_d^{B_s}\langle B\rangle_s \quad (26)$$

$$K_{B_s}\cdot[B] = \theta_{B_s}/(1 - \theta_{A_s} - \theta_{B_s}) \quad (27)$$

Combining eqs (23) and (25) and solving for θ_{A_s} and θ_{B_s}:

$$\theta_{A_s} = K_{A_s}\cdot[A] / (1 + K_{A_s}\cdot[A] + K_{B_s}\cdot[B]) \quad (28)$$

$$\theta_{B_s} = K_{B_s}\cdot[B] / (1 + K_{A_s}\cdot[A] + K_{B_s}\cdot[B]) \quad (29)$$

Considering that the sites are completely independent regardless of whether they belong to the same or to different sets. They do compete with each other to capture the molecules of the ligands A and B. The total concentration of each compound is distributed between the different sets as:

$$[M]_T = [M] + [M]_T \sum_s n_s\cdot(\theta_{A_s} + \theta_{B_s}) \quad (30)$$

$$[A]_T = [A] + [M]_T \sum_s n_s\cdot\theta_{A_s} \quad (31)$$

$$[B]_T = [B] + [M]_T \sum_s n_s\cdot\theta_{B_s} \quad (32)$$

Note that, in contrast to the stoichiometric equilibrium scheme, the equations for M are different from those for A and B. This is because the sites are assumed to be located in M and the model is not symmetrical in this sense. Thus, the application of this model using AFFINImeter requires the presence of at least a macromolecule M in the sample cell and a ligand A in the syringe.

Again, the model can be applied to any property that is sensitive to the fraction of occupied sites for the different sets. For the specific case of ITC, the equation equivalent to eq. (19) in this interaction scheme is:

$$\Delta Q_i = \{(Q_{i+1} - Q_i) + \Delta Q_{corr,i} + \Delta H_{dil}\cdot([A_{syr}] - [A]_{T,i}) + Q_{db}\} / ([A_{syr}]\cdot v_{inj,i}) \quad (33)$$

The term $Q_{syr,i}$ was removed since in its current version for this model the macromolecule M cannot be in the syringe and the model does not consider the possibility of binding between A and B or their self-association. All the terms in equation (33) are identical to those in eq. (19) except Q_i and Q_{i+1}, which are given by:

$$Q_i = [M]_{T,i}\ V_i \left\{\sum_s n_s\cdot\left[(\theta_{A_s})_i\cdot\Delta H_{A_s} + (\theta_{B_s})_i\cdot\Delta H_{B_s}\right]\right\} \quad (34)$$

This model is well suited mainly for the study of molecular interactions with macromolecules with multiple binding sites under the assumption that they are independent to each other. Notably, with our implementation, it is possible to study competitive binding in this kind of systems, and to consider also multiple sets of binding sites. Actually, an IS model is defined by the number of sets available for binding. For each new set there are, in principle, three new parameters (the number of sites, the site equilibrium constant and the associated enthalpy). As in the case of stoichiometric equilibrium models, the dilution enthalpy and Q_{db} could also be globally fitted. Some examples of the application

of the IS family of models using AFFINImeter can be found in Refs. [19–21].

2.2.5. Concentration correction

The determination of equilibrium constants is based on the concentrations of the different chemical species present in the sample. Such concentrations are calculated from the nominal concentrations of the participating compounds. Mismatch between nominal and true active concentrations (due to *i.e.* chemical degradation, aggregation or conformational changes that prevent the binding of a fraction of the reactant present) have a serious impact in the results. In order to quantitatively consider these events, we have introduced a correction factor for each compound: r_M, r_A and r_B; that are equivalent to the ratio between active concentration and nominal concentration of M, A or B, respectively. The introduction in the equations is simple since the concentration of each compound is replaced by its product with the corresponding factor. The only additional consideration is the determination of ΔQ_i when r_A is different from unity. By convention, ΔQ_i is the heat absorbed or delivered per mole of A added during the injection i. The values of the experimental binding isotherm are calculated using the concentration of nominal A, without any correction. Accordingly, the value of A_{syr} in the denominator of equations 19 and 33 is not corrected, allowing the comparison between the fitted and the experimental values.

Thus equations (19) and (33) corresponding to the SE and IS models, respectively, became:

$$\Delta Q_i = \{ -Q_{syr,i} + (Q_{i+1} - Q_i) + Q_{corr,i} + \Delta H_{dil}\cdot([A_{syr}] - [A]_{T,i}) + Q_{db}\} / ([A_{syr}]^{nominal}\cdot v_{inj,i}) \quad (35)$$

$$\Delta Q_i = \{(Q_{i+1} - Q_i) + \Delta Q_{corr,i} + \Delta H_{dil}\cdot([A_{syr}] - [A_T]_i) + Q_{db}\} / ([A_{syr}]^{nominal}\cdot v_{inj,i}) \quad (36)$$

were $[A_{syr}]^{nominal}$ is the nominal, non-corrected concentration of A.

2.2.6. Non-fitted parameters and hybrid SE/IS models

In the previous sections, we have described in detail how the SE and the IS models are implemented in AFFINImeter. For SE models we have 2 fitting parameters for each chemical reaction while for IS models there are 3 additional fitting parameters *per* set of sites. Additionally the ΔH_{dil}, Q_{db} and the r_M, r_A and r_B values can be fitted for each equilibrium isotherm. Often, it is convenient to keep constant some of these parameters, to avoid overparameterization while enough degrees of freedom in the fitting should be taken to make it valuable. For instance, if the concentrations are well known, the three correction factors introduced for this aim must be set to 1 and not allowed to vary. It is also experimentally found that in most cases, the "external" heat contributions considered by Q_{db} can be dismissed, and sometimes the ΔH_{dil} is not significant and can be neglected. This can be easily tested by performing the fitting allowing their variation or keeping them fixed. Additionally, the value of any other parameter might be known from other experimental or theoretical source, and thus be introduced as a fixed parameter. On the other hand, AFFINImeter allows mathematical and logical relationships between parameters. This is a powerful functionality for parameters that we wish to restraint as a combination of values of other parameters, *i.e.* they are not fitted nor kept constants but dynamically changed during the iterative minimization. This kind of dynamical restrictions can also be set for the upper and lower bounds of parameters that are fitted. By using such relationships it is possible to introduce hybrid models in AFFINImeter, i.e. models that combine independent and stoichiometric binding sites. For instance, we could have a macromolecule with four binding sites where only two of them are independent and equivalent. If the non-independent sites cannot be occupied before the saturation of the independent ones, we could use a SE model with only two parameters for the first two sites, by using eq. (12) to connect the stepwise stoichiometric binding constants and matching the enthalpies for the first two reactions. The dynamical relationships between fitting parameters can be employed to introduce a large variety of restrictions that minimize the number of fitting parameters. Such functionality is usually employed when specific experimental information is available to connect the parameters on a rational basis. Another application would be the fitting of data corresponding to the same system at different temperatures, by using the van't Hoff equation to connect the equilibrium constants (see section 3).

2.3. Minimization procedure

For ITC data, the fitting parameters for each model are numerically determined by minimizing the objective function:

$$\chi^2 = \frac{1}{p}\sum_{1}^{p}\frac{(\Delta Q_i^{exp} - \Delta Q_i)^2}{\sigma_i^2} \quad (37)$$

where p is the total number of points, (ΔQ_i^{exp}) the values of the experimental equilibrium isotherm, ΔQ_i is given by eq (19) or (33) (depending on the model), and σ_i is the uncertainty of each point (see Ref. [10] and section 2.1.). In order to optimize the quality and the speed of convergence, the Simulated Annealing and Levenberg-Marquardt algorithms are sequentially used [22]. In addition, for each combination of proposed fitting parameters during the iterative process, a damped Newton-Raphson algorithm using the Armijo rule [23] was employed to obtain the concentration of free M, A and B compounds from equations (16)–(18) or (30)–(32). This latter calculation is individually performed for every point in the equilibrium isotherm, although global controls, such as backpropagation fittings based on the homogeneous increasing/decreasing of the free concentrations as the total concentration of M, A and B change, were introduced in the code to guarantee the consistency of the results.

From eq. (37) it is clear that the lower the χ^2 value the better the fitting. Ideally, for a combination of reasonably good experimental measurements, fair estimation of uncertainties, and right selection of the interaction model, the χ^2 value should approach the unity, which means that the differences between the ΔQ_i^{exp} and the ΔQ_i are essentially accounted for by the uncertainties σ_i. Actually, the estimation of the uncertainties is not a trivial task. Thus, good fittings with χ^2 significantly larger than 1 are expected if the σ values are unrealistically low and vice versa (equation (37)). Although in general the uncertainties in AFFINImeter seem to be fairly determined, we have detected some trend towards underestimated uncertainty values for each individual titration point (used as weighting factors in equation (37)).

In theory, if the uncertainties are well estimated, the χ^2 distribution gives us the probability of obtaining a value of the χ^2 above, or below, some threshold. However, in practice, the value of χ^2 may be difficult to translate into an informative measure of the quality of the fitting that guides the user in the selection of the right model to analyze the data. In general, χ^2 values around unity correspond to good fittings, but the absolute value of this parameter depends too much on the uncertainties of the points and its value is not bounded, so it is difficult to say whether or not a value of χ^2 around 5, 10 or 20 is acceptable. So we have implemented a Goodness of Fit (GoF) estimation, defined as the probability of finding the fitted value of each experimental point within a normal distribution with half-width equal to the corresponding uncertainty. This parameter is basically a normalization of χ^2 expressed in percentage units. The GoF of a given curve is determined as the mean GoF of all its points. Ideally, the GoF value of a perfect fit would be 100%. The advantage of this descriptor is that it is bounded between 0 and 100, so it is easy to interpret. Nevertheless, one should not forget that it still depends too much on the uncertainties of the experimental points. Improvements of this parameter to solve this problem are expected to be included in AFFINImeter in the future.

2.4. Seeds and local minima

Non-trivial models may have a large number of fitting parameters, increasing the probability of reaching and being stuck at local minima. In order to identify the presence of such results, we have implemented the possibility of repeating the fittings starting from different seeds/initial values for the parameters. By default, 20 different independent minimizations are performed using 20 different sets of random seeds. The number of independent sets can be changed by the user. Unless the user modifies the default options, the seeds are always randomly chosen between the lower and upper bounds allowed for each fitting parameter. By default, constant values are provided for such bounds ([1, 10^8] M^{-1} for the equilibrium constants and [-10^5, 10^5] J/mol for the enthalpies). The results for each independent fitting are shown at the bottom of the results' window, and they can be downloaded in csv format for further treatment. Several minima with low χ^2 values different from each other likely indicate that the model is overparameterized. Ideally, all the minimizations should converge to the same result regardless of the employed initial value, but in some cases local minima can be identified. This can be used as a consistency test. A fitting where the lowest χ^2 only appears once is an evidence of convergence problems. When this happens, the number of independent minimizations should be increased. A maximum of 1000 repeats is allowed in AFFINImeter. Obviously, the larger the number of repeats, the longer the time taken to achieve the results.

2.5. Uncertainties

Uncertainties are part of the results in any quantitative scientific experiment. We have made an effort to provide reliable estimation of uncertainties for the fitting parameters by determining them in two different ways, named in AFFINImeter as standard and statistical errors. The standard errors are determined as the square root of the diagonal elements of the variance-covariance matrix, obtained as the inverse of the Hessian matrix (the matrix of the second partial derivatives $\partial^2\chi^2/\partial p_i \partial p_j$ of the objective function with respect to the fitting parameters). These uncertainties are determined on the flight, since the Hessian matrix is already required for the Levenberg-Marquardt method used for the minimization; therefore no expensive extra calculations are required. Since our implementation of the models is fully general, as described in the previous sections, we do not use explicit analytical derivatives and the elements of the Hessian matrix are numerically obtained. The uncertainties determined in this way are less reliable than those obtained from analytical derivatives. Thus, we decided to implement a non-parametric bootstrap method to obtain what we call in AFFINImeter statistical errors: the Jackknife resampling method [24,25]. These uncertainties are more reliable, since they are determined from the standard deviations of the parameters obtained by repeating the fitting as many times as experimental points are available in the target experiment, each time ignoring one point in these extra fittings. For instance, in an equilibrium isotherm consisting of 30 points, all of them are employed in the main minimization process. The resulting parameters are used as seeds for 30 independent fittings (of 29 points each) where the data points are sequentially removed, one at a time. In this case, AFFINImeter gets 30 independent solutions for each parameter (in addition to the one provided by the main fitting). Then, the standard deviation for each parameter, using the values obtained in these 30 independent fittings, is obtained and taken as "statistical uncertainty". The removal of the points with a high weight in the fittings induces a significant change in the parameters and so increases the standard deviations. By default, the statistical uncertainties are activated in AFFINImeter, but the user can also access to the standard errors by clicking on the corresponding option.

2.6. Global analysis

In the previous sections we have described how AFFINImeter works to fit the parameters of a model to the molar enthalpies obtained from an ITC experiment. Note that a single experiment in any technique is rarely conclusive. One always needs to perform several repeats of the same assay and to fit all the results either together or individually using the same or complementary models. AFFINImeter allows global fitting of multiple experiments for this aim.

Further, in cases of competitive binding studies of two different ligands A and B to a given macromolecule M, several experiments can be designed to study the interactions between these molecules: the titration of A or B separately into a solution of M, the titration of both A and B together into the same solution, the titration of A into a solution of M + B, and the titration of B into a solution of M + A. Additionally this can be done at different concentrations of each compound. AFFINImeter allows analyzing all these experiments together, by optionally sharing the fitting parameters. Other example is the case where the same system is studied at several temperatures. In that case, the equilibrium constants can be connected to each other by using the van't Hoff equation and the enthalpies can also be restrained by assuming a linear or quadratic dependence involving the heat capacity change upon binding (see section 3). Similar situations can be proposed for many other interactions. The results obtained in this way are expected to be much more robust than fitting individual experiments separately.

2.7. Fitting results, simulation tool and report

In the previous sections we have explained how the SE and IS models have been implemented in AFFINImeter, including parameters to consider the ratio or percentage of active compounds in the solution, corrections for volume displacement, external contributions to the heat signal, and dilution of the injected compound. Those equations can be used to fit experiments as well as to perform simulations. The simulations are useful in order to design experiments −if the user has an estimation of the expected parameters−, to understand the sensitivity of the isotherm to the different parameters, and also to understand better the interaction mechanisms. As explained above, the evaluation of equations (19) and (33) require the determination of the concentration of free species, as well as the concentration of every complex present in the solution (or fraction of occupied sites in the case of IS models). This allows determining the contribution of each chemical species to the total molar heat. The combination of the three plots (total molar heat, species distribution, and different contributions to the total signal, together with the value of the model parameters) indicate which stoichiometry or binding site dominates at specific concentration ranges, and it is useful both for optimizing new experiments and to understand complex interaction mechanisms. An example is shown in Fig. 5. All this information is provided in csv (numerical data for further external treatment), html or pdf formats, and can be freely shared by e-mail from the AFFINImeter software.

2.8. The evaluation of kinetic constants using kinITC

ITC raw data have intrinsically kinetic information, as they are heat power as a function of time. Traditionally, the perturbations in this signal caused by the injection of small aliquots of one titrant solution into a titrate solution are integrated thus leading to an energy (heat) profile as a function of the stoichiometric ratio. Such processed data can be employed for the application of thermodynamic models, thus contributing to elucidate interaction mechanisms as well as the entropic and enthalpic contributions to the Gibbs energy change corresponding to the formation of the different chemical species. This classical treatment, however, results in the loss of useful kinetic information. Although the possibility of obtaining kinetic information from ITC experiments has long been known, strangely it was not at all used in

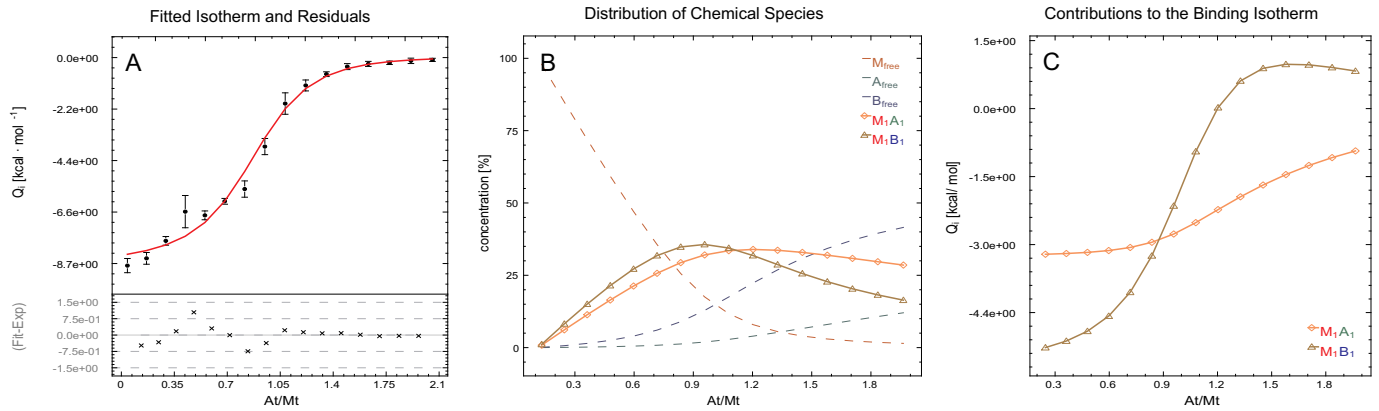


Fig. 5. Example of plots generated in AFFINImeter after data analysis. A) Binding isotherm and fitting result; B) Species distribution plot; C) Contribution of complexes formation to the overall signal. In this example the data analyszed were for a titration where a receptor M is titrated with a mixture of ligands in syringe (A + B). The competitive model MA ⇔ FS ⇔ MB was used.

biology and even considered as impossible by many users. A few years ago, the ITC community was re-awakened to this possibility [8] the method was named kinITC. A simplification of this method that considers the variation of the time of return to equilibrium at each injection [26] has been implemented into AFFINImeter [9]. It is worth mentioning that ordinary titration data with reasonable values of the Wiseman parameter are often amenable to this analysis. Thus, even old ITC data can be directly reanalysed to extract potential kinetic information. In a recent review, a compilation of kinITC studies using AFFINImeter has been summarized [18]. Also a paper was recently published by Zihlmann et al. [27], who retrieved the kinetic constants of 29 mannosides binding to the bacterial adhesion FimH using the kinITC method implemented in AFFINImeter and performed a thoughtful validation of results with SPR data. The kinITC method provides results that are in excellent agreement with those obtained by SPR for a wide range of Kd values.

2.9. Accessibility and management of lab projects

The default version of AFFINImeter is a cloud software with user accounts protected by password. This means that it can be accessed from the web browser of any device with internet connection. The calculations required to fit experimental data often require a significant computational cost that is performed using the AFFINImeter servers. Local installations of AFFINImeter are also available upon request. Once the user access to his/her account, all the past projects are available and they can be read or edited. They can also be organized in folders and the results of complete fitting or simulation projects can be shared with other people by introducing the corresponding e-mail address.

3. Example of how to use AFFINImeter to analyze complex interactions with multiple ITC measurements

Although AFFINImeter has been made public recently, many research groups from academia, research institutes and pharmaceutical companies have already benefited from the advanced tools of analysis that the software offers. Indeed, a number of research papers have been published that manifest the value of AFFINImeter for the robust thermodynamic and kinetic analysis of ITC data. Referencing all these works is out of the scope of this paper but a rather comprehensive review is provided in a recent literature review article [18]. A book chapter has also been recently published with a detailed analysis on a number of heparin derivatives [29]. As illustrative examples we would like to highlight the work performed by Shiu-Hin Chan et al. [17] and the work performed by Marques-Carvalho et al. [28] where advanced stoichiometric models were used in the thermodynamic and mechanistic characterization of complex interactions. Besides, the excellent work performed by Zihlmann et al. focused on testing the reliability of KinITC-ETC to retrieve kinetic information [27].

In this section we will show that AFFINImeter is well suited to analyze complex intermolecular mechanisms, without the need of developing and validating new code, thus saving time and effort. To this end, we show now a global multitemperature analysis –using the van't Hoff equation to connect the equilibrium constants and the change in heat capacity to linearly constrain the corresponding enthalpies at different temperatures– for a set of measurements of a system exhibiting cooperative 1:2 interactions (a similar analysis has been published in Ref. [8]). First we provide a description of the system, which is required to understand the interaction mechanism, and then the analysis method using AFFINImeter is explained in detail. Finally, the obtained results following such methodology are shown.

3.1. Description of the system and analysis performed in the literature

NQO1 NAD(P)H (NADH, nicotinamide adenine dinucleotide) quinone dehydrogenase 1 (EC 1.6.5.2) is a cytosolic FAD-binding (FAD, flavin adenine dinucleotide) homodimeric protein responsible for the two-electron reduction of quinones to hydroquinones, with preference for short-chain acceptor quinones, thus preventing the one-electron reduction of radical species, intervening in detoxification processes and activation of antitumor quinone-related prodrugs [30]. NQO1 stabilizes and protects tumor suppressor p53 from degradation. Thus, decreased expression of NQO1 is associated with decreased p53 stability, as well as chemoresistance stemming from diminished prodrug bioactivation [30]. P187S is a widespread polymorphism in NQO1 associated with different types of cancer and low efficacy of anticancer drugs. P187S causes lowered structural stability and activity. NQO1-FAD is an excellent biological system to study 1:2 protein:ligand interaction: 1) NQO1 is able to bind two FAD molecules per dimer; 2) the binding of the two FAD molecules is cooperative (homotropic interaction); 3) FAD binding and FAD homotropy are highly temperature dependent; and 4) mutations or polymorphisms in NQO1, in particular P187S associated with cancer susceptibility, result in considerable distortion of the cooperativity of binding. Therefore, NQO1-FAD interaction is an appropriate system to perform a global analysis of calorimetric titrations conducted at different temperatures applying a 1:2 model with homotropic binding cooperativity and variable temperature (considering the extended van't Hoff equation with non-zero binding heat capacity) in order to estimate the intrinsic FAD binding parameters and the cooperative FAD binding parameters. At particular temperatures each variant (wild-type and P187S NQO1) shows an apparent non-

cooperative binding behaviour (because of the temperature-dependency of the cooperativity binding parameters); therefore, in biological systems with stoichiometry higher than 1 it is always advisable to perform titrations at different temperatures in order to confirm whether or not the binding is cooperative. It was hypothesized that the apparent binding cooperativity features observed in NQO1-FAD titrations were in fact the manifestation of a significant percentage of aggregated protein in the calorimetric cell, and, consequently, reverse titrations (FAD in cell and NQO1 in syringe) were more appropriate. However, it was later demonstrated that there is true binding cooperativity in NQO1-FAD interaction, that NQO1 potential aggregation has no influence on the titration features (different from reducing the fraction of active binding-competent protein), and that direct and reverse titrations provided a common set of estimated intrinsic and cooperative parameters [30] applying the same 1:2 model with binding cooperativity.

3.2. Analysis with AFFINImeter

The calorimetric titrations for FAD binding to wild-type and P187S NQO1 were reanalysed using AFFINImeter. We used the model builder tool (https://www.youtube.com/watch?v=dhfW-PQ-qVA) to apply the model described in the original reference [30] (Fig. 6).

The binding constants corresponding to the formation of the complexes with stoichiometries 1:1 and 1:2 were connected by a cooperativity constant. The model assumes that there are two identical binding sites with cooperativity. There are two sets of binding parameters: K_a, ΔH, and ΔC_P are the association constant, the binding enthalpy, and the binding heat capacity for each the two identical binding sites; α, Δh, and Δc_P are the cooperativity interaction constant, the cooperativity binding enthalpy, and the cooperativity binding heat capacity for the binding of the second ligand. Thus, the first ligand binds with binding parameters: K_a, ΔH, and ΔC_P; and the second ligand binds with binding parameters: $K_a\alpha$, $\Delta H+\Delta h$, and $\Delta C_P+\Delta c_P$. Because experiments were performed at different temperatures, the van't Hoff relationship was employed to establish the temperature dependency of the equilibrium constants (K_a and α) as a function of the enthalpies and heat capacities (ΔH, ΔC_P, Δh, and Δc_P), and the enthalpies were assumed to vary linearly with temperature. Thus, the estimated parameters are those at 25 °C.

The equations describing the temperature dependence of the enthalpy, overall equilibrium constants and cooperativity constant can be found in the original reference [30]. The introduction of those equations into AFFINImeter was performed by using the following procedure: i) using the model builder, a dummy reaction was added to the model for each global parameter (α, ΔC_p, Δh and Δc_p); ii) for each dummy reaction (let's say the formation of A_2 from free species) we set an equilibrium constant equal to zero and we use the corresponding "enthalpy" as a global parameter that can be introduced in the equations to connect the equilibrium constants or the enthalpies. Using this procedure, the variety of models that can be applied with AFFINImeter is significantly expanded since any kind of global parameters and restrictions between the actual chemical reactions describing the system can be introduced, including heat capacity changes and cooperativity constants. In particular, the equations describing the model applied in Ref. [30] are easily implemented in the model builder. The results of the analysis using AFFINImeter are shown in Figs. 7–8 and in Table 1. It can be seen that the global fitting of the two sets of data is good and that the parameters compare well with those published in the main paper (Table 1). Differences can be ascribed mainly to the fact that the analysis performed with AFFINImeter is done by weighting the uncertainties of the molar heat values (see Figs. 7 and 8). It is worth to comment that the analysis applied here is not directly implemented in any public software. For its application in the original paper [30] it was necessary to develop specific computational code. In AFFINImeter, the model is easily constructed using the model builder tool. The introduction of the global fitting parameters connecting equilibrium constants and enthalpies is done by adding dummy reactions in the model builder, with the corresponding mathematical relationships in the "fit setting" form (see Table 2).



Fig. 6. Equilibrium equation describing the interaction model applied for FAD binding to wild-type and P187S NQO1. Dummy reactions were also introduced in the model builder tool in order to account for the global parameters employed in the model (using the "enthalpy" as a global parameter and setting the corresponding equilibrium constant to zero).

4. Best-practice recommendations for analysis of molecular interactions

A number of recommendations, of global use are appropriate at this stage, to improve the quality of the retrieved results.

- **Raw data processing.**

In a first step, AFFINImeter performs the automatic processing of the raw data and automatic thermodynamic and kinetic analysis using a 1:1 simple model. Although this automated process is already optimized, in some cases manual refinement could be convenient, especially when the data are of poor quality. For this, it is important to verify peak by peak the processed thermogram to assess that the processing (baseline correction, noise removal, peak integration and molar heat uncertainty) is adequate.

- **Generating and using tailored binding models.**

When creating a new binding model, use the minimum amount of complex species that are expected to be present in the binding event, although including all the species that are assumed to be formed. The application of a wrong model is an important source of error in the analysis of intermolecular interactions, so the model to perform the final analysis should be reasonably and carefully validated.

- **Global analysis.**

Performing global analysis is always recommended, as well as its comparison to individual fitting. Even for the characterization of a 1:1 interaction, where it is advisable to perform at least 2–3 repeats. For the characterization of complex binding systems with models involving more than one equilibrium, global analysis is typically a requirement in order to reduce the number of degrees of freedom in the fitting process. In these cases, it is recommended to perform several titration experiments using different experimental setups *i.e.* direct and reverse experiments, and/or modification of titrant and/or titrate concentrations. Global analysis of this dataset will give much more robust results and will prevent over-parameterized fittings. The determination of uncertainties for global analysis of several experiments is exactly the same as for the single experiments (see below).

- **Use or error bars.**

AFFINImeter automatically includes the uncertainty associated to the integral calculation of each peak in the binding isotherm (error bars). By default, the software takes into account these uncertainties throughout the fitting to yield a more reliable result. However, the unweighted fitting (disregarding the error bars) can also be performed.

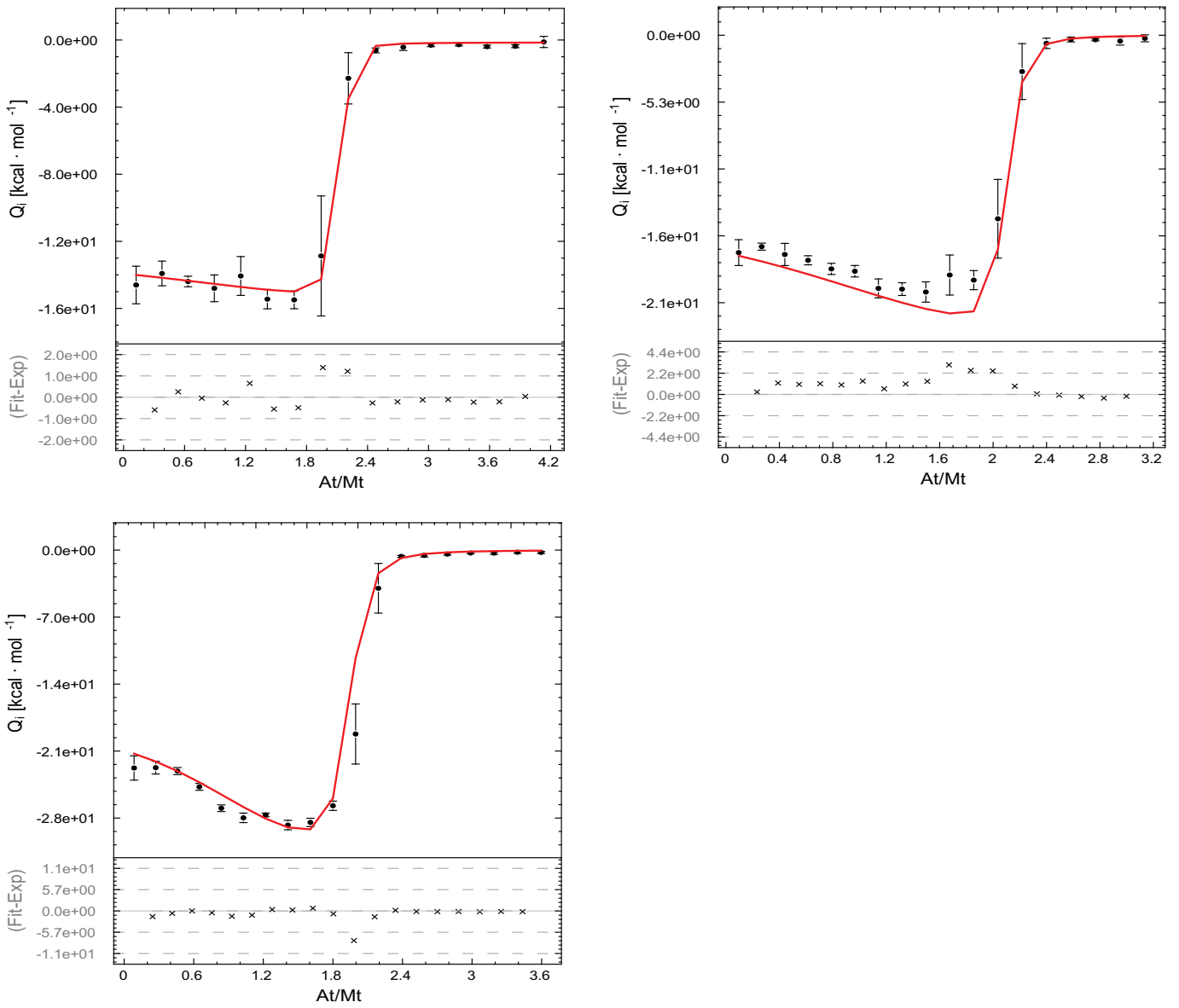


Fig. 7. Experimental binding isotherms obtained for the interaction between FAD and the wild type NQO1 at 288.15, 293.15, and 298.15 K, together with the curves obtained by a global fitting of the three experiments together to the model described in Ref. [30] using AFFINImeter, as explained in the text.

- **Use of the parameter Q_{dil} to account for the heat of dilution.**

Blank experiments are useful in order to investigate self-association or aggregation in the titrant solution. Self-association and some kind of aggregation can be considered in AFFINImeter by stoichiometric equilibrium models. Non-specific dilution effects can be modelled using the Q_{dil} parameter. In many cases, the use of this parameter is a very convenient option that can replace the blank subtraction operation (although it is always convenient to perform the blank experiment in order to test for possible extraneous heat effects and to have an experimental estimate of the dilution heat).

- **Validation tools.**
  - Visual inspection: use it to determine if differences between the experimental data and theoretical curve are random or systematic. In the second case, it can be an indication that the model employed is not appropriate.
  - GoF: use it to compare the goodness of fit between different analyses of the same isotherm with the same number of fitting parameters.
  - Uncertainty associated to a parameter value: very large uncertainties (larger than the nominal value itself) are a sign of over-parameterized fitting.
  - List of local minima: use it to check for potential over-parameterization.
  - Parameter saturation: check that the result obtained for all the fitting parameters are not equal to the maximum or minimum allowed value. If that is the case that parameter should be kept as a constant or, alternatively, modify the fitting range the parameter can access during the fitting process. By default, such range is fixed to several orders of magnitude for each fitting parameter but it can be manually modified by the user.

- **Statistical & standard errors**

As explained in the main text, AFFINImeter provides both statistical and standard errors. By default, the statistical errors are activated, since we consider they are a more reliable estimation of the parameter

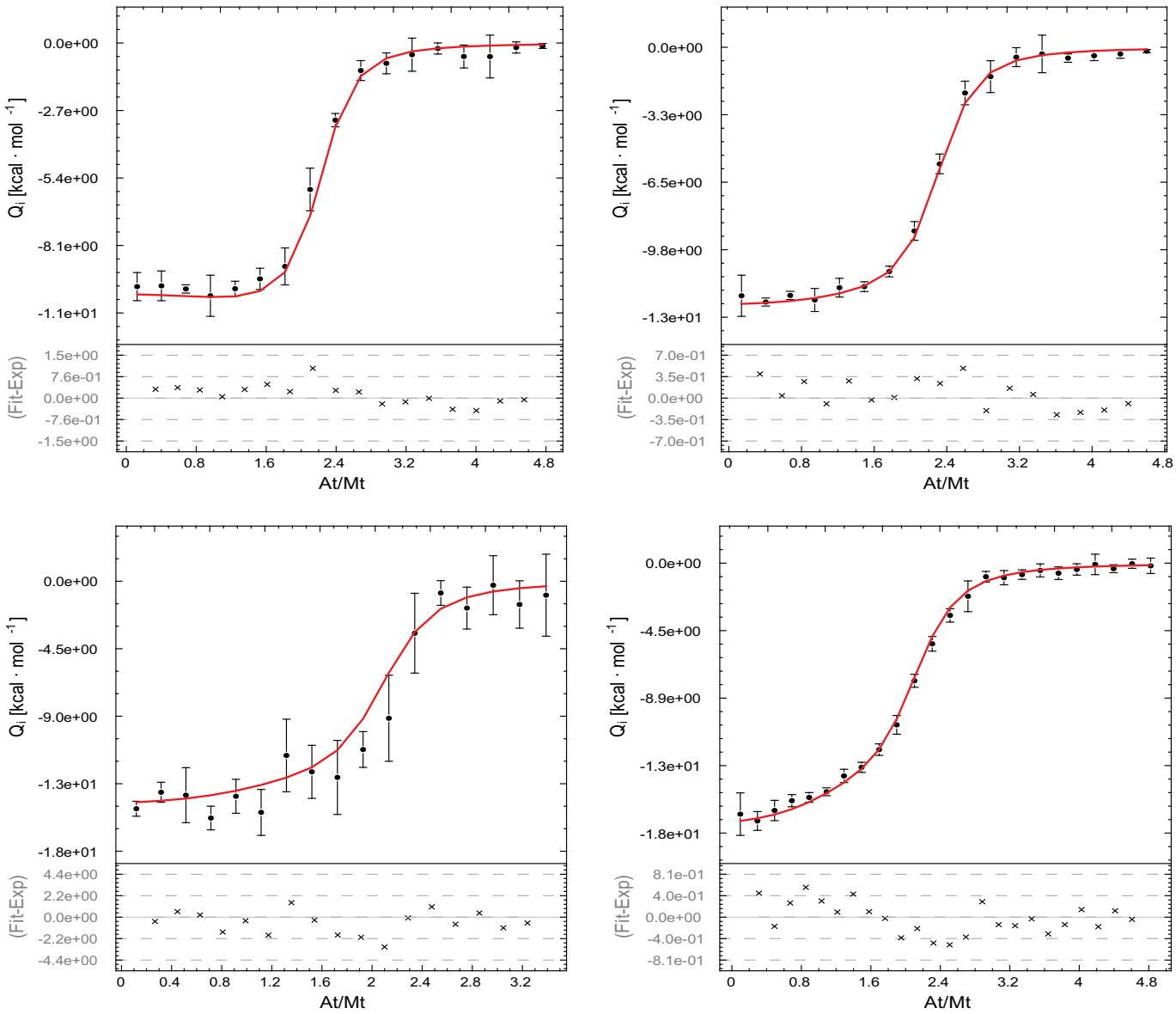


Fig. 8. Experimental binding isotherms obtained for the interaction between FAD and the P187S NQO1 mutant at 288.15, 292.15, 295.15 and 298.15 K, together with the curves obtained by a global fitting of the four experiments together to the model described in Ref. [30] using AFFINImeter, as explained in the text.

Table 2
Values of the parameters obtained from the fitting of the data shown in Figs. 7 and 8 to the model described in Ref. [30] using AFFINImeter, as described in the text.

		K_a (10^7) (M^{-1})	ΔH (kcal mol^{-1})	ΔC_p (kcal mol^{-1} K^{-1})	α	Δh (kcal mol^{-1})	Δc_p (kcal mol^{-1} K^{-1})
WT	AFFINImeter	5.8 ± 3.7	−20.69 ± 0.12	−0.699 ± 0.033	0.585 ± 0.092	−11.38 ± 0.32	−0.98 ± 0.23
	Ref. [30]	8.8 ± 0.9	−22.2 ± 0.5	−0.8 ± 0.1	0.53 ± 0.04	−12.0 ± 0.6	−1.1 ± 0.2
P187S	AFFINImeter	1.13 ± 0.48	−17.22 ± 0.35	−0.798 ± 0.047	0.35 ± 0.17	2.40 ± 0.87	0.34 ± 0.14
	Ref. [30]	0.81 ± 0.09	−17.6 ± 0.5	−0.9 ± 0.1	0.62 ± 0.05	3.1 ± 0.4	0.6 ± 0.2

These binding parameters are related to those introduced in previous sections.
K_a is equal to K_{s1} and K_{s2} (two identical binding sites) and equal to $K_{11}/2$.
$K_a\alpha$ is equal to K_{s1s2} and K_{s2s1} and equal to $2K_{12}$.

uncertainties. However the user has also access to the standard errors. For highly involved models it could be convenient to ask for many independent fitting repeats (a maximum of 1000 repeats can be performed in AFFINImeter) to then perform a statistical study of the results (all the independent minima can be downloaded in csv format from the results window).

- **Visualization and fitting of ETC.**

The ETC curve represents the duration of the different peaks throughout the titrations as a function of the concentration ratio ([A]/[M]). Typically the high concentration region of standard sigmoidal isotherms where saturation is reached ([A]/[M] significantly larger than 1) is noisy (low heat effects) and does not provide much kinetic information. Thus, by default, AFFINImeter sets only uses the concentration region where the ETC curve contains useful information. However all the data range is accessible by just activating the corresponding option below the ETC plot. The duration of the experiments in the ETC curve is automatically detected, but it can also be modified by the user.

5. Perspectives

The current version of AFFINImeter for the analysis of ITC measurements offers an unlimited number of thermodynamic models that can be freely designed by the user. Although this software is relatively new and its potential is still far from being fully exploited, a number of groups have already took advantage of its original functionalities and analysis methods (see Refs. [27–30] and references therein). New experiments can now be designed, performed and properly analysed, leading to characterization of non-trivial interactions (see for instance those shown in the Appendix). In the present manuscript we aimed at describing in detail the theory behind the software in order to facilitate its correct use by the scientific community interested in the characterization of intermolecular interactions using experimental techniques, in the present case mainly ITC. Optimization of available instruments regarding automation, reduction of sample consumption, sensitivity, implementation of simultaneous channels for measurements under the same conditions (for reproducibility or statistics) or different one (such as concentrations or temperature, to be used in global analysis), would allow the community to take more advantage of AFFINImeter. We foresee that there is also room for improvement and development in the software along the following lines: (i) the removal of unnecessary assumptions in the employed equations; (ii) the improvement of algorithms for better or/and faster convergence; (iii) the expansion of functionalities; and (iv) the inclusion of new applications to other experimental techniques. As an example of developments in progress, more rigorous equations for the analysis of ITC data [31] are being incorporated – these include exact concentration corrections due to the displacement of volume and exact equations for the effect of dilution in the molar heat resulting from the titration. One major problem that is solved by these exact equations is the erroneous asymptotic heat value obtained at large molar ratios [Mt]/[At]. The implementation of these results will allow obtaining equilibrium constant and enthalpic terms not affected by this up-to-now erroneous basic estimate. AFFINImeter is also continuously evolving by taking advantage of new algorithms and more powerful computational resources. The expansion of functionalities will be reflected mainly in a redesign of the software to facilitate the multi-temperature and global analysis, amongst a number of specific interaction models. Finally, the recent release of AFF-NMR and AFF-Spectroscopy shows that the strategy of the AFFINImeter's Scientific and Development team is to develop a multi-technique software for the orthogonal analysis of intermolecular interactions within the same platform.

Acknowledgments

The authors thank the financial support of the Spanish Ministry of Economy and Competitiveness (projects MAT2015-71826-P to Á. P., BFU2016-78232-P to A.V.C. and CTQ2017-84354-P to L. G-R), Xunta de Galicia (projects AGRUP2015/11, GPC ED431B 2017/21, GR 2007/085, IN607C 2016/03 and Centro singular de investigación de Galicia accreditation 2016-2019, ED431G/09), and Fundação para a Ciência e a Tecnologia (project UID/QUI/0081/2013 to M.B.). These research projects were partially supported by FEDER. Financial support from PAIP-FQ-UNAM (grant 5000-9018 to M.C.) and FEDER (project Norte-01-0145-FEDER-000028 to M. B.) is acknowledged. P. F. G. thanks the Spanish Ministry of Economy and Competitiveness and the European Social Fund for his predoctoral research grant, reference BES-2016-076761. Facilities provided by the Galician Supercomputing Centre (CESGA) are also acknowledged.

Appendix. The use of the AFFINImeter simulation tool

Using two examples, we illustrate the employment of the AFFINImeter simulation tool to determine the binding isotherms of the possible ITC experiments and the corresponding species distributions.

First we considered a system consisting of a ligand **L** with a protein **P** that is already bound to another ligand **L'**. The first ligand **L** is assumed to self-associate forming dimers, but only the monomeric species can interact with the protein. In the notation employed in AFFINImeter, the main compounds in the syringe and in the cell are A and M, respectively. An additional compound B can be in the sample cell, in the syringe or in both. The chosen system can be studied by using the protein as titrant or as a titrate. This system will be simulated using an equilibrium stoichiometry (SE) model. Thus, using the model builder tool (https://www.youtube.com/watch?v=dhfW-PQ-qVA), the reaction schemes required to simulate both the direct and the reverse experiments are shown in Fig. A.1. In one case the protein and **L'** are in the syringe at the same concentration forming 1:1 complexes, while **L** is in the sample cell with both monomers and dimers in equilibrium. When the protein is titrated to the cell, the **PL'** complex and the $\mathbf{L_2}$ dimers dissociate to form the **PL** complex and free **L'** molecules. This occurs because the equilibrium constant corresponding to the formation of **PL** has been chosen to be much higher than those corresponding to the formation of **PL'** and $\mathbf{L_2}$ (see Table A.1.). Once all the **L** molecules reacted with **P**, the **PL'** complexes remain formed upon injection because there are no free **L** molecules to compete with **L'** for the interaction with **P** (Fig. A.1, top). In the second case, i.e. when the dimer $\mathbf{L_2}$ is injected from the syringe, it dissociates forming monomers that then interact with **P**. Again, **L** competes with **L'** for the interaction with **P**. Once the protein is saturated with **L**, all the **L'** molecules are free in the cell. Beyond that injection, **L** remains in dimeric form when injected from the syringe (Fig. A.1, bottom).

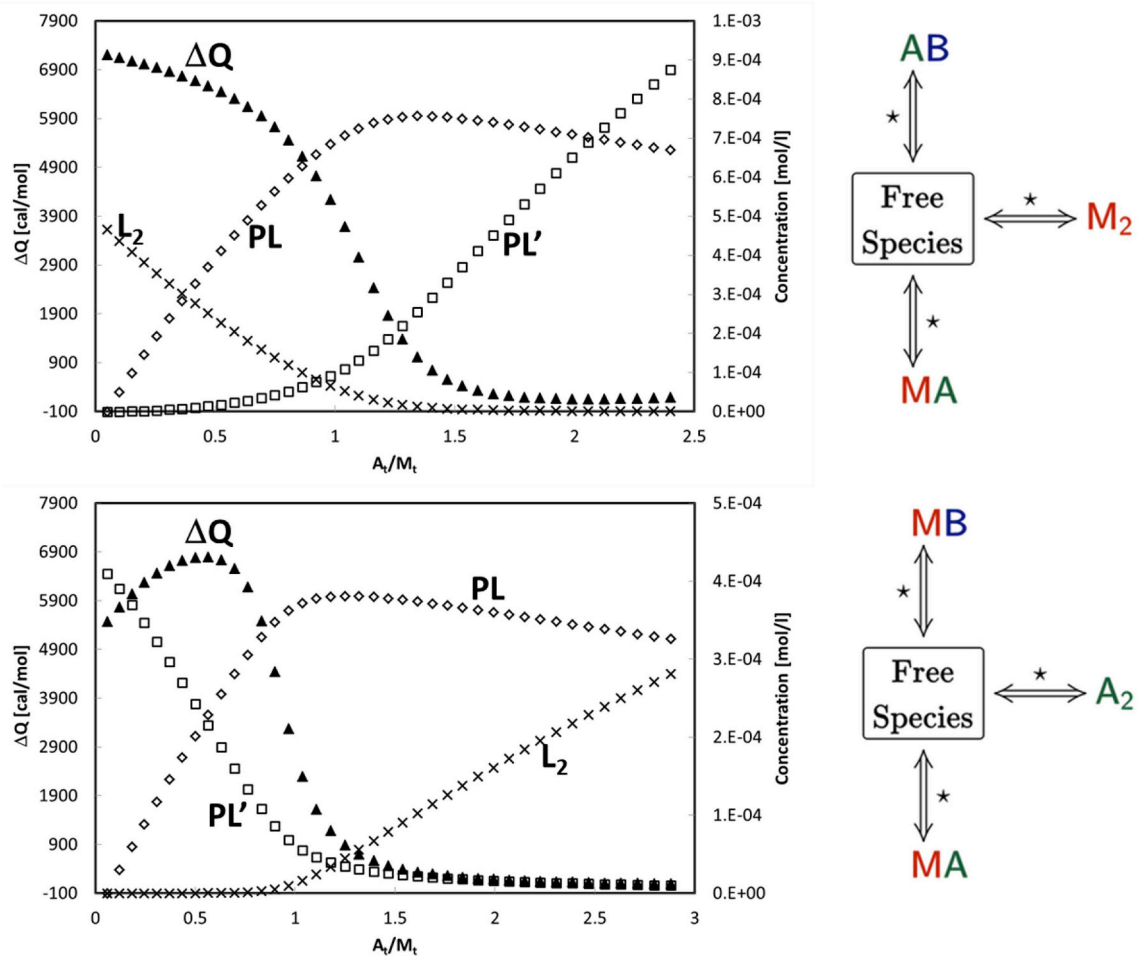


Fig. A.1. Simulated binding isotherms (▲; left axes) for the reaction schemes showed on the right of each plot, together with the concentration in the sample cell of the different chemical species (see labels in the plots; right axes). The two reaction schemes describe exactly the same molecular interactions for the direct and reverse experiments (see main text). The concentrations employed for these simulation are: {[M] = [**L**] = 1 mM; [A_{syr}] = [**P**] = 5 mM; [B_{syr}] = [**L'**] = 5 mM} for the top plot and {[M] = [**P**] = 0.5 mM; [A_{syr}] = [**L**] = 3 mM; [B_{cell}] = [**L'**] = 0.5 mM} for the bottom plot. The employed thermodynamic parameters are in Table A.1. In all cases 40 injections of 2 μl each in a sample cell of 0.2 ml were performed.

Table A.1
Thermodynamic parameters employed for the simulation of the curves shown in Fig. A.1.

	K	ΔH
FS↔ L_2	10^5	-10^3
FS↔PL	10^7	$3{\cdot}10^3$
FS↔PL'	$5{\cdot}10^4$	$-4{\cdot}10^3$

Clearly, the simulation tool is useful to understand the behaviour of a molecular system for a given set of thermodynamic parameters. Additionally, it is also useful to design the ITC experiments. In this example, the fitting of the model to the experiment corresponding to the first simulation (Fig. A.1, top) will probably be overparameterized since it requires at least 6 parameters to describe a smooth curve. However, the binding isotherm corresponding to the second simulation (Fig. A.1, bottom) present stronger curvature changes and more parameters would be statistically justified. Of course, if the two experiments are performed the global fitting of both binding isotherms would provide more reliable values for the parameters.

The second simulation corresponds to the interaction of a hypothetical nanoparticle (**NP**) initially located in the sample cell at 0.5 mM with two competitor ligands initially at 40 mM in the syringe (**A**) and at 5 mM or 10 mM in the sample cell (**B**). **NP** is assumed to have two different interaction regions with 20 and 5 sites, respectively. It is also assumed that all the interaction sites in both regions are independent from each other. This system is well suited for an IS model. The employed site affinity constants and enthalpies for each ligand and site are given in Table A.2.

Table A.2
Thermodynamic parameters employed for the simulation of the curves shown in Fig. A.2.

	Region 1; n = 20		Region 2; n = 5	
	A	B	A	B
K	10^8	10^6	10^7	10^4
ΔH	$-5{\cdot}10^3$	-10^3	10^3	$5{\cdot}10^3$

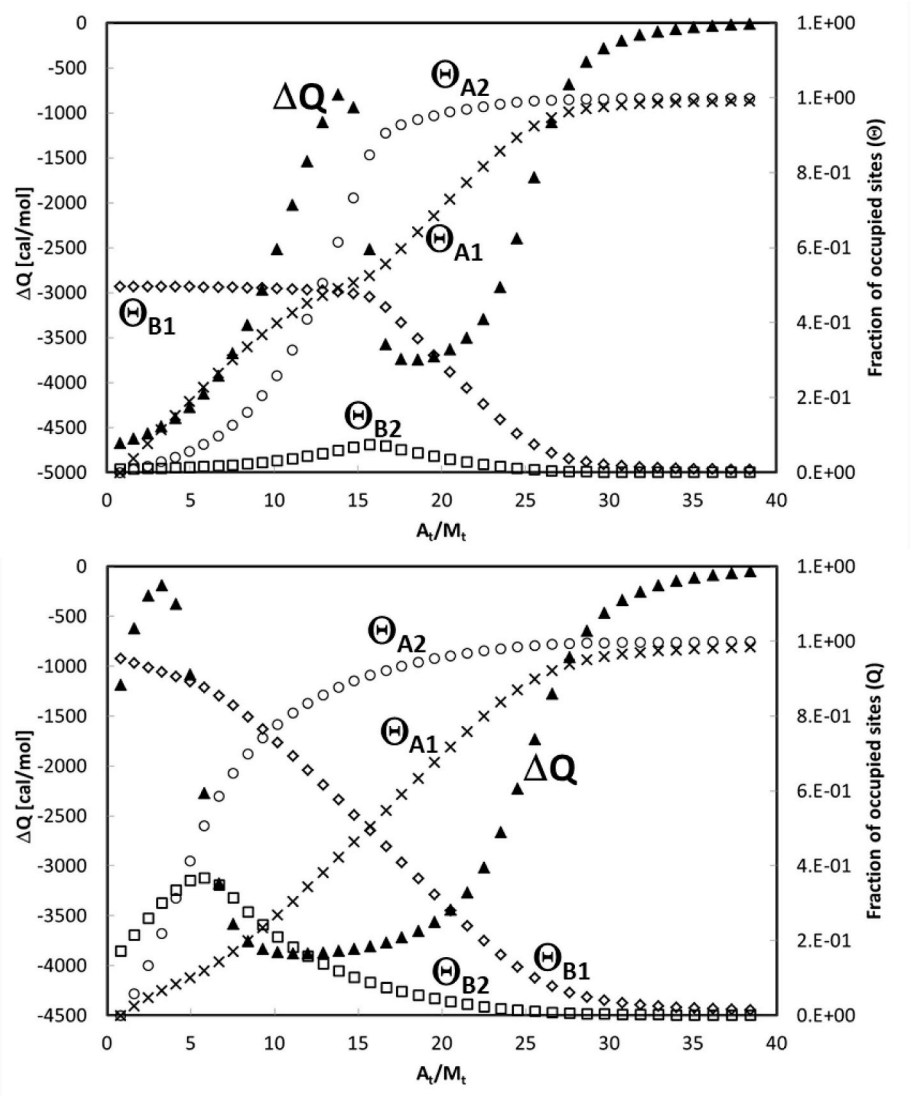


Fig. A.2. Simulated binding isotherms (▲; left axes) for the interaction of a hypothetical nanoparticle with two competitor ligands (see main text), together with the fraction of occupied sites (see labels in the plots; right axes) for the two interaction regions (subscripts 1 and 2). The two binding isotherms reflect the same molecular interactions at slightly different concentrations of B in the sample cell (5 mM for the top plot and 10 mM for the bottom plot).

At the beginning of the experiment the concentration of A in the cell is null and the concentration of B (5 mM) is not enough to saturate both regions of NP. In the first experiment the first region (with n = 20) is half saturated of B while the second region is empty, as expected from the corresponding equilibrium constants. The addition of A displaces B from the first region and it starts to populate the second region (see the small maximum at At/Mt ~ 16). Then A also displaces B from the second region. At the end of the experiment, the whole NP is saturated by molecules of A ($\Theta_{A1} = \Theta_{A2} = 1$) while B remains free in solution ($\Theta_{B1} = \Theta_{B2} = 0$). The second experiments (B concentration 10 mM) behaves similarly but it begins at a larger concentration of B, enough to saturate the first region and to partially populate the second one. Note that the binding isotherms are quite different for each of these two hypothetical experiments and hence they would be well suited to perform a global fitting and obtain a good thermodynamic characterization.

References

[1] M.J. Rosen, J.T. Kunjappu, Surfactants and Interfacial Phenomena, Wiley & Sons, 978-0-470-54194-4, 2012.

[2] J.M. Ruso, Á. Piñeiro (Eds.), Proteins in Solution and at Interfaces: Methods and Applications in Biotechnology and Materials Science, Wiley & Sons, 978-0-470-95251-1, 2013.

[3] K.A. Connors, Binding Constants. The Measurement of Molecular Complex Stability, John Wiley & Sons, 978-0471830832, 1987.

[4] S. Vega, O. Abian, A. Velazquez-Campoy, A unified framework based on the binding polynomial for characterizing biological systems by isothermal titration calorimetry, Methods 76 (2015) 99–115, https://doi.org/10.1016/j.ymeth.2014.09.010.

[5] A. Velazquez-Campoy, Allostery and cooperative interactions in proteins assessed by Isothermal Titration Calorimetry (Chapter 12), in: M. Bastos (Ed.), Biocalorimetry: Foundations and Contemporary Approaches, CRC Press, Taylor & Francis Group, Boca Raton, FL, 2016, pp. 223–246, , https://doi.org/10.1201/b20161-16 ©20 ©2015. ISBN: 9781482246667 148224666X.

[6] X. Pang, H.-X. Zhou, Rate constants and mechanisms of protein–ligand binding, Annu. Rev. Biophys. 46 (2017) 105–130, https://doi.org/10.1146/annurev-biophys-070816-033639.

[7] COST action CA15126, Between atom and cell; integrating molecular Biophysics approaches for biology and Health care, Working Group 4, 'Optimization of data quality' https://arbre-mobieu.eu/.

[8] D. Burnouf, E. Ennifar, S. Guedich, B. Puffer, G. Hoffmann, G. Bec, F. Disdier, M. Baltzinger, Dumas P. kinITC, A new method for obtaining joint thermodynamic and kinetic data by isothermal titration calorimetry, J. Am. Chem. Soc. 134 (1) (2012) 559–565, https://doi.org/10.1021/ja209057d.

[9] P. Dumas, E. Ennifar, G. Bec, Á. Piñeiro, J. Sabín, E. Muñoz, J. Rial, Implementation of kinITC into AFFINImeter, Malvern Panalytical Application Note, 2015, https://www.malvernpanalytical.com/en/learn/knowledge-center/application-notes/AN150427kinItcAffiniMeter.html.

[10] E. Muñoz, J. Sabín, J. Rial, D. Pérez, E. Ennifar, P. Dumas, Á. Piñeiro, Thermodynamic and kinetic analysis of isothermal titration calorimetry experiments by using kinITC in AFFINImeter, in: Eric Ennifar (Ed.), Microcalorimetry of Biological Molecules: Methods and Protocols, Springer, 978-1-4939-9178-5, 1964series title: Methods Molecular Biology.

[11] P. Dumas, E. Ennifar, C. Da Veiga, G. Bec, W. Palau, C. Di Primo, Á. Piñeiro, J. Sabin, E. Muñoz, J. Rial, Chapter seven - extending ITC to kinetics with kinITC, Methods Enzymol. 567 (2016) 157–180, https://doi.org/10.1016/bs.mie.2015.08.026.

[12] S. Keller, C. Vargas, H. Zhao, G. Piszczek, C.A. Brautigam, P. Shuck, High-precision isothermal titration calorimetry with automated peak-shape analysis, Anal. Chem. 84 (2012) 5066–5073, https://doi.org/10.1021/ac3007522.

[13] E. Vigonsky, I. Fish, N. Livnat-Levanon, E. Ovcharenko, N. Ben-Tal, O. Lewinson, Metal binding spectrum and model structure of the Bacillus anthracis virulence determinant MntA, Metall 7 (10) (2015) 1407–1419, https://doi.org/10.1039/c5mt00100e.

[14] M.J. Marques-Carvalho, J.H. Morais-Cabral, Interaction of calmodulin with the EAG1 potassium channel, Biophys. J. 108 (2) (2015), https://doi.org/10.1016/j.bpj.2014.11.150 23A.

[15] B. Gómez-González, V. Francisco, R. Montecinos, L. García-Río, Investigation of the binding modes of a positively charged pillar[5]arene: internal and external guest complexation, Org. Biomol. Chem. 15 (2017) 911–919, https://doi.org/10.1039/C6OB02573K.

[16] L.Y. Rivera-Najera, G. Saab-Rincón, M. Battaglia, C. Amero, N.O. Pulido, E. García-Hernández, R.M. Solórzano, J.L. Reyes, A.A. Covarrubias, A group 6 late embryogenesis abundant protein from common bean is a disordered protein with extended Helical structure and oligomer-forming properties, J. Biol. Chem. 289 (2014) 31995–32009, https://doi.org/10.1074/jbc.M114.583369.

[17] D.S.-H. Chan, W.-G. Seetoh, B.N. McConnell, D. Matak-Vinković, S.E. Thomas, V. Mendes, M. Blaszczyk, A.G. Coyne, T.L. Blundell, C. Abell, Structural insights into the EthR–DNA interaction using native mass spectrometry, Chem. Commun. 53 (2017) 3527–3530, https://doi.org/10.1039/C7CC00804J.

[18] E. Muñoz, Á. Piñeiro, AFFINImeter software: from its beginnings to future trends a literature review, J. Appl. Bioanal. 4 (4) (2018) 123–138 https://doi.org/10.17145/jab.18.017.

[19] T. Silva, B. Claro, B.F.B. Silva, N. Vale, P. Gomes, M.S. Gomes, S. Funari, J. Teixeira, D. Uhríková, M. Bastos, Unravelling a mechanism of action for a cecropin A-melittin hybrid antimicrobial peptide: the induced formation of multilamellar lipid stacks, Langmuir 34 (5) (2018) 2158–2170, https://doi.org/10.1021/acs.langmuir.7b03639.

[20] R. Dias, N.F. Brás, I. Fernandes, M. Pérez-Gregorio, N. Mateus, V. Freitas, Molecular insights on the interaction and preventive potential of epigallocatechin-3-gallate in Celiac Disease, Int. J. Biol. Macromol. 112 (2018) 1029–1037, https://doi.org/10.1016/j.ijbiomac.2018.02.055.

[21] S. Soares, I. García-Estévez, R. Ferrer-Galego, N.F. Brás, E. Brandão, M. Silva, N. Teixeira, F. Fonseca, S.F. Sousa, F. Ferreira-da-Silva, N. Mateus, V. de Freitas, Study of human salivary proline-rich proteins interaction with food tannins, Food Chem. 243 (2018) 175–185, https://doi.org/10.1016/j.foodchem.2017.09.063.

[22] W.H. Press, B.P. Flannery, S.A. Teukolsky, W.T. Vetterling, Numerical Recipes in C: the Art of Scientific Computing, second ed. second ed., Cambridge University Press, 1988 ISBN-10: 0521431085.

[23] L. Armijo, Minimization of Functions having Lipschitz continuous first partial derivatives, Pac. J. Math. 16 (1) (1966) 1–3 https://projecteuclid.org/euclid.pjm/1102995080.

[24] J.W. Tukey, Bias and confidence in not quite large samples, Ann. Math. Stat. 29 (2) (1958) 614, https://doi.org/10.1214/aoms/1177706647.

[25] B. Efrom, C. Stein, The Jackknife estimate of variance, Ann. Stat. 9 (3) (1981) 586–596 https://projecteuclid.org/euclid.aos/1176345462.

[26] P. Dumas, Joining thermodynamics and kinetics by kinITC (Chapter 15), in: M. Bastos (Ed.), Biocalorimetry: Foundations and Contemporary Approaches, CRC Press, Taylor & Francis Group, Boca Raton, FL, 2016, pp. 281–300, , https://doi.org/10.1201/b20161-19 ©20 ©2015. ISBN: 9781482246667 148224666X.

[27] P. Zihlmann, M. Slbermann, T. Sharpe, X. Jiang, T. Mühlethaler, R. Jakob, S. Rabbani, C. Sager, P. Frei, T. Maier, B. Ernst, KinITC - one method supports both thermodynamic and kinetic SARs as exemplified on FimH antagonists, Chem. Eur J. 24 (49) (2018) 13049–13057, https://doi.org/10.1002/chem.201802599.

[28] M. Marques-Carvalho, J. Oppermann, E. Muñoz, A. Fernandes, G. Gabant, M. Cadene, S. Heinemann, R. Schönherr, J. Morais-Cabral, Molecular insights into the mechanism of calmodulin inhibition of the EAG1 potassium channel, Structure 24 (10) (2016) 1742–1754, https://doi.org/10.1016/j.str.2016.07.020.

[29] E. Muñoz, J. Sabín, Á. Piñeiro, G. Franco Rodríguez, The use of ITC and the software AFFINImeter for the quantification of the anticoagulant pentasaccharide in low molecular weight heparin, in: Eric Ennifar (Ed.), Microcalorimetry of Biological Molecules, Methods and Protocols, Springer, 978-1-4939-9178-5, 1964series title: Methods Molecular Biology.

[30] R. Clavería-Gimeno, A. Velazquez-Campoy, A.L. Pey, Thermodynamics of cooperative binding of FAD to human NQO1: implications to understanding cofactor-dependent function and stability of the flavoproteome, Arch. Biochem. Biophys. 636 (2017) 17–27, https://doi.org/10.1016/j.abb.2017.10.020.

[31] P. Dumas, Rigorous Equations for Isothermal Titration Calorimetry: Theoretical and Practical Consequences, (2019) https://doi.org/10.1101/512780.

USC UNIVERSIDADE DE SANTIAGO DE COMPOSTELA

8.2. Paper V

"Simple aproximaTion for Aggregation Number Determination by Isothermal Titration Calorimetry: STAND-ITC", published in *Langmuir* (online 2021), is a regular article where a model to characterize micellization by ITC and to obtain, among other parameters, the aggregation number, is presented. The model is tested on four different surfactant solutions and compared with literature. This work has been developed in collaboration with people from: (1) Departamento de Física Aplicada, Facultade de Física, Universidade de Santiago de Compostela; (2) CIQUS, Departamento de Quimica Física, Universidade de Santiago de Compostela. The list of authors is presented below, by order and with their corresponding affiliations. The corresponding authors are marked with a *:

Pablo F. Garrido (1), Pedro Rodríguez-Dafonte (2), Luis García-Río (2), Ángel Piñeiro (1)*.

According to the CRediT authorship contribution statement (Brand *et al.*, 2015), my contributions to this publication are: Software, Validation; Formal analysis; Investigation; Writing - Review & Editing; Visualization.

Reprinted with permission from Garrido PF, Rodríguez-Dafonte P, García-Río L, Piñeiro Á (available online: September 27, 2021). Simple approximaTion for Aggregation Number Determination by Isothermal Titration Calorimetry: STAND-ITC. *Langmuir*. ISSN 0743-7463. doi: 10.1021/acs.langmuir.1c01727. URL https://doi.org/10.1021/acs.langmuir.1c01727 Copyright 2021 American Chemical Society

Supporting Information is included in the Appendix B

USC UNIVERSIDADE DE SANTIAGO DE COMPOSTELA

USC
UNIVERSIDADE
DE SANTIAGO
DE COMPOSTELA

LANGMUIR

pubs.acs.org/Langmuir Article

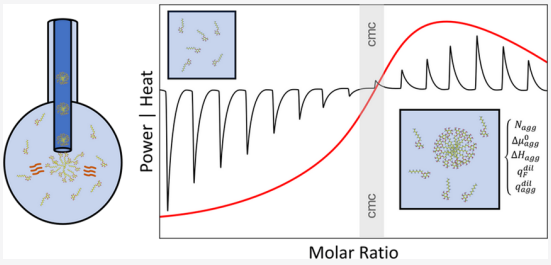
Simple ApproximaTion for Aggregation Number Determination by Isothermal Titration Calorimetry: STAND-ITC

Pablo F. Garrido, Pedro Rodríguez-Dafonte, Luis García-Río, and Ángel Piñeiro*

Cite This: https://doi.org/10.1021/acs.langmuir.1c01727 Read Online

ACCESS | Metrics & More | Article Recommendations | Supporting Information

ABSTRACT: A new proposal to obtain aggregation numbers from isothermal titration calorimetry dilution experiments is described and tested using dodecyl trimethyl ammonium bromide, dodecyl methylimidazolium chloride, dodecyl methylimidazolium sulfonate, and didecyl methylimidazolium chloride aqueous solutions at different temperatures. The results were compared to those obtained from fluorescence measurements and also with data from the literature. In addition to the aggregation number, the molar free energy to transfer a solute molecule from the aggregate to the bulk solution, the enthalpy corresponding to the formation of the self-assembled suprastructures, the molar heat corresponding to the dilution of monomers and aggregates, and an offset parameter to account for unpredictable external contributions are simultaneously obtained using the same method. The new equations are compared to those obtained from previous proposals, and they are also analyzed in detail to assess the impact of each fitting parameter in the profile of the calorimetric isotherm. This new approach has been implemented in a computational code that automatically determines the fitting parameters as well as the corresponding statistical uncertainties for the large variety of calorimetric profiles that have been tested. Given the high sensitivity of the dilution experiments to the aggregation number for relatively small assemblies, our approach is proposed also to quantify the oligomerization state of biomolecules such as proteins and peptides.



Downloaded via UNIV DE SANTIAGO DE COMPOSTELA on September 28, 2021 at 15:33:23 (UTC).
See https://pubs.acs.org/sharingguidelines for options on how to legitimately share published articles.

INTRODUCTION

The surfactant industry is ubiquitous and highly dynamic. The main market is related to household or industrial detergents for cleaning, but many other applications including some related to the agricultural chemicals, pharmaceutical, paints, coatings, textile, and food industries are also extremely important.[1−7] New surfactants, both natural and artificially synthesized, are continuously being discovered and employed to optimize commercial products by lowering their toxicity, making them cheaper or increasing the control of their properties for a better performance.[3,8−13]

The critical micelle concentration (*cmc*) and the average aggregation number (N_{agg}) are probably the most important parameters that require to be considered in the development of surfactant-based commercial products as well as in fundamental applications involving this kind of molecules. The *cmc* has been quantitatively defined in different ways but it is generally understood as the free surfactant concentration beyond which the molecules begin to form nanoaggregate structures called micelles. The *cmc* can be assessed by different techniques producing slightly different values.[14] N_{agg} is the average number of molecules forming the micelles, thus providing an estimation of the size of these nanoaggregates. The combination of both numbers allows determining the concentration of micelles for a given nominal surfactant concentration and so its ability to encapsulate a certain co-solute in aqueous solution. Other thermodynamic parameters such as Gibbs energy, enthalpy, or entropy corresponding to the micelle formation process are also keys in the characterization of these molecules since they allow the introduction of rational chemical modifications in their structure to modify their stability, diffusion rate, and other physicochemical properties.

The most accessible experiments aimed to determine micelle aggregation numbers require using a fluorescent probe and a quencher,[15] although other methods including light scattering and small-angle neutron scattering are also occasionally employed.[16,17] Several authors have also proposed an alternative method based on surface tension measurements.[18−21] The reliability of the results is often dependent on the physicochemical properties of the employed molecules. Additionally, these techniques present some limitations such as the temperature and concentration ranges of the target surfactant. For some of these methods, the employed concentrations are far above the *cmc*, leading to higher-than-expected N_{agg} values coming from larger aggregates that dominate the solutions in such scenarios. Note that the size and shape of these supramolecular aggregates

Received: June 28, 2021
Revised: September 10, 2021

ACS Publications

© XXXX The Authors. Published by American Chemical Society

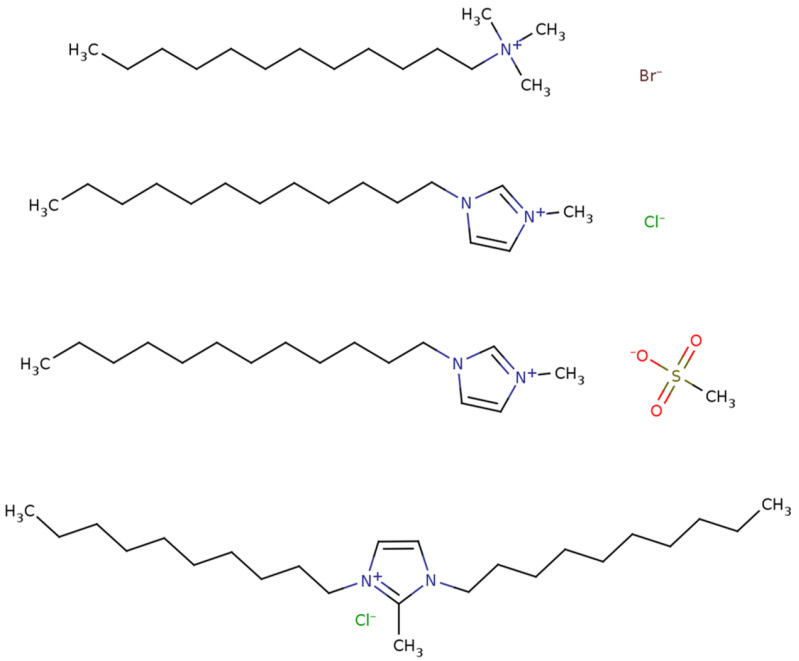


Figure 1. Structures of the molecules employed for the ITC and fluorescence experiments. From top to bottom: dodecyl trimethyl ammonium bromide (C_{12}TAB), dodecyl methylimidazolium chloride ($[C_{12}mim^+][Cl^-]$), dodecyl methylimidazolium sulfonate ($[C_{12}mim^+][CH_3SO_3^-]$), and didecyl methylimidazolium chloride ($[C_{10}C_{10}mim^+][Cl^-]$).

depend on the solute concentration[22] and the smallest and simplest micelles are typically obtained around the *cmc*. Last generation isothermal titration calorimetry (ITC) significantly increased their sensitivity, while the sample cell volume has been reduced. Taking advantage of this, a method to get surface tension values of liquid samples from the injection of air bubbles in the sample cell of an ITC system has been recently developed, thus opening new possibilities for calorimetry at fluid interfaces.[23,24] Nowadays, it is also possible to register the signal of demicellization processes, as well as of other coupled events, with high precision using a tiny amount of material. This is based on standard ITC experiments corresponding to the dilution of surfactant solutions above the *cmc*, which have shown to be clearly sensitive to the structure of the molecules and so to that of the corresponding aggregates. Both empirical and theoretical attempts have been made to get physicochemical and structural parameters for the processes involved in this kind of measurement.[25−31] In general, two different model families are applied to the analysis of micelle formation/rupture processes observed by different experimental techniques, namely, the pseudo-phase separation and the mass action approaches. The former type of model is normally easier to apply since it assumes the micelles as a different phase in equilibrium with monomers, disregarding the number of surfactant molecules in each nanoaggregate. Models from the latter family typically assume that N_{agg} is the same for all micelles.[25] Mass action-type models explicitly contemplate the equilibrium between monomers and micelles, and they are considered to be more rigorous than pseudo-phase separation models. The direct information obtained from the analysis of demicellization ITC isotherms is typically the value of the *cmc* and the enthalpy of the micelle formation process, but more thermodynamic information including the free energy of micellization, solute dilution enthalpy, and even an estimation of the aggregation number can be obtained.[25−34] Several approaches have been proposed to optimize the analysis of these experiments, including the simultaneous use of different calorimetric techniques,[25] global multitemperature fittings,[30] or manipulations in the equations to decouple the fitting parameters,[29] thus facilitating the application of the model.

In the present work, it is shown that the direct application of the mass action law to simple ITC demicellization experiments leads to reasonable aggregation numbers of surfactant micelles with a small uncertainty. Additionally, complete thermodynamic characterization of the demicellization isotherms, including the dilution heat of surfactant monomers and micelles as well as the enthalpy and the Gibbs energy changes for the molecular transfer from the solution to the aggregates, is obtained. In our proposal, the *cmc* is not explicitly considered as a fitting parameter since a continuous equilibrium between surfactants and micelles is assumed. Complementarily, a value for the *cmc* can be determined from the free surfactant and micelle concentration profiles obtained from the model. The sensitivity of our proposal to the different fitting parameters is carefully examined, allowing the design of optimal experiments with specific sampling in certain concentration regions. A variety of ionic liquids with different chain lengths and polar head groups at different temperatures are employed to validate the method with information obtained from fluorescence experiments. For the same systems, a literature review of previously published aggregation number values using different methods is also presented, showing a large discrepancy between the different sources of data. The proposed model is expected to be publicly available soon from the AFFINImeter platform.[35,36]

MATERIALS AND METHODS

Experimental Section. *Materials.* The ionic liquids dodecyl methylimidazolium chloride ($[C_{12}mim^+][Cl^-]$) and didecyl methylimidazolium chloride ($[C_{10}C_{10}mim^+][Cl^-]$) were obtained from Iolitec (Germany) with a mass fraction purity better than 0.98 and used as received. In an effort to avoid the absorption of atmospheric water, the compound was stored under vacuum in a desiccator filled with

https://doi.org/10.1021/acs.langmuir.1c01727
Langmuir XXXX, XXX, XXX−XXX

molecular sieves, and only fresh samples were used. The surfactant dodecyl trimethyl ammonium bromide (C_{12}TAB) was of the highest commercially available purity (>98%) (Sigma-Aldrich) and was used without further purification. The synthesis of the ionic liquid dodecyl methylimidazolium sulfonate ($[C_{12}mim^+][CH_3SO_3^-]$) followed a method previously reported. The structure of all the employed surfactants is shown in Figure 1.[37] Pyrene (>99%) and cetylpyridinium chloride (>99%) (CPC), employed in the fluorescence experiments, were purchased from Aldrich, of the highest available purity, and they were used without further purification.

ITC. The ITC experiments were performed with a VP-ITC instrument (MicroCal, Inc.). In a typical experiment, both the reference and reaction cells were filled with doubly distilled and degassed water. For $[C_{12}mim^+][Cl^-]$, $[C_{12}mim^+][CH_3SO_3^-]$, and C_{12}TAB, the injection syringe was filled with a concentrated solution of surfactant (150 mM); this was injected at 5 min intervals in 90 steps (the first injection of 2 μL was followed by 4 μL injections in each step) into the pure water in the reaction cell under constant stirring conditions (250 rpm) at a specified temperature. For $[C_{10}C_{10}mim^+][Cl^-]$, the injection syringe was filled with a concentrated solution of surfactant (8, 6, or 5 mM); this was injected at 5 min intervals in 34 steps (the first injection of 4 μL was followed by 8 μL injections in each step) into the pure water in the reaction cell under constant stirring conditions (250 rpm) at a specified temperature. The heat absorbed or released at each step of the dilution of the surfactant solution was recorded, and the enthalpy per mole of injectant (ΔH_{obs}) was obtained by integrating the area of the peaks in the plot of thermal power against time by using ITC software.[38]

Fluorescence. Steady-state fluorescence experiments were recorded using a Cary Eclipse fluorescence spectrophotometer. The fluorescence spectrum of pyrene was measured with an excitation wavelength of 334 nm. All emission spectra were corrected for the emission monochromator response and were background-subtracted using appropriate blanks. Slits and rates of acquisition were chosen for a convenient signal-to-noise ratio. The micelle aggregation number (N_{agg}) of surfactants can be determined by static luminescence quenching according to the Turro−Yekta method.[39] Pyrene was selected as the fluorescent probe and cetylpyridinium chloride (CPC) was assigned to be the quencher of pyrene. Thus, N_{agg} can be calculated on the basis of the following equation:

$$\ln\left(\frac{I_0}{I}\right) = N_{agg}\frac{[Qc]}{[S_T] - cmc} \tag{1}$$

where I_0 and I are the fluorescent intensities of pyrene in the absence and presence of CPC and $[Qc]$ and $[S_T]$ are the concentration of CPC (4.0×10^{-7} M) and surfactant (slightly above the *cmc*), respectively. This equation relies on the assumption that pyrene and CPC are completely solubilized in the micelle phase and their distributions follow the Poisson behavior.

Theory. The proposed approach is based on the equilibrium between the N_{agg} surfactant monomers (S) and the corresponding micelles (M):

$$N_{agg}S \leftrightarrow S_N \tag{2}$$

where S_N represents an aggregate of N S molecules, i.e., a micelle (M). Note that the counterions of the surfactant molecules are not explicitly considered in the previous reaction. The overall equilibrium constant corresponding to eq 2 is given by:

$$K = [M]/[S_F]^{N_{agg}} \tag{3}$$

where $[S_F]$ is the molar concentration of the free surfactant and $[M]$ is the molar concentration of micelles. Thus, the total concentration of surfactant in a given solution can be expressed as

$$[S_T] = [S_F] + N_{agg}[M] = [S_F] + N_{agg}K[S_F]^{N_{agg}} \tag{4}$$

Also, the free energy for the micelle formation process per mole of surfactant molecule, assuming a hypothetical concentration of 1 M as the standard state, is given by

$$\Delta\mu^0_{agg} = -RT\ln(K)/N \tag{5}$$

For a typical ITC experiment designed to observe the demicellization process, small aliquots of a relatively highly concentrated surfactant solution (above the *cmc*) are successively introduced in the sample cell, which is initially filled with the pure solvent (see the Experimental Section). Due to the equilibrium described by eq 2, the micelles contained in the aliquots break down into monomeric species upon dilution in the sample cell. This process stands while the surfactant concentration in the measuring cell is lower than the *cmc*. Note that the *cmc* is being employed as a reference concentration in order to describe the experiments, but this parameter does not explicitly appear in eqs 2−5.

The total heat exchanged due to the transfer of all the surfactant molecules from the micelles contained in a certain volume V to the solution as free species would be

$$Q = VN_{agg}\Delta H_{agg}[M] \tag{6}$$

where ΔH_{agg} is the enthalpy corresponding to the transfer of one mole of surfactants from the solution to micelles. The previous equations describe the micelle formation/rupture process, but the calorimetric signal also contains the contribution due to the dilution of the free surfactant molecules and that of due to the dilution of micelles. These contributions can be reasonably approached by a linear dependence on the nominal surfactant concentration (see below). The experimental stepwise heat change corresponding to the injection number i can be expressed as

$$\Delta Q_i = -Q_{syr} + (Q_i - Q_{i-1}) + (q_F^{dil}[\Delta S_F]_i + q_{agg}^{dil}N_{agg}[\Delta M]_i)\Delta V \tag{7}$$

where Q_{syr} and Q_i are the total heat corresponding to the rupture of all the micelles within the titration volume ΔV and in the sample cell after i titrations, respectively, q_F^{dil} and q_{agg}^{dil} are the molar enthalpies corresponding to the dilution of free surfactants and micelles, and $[\Delta S_F]_i$ and $[\Delta M]_i$ are the differences in the free surfactant and micelle concentration between the syringe and the sample cell for the titration i: $[\Delta S_F]_i = [S_F{}^{syr}] - [S_F{}^{cell}]_i$ and $[\Delta M]_i = [M^{syr}] - [M^{cell}]_i$. These two terms are included to ensure that the dilution heat becomes zero when the concentration of the syringe and the sample cell are the same.

A correction due to the volume displacement upon injection should be introduced:

$$Q_i^c = \Delta V/(2V)(Q_i + Q_{i-1}) \tag{8}$$

Finally, a constant correction to the baseline (Q_b) due to a variety of external reasons (electric noise, the heat due to the friction of the stirrer, etc.) should also be considered. Thus, the final stepwise molar heat change per injection should be

$$\Delta q_i = (\Delta Q_i + Q_i^c + Q_b)/([S^{syr}]\Delta V) \tag{9}$$

where $[S^{syr}]$ is the total surfactant concentration in the syringe (generally a constant).

Since eq 9 contains all the previously described contributions and parameters, by fitting the experimental ITC isotherms to it, it is possible to obtain the values of N_{agg}, $\Delta\mu^0_{agg}$, ΔH_{agg}, q_F^{dil}, q_{agg}^{dil}, and Q_b in a single fitting. A simulated annealing algorithm was employed to minimize the objective function (χ^2) given by eq 10, following the same protocol of previous publications.[40]

$$\chi^2 = (n - \nu)^{-1}\sum_i [(\Delta q_i^{exp} - \Delta q_i^{teo})([S^{syr}]\Delta V)]^2 \tag{10}$$

where n is the number of injections of the target isotherm (number of points consisting the heat profile), ν is the number of fitting parameters, and Δq_i^{exp} and Δq_i^{teo} are the experimental and theoretical (given by eq 9) stepwise molar heat corresponding to each titration. The standard deviation of the fitting parameters was estimated by the jackknife method,[41] which has been previously applied for other ITC analysis.[40]

https://doi.org/10.1021/acs.langmuir.1c01727
Langmuir XXXX, XXX, XXX−XXX

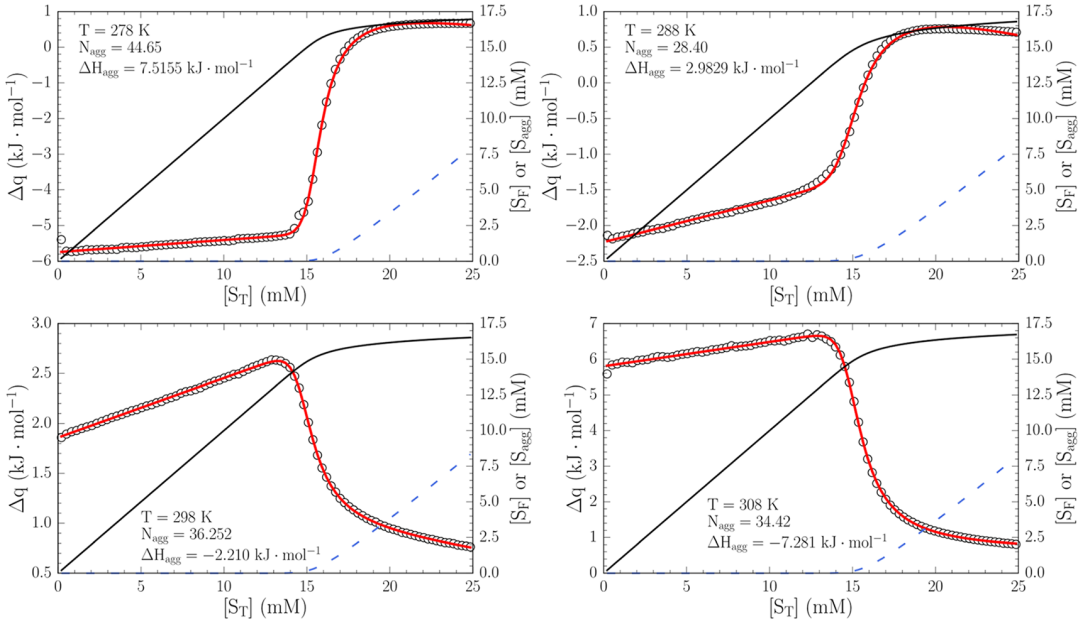


Figure 2. Experimental ITC isotherms (circles) together with the corresponding fitted curves (red solid line) obtained as indicated in the theoretical section for dodecyl trimethylammonium bromide (C_{12}TAB) at the temperatures indicated in the plots. The concentration of free surfactants (solid black line) as well as that of surfactant molecules in micelles (dashed blue line) are also included (both are referred to the secondary *y* axis). The enthalpy corresponding to the micelle formation process and the obtained aggregation number for each system are included in each plot. Other thermodynamic information obtained from the fittings is specified in Table 1.

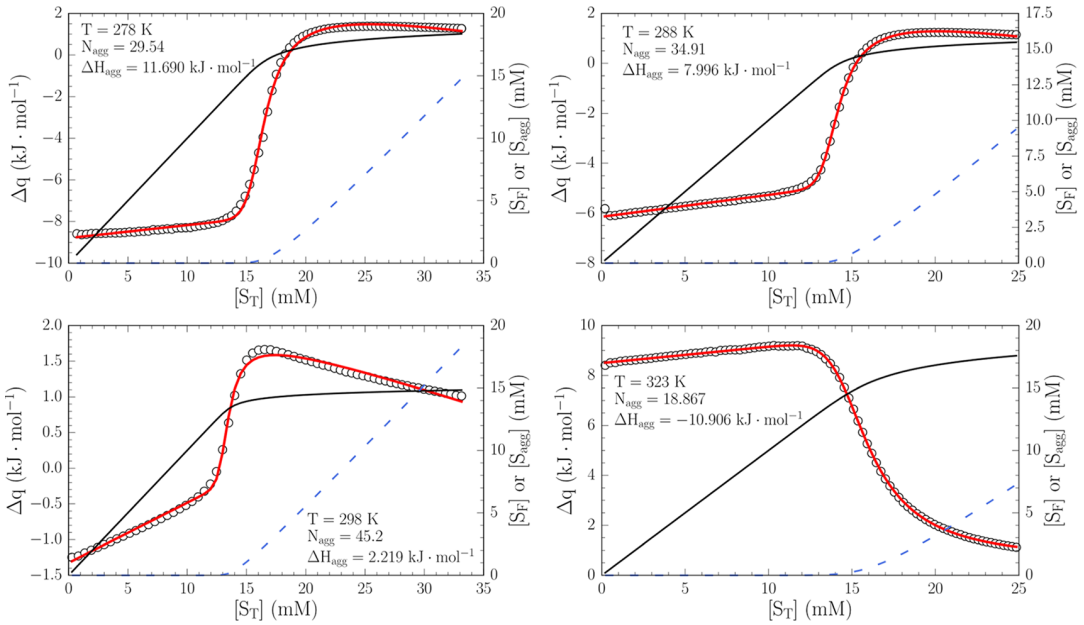


Figure 3. Experimental ITC isotherms (circles) together with the corresponding fitted curves (red solid line) obtained as indicated in the theoretical section for dodecyl methylimidazolium chloride ($[C_{12}mim^+][Cl^-]$) at the temperatures indicated in the plots. The concentration of free surfactants (solid black line) as well as that of surfactant molecules in micelles (dashed blue line) are also included (both are referred to the secondary *y* axis). The enthalpy corresponding to the micelle formation process and the obtained aggregation number for each system are included in each plot. Other thermodynamic information obtained from the fittings is specified in Table 1.

RESULTS AND DISCUSSION

Different methods for N_{agg} determination by ITC have already been introduced. Garidel *et al.*[31] as well as Majhi and Blume[25] proposed a calorimetric analysis based on ITC and on differential scanning calorimetry (DSC). Their scheme is simple and easy to understand, but it provides very low values for N_{agg}. They have reported a low sensitivity of the model as the aggregate grows in size. Olesen *et al.*[29] ended up with an alternative proposal that explicitly uses the *cmc* as a reference parameter. They perform an interesting treatment on the equations to overcome the correlation between the different parameters of the model as well as to make its mathematical implementation easier. These authors also explicitly consider the heat of dilution as a constant to all peaks in the isotherm. Šarac *et*

https://doi.org/10.1021/acs.langmuir.1c01727
Langmuir XXXX, XXX, XXX−XXX

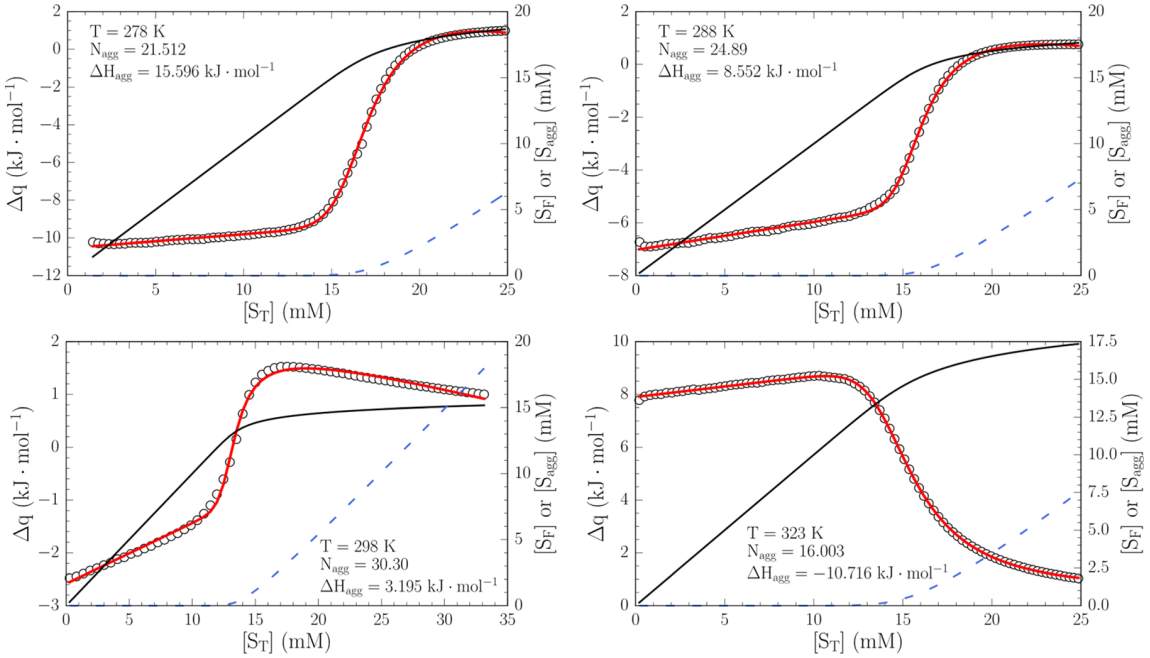


Figure 4. Experimental ITC isotherms (circles) together with the corresponding fitted curves (red solid line) obtained as indicated in the theoretical section for dodecyl methylimidazolium sulfonate ($[C_{12}mim^+][CH_3SO_3^-]$) at the temperatures indicated in the plots. The concentration of free surfactants (solid black line) as well as that of surfactant molecules in micelles (dashed blue line) are also included (both are referred to the secondary *y* axis). The enthalpy corresponding to the micelle formation process and the obtained aggregation number for each system are included in each plot. Other thermodynamic information obtained from the fittings is specified in Table 1.

al.[30] have also introduced an ITC-based approach for demicellization processes that also uses six fitting parameters including N_{agg}, $\Delta\mu^0_{agg}$, ΔH^0_{agg}, ΔC^0_{agg}, and two additional parameters that depend on the solvent properties at each temperature. These authors apply a global multitemperature fitting to reduce the number of degrees of freedom in the minimization process, thus increasing the statistical confidence. N_{agg} is considered as a constant for all the temperatures, and the dilution enthalpies of free monomers and micelles are disregarded in this work. A reason to introduce different approaches in the models is to prevent the cross-correlation between fitting parameters, in particular between N_{agg} and $\Delta\mu^0_{agg}$, as it has been pointed out by Lah *et al.*[42] This issue has been discussed in detail in a previous work that also uses the mass action law to determine N_{agg} from surface tension measurements.[19] In that work, it is shown that the cross-correlation between N_{agg} and $\Delta\mu^0_{agg}$ is restricted to a range of values that can be associated to the statistical uncertainties. Thus, beyond the uncertainties' interval, the cross-correlation is negligible. This is why we have decided to make an effort to provide a reasonable estimation of the statistical uncertainties of all the fitting parameters. Note that this estimation does not consider other possible sources of error that can significantly increase the uncertainty of the parameters with physical meaning. Tso *et al.* have also provided a method to analyze demicellization ITC experiments based on the pseudo-phase separation approach, although it does not provide aggregation numbers.[43] In contrast to several previous approaches,[25,29−31] we have included two independent dilution contributions for both the free monomers and the micelles, which makes the description of the molar heat profile more realistic. An alternative model that also considers the dilution enthalpy of free monomers and micelles in a completely different way has been recently proposed.[32−34] Our choice to model these contributions is based on the linear interpolation between the minimum dilution enthalpy, which by definition should correspond to the point where the concentrations of the mixed liquids are identical, and the maximum, expected when the concentration difference between the cell and syringe is maximum. In this way, a single parameter is required to model each dilution contribution and the results are easy to interpretate. Additionally, a computational code has been developed to fit the whole isotherm to the same equations, *i.e.*, the same equilibria and approaches are employed over the whole concentration range. This strategy is opposite to that introduced by Olesen *et al.*, who made an effort to decouple the different contributions and to simplify the equations. Using the model described in the Theory section, a good description for a wide variety of ITC profiles has been obtained (Figures 2−5).

The obtained N_{agg} values for all the systems and temperatures range from 10 to 45 are in good agreement with those obtained from fluorescence experiments (Table 1) with the exception of $[C_{10}C_{10}mim^+][Cl^-]$, for which the values obtained from fluorescence are clearly lower than those from ITC. From previous studies,[44] this behavior can be explained because of its more complex aggregation process due to the presence of the double chain and the formation of pre-micelles. Notably, there are no clear trends with temperature, although the differences in N_{agg} for the same system as a function of temperature are significant in several cases. It is worth to comment on the case of $[C_{12}mim^+][CH_3SO_3^-]$, with N_{agg} = 24.89, 30.30, and 16.003 at 288, 298, and 323 K, respectively (obtained by ITC), and N_{agg} = 19.2, 33.1, and 19.5 at the same temperatures (obtained by fluorescence) (Table 1). Thus, based on the available experimental data and on the results of our fittings, it seems that significant dependence of N_{agg} with temperature can exist and that this dependence does not change monotonically. The uncertainties reported in Table 1 were obtained as 1.96 times the standard deviation upon applying the jackknife method to the

https://doi.org/10.1021/acs.langmuir.1c01727
Langmuir XXXX, XXX, XXX−XXX

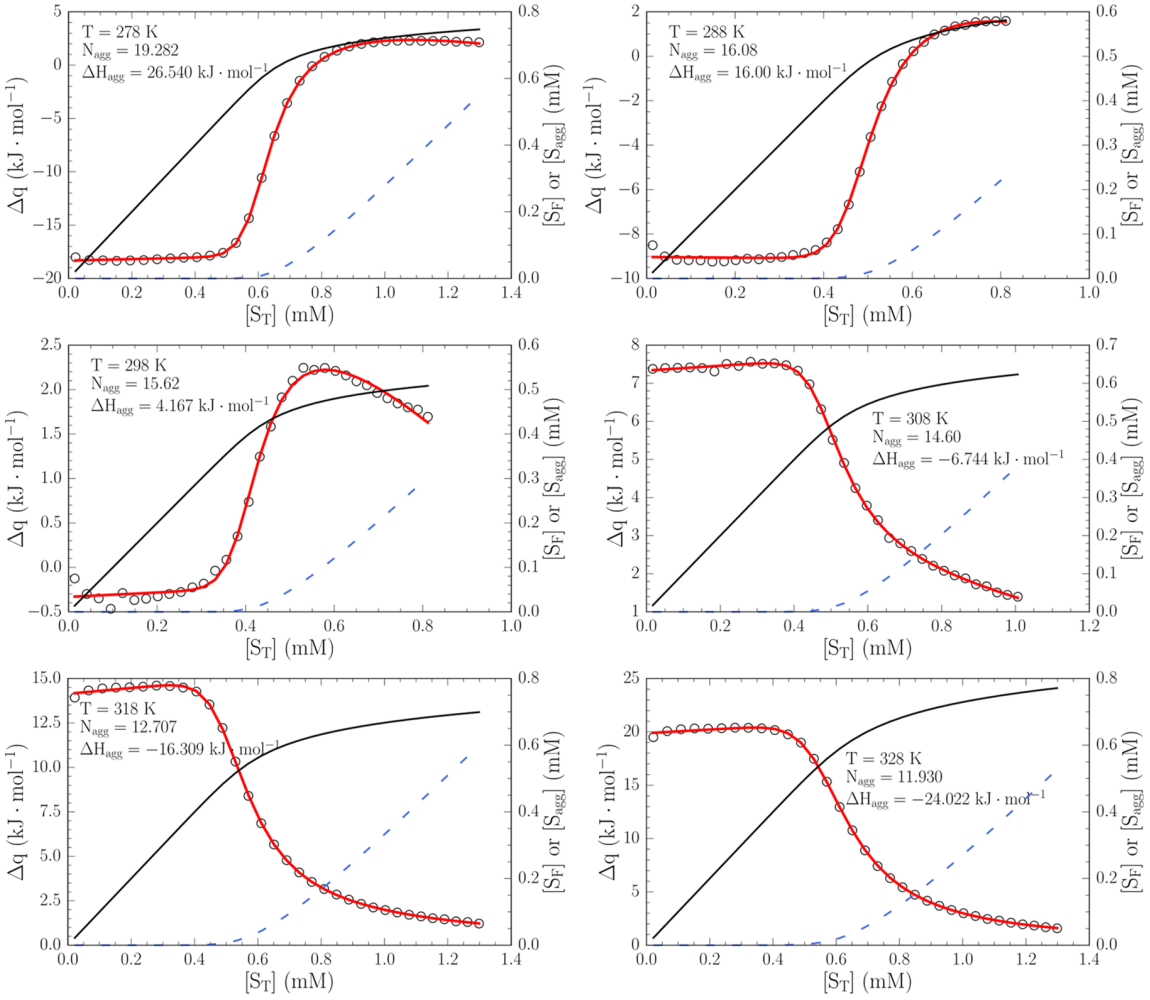


Figure 5. Experimental ITC isotherms (circles) together with the corresponding fitted curves (red solid line) obtained as indicated in the theoretical section for didecyl methylimidazolium chloride ($[C_{10}C_{10}mim^+][Cl^-]$) at the temperatures indicated in the plots. The concentration of free surfactants (solid black line) as well as that of surfactant molecules in micelles (dashed blue line) are also included (both are referred to the secondary *y* axis). The enthalpy corresponding to the micelle formation process and the obtained aggregation number for each system are included in each plot. Other thermodynamic information obtained from the fittings is specified in Table 1.

isotherms. Actual errors in the parameters, mainly N_{agg}, are expected to be significantly larger than these statistical uncertainties due to systematic errors as well as noise in the ITC measurements. In particular, errors for N_{agg} are not expected to be lower than 1.

A large list of N_{agg} values has been reported for the studied systems under different conditions (Table S1),[30,45−79] principally for C_{12}TAB (Figure 6). These values exhibit a significant discrepancy that is mainly due to the concentration where they have been measured. These literature results reflect the difficulty to obtain reliable N_{agg} values under controlled conditions.

No literature data is available for comparison to the rest of the fitting parameters, but it is worth to discuss the results by themselves. The $\Delta\mu^0_{agg}$ values are always negative, as expected for systems spontaneously forming micelles, and they also show temperature dependence for all the solutions. In this case, the values exhibit a clear trend to decrease as the temperature increases. The trend for ΔH_{agg} is perfectly linear, with positive values at low temperatures and negative values at high temperatures. By interpolation of these data, it is possible to find a temperature where the process is fully entropic. This happens at 294, 302, 304, and 303 K for C_{12}TAB, $[C_{12}mim^+][Cl^-]$, $[C_{12}mim^+][CH_3SO_3^-]$, and $[C_{10}C_{10}mim^+][Cl^-]$, respectively. In the vicinity of those temperatures, the heat corresponding to the demicellization is weak (Figures 2−5), although other contributions such as those corresponding to the dilution of monomers and micelles are relatively high in these cases. Consequently, the scale of the plots close to those temperatures is more amplified and the fittings seem to be worse than those corresponding to other temperatures. This does not seem to be translated in significantly larger errors for the parameters obtained from those experiments, although the highest differences between results obtained from fluorescence and ITC are precisely those corresponding to $[C_{12}mim^+][Cl^-]$ at 298 K, one of the experiments with the lowest micellization enthalpy. The behavior of the dilution contributions of micelles is also quite linear with temperature, with negative slopes of −0.266, −0.345, −0.850, and −0.652 kJ·mol^{-1}·K^{-1} for C_{12}TAB, $[C_{12}mim^+][Cl^-]$, $[C_{12}mim^+][CH_3SO_3^-]$, and $[C_{10}C_{10}mim^+][Cl^-]$, respectively. The enthalpy of dilution of free monomers also decreases with temperature although the trend is less clear.

The sensitivity of the model to the different parameters over the whole concentration range was examined by simulating

https://doi.org/10.1021/acs.langmuir.1c01727
Langmuir XXXX, XXX, XXX−XXX

Table 1. Model Parameter Values Obtained from the Fitting of the ITC Isotherms to the Model Described in the Theory Section[b]

	T	N_{agg}		$\Delta\mu^0_{agg}$	ΔH_{agg}	q_F^{dil}	q_{agg}^{dil}	Q_b
compound	K	ITC	fluorescence[a]	kJ·mol^{-1}	kJ·mol^{-1}	kJ·mol^{-1}	kJ·mol^{-1}	mJ
C_{12}TAB	278	44.65 ± 0.17		−8.9780 ± 0.0020	7.5155 ± 0.0076	−5.092 ± 0.025	8.96 ± 0.14	−2.881 ± 0.051
	288	28.40 ± 0.17	28.1	−9.0977 ± 0.0053	2.9829 ± 0.0082	−8.747 ± 0.026	9.50 ± 0.10	−3.090 ± 0.038
	298	36.252 ± 0.061	30	−9.5943 ± 0.0011	−2.210 ± 0.018	−8.948 ± 0.048	4.475 ± 0.016	−1.3357 ± 0.0062
	308	34.42 ± 0.16		−9.8543 ± 0.0032	−7.281 ± 0.036	−10.237 ± 0.090	1.76 ± 0.13	−0.409 ± 0.047
	323		29.8					
$[C_{12}mim^+][Cl^-]$	278	29.54 ± 0.18		−8.6461 ± 0.0032	11.690 ± 0.026	−12.26 ± 0.15	16.56 ± 0.19	−7.171 ± 0.095
	288	34.91 ± 0.17	31.5	−9.4183 ± 0.0032	7.996 ± 0.015	−13.16 ± 0.14	14.02 ± 0.18	−4.518 ± 0.067
	298	45.2 ± 1.0	29.4	−10.0034 ± 0.0091	2.219 ± 0.011	−16.823 ± 0.094	10.621 ± 0.091	−6.203 ± 0.072
	323	18.867 ± 0.058		−9.7335 ± 0.0041	−10.906 ± 0.026	−9.869 ± 0.055	1.30 ± 0.42	−0.32 ± 0.13
$[C_{12}mim^+][CH_3SO_3^-]$	278	21.512 ± 0.082		−8.3266 ± 0.0041	15.596 ± 0.051	−10.978 ± 0.075	43.30 ± 0.76	−14.72 ± 0.27
	288	24.89 ± 0.15	19.2	−8.8865 ± 0.0052	8.552 ± 0.025	−15.80 ± 0.12	19.13 ± 0.36	−6.35 ± 0.13
	298	30.30 ± 0.46	33.1	−9.770 ± 0.014	3.195 ± 0.015	−22.95 ± 0.12	11.89 ± 0.12	−6.952 ± 0.080
	323	16.003 ± 0.030	19.5	−9.6018 ± 0.0029	−10.716 ± 0.016	−11.951 ± 0.038	0.50 ± 0.19	−0.053 ± 0.070
$[C_{10}C_{10}mim^+][Cl^-]$	278	19.282 ± 0.070		−15.3862 ± 0.0044	26.540 ± 0.061	−5.49 ± 0.31	34.60 ± 0.42	−1.596 ± 0.022
	288	16.08 ± 0.15	7.6	−16.180 ± 0.017	16.00 ± 0.11	0.92 ± 0.38	31.9 ± 1.1	−0.912 ± 0.033
	298	15.62 ± 0.35	6.6	−17.069 ± 0.043	4.167 ± 0.065	−1.16 ± 0.32	24.88 ± 0.51	−0.736 ± 0.016
	308	14.60 ± 0.14	5.2	−17.050 ± 0.020	−6.744 ± 0.049	−3.83 ± 0.11	15.23 ± 0.30	−0.549 ± 0.012
	318	12.707 ± 0.045	4.1	−17.1379 ± 0.0080	−16.309 ± 0.061	−13.21 ± 0.60	7.36 ± 0.17	−0.359 ± 0.011
	328	11.93 ± 0.053	6.6	−17.254 ± 0.011	−24.022 ± 0.082	−13.70 ± 0.70	5.65 ± 0.44	−0.295 ± 0.023

[a]The uncertainty of the aggregation numbers obtained from fluorescence measurements was estimated to be around 10% of the values in all cases; this uncertainty is obtained by applying the classical propagation error expression to eq 1; the main contribution to the error is the concentration difference in the denominator of eq 1 since the experiments are performed close to the *cmc*. [b]The uncertainties were obtained as 1.96 times the standard deviation upon applying the jackknife method to the isotherms (see Theory section); results for the aggregation numbers obtained from the available fluorescence experiments are also included.

https://doi.org/10.1021/acs.langmuir.1c01727
Langmuir XXXX, XXX, XXX−XXX

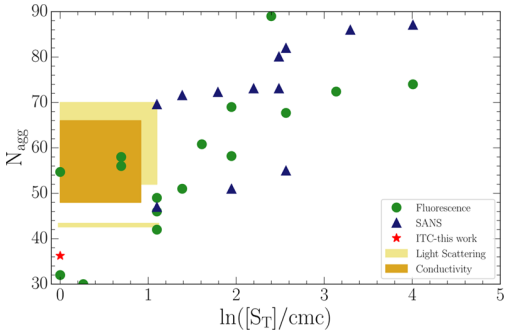


Figure 6. N_{agg} values obtained for C_{12}TAB at 298 K from different sources. The complete list and the corresponding references can be found in Table S1.

dilution curves. These curves were obtained by varying one of the model parameters at a time (except for Q_b, which is just a constant offset) while keeping constant the rest of them (Figure 7). The model proved to be highly sensitive to changes in the aggregation number of low values of this parameter. As the aggregation number increases, the sensitivity is reduced to a narrow range of concentrations, around the inflection point of the isotherm. This means that the ITC experiment can be designed to optimize the determination of N_{agg}, by increasing the sampling in that concentration region. Additionally, the simulated curves suggest that this model is well suited to determine the degree of oligomerization of a given molecule when this number is expected to be low, for instance, in the case of proteins or peptides.

It has been said that N_{agg} and $\Delta\mu^0_{agg}$ are highly coupled. We have previously shown that this coupling is limited to a relatively narrow range of both parameters, which can be bound by the

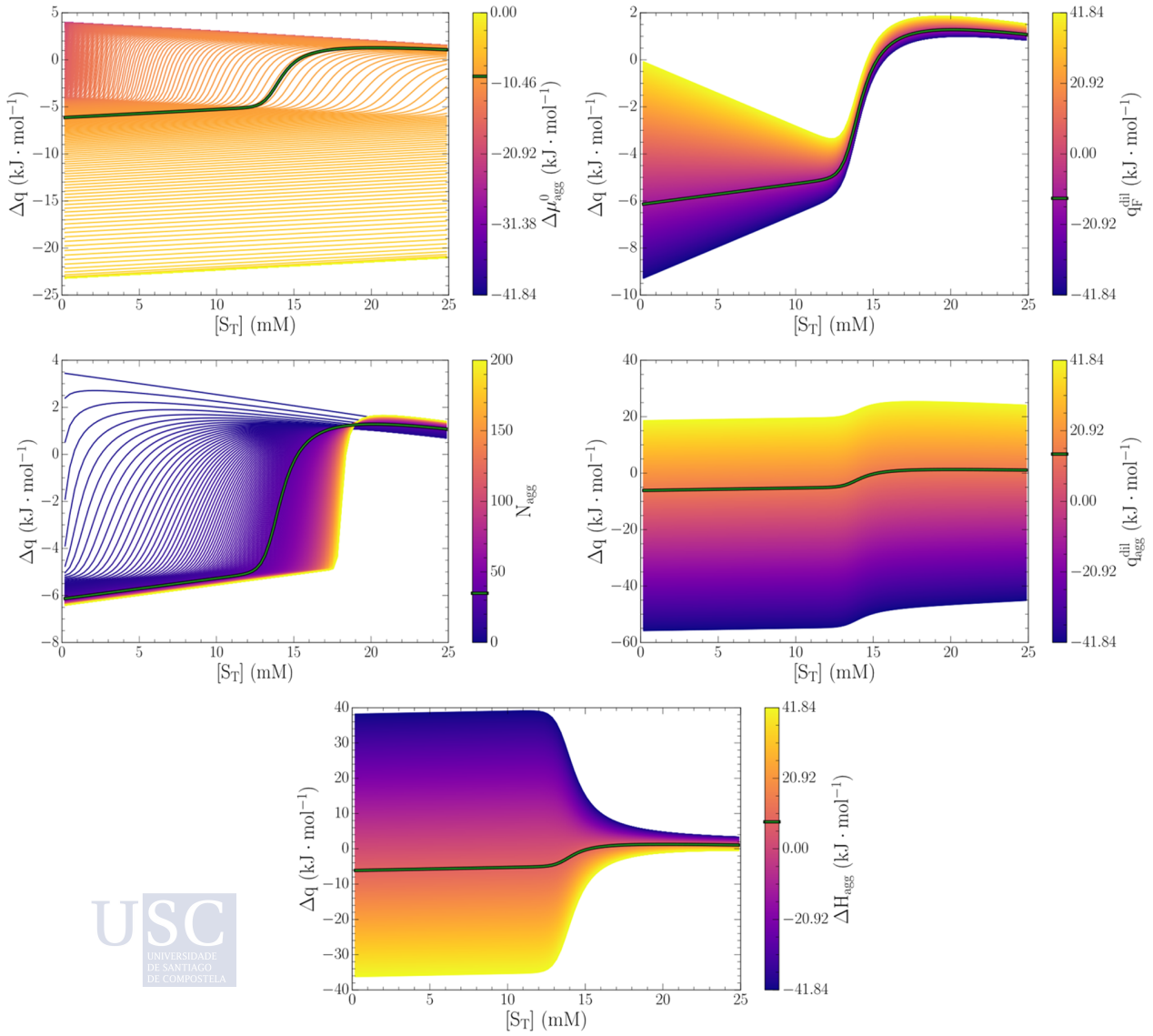


Figure 7. Simulated isotherms obtained for dilution experiments using the model described in the Theory section. A reference set of parameters given by N_{agg} = 34.91, $\Delta\mu^0_{agg}$ = −9.4183 kJ·mol^{-1}, ΔH_{agg} = 7.996 kJ·mol^{-1}, q_F^{dil} = −13.16 kJ·mol^{-1}, q_{agg}^{dil} = 14.02 kJ·mol^{-1}, and Q_b = −4.518 mJ was employed and represented by a green solid line. All the parameters are kept constant except that indicated in each plot, which varies in the range indicated in the corresponding color bar.

https://doi.org/10.1021/acs.langmuir.1c01727
Langmuir XXXX, XXX, XXX−XXX

uncertainties.[19] It is seen here that the response of the model to the variation of each of these parameters is different, thus indicating that an effective fitting protocol should be able to distinguish them. The impact of ΔH_{agg} is quite obvious, controlling the Δq drop/rise between both sides of the inflection point. The dilution enthalpies of free monomers and micelles also exhibit the expected behavior. The dilution of free monomers defines the slope along the low concentration region, with a much lower impact at higher concentrations. In contrast, the dilution of micelles is similar to a flat offset over all isotherms. This is because the concentration of the injected solution, and so the concentration of injected micelles, is constant along the whole experiment. The derivatives of the simulated curves with respect to each fitting parameter as a function of the concentration provide a complementary view of the previous discussion (Figure S1), confirming the abovementioned conclusions. Overall, this analysis shows that, in general, the different parameters of the model affect in a different way the different concentration ranges, and so they can be simultaneously fitted provided that enough sampling is considered and the experimental noise is reasonable. This information can also be employed to design experiments aimed to optimize the determination of certain parameters, by increasing the sampling of the experiment in the most sensitive region of the concentration range.

CONCLUSIONS AND PERSPECTIVES

A new approach to perform thermodynamic characterization of surfactant dilution experiments is proposed and tested here using experimental data for a variety of systems that exhibit a range of molar heat vs concentration profiles. The fitting parameters (N_{agg}, $\Delta\mu^0_{agg}$, ΔH_{agg}, q_F^{dil}, q_{agg}^{dil}, and Q_b) showed to be sensitive to the concentration and also to the temperature. In general, the obtained aggregation numbers agree well with a range of values obtained from fluorescence experiments and also from other methods and sources previously reported. However, a large discrepancy in the determination of N_{agg} has been found in the literature, reflecting the difficulty to determine this structural parameter. The analysis performed using simulation curves indicates that the experiments can be designed to optimize the determination of the aggregation numbers, by increasing the sampling along the inflection point of the isotherm. It is also suggested that this model could be employed to predict the oligomerization state of more complex systems, such as proteins or peptides, since it showed to be highly sensitive to the stoichiometry of the self-assembled structure at low aggregation numbers.

Some obvious limitations of the model described in the present work are that it ignores the presence of counterions as well as the distribution of sizes and shapes of the aggregates. In order to explicitly consider these variables, more fitting parameters should be included in the equations, which is not feasible considering the analysis of the uncertainties and concentration data dependence illustrated in Figure 7. However, using a more elaborate protocol, by combining multitemperature experiments with a global fitting, it is possible to reduce the number of degrees of freedom during the minimization process. This has already been done by several authors to explicitly include the effect of counterions.[32−34] Although this method is definitely interesting, it cannot be applied to single demicellization isotherms, which is the aim of the present work, due to the large number of fitting parameters required.

A similar model to that described and tested in the present work, based on surface tension measurements, has been proposed a few years ago.[19] Both approaches share N_{agg} and $\Delta\mu^0_{agg}$ as fitting parameters. Equivalent proposals can be developed for different experimental methods such as spectroscopy, light scattering, or any other physical observable that is sensitive to the presence of molecular assemblies in solution. This opens the possibility to orthogonal multitechnique analysis that would provide much more accurate values for the fitting parameters. Additionally, the extension of this model to consider hybrid assemblies is straightforward from the theoretical point of view, and the corresponding results would be useful to determine the proportion of different subunits in a complex heteroassembly. The limitation of the model for this application would be the amount of information required to get reliable results since the number of fitting parameters would increase and so more data would be required to restrain the additional degrees of freedom. This limitation is expected to be amended with the increasing automation of the instruments, allowing easier, cheaper, and faster collection of experimental measurements. The development of public software will also facilitate the analysis of the data as well as the comparison between different sources. The model described in the present paper is expected to be implemented in the AFFINImeter platform.[36]

ASSOCIATED CONTENT

Supporting Information

The Supporting Information is available free of charge at https://pubs.acs.org/doi/10.1021/acs.langmuir.1c01727.

(Table S1) A comparison between aggregation numbers obtained from different sources, with the corresponding references and (Figure S1) the derivatives of simulated isotherms with respect to each of the fitting parameters (PDF)

AUTHOR INFORMATION

Corresponding Author

Ángel Piñeiro − *Departamento de Fisica de Aplicada, Facultade de Fisica, Universidade de Santiago de Compostela, E-15782 Santiago de Compostela, Spain;* orcid.org/0000-0001-9350-8468; Email: Angel.Pineiro@usc.es

Authors

Pablo F. Garrido − *Departamento de Fisica de Aplicada, Facultade de Fisica, Universidade de Santiago de Compostela, E-15782 Santiago de Compostela, Spain*

Pedro Rodríguez-Dafonte − *CIQUS, Departamento de Quimica Física, Universidade de Santiago de Compostela, E-15782 Santiago de Compostela, Spain*

Luis García-Río − *CIQUS, Departamento de Quimica Física, Universidade de Santiago de Compostela, E-15782 Santiago de Compostela, Spain*

Complete contact information is available at: https://pubs.acs.org/10.1021/acs.langmuir.1c01727

Notes

The authors declare no competing financial interest.

ACKNOWLEDGMENTS

The authors thank the financial support of the Spanish Ministry of Economy and Competitiveness and the Agencia Estatal de Investigación (AEI) (projects MAT2015-71826-P, CTQ2017-

84254-P, and PID2019-111327GB-I00 to Á.P.), Xunta de Galicia (GR 2007/085 and IN607C 2016/03), and Centro Singular de Investigación de Galicia accreditation 2016-2019 (ED431G/09). P.F.G. thanks the Spanish Ministry of Economy and Competitiveness and the European Social Fund for his predoctoral research grant, reference BES-2016-076761. These research projects were partially supported by European ERDF Funds (MCIU/AEI/FEDER, EU). Facilities provided by the Galician Supercomputing Centre (CESGA) are also acknowledged.

REFERENCES

(1) *Surfactants*; Schramm, L. L., Ed.; Cambridge University Press, 2000, DOI: 10.1017/CBO9780511524844.
(2) Mukherjee, N.; Bansal, B.; Chen, X. D. Measurement of Surface Tension of Homogenised Milks. *Int. J. Food Eng.* **2005**, *1*, 1−6.
(3) Mulligan, C. N. Environmental Applications for Biosurfactants. *Environ. Pollut.* **2005**, *133*, 183−198.
(4) Karbowiak, T.; Debeaufort, F.; Voilley, A. Importance of Surface Tension Characterization for Food, Pharmaceutical and Packaging Products: A Review. *Crit. Rev. Food Sci. Nutr.* **2006**, *46*, 391−407.
(5) Hill, C.; Eastoe, J. Foams: From Nature to Industry. *Advances in Colloid and Interface Science*. Elsevier B.V. September 1, 2017, pp. 496−513, DOI: 10.1016/j.cis.2017.05.013.
(6) Seo, S.; Mastiani, M.; Mosavati, B.; Peters, D. M.; Mandin, P.; Kim, M. Performance Evaluation of Environmentally Benign Nonionic Biosurfactant for Enhanced Oil Recovery. *Fuel* **2018**, *234*, 48−55.
(7) Farias, C. B. B.; Almeida, F. C. G.; Silva, I. A.; Souza, T. C.; Meira, H. M.; Soares da Silva, R. d. C. F.; Luna, J. M.; Santos, V. A.; Converti, A.; Banat, I. M.; Sarubbo, L. A. Production of Green Surfactants: Market Prospects. *Electron. J. Biotechnol.* **2021**, *51*, 28−39.
(8) Souza, E. C.; Vessoni-Penna, T. C.; de Souza Oliveira, R. P. Biosurfactant-Enhanced Hydrocarbon Bioremediation: An Overview. *Int. Biodeterior. Biodegrad.* **2014**, *89*, 88−94.
(9) Varjani, S. J.; Upasani, V. N. Critical Review on Biosurfactant Analysis, Purification and Characterization Using Rhamnolipid as a Model Biosurfactant. *Bioresour. Technol.* **2017**, *232*, 389−397.
(10) Jimoh, A. A.; Lin, J. Biosurfactant: A New Frontier for Greener Technology and Environmental Sustainability. *Ecotoxicol. Environ. Saf.* **2019**, *184*, 109607.
(11) Hu, J.; Luo, J.; Zhu, Z.; Chen, B.; Ye, X.; Zhu, P.; Zhang, B. Multi-Scale Biosurfactant Production by Bacillus Subtilis Using Tuna Fish Waste as Substrate. *Catalysts* **2021**, *11*, 456.
(12) Silva, M. E. T.; Duvoisin, S., Jr.; Oliveira, R. L.; Banhos, E. F.; Souza, A. Q. L.; Albuquerque, P. M. Biosurfactant Production of Piper Hispidum Endophytic Fungi. *J. Appl. Microbiol.* **2021**, *130*, 561−569.
(13) Nunes, A.; Marques, P.; Marto, J.; Ascenso, A.; Gonçalves, L.; Fitas, M.; Pinto, P.; Sotomayor, J.; Ribeiro, H. M. Sugar Surfactant-Based Shampoos. *J. Surfactants Deterg.* **2020**, *23*, 809−819.
(14) Adamson, A. W.; Gast, A. P. *Physical Chemistry of Surfaces*, 6th ed.; John Wiley & Sons: New York, 1997.
(15) Tummino, P. J.; Gafni, A. Determination of the Aggregation Number of Detergent Micelles Using Steady-State Fluorescence Quenching. *Biophys. J.* **1993**, *64*, 1580−1587.
(16) Attwood, D.; Jagielski, C. E.; McDonald, C.; Wilkinson, A. E. The Solution Properties of Some Nonionic Surface-Active Agents in Non-Aqueous Solvents. *Colloid Polym. Sci.* **1974**, *252*, 991−996.
(17) Penfold, J.; Staples, E.; Tucker, I.; Cummins, P. The Structure of Nonionic Micelles in Less Polar Solvents. *J. Colloid Interface Sci.* **1997**, *185*, 424−431.
(18) Capalbi, A.; Gente, G.; La Mesa, C. Solution Properties of Alkyl Glucosides, Alkyl Thioglucosides and Alkyl Maltosides. *Colloids Surf., A* **2004**, *246*, 99−108.
(19) Garrido, P. F.; Brocos, P.; Amigo, A.; García-Río, L.; Gracia-Fadrique, J.; Piñeiro, Á. STAND: Surface Tension for Aggregation Number Determination. *Langmuir* **2016**, *32*, 3917−3925.
(20) Rusanov, A. I. On the Problem of Determining Aggregation Numbers from Surface Tension Measurements. *Langmuir* **2017**, *33*, 12643−12650.
(21) López-Cervantes, J. L.; Sandoval-Ibarra, F. D.; Gracia-Fadrique, J. Equilibrium Model for Estimating Micellar Aggregation Number from Surface Equation. *Fluid Phase Equilib.* **2021**, *528*, 112844.
(22) Hassan, N.; Ruso, J. M.; Piñeiro, Á. Hydrogenated/Fluorinated Catanionic Surfactants as Potential Templates for Nanostructure Design. *Langmuir* **2011**, *27*, 9719−9728.
(23) Garrido, P. F.; Bastos, M.; Piñeiro, Á. Method for Determining Interfacial Tension. WO2020043792A1, 2020.
(24) Garrido, P. F.; Bastos, M.; Velázquez-Campoy, A.; Dumas, P.; Piñeiro, Á. Fluid Interface Calorimetry. *J. Colloid Interface Sci.* **2021**, *596*, 119−129.
(25) Majhi, P. R.; Blume, A. Thermodynamic Characterization of Temperature-Induced Micellization and Demicellization of Detergents Studied by Differential Scanning Calorimetry. *Langmuir* **2001**, *17*, 3844−3851.
(26) D'Andrea, M. G.; Domingues, C. C.; Malheiros, S. V. P.; Neto, F. G.; Barbosa, L. R. S.; Itri, R.; Almeida, F. C. L.; De Paula, E.; Bianconi, M. L. Thermodynamic and Structural Characterization of Zwitterionic Micelles of the Membrane Protein Solubilizing Amidosulfobetaine Surfactants ASB-14 and ASB-16. *Langmuir* **2011**, *27*, 8248−8256.
(27) Loh, W.; Brinatti, C.; Tam, K. C. Use of Isothermal Titration Calorimetry to Study Surfactant Aggregation in Colloidal Systems. *Biochim. Biophys. Acta, Gen. Subj.* **2016**, *1860*, 999−1016.
(28) Heintz, A.; Lehmann, J. K.; Kozlova, S. A.; Balantseva, E. V.; Bazyleva, A. B.; Ondo, D. Micelle Formation of Alkylimidazolium Ionic Liquids in Water and in Ethylammonium Nitrate Ionic Liquid: A Calorimetric Study. *Fluid Phase Equilib.* **2010**, *294*, 187−196.
(29) Olesen, N. E.; Holm, R.; Westh, P. Determination of the Aggregation Number for Micelles by Isothermal Titration Calorimetry. *Thermochim. Acta* **2014**, *588*, 28−37.
(30) Šarac, B.; Medoš, Ž.; Cognigni, A.; Bica, K.; Chen, L.-J.; Bešter-Rogač, M. Thermodynamic Study for Micellization of Imidazolium Based Surface Active Ionic Liquids in Water: Effect of Alkyl Chain Length and Anions. *Colloids Surf., A* **2017**, *532*, 609−617.
(31) Garidel, P.; Hildebrand, A.; Neubert, R.; Blume, A. Thermodynamic Characterization of Bile Salt Aggregation as a Function of Temperature and Ionic Strength Using Isothermal Titration Calorimetry. *Langmuir* **2000**, *16*, 5267−5275.
(32) Medoš, Ž.; Bešter-Rogač, M. Two-Step Micellization Model: The Case of Long-Chain Carboxylates in Water. *Langmuir* **2017**, *33*, 7722−7731.
(33) Čobanov, I.; Šarac, B.; Medoš, Ž.; Vraneš, M.; Gadžurić, S.; Zec, N.; Bešter-Rogač, M. Effect of Cationic Structure of Surface Active Ionic Liquids on Their Micellization: A Thermodynamic Study. *J. Mol. Liq.* **2018**, *271*, 437−442.
(34) Medoš, Ž.; Friesen, S.; Buchner, R.; Bešter-Rogač, M. Interplay between Aggregation Number, Micelle Charge and Hydration of Catanionic Surfactants. *Phys. Chem. Chem. Phys.* **2020**, *22*, 9998−10009.
(35) Muñoz, E.; Piñeiro, A. AFFINImeter Software: From Its Beginnings to Future Trends- A Literature Review. *J. Appl. Bioanal.* **2018**, *4*, 124−139.
(36) AFFINImeter- The software for molecular interactions https://www.affinimeter.com (accessed Jun 7, 2021).
(37) Brown, P.; Butts, C. P.; Eastoe, J.; Fermin, D.; Grillo, I.; Lee, H. C.; Parker, D.; Plana, D.; Richardson, R. M. Anionic Surfactant Ionic Liquids with 1-Butyl-3-Methyl-Imidazolium Cations: Characterization and Application. *Langmuir* **2012**, *28*, 2502−2509.
(38) Basílio, N.; Garcia-Rio, L. Calixarene-Based Surfactants: Conformational-Dependent Solvation Shells for the Alkyl Chains. *ChemPhysChem* **2012**, *13*, 2368−2376.
(39) Turro, N. J.; Yekta, A. Luminescent Probes for Detergent Solutions. A Simple Procedure for Determination of the Mean Aggregation Number of Micelles. *J. Am. Chem. Soc.* **1978**, *100*, 5951−5952.

https://doi.org/10.1021/acs.langmuir.1c01727
Langmuir XXXX, XXX, XXX−XXX

(40) Piñeiro, Á.; Muñoz, E.; Sabín, J.; Costas, M.; Bastos, M.; Velázquez-Campoy, A.; Garrido, P. F.; Dumas, P.; Ennifar, E.; García-Río, L.; Rial, J.; Pérez, D.; Fraga, P.; Rodríguez, A.; Cotelo, C. AFFINImeter: A Software to Analyze Molecular Recognition Processes from Experimental Data. *Anal. Biochem.* **2019**, *577*, 117−134.
(41) Efron, B.; Stein, C. The Jackknife Estimate of Variance. *Ann. Stat.* **1981**, *9*, 586−596.
(42) Lah, J.; Bešter-Rogač, M.; Perger, T. M.; Vesnaver, G. Energetics in Correlation with Structural Features: The Case of Micellization. *J. Phys. Chem. B* **2006**, *110*, 23279−23291.
(43) Tso, S. C.; Mahler, F.; Höring, J.; Keller, S.; Brautigam, C. A. Fast and Robust Quantification of Detergent Micellization Thermodynamics from Isothermal Titration Calorimetry. *Anal. Chem.* **2020**, *92*, 1154−1161.
(44) Figueira-González, M.; Francisco, V.; García-Río, L.; Marques, E. F.; Parajó, M.; Rodríguez-Dafonte, P. Self-Aggregation Properties of Ionic Liquid 1,3-Didecyl-2-Methylimidazolium Chloride in Aqueous Solution: From Spheres to Cylinders to Bilayers. *J. Phys. Chem. B* **2013**, *117*, 2926−2937.
(45) Tehrani-Bagha, A. R.; Kärnbratt, J.; Löfroth, J. E.; Holmberg, K. Cationic Ester-Containing Gemini Surfactants: Determination of Aggregation Numbers by Time-Resolved Fluorescence Quenching. *J. Colloid Interface Sci.* **2012**, *376*, 126−132.
(46) Pal, A.; Pillania, A. Modulating Effect of Ionic Liquid 1-Butyl-2,3-Dimethylimidazolium Chloride on Micellization Behaviour of Cationic Surfactant Dodecyltrimethylammonium Bromide in Aqueous Media. *Fluid Phase Equilib.* **2015**, *389*, 67−73.
(47) Berr, S.; Jones, R. R. M.; Johnson, J. S., Jr. Effect of Counterion on the Size and Charge of Alkyltrimethylammonium Halide Micelles as a Function of Chain Length and Concentration as Determined by Small-Angle Neutron Scattering. *J. Phys. Chem.* **1992**, *96*, 5611−5614.
(48) Jalšenjak, N.; Težak, Đ. A New Method for Simultaneous Estimation of Micellization Parameters from Conductometric Data. *Chem. - Eur. J.* **2004**, *10*, 5000−5007.
(49) Pal, A.; Pillania, A. Thermodynamic and Aggregation Properties of Aqueous Dodecyltrimethylammonium Bromide in the Presence of Hydrophilic Ionic Liquid 1,2-Dimethyl-3-Octylimidazolium Chloride. *J. Mol. Liq.* **2015**, *212*, 818−824.
(50) Anacker, E. W.; Rush, R. M.; Johnson, J. S. Equilibrium Ultracentrifugation and Light Scattering of Sodium Lauryl Sulfate and Dodecyltrimethylammonium Bromide Solutions. *J. Phys. Chem.* **1964**, *68*, 81−93.
(51) Danov, K. D.; Kralchevsky, P. A.; Ananthapadmanabhan, K. P. Micelle-Monomer Equilibria in Solutions of Ionic Surfactants and in Ionic-Nonionic Mixtures: A Generalized Phase Separation Model. *Adv. Colloid Interface Sci.* **2014**, *206*, 17−45.
(52) Moyá, M. L.; Rodríguez, A.; del Mar Graciani, M.; Fernández, G. Role of the Solvophobic Effect on Micellization. *J. Colloid Interface Sci.* **2007**, *316*, 787−795.
(53) Junquera, E.; Aicart, E. Mixed Micellization of Dodecylethyldimethylammonium Bromide and Dodecyltrimethylammonium Bromide in Aqueous Solution. *Langmuir* **2002**, *18*, 9250−9258.
(54) Rodríguez, A.; Junquera, E.; Del Burgo, P.; Aicart, E. Conductometric and Spectrofluorimetric Characterization of the Mixed Micelles Constituted by Dodecyltrimethylammonium Bromide and a Tricyclic Antidepressant Drug in Aqueous Solution. *J. Colloid Interface Sci.* **2004**, *269*, 476−483.
(55) Caponetti, E.; Martino, D. C.; Floriano, M. A.; Triolo, R.; Wignall, G. D. Effect of Crown Ether 1,4,7,10,13,16-Hexaoxacyclooctadecane on the Structure of Sodium Dodecyl Sulfate and Dodecyltrimethylammonium Bromide Aqueous Micellar Solutions. *Langmuir* **1995**, *11*, 2464−2470.
(56) Pisárčik, M.; Devínsky, F.; Pupák, M. Determination of Micelle Aggregation Numbers of Alkyltrimethylammonium Bromide and Sodium Dodecyl Sulfate Surfactants Using Time-Resolved Fluorescence Quenching. *Open Chem.* **2015**, *13*, 922−931.
(57) Herrington, K. L.; Kaler, E. W.; Miller, D. D.; Zasadzinski, J. A.; Chiruvolu, S. Phase Behavior of Aqueous Mixtures of Dodecyltrimethylammonium Bromide (DTAB) and Sodium Dodecyl Sulfate (SDS). *J. Phys. Chem.* **1993**, *97*, 13792−13802.
(58) Caponetti, E.; Causi, S.; De Lisi, R.; Floriano, M. A.; Milioto, S.; Triolo, R. Dodecyltrimethylammonium Bromide in Water-Urea Mixtures: Structure and Energetics. *J. Phys. Chem.* **1992**, *96*, 4950−4960.
(59) Lusvardi, K. M.; Full, A. P.; Kaler, E. W. Mixed Micelles of Dodecyltrimethylammonium Bromide and Didodecyldimethylammonium Bromide. *Langmuir* **1995**, *11*, 487−492.
(60) Dar, A. A.; Chatterjee, B.; Rather, G. M.; Das, A. R. Mixed Micellization and Interfacial Properties of Dodecyltrimethylammonium Bromide and Tetraethyleneglycol Mono-n-Dodecyl Ether in Absence and Presence of Sodium Propionate. *J. Colloid Interface Sci.* **2006**, *298*, 395−405.
(61) Mahajan, R. K.; Vohra, K. K.; Aswal, V. K. Small Angle Neutron Scattering Measurements of Aggregation Behaviour of Mixed Micelles of Conventional Surfactants with Triblock Polymer L64. *Colloids Surf., A* **2008**, *326*, 48−52.
(62) Fafati, A. A.; Gharibi, H.; Iloukhani, H.; Safdari, L. Aggregation Number of Ionic Surfactants and Its Application for Alkyltrimethyl Ammonium Bromides and Sodium Tetradecyl Sulfate by Potentiometric Technique. *Phys. Chem. Liq.* **2003**, *41*, 227−238.
(63) Griffiths, P. C.; Paul, A.; Khayat, Z.; Heenan, R. K.; Ranganathan, R.; Grillo, I. A Small-Angle Neutron Scattering Study of Biologically Relevant Mixed Surfactant Micelles Comprising 1,2-Diheptanoyl-Sn-Phosphatidylcholine and Sodium Dodecyl Sulfate or Dodecyltrimethylammonium Bromide. *Soft Matter* **2005**, *1*, 152−159.
(64) Naskar, B.; Dey, A.; Moulik, S. P. Counter-Ion Effect on Micellization of Ionic Surfactants: A Comprehensive Understanding with Two Representatives, Sodium Dodecyl Sulfate (SDS) and Dodecyltrimethylammonium Bromide (DTAB). *J. Surfactants Deterg.* **2013**, *16*, 785−794.
(65) Bergström, M.; Pedersen, J. S. Structure of Pure SDS and DTAB Micelles in Brine Determined by Small- Angle Neutron Scattering (SANS). *Phys. Chem. Chem. Phys.* **1999**, *1*, 4437−4446.
(66) Bai, G.; Lopes, A.; Bastos, M. Thermodynamics of Micellization of Alkylimidazolium Surfactants in Aqueous Solution. *J. Chem. Thermodyn.* **2008**, *40*, 1509−1516.
(67) Kennedy, C. A.; MacMillan, S. N.; McAlduff, M. J.; Marangoni, D. G. The Interaction of Isomeric Hexanediols with Sodium Dodecyl Sulfate and Dodecyltrimethylammonium Bromide Micelles. *Colloid Polym. Sci.* **2001**, *279*, 1−7.
(68) Pal, A.; Yadav, S. Thermodynamic and Surface Properties of Aqueous 1-Dodecyl-3-Methylimidazolium Chloride [C12mim][Cl] Solution in the Presence of a Series of Inorganic Salts. *J. Surfactants Deterg.* **2020**, *23*, 53−65.
(69) Łuczak, J.; Jungnickel, C.; Markiewicz, M.; Hupka, J. Solubilization of Benzene, Toluene, and Xylene (BTX) in Aqueous Micellar Solutions of Amphiphilic Imidazolium Ionic Liquids. *J. Phys. Chem. B* **2013**, *117*, 5653−5658.
(70) Chabba, S.; Kumar, S.; Aswal, V. K.; Kang, T. S.; Mahajan, R. K. Interfacial and Aggregation Behavior of Aqueous Mixtures of Imidazolium Based Surface Active Ionic Liquids and Anionic Surfactant Sodium Dodecylbenzenesulfonate. *Colloids Surf., A* **2015**, *472*, 9−20.
(71) El Seoud, O. A.; Pires, P. A. R.; Abdel-Moghny, T.; Bastos, E. L. Synthesis and Micellar Properties of Surface-Active Ionic Liquids: 1-Alkyl-3-Methylimidazolium Chlorides. *J. Colloid Interface Sci.* **2007**, *313*, 296−304.
(72) Sastry, N. V.; Vaghela, N. M.; Aswal, V. K. Effect of Alkyl Chain Length and Head Group on Surface Active and Aggregation Behavior of Ionic Liquids in Water. *Fluid Phase Equilib.* **2012**, *327*, 22−29.
(73) Kaur, R.; Kumar, S.; Aswal, V. K.; Mahajan, R. K. Influence of Headgroup on the Aggregation and Interactional Behavior of Twin-Tailed Cationic Surfactants with Pluronics. *Langmuir* **2013**, *29*, 11821−11833.
(74) Bales, B. L.; Zana, R. Characterization of Micelles of Quaternary Ammonium Surfactants as Reaction Media I: Dodeclytrimethylammonium Bromide and Chloride. *J. Phys. Chem. B* **2002**, *106*, 1926−1939.

https://doi.org/10.1021/acs.langmuir.1c01727
Langmuir XXXX, XXX, XXX−XXX

(75) Jones, M. N.; Piercy, J. Light Scattering Studies on N-Dodecyltrimethylammonium Bromide and n-Dodecylpyridinium Iodide. *J. Chem. Soc., Faraday Trans. 1* **1972**, *68*, 1839−1848.
(76) Mata, J.; Varade, D.; Bahadur, P. Aggregation Behavior of Quaternary Salt Based Cationic Surfactants. *Thermochim. Acta* **2005**, *428*, 147−155.
(77) Lianos, P.; Zana, R. Fluorescence Probe Studies of the Effect of Concentration on the State of Aggregation of Surfactants in Aqueous Solution. *J. Colloid Interface Sci.* **1981**, *84*, 100−107.
(78) Malliaris, A.; Le Moigne, J.; Sturm, J.; Zana, R. Temperature Dependence of the Micelle Aggregation Number and Rate of Intramicellar Excimer Formation in Aqueous Surfactant Solutions. *J. Phys. Chem.* **1985**, *89*, 2709−2713.
(79) Rodenas, E.; Dolcet, C.; Valiente, M.; Valeron, E. C. Physical Properties of Dodecyltrimethylammonium Bromide (DTAB) Micelles in Aqueous Solution and Their Behavior as the Reaction Medium. *Langmuir* **1994**, *10*, 2088−2094.

USC UNIVERSIDADE DE SANTIAGO DE COMPOSTELA

https://doi.org/10.1021/acs.langmuir.1c01727
Langmuir XXXX, XXX, XXX−XXX

Chapter 9

Surfactant aggregation studies

Avengers, assemble!

Steve Rogers/Captain America, fictional character

In parallel to the ITC experiments, other techniques have been applied in order to characterize and to get a better understanding of surfactant aggregation processes. These complementary experiments are expected to be useful to optimize and validate results obtained from new methods, specially from Fluid Interface Calorimetry measurements. Some side results were obtained from this work. One of them is a software aimed to automatically obtain aggregation number of micelles from surface tension measurements. This software contains an original model developed during my Master degree in the same group (Garrido *et al.*, 2016) and it is expected to be included in the AFFINImeter platform at the short term. The certificate of the software registration is included as a part of the results obtained during this project. The full documentation is not included here to save space, but the flux diagram of the software and a brief explanation about the model are presented.

The second work included in this chapter is part of a project aimed to characterize bulk and interfacial properties of glucosides and maltosides surfactants. These compounds have been studied by means of surface tension, sound velocity and density, combining interfacial and bulk characterization. A selection of some of these molecules has been used in the development of the Fluid Interface Calorimetry too. In Paper VI, the results for decyl-β-D-glucopyranoside characterization by surface tension, sound velocity and density are shown.

USC
UNIVERSIDADE DE SANTIAGO DE COMPOSTELA

USC
UNIVERSIDADE
DE SANTIAGO
DE COMPOSTELA

9.1. Software registration

"STAND: Surface Tension for Aggregation Number Determination ", is a software registered on December, 2016. It has been developed for the analysis of surfactant sulutions' surface tension isotherms, based on a previous publication (Garrido *et al.*, 2016). This work has been developed in collaboration with people from: (1) Departamento de Física Aplicada, Facultade de Física, Universidade de Santiago de Compostela. The list of authors is presented below with their corresponding affiliations. The rights distribution is shown in %.

Ángel Piñeiro (1) 60 %, **Pablo F. Garrido** (1) 20 %, Roberto Rosende Dopazo (1) 20 %.

According to the CRediT authorship contribution statement (Brand *et al.*, 2015), my contributions to this publication are: Methodology; Validation; Formal analysis; Investigation; Writing - Original Draft; Writing - Review & Editing; Visualization.

USC UNIVERSIDADE DE SANTIAGO DE COMPOSTELA

USC
UNIVERSIDADE
DE SANTIAGO
DE COMPOSTELA

REGISTRO TERRITORIAL
DE LA PROPIEDAD INTELECTUAL

XUNTA DE GALICIA

GOBIERNO DE ESPAÑA MINISTERIO DE EDUCACIÓN, CULTURA Y DEPORTE

REGISTRO GENERAL DE LA PROPIEDAD INTELECTUAL

Según lo dispuesto en la Ley de Propiedad Intelectual (Real Decreto Legislativo 1/1996, de 12 de abril), quedan inscritos en este Registro los derechos de propiedad intelectual en la forma que se determina seguidamente:

NÚMERO DE ASIENTO REGISTRAL 03 / 2017 / 86

Título: STAND: Surface Tension for Aggregation Number Determination

Objeto de propiedad intelectual: Programa de ordenador

Clase de obra: Programa de ordenador

PRIMERA INSCRIPCIÓN

Autor/es y titular/es originarios de derechos

- **Apellidos y nombre**: PIÑEIRO GUILLÉN, Ángel
  Nacionalidad: España **D.N.I./N.I.F./Pasaporte**: 33296324Y
  Parte de la obra de la que es autor: 60%
- **Apellidos y nombre**: FERNÁNDEZ GARRIDO, Pablo
  Nacionalidad: España **D.N.I./N.I.F./Pasaporte**: 47436389Q
  Parte de la obra de la que es autor: 20%
- **Apellidos y nombre**: ROSENDE DOPAZO, Roberto
  Nacionalidad: España **D.N.I./N.I.F./Pasaporte**: 44472988G
  Parte de la obra de la que es autor: 20%

Transmisión de derechos

- **Titular cesionario**: UNIVERSIDADE DE SANTIAGO DE COMPOSTELA
  Nacionalidad: España **D.N.I./N.I.F./Pasaporte**: Q1518001A

  Es titular en exclusiva de los derechos de explotación de esta obra por mediar relación laboral y estar creada en el ejercicio de las funciones asignadas en la empresa al autor/es o siguiendo las instrucciones de su empresario.

USC UNIVERSIDADE DE SANTIAGO DE COMPOSTELA

- **Cedente**: PIÑEIRO GUILLÉN, Ángel
  Nacionalidad: España **D.N.I./N.I.F./Pasaporte**: 33296324Y
- **Cedente**: FERNÁNDEZ GARRIDO, Pablo
  Nacionalidad: España **D.N.I./N.I.F./Pasaporte**: 47436389Q

03/2017/86

REGISTRO TERRITORIAL
DE LA PROPIEDAD INTELECTUAL

XUNTA DE GALICIA

GOBIERNO DE ESPAÑA
MINISTERIO DE EDUCACIÓN, CULTURA Y DEPORTE

• **Cedente**: ROSENDE DOPAZO, Roberto

Nacionalidad: España **D.N.I./N.I.F./Pasaporte**: 44472988G

Datos de la solicitud

Núm. solicitud: SC-366-2016

Fecha de presentación y efectos: 23/12/2016 Hora: 09:07

En Santiago de Compostela, a veintisiete de enero de dos mil diecisiete
El/La titular del Registro

Firmado: José Mª Guijo Vázquez

USC UNIVERSIDADE DE SANTIAGO DE COMPOSTELA

STAND is a software for data analysis of surfactants solutions surface tension measurements. From the surface tension data and the surfactant concentration, the software provides:

- Micellar aggregation number
- Micellization free energy
- Adsorption constant
- Maximum surface excess concentration (or minimum area per molecule at the interface)
- Solute distribution in the liquid phase between free monomers and micelled molecules (from which the critical micelle concentration can be obtained)
- Surface coverage

The software is designed for the experimental data analysis and to obtain the previously cited magnitudes. However, it also allows the simulation of the surface tension adsorption isotherms. STAND was available online, but it is currently stopped for maintenance and improving, looking for its inclusion in the AFFINImeter platform. The old available version was developed using PHP as server language and HTML5 with CSS for the client part and visualization. The data storage was done by files located in the same server as the execution program. The needed environment for its execution was based in a Apache2 server with support for PHP5. The code is developed in C++ and its execution is made by PHP calls. The plots are generated using gnuplot. A screenshot of the old version is shown in Figure 9.1. At the present time, the algorithm is being redesigned in Python language.

USC
UNIVERSIDADE DE SANTIAGO DE COMPOSTELA

STAND: Surface Tension for Aggregation Number Determination

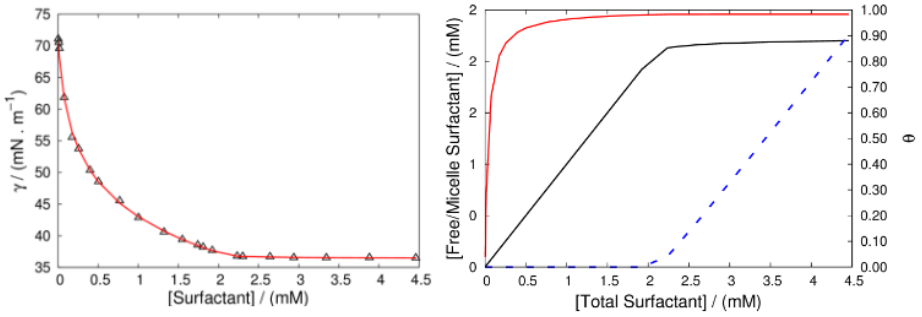


Figure 1.– Experimental data (triangles) and fitted curve (red line) vs the surfactant concentration
Figure 2.– Concentration of free (solid black line) and in–micelle (dashed blue line) surfactant (left axis), and surface coverage (red line; right axis) vs the surfactant concentration

*If you do not see two plots above, the input data file is wrong or the seeds in the table below are not reasonable.
Please check your input file or edit the seeds below and press on the "Repeat Fitting" buttom

γ Solvent (mN/m):	71.06
Temperature (K):	298

*Make sure that these values are correct since they will strongly affect the values of the fitting parameters.

		Seeds/Initial Values (Edit to optimize the fitting)			See results		
Parameter name	**Fit**	Value	Lower Limit	Upper Limit	Fitted Value	STD Error	Dependency
N_{agg}	☑	30	1	300	93.5218	4.95806	0.992208
$\Delta\mu^0_{(M=1)}$ (J/mol)	☑	-8500	-1e5	0	-14879.6	15.1175	0.992213
β (L/mol)	☑	20000	1	1e8	26447.7	45.0084	0.969051
Γ_{max} (μmol/m^2)	☑	5	0	15	3.41679	0.0017419	0.973849
						χ^2	1466.98

Repeat Fitting

IMPORTANT INFORMATION:
The minimum area that the surfactant molecule can occupy at the interface can be determined from Γ_{max}:
A_{min}=0.48592455930738 nm^2

The micellization Gibbs energy included in the table corresponds to a reference state 1 M.
The micellization Gibbs energy corresponding to x=1 as a reference state is given by:
$\Delta\mu^0_{(x=1)} = \Delta\mu^0_{(M=1)} - 4RT = -24790.4388232$ J/mol

Figure 9.1: Screenshot of the old web version of STAND.

USC UNIVERSIDADE DE SANTIAGO DE COMPOSTELA

STAND is based on the physical model with the same name (Garrido *et al.*, 2016). The model was the first attempt in the group to relate the aggregation and the adsorption effects, an idea that has been extensively exposed in this dissertation. It relates the surface tension as a function of the surfactant concentration with the aggregation number of the first formed micelles. STAND is based on three already known equations and models:

- The mass action approach, that states an equilibrium between two different species: the free surfactant monomers (S_F) and the micelles (M). Under equilibrium, N_{agg} monomers can form a micelle:

$$N_{agg} S_F \leftrightarrow M \tag{9.1}$$

  For any thermodynamic equilibrium, the corresponding constant can be defined. In this case, the micellization constant, K_{mic}:

$$K_{mic} = \frac{[M]}{[S_F]^{N_{agg}}} \tag{9.2}$$

  And its corresponding free energy per mole of surfactant molecule:

$$\Delta\mu^0 = -\frac{RT}{N_{agg}} ln(Kmic) \tag{9.3}$$

  The final consideration to take into account from the mass action model is the approach to the total surfactant concentration. If the adsorbed surfactant molecules can be negleted with respect to the monomer bulk form or the micelled monomers, the total concentration of surfactants in solution can be expressed as:

$$[S_T] = [S_F] + N_{agg}[M] = [S_F] + N_{agg} K_{mic} [M] [S_F]^{N_{agg}} \tag{9.4}$$

- The Langmuir adsorption isotherm, which relates the surface coverage, Θ (fraction of ocuppied sites at the interface) in terms of the free surfactant concentracion and the adsorption constant β

$$\Theta = \frac{\beta[S_F]}{1 + \beta[S_F]} \tag{9.5}$$

  Where $\Theta = \Gamma / \Gamma_{max}$

- The Gibbs adsorption equation, already presented in Section 1.2, but expressed in terms of the free surfactant concentration too:

$$d\pi = \Theta \Gamma_{max} RT \frac{d[S_F]}{[S_F]} \tag{9.6}$$

  Here π represents the surface pressure, the difference between the surface tension of the pure solvent and the solution ($\pi = \gamma_0 - \gamma$)

USC UNIVERSIDADE DE SANTIAGO DE COMPOSTELA

The Equations 9.3, 9.4, 9.5 and 9.6, together with the fitting procedure, compose the core of the STAND model and software.

USC
UNIVERSIDADE
DE SANTIAGO
DE COMPOSTELA

9.2. Paper VI

"Boosting the use of thermoacoustimetry in micellization thermodynamics studies by easing an objective determination of the cmc", published in *Fluid Phase Equilibria* (2018), is a regular article where a surfactant, the devyl-β-D-glucopyranoside, is studied by speed of sound, density and surface tension at multiple temperatures. This work has been developed in collaboration with people from: (1) Departamento de Física Aplicada, Facultade de Física, Universidade de Santiago de Compostela. The corresponding authors are marked with a *:

Goretti Castro (1), **Pablo F. Garrido** (1), Alfredo Amigo (1),Pilar Brocos (1)*.

According to the CRediT authorship contribution statement (Brand *et al.*, 2015), my contributions to this publication are: Software, Validation; Formal analysis;

Castro G, Garrido PF, Amigo A, Brocos P (2018). Boosting the use of thermoacoustimetry in micellization thermodynamics studies by easing an objective determination of the cmc. *Fluid Phase Equilib.*, **478**, 1–13. ISSN 03783812. doi: 10.1016/j.fluid.2018.08.011. URL https://www.doi.org/10.1016/j.fluid.2018.08.011

Supplementary data can be accessed by this link: https://ars.els-cdn.com/content/image/1-s2.0-S0378381218303431-mmc1.pdf

USC UNIVERSIDADE DE SANTIAGO DE COMPOSTELA

USC
UNIVERSIDADE
DE SANTIAGO
DE COMPOSTELA

Fluid Phase Equilibria 478 (2018) 1–13

Contents lists available at ScienceDirect

Fluid Phase Equilibria

journal homepage: www.elsevier.com/locate/fluid

Boosting the use of thermoacoustimetry in micellization thermodynamics studies by easing an objective determination of the cmc☆

Goretti Castro, Pablo F. Garrido, Alfredo Amigo, Pilar Brocos*

Departamento de Física Aplicada, Universidade de Santiago de Compostela, Campus Vida, E-15782, Santiago de Compostela, Spain

ARTICLE INFO

Article history:
Received 12 May 2018
Received in revised form
4 August 2018
Accepted 19 August 2018
Available online 21 August 2018

Keywords:
Speed of sound
Isentropic compressibility
Phillips definition of cmc
van't Hoff micellization enthalpy
Standard micellization entropy
Surface tension

ABSTRACT

The thermodynamics of micellization of decyl-β-D-glucopyranoside (β-$C_{10}G_1$) in aqueous solution is studied from multiple-temperature (283.15–323.15 K) speed of sound and density measurements. The Williams method being unsuited to estimate the cmc, we propose the Carpena method (widely used in the cmc determination from conductivity data) as an objective and easy-to-use alternative. Its performance is checked by comparison with a well-established but quite complex procedure: the combination of the Runge-Kutta numerical integrations method and the Levenberg–Marquardt least-squares fitting algorithm. As a result of this investigation, three temperature regions are associated to a β-$C_{10}G_1$ micellization governed by entropy (I), by enthalpy (III), or by both of them (II). Besides, the adsorption of β-$C_{10}G_1$ and β-$C_{12}G_1$ at the solution/air interface is revisited from surface tension measurements at several temperatures and reviews of literature data.

© 2018 Elsevier B.V. All rights reserved.

1. Introduction

Thermoacoustimetry is defined by the IUPAC as "a technique in which the characteristics of imposed acoustic waves are measured as a function of temperature after passing through a substance (and/or its reaction product(s)) whilst the substance is subjected to a controlled temperature program" [1]. We have recently stressed the potential of this technique in micellization thermodynamics studies by analyzing speed of sound (u) and isentropic compressibility (κ_S) data of octyl-β-D-glucopyranoside (β-C_8G_1) aqueous solutions [2], to finally get thermodynamic parameters of micelle formation in excellent agreement with those reported by others from isothermal titration calorimetry. However, a thorough revision of the literature reveals that micellization thermodynamics studies based on thermoacoustimetry are scarce, despite being an attractive alternative in terms of handiness and ease of use.

We have examined all relevant papers (around 80) reporting speed of sound measurements of (mainly aqueous) solutions of surfactants from the 1980s onwards. Only about 11% of them use u or κ_S data to derive, through the temperature dependence of the critical micelle concentration (cmc), standard enthalpies and entropies of micellization [3–11]. In other instances, either the cmc was not even determined (~31%) [12–24] or, in the cases where it was, the speeds of sound were just measured at a single temperature (~30%) [25–37]. Finally, around 28% of the revised papers reported u data at several temperatures accompanied by the corresponding cmc values, but the opportunity for addressing the thermodynamics of micellization was not taken [38–53]. Interestingly, the van't Hoff equation was indeed used in some of these latter works to get the thermodynamic parameters of micelle formation from a cmc(T) function derived from conductivity data [45,49–52]. Thus, it seems from this revision that the potential of thermoacoustimetry in micellization thermodynamics is underused. The references cited above are not intended to be comprehensive, but just representative of each case.

The issue underlying the scarcity of micellization thermodynamics studies based on thermoacoustimetry is the difficulty of obtaining reliable cmc values from speed of sound data. The most popular way of estimating the cmc is the Williams method, consisting in the intersection of two straight lines [3,4,9,10,26–28,30–37,39,42,43,45,47,49–53]. This method assumes a strict compliance with the pseudo-phase separation model of micelle formation, in such a way that the first derivative of $f(c)$ (f being the

☆ Electronic Supplementary Material (ESM) available: Analysis of ^{1}H NMR and ESI-TOF mass spectra for β-$C_{10}G_1$ and β-$C_{12}G_1$. Tables S1–S10 and Figs. S1–S4.

* Corresponding author.
E-mail addresses: Goretti.Castro@gmail.com (G. Castro), Pablo.Fernandez@usc.es (P.F. Garrido), Alfredo.Amigo@usc.es (A. Amigo), Pilar.Brocos@usc.es (P. Brocos).

https://doi.org/10.1016/j.fluid.2018.08.011
0378-3812/© 2018 Elsevier B.V. All rights reserved.

physical property under investigation and c the nominal concentration) would be discontinuous at the cmc. However, in many instances the change of slope of $f(c)$ is not sudden because the micellization process is not cooperative, taking way more gradually. The sensitivity of the working property to the micelle formation may also play a role. The use of the Williams method is not advisable in such cases as it entails a high level of subjectivity, leaving room for inaccurate cmc estimations.

An alternative approach for the cmc determination (based on the mass-action model of micelle formation) is the use of the Phillips definition, which identifies the cmc as an inflection point in the first derivative of $f(c)$ [54]. In the course of the review made (see above), several methods of calculating this inflection point in $u(c)$ or $\kappa_S(c)$ have been found, from the crudest to the most rigorous. Thus, Priev et al. [29] fitted the experimental speeds of sound/concentration data to an empirical function describing them closely and then calculated analytically its second derivative, whose minimum was identified as the cmc. A rudimentary numerical variant of this method was adopted by Jamal et al. [44,46], who averaged the slopes of every pair of adjacent experimental data to get first (and subsequently, second) derivative data points, followed by a Gaussian fit of the second derivative. Finally, a few authors [5–7,32,38,40,41,48] applied a much more precise procedure that had been earlier proposed by Pérez-Rodríguez et al. [55] in the context of electrical conductivity studies on surfactant solutions. Starting from the assumption that the second derivative of $f(c)$ is a Gaussian function, the procedure combines the Runge-Kutta numerical integrations method with the Levenberg-Marquardt least-squares fitting algorithm. This method (hereinafter referred to as RK-LM) requires programming skills and expertise in numerical computation techniques, which explains its limited use. For a more generic and extensive revision of approaches to cmc estimation, refer to Al-Soufi et al. [56].

With the aim of boosting the use of thermoacoustimetry in micellization thermodynamics studies, we propose to borrow a method that has been widely used for the cmc determination from conductivity data over the last 16 years. It was presented by Carpena et al. in a paper [57] that totals more than 200 citations to this day. The Carpena method lies on the assumption that the first derivative of $f(c)$ behaves as a sigmoid (f being the electrical conductivity), so that $f(c)$ itself should behave as the integral of such sigmoid. The procedure for the cmc determination is simple and accessible to everybody (to the extent of being applied at the undergraduate level [58]), just requiring the use of any nonlinear fitting software.

The Carpena and RK-LM methods were confronted in this work to test the performance of the first one in the context of thermoacoustimetry. The comparison was undertaken in the framework of our studies on the adsorption and micellization of even hydrocarbon chain sugar-based surfactants (nonionic surfactants derived from carbohydrates). Following our research into β-C_8G_1 thermodynamics [2], we focus here our attention on decyl-β-D-glucopyranoside (β-$C_{10}G_1$) and dodecyl-β-D-glucopyranoside (β-$C_{12}G_1$). Measurements of surface tension (σ), density (ρ), and speed of sound are reported for β-$C_{10}G_1$ in the range 10–50 °C, together with surface tension data at 37 and 50 °C for β-$C_{12}G_1$. To our knowledge, the thermodynamics of micellization of β-$C_{10}G_1$ has not been investigated yet, while multiple-temperature studies on the thermodynamics of adsorption are scarce and limited for both surfactants [59–61].

2. Materials and methods

2.1. Materials

Decyl-β-D-glucopyranoside and dodecyl-β-D-glucopyranoside were purchased from Anatrace, kept in a dark place at 256 K, and used as received (see Table 1). Their purity (≥99%) was checked by one- and two-dimensional ^{1}H NMR spectra, as well as by electrospray ionization mass spectrometry; details can be found in the Electronic Supplementary Material (ESM). Water content was determined with a C20 coulometric Karl Fischer titrator from Mettler Toledo. On dry mass basis it amounted to 0.79% and 0.70% for β-$C_{10}G_1$ and β-$C_{12}G_1$, respectively. Boiled and mechanically degassed ultrapure water (Elix 3 purification system, Millipore Corp.) was used in sample preparation. Solutions were carefully prepared by mass (balance models: AT250 from Mettler (Switzerland) with resolution $1\cdot10^{-5}$ g, and SV-1000 MS from Gram Precision (Spain) with resolution $1\cdot10^{-3}$ g) with the procedure of diluting aliquots from a mother solution, in whose preparation the water content of the glucosides was considered. The relative uncertainty in the concentration of the final solutions was estimated to be less than 0.04% and 0.3% for β-$C_{10}G_1$ and β-$C_{12}G_1$, respectively.

2.2. Experimental techniques

Surface tensions were measured with a Lauda drop volume tensiometer (TVT 2 model, Germany) using the standard mode, which from our experience is suitable for not bulky surfactants [2,62]. A syringe of 2.5 ml, incompletely filled and attached to a steel capillary with an inner radius of 1.345 mm, furnished between 30 and 50 drops of each sample, depending on its concentration and temperature. Both the equipment and the procedure were described in detail in the past [62–64]. In contrast with previous experiences [2,65,66], the experimental densities of the aqueous solutions were not useful to get drop masses from drop volumes, since they differ from that of pure water by less than the precision required by the method ($1\cdot10^{-3}$ g cm^{-3}). Depending on the working concentration (from 0 to 4 mM) and temperature (283.15, 298.15, 310.15, and 323.15 K), the surface tension of diluted β-$C_{10}G_1$ was determined with an expanded uncertainty ranging from ±0.01 to ±0.04 mN m^{-1} at the 95% confidence level (see Table S1), the temperature precision being better than 0.10 K. As regards β-$C_{12}G_1$, its very low solubility in water was an added source of error and prevented us from doing measurements at 283.15 and 298.15 K. For this surfactant, the expanded uncertainty ($k = 2$) of surface tension data is higher in the saturated region, going up to ±0.10 mN m^{-1} (see Table S2).

Densities and ultrasound speeds (~3 MHz) were measured using a DSA 5000 equipment (Anton Paar, Austria) calibrated with water

USC UNIVERSIDADE DE SANTIAGO DE COMPOSTELA

Table 1
Provenance and purity of the synthesis material.

Chemical (CAS number)	Abbreviation	Supplier	Sample purity	
			Mass fraction	Mass fraction water content[a]
Decyl-β-D-glucopyranoside (58846-77-8)	β-$C_{10}G_1$	Anatrace	≥0.99	0.0079
Dodecyl-β-D-glucopyranoside (59122-55-3)	β-$C_{12}G_1$	Anatrace	≥0.99	0.0070

[a] The uncertainty of this quantity was estimated to be less than 2.5%.

and dry air that has been described elsewhere [2,67]. Every sample of diluted β-$C_{10}G_1$ was studied in the range 283.15–323.15 K (10–50 °C), with a decreasing temperature sweep (to minimize bubble formation) in steps of 2.5 K. Previous measurements of β-C_8G_1 solutions [2] had been successfully made with temperature steps of 5 K. However, in the present case a higher precision was needed to compensate for the lower sensitivity of the measured properties to the change from monomeric to micellar domain (see section 3.2). As with β-C_8G_1, the marked tendency of β-$C_{10}G_1$ solutions to develop bubbles in the measuring cells at high temperatures prevented us from extending the working T range above 50 °C. The expanded uncertainties ($k = 2$) of our ρ and u data were estimated to be $\pm 10 \cdot 10^{-6}$ g cm^{-3} and ± 0.20 m s^{-1}, respectively.

2.3. The working region in the temperature-concentration phase diagram

Despite the publication of a number of papers devoted to the adsorption and micellization of β-$C_{10}G_1$ [59,60,68–81] and β-$C_{12}G_1$ [59,61,70,72,74,76,78,82–86] in aqueous solution, or to their micelle properties [59,87–90], there is still some controversy as to the suitability of performing such kind of studies with these glucosides. This is partially due to discrepancies in their reported binary surfactant–water phase diagrams. Drummond and coworkers [60,91] found that both glucosides undergo a phase separation at the cmc, which should be named cac (critical aggregation concentration) instead. In their words, "the miscibility gap region (L_1+L_2) comprises a dense isotropic hydrated liquid surfactant phase (L_2) and a surfactant-poor isotropic solution which may or may not contain micelles, sitting above the L_2 layer". According to them, such phase separation extends up to ~15 wt % and ~40 wt % for decyl and dodecyl glucoside, respectively. A similar result for β-$C_{10}G_1$ had been gathered in a previous review by Shinoda et al. [92]. However, focusing the attention on the low surfactant concentration region of the phase diagram and using more accurate techniques, other authors reported that the miscibility gap does not begin at the cmc, but at a concentration slightly above: around 0.1 wt % (3.1 mM) and 0.005% wt % (0.13 mM) for β-$C_{10}G_1$ [88,93–95] and β-$C_{12}G_1$ [94], respectively. It should be noted that the later values correspond in all cases to chemicals supplied by Sigma, with a certified purity of 98%, and that the phase boundaries were typically determined to within 0.5 wt % accuracy [88,95].

Another drawback to perform micellization studies of these two glucosides is that they have a relatively high Krafft boundary (temperature below which the surfactant in water remains in crystalline form): 22.5 °C (β-$C_{10}G_1$) and 37.5 °C (β-$C_{12}G_1$) [60,92,94]. This would preclude making measurements below such temperatures if it were not for the fact that the solutions are metastable at these conditions. Actually, crystallization is kinetically retarded to a considerable extent [96], in such a way that crystals form only after a long induction time [94]. At this respect, Rybinski and Hill stated in their review [96] about glucoside surfactants that the Krafft boundary "changes position with storage time", which explains the absence of the crystals + H_2O region in some of the published phase diagrams for β-$C_{10}G_1$ [88,93].

To ensure that we were always working in the L1 region and above the (moving) Krafft boundary, the following precautions were taken: use of relatively fresh samples, storage at room temperature, magnetic stirring for at least 30 min before making dilutions or before measuring, and regular visual examination of the solutions with the unaided eye under a lamp. In the case of β-$C_{12}G_1$, these preventive measures led us to avoid performing surface tension measurements far below the Krafft temperature.

3. Results and discussion

The experimental surface tension data for water and aqueous solutions of β-$C_{10}G_1$ at four temperatures (283.15, 298.15, 310.15, and 323.15 K) are listed in Table S1 and plotted in Fig. 1a, while those concerning β-$C_{12}G_1$ at 310.15 and 323.15 K are presented in Table S2 and Fig. 1b. Still on β-$C_{10}G_1$ solutions, the experimental density and speed of sound data at 17 temperatures in the range 283.15–323.15 K are listed in Tables S3 and S4. Table S5 shows the corresponding isentropic compressibilities, calculated by using the Newton-Laplace equation: $\kappa_S = 1/(\rho\, u^2)$. The temperature dependence of these three bulk properties is illustrated in Fig. 2, showing that the studied β-$C_{10}G_1$ solutions expand, become less compressible, and exhibit increasing speeds of sound when heated in the working T interval. Unlike for β-C_8G_1 [2], the curves for the pure solvent and the mother solution (4.01 mM) are nearly indistinguishable. As representative examples of concentration dependence, isotherms at 283.15, 298.15, and 313.15 K are displayed in Figs. S1, 3, and S2, respectively. Their inspection reveals that an increase of the β-$C_{10}G_1$ concentration results in higher sound

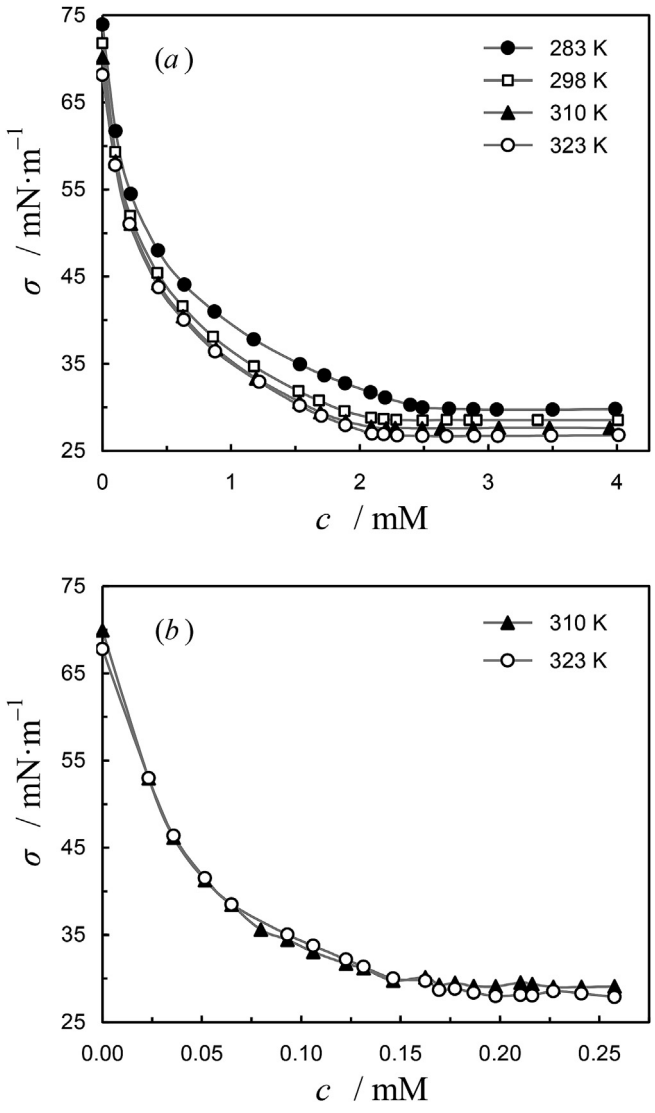


Fig. 1. Surface tension data for aqueous solutions of (*a*) β-$C_{10}G_1$ and (*b*) β-$C_{12}G_1$ at different temperatures. The lines connecting the dots are just eye-guides. (The unit mM means 10^{-3} mol dm^{-3}).

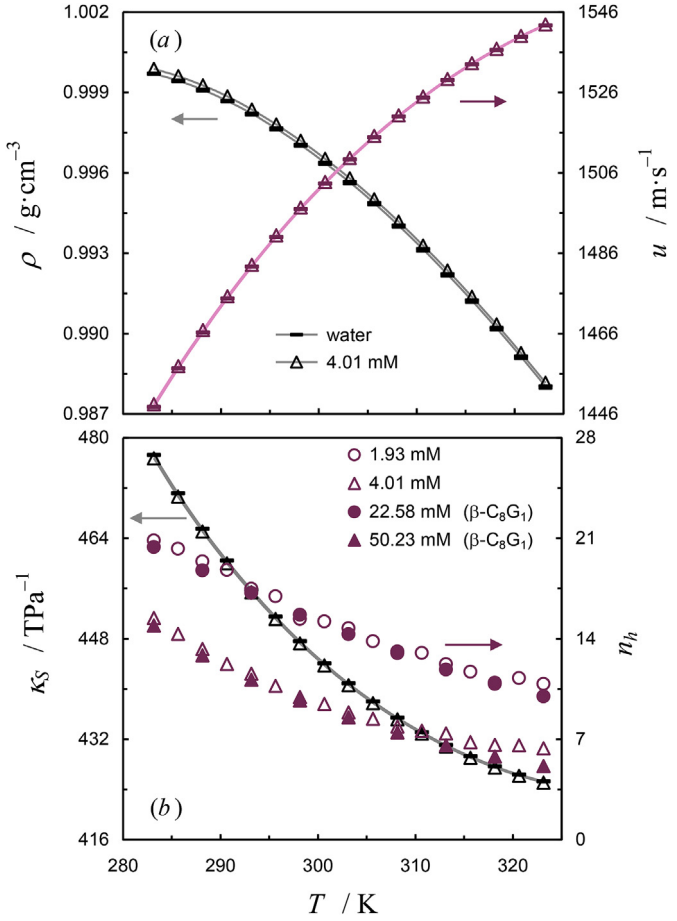


Fig. 2. Temperature dependence of (*a*) density, speed of sound, (*b*) isentropic compressibility, and hydration number for water and selected aqueous solutions of β-$C_{10}G_1$. The lines connecting the dots are just eye-guides. The legend in (*a*) is common to both parts. Two hydration number datasets sampling the premicellar and saturated regions of β-C_8G_1 [2] are included for comparison purposes.

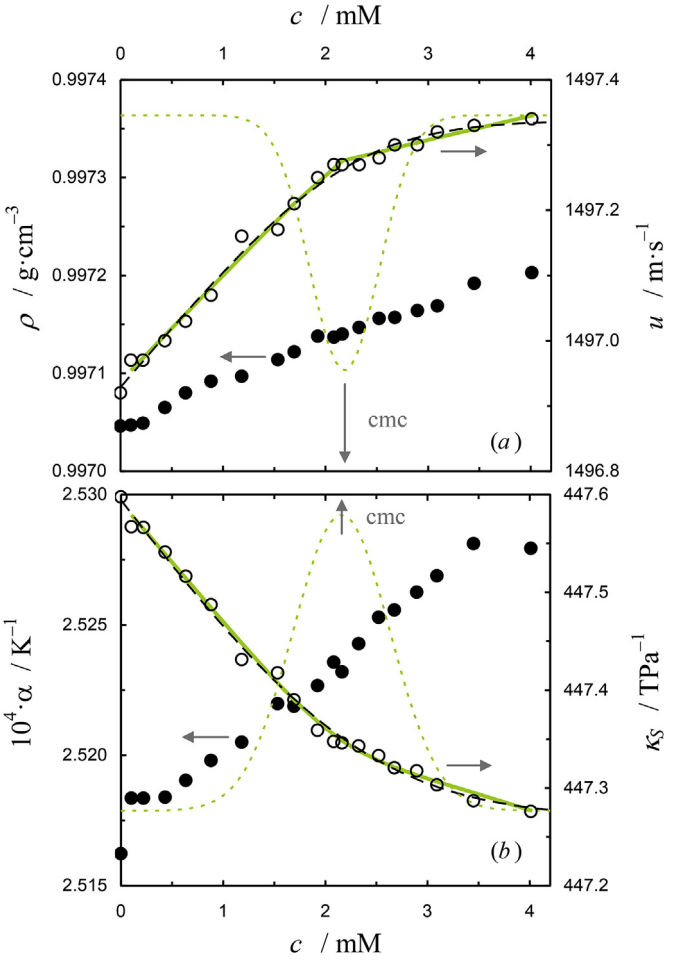


Fig. 3. Isotherms of (*a*) density, speed of sound, (*b*) thermal expansion coefficient, and isentropic compressibility at 298.15 K for aqueous solutions of β-$C_{10}G_1$. The fitting curves of u and κ_S data have been obtained either by the Carpena method (dashed) or by applying a combination of the Runge-Kutta numerical integrations method and the Levenberg–Marquardt least-squares fitting algorithm (solid). In the later case, the Gaussian fit of its 2nd derivative is the dotted line. (The unit mM means 10^{-3} mol dm^{-3}).

propagation speeds and in denser and less compressible solutions, such effects becoming less significant with increasing temperature.

A fourth bulk property displayed in part b of Figs. S1, 3, and S2 is the thermal expansion coefficient (α), defined as $(-1/\rho)(\partial\rho/\partial T)_p$ and calculated at each concentration from a second-order polynomial regression to get $\rho(T)$. Although the high uncertainty associated to these values (~$0.6\cdot10^{-4}$ K^{-1}) made their tabulation inadvisable, it is noteworthy that α clearly increases with T, going from ~$1.2\cdot10^{-4}$ K^{-1} at 283 K up to ~$4.8\cdot10^{-4}$ K^{-1} at 323 K.

A typical feature of aqueous solutions is the hydration number (n_h), which was estimated from the Pasynski equation (Eq. (1)) [97–99] and plotted as a function of T for two selected concentrations sampling the premicellar and saturated regions of β-$C_{10}G_1$ (see Fig. 2b). For comparison purposes, two more datasets for β-C_8G_1 under similar conditions (pre-cmc and at c/cmc ≈ 2) were included too [2]. The hydration number is defined as the number of water molecules located in the hydration shell of the solute and thus having properties that differ from those of bulk solvent. The Pasynski equation assumes that these water molecules are held so tightly as to be considered incompressible and that the solute itself is also incompressible, which is a good approach for the glucose moiety [97].

$$n_h = \frac{n_w}{n}\left(1 - \frac{\kappa_S}{\kappa_{S,w}}\right) \quad (1)$$

Here n and n_w stand for the number of moles of solute and water, respectively, at a given concentration. It should be noted that both the hydrophobic and the hydrophilic hydration are accounted for in n_h [100,101]. Hence Fig. 2b illustrates the dehydration suffered by β-$C_{10}G_1$ (and β-C_8G_1) with increasing temperature and concentration.

3.1. Analysis of surface tension data

The comparison of experimental surface tensions with those previously reported by others is often hindered by the scarcity of tabulated σ data for aqueous solutions of surfactants. This is not entirely the case, as we have found numerical σ data by Shinoda et al. [72] for the two investigated systems (see Fig. S3). As for other works reporting surface tensions of decyl [59,60,68–71,73–78,102,103] and/or dodecyl [59,61,70,74,76,78,82–85,103,104] glucosides just in a graphical way, the comparison will be limited to derived quantities such as the critical micelle concentration or the minimum area per solute molecule at the solution/air interface (see Tables S6 and S7).

Despite the different working temperatures, there is clear disagreement between our data and those reported by Shinoda et al. [72] as regards the extent of surface tension reduction in β-

$C_{12}G_1$ solutions (see Fig. S3b). To get more insight into this issue, Table S7 contains the column σ_{min} (surface tension at saturation conditions). The large discrepancies found at 298 K between σ_{min} data from different sources are remarkable: while half of them stay in the range of 27–29 mN m^{-1} [61,78,82,83,103], the other half ranges from 32 to 58 mN m^{-1} [72,74,76,84]. Higher σ_{min} are most likely due to the presence of β-$C_{12}G_1$ in crystalline form, as a result of working far below the Krafft temperature (see section 2.3).

The cmc has been determined by means of Eq. (2), obtained by integration of the Gibbs adsorption isotherm (GAI), $\Gamma RT = (d\pi/d\ln x)_T$, in the vicinity of the cmc [2,105]:

$$\pi = [\pi_{max} - \Gamma_{max} RT \ln x_{cmc}] + \Gamma_{max} RT \ln x \quad (2)$$

Here x is the solute mole fraction, Γ_{max} the maximum value of the excess surface concentration, and π the surface pressure, defined as $\sigma_w - \sigma$. This equation accounts for the (almost) linear behavior of the function $\pi(\ln x)$ just below the cmc. According to Rosen [106], that trend begins around $\pi = 20$ mN m^{-1}. The linear fit of the selected data points allows the simultaneous determination of Γ_{max} and x_{cmc} from the slope and the intercept of Eq. (2), respectively. Then, the minimum area per solute molecule at the solution/air interface is calculated as $A_{min} = (\Gamma_{max} N_{Av})^{-1}$, where N_{Av} is the Avogadro's number. The value of π_{max} is previously obtained by averaging π data in the surface saturation region. Note that the cmc determination from Eq. (2) is fully equivalent to the application of the Williams method in a π vs. ln$x$ plot, where the intersection of two straight lines (one of them horizontal) gives x_{cmc}.

Our results for the cmc (expressed in mM units instead of mole fraction), π_{max}, Γ_{max}, and A_{min} are collected in Table 2. The cmc values for β-$C_{10}G_1$ are compatible with a U-shaped cmc(T) function, as had been predicted theoretically [87] and in line with the trend already reported for the octyl glucoside [2]. As also found in the case of β-C_8G_1 [2], the extent of surface tension reduction at surface saturation conditions (measured by π_{max}) decreases with rising temperature, meaning that both β-$C_{10}G_1$ and β-$C_{12}G_1$ become less effective surfactants upon heating. This is the result, more than anything else, of decreasing the surface tension of water itself. The minimum surface molecular area, which accounts for the degree of packing at the saturated interface, increases with rising temperature as a result of increased thermal motion. This feature is also shared with β-C_8G_1 which, interestingly, exhibits larger values of A_{min} [2] than β-$C_{10}G_1$ or β-$C_{12}G_1$. Similar remarks were recently made by Barzyk et al. [68] and Krawczyk [61] in studies where the adsorption properties of octyl glucoside were compared to those of decyl and dodecyl glucoside, respectively. Noteworthy, the increase of A_{min} with T seems to be in contradiction with the hydrophilic dehydration of surfactants on heating, which should result in the opposite trend. This paradox is only apparent: several works [68,107] have concluded that the amount of water in the densest packed monolayers of glucopyranosides is insignificant due to the formation of H-bonds between sugar units. (In fact, such process is enthalpy-driven and accounts for the high stability of foams generated with sugar-based surfactants [108]). In other words, the glucose moiety of the adsorbed molecule is already practically dehydrated in saturation conditions. Hence the surface dehydration caused by heating would be insignificant too, so that the increased thermal motion would be the dominant contribution to the temperature dependency of A_{min}.

Tables S6 (for β-$C_{10}G_1$) and S7 (for β-$C_{12}G_1$) allow the comparison of cmc and A_{min} with literature values [59–61,68–78,82–85,102–104,109,110], in most cases at a single temperature and in a few instances at two [59,60] or three [61] working temperatures. There is an open discussion [111–119] about the suitability of the Gibbs adsorption isotherm to derive minimum surface molecular areas (note that the GAI is only applicable for $c <$ cmc, unless it is expressed in terms of the *free* surfactant concentration [120]). In short, the conventional Gibbs analysis starting from the assumption of linearity in $\pi(\ln x)$ below the cmc may lead to inaccurate values of A_{min} (Γ_{max}), which would be overestimated (underestimated) [115]. As the plot of π against ln$x$ is actually slightly curved below the cmc, it should rather be fitted locally to a polynomial [121] (the 2nd degree being usually enough [119]). Values of Γ_{cmc} obtained experimentally (by neutron reflectivity) and from quadratic fits of π vs. ln$x$ compare very well with each other [118,119], both for nonionic and ionic surfactants. In the case of nonionics it is safe to assimilate Γ_{cmc} to Γ_{max}, as the surface is already saturated when the micelles are formed [118,119]. However, the quadratic local fit of π vs. ln$x$ below the cmc requires highly accurate surface tension values to be statistically justified [121]. A linear fit restricted to data points immediately below the cmc gives equally good results [117,118]. Applied to Eq. (2), this means that the fitting concentration range may be tentatively fixed by using the Rosen's criterion ($\pi > 20$ mN m^{-1}), to subsequently determine visually where the plot becomes linear (see for example Fig. S2 in Ref. [2]). In Table S6, the comparison of A_{min} from different sources shows that our values are in the lower end of the spectrum (and hence, least likely to be overestimated) and in good agreement with those

Table 2
Critical micelle concentration and standard Gibbs energy of micellization from surface tension data, surface pressure at saturation conditions and at the cmc, maximum surface concentration of solute, minimum area per solute molecule at the solution/air interface, standard Gibbs energy of adsorption as calculated from Eqs. (7) and (8), limiting value of $\ln(\pi^*/x)$ according to the Volmer SEOS (Eq. (3)), and bulk activity coefficient at infinite dilution for β-$C_{10}G_1$ and β-$C_{12}G_1$ at different temperatures.[a,b]

	T/K	cmc/mM	ΔG^0_{mic}/kJ·mol^{-1}	π_{max}/mN·m^{-1}	π_{cmc}/mN·m^{-1}	Γ_{max}/μmol·m^{-2}	A_{min}/Å^2	$\Delta G^{0(1)}_{ads}$/kJ·mol^{-1}	$\ln(\pi^*/x)_{x\to 0}$	$\Delta G^{0(2)}_{ads}$/kJ·mol^{-1}	γ^∞
β-$C_{10}G_1$	283.15	2.53	−23.54	44.14	43.94	4.418	37.58	−33.48	12.969	−39.45	22460
		(0.16)	(0.15)	(0.06)		(0.019)	(0.16)	(0.16)	(0.013)	(0.03)	(470)
	298.15	2.09	−25.26	43.23	42.97	4.336	38.29	−35.17	12.958	−41.46	27110
		(0.17)	(0.20)	(0.03)		(0.023)	(0.21)	(0.21)	(0.015)	(0.04)	(640)
	310.15	2.03	−26.35	42.51	42.26	4.218	39.36	−36.37	12.854	−42.81	28120
		(0.16)	(0.21)	(0.04)		(0.023)	(0.21)	(0.21)	(0.017)	(0.04)	(760)
	323.15	2.13	−27.32	41.42	41.17	4.046	41.04	−37.49	12.698	−44.12	26730
		(0.25)	(0.32)	(0.03)		(0.032)	(0.33)	(0.33)	(0.017)	(0.05)	(730)
β-$C_{12}G_1$	310.15	0.153	−33.0	40.71	40.24	4.16	39.9	−42.7	15.39	−49.23	366000
		(0.093)	(1.6)	(0.07)		(0.14)	(1.3)	(1.6)	(0.12)	(0.32)	(69000)
	323.15	0.182	−33.9	39.60	39.22	3.839	43.2	−44.1	15.248	−50.85	307000
		(0.080)	(1.2)	(0.09)		(0.092)	(1.0)	(1.2)	(0.094)	(0.25)	(43000)

[a] Uncertainties are given in parentheses.
[b] The unit mM means 10^{-3} mol dm^{-3}.

determined from quadratic fits: at 25 °C, 38.29 Å^2 compares well with 38 Å^2 from Boyd et al. [60] and with 37.5 Å^2 from Persson et al. [69] (at 22 °C).

Solvents other than pure water (as salt solutions or buffer) were ignored in the compilation made in Tables S6-S7. Aside from this it is worth mentioning a paper from Hu et al. [81] that reports surface tension measurements of β-$C_{10}G_1$ at 310 K (37 °C, the temperature of human body) in cell culture medium ($\sigma = 72$ mN m^{-1} at 37 °C). They obtained a cmc of 2.3 mM (against our (2.03 ± 0.16) mM in water) and a maximum surface tension reduction of 40.7 mN m^{-1} (against our $\pi_{max} = 42.51$ mN m^{-1}). It results from this comparison that the presence of cells delays the onset of micellization and makes β-$C_{10}G_1$ a less effective surfactant, as also found in the case of β-C_8G_1 [2].

3.1.1. Activity coefficients at infinite dilution

The limiting value of the surfactant activity coefficient in the bulk phase defined under the symmetric convention ($\gamma \to 1$ when $x \to 1$ and $\gamma \to \gamma^{\infty}$ when $x \to 0$) can be estimated from surface tension data by using a method developed by Gracia-Fadrique and coworkers [122]. The procedure lies on the assumption that molecular interactions between adsorbed molecules are negligible below the cmc, so that the Volmer surface equation of state is applicable: $\pi(a - a_0) = RT$. Here a stands for the molar area, $a = 1/\Gamma$, while a_0 is a van der Waals type constant to account for deviations from surface ideality ($\pi\, a = RT$) through repulsive lateral interactions. For any solution/air interface obeying the Volmer SEOS, the plot of $\ln(\pi^*/x)$ versus π in the dilute region (with $\pi^* = \pi/\pi_{max}$) should be a straight line with negative slope:

$$\ln\left(\frac{\pi^*}{x}\right) = \ln\left(\frac{\pi^*}{x}\right)_{x\to 0} - \frac{\pi a_0}{RT} \tag{3}$$

The linear fit of data in the selected π range (see for example Fig. S5 in Ref. [2]) furnishes the constants $-a_0/RT$ and $\ln(\pi^*/x)_{x\to 0}$ from the slope and intercept of Eq. (3), respectively. Then, their substitution in Eq. (4) gives the bulk activity coefficient at infinite dilution:

$$\ln\gamma^{\infty} = \ln\left(\frac{\pi^*}{x}\right)_{x\to 0} - \frac{\pi_{max} a_0}{RT} \tag{4}$$

For a brief overview of how Eqs. (3) and (4) are obtained from the combination of the Volmer SEOS with the GAI, refer to section 3.4 in Ref. [2].

The γ^{∞} values for β-$C_{10}G_1$ and β-$C_{12}G_1$ in aqueous solution are listed in Table 2. Assuming that the activity coefficient of a surfactant in aqueous solution keeps constant below the cmc, Eq. (5) is usually employed to have a rough estimation of its value at infinite dilution [122]

$$\gamma_{cmc} = (x_{cmc})^{-1} \cong \gamma^{\infty} \tag{5}$$

and to explain qualitatively some typical behavior patterns. Thus, while the cmc decreases by one order of magnitude for every pair of CH_2 groups added to the hydrocarbon chain of the glucoside, γ^{∞} follows the opposite trend. For example, their sequences at 323 K are as follows:

For cmc (mM): β-C_8G_1 (22.5 ± 1.2) > β-$C_{10}G_1$ (2.13 ± 0.25) > β-$C_{12}G_1$ (0.182 ± 0.080)

For γ^{∞}: β-C_8G_1 (2570 ± 160) < β-$C_{10}G_1$ (26730 ± 730) < β-$C_{12}G_1$ (307000 ± 43000)

In the same way, the temperature dependency of γ^{∞} for the three glucosides closely follows that of cmc in an inverse manner (see Table 3 in Ref. [2] and Table 2 here).

If $\gamma(x)$ is a decreasing function in the range $(0, x_{cmc})$, as usual in aqueous solutions of surfactants [123–126], then the use of Eq. (5) to get γ^{∞} from x_{cmc} will provide an underestimated value of the bulk activity coefficient at infinite dilution. If, on the contrary, reliable γ^{∞} values are available and $\gamma(x)$ is assumed to be a constant function below the cmc, then Eq. (5) will underestimate x_{cmc}. In a previous work [2] we proposed to exploit this to get a lower boundary for x_{cmc} that would allow the identification of unreliable cmc values. In the case of β-C_8G_1 such criterion was found to be very useful. However, its utility within a given family of surfactants is expected to decrease as the hydrophilic-lipophilic balance (HLB value) becomes lower and Eq. (5) is increasingly a better approach [127]. Thus, the cmc values of β-$C_{12}G_1$ obtained from the infinite dilution activity coefficients are nearly identical to those calculated directly from surface tension data (Table S7). As for β-$C_{10}G_1$, which represents an intermediate scenario, the proposed lower boundary criterion clearly identifies unreliable cmc values from the literature at 298 K (from 0.78 to 1 mM [77,78,102,103]) and 323 K (1.61 mM [60]), as can be checked in Table S6. We will come back to that later (last paragraph in sect. 3.2).

3.1.2. Standard Gibbs energies of micellization and adsorption

Another quantity included in Table 2 is the standard Gibbs energy of micellization per mole of monomer (ΔG^0_{mic}). For nonionic surfactants it can be approximated by Eq. (6), whose standard state is the hypothetical state of unit mole fraction extrapolated along the Henry's law line.

$$\Delta G^0_{mic} = RT \ln x_{cmc} \tag{6}$$

This expression supposes ideal behavior (in the sense of Henry's law) of the free surfactant molecules below the cmc, which amounts to a constant bulk activity coefficient in that interval. Note that such assumption is more realistic for lower cmc surfactants [127]. On the other hand, Eq. (6) can be derived either from the pseudophase separation model [128] or from the association model of mass action law, assuming in this case monodisperse micelles with a fairly large aggregation number (≥50) [128–130]. The later condition is fulfilled by β-$C_{10}G_1$ [120] and according to theoretical predictions it is also likely to apply to β-$C_{12}G_1$ [87].

As for the standard Gibbs energy of adsorption (ΔG^0_{ads}), which characterizes the transference from bulk to surface in the selected standard states, we have considered two different definitions. Both of them have in common the choice of the standard state in the bulk phase (the hypothetical state of unit mole fraction extrapolated along the Henry's law line), with the aim of enabling comparisons between ΔG^0_{mic} and ΔG^0_{ads}. Rosen and Aronson [131] defined ΔG^0_{ads} by choosing as reference for the surface phase "a hypothetical monolayer of the surfactant at its closest packing but at a surface pressure of zero". For nonionic surfactants obeying Eq. (6), this choice affords [106].

$$\Delta G^{0(1)}_{ads} = RT \ln x_{cmc} - \pi_{cmc} a_{min} = \Delta G^0_{mic} - \pi_{cmc} a_{min} \tag{7}$$

where a_{min} stands for the minimum surface molar area. Another classical choice for the standard state at the surface is that of unit surface pressure, $\pi = 1$ mN m^{-1}, which yields Eq. (8) for all surfactant types:

$$\Delta G^{0(2)}_{ads} = -RT \ln\left(\frac{\pi}{x}\right)_{x\to 0} \tag{8}$$

Table 3
Critical micelle concentrations determined from speed of sound analysis [a,b] and the corresponding thermodynamic parameters for the micellization of β-$C_{10}G_1$ at different temperatures.[c]

T/K	cmc/mM		ΔG^0_{mic}/kJ·mol^{-1}		ΔH^0_{mic}/kJ·mol^{-1}		$T\Delta S^0_{mic}$/kJ·mol^{-1}	
	RK-LM	C	RK-LM	C	RK-LM	C	RK-LM	C
283.15	2.85	2.89	−23.43	−23.26	19.5	26.2	42.9	49.5
	(0.91)	(0.17)	(0.39)	(0.39)	(9.1)	(7.5)	(8.7)	(7.2)
285.65	2.59	2.63	−23.80	−23.68	17.4	23.7	41.2	47.3
	(0.45)	(0.18)	(0.33)	(0.33)	(8.2)	(6.9)	(7.9)	(6.6)
288.15	2.45	2.41	−24.16	−24.08	15.4	21.1	39.5	45.2
	(0.31)	(0.21)	(0.26)	(0.28)	(7.3)	(6.3)	(7.0)	(6.1)
290.65	2.16	2.16	−24.49	−24.47	13.3	18.5	37.8	43.0
	(0.14)	(0.19)	(0.21)	(0.23)	(6.4)	(5.7)	(6.2)	(5.5)
293.15	1.94	1.85	−24.81	−24.82	11.2	15.9	36.0	40.7
	(0.14)	(0.14)	(0.17)	(0.19)	(5.6)	(5.1)	(5.4)	(5.0)
295.65	2.01	1.99	−25.10	−25.16	9.1	13.3	34.2	38.5
	(0.17)	(0.22)	(0.13)	(0.16)	(4.7)	(4.6)	(4.6)	(4.4)
298.15	2.18	2.19	−25.38	−25.48	7.1	10.8	32.5	36.2
	(0.15)	(0.23)	(0.11)	(0.13)	(3.9)	(4.1)	(3.9)	(4.0)
300.65	1.86	1.78	−25.65	−25.77	5.0	8.2	30.6	34.0
	(0.15)	(0.14)	(0.09)	(0.11)	(3.2)	(3.6)	(3.2)	(3.5)
303.15	2.04	1.98	−25.89	−26.04	2.9	5.6	28.8	31.6
	(0.11)	(0.12)	(0.08)	(0.09)	(2.7)	(3.3)	(2.6)	(3.2)
305.65	1.80	1.70	−26.12	−26.29	0.8	3.0	27.0	29.3
	(0.16)	(0.21)	(0.07)	(0.08)	(2.3)	(3.0)	(2.3)	(3.0)
308.15	1.77	1.71	−26.34	−26.52	−1.2	0.4	25.1	27.0
	(0.13)	(0.12)	(0.08)	(0.07)	(2.4)	(2.9)	(2.4)	(2.9)
310.65	1.81	1.69	−26.53	−26.73	−3.3	−2.1	23.2	24.6
	(0.19)	(0.16)	(0.08)	(0.08)	(2.7)	(3.0)	(2.8)	(3.0)
313.15	1.81	1.68	−26.71	−26.92	−5.4	−4.7	21.3	22.2
	(0.21)	(0.21)	(0.09)	(0.09)	(3.3)	(3.2)	(3.4)	(3.2)
315.65	2.14	1.93	−26.87	−27.08	−7.4	−7.3	19.4	19.8
	(0.16)	(0.13)	(0.11)	(0.10)	(4.1)	(3.5)	(4.2)	(3.6)
318.15	2.04	1.91	−27.02	−27.23	−9.5	−9.9	17.5	17.4
	(0.25)	(0.20)	(0.14)	(0.12)	(4.9)	(3.9)	(5.0)	(4.0)
320.65	2.05	1.72	−27.15	−27.36	−11.6	−12.5	15.6	14.9
	(0.24)	(0.27)	(0.18)	(0.15)	(5.7)	(4.4)	(5.9)	(4.5)
323.15	1.6*	1.49*	−27.26	−27.46	−13.7	−15.0	13.6	12.4
	(1.2)	(0.52)	(0.22)	(0.18)	(6.6)	(4.9)	(6.8)	(5.1)

[a] Each isotherm was analyzed in two ways: (*i*) by applying a combination of the Runge-Kutta numerical integrations method and the Levenberg–Marquardt least-squares fitting algorithm (RK-LM), and (*ii*) by using the Carpena method.
[b] The values marked with an asterisk (cmc at 323.15 K) have not been included in the subsequent fits of Eq. (14) to cmc data.
[c] Uncertainties are given in parentheses.

The direct calculation of the limit in the right-hand side of the equation would require surface tension data in the π range (0, 3) mN m^{-1} [106], where reliable values are difficult to obtain. However, we can get it in an indirect way from the Volmer SEOS, through the intercept of the linear fit of $\ln(\pi^*/x)$ vs. π data in the dilute region (calculated from Eq. (3) and included in Table 2). Then, the sought limit is obtained just by adding $\ln\pi_{max}$ to that intercept.

Our results (Table 2) show that adsorption is more spontaneous than micellization ($\Delta G^0_{ads} < \Delta G^0_{mic} < 0$), as expected. As with β-C_8G_1 [2], both adsorption and micellization Gibbs energies become more negative with the increase of temperature, which could be ascribed to the dehydration of the glucose moiety upon heating. Interestingly, the difference $\Delta G^0_{ads} - \Delta G^0_{mic}$ seems not to depend on the glucoside chain length nor on the temperature, meaning that adsorption and micellization are equally favored upon lengthening the hydrophobic moiety or upon heating. Such difference, called effective Gibbs free energy change [132], amounts to −10 kJ mol^{-1} and −16 kJ mol^{-1} for $\Delta G^{0(1)}_{ads}$ and $\Delta G^{0(2)}_{ads}$, respectively. Note that in the case of $\Delta G^{0(1)}_{ads}$ that temperature independent quantity can be written as $-\pi_{cmc}a_{min}$ (see Eq. (7)).

3.2. Determination of the cmc from thermoacoustimetry

The inspection of Figs. S1, 3, and S2 shows that the Williams method for the cmc determination would be hardly applicable. The gradual variation of u and κ_S data around the cmc region, along with some data scattering related to specific problems in working with β-$C_{10}G_1$ solutions (see sections 2.2 and 2.3), would allow for a high degree of subjectivity in selecting the concentration intervals for each of the two linear fits. So this scenario is clearly suited to check the applicability of the Carpena method in thermoacoustimetry.

The origin of the Carpena method [57] lies on the qualitative examination of a typical plot of conductivity vs. concentration data for aqueous solutions of ionic surfactants. It presents two regions with linear behavior but different slopes (A_1 and A_2) connected by a narrower or larger transition zone centered at the cmc, in such a way that its first derivative plot could be described by a Boltzmann type sigmoid,

$$f'(c) = \frac{A_1 - A_2}{1 + \exp[(c - \mathrm{cmc})/\Delta c]} + A_2 \tag{9}$$

where Δc is the width of the transition zone. Then the analytical integration of such sigmoid should yield the original function $f(c)$:

$$f(c) = f(0) + A_1 c + \Delta c(A_2 - A_1)\ln\left(\frac{1 + \exp[(c - \mathrm{cmc})/\Delta c]}{1 + \exp(-\mathrm{cmc}/\Delta c)}\right) \tag{10}$$

The qualitative description of the conductivity vs. concentration

plots made above could also apply to other physical properties used in the characterization of surfactant solutions (for instance, first derivatives of refractometric data have been fitted to Eq. (9) [133]), and particularly to speeds of sound and isentropic compressibilities. On this basis, we propose to use Eq. (10) to fit u or κ_S data, allowing to easily remove all subjectivity in the cmc determination from these quantities.

All adjustments were made with Origin Pro (version 8.0724), utilizing the simplex method to ensure finding the global minimum and (once the chi-square can not be further reduced) doing a final iteration with Levenberg-Marquardt. The values of the adjustable parameters in Eq. (10) are listed in Tables S8 and S9 for $f = u$ and $f = \kappa_S$, respectively. It is worth mentioning that we fixed $A_2 = 0$ when its fitting was not statistically justified (by examining both the relative uncertainties of parameters and the adjusted r-squared). Note also that $f(0)$ refers to the pure solvent, so that it could be treated as a constant if desired. From our experience, this choice is advisable in cases of low data scattering to avoid an overparameterized fitting function. Thus, while $f(0)$ was considered an adjustable parameter for β-$C_{10}G_1$ solutions, it was fixed when our earlier reported u and κ_S isotherms for β-C_8G_1 [2] were used to make additional tests of the Carpena method (Fig. S4).

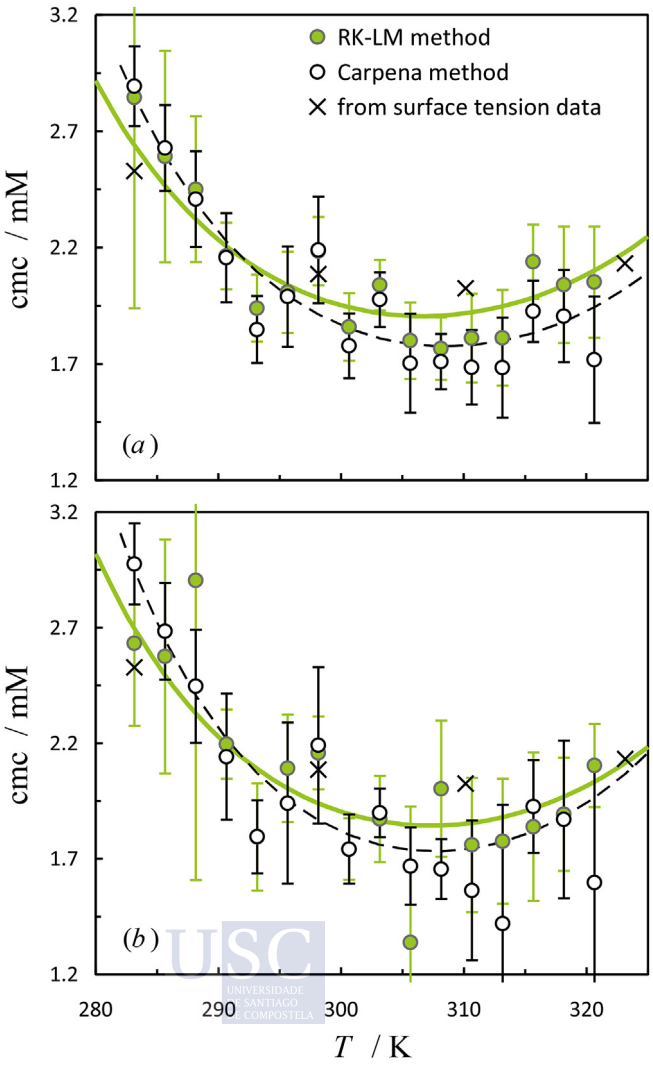


Fig. 4. Temperature dependence of the critical micelle concentration of β-$C_{10}G_1$, as estimated in this work by analyzing (*a*) speed of sound and (*b*) isentropic compressibility data following two procedures. The lines stand for fits of Eq. (14) to datasets obtained from the RK-LM (solid) and Carpena (dashed) methods. The cmc values estimated from surface tension data are included for comparison purposes both in (*a*) and (*b*). The legend applies to both plots.

To check the validity of Eq. (10) in the context of thermoacoustimetry, a comparison was established between the cmc values obtained with the Carpena and RK-LM methods (using in the later case a home-made program). Some examples of the application of both procedures are shown in Figs. S1, 3, and S2. The comparative analysis from speed of sound isotherms is made in Table 3 and Fig. 4a, while that from isentropic compressibility isotherms is displayed in Table S10 and Fig. 4b. As can be easily checked in Fig. 4, the cmc values from both methods agree within uncertainty. This agreement also holds in the case of β-C_8G_1 solutions, shown in Fig. S4, where the results from the conventional procedure (Williams) were included too [2].

All the cmc data for β-$C_{10}G_1$ determined from u and κ_S with either of the two methods were included in Table S6 for the sake of comparison with literature. It is striking that all the literature values in Tables S6-S7 derive from a single property (surface tension), which stresses the current need of providing reliable and easy methods for the cmc determination from other quantities. At 50 °C (323.15 K), we note that the four values obtained from thermoacoustimetry are much lower than that determined from the infinite dilution activity coefficient (Eq. (5)). Thus, the application of the lower boundary criterion for the cmc (section 3.1.1), together with unacceptably high relative uncertainties, advise us to ignore the cmc values at 50 °C for the subsequent estimation of the cmc(T) function.

3.3. Thermodynamics of micellization

Assuming a linear dependence of the heat capacity change of micellization (and of the degree of ionization) with temperature,

$$\Delta C^0_{p,\mathrm{mic}} = \Delta C^{0*}_{p,\mathrm{mic}} + \beta(T - T^*) \tag{11}$$

Rodríguez et al. [134] modified the Muller equation [135] to get a more accurate description of U-shaped $x_{\mathrm{cmc}}(T)$ curves. In the case of nonionic surfactants, their proposal reduces to

$$\ln x_{\mathrm{cmc}} = \ln x^*_{\mathrm{cmc}} + \frac{\Delta C^{0*}_{p,\mathrm{mic}}}{R}\left(\ln\frac{T^*}{T} + \frac{T - T^*}{T}\right) + \frac{\beta}{R}\left(\frac{T^{*2} - T^2}{2T} - T^* \ln\frac{T^*}{T}\right) \tag{12}$$

where $(T^*, x^*_{\mathrm{cmc}})$ is the minimum of the $x_{\mathrm{cmc}}(T)$ function. Eq. (12) can be simplified for fitting purposes by means of two changes of variables:

$$\Delta C^{0*}_{p,\mathrm{mic}} = -2BRT^* - CR \qquad \beta = -2BR \tag{13}$$

affording Eq. (14),

$$\ln x_{\mathrm{cmc}} = \ln x^*_{\mathrm{cmc}} + B\frac{(T - T^*)^2}{T} - C\left(\ln\frac{T^*}{T} + \frac{T - T^*}{T}\right) \tag{14}$$

which has also four fitting parameters (T^*, $\ln x^*_{\mathrm{cmc}}$, B, and C). This later expression can be alternatively obtained from the Lim equation [136] ($\ln x_{\mathrm{cmc}} = A + BT + C\ln T + D/T$) by making variable changes to rewrite the constants A and D as a function of the coordinates of the minimum, as shown in a previous work [2].

All adjustments were made with Origin Pro in the same manner as described above (section 3.2). The four-parameter fit was not statistically justified with the available cmc data (whether obtained from u or κ_S, with either method). As with β-C_8G_1 [2] we had to fix

$B = 0$, which entails assuming the heat capacity change of micellization constant in the working T range ($\beta = 0$ in Eq. (11)). Table 4 shows the results of the weighted fit of Eq. (14) to the cmc data obtained from u or κ_S with either method (RK-LM or Carpena). (For convenience, cmc* is furnished instead of x^*_{cmc}.) The values of the fitting parameters obtained from both datasets or from both procedures agree within error. The calculated curves are plotted in Fig. 4.

The estimation of the thermodynamic parameters of micelle formation starts from the combination of Eqs. (6) and (14) to get the temperature dependence of the standard Gibbs energy of micellization, $\Delta G^0_{mic}(T)$. (Note that although the cmc is expressed in mM units in Tables 3 and S10, Eq. (6) requires the use of mole fractions.) Then the enthalpy of micelle formation is obtained through the Gibbs-Helmholtz relation $\Delta H^0_{mic} = -T^2\partial(\Delta G^0_{mic}/T)/\partial T$:

$$\Delta H^0_{mic} = -BR\left(T^2 - T^{*2}\right) - CR(T - T^*) \quad (15)$$

It appears from this equation that the x-coordinate of the minimum in $x_{cmc}(T)$ is in fact the isenthalpic temperature: $T^* \equiv T_{\Delta H=0}$. It is worth pointing out that we are dealing with a van't Hoff enthalpy, as ΔH^0_{mic} is ultimately derived from the temperature dependence of the micellization equilibrium constant (K):

$$\Delta G^0_{mic} = -\frac{RT}{N}\ln K \cong RT\ln x_{cmc} \quad (16)$$

Hence Eq. (15) is valid only under the assumption of a temperature independent aggregation number (N) in the working T range [38,137].

Next, the standard entropy of micellization is calculated from the relation $T\Delta S^0_{mic} = \Delta H^0_{mic} - \Delta G^0_{mic}$. It is helpful to express it as a function of the adjustable parameters:

$$\Delta S^0_{mic} = -R\ln x^*_{cmc} - 2BR(T - T^*) + CR\ln\frac{T^*}{T} \quad (17)$$

to get (only for $B = 0$) the isentropic temperature:

$$\ln T_{\Delta S=0} = \ln T_{\Delta H=0} - \frac{\ln x^*_{cmc}}{C} \quad (18)$$

Finally, the first temperature derivative of ΔH^0_{mic} affords an expression for $\Delta C^0_{p,mic}$

$$\Delta C^0_{p,mic} = -2BRT - CR \quad (19)$$

that would bring us back to Eq. (11) by undoing the variable changes (Eq. (13)).

Tables 3 and S10 gather the calculated thermodynamic parameters that were ultimately obtained from speeds of sound and from isentropic compressibilities, respectively. The process of micelle formation becomes more spontaneous with increasing T, as already discussed in section 3.1.2. Three temperature regions can be considered, as illustrated by Fig. 5: The micellization is endothermic and hence entropy driven up to ~34 °C (I), whereas it is governed by both enthalpy and entropy above that temperature (II); afterwards, the entropy term might change sign around 65 °C (see $T_{\Delta S=0}$ in Table 4), where the formation of micelles would become enthalpy driven (III). However, this extrapolated trend should be taken with caution. Positive ΔH^0_{mic} and ΔS^0_{mic} (region I) are usually ascribed to the removal of hydrophobic hydration, as water molecules around the hydrophobic moiety of the monomers are highly structured [110,138]. The increase of thermal motion partially disrupts the water structure around the monomeric alkyl

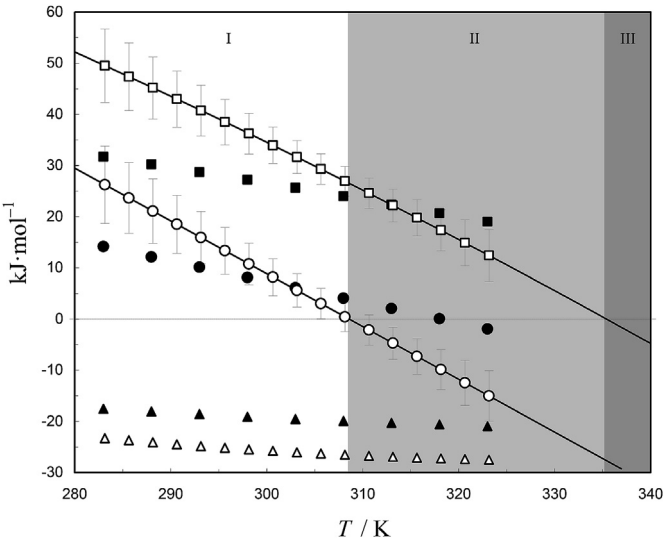


Fig. 5. Temperature dependence of the thermodynamic parameters of micelle formation for β-$C_{10}G_1$ (white dots) and β-C_8G_1 [2] (black dots): ΔG^0_{mic} (triangle), ΔH^0_{mic} (circle), and $T\cdot\Delta S^0_{mic}$ (square). The lines corresponding to the enthalpic and entropic functions for β-$C_{10}G_1$ help to define three temperature ranges for this surfactant: (I) $\Delta H^0_{mic} > 0$, $\Delta S^0_{mic} > 0$; (II) $\Delta H^0_{mic} < 0$, $\Delta S^0_{mic} > 0$; (III) $\Delta H^0_{mic} < 0$, $\Delta S^0_{mic} < 0$. All these quantities were derived from speed of sound analysis, using the Carpena (β-$C_{10}G_1$) and Williams (β-C_8G_1) methods for the cmc determination.

Table 4
Adjustable parameters in Eq. (14) after having fixed $B = 0$ (C coefficient, minimal cmc value, and isenthalpic temperature),[a] isentropic temperature, and heat capacity change of micellar formation.[b,c]

		C	$\frac{cmc^*}{mM}$	$\frac{T^*\equiv T_{\Delta H=0}}{K}$	$\frac{T_{\Delta S=0}}{K}$	$\frac{\Delta C^0_{p,mic}}{kJ\cdot mol^{-1}\cdot K^{-1}}$
from u	RK-LM	100	1.905	306.7	340	−0.83
		(45)	(0.056)	(2.8)	(16)	(0.37)
	Carpena	124	1.775	308.6	335.4	−1.03
		(33)	(0.050)	(2.8)	(8.0)	(0.27)
from κ_S	RK-LM	110	1.844	307.3	337	−0.92
		(44)	(0.075)	(2.8)	(13)	(0.36)
	Carpena	149	1.732	307.7	329.8	−1.24
		(43)	(0.061)	(3.3)	(7.5)	(0.36)

[a] Performing a weighted fit to account for the different uncertainties of cmc values. Note that although the minimal cmc is given in mM units, calculations were actually made in terms of mole fractions.
[b] A comparison is made between the results obtained from four sets of cmc data, derived from speed of sound and isentropic compressibility analyses using two different procedures (see Tables 3 and S10).
[c] Uncertainties are given in parentheses.

chains and thus the effects of breaking down the hydrophobic hydration layer upon micellization reduce gradually (region II) until they eventually disappear (region III).

Both the isenthalpic and the isentropic temperatures (Table 4) are significantly lower than those estimated for β-C_8G_1 [2], as can be seen in Fig. 5. In the case of $T_{\Delta H=0}$ this is consistent with the observed trend for T^* in homologous series of surfactants [134], being shifted to lower temperatures on increasing the alkyl chain length.

The so-called enthalpy-entropy compensation is reflected by a linear fit of ΔH^0_{mic} vs. ΔS^0_{mic} with a high correlation coefficient (r = 0.9998, not shown). The compensation temperature (slope of the straight) is identical from any of the two data sources (u or κ_S) with either method of cmc determination (RK-LM or Carpena): $T_{com} = (302.8 \pm 1.4)$ K, agreeing within error with the central value of the experimental temperature interval, as expected [139].

The heat capacity change of micellization of β-$C_{10}G_1$ is negative, as expected for a process involving strong dehydration [140], and it is roughly twice as large as that obtained for β-C_8G_1 [2]. Its relatively high uncertainty (see Table 4) should be partly ascribed to the assumption of constancy in the working T range (by fixing $B = 0$ in the adjustments).

4. Conclusions

An exhaustive revision of literature has highlighted the lack of a simple but objective procedure for the determination of the cmc from u or κ_S data, which translates into an underuse of the potential of thermoacoustimetry in micellization thermodynamics studies. To tackle the problem we propose to borrow a method from Carpena et al. [57] that fulfills both conditions (simple and objective) and that has been successfully used over the last 16 years to estimate the cmc from conductivity data. Let us stress that this choice does not require programming experience nor expertise in numerical computation techniques, in contrast with other procedures like the one employed here for comparison purposes (combination of the Runge-Kutta numerical integrations method and the Levenberg–Marquardt least-squares fitting algorithm). On the other hand, our working surfactant (β-decyl-β-D-glucopyranoside) is specially suitable to check that proposal: The Williams method for the cmc determination can not be applied to it because of (*i*) the low sensitivity of u and κ_S to the change from monomeric to micellar domain, and (*ii*) some data scattering ascribed to system-related experimental difficulties (sections 2.2 and 2.3).

Densities, speeds of sound, and isentropic compressibilities at 17 temperatures (10–50 °C) have been tabulated for aqueous solutions of β-$C_{10}G_1$, ranging from the dilute region up to around twice the cmc. To get the analytical cmc(T) function we have rewritten the Muller [135] fitting equation modified by Rodríguez et al. [134] in a way that allows to subsequently determine most of the derived thermodynamic quantities with lower uncertainties [2] (Eq. (14)). The extrapolation of the obtained cmc(T) function beyond the working T range allows to identify three temperature regions as regards the nature of β-$C_{10}G_1$ micellization: entropy driven below ~34 °C and enthalpy driven above ~65 °C, while in the middle it would be governed by both entropy and enthalpy. The existence of the third region ($\Delta H^0_{mic} < 0$, $\Delta S^0_{mic} < 0$) was not that clear in the case of β-C_8G_1, which showed higher isentropic and isenthalpic temperatures [2].

The adsorption of β-$C_{10}G_1$ and β-$C_{12}G_1$ at the solution/air interface was investigated by making surface tension measurements at several temperatures (including that of human body). A comprehensive revision of literature data revealed significant discrepancies between different sources. In the case of β-$C_{12}G_1$ they were ascribed to the fact of working far below the Krafft temperature. For β-$C_{10}G_1$, the setting of a cmc lower boundary (calculated as the inverse of the limiting activity coefficient of the surfactant defined under the symmetric convention [2]) has shown its utility as a criterion to identify unreliable cmc values. As for the adsorption behavior of the two working surfactants, the observed trends were identical to those encountered for β-C_8G_1 [2]: Both chemicals become less effective surfactants upon heating and their minimum area at the surface (while keeping lower than that of β-C_8G_1) increases with T, dominated by increased thermal motion. The spontaneity of the adsorption and micellization processes also increases with T due to a lowering of the hydration number, the difference between ΔG^0_{ads} and ΔG^0_{mic} being temperature and chain length independent. Furthermore, the analysis of surface tension data for β-$C_{10}G_1$ was useful to confirm that its cmc(T) function is U-shaped, as with β-C_8G_1 [2].

Acknowledgements

We thank Dr. Ángel Piñeiro for assistance in the design of experiments and useful suggestions. The raw NMR and mass spectra were furnished by technicians from the RIAIDT. This work was supported by grants from XUGA-Spain (INCITE08PXIB206050PR) and MINECO (MAT2015-71826-P). P.F. Garrido also wants to thank the Spanish Ministry of Education, Culture and Sport for a Departmental Collaboration Grant during the 2014/2015 academic year, as well as the Spanish Ministry of Economy and Competitiveness for supporting him with the FPI grant BES-2016-076761.

List of symbols

a	surface molar area
a_0	van der Waals type constant in the Volmer SEOS
a_{min}	minimum surface molar area
A_1 (A_2)	asymptotic value for small (large) concentration values in the Boltzmann type sigmoid $f'(c)$
A_{min}	minimum surface area per solute molecule
c	nominal concentration
cmc*	x^*_{cmc} expressed in molar concentration units
f	generic physical property used to detect the change from monomeric to micellar domain (the electrical conductivity in the context of the original Carpena method)
$f(0)$	value of f for the pure solvent (water in this work)
GAI	Gibbs adsorption isotherm
K	micellization equilibrium constant
n	number of moles of solute
n_h	hydration number
n_w	number of moles of water
N	aggregation number
N_{Av}	Avogadro's number
R	ideal gas constant
RK-LM	combination of the Runge-Kutta numerical integrations method with the Levenberg-Marquardt least-squares fitting algorithm
SEOS	surface equation of state
T	temperature
T^*	x-coordinate of the minimum of a U-shaped $x_{cmc}(T)$ function
T_{com}	compensation temperature
$T_{\Delta H=0}$	isenthalpic temperature (T value such as $\Delta H^0_{mic} = 0$)
$T_{\Delta S=0}$	isentropic temperature (T value such as $\Delta S^0_{mic} = 0$)
u	speed of sound
x	solute mole fraction
x^*_{cmc}	y-coordinate of the minimum of a U-shaped $x_{cmc}(T)$ function

Subscripts

cmc	critical micelle concentration
w	pure water

Greek letters

α	thermal expansion coefficient
β	slope of the $\Delta C^0_{p,\mathrm{mic}}(T)$ function
Δc	width of the transition zone in the Boltzmann type sigmoid $f'(c)$
$\Delta C^0_{p,\mathrm{mic}}$	heat capacity change of micellization
$\Delta C^{0\,*}_{p,\mathrm{mic}}$	value of $\Delta C^0_{p,\mathrm{mic}}$ at $x = x^*_{\mathrm{cmc}}$
$\Delta G^0_{\mathrm{ads}}$	standard Gibbs energy of adsorption
$\Delta G^0_{\mathrm{mic}}$	standard Gibbs energy of micellization (per mole of monomer)
$\Delta H^0_{\mathrm{mic}}$	enthalpy of micellization (per mole of monomer)
$\Delta S^0_{\mathrm{mic}}$	standard entropy of micellization (per mole of monomer)
γ	surfactant activity coefficient in the bulk phase, defined under the symmetric convention
γ^{∞}	limiting value (when $x \to 0$) of the activity coefficient
Γ	excess surface concentration
$\Gamma_{\max}$	maximum value of the excess surface concentration
κ_S	isentropic compressibility
π	surface pressure (defined as $\sigma_w - \sigma$)
π^*	$\pi/\pi_{\max}$
$\pi_{\max}$	surface pressure at saturation conditions
ρ	density
σ	surface tension
$\sigma_{\min}$	surface tension at saturation conditions

Appendix A. Supplementary data

Supplementary data related to this article can be found at https://doi.org/10.1016/j.fluid.2018.08.011.

References

[1] IUPAC Compendium of Chemical Terminology - The Gold Book, https://goldbook.iupac.org/.
[2] G. Castro, A. Amigo, P. Brocos, Squeezing experimental measurements for a proper analysis of surfactant thermodynamics: octyl-β-D-glucopyranoside as a case study, Fluid Phase Equil. 376 (2014) 31–39.
[3] E. Junquera, L. Peña, E. Aicart, Influence of temperature on the micellization of sodium dodecylsulfate in water from speed of sound measurements, J. Solut. Chem. 23 (1994) 421–430.
[4] M.R. Islam, S. Ara, Thermodynamics of hexadecyltrimethyl-ammonium bromide in water and in aqueous NaBr solution, Acoust. Lett. 20 (1996) 99–106.
[5] J.M. Ruso, A. González-Pérez, G. Prieto, F. Sarmiento, Thermodynamic study of self-assembly behavior of propranolol hydrochloride in aqueous solutions as a function of electrolyte concentration and temperature, J. Chem. Eng. Data 48 (2003) 1597–1602.
[6] P. Taboada, M. Gutiérrez-Pichel, S. Barbosa, V. Mosquera, A thermodynamic study of two anionic amphiphilic penicillins in aqueous solution by ultrasound speed measurements, Colloids Surf., A 220 (2003) 29–34.
[7] P. Taboada, M. Gutiérrez-Pichel, V. Mosquera, Effects of self-aggregation on the hydration of an amphiphilic antidepressant drug in different aqueous media, Chem. Phys. 298 (2004) 65–74.
[8] R. Sadeghi, S. Shahabi, A comparison study between sodium dodecyl sulfate and sodium dodecyl sulfonate with respect to the thermodynamic properties, micellization, and interaction with poly(ethylene glycol) in aqueous solutions, J. Chem. Thermodyn. 43 (2011) 1361–1370.
[9] H.I. Tantry, F.A. Sheikh, P.A. Bhat, Micellization behavior of dodecylethyldimethylammonium bromide as a function of temperature and concentration, J. Mol. Liq. 183 (2013) 79–84.
[10] A. Ali, F. Nabi, N.A. Malik, S. Tasneem, S. Uzair, Study of micellization of sodium dodecyl sulfate in non-aqueous media containing lauric acid and dimethylsulfoxide, J. Surfactants Deterg. 17 (2014) 151–160.
[11] D.M. Bhattacharya, U.R. Pratap, A.V. Wankhade, S.P. Zodape, Volumetric and ultrasonic approach in the investigation of critical micellar phenomenon of amphiphilic drugs in aqueous solutions at different temperatures, J. Mol. Liq. 214 (2016) 117–127.
[12] S.K. Mehta, N. Bala, S. Sharma, Thermodynamics of aggregation of Tweens in the presence of diclofenac sodium, Colloids Surf., A 268 (2005) 90–98.
[13] J.L. López-Fontán, A. González-Pérez, J. Costa, J.M. Ruso, G. Prieto, P.C. Schulz, F. Sarmiento, Thermodynamics of micellization of tetraethylammonium perfluorooctylsulfonate in water, J. Colloid Interface Sci. 297 (2006) 10–21.
[14] M.A. Cheema, P. Taboada, S. Barbosa, E. Castro, M. Siddiq, V. Mosquera, A comparative study of the thermodynamic properties at the air–water interface and in the bulk of structurally related phenothiazine drugs aqueous solutions, J. Chem. Thermodyn. 40 (2008) 298–308.
[15] E. Fisicaro, C. Compari, M. Biemmi, E. Duce, M. Peroni, G. Donofrio, F. Sansone, B. Różycka-Roszak, H. Pruchnik, N. Barbero, G. Viscardi, P. Quagliotto, Thermodynamics and biological properties of the aqueous solutions of new glucocationic surfactants, J. Phys. Chem. B 112 (2008) 9360–9370.
[16] S. Chauhan, V. Sharma, K. Sharma, Maltodextrin–SDS interactions: volumetric, viscometric and surface tension study, Fluid Phase Equil. 354 (2013) 236–244.
[17] N. Dubey, CTAB aggregation in solutions of higher alcohols: thermodynamic and spectroscopic studies, J. Mol. Liq. 184 (2013) 60–67.
[18] D. Kaushal, D.S. Rana, S. Chauhan, Effect of Furosemide on denaturation of lysozyme in the presence of ionic surfactant at different temperatures, Fluid Phase Equil. 360 (2013) 239–247.
[19] A. Pal, S. Chaudhary, Ionic liquid induced alterations in the physicochemical properties of aqueous solutions of sodium dodecylsulfate (SDS), Colloids Surf., A 430 (2013) 58–64.
[20] V. Bhardwaj, S. Chauhan, P. Sharma, Probing effect of lipophilic butylated hydroxytoluene on anionic surfactant properties for potential food and pharmaceutical applications: thermo-acoustic and spectroscopic study, Fluid Phase Equil. 373 (2014) 63–71.
[21] H. Kumar, C. Chadha, Conductometric and spectroscopic studies of cetyltrimethylammonium bromide in aqueous solutions of imidazolium based ionic liquid 1-butyl-3-methylimidazolium tetrafluoroborate, J. Mol. Liq. 211 (2015) 1018–1025.
[22] K. Sharma, S. Chauhan, B. Priya, Surface, compressibility and viscometric measurements of binary system containing cationic surfactant with achiral amino acid at different temperatures, J. Mol. Liq. 222 (2016) 407–414.
[23] K. Szymczyk, A. Taraba, Properties of aqueous solutions of nonionic surfactants, Triton X-114 and Tween 80, at temperatures from 293 to 318K: spectroscopic and ultrasonic studies, Chem. Phys. 483–484 (2017) 96–102.
[24] S.T. Huerta-Marcial, E.B. Figueroa-Ochoa, L.C. Rosales-Rivera, M.V. Ramallo, J.M. Ruso, J.F.A. Soltero, Changes in thermodynamic and structural characteristics of polymerized and monomer surfactants induced by introduction of a hydrotrope, J. Mol. Liq. 246 (2017) 197–207.
[25] J.E. Desnoyers, G. Caron, R. DeLisi, D. Roberts, A. Roux, G. Perron, Thermodynamic properties of alkyldimethylamine oxides in water. Application of a mass-action model for micellization, J. Phys. Chem. 87 (1983) 1397–1406.
[26] M.J. Suárez, J.L. López-Fontán, F. Sarmiento, V. Mosquera, Thermodynamic study of the aggregation behavior of sodium n-hexyl sulfate in aqueous solution, Langmuir 15 (1999) 5265–5270.
[27] J.A. MacInnis, D.G. Marangoni, R. Palepu, A study of micellization and the thermodynamic properties of a series of aqueous sodium cyclohexyl alkanoate surfactants, Can. J. Chem. 78 (2000) 1222–1232.
[28] M. Gutiérrez-Pichel, P. Taboada, L.M. Varela, D. Attwood, V. Mosquera, Solute and solvent structure effects on the volume and compressibilities of some colloidal penicillins in aqueous solution, Langmuir 18 (2002) 3650–3654.
[29] A. Priev, S. Zalipsky, R. Cohen, Y. Barenholz, Determination of critical micelle concentration of lipopolymers and other amphiphiles: Comparison of sound velocity and fluorescent measurements, Langmuir 18 (2002) 612–617.
[30] E. Junquera, F. Ortega, E. Aicart, Aggregation process of the mixed ternary system dodecylethyldimethylammonium bromide/dodecylpyridinium chloride/H_2O: an experimental and theoretical approach, Langmuir 19 (2003) 4923–4932.
[31] A. González-Pérez, L.M. Varela, M. García, J.R. Rodríguez, Sphere to rod transitions in homologous alkylpyridinium salts: a Stauff-Klevens-type equation for the second critical micelle concentration, J. Colloid Interface Sci. 293 (2006) 213–221.
[32] M.A. Cheema, M. Siddiq, S. Barbosa, P. Taboada, V. Mosquera, Surface and bulk properties of two amphiphilic phenothiazine drugs in different aqueous media, J. Chem. Eng. Data 53 (2008) 368–373.
[33] K. Kishore, S.K. Upadhyaya, Acoustic behaviour of terbium laurate and myristate solutions in 60/40 benzene-methanol mixture (v/v), J. Pure Appl. Ultrason. 33 (2011) 39–42.
[34] H.M. Kwaambwa, F.M. Nermark, Interactions in aqueous solution of a zwitterionic surfactant with a water treatment protein from *Moringa oleifera* seeds studied by surface tension and ultrasonic velocity measurements, Green Sustain. Chem. 3 (2013) 135–140.
[35] H. Høiland, E. Alagic, G.M. Førland, Solubilization of 1-hexanol in aqueous solutions of sodium dodecyl sulfate at pressures up to 140 MPa: partial molar volumes, compressibilities, and partition coefficients, Langmuir 30 (2014) 7962–7967.
[36] M.K. Sangeeta, Rawat, Ultrasonic velocity and other allied parameters of dysprosium laurate and myristate, J. Applicable Chem. 3 (2014) 354–359.
[37] S. Shirzad, R. Sadeghi, Micellization properties and related thermodynamic parameters of aqueous sodium dodecyl sulfate and sodium dodecyl sulfonate solutions in the presence of 1-propanol, Fluid Phase Equil. 377 (2014) 1–8.
[38] M. Gutiérrez-Pichel, D. Attwood, P. Taboada, V. Mosquera, Influence of

external factors on the self-assembly of two structurally related antidepressant drugs: a thermodynamic study, Mol. Phys. 101 (2003) 3455–3465.
[39] P. Taboada, M. Gutiérrez-Pichel, S. Barbosa, D. Attwood, V. Mosquera, Effect of temperature on the volume and compressibilities of some amphiphilic penicillins in aqueous solution, Phys. Chem. Chem. Phys. 5 (2003) 703–709.
[40] P. Taboada, S. Barbosa, V. Mosquera, Thermodynamic properties of a diblock copolymer of poly(oxyethylene) and poly(oxypropylene) in aqueous solution, Langmuir 20 (2004) 8903–8908.
[41] M.A. Cheema, P. Taboada, S. Barbosa, M. Siddiq, V. Mosquera, Effect of molecular structure on the hydration of structurally related antidepressant drugs, Mol. Phys. 104 (2006) 3203–3212.
[42] P. Gianni, L. Bernazzani, R. Carosi, V. Mollica, Micellization of lithium perfluoroheptanoate and its aggregation on poly(ethylene glycol) oligomers in water, Langmuir 23 (2007) 8752–8759.
[43] A. González-Pérez, J.M. Ruso, Temperature dependence of micellar sphere-to-rod transition using adiabatic compressibility, Colloids Surf., A 356 (2010) 84–88.
[44] M.A. Jamal, K. Shahzad, A. Bahadur, Self aggregation of a selective serotonin reuptake inhibitor drug paroxetine hydrochloride: a thermodynamic study, Phys. Chem. Indian J. 6 (2011) 182–185.
[45] F.A. Sheikh, P.A. Bhat, Effect of temperature and concentration on density, apparent molar volume, ultrasound velocity, isoentropic compressibility, viscosity, and conductivity of hexadecyldimethylethylammonium bromide, J. Chem. Eng. Data 57 (2012) 3368–3374.
[46] M.A. Jamal, I.H. Bukhari, M. Muneer, K. Shahzad, Influence of external factors on self-aggregation of amphiphilic antidepressant drug: a thermodynamic study, J. Chem. Soc. Pakistan 35 (2013) 262–266.
[47] A. Gupta, S.K. Upadhyaya, Acoustical behavior of cerium and thorium myristate in mixed organic solvents, Cellul. Chem. Technol. 47 (2013) 77–82.
[48] G. Savaroglu, L. Genc, Determination of micelle formation of ketorolac tromethamine in aqueous media by acoustic measurements, Thermochim. Acta 552 (2013) 5–9.
[49] P.A. Bhat, F.A. Sheikh, H.I. Tantry, Effect of electrolyte and temperature on micellization behavior of N-ethyl-N,N-dimethyl-1-hexadecanaminium bromide, J. Chem. Eng. Data 59 (2014) 2013–2020.
[50] S. Chauhan, S. Kumari, K. Kumar, A. Umar, C.N. Sundaresan, R. Gupta, Influence of iso-perthiocyanic acid and temperature on the aggregation properties of sodium dodecylsulphate in dimethylsulphoxide, J. Mol. Liq. 211 (2015) 338–345.
[51] S. Chauhan, R. Singh, K. Sharma, K. Kumar, Interaction study of anionic surfactant with aqueous non-ionic polymers from conductivity, density and speed of sound measurements, J. Surfactants Deterg. 18 (2015) 225–232.
[52] O. Naderi, R. Sadeghi, Effect of temperature on the aggregation behaviour and thermodynamic properties of surface active ionic liquid 1-decyl-3-methylimidazolium bromide in aqueous solutions: surface tension, vapour pressure osmometery, conductivity, volumetric and compressibility study, J. Chem. Thermodyn. 102 (2016) 68–78.
[53] M.R. Khatun, M.M. Islam, F.R. Rima, M.N. Islam, Apparent molar volume, adiabatic compressibility, and critical micelle concentration of flucloxacillin sodium in aqueous NaCl solutions at different temperatures, J. Chem. Eng. Data 61 (2016) 102–113.
[54] Y. Moroi, Micelles: Theoretical and Applied Aspects, Springer Science & Business Media, New York, 1992.
[55] M. Pérez-Rodríguez, G. Prieto, C. Rega, L.M. Varela, F. Sarmiento, V. Mosquera, A comparative study of the determination of the critical micelle concentration by conductivity and dielectric constant measurements, Langmuir 14 (1998) 4422–4426.
[56] W. Al-Soufi, L. Piñeiro, M. Novo, A model for monomer and micellar concentrations in surfactant solutions: application to conductivity, NMR, diffusion, and surface tension data, J. Colloid Interface Sci. 370 (2012) 102–110.
[57] P. Carpena, J. Aguiar, P. Bernaola-Galván, C. Carnero Ruiz, Problems associated with the treatment of conductivity–concentration data in surfactant solutions: Simulations and experiments, Langmuir 18 (2002) 6054–6058.
[58] J.M. Goronja, A.M. Janošević Ležaić, B.M. Dimitrijević, A.M. Malenović, D.R. Stanisavljev, N.D. Pejić, Determination of critical micelle concentration of cetyltrimethylammonium bromide: different procedures for analysis of experimental data, Hem. Ind. 70 (2016) 485–492.
[59] A. Capalbi, G. Gente, C. La Mesa, Solution properties of alkyl glucosides, alkyl thioglucosides and alkyl maltosides, Colloids Surf., A 246 (2004) 99–108.
[60] B.J. Boyd, C.J. Drummond, I. Krodkiewska, F. Grieser, How chain length, headgroup polymerization, and anomeric configuration govern the thermotropic and lyotropic liquid crystalline phase behavior and the air–water interfacial adsorption of glucose-based surfactants, Langmuir 16 (2000) 7359–7367.
[61] J. Krawczyk, Temperature impact on the water-air interfacial activity of n-octyl and n-dodecyl-β-D-glucopyranosides, Colloids Surf., A 533 (2017) 61–67.
[62] J. Hernández-Pascacio, X. Banquy, S. Pérez-Casas, M. Costas, A. Amigo, Á. Piñeiro, A small molecular size system giving unexpected surface effects: α-cyclodextrin + sodium dodecyl sulfate in water, J. Colloid Interface Sci. 328 (2008) 391–395.
[63] Á. Piñeiro, P. Brocos, A. Amigo, M. Pintos, R. Bravo, Surface tensions and refractive indices of (tetrahydrofuran plus n-alkanes) at T=298.15 K, J. Chem. Thermodyn. 31 (1999) 931–942.
[64] C. Bermúdez-Salguero, J. Gracia-Fadrique, A. Amigo, Surface tension data of aqueous binary mixtures of methyl, ethyl, propyl, and butyl acetates at 298.15 K, J. Chem. Eng. Data 55 (2010) 2905–2908.
[65] C. Bermúdez-Salguero, J. Gracia-Fadrique, E. Calvo, A. Amigo, Densities, refractive indices, speeds of sound, and surface tensions for dilute aqueous solutions of 2-methyl-1-propanol, cyclopentanone, cyclohexanone, cyclohexanol, and ethyl acetoacetate at 298.15 K, J. Chem. Eng. Data 56 (2011) 3823–3829.
[66] J.L. López-Cervantes, J. Gracia-Fadrique, E. Calvo, A. Amigo, Surface tensions, densities, and speeds of sound for aqueous solutions of lauryl ether ethoxylates, Fluid Phase Equil. 356 (2013) 193–200.
[67] T.J. Fortin, A. Laesecke, M. Freund, S. Outcalt, Advanced calibration, adjustment, and operation of a density and sound speed analyzer, J. Chem. Thermodyn. 57 (2013) 276–285.
[68] W. Barzyk, K. Lunkenheimer, P. Warszyński, B. Jachimska, A. Pomianowski, Effect of molecular structure of amphiphiles on the surface pressure and electric surface potential isotherms at the air/solution interface, Colloids Surf., A 443 (2014) 515–524.
[69] C.M. Persson, A.J. Kumpulainen, J.C. Eriksson, Adsorption of n-decyl-β-D-glucopyranoside and n-decyl-β-D-maltopyranoside mixtures at the liquid–vapor interface, Langmuir 19 (2003) 6110–6114.
[70] M.L. Sierra, M. Svensson, Mixed micelles containing alkylglycosides: Effect of the chain length and the polar head group, Langmuir 15 (1999) 2301–2306.
[71] M.A. Deyab, Decyl glucoside as a corrosion inhibitor for magnesium–air battery, J. Power Sources 325 (2016) 98–103.
[72] K. Shinoda, T. Yamaguchi, R. Hori, The surface tension and the critical micelle concentration in aqueous solution of β-D-alkyl glucosides and their mixtures, Bull. Chem. Soc. Jpn. 34 (1961) 237–241.
[73] B. Niraula, T.C. King, T.K. Chun, M. Misran, Rheology properties of glucopyranoside stabilized oil–water emulsions: effect of alkyl chain length and bulk concentration of the surfactant, Colloids Surf., A 251 (2004) 117–132.
[74] C. Rodgers, J. Moulins, R. Palepu, Mixed micellar systems of n-alkyl-β-D glucopyranosides with hexadecyl cationic surfactants, Tenside Surfactants Deterg. 43 (2006) 310–316.
[75] R. Aveyard, B.P. Binks, J. Chen, J. Esquena, P.D.I. Fletcher, R. Buscall, S. Davies, Surface and colloid chemistry of systems containing pure sugar surfactant, Langmuir 14 (1998) 4699–4709.
[76] V.C. Reinsborough, V.C. Stephenson, Inclusion complexation involving sugar-containing species: β-cyclodextrin and sugar surfactants, Can. J. Chem. 82 (2004) 45–49.
[77] I. Varga, R. Mészáros, C. Stubenrauch, T. Gilányi, Adsorption of sugar surfactants at the air/water interface, J. Colloid Interface Sci. 379 (2012) 78–83.
[78] S. Matsumura, K. Imai, S. Yoshikawa, K. Kawada, T. Uchibori, Surface activities, biodegradability and antimicrobial properties of n-alkyl glucosides, mannosides and galactosides, J. Am. Oil Chem. Soc. 67 (1990) 996–1001.
[79] M.J. Rosen, S.B. Sulthana, The interaction of alkylglycosides with other surfactants, J. Colloid Interface Sci. 239 (2001) 528–534.
[80] A.J. Kumpulainen, C.M. Persson, J.C. Eriksson, n-Decyl-glucopyranoside and n-decyl-maltopyranoside Gibbs monolayers. Phase changes in the dilute liquid-expanded range, Langmuir 20 (2004) 10534–10541.
[81] W. Hu, J.J. Rathman, J.J. Chalmers, An investigation of small-molecule surfactants to potentially replace pluronic F-68 for reducing bubble-associated cell damage, Biotechnol. Bioeng. 101 (2008) 119–127.
[82] P. Wydro, M. Paluch, Surface properties of cationic–nonionic mixed surfactant systems, Colloids Surf., A 245 (2004) 75–79.
[83] P. Wydro, The influence of the size of the hydrophilic group on the miscibility of zwitterionic and nonionic surfactants in mixed monolayers and micelles, J. Colloid Interface Sci. 316 (2007) 107–113.
[84] T. Böcker, J. Thiem, Synthesis and properties for nonionic surfactants, Tenside Surfactants Deterg. 26 (1989) 318–323.
[85] G. Garofalakis, B.S. Murray, D.B. Sarney, Surface activity and critical aggregation concentration of pure sugar esters with different sugar headgroups, J. Colloid Interface Sci. 229 (2000) 391–398.
[86] B. Havlinova, J. Zemanovic, M. Koëik, A. Blazej, Synthesis and properties of surfactants based on carbohydrates. II. Some properties of O-dodecyl aldoses, Tenside Deterg 15 (1978) 119–121.
[87] S. Enders, D. Häntzschel, Thermodynamics of aqueous carbohydrate surfactant solutions, Fluid Phase Equil. 153 (1998) 1–21.
[88] F. Nilsson, O. Söderman, P. Hansson, I. Johansson, Physical–chemical properties of C_9G_1 and $C_{10}G_1$ β-alkylglucosides. Phase diagrams and aggregate size/structure, Langmuir 14 (1998) 4050–4058.
[89] K.J. Tiefenbach, H. Durchschlag, R. Jaenicke, Spectroscopic and hydrodynamic investigations of nonionic and zwitterionic detergents, in: H. Cölfen (Ed.), Analytical Ultracentrifugation V, Springer Berlin Heidelberg, Berlin, Heidelberg, 1999, pp. 135–141.
[90] R.C. Oliver, J. Lipfert, D.A. Fox, R.H. Lo, S. Doniach, L. Columbus, Dependence of micelle size and shape on detergent alkyl chain length and head group, PLoS One 8 (2013), e62488.
[91] B.J. Boyd, C.J. Drummond, I. Krodkiewska, A. Weerawardena, D.N. Furlong, F. Grieser, Alkyl chain positional isomers of dodecyl β-D-glucoside: thermotropic and lyotropic phase behavior and detergency, Langmuir 17 (2001) 6100–6107.
[92] K. Shinoda, A. Carlsson, B. Lindman, On the importance of hydroxyl groups in the polar head-group of nonionic surfactants and membrane lipids, Adv. Colloid Interface Sci. 64 (1996) 253–271.
[93] M. Kahlweit, G. Busse, B. Faulhaber, Preparing microemulsions with alkyl

monoglucosides and the role of n-alkanols, Langmuir 11 (1995) 3382–3387.
[94] L.D. Ryan, E.W. Kaler, Role of oxygenated oils in n-alkyl β-D-monoglucoside microemulsion phase behavior, Langmuir 13 (1997) 5222–5228.
[95] F. Nilsson, O. Söderman, J. Reimer, Phase separation and aggregate–aggregate interactions in the $C_9G_1/C_{10}G_1$ β-alkyl glucosides/water system. A phase diagram and NMR self-diffusion study, Langmuir 14 (1998) 6396–6402.
[96] W. von Rybinski, K. Hill, Alkyl polyglycosides—properties and applications of a new class of surfactants, Angew. Chem. Int. Ed. 37 (1998) 1328–1345.
[97] S.P. Moulik, S. Gupta, A.R. Das, Hydration studies on some polyhydroxy non-electrolytes and non-ionic surfactants, Can. J. Chem. 67 (1989) 356–364.
[98] O. Pastor, E. Junquera, E. Aicart, Hydration and micellization processes of n-octyl β-D-glucopyranoside in aqueous solution. A thermodynamic and fluorimetric study in the absence and presence of salts, Langmuir 14 (1998) 2950–2957.
[99] J.O.M. Bockris, A.K.N. Reddy, Modern Electrochemistry: Ionics, second ed., Plenum Press, New York, 1998.
[100] J. Gliński, A. Burakowski, Is the hydration number of a non-electrolyte additive with length and constituents of the solute molecule? Eur. Phys. J. Spec. Top. 154 (2008) 275–279.
[101] A. Burakowski, J. Gliński, Hydration numbers of nonelectrolytes from acoustic methods, Chem. Rev. 112 (2012) 2059–2081.
[102] M.M.A. El-Sukkary, N.A. Syed, I. Aiad, W.I.M. El-Azab, Synthesis and characterization of some alkyl polyglycosides surfactants, J. Surfactants Deterg. 11 (2008) 129–137.
[103] M.M.A. El-Sukkary, N.A. Syed, I. Aiad, S.M. Helmy, W.I.M. El-Azab, Aqueous solution properties, biodegradability, and antimicrobial activity of some alkylpolyglycosides surfactants, Tenside Surfactants Deterg. 46 (2009) 311–316.
[104] D. Nickel, C. Nitsch, P. Kurzendörfer, W. von Rybinski, Interfacial properties of surfactant mixtures with alkyl polyglycosides, in: C. Helm, M. Lösche, H. Möhwald (Eds.), Trends in Colloid and Interface Science VI, Steinkopff, 1992, pp. 249–252.
[105] A.M. Novelo-Torres, J. Gracia-Fadrique, Concentración micelar crítica mediante la ecuación de adsorción de Gibbs, Educ. Quím. 16 (2005) 63–67.
[106] M.J. Rosen, Surfactants and Interfacial Phenomena, third ed., John Wiley & Sons, Inc., New Jersey, 2004.
[107] H. Matsubara, H. Obata, T. Matsuda, T. Takiue, M. Aratono, Surface adsorption and aggregate formation of aqueous binary mixture of cationic surfactant and sugar surfactant, Colloids Surf., A 315 (2008) 183–188.
[108] C. Stubenrauch, M. Hamann, N. Preisig, V. Chauhan, R. Bordes, On how hydrogen bonds affect foam stability, Adv. Colloid Interface Sci. 247 (2017) 435–443.
[109] D. Balzer, Cloud point phenomena in the phase behavior of alkyl polyglucosides in water, Langmuir 9 (1993) 3375–3384.
[110] J.A. Molina-Bolívar, C. Carnero Ruiz, Self-assembly and micellar structures of sugar-based surfactants: effect of temperature and salt addition, in: C. Carnero Ruiz (Ed.), Sugar-based Surfactants. Fundamentals and Applications, Taylor & Francis Group, Boca Raton, 2009, pp. 61–104.
[111] F.M. Menger, L. Shi, Electrostatic binding among equilibrating 2-D and 3-D self-assemblies, J. Am. Chem. Soc. 131 (2009) 6672–6673.
[112] F.M. Menger, L. Shi, S.A.A. Rizvi, Re-evaluating the Gibbs analysis of surface tension at the air/water interface, J. Am. Chem. Soc. 131 (2009) 10380–10381.
[113] F.M. Menger, L. Shi, S.A.A. Rizvi, Additional support for a revised Gibbs analysis, Langmuir 26 (2010) 1588–1589.
[114] J. Laven, G. de With, Should the Gibbs analysis be revised? Langmuir 27 (2011) 7958–7962.
[115] F.M. Menger, S.A.A. Rizvi, L. Shi, Reply to “Should the Gibbs analysis be revised?”, Langmuir 27 (2011) 7963–7965.
[116] F.M. Menger, S.A.A. Rizvi, Relationship between surface tension and surface coverage, Langmuir 27 (2011) 13975–13977.
[117] C. Bermúdez-Salguero, J. Gracia-Fadrique, Analysis of Gibbs adsorption equation and thermodynamic relation between Gibbs standard energies of adsorption and micellization through a surface equation of state, J. Colloid Interface Sci. 355 (2011) 518–519.
[118] A.A. Shahir, K.T. Nguyen, A.V. Nguyen, A sum-frequency generation spectroscopic study of the Gibbs analysis paradox: monolayer or sub-monolayer adsorption? Phys. Chem. Chem. Phys. 18 (2016) 8794–8805.
[119] L. Martínez-Balbuena, A. Arteaga-Jiménez, E. Hernández-Zapata, C. Márquez-Beltrán, Applicability of the Gibbs Adsorption Isotherm to the analysis of experimental surface-tension data for ionic and nonionic surfactants, Adv. Colloid Interface Sci. 247 (2017) 178–184.
[120] P.F. Garrido, P. Brocos, A. Amigo, L. García-Río, J. Gracia-Fadrique, Á. Piñeiro, STAND: surface tension for aggregation number determination, Langmuir 32 (2016) 3917–3925.
[121] J.R. Lu, R.K. Thomas, J. Penfold, Surfactant layers at the air/water interface: structure and composition, Adv. Colloid Interface Sci. 84 (2000) 143–304.
[122] J. Viades-Trejo, A. Amigo, J. Gracia-Fadrique, Activity coefficients at infinite dilution for surfactants, Fluid Phase Equil. 250 (2006) 158–164.
[123] T.E. Burchfield, E.M. Woolley, Model for thermodynamics of ionic surfactant solutions. 1. Osmotic and activity coefficients, J. Phys. Chem. 88 (1984) 2149–2155.
[124] M.L. Antonelli, M.G. Bonicelli, G. Ceccaroni, C. La Mesa, B. Sesta, Solution properties of octyl-β-D-glucoside. Part 2: thermodynamics of micelle formation, Colloid Polym. Sci. 272 (1994) 704–711.
[125] P. Sharma, J.A. MacNeil, J. Bowles, D.G. Leaist, The unusual importance of activity coefficients for micelle solutions illustrated by an osmometry study of aqueous sodium decanoate and aqueous sodium decanoate + sodium chloride solutions, Phys. Chem. Chem. Phys. 13 (2011) 21333–21343.
[126] J.A. MacNeil, G.B. Ray, P. Sharma, D.G. Leaist, Activity coefficients of aqueous mixed ionic surfactant solutions from osmometry, J. Solut. Chem. 43 (2014) 93–108.
[127] R. Strey, Y. Viisanen, M. Aratono, J.P. Kratohvil, Q. Yin, S.E. Friberg, On the necessity of using activities in the Gibbs equation, J. Phys. Chem. B 103 (1999) 9112–9116.
[128] K. Shinoda, E. Hutchinson, Pseudo-phase separation model for thermodynamic calculations on micellar solutions, J. Phys. Chem. 66 (1962) 577–582.
[129] C. Tanford, The Hydrophobic Effect: Formation of Micelles and Biological Membranes, second ed., John Wiley & Sons, Inc., New York, 1980.
[130] H.-U. Kim, K.-H. Lim, A model on the temperature dependence of critical micelle concentration, Colloids Surf., A 235 (2004) 121–128.
[131] M.J. Rosen, S. Aronson, Standard free energies of adsorption of surfactants at the aqueous solution/air interface from surface tension data in the vicinity of the critical micelle concentration, Colloids Surf., A 3 (1981) 201–208.
[132] M.S. Borse, S. Devi, Importance of head group polarity in controlling aggregation properties of cationic gemini surfactants, Adv. Colloid Interface Sci. 123–126 (2006) 387–399.
[133] M.A. Desando, Refractive index in relation to solvent effects on the amphiphilic association of n-alkylammonium carboxylates, Colloid Polym. Sci. 294 (2016) 1789–1805.
[134] J.R. Rodríguez, A. González-Pérez, J.L. Del Castillo, J. Czapkiewicz, Thermodynamics of micellization of alkyldimethylbenzylammonium chlorides in aqueous solutions, J. Colloid Interface Sci. 250 (2002) 438–443.
[135] N. Muller, Temperature dependence of critical micelle concentrations and heat capacities of micellization for ionic surfactants, Langmuir 9 (1993) 96–100.
[136] K.-H. Lim, Thermal behavior of critical micelle concentration from the standpoint of Flory-Huggins model, Bull. Kor. Chem. Soc. 30 (2009) 2001–2006.
[137] A. Chatterjee, S.P. Moulik, S.K. Sanyal, B.K. Mishra, P.M. Puri, Thermodynamics of micelle formation of ionic surfactants: A critical assessment for sodium dodecyl sulfate, cetyl pyridinium chloride and dioctyl sulfosuccinate (Na salt) by microcalorimetric, conductometric, and tensiometric measurements, J. Phys. Chem. B 105 (2001) 12823–12831.
[138] J.A. Molina-Bolívar, J. Aguiar, J.M. Peula-García, C. Carnero Ruiz, Surface activity, micelle formation, and growth of n-octyl-β-D-thioglucopyranoside in aqueous solutions at different temperatures, J. Phys. Chem. B 108 (2004) 12813–12820.
[139] M.P. Vázquez-Tato, F. Meijide, J.A. Seijas, F. Fraga, J. Vázquez Tato, Analysis of an old controversy: the compensation temperature for micellization of surfactants, Adv. Colloid Interface Sci. 254 (2018) 94–98.
[140] P. Brocos, X. Banquy, N. Díaz-Vergara, S. Pérez-Casas, Á. Piñeiro, M. Costas, A critical approach to the thermodynamic characterization of inclusion complexes: multiple-temperature isothermal titration calorimetric studies of native cyclodextrins with sodium dodecyl sulfate, J. Phys. Chem. B 115 (2011) 14381–14396.

USC UNIVERSIDADE DE SANTIAGO DE COMPOSTELA

USC
UNIVERSIDADE
DE SANTIAGO
DE COMPOSTELA

Chapter 10

MD simulations

A scientist in his laboratory is not a mere technician: he is also a child confronting natural phenomena that impress him as though they were fairy tales

Maria Skłodowska-Curie, Polish-French scientist

MD simulations were proposed in the initial planning of the thesis as a complementary tool to provide more information about the adsorption phenomena that could also be studied by calorimetry. However, because of the COVID-19 pandemic and the lockdown, no experiments were possible during some time and MD simulations became more relevant in this project. Some of the results obtained from MD simulations are still unpublished (or under revision) but one publication is included as part of this thesis and another work, to which I have significantly contributed by developing trajectory analysis, has already been published as a collaboration (Blanco-González *et al.*, 2021).

Using MD simulations we aim to characterize specific systems that can later be studied by Fluid Interface Calorimetry with a good understanding on the interactions dominating the adsorption processes. Based on the previous work of our research group, we decided to investigate a mixture of cyclodextrins and surfactant molecules (sodium dodecyl sulphate) that exhibits a particular behaviour, unexplained in detail yet, at the water/air interface. These CDs complexes can aggregate and adsorb at the interface but, more important, they can mimic proteins and surfactant structures (Yang *et al.*, 2017). The results of this work are presented in Paper VII. In line with the general aim of this project, which is to develop new analysis methods for the characterization of interfaces, a method to speed up the simulations, named Hydrogen Isotope Exchage (HIE) was tested here. It showed to speed up the simulations by a factor of 3 without loss of resolution in the system nor significant changes in the main structural features, including the interaction with the solvent molecules. This method has already been tested with other systems (peptides nanotubes in membrane models) producing similar results (work under revision).

USC
UNIVERSIDADE
DE SANTIAGO
DE COMPOSTELA

10.1. Paper VII

"Rings, Hexagons, Petals, and Dipolar Moment Sink-Sources: The Fanciful Behavior of Water around Cyclodextrin Complexes", published in *Biomolecules* (2020), is a regular article where a CD complex encapsulating a surfactant (2 CD, 1 surfactant molecule) is studied by MD simulations. Two main contributions come from this work: the applicability of speed-up techniques for bulk and interfacial simulations and the results obtained from the water organization around the CD complex. This work has been developed in collaboration with people from: (1) Departamento de Física Aplicada, Facultade de Física, Universidade de Santiago de Compostela; (2) Departamento de Química Orgánica, Center for Research in Biological Chemistry and Molecular Materials, Universidade de Santiago de Compostela. The list of authors is presented below, by order and with their corresponding affiliations. The corresponding authors are marked with a *:

Pablo F. Garrido (1), Martín Calvelo (2), Rebeca Garcia-Fandino (2)*, Ángel Piñeiro (1)*.

According to the CRediT authorship contribution statement (Brand *et al.*, 2015), my contributions to this publication are: Conceptualization; Software; Validation; Formal analysis; Investigation; Writing - Review & Editing; Visualization

Garrido PF, Calvelo M, Garcia-Fandiño R, Piñeiro Á (2020b). Rings, Hexagons, Petals, and Dipolar Moment Sink-Sources: The Fanciful Behavior of Water around Cyclodextrin Complexes. *Biomolecules*, **10**(3), 431. ISSN 2218-273X. doi: 10.3390/biom10030431. URL https://www.doi.org/10.3390/biom10030431

Supplementary Material can be accessed by this link: https://www.mdpi.com/2218-273X/10/3/431/s1

USC UNIVERSIDADE DE SANTIAGO DE COMPOSTELA

USC
UNIVERSIDADE
DE SANTIAGO
DE COMPOSTELA

biomolecules

MDPI

Article

Rings, Hexagons, Petals, and Dipolar Moment Sink-Sources: The Fanciful Behavior of Water around Cyclodextrin Complexes

Pablo F. Garrido [1], Martín Calvelo [2], Rebeca Garcia-Fandiño [2,*] and Ángel Piñeiro [1,*]

[1] Departamento de Física de Aplicada, Facultade de Física, Universidade de Santiago de Compostela, E-15782 Santiago de Compostela, Spain; pablo.fernandez@usc.es

[2] Departamento de Química Orgánica, Center for Research in Biological Chemistry and Molecular Materials, Universidade de Santiago de Compostela, Campus Vida s/n, E-15782 Santiago de Compostela, Spain; martin.calvelo.souto@usc.es

* Correspondence: rebeca.garcia.fandino@usc.es (R.G.-F.); Angel.Pineiro@usc.es (A.P.); Tel.: +34-8818-14042 (A.P.)

Received: 30 January 2020; Accepted: 4 March 2020; Published: 10 March 2020



Abstract: The basket-like geometry of cyclodextrins (CDs), with a cavity able to host hydrophobic groups, makes these molecules well suited for a large number of fundamental and industrial applications. Most of the established CD-based applications rely on trial and error studies, often ignoring key information at the atomic level that could be employed to design new products and to optimize their use. Computational simulations are well suited to fill this gap, especially in the case of CD systems due to their low number of degrees of freedom compared with typical macromolecular systems. Thus, the design and validation of solid and efficient methods to simulate and analyze CD-based systems is key to contribute to this field. The behavior of supramolecular complexes critically depends on the media where they are embedded, so the detailed characterization of the solvent is required to fully understand these systems. In the present work, we use the inclusion complex formed by two α-CDs and one sodium dodecyl sulfate molecule to test eight different parameterizations of the GROMOS and AMBER force fields, including several methods aimed to increase the conformational sampling in computational molecular dynamics simulation trajectories. The system proved to be extremely sensitive to the employed force field, as well as to the presence of a water/air interface. In agreement with previous experiments and in contrast to the results obtained with AMBER, the analysis of the simulations using GROMOS showed a quick adsorption of the complex to the interface as well as an extremely exotic behavior of the water molecules surrounding the structure both in the bulk aqueous solution and at the water surface. The chirality of the CD molecule seems to play an important role in this behavior. All together, these results are expected to be useful to better understand the behavior of CD-based supramolecular complexes such as adsorption or aggregation driving forces, as well as to introduce new methods able to speed up general MD simulations.

Keywords: cyclodextrins; molecular dynamics simulations; bulk; interface; solvent order; sampling improvement

USC
UNIVERSIDADE
DE SANTIAGO
DE COMPOSTELA

1. Introduction

The behavior of native cyclodextrins (CDs) in aqueous solution and at the air/water interface is much more complex than expected just considering their apparently simple molecular structure [1–3]. Consequently, the correct prediction of their properties and skills such as their solubility, their ability to adsorb at interfaces, or to encapsulate a variety of molecules is not straightforward; not to mention

their propensity to aggregate forming different patterns in the bulk solution and at the water/air interface [4–6]. It is not a surprise then that the behavior of native and modified CDs, as well as that of the supramolecular complexes they form upon interacting with different types of molecules, is not trivial [7].

In spite of their great potential for a large number of applications, atomic level information of CD molecules, which is key to understand how structure relates to function, is really scarce. It is also important to remember that, like most functional supramolecular systems, CDs are not static and that only by visualizing them in action it is possible to understand how structure and function are connected. Moreover, a detailed structural-dynamic description at atomic resolution that explicitly includes the surrounding molecules is crucial to fully understand the behavior of supramolecular complexes since such behavior is strongly correlated with the entire multi-component system where they are embedded. Without the ability to understand dynamic structural changes, the design, development, and optimization of applications using CDs has been traditionally based on empirical trial-and-error essays as well as a fair degree of serendipity.

Computational simulations are commonly employed to study a large variety of systems including proteins, peptides, DNA, lipids, surfactants, and heterogeneous mixtures of different molecules in different solvents [8,9]. More specifically, molecular dynamics (MD) simulations are increasingly popular because they can provide structural, energetic, dynamic, and even mechanistic information. Computational studies of CDs are not so common, although a significant number of works based on MD simulations and docking of these molecules have already been published [10–12]. The number of degrees of freedom of single (native or modified) CDs is much lower than that of typical macromolecules. So, computational studies of these cyclic oligosaccharides are expected to be able to easily sample their conformational space and so to provide a good understanding of their behavior at the atomic level, as well as the connection of such behavior with macroscopic properties. Single CDs and CD complexes can be computationally studied in aqueous solution using relatively small simulation boxes and explicit solvent: ~3000 water molecules at room temperature and atmospheric pressure are typically enough to exhibit negligible direct interaction of these molecules with their periodic images. Using last-generation computational resources, it is feasible to get atomistic trajectories of such systems in the microsecond timescale. However, CDs and CD complexes at concentrations employed in typical applications often aggregate, adsorb to interfaces, penetrate other media such as lipid bilayers, and acquire new levels of organization both in bulk solution and at interfaces. The study of such aggregates requires longer timescales and larger simulation boxes, and so, much more computational effort than that required for the study of single molecules. The implementation of methods to increase the sampling of the conformational space at lower computational cost is then convenient to better approach the convergence of the most important properties of the studied systems. A practical general solution to speed up MD simulations is to use the so called coarse-grained (CG) force fields, where groups of atoms are represented by single beads [13], hence decreasing the number of degrees of freedom, mainly those that move faster. This also allows increasing the time step for the integration of the motion equations by more than one order of magnitude, as well as to smooth the energy landscape, avoiding kinetically trapped states and facilitating the evolution of the system towards the equilibrium. This method proved to work exceptionally well mainly for lipid membranes. Using this approach, it is more difficult to describe the behavior of other molecules -such as proteins or DNA- in a realistic way, so internal restraints are typically used to overcome obvious artifacts [14]. In any case, the atomistic structure of the systems simulated at CG resolution can be recovered by applying different algorithms [15,16]. CG parameterizations of CDs have been made in the past [17] but they are not expected to be fully reliable since the larger van der Waals radius of CG beads significantly reduces the volume of the cavity, thus seriously affecting their ability to encapsulate molecules as well as the accessible conformational space of the system. An alternative to save computational time is the use of multiple time-step algorithms such as RESPA (Reference System Propagator Algorithm) [18,19], but they have proved to introduce serious artifacts in some cases [20,21].

A different and very simple general method to efficiently increase the sampling of MD simulations was proposed by Feenstra et al. 20 years ago [22]. The method consists of transferring mass from heavy atoms to hydrogens (Hs) to slow their movement. This allows significantly increasing the time step for the integration of the motion equations. As a result, it is possible to reach longer trajectories as well as to smooth the energy landscape (as in CG simulations) by keeping the atomistic resolution of the system (in contrast to CG simulations). It is worth mentioning that the mass of the atoms is definitely much less critical for equilibrium properties than topological features (bond distances, angles, dihedrals, torsions, etc.), van der Waals, and electrostatic interactions. This can be experimentally demonstrated by the fact that structural and thermodynamic properties of many deuterated systems are indistinguishable from those of the equivalent hydrogenated structures (this has been specifically verified for CD systems) [23]. The Feenstra method, also called the HMR (hydrogen mass repartitioning) method, has been tested for many systems providing good results [24,25]. CD systems have also been simulated using this method for all-atom (AA) force fields with a mass transfer of 2 Da per H and a time step of 4 fs instead of the standard 2 fs [26]. In general, AA force fields allow transferring a maximum of 2 Da from heavy to the bound H atoms due to the possible presence of methyl groups. A mass transfer of 2 Da from a single C atom to three H implies reducing the mass of such carbon atom from 12 to 6 Da. This makes it impossible to transfer more mass without leaving the carbon lighter than the Hs to which it is bound. In contrast to AA force fields, the HMR method applied to united atom (UA) force fields such as GROMOS allows transferring up to 3 Da from heavy atoms to the bound polar H atoms (non-polar H atoms are implicit in this force field and so not explicit methyl groups nor Hs in aliphatic chains are present in this case). Consequently, using the mass transfer approach, the time step in UA force fields could be increased up to 7 fs, instead of 4 fs. It is worth to test the effect of a direct mass increase in the explicit Hs of UA force fields, avoiding the repartition proposed by Feenstra to increase the time step. The application of this method would not have the limitation implicit in AA force fields due to the large number of explicit H atoms present in that representation, which would imply a significant increment of mass, thus making the movement of the total molecule too slow. As a consequence, the increase of mass in AA force fields could reduce the sampling even if the time step is increased. The mass increase of just polar Hs from 1 to 2 Da is justified based on the experimental fact that only the polar H atoms are spontaneously deuterated (thus doubling their mass) when they are solvated in deuterated water [1,23]. In the present work, we propose to also test the mass increase of just the polar H up to 4 Da. This is expected to virtually mimic the behavior of the molecules with a heavier isotope of H (quadium) without the risk of subtracting too much mass to the bound carbon atoms, thus compromising the thermodynamic behavior of the global system. This last method will be named H2Q from here on. To our knowledge, the HMR method using UA force fields has not been tested yet for CD systems and the H2Q method has been marginally essayed (a literature revision is included in [22]) but not analyzed in detail.

The validation of any new methodology implies the comparison to a recognizable reference method to demonstrate equivalence of the obtained results. The selection of a system sensitive enough to subtle and precise discrepancies among the different methodologies is also crucial. In the present paper, we will focus on the behavior of the supramolecular 2:1 complex formed by α-CD and sodium dodecyl sulfate (SDS) (see Figure 1) in the bulk of aqueous solutions and also at water/air interfaces. CD-surfactant mixtures are especially interesting because they proved to exhibit interesting aggregation, mechanical, and adsorption properties under certain experimental conditions (concentration range and temperature) where the presence of 2:1 complexes dominate the solution [4–6,27–30] but the molecular interactions leading to such behavior are unclear. This can be illustrated by an specific example: The adsorption of α-CD_2SDS_1 complexes at interfaces leading to a monolayer has been conclusively demonstrated by different methods including surface tension, rheology, ellipsometry, Brewster angle microscopy (BAM), atomic force microscopy (AFM), and neutron reflectometry (NR), [5,6,23] although the adsorption driving force of those structures at the interface are still unknown. Additionally, preliminary work from our group indicates that this system is extremely sensitive to the parameterization, as will be

shown in the present work. The selection of this highly sensitive system for which a lot of experimental information is available, and its study both in bulk and in the presence of an air/water interface, will allow testing several force field parameterizations as well as methods to speed up MD simulations of CD complexes at the time that the obtained information can be connected to the macroscopic properties of the system. The essayed methods could be later trustingly employed in larger and longer scale studies of similar systems. We will especially focus on the detailed analysis of the packing and structure of the solvent around the target complex, assuming that they have an important impact in its behavior, including their adsorption or penetration to media of different polarity, as well as to define their stoichiometry, topology, and also the stability of the corresponding structures. The role of the solvent structure for the aggregation and adsorption of different molecules has been discussed for many decades in the context of the hydrophobic effect [31]. However, the organization of the solvent in the immediate environment of solutes is not commonly characterized in detail and so the impact of such organization is often implicitly ignored. The strong correlation between the order of the lipids induced by pore proteins or modified carbon nanotubes in a membrane and the toxicity of the systems [32] has been recently reported. The structure of water around proteins has also been widely analyzed [33,34]. In the case of CD systems, many interaction mechanisms are unknown, and they are simply ignored in benefit of experimentally improving formulations just based on trial-and-error essays. The order of the solvent around CD complexes is expected to be key to explain many of such mechanisms, including how they aggregate, adsorb and organize at interfaces, or sequester molecules from lipid membranes. Several studies have analyzed this behavior for native and modified CDs using different methods [35–37] and some groups called the attention on the order of water around CD complexes [26], but no detailed studies have been performed on this latter issue.

In what follows, we will describe a number of methods employed to simulate CD-based complexes in the water solution and at water/air interfaces. The α-CD_2SDS_1 structure will be taken as a reference system for the present study. Then, the obtained results will be analyzed in detail with specific strength in the local density and order of water molecules around the complex using different simulation methods.

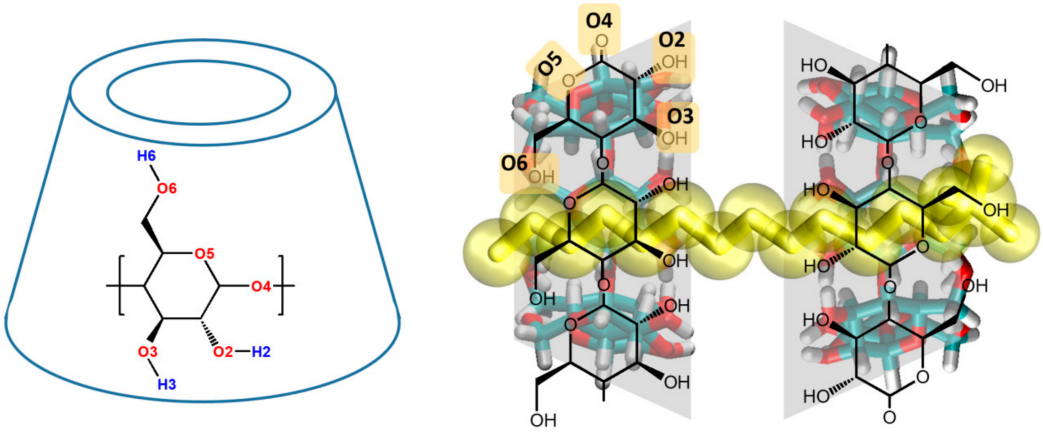


Figure 1. Two-dimensional representation of an α-cyclodextrin (CD) (left) and of an α-CD_2SDS_1 complex (right) with the oxygen atoms labelled. Just the polar H atoms are shown in the left figure. The surfactant molecule is represented in yellow sticks and transparent spheres while the two CDs in the complex are presented in lines and sticks.

2. Materials and Methods

2.1. Set Up of the Simulation Boxes and MD Simulation Parameters

Several sets of MD simulations were performed starting from one preassembled α-CD_2SDS_1 complex located at random positions and orientations in pre-equilibrated 5 × 5 × 5 nm^3 water boxes. The GROMOS [38] and AMBER [39,40] force fields were tested. For the simulations with

GROMOS, the topology of SDS was built based on the 54a7 parameters and SPC water molecules were employed as explicit solvent [41]. For the α-CD molecule, different GROMOS parameterizations were essayed in order to slow down high-frequency motions thus allowing to increase the time step for the integration of the motion equation (see Section 2.2). TIP3P water molecules [42] were used for all the simulations with AMBER [39,40], and three different parameterizations were also employed for the SDS and α-CD molecules in this force field (see Section 2.2). The initial structure of the complex was taken from previous works [43]. For the studies at the interface, the Z dimension of the water boxes was enlarged by a factor of three thus getting $5 \times 5 \times 15$ nm^3 boxes with two water/air interfaces parallel to the XY plane. In all cases, one Na^+ ion was introduced using the *genion* tool from the GROMACS 2018 package to neutralize the system. The same simulation parameters were employed for all the simulations, regardless the parameterization method. First, the simulation boxes were energy minimized using the steepest descent method. Approximately 500-ns-long MD trajectories for the simulations based on the GROMOS force field and 150-ns-long trajectories for the simulations using AMBER, all of them at 283 K, were generated. This temperature was employed because both the adsorption and the formation of 2:1 complexes are much more favorable at 283 K than at 298 K [5,6,23]. The NPT ensemble was employed for the simulations in solution and in the NVT ensemble for the simulation in the presence of water/air interfaces. Between one and three replicas of every simulation using different initial random velocities from a Maxwell–Boltzmann distribution at 283 K were performed. The GROMACS 2018 engine [44,45] was employed to get all the MD trajectories. The temperature was controlled using the V-rescale thermostat [46] with a coupling constant of 0.1 ps. For the simulations at constant pressure (1 bar), a Parrinello-Rahman barostat [47] with a compressibility of $4.5 \cdot 10^{-5}$ bar^{-1} was employed. The coupling constant for the barostat was 0.5 ps for the simulations with a time step of 2 fs and 1.5 ps for the simulations with a time step of 7 fs. Long range electrostatic interactions were calculated using the particle mesh Ewald method [48,49] with a real-space cutoff of 1.2 nm, a 0.15 nm spaced grid, and fourth-order B-spline interpolation. The Ewald sum in three dimensions with a correction term (EW3DC) was used to avoid artifacts due to interactions between periodic images in the Z direction for the simulations with slab geometry. The equations of motion were integrated using the leapfrog method [50]. The SETTLE [51] algorithm was employed to constrain the bond lengths and angles of water molecules while the LINCS [52] algorithm was employed to constrain the bond lengths of the CD molecules. During the MD simulations, coordinates and energies were stored every 10 ps for analysis.

2.2. Parameterization Methods

Five types of simulations were performed using a standard parameterization of the GROMOS 54a7 force field for the SDS molecule and different modifications for α-CD molecule in order to increase the sampling (see Introduction section), namely: (i) Simulations using the GROMOS 54a7 force field [38] based on a parametrization of the glucopyranoside (GPU) units as building blocks [53] and using a time step of 2 fs for the integration of the motion equations (**G_2**); (ii) an alternative parameterization for the CDs based on G_2 but including the transference of 3 Da of mass to the H atoms from the bounded heavy atoms (O2, O3 or O6) and using the same time step (**HMR_2**); (iii) the latter parameterization (using the mass transfer to the H atoms) but with a time step of 7 fs (**HMR_7**) [22]; (iv) another alternative parameterization for the CDs also based on the G_2 parameterization but increasing the mass of the polar H atoms (H2, H3, and H6) from 1 to 4 Da, while the mass of the rest of the atoms remains unchanged, and using a time step of 2 fs (**H2Q_2**); and (v) the latter parameterization (mass increase in the polar H atoms of 3 additional Da) but using a time step of 7 fs (**H2Q_7**). Additionally, three different AMBER/GAFF parameterizations for the CD molecule were employed: (i) A first parameterization obtained by applying the *antechamber* [54,55] tool to the whole molecule and using RESP (Restrained Electrostatic Potential) charges (**AMBER RESP**); (ii) a second parameterization also using RESP charges and the antechamber tool applied just to the methylated GPU rings, which were then pasted together to form the topology of the whole CD (this method will be named **AMBER BB-RESP**); and (iii) a last

parameterization equivalent to the previous one, i.e., using the GPUs as building blocks, but using AM1-BCC charges instead of RESP (this will be named **AMBER BB-AM1**). The SDS molecule was parameterized as a single entity in all cases, using the RESP and AM1-BCC charges, thus obtaining two different parameter sets. All the simulations using GROMOS were performed with the SPC water model [41] while the simulations with AMBER/GAFF were performed using the TIP3P water model [42,56] for the solvent. For the simulations using AMBER, no modification in the mass of the H atoms was performed.

2.3. Analysis of the Trajectories

For the simulations in the bulk solution, the 12 O4 atoms (Figure 1) of the two CDs were employed to fit the structure of the complex along each trajectory. Additionally, in order to facilitate the analysis, the segment joining the center of the O4 atoms of each CDs was aligned with one of the coordinate axes. The behavior of the water molecules around the complexes and the internal motion of the different CD atoms within the complex were analyzed in three different ways: (i) Water density maps for 3-Å-width slices perpendicular to the symmetry axis of the complex were determined using the last 10,000 frames of each trajectory with a resolution of 0.5×0.5 Å^2. A total of 9 slices per structure were set, taking the center of the 12 O4 atoms of the two CDs as a reference. The first slice includes 1.5 Å towards each CD while the remaining 8 slices are located between 1–4, 4–7, 7–10, and 10–13 Å towards each CD of the complex. Thus, the segment going from 1 to 1.5 Å in the direction of each CD is accounted for in two different slices. In order to assess the specificity in the local orientation of the water molecules, the average dipolar moment was determined for the same slices, over the same number of frames, and for the same resolution. (ii) A single 3-Å-width slice parallel to and including the symmetry axis of the complex was taken and again the density of water molecules as well as their average dipolar moment in that plane was determined using the same resolution and frames from the MD trajectories; and (iii) 13 1-Å-width concentric shells centered in the symmetry axis of the complex were taken and the same analysis was performed using cylindrical coordinates.

For the simulations of a single complex in the presence of water/air interfaces, the final conformation, regardless whether or not it is located at the water surface, was aligned with one of the coordinate axes and the resulting structure was employed to align the whole trajectory again using the O4 atoms as a reference. The distance between the center of the O4 atoms and the center of mass of the water, as well as the yaw, pitch, and roll angles, referred to the water surface, as a function of time were determined (see Figure 2). The hydration of each GPU unit within the complex, also as a function of time, was also determined using cutoff values of 3 and 5 Å around any atom of these rings. The same calculation was performed taking as a reference just the center of each ring with the same cutoff values measured from this point. The water density maps and dipolar moment analysis were determined for the trajectory segments where each of the six rings of one of the CDs exhibits the minimum hydration, thus guaranteeing that such a ring is orientated towards the air in when the structure is adsorbed. Thus, for the simulations at the interface, a set of density maps and dipolar moment distribution plots was obtained for each GPU group.

For all the simulations, the number of CD-CD and CD-water hydrogen bonds (H-bonds), as well as their lifetime, were also determined using the *hbonds* tool from the GROMACS 2018 package. The rest of the analysis was performed using our own code based on the *MDanalysis* python package [57,58].

USC UNIVERSIDADE DE SANTIAGO DE COMPOSTELA

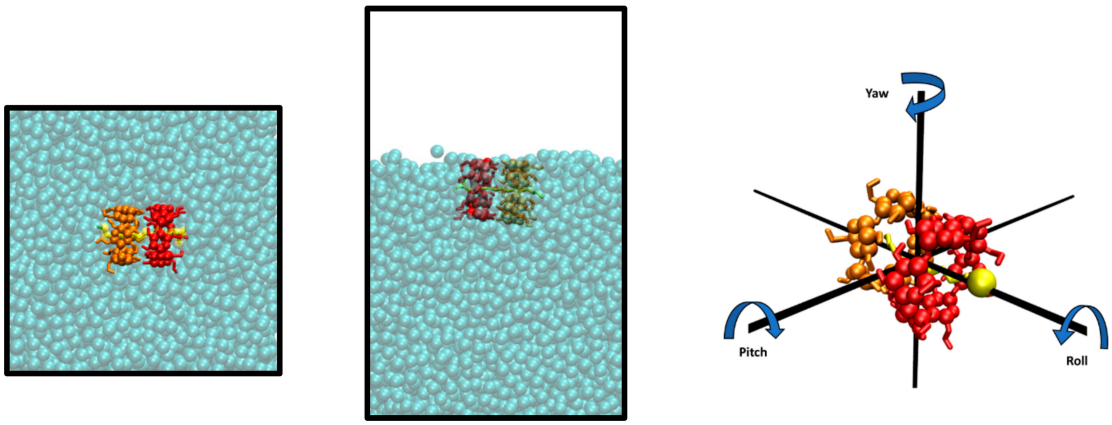


Figure 2. Representation of simulation boxes with an α-CD_2SDS_1 complex in the bulk aqueous solution (left) and in the presence of an air/water interface (middle). The supramolecular structure in the second image appears adsorbed with the symmetry axis parallel to the interface. Definition of the yaw, pitch, and roll angles for an α-CD_2SDS_1 complex (right). The three rotation angles are defined with respect to the interface shown in the central image. The CD molecules that are closer (CD1) and further (CD2) from the SDS polar head in the complex are represented in red and orange, respectively, with the glucopyranoside (GPU) rings in sphere representation and the hydroxyl groups in sticks. The sodium dodecyl sulfate (SDS) molecule is in yellow sticks, with the Sulphur atom as a sphere.

3. Results

First, 500-ns-long trajectories of one α-CD_2SDS_1 complex in the bulk aqueous solution and exposed to the water/air interface were generated using five different simulation methods for the GROMOS force field: G_2, HMR_2, HMR_7, H2Q_2, and H2Q_7. For the simulations using the three different parameterizations of the AMBER/GAFF force field, 150-ns-long trajectories, also in the bulk solution and at the water/air interface, were generated. In short, the complexes were stable in all the MD simulations. For the simulations using GROMOS in the presence of interfaces, they were spontaneously adsorbed during the first few ns and remained floating during the rest of the trajectory with the symmetry axis parallel to the water surface (Figure 2 (middle) and Figure 3). The complexes were much less tight in the simulations using AMBER/GAFF and, in contrast with experimental evidences and with the results obtained with GROMOS, they did not adsorb to the interface using this force field. When they reached the interface by diffusion using AMBER/GAFF, they stayed with the symmetry axis perpendicular to the surface during a few ns and then they went back to the bulk solution. Thus, the results from the two force fields, regardless the parameterization method, were opposite in this sense. The next sections will present the results obtained from the G_2 method in the bulk aqueous solution, used as reference for the validation of the rest of the methodologies, and a description of the main similitudes and differences is performed.

3.1. Simulations in the Bulk Aqueous Solutions Using the G_2 Metho

The water density map as well as the local dipole moment of the water molecules as a function of the position was determined in several slices (see Methods) perpendicular and parallel to the symmetry axis of the complex (Figures 3 and 4), as well as in cylindrical coaxial shells centered in the same symmetry axis (Figure 5). The slice parallel to and centered in the nanocylinder symmetry axis showed a fanciful distribution and orientation of the water molecules around the 2:1 structure (Figure 3). The water had three 1.5-Å-width high–low–high-density layers, respectively, before reaching the bulk behavior. The water density distribution along the complex symmetry axis was very similar on both sides of the structure (i.e., for both CD molecules) but the water orientation changed significantly as a function of the distance to the oxygen atoms of the CDs (O2, O3, O4, O5, and O6) as well as of

the distance to the sulfur atom of the SDS head. There were four zones where the water orientation was very specific, namely around the O6 atoms of both CDs, around the O2-O3 atoms of the CD that is closer to the SDS head, and a last region surrounding the sulfur atom of the SDS. The highly orientated water molecules were located in the first layer around the complex, where the density of the solvent was high. There were also zones where the water density was significantly higher compared to the bulk solution but where the average dipole moment of water molecules was negligible. The orientation of the water molecules in the second and third 1.5-Å-width layers around the supramolecular structure (with low and high density, respectively) also canceled the average dipolar moment. In addition to the water density and orientation, the position of the CD oxygen atoms throughout the last 10,000 frames of the studied trajectories was represented (Figure 3, in red, black, purple, grey, and green, for O2, O3, O4, O5, and O6, respectively). The motion amplitude of the different oxygen atoms was much larger for O6 than for O2, O3, O4, and O5; and slightly larger for O2 and O3 than for O4 and O5. This justifies using O4 as reference atoms to align CD structures.

The same analysis was performed for nine additional 3-Å-width slices along and perpendicular to the nanocylinder symmetry axis (Figure 4). This view of the water density and ordering allowed a more detailed perspective of the water around the complex. In contrast to the density profile, the water dipolar moment of equivalent slices (at the same distance from the center of the CD-CD interface) for both CDs was significantly different. The reason for this difference is clearly the proximity to the charged SDS head, as shown in the perpendicular slice (Figure 3). The petal-shaped density profiles observed for the slices between 7 and 10 Å from the center of the CD-CD interface revealed a highly anisotropic motion of the O6 atoms of both CDs (Figures 3–5) likely due to the chirality of GPU rings of the CD molecules. It can be clearly seen that the orientation of the petals was clockwise and counterclockwise in the CDs that were further and closer to the head of the SDS molecule, respectively. This is because the O6 atoms producing this motion were orientated towards opposite directions along the symmetry axis of the complex. This particular motion of the O6 atoms seemed to be accompanied by water molecules since a high-density layer with similar geometry appears for both CDs. An interesting transition from a circular to hexagonal and again to circular density profile was observed for the slices centered at the interface between both CDs, as well as for those between 1–4 Å and 4–7 Å on both sides of the structure. This apparent shift results from the six-ring topology of both CDs combined with the opposite orientation of one CD with respect to the other in the complex. The GPU rings of both CD molecules were perfectly aligned, forming quite stable O2-H2-O3 and O2-H3-O3 intermolecular CD1-CD2 H-bonds (Table 1). The hexagons formed by the O5 atoms of both CDs were rotated 60 degrees with respect to each other in this conformation, which fit exactly with the relative orientation of the two hexagons appearing for the two slices at 1–4 Å from the center of the complex. Notably, there were six specific sources of the dipole moment vector field in the slice corresponding to the interface between both CDs. Such dipole moments had radial symmetry in this plane and the location of the corresponding sources was slightly shifted towards the head of the SDS molecule, as it had been previously mentioned (Figures 3 and 4). This was reflected in significant differences between both CDs in the H-bond pattern and lifetimes involving O2-H2 and O3-H3 hydroxyls (see below). The O5 atoms were in the slices at 4–7 Å from the center of the complex while the O4 and O6 atoms of the CDs, as well as the sulfur atom of the surfactant molecule, fluctuated between the same slice and that at 7–10 Å. As in the slices corresponding to ±1.5 Å and 1–4 Å, the three high–low–high-density water layers between the solute and the bulk solution were perfectly visible at 4–7 Å. In this case, the hexagonal symmetry was lost, probably due to the influence of the O6 atoms movement. For the CD that was closer to the SDS head (CD1), some of these water molecules were significantly ordered in this slice. Finally, for the most external layers corresponding to 10–13 Å from the center of the structure, only the effect of the solute in the water molecules, translated into a petal-shaped density profile, can be seen. Some order in the water molecules that were closer to the SDS head can also be envisaged from the orientation of their dipole moments in this region.

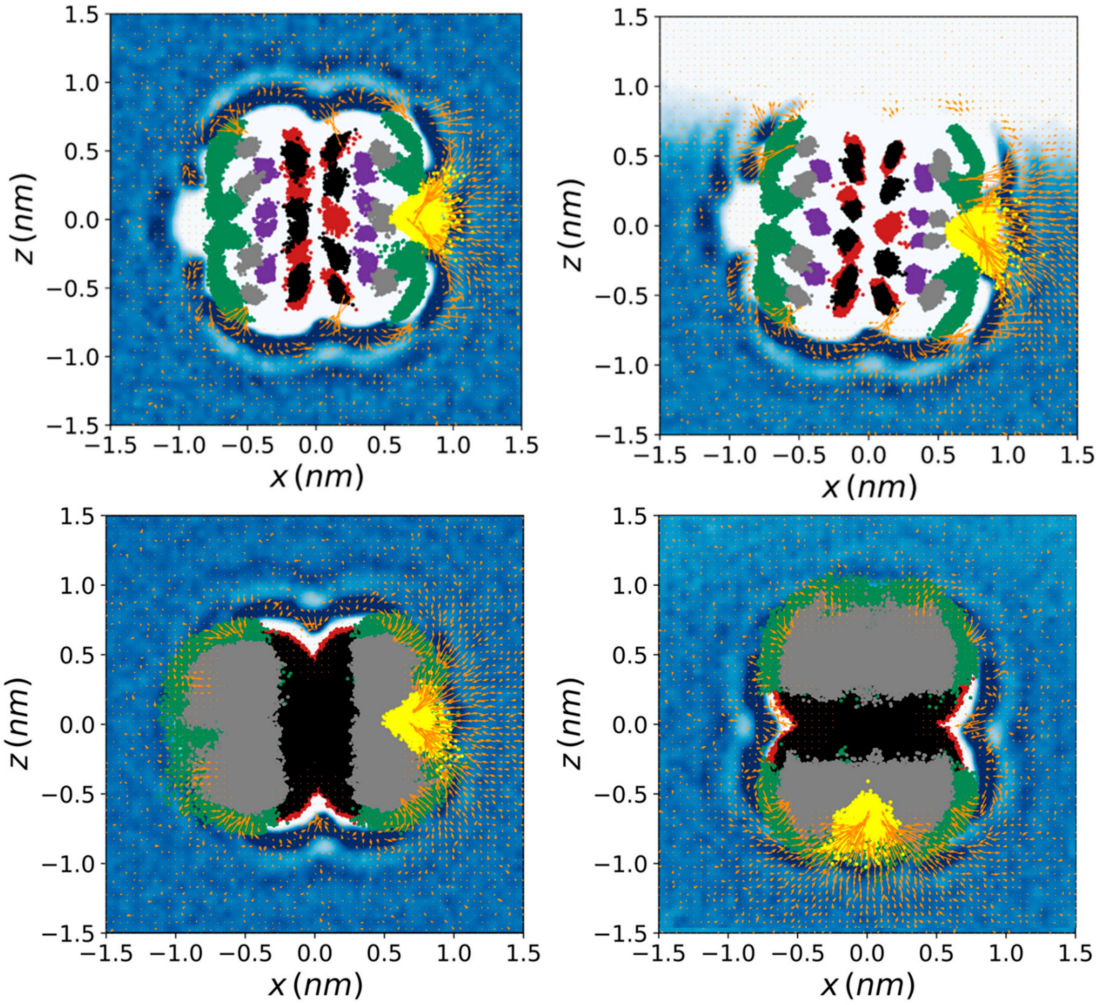


Figure 3. Water density (blue-white gradient from highest to lowest) and average water dipole moment (orange vectors) around the α-CD_2SDS_1 complex in the aqueous solution (left) and in the presence of water/air interface (right) for four trajectories generated using the GROMOS force field with the G_2 method (original GROMOS 54a7 force field with 2 fs time step) (top) and the AMBER/GAFF building block parameterization based on GPU rings with RESP charges (bottom). The O2 (red), O3 (black), O4 (purple), O5 (grey), and O6 (green) atoms of the two CDs comprising the complex, together with the sulfur atom of the SDS molecule (yellow), are also represented. The last 10,000 frames of one trajectory with the complex aligned to the O4 atoms were employed for these calculations. A resolution of 0.5 × 0.5 $Å^2$ in the XZ plane for a 3 Å width slice perpendicular to the Y axis and centered in the symmetry axis of the complex was considered to generate the plot.

The analysis shown in Figure 5 is complementary to those of Figures 3 and 4. Thirteen 1-Å-thick coaxial shells centered in the symmetry axis of the complex were considered and cylindrical coordinates were employed. It can be noticed that the deepest water molecules appeared at 7–8 Å from the center of the structure, just between the O2 and O3 atoms, i.e., at the interface between both CDs. At 8–9 Å, the shape of the rings can be perfectly appreciated from the high density of water around them. The complementary profile was observed between 9–10 Å while the water density was uniform at more than 12 Å from the center of the complex. Overall, these complementary views of the water density, oxygen atoms, and water dipolar moment indicate that the solvent fits perfectly well to the complex structure.

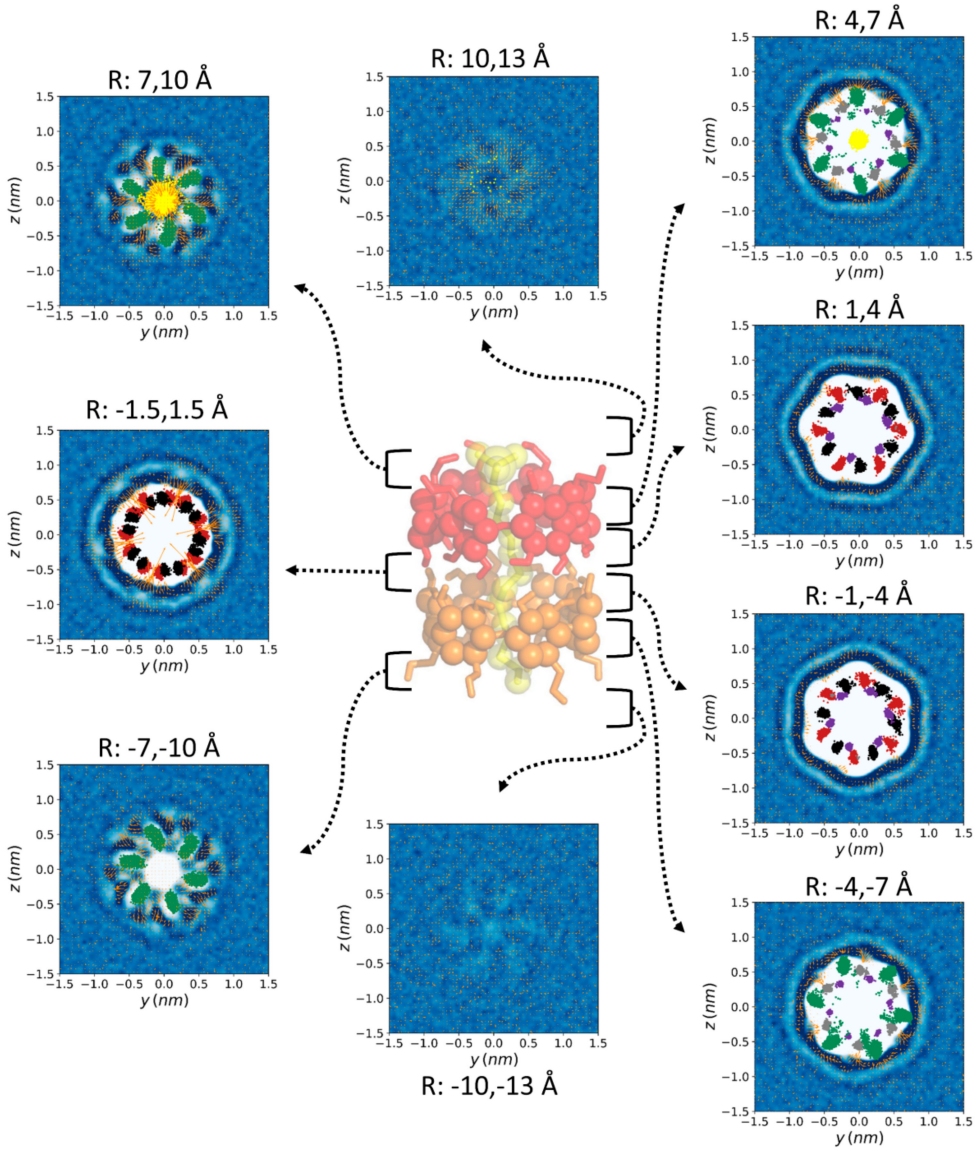


Figure 4. Water density (blue–white gradient from highest to lowest) and average water dipole moment (orange vectors) around the α-CD_2SDS_1 structure in aqueous solution for a trajectory generated using the G_2 method (original GROMOS 54a7 force field with 2 fs time step). Nine 3 Å width slices perpendicular to the symmetry axis of the complex and comprising the atoms at the indicated distances (R) from the center of the structure, were considered. The position of each slice is indicated by the brackets and arrows. The O2 (red), O3 (black), O4 (purple), O5 (grey), and O6 (green) atoms of the two CDs comprising the complex, together with the sulfur atom of the SDS molecule (yellow), are also represented. The last 10,000 frames of one trajectory with the complex aligned to the O4 atoms were employed for these calculations. A resolution of 0.5 × 0.5 $Å^2$ in the YZ plane was considered to generate each plot. Equivalent plots for the rest of the studied parameterization methods are shown in the Supplementary Materials.

USC
DE SANTIAGO
DE COMPOSTELA

In order to study the internal motion of the CD molecules, the area of the hexagons formed by the different oxygen atoms of the two CDs was monitored as a function of time (see Figure 6). The significant difference between the areas of the hexagons formed by O2 and those formed by O3 can be explained by the intramolecular and intermolecular H-bond pattern involving the corresponding hydroxyl groups. The hydroxyls containing O2 always donate the H2 atom to the O3 atom of the GPU unit in the opposite CD, thus participating in an intermolecular H-bond. In turn, the hydroxyls containing the O3 atoms always donate the corresponding H3 to the O2 atom belonging to the contiguous

GPU group within the same CD, thus participating in an intramolecular H-bond. Experimental evidence of this specific behavior has been previously observed [59]. The correlation between the areas of the hexagons formed by the different oxygen atoms and the H-bonds of the corresponding hydroxyl groups is illustrated in Figure 6. Abrupt increases in the area of the hexagon formed by a given oxygen type were always accompanied by the rupture of H-bonds involving the corresponding hydroxyl group, and vice versa. There were slight differences of just 1–2 Å^2 between the areas of the hexagons formed by the same type of oxygens from different CDs, larger for O3 and O5 of the CD that was closer to the SDS head (CD1) and for the O2 of the CD that was further (CD2). In general, these areas were practically constant with time, mainly those obtained from O4 atoms. The O6 was an exception to this behavior, showing sharp variations of more than 40 Å^2 between minimum and maximum areas. Such variations were related to the high amplitude of the movement of these atoms leading to the petal-shaped patterns shown in Figure 4.

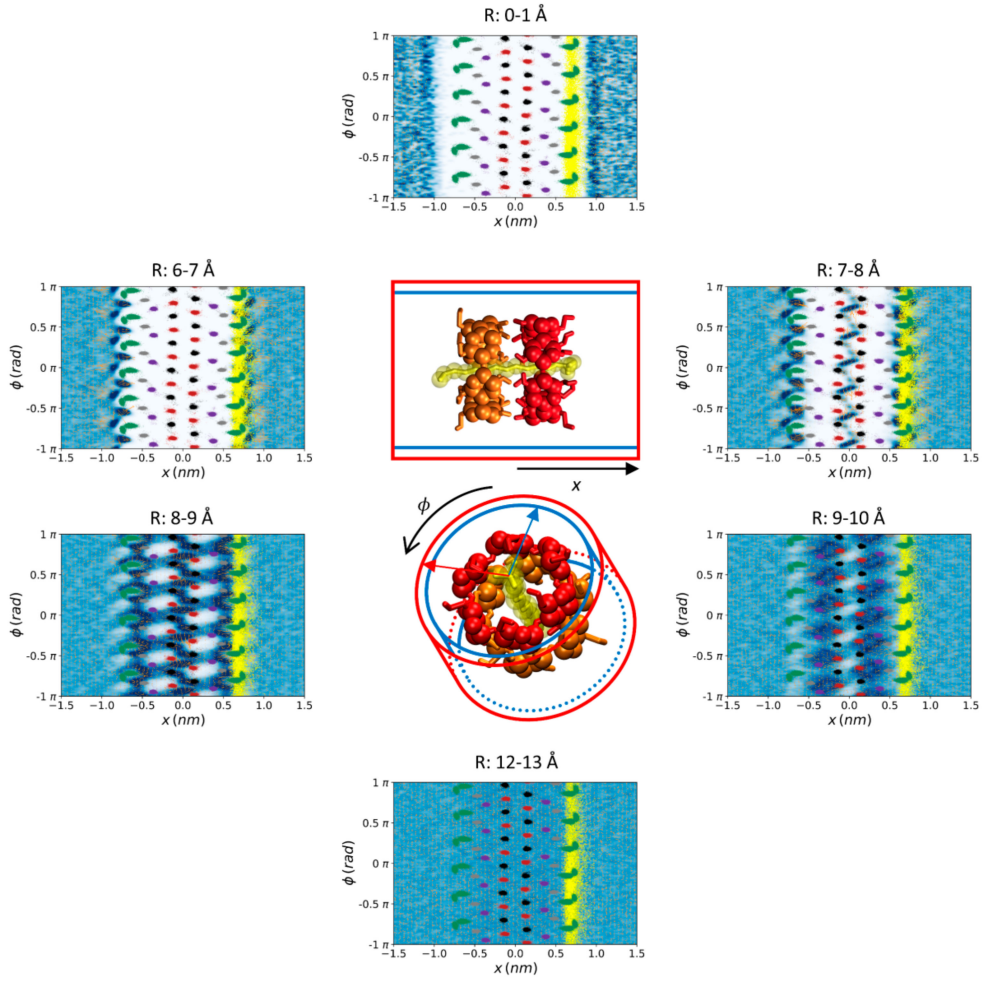


Figure 5. Water density (blue–white gradient from highest to lowest) and average water dipole moment (orange vectors) around the α-CD_2SDS_1 structure in aqueous solution for a trajectory generated using the G_2 method (original GROMOS 54a7 force field with 2 fs time step). Thirteen 1 Å thick coaxial shells centered in the symmetry axis of the complex were considered but only the more representative six are shown with the corresponding maximum and minimum radius indicated in each image. Cylindrical coordinates are employed, for clarity. The distances to the symmetry axis corresponding to each shell are indicated in the figure. The O2 (red), O3 (black), O4 (purple), O5 (grey), and O6 (green) atoms of

the two CDs comprising the complex, together with the sulfur atom of the SDS molecule (yellow), are represented in all the images as a reference even though they are not within the indicated radii. The last 10,000 frames of one trajectory with the complex aligned to the O4 atoms were employed for these calculations. A resolution of 0.5 × 0.5 $Å^2$ in the φx plane was considered to generate each plot. Equivalent plots for the rest of the studied parameterization methods are shown in the Supplementary Materials.

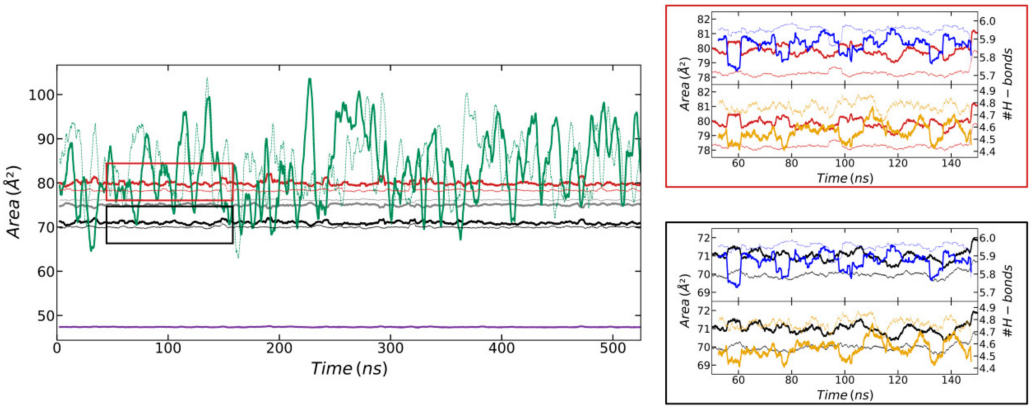


Figure 6. Area of the hexagons formed by the six O2 (red), O3 (black), O4 (purple), O5 (grey), and O6 (green) atoms of the CD molecules that are closer (solid thick lines) and further (dotted thin lines) from the SDS head. The right-upper plot (red-squared) shows the area of the hexagons formed by the six O2 of CD1 (thick red line) and CD2 (thin red line) between 50 and 150 ns together with: (i) The intramolecular H-bonds between the hydroxyl groups 2 and 3 of the CD that is closer and further to the SDS head (thick and thin blue lines, respectively); and (ii) the intermolecular H-bonds between the hydroxyl groups 2 and 3 of the first CD and second CD (thick yellow line) and vice versa (thin yellow line). The right-lower plot (black-squared) shows the same H-bond information as in the red-squared box, compared to the area of the hexagon formed by the six O3 of CD1 (thick black line) and CD2 (thin black line). This figure was obtained from the simulation of the α-CD_2SDS_1 structure in aqueous solution for a trajectory generated using the G_2 method (original GROMOS 54a7 force field with 2 fs time step). All the curves were moving-averaged over 3.5 ns in order to remove noise. Equivalent plots for the rest of the studied parameterization methods are shown in the Supplementary Materials.

3.2. Comparison between G_2 and Other Simulation Methods Using GROMOS and AMBER/GAFF Force Fields in the Bulk Aqueous Solution

The 2:1 complexes in the simulations using GROMOS with the HMR and the H2Q methods with both time steps (2 and 7 fs) were stable and provided indistinguishable water density and dipolar moment profiles compared to the G_2 method (see Figures S2–S5 and Figures S8–S11). The projection of the motion of the different oxygen atoms along the trajectories was also identical for each group of simulations, indicating that the pathway and the amplitude of the internal motions of the CD groups and SDS molecule remained unaffected by the mass transfer or mass increase. This was also reflected in the indistinguishable areas of the hexagons formed by the oxygen atoms (Figures S12–S15). However, the results were quite different for the simulations using the AMBER/GAFF force field. In this case, the three high–low–high-density water layers were also visible, together with the dipole moment vector field of water molecules, but the motion of the CD oxygens was much more important and isotropic i.e., no privileged directions were observed in their motions. In Figure 3 and Figure S1, only the position of O5, O3, and O6 atoms were visible, O2 and O4 being shielded by them. Figures S6 and S7 show that the hexagonal shape water layer that was clear with the different parameterizations of GROMOS at 1–4 Å from the center of the structure was not visible when using the AMBER/GAFF force field. Additionally, the petal-shaped projection of the O6 motion was not present at all when using AMBER/GAFF. The three parameterizations of the AMBER/GAFF force field provided similar water densities and dipole moment profile, regardless of the method used to determine the partial

charges and to parameterize the molecule (Figure 3, Figures S1, S6, and S7). For the AMBER/GAFF force field, the analysis of water density in concentric shells produced completely uniform patterns (not shown). There was also an important dipole moment vector field of water molecules around the structure of the complex, mainly near the SDS head, for the simulations with this force field. The areas formed by different types of oxygens using the AMBER/GAFF parameterization based on GPUs building blocks are shown in Figures S16 and S17. When using the AM1-BCC charges, the area of the hexagons formed by the six O6 atoms was significantly shorter than for the RESP charges. For this latter parameterization, the areas were more similar to those using the different versions of the GROMOS force field. In general, the areas obtained from AMBER/GAFF simulations were lower and fluctuated more than those using GROMOS.

3.3. H-Bond Analysis of Simulations in the Bulk Aqueous Solution

The number of intramolecular, CD-CD, and CD-water H-bonds were also equivalent for all the simulations using variations of the GROMOS force field (Table 1). In contrast, significant differences were observed for the corresponding H-bond lifetimes. In general, lifetimes of simulations using a time step of 7 fs were between 1.7 and 3.5 times larger than the equivalent simulations using a time step of 2 fs. The impact of the mass change at a constant time step in the H-bond lifetime was negligible for most H-bonds. The largest difference appeared for the lifetimes of the intramolecular H-bonds of the CD that was further from the SDS head. Even though the number of H-bonds was practically identical, their lifetimes for G_2 were 1640 ps while for HMR_2 was 1437 ps and for H2Q_2 was 1678 ps. It is interesting to see the different behavior of the interfacial hydroxyl groups (O2H2 and O3H3) between both CDs. The hydroxyl groups of CD1 formed significantly more H-bonds with water molecules than those of CD2. As a result, the intramolecular H-bonds of CD2 were twice more stable than those of CD1. This is reproducible with all methods based on the GROMOS and also on AMBER/GAFF force field, and it could be related to the higher order of water molecules around the hydroxyl groups of CD1 than of CD2 (see Figures 3–5 and Figures S1–S8) induced by the closer proximity to the ionic SDS head. In general, the number of H-bonds obtained from any of the simulations using the AMBER/GAFF force field were very different from those obtained from the simulations based on the GROMOS force field. As shown in Table 1, for the simulations using AMBER/GAFF, the average number of CD1-CD2 intermolecular H-bonds was almost half (~9.4 vs. 5.5–5.8) of that using any of the GROMOS methods. The lifetime of these H-bonds obtained using the three AMBER/GAFF parameterizations was also significantly different to each other: 20.56, 37.61, and 18.21 ps for AMBER RESP, AMBER BB-RESP, and AMBER BB-AM1, respectively. In contrast, the number of intramolecular H-bonds was similar for all the AMBER/GAFF and GROMOS simulations, although the lifetime was much lower in AMBER than for the GROMOS parameterizations. The reduction in intermolecular CD1-CD2 H-bonds with AMBER/GAFF was compensated by a significant increase in the number of H-bonds between the O2H2 or O3H3 hydroxyls of both CDs and water molecules. The lifetime of such H-bonds was similar for AMBER/GAFF and for the GROMOS parameterizations. The O5 atom also participated in a larger number of H-bonds with water when using AMBER/GAFF than GROMOS, although the corresponding lifetime was similar. The number of H-bonds involving O6 was similar for all the parameterizations, just slightly lower for AMBER/GAFF.

USC UNIVERSIDADE DE SANTIAGO DE COMPOSTELA

Table 1. Average number of different H-bonds contributions and simulation methods together with the corresponding lifetimes in ps (in brackets) for the different molecular dynamics (MD) simulations in the bulk solution.

Donor/Acceptor	G_2	HMR_2	HMR_7	H2Q_2	H2Q_7	AMBER RESP	AMBER BB-RESP	AMBER BB-AM1
CD1-CD2	9.37 (41.01)	9.37 (41.00)	9.47 (148.42)	9.40 (41.75)	9.42 (145.47)	5.87 (20.56)	5.45 (37.61)	4.85 (18.21)
O2H2 (CD1)-O3H3 (CD2)	4.55 (37.78)	4.52 (37.87)	4.60 (138.35)	4.56 (38.63)	4.59 (137.23)	2.58 (21.42)	1.57 (41.36)	1.96 (18.64)
O2H2 (CD2)- O3H3 (CD1)	4.76 (44.37)	4.74 (43.93)	4.77 (158.85)	4.74 (44.78)	4.74 (153.70)	2.60 (21.51)	1.59 (42.60)	1.93 (18.81)
CD1-CD1	5.87 (852)	5.82 (856)	5.86 (2624)	5.85 (849)	5.87 (2696)	5.80 (250.07)	5.46 (145.83)	5.73 (210.60)
O3H3 (CD1)- O2H2 (CD1)	5.87 (856)	5.82 (859)	5.86 (2631)	5.85 (853)	5.87 (2701)	5.77 (291.50)	5.43 (155.73)	5.71 (227.72)
CD1-SDS	1.48 (52.26)	1.35 (53.58)	1.39 (93.65)	1.55 (52.70)	1.41 (89.89)	2.02 (17.98)	0.89 (19.63)	2.55 (21.00)
CD2-CD2	5.94 (1640)	5.93 (1437)	5.92 (4484)	5.92 (1678)	5.92 (4586)	5.89 (310.17)	5.66 (209.38)	5.81 (233.32)
O3H3 (CD2)- O2H2 (CD2)	5.94 (1645)	5.93 (1444)	5.92 (4494)	5.92 (1678)	5.92 (4607)	5.84 (400.60)	5.64 (223.52)	5.76 (271.77)
O2H2 (CD1)-water	2.32 (6.90)	2.37 (7.03)	2.36 (19.47)	2.34 (6.95)	2.33 (19.35)	3.45 (7.49)	4.41 (9.72)	3.14 (7.94)
O2H2 (CD2)-water	1.97 (6.45)	1.95 (6.54)	2.01 (19.09)	1.99 (6.65)	2.01 (19.11)	3.18 (7.24)	3.91 (9.45)	2.89 (7.85)
O3H3 (CD1)-water	1.40 (6.23)	1.43 (6.35)	1.38 (18.64)	1.39 (6.24)	1.39 (18.73)	2.98 (6.99)	3.29 (8.39)	3.26 (7.45)
O3H3 (CD2)-water	1.19 (5.87)	1.17 (5.82)	1.18 (18.30)	1.21 (5.85)	1.20 (18.43)	2.72 (7.06)	2.98 (8.27)	3.00 (7.48)
O5 (CD1)-water	1.93 (6.60)	1.93 (6.62)	1.98 (18.79)	1.95 (6.75)	1.97 (18.77)	2.80 (6.50)	4.67 (9.43)	2.78 (6.80)
O5 (CD2)-water	1.63 (6.47)	1.60 (6.43)	1.64 (18.67)	1.62 (6.50)	1.62 (18.74)	2.42 (6.33)	4.40 (9.28)	2.32 (6.55)
O6H6 (CD2)-water	12.44 (14.49)	12.46 (14.76)	12.56 (27.73)	12.45 (14.82)	12.52 (28.27)	9.71 (7.48)	10.96 (7.96)	9.53 (7.69)
O6H6 (CD1)-water	11.59 (12.16)	11.68 (12.36)	11.73 (24.84)	11.50 (12.30)	11.72 (24.87)	10.72 (8.16)	11.31 (8.75)	10.99 (8.32)
SDS-water	3.69 (12.35)	3.74 (12.53)	3.74 (25.70)	3.63 (12.38)	3.72 (25.67)	3.53 (8.96)	3.75 (11.35)	3.37 (8.64)

3.4. Simulations at the Water/Air Interface Using the Different Parameterizations of the GROMOS Force Field

The α-CD_2SDS_1 complex was quickly adsorbed in the simulations where the interface was present, and it remained "floating" with the symmetry axis parallel to the water surface for the rest of the trajectories. A few exceptions to this behavior took place in some replicas of our simulations, where the structure rotated 90° and remained close to the interface with the symmetry axis perpendicular to the water surface. This behavior does not seem to depend on the different variations of the simulation method based on GROMOS and it is quite general for this force field, but it eventually appeared in some of the trajectories. An example of this behavior is shown in Figure S36 for the H2Q method with a time step of 2 fs, where the rotation took place at approximately 430 ns. The impact of the rotation of the structure was perfectly clear in the distance between the center of mass of the structure and that of the water molecules in the simulation box as well as in the pitch, yaw, and roll angles (see definition in Figure 2). The pitch angle went to 90° and the yaw and roll angles became much noisier (Figure S36). Notably, the hydration level of the different GPU residues after the rotation was lower than the maximum values reached by some residues when the structure was parallel to the interface. The possible presence of these alternative orientations for the complex (parallel and perpendicular to

the interface) has been discussed in the past [23] using a battery of experimental data. Our simulations clearly indicate that the most probable orientation is that with the symmetry axis parallel to the surface but the rotation that appears in some simulations suggests that it could also be a marginal population of the perpendicular orientation. When the orientation of the complex was parallel to the surface, the level of water at which the 2:1 structure floats fluctuated significantly (± 3 Å), as indicated by the distance between the center of mass of the water molecules and that of the 2:1 complex (Figure 7, first row). The pitch angle was very small in all cases, indicating that the α-CD_2SDS_1 complex was really parallel to the water surface and it did not fluctuate significantly. The yaw angle changed slowly, although it did not seem to have a unidirectional rotation. However, the roll angle exhibited a clear trend to increase in the trajectory shown in Figure 7, completing more than four full turns after 450 ns. A similar increase in the roll angle can be seen in Figure S34 for one of the replicas of the HMR method with a time step of 2 fs and, to a lesser extent, in the H2Q simulation with time step of 7 fs shown in Figure S37. For the HMR_7 simulation shown in Figure S35, the average roll angle also increased although the structure only rotated 1.5 turns after 500 ns, while in the simulation shown in Figure S36, corresponding to the H2Q method with a time step of 2 fs, the rotation was small and it took place in the opposite direction. The anisotropic motion of the O6 atoms might favor the rotation of the roll angle in a single direction, although this could be shielded by other coupled movements. Actually, it is interesting to observe the orientation change of the α-CD_2SDS_1 complex at the interface, from parallel to perpendicular, which took place in the simulation where the roll angle decreased. The hydration level of the different GPU rings in the two CDs showed an interesting behavior with different patterns along the trajectories (see Figure 7 and Figures S34–S37, rows 3–5). For some periods, the hydration of most residues was quite high and fluctuated (around 50 ns in Figure 7) while for other periods the level of hydration of all residues was significantly lower (long period around 225 ns in Figure 7). The periods corresponding to low hydration seem to correlate with the regions where the distance between the complex and the center of mass of the water was larger and relatively stable, while the regions with high fluctuations seem to correspond to those where the complex was more buried in the water phase (shorter distance to the center of mass of the water molecules). Notably, the level of hydration in all residues was relatively low after the 90° rotation in the trajectory shown in Figure S36, even though the structure was less exposed to the air in that case.

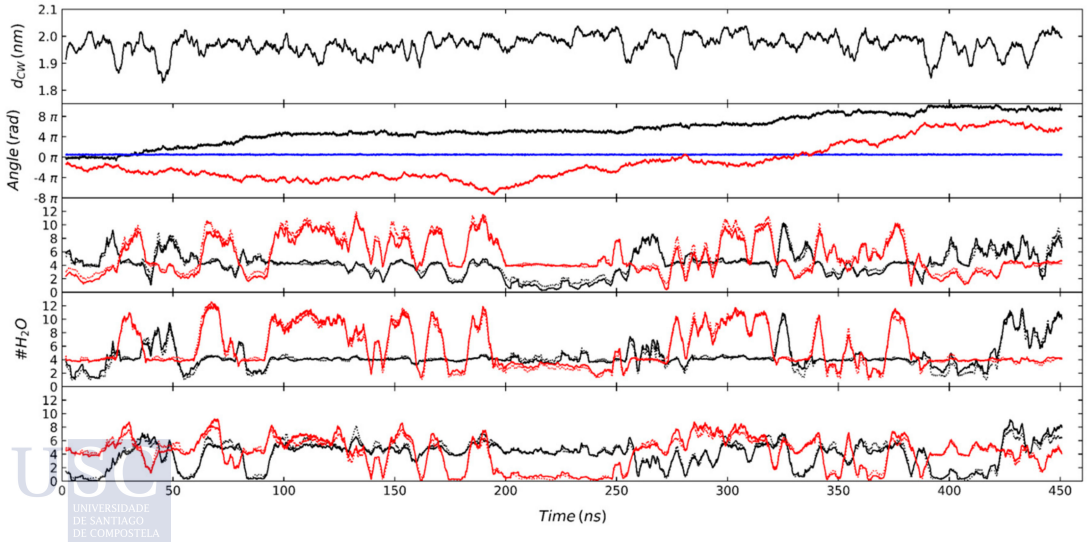


Figure 7. Distance between the center of the O4 atoms of the two CDs in the α-CD_2SDS_1 structure and the center of mass of the water molecules (first row). Yaw (red), pitch (blue), and roll (black) angles of the 2:1 complex as defined in Figure 2 with respect to the water/air interface (second row). Number of

water molecules at less than 3 Å of any atom of the CD that is closer (solid lines) and further (dashed lines) to the SDS head in the complex (third to fifth rows). Rows 3, 4, and 5 represent GPU units {1,4}, {2,5}, and {3,6} for one CD (black lines), respectively, and the corresponding GPU units (i.e., those in the same generatrix of the nanocylinder-shaped structure) of the opposite CD (red lines). This plot results from the analysis of a MD trajectory using the G_2 parameterization method in the presence of a water/air interface. Equivalent plots for the rest of the studied parameterization methods are shown in the Supplementary Materials.

For the calculation of the density maps, only the frames corresponding to the minimum hydration level of each GPU group were selected, assuming that the rings with the minimum hydration level for a given frame are orientated towards the air. The density maps were similar to those corresponding to the complex in the bulk solution, but in this case, the exposition to the air left a region completely dried. The complementary density maps are shown in Figure 3 (right-top) as well as in Figures 8 and 9. Figure 3 displays the comparison between the water density profile in the bulk solution and that at the interface. Upon adsorption, a significant number of highly packed water molecules were released, which could provide an entropic contribution to the adsorption. Notably, the high orientation of the water molecules around the complex also seemed to decrease, as revealed by the shorter dipole moment vector field shown around the complex structure (Figures 3, 8 and 9, Figures S18–S21, and Figures S24–S27). However, the wet region of the complex maintained the water structure around with a pattern that was quite similar to that in the bulk solution. The density maps shown as a function of the distance to the symmetry axis of the complex (Figure 3, right-top) reveals that the SDS head was slightly bent towards the water, since the density of sulfur in the dried region was slightly lower than that in the wet region.

The transition from a circular to hexagonal and again to circular density profile that had been observed in the bulk solution was also maintained at the interface despite the partial drying of the complex (Figure 8). Notably, even the petal-shaped density profiles induced by the particular movement of the O6 atoms were clearly seen in the presence of air/water interface (Figure 8). This suggests that just a few water molecules were required to avoid the loss of symmetry around the complex caused by the movement of the O6 groups. The complementary analysis shown in Figure 9 reveals that a thin layer of water appeared at a radius from the center of 7–8 Å, just between the O2 and O3 atoms, at the interface between both CDs, as happened in the case of the bulk simulations. However, even at this distance, the layer of waters was not completely uniform.

The area of the hexagons formed by the six O2, O3, O4, or O5 atoms for the simulation at the interface were similar to those corresponding to the simulation in the bulk solution (Figure 10 and Figures S28–S31). The O6 again presented strong variations between the minimum and the maximum area. However, the amplitudes of the motion of these atoms leading to the petal-shaped patterns shown in Figure 9 were now a bit decreased in comparison to the results in the bulk (Figure 6 and Figures S12–S15).

3.5. H-Bond Analysis of Simulations at the Water/Air Interfaces Using the Different Parameterizations of the GROMOS Force Field

As in the case of the bulk solution, the number of intramolecular, CD-CD, and CD-water H-bonds were also equivalent for all the simulation methods (Table 2). In general, the average number of H-bonds seemed to be higher at the interface than in the bulk solution, although the discrepancies were not large. Again, important differences were observed in the H-bond lifetimes with all simulation methods. The most significant variation was observed between the lifetime of intramolecular H-bonds of CD1 vs. the same contribution in CD2, as in the case of the simulations in the bulk solution. That difference was attributed to the long-range effect of the charged SDS head, which induced a significant dipolar moment in the water molecules around CD1 and favored the interaction the O2-H2 and O3-H3 of this CD with water, compared to the equivalent interactions of CD2. In turn, the intramolecular H-bonds between O2-H2 and O3-H3 of CD2 were more stable than those for CD1. In this case,

the relative difference is not as large as in the case of the simulations in the bulk solution, which might be due to the significant decrease in the dipolar moment of water around the complex in the bulk solution compared to the simulations at the interface. For the simulation using G_2, the lifetime values of the intramolecular H-bonds of CD1 and CD2 in aqueous solution were ~852 ps and ~1640 ps, respectively, while the equivalent interactions at the interface were ~1248 ps and ~1989 ps. In contrast with the simulations in the bulk aqueous solution, the presence of O4-water H-bonds was significant, although relatively low, at the interface. The H-bond pattern, completely reproducible with all the tested simulation methods using GROMOS (considering the correction factor observed in the simulations with a 7 fs time step), illustrates the significant increase in the number and stability of H-bonds from bulk to interface as well as the differences between both CDs in the supramolecular complex.

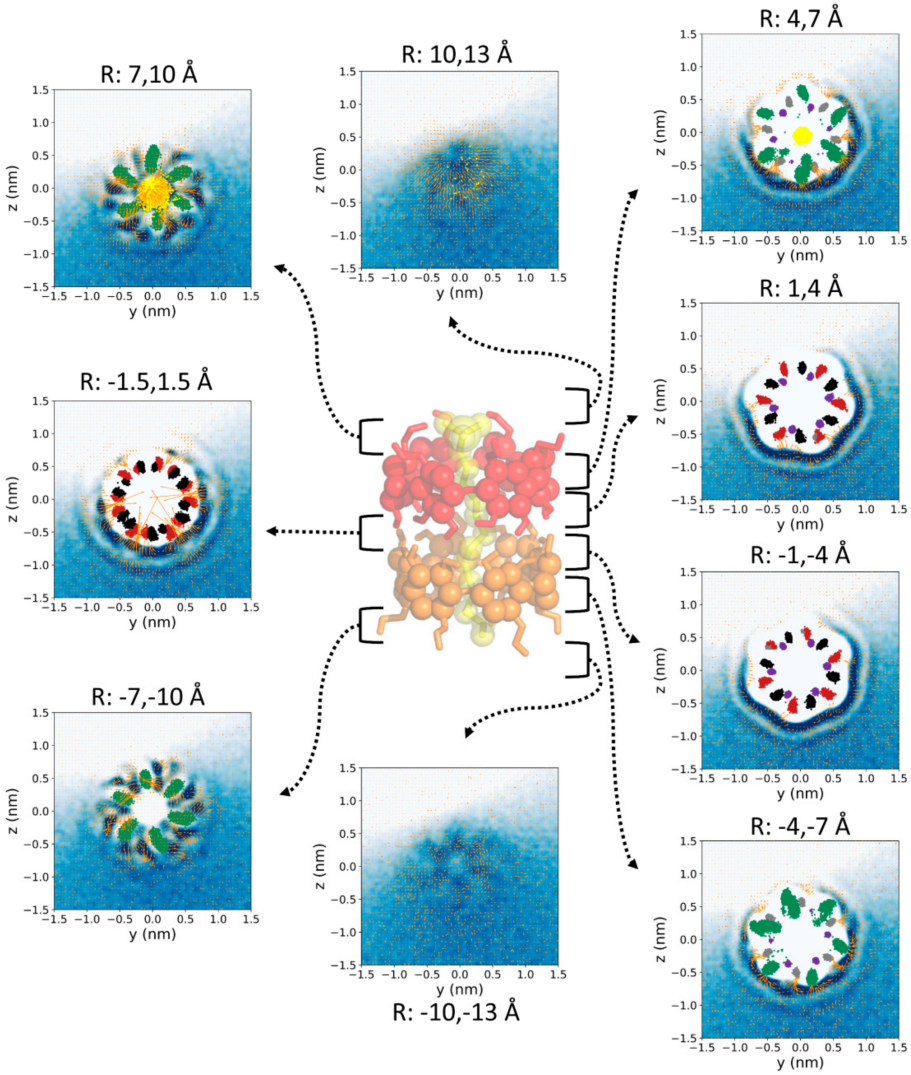


Figure 8. Water density (blue–white gradient from highest to lowest) and average water dipole moment (orange vectors) around the α-CD_2SDS_1 structure at the water/air interface for a trajectory generated using the G_2 method (original GROMOS 54a7 force field with 2 fs time step). Nine 3 Å width slices perpendicular to the symmetry axis of the complex were considered. The position of each slice is indicated by the brackets and arrows. The O2 (red), O3 (black), O4 (purple), O5 (grey), and O6 (green) atoms of the two CDs comprising the complex, together with the sulfur atom of the SDS molecule (yellow), are also represented. A selection of the last 10,000 frames of one trajectory with the complex aligned to the O4 atoms, corresponding to the frames where the GPU number 1 of the first CD has the minimum hydration, were employed for these calculations. A resolution of 0.5 × 0.5 $Å^2$ in the YZ plane was considered to generate each plot. Equivalent plots for the rest of the studied parameterization methods are shown in the Supplementary Materials.

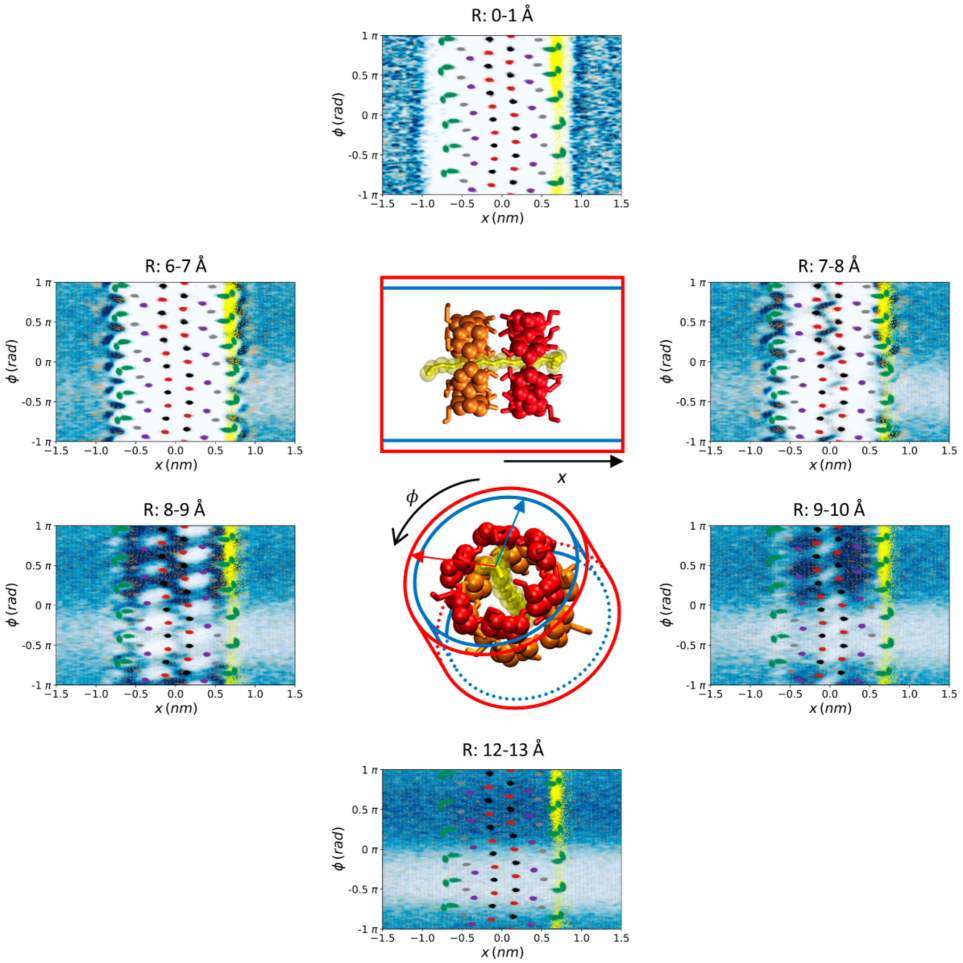


Figure 9. Water density (blue–white gradient from highest to lowest) and average water dipole moment (orange vectors) around the α-CD_2SDS_1 structure at the water/air interface for a trajectory generated using the G_2 method (original GROMOS 54a7 force field with 2 fs time step). Six 1 Å thick coaxial shells centered in the symmetry axis of the complex were considered and cylindrical coordinates are employed, for clarity. The distances to the symmetry axis corresponding to each shell is indicated in the figure. The O2 (red), O3 (black), O4 (purple), O5 (grey), and O6 (green) atoms of the two CDs comprising the complex, together with the sulfur atom of the SDS molecule (yellow), are also represented. The last 10,000 frames of one trajectory with the complex aligned to the O4 atoms were employed for these calculations. A resolution of 0.5 × 0.5 $Å^2$ in the φx plane was considered to generate each plot. Equivalent plots for the rest of the studied parameterization methods are shown in the Supplementary Materials.

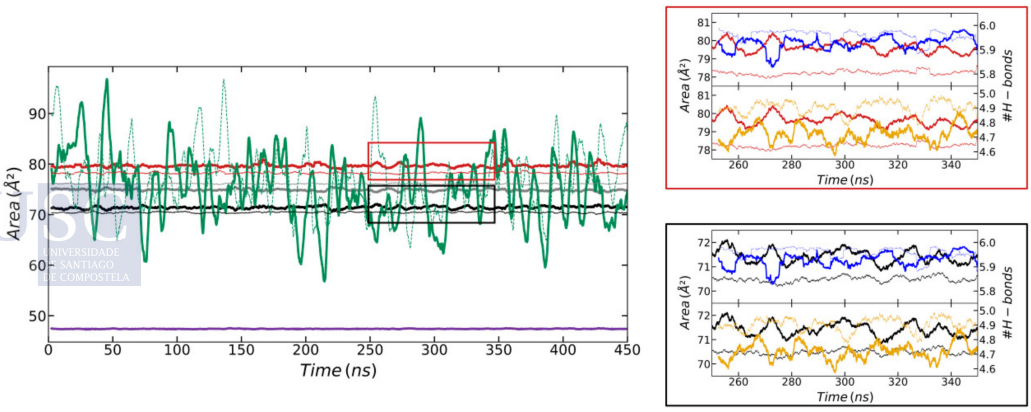


Figure 10. Area of the hexagons formed by the six O2 (red), O3 (black), O4 (purple), O5 (grey), and O6 (green) atoms of the CD molecules that are closer (solid lines) and further (dashed lines) from

the SDS head. This plot corresponds to the simulation of the α-CD_2SDS_1 structure at the water/air interface for a trajectory generated using the G_2 method (original GROMOS 54a7 force field with 2 fs time step). Equivalent plots for the rest of the studied parameterization methods are shown in the Supplementary Materials.

Table 2. Average number of different H-bonds contributions and simulation methods together with the corresponding lifetimes in ps (in brackets) for the different simulations at the water/air interface.

Donor/Acceptor	G_2	HMR_2	HMR_7	H2Q_2	H2Q_7	AMBER RESP	AMBER BB-RESP	AMBER BB-AM1
CD1-CD2	9.64 (46.60)	9.65 (46.58)	9.71 (166.19)	9.61 (45.75)	9.67 (163.43)	5.87 (20.50)	5.40 (36.66)	4.86 (18.81)
O2H2 (CD1)-O3H3 (CD2)	4.71 (42.81)	4.72 (42.66)	4.76 (155.15)	4.69 (42.10)	4.70 (147.75)	2.55 (21.27)	1.61 (39.79)	1.98 (19.66)
O2H2 (CD2)- O3H3 (CD1)	4.90 (50.71)	4.91 (50.94)	4.93 (178.41)	4.89 (49.77)	4.93 (181.16)	2.64 (21.37)	1.54 (41.16)	1.98 (19.21)
CD1-CD1	5.91 (1248)	5.92 (1381)	5.93 (3852)	5.91 (1298)	5.90 (3662)	5.79 (244.78)	5.47 (151.57)	5.73 (208.11)
O3H3 (CD1)- O2H2 (CD1)	5.91 (1262)	5.92 (1398)	5.93 (3878)	5.91 (1311)	5.90 (3695)	5.76 (284.60)	5.45 (160.66)	5.71 (223.89)
CD1-SDS	2.09 (47.35)	1.89 (48.18)	1.99 (104.61)	2.05 (56.39)	2.16 (93.78)	1.96 (18.15)	1.01 (19.74)	2.25 (20.96)
CD2-CD2	5.96 (1989)	5.97 (2505)	5.96 (5624)	5.96 (2144)	5.97 (8040)	5.89 (318.85)	5.56 (182.09)	5.82 (251.10)
O3H3 (CD2)- O2H2 (CD2)	5.96 (2117)	5.96 (2632)	5.96 (5869)	5.96 (2307)	5.96 (8421)	5.84 (411.09)	5.54 (191.28)	5.78 (289.62)
O2H2 (CD1)-water	2.51 (6.17)	2.39 (6.19)	2.76 (18.49)	2.34 (6.22)	2.28 (18.77)	3.51 (7.42)	4.53 (9.77)	3.17 (7.79)
O2H2 (CD2)-water	2.24 (5.85)	2.16 (5.88)	2.52 (18.24)	2.08 (5.99)	2.03 (18.43)	3.23 (7.25)	3.97 (9.35)	3.00 (7.86)
O3H3 (CD1)-water	1.87 (5.62)	1.72 (5.65)	2.10 (18.04)	1.67 (5.68)	1.62 (18.24)	2.99 (7.03)	3.37 (8.28)	3.33 (7.52)
O3H3 (CD2)-water	1.72 (5.45)	1.61 (5.44)	1.99 (17.94)	1.51 (5.48)	1.49 (17.95)	2.79 (6.89)	2.99 (8.23)	3.07 (7.36)
O4 (CD1)-water	0.56 (5.10)	0.47 (5.09)	0.69 (17.75)	0.39 (5.09)	0.40 (17.53)	–	–	–
O4 (CD2)-water	0.55 (5.10)	0.50 (5.08)	0.68 (17.50)	0.44 (5.09)	0.40 (17.58)	–	–	–
O5 (CD1)-water	2.05 (6.07)	2.01 (6.13)	2.27 (18.26)	1.97 (6.10)	1.94 (18.41)	2.83 (6.48)	4.70 (9.44)	2.82 (6.84)
O5 (CD2)-water	1.82 (5.95)	1.75 (6.01)	1.98 (18.07)	1.68 (5.94)	1.68 (18.40)	2.46 (6.26)	4.46 (9.07)	2.37 (6.45)
O6H6 (CD2)-water	11.33 (11.89)	11.36 (12.13)	11.74 (24.99)	11.24 (12.12)	11.12 (25.27)	9.83 (7.48)	10.98 (7.90)	9.80 (7.65)
O6H6 (CD1)-water	12.79 (15.68)	12.70 (15.83)	12.95 (31.75)	12.74 (15.83)	12.65 (32.11)	10.89 (8.13)	11.55 (8.55)	11.17 (8.27)
SDS-water	3.49 (11.01)	3.59 (11.34)	3.61 (24.84)	3.42 (11.13)	3.34 (25.07)	3.62 (8.97)	3.66 (11.18)	3.62 (8.80)

USC UNIVERSIDADE DE SANTIAGO DE COMPOSTELA

For the simulations at the interface, the distance between the center of mass of the simulation box and that of the complex, the roll, yaw, and pitch angles, the profile of the number of water molecules for each glucopyranoside ring as a function of time, and the area of the hexagons formed by different groups of oxygen atoms were also indistinguishable using the different GROMOS simulation methods and time steps of 2 and 7 fs (see Supplementary Materials). The number of intermolecular CD-CD and CD-water H-bonds were also equivalent between the two groups of simulations. As in the case of the simulations in the bulk solution, only the H-bond lifetimes were significantly increased.

This indicates that both the HMR and the H2Q methods lead to identical structural results also in the interface and that the internal relative movements of the solute atomic groups are also identical.

3.6. Analysis of Simulations Using the AMBER Force Field in the Presence of the Water/Air Interfaces

Using the AMBER force field, the α-CD_2SDS_1 complex did not significantly adsorb at the interface and so the water density analysis and the determination of H-bonds for comparison with the simulations based on the GROMOS force field cannot be properly done. The complex can be observed very close to the interface at times during the MD trajectories due to its diffusion but it was not stable enough to perform a reasonable characterization (see Figures S38 and S39). Interestingly, when it was close to the interface, it appeared with the symmetry axis in the perpendicular orientation. The density profile corresponding to these simulations is shown in Figure 3 (right-bottom) and Figure S1 but the water/air interface cannot be appreciated because the complex does not stay at the interface for a significant time. Thus, the water density profile, dipole moment vector field, and H-bond pattern (Table 2) of these trajectories were quite similar to those obtained for the same force field in the bulk solution.

4. Discussion

The system selected for this study, a α-CD_2SDS_1 complex, proved to be extremely sensitive to different factors including temperature, concentration range, and the presence of water/air interface. A number of different experimental methods including calorimetry, surface tension, rheology, neutron reflectometry, ellipsometry, and several microscopies were employed to characterize its behavior under different conditions [1,5,6,23]. Several studies were also performed by using β-CD_2SDS_1 instead of α-CD_2SDS_1 complexes [4,27,28], as well as other similar structures that provide interesting self-assembly patterns in the bulk solution and at interfaces [29,30]. However, the driving forces responsible for those events and arrangements are not clear. The connection between atomistic and macroscopic level information might be employed to design new applications as well as to optimize the already established employments of these systems. CDs are well suited for atomic resolution computational studies due to their small size and low number of degrees of freedom. A number of docking and computational studies involving CDs have been published [10–12,26] but the use of these tools is much less extended for these molecules than in protein, peptide, or lipid systems. Thus, the proposal and validation of reliable and efficient computational methods for CD systems is expected to contribute to acquire a better knowledge able to complement the interpretation of wet-lab measurements.

Here, we performed MD simulations of α-CD_2SDS_1 complexes in the bulk aqueous solution as well as in the presence of water/air interfaces using five different parameterizations of the GROMOS force field and three different parameterizations of the AMBER/GAFF force field. The different parameterizations tested using GROMOS were aimed at optimizing the sampling, minimizing the use of computational resources. For this, we took advantage of manipulating the highest frequency motions, which in any molecule corresponds to the lightest atoms, i.e., the Hs. The time step employed in MD simulations for the integration of the motion equation is necessarily limited by these fastest degrees of freedom. For this reason, a time step of 2 fs is employed in most atomic force fields. Different methods have been proposed and tested to overcome this limitation. We decided to compare MD simulations using the standard GROMOS 54a7 force field (G_2), simulations transferring 3 Da of mass to the H atoms from the bound heavy atoms with 2 fs (HMR_2) and 7 fs (HMR_7) time steps, and simulations increasing the mass of H atoms from 1 to 4 Da with the same time steps (H2Q_2 and H2Q_7). Preliminary work performed in our lab indicated that simulations using AMBER behave significantly different from those using GROMOS for CD systems. Thus, we decided to test three different parameterizations of this force field, trying to explain the source of such discrepancy with experiments as well as with results using GROMOS. Simulations of the α-CD_2SDS_1 complex using the eight different parameterizations were performed in the bulk aqueous solution and also in the presence of water/air interfaces. As expected, the mass increase of H in the GROMACS

parameterization using the H2Q method slows down the motion of these atoms, thus producing stable trajectories even with a time step of 7 fs. It has been said that the application of this method could negatively contribute to the sampling when applied to AA force fields, even if the time step is larger, due to slower diffusion that the resulting heavier molecules would exhibit [22]. However, for UA force fields, the impact of the mass increase is much lower. This can be illustrated by a simple calculation: by increasing the mass of all H atoms of the α-CD molecules in 3 Da, the total mass increase of the molecule would be 18.5% in an AA representation and just 5.5% when using the GROMOS force field. The difference is even larger for the SDS molecule since the total mass increase using an AA force field would be 26% while the lack of polar H atoms in this molecule implies that the mass does not change at all upon the application of this method using the GROMOS force field. In addition to the latter argument, the mass increase just in the polar H atoms for the UA force fields can also be justified based on the experimental fact that only the polar H atoms are spontaneously deuterated (thus doubling their mass) when they are solvated in deuterated water [1,23]. This experimental increase of mass just in the α-CD polar Hs maintains the stoichiometry, enthalpies, and equilibrium constants of the binding with SDS molecules, as revealed by ITC measurements performed using different isotopic contrasts, namely α-CD with hydrogenated and deuterated SDS in deuterated and non-deuterated water [23]. Our proposal of increasing the H mass from 1 to 4 Da is based on the hypothesis that the use of quadium instead of deuterium (another mass increase by a factor of 2) also maintains the thermodynamic behavior of this system. Note that in this work, we did not change the parameterization of the water, which is equivalent to using one of the several possible isotopic contrasts. Our results provide almost indistinguishable results using the different GROMOS parameterizations, regardless of the mass of the H atoms. The highly specific density maps as well as the water dipole moment vector field were absolutely reproducible in all the details, both in the bulk solution and at the interface. It is worth to mention that the application of the mass increase just for the polar H atoms in AA force fields would not represent any advantage since the presence of nonpolar light H atoms would not make possible to increase the time step.

The simulations using the AMBER/GAFF force field provided completely different results, illustrating the high sensitivity of this system. In all the simulations performed in the presence of water/air interface using the different parameterizations of the GROMOS force field, the complex quickly adsorbed with the symmetry axis parallel to the surface. The perpendicular orientation was also observed in some marginal cases of this force field. Again, these results do not seem to depend on the method employed to deal with the mass of the H atoms nor on the time step. However, for the simulations performed using the AMBER force field, the affinity of the complex by the interface is negligible. In these simulations, the complex does not adsorb to the interface at all or, when it is adsorbed, the orientation is perpendicular to the surface (see Results section). The source of this discrepancy seems to be in the low number of intramolecular CD1-CD2 H-bonds in the complex for this force field, almost half the amount observed for all the parameterizations using GROMOS. Since the strength of the H-bonds critically depends on the partial charges, the three AMBER/GAFF parameterizations tested were performed in completely different ways, namely (*i*) using the *antechamber* tool with RESP charges for the whole CD; (*ii*) using the antechamber tool with RESP charges to parameterize the methylated GPUs and then manually pasting them together to build the topology of the whole CD; and (*iii*) same as (*ii*) but using AM1-BCC charges. The first strategy introduces an artificial asymmetry in the charge distribution for chemically equivalent groups so the other two approaches, based on the building block strategy, could be considered as more reliable. The results coming from the three different AMBER/GAFF parameterizations are significantly different to each other but they match in the number of intramolecular CD1-CD2 H-bonds in the complex, approximately half of that observed for all the simulations using GROMOS, as well as in the larger number of H-bonds between the hydroxyls involving O2 and O3 with the solvent molecules. Thus, the differences between the two force fields rely on the intrinsic force field parameters (bond and angle constants) more than in the partial charges. The impact of this specific difference between both force fields is extremely

serious for this system due to its high sensitivity to the presence of the water/air interface. As a result, the α-CD_2SDS_1 complexes exhibit no significant affinity to the interface with AMBER/GAFF, in contrast to experimental results and with the simulations using the different parameterizations of the GROMOS force field. These results indicate that the AMBER/GAFF force field does not describe the behavior of this system in a reliable way, regardless of the method employed to get the partial charges. Additionally, the simulations using GROMOS suggest a possible driving force for the adsorption of the CD-based complexes. The high specificity of the water distribution around the complex, like a well-fitted dress over the structure, with a relatively low number of H-bonds between the CDs and the water, play the role of a hydrophobic solvent shell that is partially released upon adsorption to the interface. This is expected to provide a favorable entropic contribution associated to this process. For the simulations using AMBER/GAFF, there is also a high-density water shell around the complex, but it is much less specific than in the case of GROMOS and the number of H-bonds with the CDs is significantly higher in the case of AMBER/GAFF. Thus, the force field parameters, providing a lower number of intermolecular CD1-CD2 H-bonds, lead to an important qualitative difference since they determine whether or not the structure adsorb to the interface. As stated above, there are conclusive experimental evidences on the adsorption of α-CD_2SDS_1 complexes at the water/air interface, but there is also an open discussion on its orientation with respect to the surface plane [23]. A combination of atomic force microscopy, neutron reflectometry, and ellipsometry experiments suggests that the symmetry axis of the complex is parallel to such surface [6,23] but there are not conclusive evidences for this. Our simulations using different parameterizations of GROMOS also indicate that the most probable orientation is the parallel one, but the perpendicular orientation also appeared marginally in some simulations. This suggests that both orientations might live together at the interface with different probability.

Some of our results could be extrapolated to other similar systems such as β-CD_2SDS_1 complexes, which exhibit an extremely interesting aggregation behavior in the bulk aqueous solution [4]. The driving force for the self-aggregation of such complexes and for the stabilization of the resulting mesoscopic structures has been discussed [27,28] but the arguments are not conclusive. Simulations of this complex in aqueous solution, using the H2Q_7 method, are expected to reproduce the aggregation pattern with atomic resolution, at least at a modest size scale of 10–15 nm. Additionally, the aggregation of α-CD_2SDS_1 complexes in the bulk solution has not been experimentally studied and it is expected to also produce interesting patterns with potential practical applications.

5. Conclusions

In the present work, we provide a detailed analysis of the behavior of the water around α-CD_2SDS_1 complexes in the bulk aqueous solution and at the water/air interface. For the simulations using different parameterizations of the GROMOS force field, highly specific density patterns and dipole moment vector fields are observed. The internal movement of the different groups within the complex are described and connected with the profile of specific regions with high water density. Especially interesting is the trajectory of the O6 atoms, showing an anisotropic petal-shaped profile probably due to the chirality of the GPU rings of the CD molecules. Such a movement seems to provoke a unidirectional rotation around the symmetry axis of the complex when it is adsorbed at the water/air interface. The adsorption of the complex is observed to be very quick (just a few ns) and the complex remains stable with its symmetry axis parallel to the water surface for the rest of the trajectory. However, a significant oscillation of the structure (~3 Å amplitude) with respect to the water surface is observed. The adsorption of the complex allows releasing of a significant number of highly packaged water molecules as well as a partial disorder of the solvent. This is translated in a decrease of the local sources and sinks of the dipolar moment vector field. Such release of packed water molecules and the associated decrease of solvent order could represent an entropic driving force for the adsorption of the complexes and also for self-assembly processes, since the aggregation of several 2:1 structures is also expected to allow releasing of neighboring water molecules.

In addition to illustrate the fanciful behavior of water molecules around the α-CD_2SDS_1 complex in water solution and at the water/air interface, the same highly specific analysis for different variations of the GROMOS force field that allow to significantly increase the sampling are tested, thus optimizing the use of computational resources. The HMR method was already proposed 20 years ago and it has been employed in a number of papers with reasonably good results. Here, we propose and test the use of what we call the H2Q method (hydrogen to quadium replacement) based on the experimental observation that deuterated CDs just in the polar Hs lead to the same stoichiometry and thermodynamic parameters than hydrogenated CDs [23] and on the assumption that the replacement of deuterium by quadium also provides similar results. This allows significantly increasing the integration time step, thus speeding up MD simulations. The results obtained using both methods are found to be identical to those using the original force field, except in the lifetime of the H-bonds involving the modified H atoms.

In contrast to wet-lab experiments and to the results obtained using different variations of the GROMOS force field, the α-CD_2SDS_1 complex does not adsorb to the water/air interface when using different parameterizations of the α-CD for the AMBER/GAFF. This suggests that the latter force field is not well suited for simulations of the studied CD systems.

Overall, this paper is expected to contribute to the understanding of the behavior of supramolecular complexes based on CDs, revealing the importance of the solvent molecules as well as of the chirality of the glucopyranoside rings. Additionally, the HMR and the H2Q methods to optimize the sampling of the simulations provided exceptionally good results, while the AMBER/GAFF force field failed even at qualitative level. Our results provide an explanation for the formation and stability of several structures that have significant practical applications, including the design of smart films with specific mechanical properties for functional coatings, the synthesis of dielectric actuators based on cyclodextrin complexes (http://www.asmi.jp/en/tec), artificial cell membranes, the so-called cyclodextrinosomes [29,30], and other recently discovered compartmentalized structures that will eventually lead to new applications [4]. All these new materials and structures were experimentally observed and characterized, but their behavior at atomic scale is still unknown. We aim to contribute to fill this gap between fundamental knowledge and practical applications. Additionally, the studied α-CD_2SDS_1 complex proved to be highly sensitive to the force field, so we propose to use it in order to test new parameters for computational simulations.

Supplementary Materials: The Supplementary Figures S1–S39 are available online at http://www.mdpi.com/2218-273X/10/3/431/s1.

Author Contributions: Conceptualization, P.F.G., M.C., R.G-.F., and Á. P.; software, P.F.G. and Á.P.; validation, P.F.G. and M.C.; formal analysis, P.F.G. and M.C.; investigation, P.F.G., M.C., R.G.-F., and Á.P.; resources, R.G.F. and Á.P.; data curation, M.C., R.G.-F., and Á.P.; writing—original draft preparation, R.G.-F. and Á.P.; writing—review and editing, P.F.G. and M.C.; visualization, P.F.G. and M.C.; supervision, R.G.-F. and Á.P.; project administration, R.G.-F. and Á.P.; funding acquisition, R.G.-F. and Á.P. All authors have read and agreed to the published version of the manuscript.

Funding: This work was supported by the Spanish Agencia Estatal de Investigación (AEI) and the ERDF (RTI2018-098795-A-I00), and by the Xunta de Galicia and the ERDF (ED431C 2017/25 and Centro singular de investigación de Galicia accreditation 2016-2019, ED431G/09). P.F.G. is funded by a predoctoral research grant (BES-2016-076761) from the Spanish Ministry of Economy and Competitiveness and the European Social Fund. M.C. is funded by a predoctoral fellowship from Xunta de Galicia. R.G.-F. is a "Ramón y Cajal" fellowship (RYC-2016-20335) from the Ministerio de Ciencia, Innovación y Universidades.

Conflicts of Interest: The authors declare no conflict of interest.

USC UNIVERSIDADE DE SANTIAGO DE COMPOSTELA

References

1. Hernandez-Pascacio, J.; Piñeiro, A.; Ruso, J.M.; Hassan, N.; Campbell, R.A.; Campos-Terán, J.; Costas, M. Complex behavior of aqueous α-cyclodextrin solutions. Interfacial morphologies resulting from bulk aggregation. *Langmuir* **2016**, *32*, 6682–6690. [CrossRef] [PubMed]
2. Ferreira, M.; Bricout, H.; Azaroual, N.; Landy, D.; Tilloy, S.; Hapiot, F.; Monflier, E. Cyclodextrin/amphiphilic phosphane mixed systems and their applications in aqueous organometallic catalysis. *Adv. Synth. Catal.* **2012**, *354*, 1337–1346. [CrossRef]
3. González-Gaitano, G.; Rodriguez, P.; Isasi, J.R.; Fuentes, M.; Tardajos, G.; Sánchez, M. The aggregation of cyclodextrins as studied by photon correlation spectroscopy. *J. Incl. Phenom. Macrocycl. Chem.* **2002**, *44*, 101–105. [CrossRef]
4. Yang, S.; Yan, Y.; Huang, J.; Petukhov, A.V.; Kroon-Batenburg, L.M.; Drechsler, M.; Zhou, C.; Tu, M.; Granick, S.; Jiang, L. Giant capsids from lattice self-assembly of cyclodextrin complexes. *Nat. Commun.* **2017**, *8*, 15856. [CrossRef]
5. Hernández-Pascacio, J.; Banquy, X.; Pérez-Casas, S.; Costas, M.; Amigo, A.; Piñeiro, Á. A small molecular size system giving unexpected surface effects: α-Cyclodextrin+ sodium dodecyl sulfate in water. *J. Colloid Interface Sci.* **2008**, *328*, 391–395. [CrossRef]
6. Hernandez-Pascacio, J.; Garza, C.; Banquy, X.; Díaz-Vergara, N.; Amigo, A.; Ramos, S.; Castillo, R.; Costas, M.; Piñeiro, Á. Cyclodextrin-based self-assembled nanotubes at the water/air interface. *J. Phys. Chem. B* **2007**, *111*, 12625–12630. [CrossRef]
7. Couto, A.R.S.; Aguiar, S.; Ryzhakov, A.; Larsen, K.L.; Loftsson, T. Interaction of native cyclodextrins and their hydroxypropylated derivatives with parabens in aqueous solutions. Part 1: Evaluation of inclusion complexes. *J. Incl. Phenom. Macrocycl. Chem.* **2019**, *93*, 309–321. [CrossRef]
8. Hollingsworth, S.A.; Dror, R.O. Molecular dynamics simulation for all. *Neuron* **2018**, *99*, 1129–1143. [CrossRef]
9. Marrink, S.J.; Corradi, V.; Souza, P.C.; Ingólfsson, H.I.; Tieleman, D.P.; Sansom, M.S. Computational modeling of realistic cell membranes. *Chem. Rev.* **2019**, *119*, 6184–6226. [CrossRef]
10. Chen, P.; Yao, S.; Chen, X.; Huang, Y.; Song, H. A new strategy for the construction of β-cyclodextrin-based magnetic nanocarriers: A molecular docking technique. *New J. Chem.* **2019**, *43*, 4282–4290. [CrossRef]
11. Khuntawee, W.; Wolschann, P.; Rungrotmongkol, T.; Wong-Ekkabut, J.; Hannongbua, S. Molecular dynamics simulations of the interaction of beta cyclodextrin with a lipid bilayer. *J. Chem. Inf. Model.* **2015**, *55*, 1894–1902. [CrossRef] [PubMed]
12. Nutho, B.; Nunthaboot, N.; Wolschann, P.; Kungwan, N.; Rungrotmongkol, T. Metadynamics supports molecular dynamics simulation-based binding affinities of eucalyptol and beta-cyclodextrin inclusion complexes. *RSC Adv.* **2017**, *7*, 50899–50911. [CrossRef]
13. Marrink, S.J.; Risselada, H.J.; Yefimov, S.; Tieleman, D.P.; De Vries, A.H. The MARTINI force field: Coarse grained model for biomolecular simulations. *J. Phys. Chem. B* **2007**, *111*, 7812–7824. [CrossRef] [PubMed]
14. Periole, X.; Cavalli, M.; Marrink, S.J.; Ceruso, M.A. Combining an elastic network with a coarse-grained molecular force field: Structure, dynamics, and intermolecular recognition. *J. Chem. Theory Comput.* **2009**, *5*, 2531–2543. [CrossRef]
15. Otero-Mato, J.M.; Montes-Campos, H.; Calvelo, M.; Garcia-Fandino, R.; Gallego, L.J.; Piñeiro, A.; Varela, L.M. GADDLE Maps: General Algorithm for Discrete Object Deformations Based on Local Exchange Maps. *J. Chem. Theory Comput.* **2018**, *14*, 466–478. [CrossRef]
16. Wassenaar, T.A.; Pluhackova, K.; Böckmann, R.A.; Marrink, S.J.; Tieleman, D.P. Going backward: A flexible geometric approach to reverse transformation from coarse grained to atomistic models. *J. Chem. Theory Comput.* **2014**, *10*, 676–690. [CrossRef]
17. López, C.A.; De Vries, A.H.; Marrink, S.J. Computational microscopy of cyclodextrin mediated cholesterol extraction from lipid model membranes. *Sci. Rep.* **2013**, *3*, 2071. [CrossRef]
18. Tuckerman, M.; Berne, B.J.; Martyna, G.J. Reversible multiple time scale molecular dynamics. *J. Chem. Phys.* **1992**, *97*, 1990–2001. [CrossRef]
19. Ma, Q.; Izaguirre, J.A.; Skeel, R.D. Verlet-I/r-RESPA/Impulse is limited by nonlinear instabilities. *SIAM J. Sci. Comput.* **2003**, *24*, 1951–1973. [CrossRef]
20. Sidler, D.; Lehner, M.; Frasch, S.; Cristófol-Clough, M.; Riniker, S. Density artefacts at interfaces caused by multiple time-step effects in molecular dynamics simulations. *F1000Research* **2018**, *7*. [CrossRef]

21. Reißer, S.; Poger, D.; Stroet, M.; Mark, A.E. Real cost of speed: The effect of a time-saving multiple-time-stepping algorithm on the accuracy of molecular dynamics simulations. *J. Chem. Theory Comput.* **2017**, *13*, 2367–2372. [CrossRef] [PubMed]
22. Feenstra, K.A.; Hess, B.; Berendsen, H.J. Improving efficiency of large time-scale molecular dynamics simulations of hydrogen-rich systems. *J. Comput. Chem.* **1999**, *20*, 786–798. [CrossRef]
23. Luviano, A.S.; Hernández-Pascacio, J.; Ondo, D.; Campbell, R.A.; Piñeiro, Á.; Campos-Teránb, J.; Costas, M. Highly Viscoelastic Films at the Water/Air Interface: α-Cyclodextrin with anionic surfactants. *J. Colloid Interface Sci.*, in press. [CrossRef] [PubMed]
24. Hopkins, C.W.; Le Grand, S.; Walker, R.C.; Roitberg, A.E. Long-time-step molecular dynamics through hydrogen mass repartitioning. *J. Chem. Theory Comput.* **2015**, *11*, 1864–1874. [CrossRef] [PubMed]
25. Balusek, C.; Hwang, H.; Lau, C.H.; Lundquist, K.; Hazel, A.; Pavlova, A.; Lynch, D.L.; Reggio, P.H.; Wang, Y.; Gumbart, J.C. Accelerating membrane simulations with Hydrogen Mass Repartitioning. *J. Chem. Theory Comput.* **2019**, *15*, 4673–4686. [CrossRef] [PubMed]
26. Henriksen, N.M.; Gilson, M.K. Evaluating force field performance in thermodynamic calculations of cyclodextrin host–guest binding: Water models, partial charges, and host force field parameters. *J. Chem. Theory Comput.* **2017**, *13*, 4253–4269. [CrossRef]
27. Jiang, L.; Peng, Y.; Yan, Y.; Deng, M.; Wang, Y.; Huang, J. "Annular Ring" microtubes formed by SDS@ 2β-CD complexes in aqueous solution. *Soft Matter* **2010**, *6*, 1731–1736. [CrossRef]
28. Jiang, L.; Peng, Y.; Yan, Y.; Huang, J. Aqueous self-assembly of SDS@ 2 β-CD complexes: Lamellae and vesicles. *Soft Matter* **2011**, *7*, 1726–1731. [CrossRef]
29. Mathapa, B.G.; Paunov, V.N. Cyclodextrin stabilised emulsions and cyclodextrinosomes. *Phys. Chem. Chem. Phys.* **2013**, *15*, 17903–17914. [CrossRef]
30. Mathapa, B.G.; Paunov, V.N. Fabrication of viable cyborg cells with cyclodextrin functionality. *Biomater. Sci.* **2014**, *2*, 212–219. [CrossRef]
31. Tanford, C. The hydrophobic effect and the organization of living matter. *Science* **1978**, *200*, 1012–1018. [CrossRef] [PubMed]
32. Garcia-Fandiño, R.; Piñeiro, A.; Trick, J.L.; Sansom, M.S. Lipid bilayer membrane perturbation by embedded nanopores: A simulation study. *ACS Nano* **2016**, *10*, 3693–3701. [CrossRef] [PubMed]
33. Laage, D.; Elsaesser, T.; Hynes, J.T. Water dynamics in the hydration shells of biomolecules. *Chem. Rev.* **2017**, *117*, 10694–10725. [CrossRef] [PubMed]
34. Bizzarri, A.R.; Cannistraro, S. Molecular dynamics of water at the Protein—Solvent interface. *J. Phys. Chem. B* **2002**, *106*, 6617–6633. [CrossRef]
35. Jana, M.; Bandyopadhyay, S. Hydration Properties of α-, β-, and γ-Cyclodextrins from Molecular Dynamics Simulations. *J. Phys. Chem. B* **2011**, *115*, 6347–6357. [CrossRef]
36. Bottari, C.; Comez, L.; Paolantoni, M.; Corezzi, S.; D'Amico, F.; Gessini, A.; Masciovecchio, C.; Rossi, B. Hydration properties and water structure in aqueous solutions of native and modified cyclodextrins by UV Raman and Brillouin scattering. *J. Raman Spectrosc.* **2018**, *49*, 1076–1085. [CrossRef]
37. Jana, M.; Bandyopadhyay, S. Vibrational spectrum of water confined in and around cyclodextrins. *Chem. Phys. Lett.* **2011**, *509*, 181–185. [CrossRef]
38. Schmid, N.; Eichenberger, A.P.; Choutko, A.; Riniker, S.; Winger, M.; Mark, A.E.; van Gunsteren, W.F. Definition and testing of the GROMOS force-field versions 54A7 and 54B7. *Eur. Biophys. J.* **2011**, *40*, 843. [CrossRef]
39. Ponder, J.W.; Case, D.A. Force fields for protein simulations. In *Advances in Protein Chemistry*; Daggett, V., Ed.; Academic Press: Cambridge, MA, USA, 2003; Volume 66, pp. 27–85. [CrossRef]
40. Maier, J.A.; Martinez, C.; Kasavajhala, K.; Wickstrom, L.; Hauser, K.E.; Simmerling, C. ff14SB: Improving the accuracy of protein side chain and backbone parameters from ff99SB. *J. Chem. Theory Comput.* **2015**, *11*, 3696–3713. [CrossRef]
41. Berendsen, H.J.; Postma, J.P.; van Gunsteren, W.F.; Hermans, J. Interaction models for water in relation to protein hydration. In *Intermolecular Forces*; Pullman, B., Ed.; Springer: Dordrecht, The Netherlands, 1981; Volume 14, pp. 331–342. [CrossRef]
42. Jorgensen, W.L.; Chandrasekhar, J.; Madura, J.D.; Impey, R.W.; Klein, M.L. Comparison of simple potential functions for simulating liquid water. *J. Chem. Phys.* **1983**, *79*, 926–935. [CrossRef]

43. Brocos, P.; Díaz-Vergara, N.; Banquy, X.; Pérez-Casas, S.; Costas, M.; Pineiro, A. Similarities and Differences between Cyclodextrin—Sodium Dodecyl Sulfate Host—Guest Complexes of Different Stoichiometries: Molecular Dynamics Simulations at Several Temperatures. *J. Phys. Chem. B* **2010**, *114*, 12455–12467. [CrossRef]
44. Berendsen, H.J.; van der Spoel, D.; van Drunen, R. GROMACS: A message-passing parallel molecular dynamics implementation. *Comput. Phys. Commun.* **1995**, *91*, 43–56. [CrossRef]
45. Abraham, M.J.; Murtola, T.; Schulz, R.; Páll, S.; Smith, J.C.; Hess, B.; Lindahl, E. GROMACS: High performance molecular simulations through multi-level parallelism from laptops to supercomputers. *SoftwareX* **2015**, *1*, 19–25. [CrossRef]
46. Bussi, G.; Donadio, D.; Parrinello, M. Canonical sampling through velocity rescaling. *J. Chem. Phys.* **2007**, *126*, 014101. [CrossRef] [PubMed]
47. Parrinello, M.; Rahman, A. Polymorphic transitions in single crystals: A new molecular dynamics method. *J. Appl. Phys.* **1981**, *52*, 7182–7190. [CrossRef]
48. Darden, T.; York, D.; Pedersen, L. Particle mesh Ewald: An N log (N) method for Ewald sums in large systems. *J. Chem. Phys.* **1993**, *98*, 10089–10092. [CrossRef]
49. Essmann, U.; Perera, L.; Berkowitz, M.L.; Darden, T.; Lee, H.; Pedersen, L.G. A smooth particle mesh Ewald method. *J. Chem. Phys.* **1995**, *103*, 8577–8593. [CrossRef]
50. Hockney, R.W.; Eastwood, J.W. *Computer Simulation Using Particles*, 1st ed.; CRC Press: Boca Raton, FL, USA, 1988. [CrossRef]
51. Miyamoto, S.; Kollman, P.A. Settle: An analytical version of the SHAKE and RATTLE algorithm for rigid water models. *J. Comput. Chem.* **1992**, *13*, 952–962. [CrossRef]
52. Hess, B.; Bekker, H.; Berendsen, H.J.; Fraaije, J.G. LINCS: A linear constraint solver for molecular simulations. *J. Comput. Chem.* **1997**, *18*, 1463–1472. [CrossRef]
53. Mixcoha, E.; Campos-Terán, J.; Piñeiro, A. Surface adsorption and bulk aggregation of cyclodextrins by computational molecular dynamics simulations as a function of temperature: α-CD vs. β-CD. *J. Phys. Chem. B* **2014**, *118*, 6999–7011. [CrossRef]
54. Wang, J.; Wang, W.; Kollman, P.A.; Case, D.A. Automatic atom type and bond type perception in molecular mechanical calculations. *J. Mol. Graph. Model.* **2006**, *25*, 247260. [CrossRef] [PubMed]
55. Wang, J.; Wolf, R.M.; Caldwell, J.W.; Kollman, P.A.; Case, D.A. Development and testing of a general AMBER force field. *J. Comput. Chem.* **2004**, *25*, 1157–1174. [CrossRef]
56. Jorgensen, W.L.; Madura, J.D. Temperature and size dependence for monte carlo simulations of TIP4P water. *Mol. Phys.* **1985**, *56*, 1381–1392. [CrossRef]
57. Gowers, R.J.; Linke, M.; Barnoud, J.; Reddy, T.J.E.; Melo, M.N.; Seyler, S.L.; Domanski, J.; Dotson, D.L.; Buchoux, S.; Kenney, I.M.; et al. MDAnalysis: A Python package for the rapid analysis of molecular dynamics simulations. In *Proceedings of the 15th Python in Science Conference, Austin, TX, USA, 11 July 2016*; Benthall, S., Rostrup, S., Eds.; SciPy: Austin, TX, USA, 2016. [CrossRef]
58. Michaud-Agrawal, N.; Denning, E.J.; Woolf, T.B.; Beckstein, O. MDAnalysis: A toolkit for the analysis of molecular dynamics simulations. *J. Comput. Chem.* **2011**, *32*, 2319–2327. [CrossRef] [PubMed]
59. Saenger, W.; Jacob, J.; Gessler, K.; Steiner, T.; Hoffmann, D.; Sanbe, H.; Koizumi, K.; Smith, S.M.; Takaha, T. Structures of the common cyclodextrins and their larger analogues—Beyond the doughnut. *Chem. Rev.* **1998**, *98*, 1787–1802. [CrossRef] [PubMed]



© 2020 by the authors. Licensee MDPI, Basel, Switzerland. This article is an open access article distributed under the terms and conditions of the Creative Commons Attribution (CC BY) license (http://creativecommons.org/licenses/by/4.0/).

Part IV

Conclusions and bibliography

This is the final part of the manuscript. The general conclusions, joining all the work, are here exposed, together with the future perspectives. The references are also included in this final part.

USC
UNIVERSIDADE
DE SANTIAGO
DE COMPOSTELA

USC
UNIVERSIDADE
DE SANTIAGO
DE COMPOSTELA

Chapter 11

Conclusions and future work

Well, that's the end of the film. Now, here's the meaning of life
...
Well, it's nothing very special. Try to be nice to people, avoid eating fat, read a good book every now and then, get some walking in, and try and live together in peace and harmony with people of all creeds and nations [...]

In "Monty Python's The Meaning of life (1983)"

All the work presented in this thesis is threaded by two intimately related terms: molecular aggregation and adsorption. These terms describe the spontaneous self-assembly that most molecules experience at some degree when they are introduced in aqueous solution as well as their spontaneous partition -and subsequent rearrangement- between polar-nonpolar interfaces of immiscible fluids or liquid-gas interfaces, and the corresponding bulk phases. When the solvent is water, both phenomena are mainly driven by the so-called hydrophobic effect: the release of highly ordered water molecules around hydrophobic groups when they find a strategy to hide from the solvent. To understand the connection between these processes and to predict or better understand the behaviour of new molecules in solution, or even to design systems for new applications, new experimental and computational methods as well as theoretical models have been proposed and tested in this thesis. Like the objectives, the conclusions will be classified into two main groups: Fluid Interface Calorimetry methodology and software development, modelling and analysis tools.

11.1. Fluid Interface Calorimetry

USC UNIVERSIDADE DE SANTIAGO DE COMPOSTELA

Throughout this thesis project, a new methodology has been developed almost from scratch: Fluid Interface Calorimetry. This technique is based on the injection of air bubbles into water, which produces a rich-in-information heat signal. This

signal has been shown to be sensitive to different liquids and to temperature changes, providing also kinetic information when the injection rate is controlled. Several heat events could be identified in the signal: the bubble appearance, its growing and release, the evaporation/condensation in the bubble, and the change in the heat capacity due to the air injection. Moreover, the proper identification of these events led us to have more control on the formation of bubbles and to perform more complex experiments. Solutions of ethanol and surfactants in water have been tested, which helped us to extend the method to obtain, from the heat signal measurements of bubble formation, the surface tension of these solutions. Finally, the methodology was tested for proteins' heat of adsorption. Only preliminary results were obtained, but it has been seen that the technique could be also sensitive to this thermal phenomenon.

Despite the most common fluid interface is that between air and liquid, it is not easy to keep it under controlled conditions, since it is easily perturbed under small pressure changes. By means of the VP-ITC, the most used calorimeter in this thesis, the bubbles cannot be completely controlled because the intrument's injector system is not adapted to this kind of experiment. For instance, our experiments require stopping the injection of air at a certain bubble's size or even decreasing it after a certain amount of time, which is not allowed by the standard injection system of the VP-ITC. This is the reason why different external injector systems have been tested. Using an external microfluidics micropump, the results are promising: highly reproducible signal and with a high control on the air injection were obtained.

Fluid Interface Calorimetry was also tested using liquid-liquid interfaces. This kind of interface showed to be easier to control and less sensitive to its surroundings but time limitations made impossible to go further in this direction. Nonetheless, it has been shown that Fluid Interface Calorimetry is also highly sensitive to the adsorption of proteins at the interface between two immiscible liquids.

The main conclusion obtained from this thesis is that it is possible to directly measure the heat associated to the creation/disruption of interfacial area by injecting air into a liquid solution. All this work has been developed using commercial ITC instruments without modifications other than some tests performed with alternative injection systems. Fluid Interface Calorimetry has just born with this work, but it has a lot of room for optimization. Slight modifications in the instruments would allow applying this method to complex systems thus favouring the development of new applications.

11.2. Software development, modelling and analysis tools

Together with the Fluid Interface Calorimetry development, other contributions, mainly focused on the development of new analytical methods for aggregation and adsorption processes, are included in this dissertation. In this sense, the AFFINImeter software is the best example: it was initially conceived in academia and then it was improved and made commercially available, providing new ITC analysis of complex models in an user-friendly way in order to make it accessible to non highly specialized researchers. My contribution to that project is small, but it allowed me to understand how to extend and develop software for external users. I have also participated in the development of the STAND software, for the analysis

USC UNIVERSIDADE DE SANTIAGO DE COMPOSTELA

of surface tension data to extract a full thermodynamics characterization of micelles in solution. Finally, another significant contribution to the analysis of data from a collaboration of a local group is included in Paper VI, where I implemented the numerical resolution of an aggregation model.

Out of the software developed for other users and regarding ITC data analysis, a simple model to determine surfactant aggregation numbers, as well as a thermodynamic characterzation of micelle formation processes, has been developed. Its name, STAND-ITC refers to the extension of the previously developed STAND model. These two models could be applied together in Fluid Interface Calorimetry to simultaneously analyze experimental information from the bulk and from the liquid/air interface.

Finally, as it was explained in the text, I was introduced to the MD simulations world during this period. Some of the obtained results are not published yet and so they have not been included in this dissertation. However, from my first publication in the field, Paper VII, two conclusions can be obtained: the first one is more technical, and regards the time step change to accelerate the simulations. It has been shown that increasing or exchanging the Hydrogen mass can help to optimize bulk and interfacial simulations. As a second conclusion, in the same paper it is shown how the water molecules are organized around the CD-SDS complexes, creating *fanciful* structures around them, both in bulk and at the interface. This speed-up methodology is now expected to be used to better understand the behavior of different kind of molecules that will be later characterized by experimental methods, including Fluid Interface Calorimetry.

Final remarks

Overall, this thesis aims to introduce significant innovations that can contribute to better understand molecular self-assembly and adsorption processes, as well as the connection between them. New experimental, theoretical and computational methods were developed and tested using real systems. This combination of elements, allowed us to visualize molecular aggregates from different perspectives, thus providing a quite complete understanding of the target systems. These methods are expected to help in the comprehension of biophysical phenomena as well as to optimize or design new biotechnological applications. There is a lot of room for improvement in the proposals contained in this work, thus I hope some of these contributions will be the basis for further works and could eventually become standard tools for researchers working around self-assembled systems at molecular level.

USC
UNIVERSIDADE DE SANTIAGO DE COMPOSTELA

USC
UNIVERSIDADE
DE SANTIAGO
DE COMPOSTELA

Chapter 12

Bibliography

Y así, del mucho leer y del poco dormir,
se le secó el celebro de manera que vino
a perder el juicio.
In "Don Quijote de la Mancha", by
Miguel de Cervantes Saavedra

Ababou A, Ladbury JE (2006). "Survey of the year 2004: Literature on applications of isothermal titration calorimetry." *J. Mol. Recognit.*, **19**(1), 79–89. ISSN 09523499. doi: 10.1002/jmr.750. URL https://www.doi.org/10.1002/jmr.750.

Ababou A, Ladbury JE (2007). "Survey of the year 2005: literature on applications of isothermal titration calorimetry." *J. Mol. Recognit.*, **20**(1), 4–14. ISSN 1099-1352. doi: 10.1002/JMR.803. URL https://www.doi.org/10.1002/JMR.803.

Abbott S (2015). *Surfactant Science: Principles and Practice*. Creative Commons license. ISBN 9781605954844.

Abreu CRA, Tuckerman ME (2020). "Molecular Dynamics with Very Large Time Steps for the Calculation of Solvation Free Energies." *J. Chem. Theory Comput.*, **16**(12), 7314–7327. doi: 10.1021/ACS.JCTC.0C00698. URL https://doi.org/10.1021/acs.jctc.0c00698.

Adamson AW, Gast AP (1997). *Physical chemistry of surfaces*. John Wiley & Sons, New York, 6 edition. ISBN 978-0-471-14873-9.

Al-Roomi Y, George R, Elgibaly A, Elkamel A (2004). "Use of a novel surfactant for improving the transportability/transportation of heavy/viscous crude oils." *J. Pet. Sci. Eng.*, **42**(2-4), 235–243. ISSN 09204105. doi: 10.1016/j.petrol.2003.12.014. URL https://www.doi.org/10.1016/j.petrol.2003.12.014.

Alahverdjieva V, Fainerman V, Aksenenko E, Leser M, Miller R (2008a). "Adsorption of hen egg-white lysozyme at the air-water interface in presence of sodium dodecyl sulphate." *Colloids Surfaces A Physicochem. Eng. Asp.*, **317**(1-3), 610–617. ISSN 09277757. doi: 10.1016/j.colsurfa.2007.11.062. URL https://www.doi.org/10.1016/j.colsurfa.2007.11.062.

Alahverdjieva V, Grigoriev D, Ferri J, Fainerman V, Aksenenko E, Leser M, Michel M, Miller R (2008b). "Adsorption behaviour of hen egg-white lysozyme at the air/water interface." *Colloids Surfaces A Physicochem. Eng. Asp.*, **323**(1-3), 167–174. ISSN 09277757. doi: 10.1016/j.colsurfa.2007.12.031. URL https://www.doi.org/10.1016/j.colsurfa.2007.12.031.

Allen MP, Tildesley DJ (2017). *Computer Simulation of Liquids*. Oxford University Press, New York, 2 edition. ISBN 9780198803195. doi: 10.1093/oso/9780198803195.001.0001. URL https://www.doi.org/10.1093/oso/9780198803195.001.0001.

Anaconda Inc (2019). "Anaconda Guide." *Anaconda*. URL https://www.anaconda.com/distribution/.

Anderson AM, Kirtadze T, Malanga M, Dinh D, Barnes C, Campo A, Clemens DM, Garcia-Fandiño R, Piñeiro Á, O'Connor MS (2021). "Cyclodextrin dimers: a versatile approach to optimizing encapsulation and their application to therapeutic extraction of toxic oxysterols." *Int. J. Pharm.*, p. 120522. ISSN 03785173. doi: 10.1016/j.ijpharm.2021.120522. URL https://www.doi.org/10.1016/j.ijpharm.2021.120522.

Araujo Marques I, Patiño-Agudelo ÁJ, Coelho YL, dos Santos Moreau P, Neves Santa Rosa L, dos Santos Pires AC, Mendes da Silva LH (2021). "Formation and self-association of host-guest complexes between βCD and nonionic surfactants Brij." *J. Mol. Liq.*, **338**, 116647. ISSN 01677322. doi: 10.1016/j.molliq.2021.116647. URL https://www.doi.org/10.1016/j.molliq.2021.116647.

Archer WR, Schulz MD (2020). "Isothermal titration calorimetry: practical approaches and current applications in soft matter." *Soft Matter*, **16**(38), 8760–8774. ISSN 1744-683X. doi: 10.1039/D0SM01345E. URL https://www.doi.org/10.1039/D0SM01345E.

Ariga K, Nishikawa M, Mori T, Takeya J, Shrestha LK, Hill JP (2019). "Self-assembly as a key player for materials nanoarchitectonics." *Sci. Technol. Adv. Mater.*, **20**(1), 51–95. ISSN 1468-6996. doi: 10.1080/14686996.2018.1553108. URL https://www.doi.org/10.1080/14686996.2018.1553108.

Arima H, Higashi T, Motoyama K (2012). "Improvement of the bitter taste of drugs by complexation with cyclodextrins: applications, evaluations and mechanisms." *Ther. Deliv.*, **3**(5), 633–644. ISSN 2041-5990. doi: 10.4155/tde.12.28. URL https://www.doi.org/10.4155/tde.12.28.

Arooj M, Gandhi NS, Kreck CA, Arrigan DW, Mancera RL (2016). "Adsorption and Unfolding of Lysozyme at a Polarized Aqueous-Organic Liquid Interface." *J. Phys. Chem. B*, **120**(12), 3100–3112. ISSN 15205207. doi: 10.1021/acs.jpcb.6b00536. URL https://www.doi.org/10.1021/acs.jpcb.6b00536.

Astray G, Gonzalez-Barreiro C, Mejuto J, Rial-Otero R, Simal-Gándara J (2009). "A review on the use of cyclodextrins in foods." *Food Hydrocoll.*, **23**(7), 1631–1640. ISSN 0268005X. doi: 10.1016/j.foodhyd.2009.01.001. URL https://www.doi.org/10.1016/j.foodhyd.2009.01.001.

USC UNIVERSIDADE DE SANTIAGO DE COMPOSTELA

Bai Y, Luo Q, Liu J (2016). "Protein self-assembly: Via supramolecular strategies." *Chem. Soc. Rev.*, **45**(10), 2756–2767. ISSN 14604744. doi: 10.1039/c6cs00004e. URL https://www.doi.org/10.1039/c6cs00004e.

Barry E, Dogic Z (2010). "Entropy driven self-assembly of nonamphiphilic colloidal membranes." *Proc. Natl. Acad. Sci.*, **107**(23), 10348–10353. ISSN 0027-8424. doi: 10.1073/PNAS.1000406107. URL https://www.doi.org/10.1073/PNAS.1000406107.

Barthelat F, Yin Z, Buehler MJ (2016). "Structure and mechanics of interfaces in biological materials." *Nat. Rev. Mater.*, **1**(4), 16007. ISSN 2058-8437. doi: 10.1038/natrevmats.2016.7. URL https://www.doi.org/10.1038/natrevmats.2016.7.

Bartlett DW, Su H, Hildebrandt IJ, Weber WA, Davis ME (2007). "Impact of tumor-specific targeting on the biodistribution and efficacy of siRNA nanoparticles measured by multimodality in vivo imaging." *Proc. Natl. Acad. Sci.*, **104**(39), 15549–15554. ISSN 0027-8424. doi: 10.1073/pnas.0707461104. URL https://www.doi.org/10.1073/pnas.0707461104.

Basílio N, Garcia-Rio L (2012). "Calixarene-based surfactants: Conformational-dependent solvation shells for the alkyl chains." *ChemPhysChem*, **13**(9), 2368–2376. ISSN 14397641. doi: 10.1002/cphc.201200175. URL https://www.doi.org/10.1002/cphc.201200175.

Bastos M (ed.) (2016). *Biocalorimetry: Foundations and Contemporary Approaches*. CRC Press, Boca Raton. ISBN 9780429171918. doi: 10.1201/b20161. URL https://www.doi.org/10.1201/b20161.

Bastos-Neto M, Azevedo DCS, Lucena SMP (2020). "Adsorption." In "Kirk-Othmer Encycl. Chem. Technol.", pp. 1–59. Wiley. ISBN 0471238961. doi: 10.1002/0471238961.0104191518212008.a01.pub3. URL https://www.doi.org/10.1002/0471238961.0104191518212008.a01.pub3.

Batchelor GK (2000). *An introduction to fluid dynamics*. Cambridge university press. ISBN 0521663962.

Beckwith DM, Fitzgerald FG, Rodriguez Benavente MC, Mercer ER, Ludwig AK, Michalak M, Kaltner H, Kopitz J, Gabius HJ, Cudic M (2021). "Calorimetric Analysis of the Interplay between Synthetic Tn Antigen-Presenting MUC1 Glycopeptides and Human Macrophage Galactose-Type Lectin." *Biochemistry*, **60**(7), 547–558. ISSN 15204995. doi: 10.1021/acs.biochem.0c00942. URL https://www.doi.org/10.1021/acs.biochem.0c00942.

Bender ML, Komiyama M (1978). *Cyclodextrin Chemistry*, volume 6 of *Reactivity and Structure Concepts in Organic Chemistry*. Springer Berlin Heidelberg, Berlin, Heidelberg. ISBN 978-3-642-66844-9. doi: 10.1007/978-3-642-66842-5. URL https://www.doi.org/10.1007/978-3-642-66842-5.

Benkő M, Király LA, Puskás S, Király Z (2014). "Complexation of β-Cyclodextrin with a Gemini Surfactant Studied by Isothermal Titration Microcalorimetry and Surface Tensiometry." *Langmuir*, **30**(23), 6756–6762. ISSN 0743-7463. doi: 10.1021/la501386j. URL https://www.doi.org/10.1021/la501386j.

Bergfreund J, Bertsch P, Fischer P (2021). "Adsorption of proteins to fluid interfaces: Role of the hydrophobic subphase." *J. Colloid Interface Sci.*, **584**, 411–417. ISSN 00219797. doi: 10.1016/j.jcis.2020.09.118. URL https://www.doi.org/10.1016/j.jcis.2020.09.118.

Berry MV (1971). "The molecular mechanism of surface tension." *Phys. Educ.*, **6**(2), 001. ISSN 00319120. doi: 10.1088/0031-9120/6/2/001. URL https://www.doi.org/10.1088/0031-9120/6/2/001.

Berthold A, Schubert H, Brandes N, Kroh L, Miller R (2007). "Behaviour of BSA and of BSA-derivatives at the air/water interface." *Colloids Surfaces A Physicochem. Eng. Asp.*, **301**(1-3), 16–22. ISSN 09277757. doi: 10.1016/j.colsurfa.2006.11.054. URL https://www.doi.org/10.1016/j.colsurfa.2006.11.054.

Bezerra FM, Lis MJ, Firmino HB, Dias da Silva JG, Curto Valle RdCS, Borges Valle JA, Scacchetti FAP, Tessaro AL (2020). "The Role of β-Cyclodextrin in the Textile Industry-Review." *Molecules*, **25**(16), 3624. ISSN 1420-3049. doi: 10.3390/molecules25163624. URL https://www.doi.org/10.3390/molecules25163624.

Bikádi Z, Kurdi R, Balogh S, Szemán J, Hazai E (2006). "Aggregation of cyclodextrins as an important factor to determine their complexation behavior." *Chem. Biodivers.*, **3**(11), 1266–1278. ISSN 16121872. doi: 10.1002/cbdv.200690129. URL https://doi.org/10.1002/cbdv.200690129.

Bilensoy E (ed.) (2011). *Cyclodextrins in Pharmaceutics, Cosmetics, and Biomedicine*. John Wiley & Sons, Inc., Hoboken, NJ, USA. ISBN 9780470926819. doi: 10.1002/9780470926819. URL https://www.doi.org/10.1002/9780470926819.

Bjelić S, Jelesarov I (2008). "A survey of the year 2007 literature on applications of isothermal titration calorimetry." *J. Mol. Recognit.*, **21**(5), 289–312. ISSN 1099-1352. doi: 10.1002/JMR.909. URL https://www.doi.org/10.1002/JMR.909.

Blanco E, Hsiao A, Mann AP, Landry MG, Meric-Bernstam F, Ferrari M (2011). "Nanomedicine in cancer therapy: Innovative trends and prospects." *Cancer Sci.*, **102**(7), 1247–1252. ISSN 13479032. doi: 10.1111/j.1349-7006.2011.01941.x. URL https://www.doi.org/10.1111/j.1349-7006.2011.01941.x.

Blanco-González A, Calvelo M, Garrido PF, Amorín M, Granja JR, Piñeiro Á, Garcia-Fandino R (2021). "Transmembrane Self-Assembled Cyclic Peptide Nanotubes Based on α-Residues and Cyclic δ-Amino Acids: A Computational Study." *Front. Chem.*, **9**, 530. ISSN 2296-2646. doi: 10.3389/fchem.2021.704160. URL https://www.doi.org/10.3389/fchem.2021.704160.

Blandamer MJ, Cullis PM, Engberts JBFN (1998). "Titration microcalorimetry." *J. Chem. Soc. Faraday Trans.*, **94**(16), 2261–2267. ISSN 09565000. doi: 10.1039/a802370k. URL https://www.doi.org/10.1039/a802370k.

Bonini M, Rossi S, Karlsson G, Almgren M, Lo Nostro P, Baglioni P (2006). "Self-Assembly of β-Cyclodextrin in Water. Part 1: Cryo-TEM and Dynamic and Static Light Scattering." *Langmuir*, **22**(4), 1478–1484. ISSN 0743-7463. doi: 10.1021/la052878f. URL https://www.doi.org/10.1021/la052878f.

USC UNIVERSIDADE DE SANTIAGO DE COMPOSTELA

Bouchemal K (2008). "New challenges for pharmaceutical formulations and drug delivery systems characterization using isothermal titration calorimetry." *Drug Discov. Today*, **13**(21-22), 960–972. ISSN 13596446. doi: 10.1016/j.drudis.2008.06.004. URL https://www.doi.org/10.1016/j.drudis.2008.06.004.

Bouchemal K, Mazzaferro S (2012). "How to conduct and interpret ITC experiments accurately for cyclodextrin-guest interactions." *Drug Discov. Today*, **17**(11-12), 623–629. ISSN 13596446. doi: 10.1016/j.drudis.2012.01.023. URL https://www.doi.org/10.1016/j.drudis.2012.01.023.

Bracco G, Holst B (eds.) (2013). *Surface science techniques*. Springer Series in Surface Sciences. Springer, Berlin, Heidelberg, Berlin, Heidelberg. ISBN 978-3-642-34243-1. doi: 10.1007/978-3-642-34243-1. URL https://www.doi.org/10.1007/978-3-642-34243-1.

Braga SS (2019). "Cyclodextrins: Emerging Medicines of the New Millennium." *Biomolecules*, **9**(12), 801. ISSN 2218-273X. doi: 10.3390/biom9120801. URL https://www.doi.org/10.3390/biom9120801.

Brand A, Allen L, Altman M, Hlava M, Scott J (2015). "Beyond authorship: attribution, contribution, collaboration, and credit." *Learned Publishing*, **28**(2), 151–155. doi: 10.1087/20150211. URL https://doi.org/10.1087/20150211.

Brewster ME, Loftsson T (2007). "Cyclodextrins as pharmaceutical solubilizers." *Adv. Drug Deliv. Rev.*, **59**(7), 645–666. ISSN 0169409X. doi: 10.1016/j.addr.2007.05.012. URL https://www.doi.org/10.1016/j.addr.2007.05.012.

Brocos P, Banquy X, Díaz-Vergara N, Pérez-Casas S, Piñeiro Á, Costas M (2011). "A critical approach to the thermodynamic characterization of inclusion complexes: Multiple-temperature isothermal titration calorimetric studies of native cyclodextrins with sodium dodecyl sulfate." *J. Phys. Chem. B*, **115**(49), 14381–14396. ISSN 15205207. doi: 10.1021/jp208740b. URL https://www.doi.org/10.1021/jp208740b.

Brow ME (ed.) (1998). *Handbook of Thermal Analysis and Calorimetry. Volume 1: Principles and Practice*. Elsevier Science B. V., Amsterdam. ISBN 978-0-444-82085-3.

Burnouf D, Ennifar E, Guedich S, Puffer B, Hoffmann G, Bec G, Disdier F, Baltzinger M, Dumas P (2012). "KinITC: A new method for obtaining joint thermodynamic and kinetic data by isothermal titration calorimetry." *J. Am. Chem. Soc.*, **134**(1), 559–565. ISSN 00027863. doi: 10.1021/ja209057d. URL https://www.doi.org/10.1021/ja209057d.

Callies O, Hernández Daranas A, Daranas AH (2016). "Application of isothermal titration calorimetry as a tool to study natural product interactions." *Nat. Prod. Rep.*, **33**(7), 881–904. ISSN 14604752. doi: 10.1039/c5np00094g. URL https://www.doi.org/10.1039/c5np00094g.

Castro G, Garrido PF, Amigo A, Brocos P (2018). "Boosting the use of thermoacoustimetry in micellization thermodynamics studies by easing an objective determination of the cmc." *Fluid Phase Equilib.*, **478**, 1–13. ISSN 03783812. doi:

USC UNIVERSIDADE DE SANTIAGO DE COMPOSTELA

10.1016/j.fluid.2018.08.011. URL https://www.doi.org/10.1016/j.fluid.2018.08.011.

Chay SK, Keating AV, James C, Aliev AE, Haider S, Craig DQM (2018). "Evaluation of the taste-masking effects of (2-hydroxypropyl)-β-cyclodextrin on ranitidine hydrochloride; a combined biosensor, spectroscopic and molecular modelling assessment." *RSC Adv.*, **8**(7), 3564–3573. ISSN 2046-2069. doi: 10.1039/C7RA11015D. URL https://www.doi.org/10.1039/C7RA11015D.

Chief Elk J, Benjamin I (2015). "β-Cyclodextrin at the Water/1-Bromobutane Interface: Molecular Insight into Reverse Phase Transfer Catalysis." *Langmuir*, **31**(18), 5086–5092. ISSN 0743-7463. doi: 10.1021/acs.langmuir.5b01025. URL https://doi.org/10.1021/acs.langmuir.5b01025.

Chiodini S, Stoliar P, Garrido PF, Albonetti C (submitted). "Differential entropy of self-similar organic islands approached by *in situ* atomic force microscopy." *Materials*.

Chodzińska A, Zdziennicka A, Jańczuk B (2012). "Volumetric and Surface Properties of Short Chain Alcohols in Aqueous Solution-Air Systems at 293 K." *J. Solution Chem.*, **41**(12), 2226–2245. ISSN 0095-9782. doi: 10.1007/s10953-012-9935-z. URL https://www.doi.org/10.1007/s10953-012-9935-z.

Cliff MJ, Gutierrez A, Ladbury JE (2004). "A survey of the year 2003 literature on applications of isothermal titration calorimetry." *J. Mol. Recognit.*, **17**(6), 513–523. ISSN 09523499. doi: 10.1002/jmr.714. URL https://www.doi.org/10.1002/jmr.714.

Cliff MJ, Ladbury JE (2003). "A survey of the year 2002 literature on applications of isothermal titration calorimetry." *J. Mol. Recognit.*, **16**(6), 383–391. ISSN 1099-1352. doi: 10.1002/JMR.648. URL https://www.doi.org/10.1002/JMR.648.

Coisne C, Tilloy S, Monflier E, Wils D, Fenart L, Gosselet F (2016). "Cyclodextrins as Emerging Therapeutic Tools in the Treatment of Cholesterol-Associated Vascular and Neurodegenerative Diseases." *Molecules*, **21**(12), 1748. ISSN 1420-3049. doi: 10.3390/molecules21121748. URL https://www.doi.org/10.3390/molecules21121748.

Coleman AW, Nicolis I, Keller N, Dalbiez JP (1992). "Aggregation of cyclodextrins: An explanation of the abnormal solubility of β-cyclodextrin." *J. Incl. Phenom. Mol. Recognit. Chem.*, **13**(2), 139–143. ISSN 0923-0750. doi: 10.1007/BF01053637. URL http://doi.org/10.1007/BF01053637.

Concha-Santos S, Pérez-Casas S, Brocos P, Piñeiro Á (2013). "Testing the effect of the cavity size and the number of molecular substitutions in host-guest complexes formed by 2-hydroxypropyl-cyclodextrins and n-octyl-β-d-glucopyranoside." *J. Chem. Thermodyn.*, **67**, 112–119. ISSN 00219614. doi: 10.1016/j.jct.2013.08.003. URL https://www.doi.org/10.1016/j.jct.2013.08.003.

Conde D, Garrido PF, Calvelo M, Piñeiro Á, Garcia-Fandiño R (submitted). "Molecular dynamics simulations of transmembrane cyclic peptide nanotubes using classical force fields, Hydrogen Mass Repartitioning and Hydrogen Isotope Exchange methods: a critical comparison." *Physical Chemistry Chemical Physics*.

USC UNIVERSIDADE DE SANTIAGO DE COMPOSTELA

Costa L, Li-Destri G, Pontoni D, Konovalov O, Thomson NH (2017). "Liquid-Liquid Interfacial Imaging Using Atomic Force Microscopy." *Adv. Mater. Interfaces*, **4**(16). ISSN 21967350. doi: 10.1002/admi.201700203. URL https://www.doi.org/10.1002/admi.201700203.

Crini G (2014). "Review: A history of cyclodextrins." *Chem. Rev.*, **114**(21), 10940–10975. ISSN 15206890. doi: 10.1021/cr500081p. URL https://www.doi.org/10.1021/cr500081p.

Cussler EL (2009). *Diffusion: Mass Transfer in Fluid Systems*. Cambridge University Press, Cambridge. ISBN 9780521871211.

Czapkiewicz J, Tutaj B (1993). "Surface tension studies on the complexation of dodecylpyridinium chloride by?-cyclodextrin in aqueous electrolyte solutions." *J. Incl. Phenom. Mol. Recognit. Chem.*, **16**(4), 377–382. ISSN 0923-0750. doi: 10.1007/BF00708717. URL http://doi.org/10.1007/BF00708717.

Dai S, Tam KC (2003). "Isothermal titration calorimetric studies of alkyl phenol ethoxylate surfactants in aqueous solutions." *Colloids Surfaces A Physicochem. Eng. Asp.*, **229**(1-3), 157–168. ISSN 09277757. doi: 10.1016/j.colsurfa.2003.09.007. URL https://www.doi.org/10.1016/j.colsurfa.2003.09.007.

DÁpolito R, Perazzo A, DÁntuono M, Preziosi V, Tomaiuolo G, Miller R, Guido S (2018). "Measuring Interfacial Tension of Emulsions in Situ by Microfluidics." *Langmuir*, **34**(17), 4991–4997. ISSN 15205827. doi: 10.1021/acs.langmuir.8b00208. URL https://www.doi.org/10.1021/acs.langmuir.8b00208.

DÁria F, Pagano B, Giancola C (2021). "Thermodynamic properties of hydroxypropyl-β-cyclodextrin/guest interaction: a survey of recent studies." *J. Therm. Anal. Calorim.*, pp. 1–9. ISSN 1388-6150. doi: 10.1007/s10973-021-10958-1. URL https://www.doi.org/10.1007/s10973-021-10958-1.

Davis ME, Brewster ME (2004). "Cyclodextrin-based pharmaceutics: Past, present and future." *Nat. Rev. Drug Discov.*, **3**(12), 1023–1035. ISSN 14741776. doi: 10.1038/nrd1576. URL https://www.doi.org/10.1038/nrd1576.

de Jesus A, Yin H (2017). "Supramolecular Membrane Chemistry." In JL Atwood (ed.), "Compr. Supramol. Chem. II," volume 5, pp. 311–328. Elsevier, 2 edition. ISBN 9780128031988. doi: 10.1016/B978-0-12-409547-2.12572-7. URL https://www.doi.org/10.1016/B978-0-12-409547-2.12572-7.

del Río JM, Grolier JPE (2017). "Isothermal Titration Calorimetry." In "Enthalpy Intern. Energy," pp. 96–132. Royal Society of Chemistry, Cambridge. doi: 10.1039/9781788010214-00096. URL https://www.doi.org/10.1039/9781788010214-00096.

Del Valle E (2004). "Cyclodextrins and their uses: a review." *Process Biochem.*, **39**(9), 1033–1046. ISSN 13595113. doi: 10.1016/S0032-9592(03)00258-9. URL https://www.doi.org/10.1016/S0032-9592(03)00258-9.

Dharmawardana UR, Christian SD, Tucker EE, Taylor RW, Scamehorn JF (1993). "A surface tension method for determining binding constants for cyclodextrin

inclusion complexes of ionic surfactants." *Langmuir*, **9**(9), 2258–2263. ISSN 0743-7463. doi: 10.1021/la00033a003. URL https://doi.org/10.1021/la00033a003.

Do TT, Van Hooghten R, Van den Mooter G (2017). "A study of the aggregation of cyclodextrins: Determination of the critical aggregation concentration, size of aggregates and thermodynamics using isodesmic and K2-K models." *Int. J. Pharm.*, **521**(1-2), 318–326. ISSN 03785173. doi: 10.1016/j.ijpharm.2017.02.037. URL https://doi.org/10.1016/J.IJPHARM.2017.02.037.

Dodziuk H (ed.) (2006). *Cyclodextrins and Their Complexes*. Wiley. ISBN 9783527312801. doi: 10.1002/3527608982. URL https://www.doi.org/10.1002/3527608982.

dos Santos C, Buera P, Mazzobre F (2017). "Novel trends in cyclodextrins encapsulation. Applications in food science." doi: 10.1016/j.cofs.2017.09.002. URL https://www.doi.org/10.1016/j.cofs.2017.09.002.

dos Santos Silva Araújo L, Lazzara G, Chiappisi L (2021). "Cyclodextrin/surfactant inclusion complexes: An integrated view of their thermodynamic and structural properties." *Adv. Colloid Interface Sci.*, **289**, 102375. ISSN 00018686. doi: 10.1016/j.cis.2021.102375. URL https://www.doi.org/10.1016/j.cis.2021.102375.

Dukhin SS, Kretzschmar G, Miller R (1995). *Dynamics of adsorption at liquid interfaces: theory, experiment, application*, volume 1. Elsevier, Amsterdam. ISBN 978-0-444-88117-5.

Dumas P, Ennifar E, Da Veiga C, Bec G, Palau W, Di Primo C, Piñeiro A, Sabin J, Muñoz E, Rial J (2016). "Extending ITC to Kinetics with kinITC." In "Methods Enzymol.", volume 567, pp. 157–180. Academic Press Inc. doi: 10.1016/bs.mie.2015.08.026. URL https://www.doi.org/10.1016/bs.mie.2015.08.026.

Durand M (2020). "Mechanical approach to surface tension and capillary phenomena." *hal*, p. 02566867. URL https://hal.archives-ouvertes.fr/hal-02566867.

Eastoe J, Dalton J (2000). "Dynamic surface tension and adsorption mechanisms of surfactants at the air-water interface." *Adv. Colloid Interface Sci.*, **85**(2-3), 103–144. ISSN 00018686. doi: 10.1016/S0001-8686(99)00017-2. URL https://www.doi.org/10.1016/S0001-8686(99)00017-2.

Erdoar N, Bilensoy E (2018). "Cyclodextrin-Based Nanosystems in Targeted Cancer Therapy." In S Fourmentin, G Crini, E Lichtfouse (eds.), "Cyclodext. Appl. Med. Food, Environ. Liq. Cryst.", pp. 59–80. Springer International Publishing, Cham. doi: 10.1007/978-3-319-76162-6_3. URL https://www.doi.org/10.1007/978-3-319-76162-6_3.

Erlekam F, Igde S, Röblitz S, Hartmann L, Weber M (2019). "Modeling of multivalent ligand-receptor binding measured by kinITC." *Computation*, **7**(3), 1–16. ISSN 20793197. doi: 10.3390/COMPUTATION7030046. URL https://www.doi.org/10.3390/COMPUTATION7030046.

USC UNIVERSIDADE DE SANTIAGO DE COMPOSTELA

Falconer RJ (2016). "Applications of isothermal titration calorimetry - the research and technical developments from 2011 to 2015." *J. Mol. Recognit.*, **29**(10), 504–515. ISSN 09523499. doi: 10.1002/jmr.2550. URL https://www.doi.org/10.1002/jmr.2550.

Falconer RJ, Collins BM (2011). "Survey of the year 2009: applications of isothermal titration calorimetry." *J. Mol. Recognit.*, **24**(1), 1–16. ISSN 1099-1352. doi: 10.1002/JMR.1073. URL https://www.doi.org/10.1002/JMR.1073.

Falconer RJ, Penkova A, Jelesarov I, Collins BM (2010). "Survey of the year 2008: applications of isothermal titration calorimetry." *J. Mol. Recognit.*, **23**(5), 395–413. ISSN 1099-1352. doi: 10.1002/JMR.1025. URL https://www.doi.org/10.1002/JMR.1025.

Falconer RJ, Schuur B, Mittermaier AK (2021). "Applications of isothermal titration calorimetry in pure and applied research from 2016 to 2020." *J. Mol. Recognit.*, **34**(10), e2901. ISSN 0952-3499. doi: 10.1002/jmr.2901. URL https://www.doi.org/10.1002/jmr.2901.

Fenyvesi F, Réti-Nagy K, Bacsó Z, Gutay-Tóth Z, Malanga M, Fenyvesi É, Szente L, Váradi J, Ujhelyi Z, Fehér P, Szabó G, Vecsernyés M, Bácskay I (2014). "Fluorescently Labeled Methyl-Beta-Cyclodextrin Enters Intestinal Epithelial Caco-2 Cells by Fluid-Phase Endocytosis." *PLoS One*, **9**(1), e84856. ISSN 1932-6203. doi: 10.1371/journal.pone.0084856. URL https://www.doi.org/10.1371/journal.pone.0084856.

Ferreira M, Bricout H, Azaroual N, Landy D, Tilloy S, Hapiot F, Monflier E (2012). "Cyclodextrin/amphiphilic phosphane mixed systems and their applications in aqueous organometallic catalysis." *Adv. Synth. Catal.*, **354**(7), 1337–1346. ISSN 16154150. doi: 10.1002/adsc.201100837. URL http://doi.org/10.1002/adsc.201100837.

Flaherty RJ, Nshime B, DeLaMarre M, DeJong S, Scott P, Lantz AW (2013). "Cyclodextrins as complexation and extraction agents for pesticides from contaminated soil." *Chemosphere*, **91**(7), 912–920. ISSN 18791298. doi: 10.1016/j.chemosphere.2013.02.005. URL https://www.doi.org/10.1016/j.chemosphere.2013.02.005.

Fliszár-Nyúl E, Lemli B, Kunsági-Máté S, Szente L, Poór M (2019). "Interactions of mycotoxin alternariol with cyclodextrins and its removal from aqueous solution by beta-cyclodextrin bead polymer." *Biomolecules*, **9**(9). ISSN 2218273X. doi: 10.3390/biom9090428. URL https://www.doi.org/10.3390/biom9090428.

Foo KY, Hameed BH (2010). "Insights into the modeling of adsorption isotherm systems." *Chem. Eng. J.*, **156**(1), 2–10. ISSN 1385-8947. doi: 10.1016/J.CEJ.2009.09.013. URL https://www.doi.org/10.1016/J.CEJ.2009.09.013.

Fortin TJ, Laesecke A, Freund M, Outcalt S (2013). "Advanced calibration, adjustment, and operation of a density and sound speed analyzer." *J. Chem. Thermodyn.*, **57**, 276–285. ISSN 00219614. doi: 10.1016/j.jct.2012.09.009. URL https://www.doi.org/10.1016/j.jct.2012.09.009.

Fourmentin S, Crini G, Lichtfouse E (eds.) (2018). *Cyclodextrin Applications in Medicine, Food, Environment and Liquid Crystals*, volume 17 of *Environmental Chemistry for a Sustainable World*. Springer International Publishing, Cham. ISBN 978-3-319-76161-9. doi: 10.1007/978-3-319-76162-6. URL https://www.doi.org/10.1007/978-3-319-76162-6.

Freire E, Mayorga OL, Straume M (1990). "Isothermal titration calorimetry." *Anal. Chem.*, **62**(18), 950A–959A. ISSN 0003-2700. doi: 10.1021/ac00217a002. URL https://www.doi.org/10.1021/ac00217a002.

Gal N, Schroffenegger M, Reimhult E (2018). "Stealth Nanoparticles Grafted with Dense Polymer Brushes Display Adsorption of Serum Protein Investigated by Isothermal Titration Calorimetry." *J. Phys. Chem. B*, **122**(22), 5820–5834. ISSN 1520-6106. doi: 10.1021/acs.jpcb.8b02338. URL https://www.doi.org/10.1021/acs.jpcb.8b02338.

Gandhi SR, Quintans JDSS, Gandhi GR, Araújo AADS, Quintans Júnior LJ (2020). "The use of cyclodextrin inclusion complexes to improve anticancer drug profiles: a systematic review." *Expert Opin. Drug Deliv.*, **17**(8), 1069–1080. ISSN 1742-5247. doi: 10.1080/17425247.2020.1776261. URL https://www.doi.org/10.1080/17425247.2020.1776261.

Garrido PF, Bastos M, Velázquez-Campoy A, Amigo A, Dumas P, Piñeiro Á (2022). "Unsupervised bubble calorimetry analysis: Surface tension from isothermal titration calorimetry." *J. Colloid Interface Sci.*, **606**, 1823–1832. ISSN 00219797. doi: 10.1016/j.jcis.2021.08.115. URL https://www.doi.org/10.1016/j.jcis.2021.08.115.

Garrido PF, Bastos M, Velázquez-Campoy A, Dumas P, Piñeiro Á (2021). "Fluid interface calorimetry." *J. Colloid Interface Sci.*, **596**, 119–129. ISSN 00219797. doi: 10.1016/j.jcis.2021.03.098. URL https://www.doi.org/10.1016/j.jcis.2021.03.098.

Garrido PF, Brocos P, Amigo A, García-Río L, Gracia-Fadrique J, Piñeiro Á (2016). "STAND: Surface Tension for Aggregation Number Determination." *Langmuir*, **32**(16), 3917–3925. ISSN 0743-7463. doi: 10.1021/acs.langmuir.6b00477. URL https://www.doi.org/10.1021/acs.langmuir.6b00477.

Garrido PF, Calvelo M, Blanco-González A, Veleiro U, Suárez F, Conde D, Cabezón A, Piñeiro Á, Garcia-Fandino R (2020a). "The Lord of the Nano-Rings: Cyclodextrins and the battle against SARS-CoV-2." *Int. J. Pharm.*, **588**, 119689. ISSN 03785173. doi: 10.1016/j.ijpharm.2020.119689. URL https://www.doi.org/10.1016/j.ijpharm.2020.119689.

Garrido PF, Calvelo M, Garcia-Fandiño R, Piñeiro Á (2020b). "Rings, Hexagons, Petals, and Dipolar Moment Sink-Sources: The Fanciful Behavior of Water around Cyclodextrin Complexes." *Biomolecules*, **10**(3), 431. ISSN 2218-273X. doi: 10.3390/biom10030431. URL https://www.doi.org/10.3390/biom10030431.

Garrido PF, Rodríguez-Dafonte P, García-Río L, Piñeiro Á (available online: September 27, 2021). "Simple approximaTion for Aggregation Number Determination by Isothermal Titration Calorimetry: STAND-ITC." *Langmuir*. ISSN

USC UNIVERSIDADE DE SANTIAGO DE COMPOSTELA

0743-7463. doi: 10.1021/acs.langmuir.1c01727. URL https://doi.org/10.1021/acs.langmuir.1c01727.

Gatiatulin AK, Ziganshin MA, Gorbatchuk VV (2020). "Smart Molecular Recognition: From Key-to-Lock Principle to Memory-Based Selectivity." *Front. Chem.*, **7**, 933. ISSN 2296-2646. doi: 10.3389/fchem.2019.00933. URL https://www.doi.org/10.3389/fchem.2019.00933.

Gèze A, Putaux JL, Choisnard L, Jéhan P, Wouessidjewe D (2004). "Long-term shelf stability of amphiphilic β -cyclodextrin nanosphere suspensions monitored by dynamic light scattering and cryo-transmission electron microscopy." *J. Microencapsul.*, **21**(6), 607–613. ISSN 0265-2048. doi: 10.1080/02652040400008457. URL https://www.doi.org/10.1080/02652040400008457.

Ghai R, Falconer RJ, Collins BM (2012). "Applications of isothermal titration calorimetry in pure and applied research-survey of the literature from 2010." *J. Mol. Recognit.*, **25**(1), 32–52. ISSN 09523499. doi: 10.1002/jmr.1167. URL https://www.doi.org/10.1002/jmr.1167.

Glöckner S, Klebe G (2021). "Simultaneous determination of thermodynamic and kinetic data by isothermal titration calorimetry." *Biochim. Biophys. Acta - Gen. Subj.*, **1865**(2), 129772. ISSN 03044165. doi: 10.1016/j.bbagen.2020.129772. URL https://www.doi.org/10.1016/j.bbagen.2020.129772.

Glöckner S, Ngo K, Sager CP, Hüfner-Wulsdorf T, Heine A, Klebe G (2020). "Conformational Changes in Alkyl Chains Determine the Thermodynamic and Kinetic Binding Profiles of Carbonic Anhydrase Inhibitors." *ACS Chem. Biol.*, **15**(3), 675–685. ISSN 15548937. doi: 10.1021/acschembio.9b00895. URL https://www.doi.org/10.1021/acschembio.9b00895.

Gogoi B, Dutta N, Goswami P, Krishna Mohan T (2003). "A case study of bioremediation of petroleum-hydrocarbon contaminated soil at a crude oil spill site." *Adv. Environ. Res.*, **7**(4), 767–782. ISSN 10930191. doi: 10.1016/S1093-0191(02)00029-1. URL https://www.doi.org/10.1016/S1093-0191(02)00029-1.

González-Gaitano G, Rodríguez P, Isasi JR, Fuentes M, Tardajos G, Sánchez M (2002). "The Aggregation of Cyclodextrins as Studied by Photon Correlation Spectroscopy." *J. Incl. Phenom. Macrocycl. Chem.*, **44**(1), 101–105. ISSN 1573-1111. doi: 10.1023/A:1023065823358. URL https://doi.org/10.1023/A:1023065823358.

Gowers R, Linke M, Barnoud J, Reddy T, Melo M, Seyler S, Domański J, Dotson D, Buchoux S, Kenney I, Beckstein O (2016). "MDAnalysis: A Python Package for the Rapid Analysis of Molecular Dynamics Simulations." In "SciPy Conf.", pp. 98–105. doi: 10.25080/Majora-629e541a-00e. URL https://www.doi.org/10.25080/Majora-629e541a-00e.

Graham D, Phillips M (1979). "Proteins at liquid interfaces." *J. Colloid Interface Sci.*, **70**(3), 415–426. ISSN 00219797. doi: 10.1016/0021-9797(79)90049-3. URL https://www.doi.org/10.1016/0021-9797(79)90049-3.

Griffiths RB (1980). "An Introduction to the Thermodynamics of Surfaces." In "Phase Transitions Surf. Film.", pp. 1–27. Springer US, Boston, MA. ISBN 9781461330578. doi: 10.1007/978-1-4613-3057-8_1. URL https://www.doi.org/10.1007/978-1-4613-3057-8_1.

Grolier JPE, Del Río JM (2012). "Isothermal titration calorimetry: A thermodynamic interpretation of measurements." *J. Chem. Thermodyn.*, **55**, 193–202. ISSN 00219614. doi: 10.1016/j.jct.2012.05.018. URL https://www.doi.org/10.1016/j.jct.2012.05.018.

Gu A, Wheate NJ (2021). "Macrocycles as drug-enhancing excipients in pharmaceutical formulations." *J. Incl. Phenom. Macrocycl. Chem.*, **100**(1-2), 55–69. ISSN 15731111. doi: 10.1007/s10847-021-01055-9. URL https://www.doi.org/10.1007/s10847-021-01055-9.

Guo R, D Wilson L (2013). "Cyclodextrin-Based Microcapsule Materials - Their Preparation and Physiochemical Properties." *Curr. Org. Chem.*, **17**(1), 14–21. ISSN 13852728. doi: 10.2174/138527213805289204. URL https://www.doi.org/10.2174/138527213805289204.

Haile JM (1997). *Molecular Dynamics Simulation: Elementary Methods*. John Wiley & Sons, New York.

Harris CR, Millman KJ, van der Walt SJ, Gommers R, Virtanen P, Cournapeau D, Wieser E, Taylor J, Berg S, Smith NJ, Kern R, Picus M, Hoyer S, van Kerkwijk MH, Brett M, Haldane A, del Río JF, Wiebe M, Peterson P, Gérard-Marchant P, Sheppard K, Reddy T, Weckesser W, Abbasi H, Gohlke C, Oliphant TE (2020). "Array programming with NumPy." *Nature*, **585**(7825), 357–362. ISSN 0028-0836. doi: 10.1038/s41586-020-2649-2. URL https://www.doi.org/10.1038/s41586-020-2649-2.

Hashidzume A, Yamaguchi H, Harada A (2019). "Cyclodextrin-Based Rotaxanes: from Rotaxanes to Polyrotaxanes and Further to Functional Materials." *European J. Org. Chem.*, **2019**(21), 3344–3357. ISSN 1434193X. doi: 10.1002/ejoc.201900090. URL https://www.doi.org/10.1002/ejoc.201900090.

Hassan N, Ruso JM, Piñeiro Á (2011). "Hydrogenated/Fluorinated Catanionic Surfactants as Potential Templates for Nanostructure Design." *Langmuir*, **27**(16), 9719–9728. ISSN 0743-7463. doi: 10.1021/la2019346. URL https://www.doi.org/10.1021/la2019346.

Hazra S, Kumar GS (2015). "Physicochemical properties of inclusion complexes of sanguinarine with natural cyclodextrins: Spectroscopy, calorimetry and NMR studies." *RSC Adv.*, **5**(3), 1873–1882. ISSN 20462069. doi: 10.1039/c4ra10204e. URL https://www.doi.org/10.1039/c4ra10204e.

Heintz A, Lehmann JK, Kozlova SA, Balantseva EV, Bazyleva AB, Ondo D (2010). "Micelle formation of alkylimidazolium ionic liquids in water and in ethylammonium nitrate ionic liquid: A calorimetric study." *Fluid Phase Equilib.*, **294**(1-2), 187–196. ISSN 03783812. doi: 10.1016/j.fluid.2010.01.022. URL https://www.doi.org/10.1016/j.fluid.2010.01.022.

USC UNIVERSIDADE DE SANTIAGO DE COMPOSTELA

Hernández-Pascacio J, Banquy X, Pérez-Casas S, Costas M, Amigo A, Piñeiro Á (2008). "A small molecular size system giving unexpected surface effects: α-Cyclodextrin + sodium dodecyl sulfate in water." *J. Colloid Interface Sci.*, **328**(2), 391–395. ISSN 00219797. doi: 10.1016/j.jcis.2008.09.002. URL https://www.doi.org/10.1016/j.jcis.2008.09.002.

Hernandez-Pascacio J, Garza C, Banquy X, Díaz-Vergara N, Amigo A, Ramos S, Castillo R, Costas M, Piñeiro Á, Hernández-Pascacio J, Garza C, Banquy X, Díaz-Vergara N, Amigo A, Ramos S, Castillo R, Costas M, Piñeiro Á (2007). "Cyclodextrin-based self-assembled nanotubes at the water/air interface." *J. Phys. Chem. B*, **111**(44), 12625–12630. ISSN 15206106. doi: 10.1021/jp076576t. URL https://www.doi.org/10.1021/jp076576t.

Hernandez-Pascacio J, Piñeiro Á, Ruso JM, Hassan N, Campbell RA, Campos-Terán J, Costas M (2016). "Complex Behavior of Aqueous α-Cyclodextrin Solutions. Interfacial Morphologies Resulting from Bulk Aggregation." *Langmuir*, **32**(26), 6682–6690. ISSN 15205827. doi: 10.1021/acs.langmuir.6b01646. URL https://www.doi.org/10.1021/acs.langmuir.6b01646.

Hiemenz PC, Rajagopalan R (2016). *Principles of Colloid and Surface Chemistry, Revised and Expanded*. CRC Press. ISBN 9781315274287. doi: 10.1201/9781315274287. URL https://www.doi.org/10.1201/9781315274287.

Hilfiger JJ (2015). *Graphing Data with R: An Introduction*. O'Reilly Media, Inc., Sebastopol, CA, USA. ISBN 9781491922613.

Hu DL, Bush JWM (2005). "Meniscus-climbing insects." *Nature*, **437**(7059), 733–736. ISSN 0028-0836. doi: 10.1038/nature03995. URL https://www.doi.org/10.1038/nature03995.

Hunt J (2019). *Advanced Guide to Python 3 Programming*. Undergraduate Topics in Computer Science. Springer International Publishing, Cham. ISBN 978-3-030-25942-6. doi: 10.1007/978-3-030-25943-3. URL https://www.doi.org/10.1007/978-3-030-25943-3.

Hunter JD (2007). "Matplotlib: A 2D Graphics Environment." *Comput. Sci. Eng.*, **9**(3), 90–95. ISSN 1521-9615. doi: 10.1109/MCSE.2007.55. URL https://www.doi.org/10.1109/MCSE.2007.55.

Igde S, Röblitz S, Müller A, Kolbe K, Boden S, Fessele C, Lindhorst TK, Weber M, Hartmann L (2017). "Linear Precision Glycomacromolecules with Varying Interligand Spacing and Linker Functionalities Binding to Concanavalin A and the Bacterial Lectin FimH." *Macromol. Biosci.*, **17**(12), 1700198. ISSN 16165195. doi: 10.1002/mabi.201700198. URL https://www.doi.org/10.1002/mabi.201700198.

Ikuta D, Hirata Y, Wakamori S, Shimada H, Tomabechi Y, Kawasaki Y, Ikeuchi K, Hagimori T, Matsumoto S, Yamada H (2019). "Conformationally supple glucose monomers enable synthesis of the smallest cyclodextrins." *Science (80-.).*, **364**(6441), 674–677. ISSN 0036-8075. doi: 10.1126/SCIENCE.AAW3053. URL https://www.doi.org/10.1126/SCIENCE.AAW3053.

Ishiguro T, Morishita E, Iohara D, Hirayama F, Wada K, Motoyama K, Arima H, Uekama K (2011). "Some pharmaceutical and inclusion properties of 2-hydroxybutyl-β- cyclodextrin derivative." *Int. J. Pharm.*, **419**(1-2), 161–169. ISSN 03785173. doi: 10.1016/j.ijpharm.2011.07.044. URL https://www.doi.org/10.1016/j.ijpharm.2011.07.044.

Jansook P, Kulsirachote P, Asasutjarit R, Loftsson T (2019). "Development of celecoxib eye drop solution and microsuspension: A comparative investigation of binary and ternary cyclodextrin complexes." *Carbohydr. Polym.*, **225**, 115209. ISSN 01448617. doi: 10.1016/j.carbpol.2019.115209. URL https://www.doi.org/10.1016/j.carbpol.2019.115209.

Jansook P, Moya-Ortega MD, Loftsson T (2010). "Effect of self-aggregation of γ-cyclodextrin on drug solubilization." *J. Incl. Phenom. Macrocycl. Chem.*, **68**(1-2), 229–236. ISSN 0923-0750. doi: 10.1007/s10847-010-9779-3. URL https://doi.org/10.1007/s10847-010-9779-3.

Jansook P, Ogawa N, Loftsson T (2018). "Cyclodextrins: structure, physicochemical properties and pharmaceutical applications." *Int. J. Pharm.*, **535**(1-2), 272–284. ISSN 03785173. doi: 10.1016/j.ijpharm.2017.11.018. URL https://www.doi.org/10.1016/j.ijpharm.2017.11.018.

Javadi A, Mucic N, Karbaschi M, Won JY, Lotfi M, Dan A, Ulaganathan V, Gochev G, Makievski AV, Kovalchuk VI, Kovalchuk NM, Krägel J, Miller R (2013). "Characterization methods for liquid interfacial layers." *Eur. Phys. J. Spec. Top.*, **222**(1), 7–29. ISSN 1951-6355. doi: 10.1140/epjst/e2013-01822-3. URL https://www.doi.org/10.1140/epjst/e2013-01822-3.

Jesús C, Socorro F, De Rivera MR, Rodríguez de Rivera M (2012). "New approach to Tian's equation applied to heat conduction and liquid injection calorimeters." *J. Therm. Anal. Calorim.*, **110**(3), 1523–1532. ISSN 13886150. doi: 10.1007/s10973-011-2117-1. URL http://doi.org/10.1007/s10973-011-2117-1.

Jimoh AA, Lin J (2019). "Biosurfactant: A new frontier for greener technology and environmental sustainability." *Ecotoxicol. Environ. Saf.*, **184**, 109607. ISSN 01476513. doi: 10.1016/j.ecoenv.2019.109607. URL https://www.doi.org/10.1016/j.ecoenv.2019.109607.

Jin ZY (2013). *Cyclodextrin Chemistry*. WORLD SCIENTIFIC / CHEMICAL INDUSTRY PRESS, CHINA. ISBN 978-981-4436-79-3. doi: 10.1142/8630. URL https://www.doi.org/10.1142/8630.

Jolicoeur C, Philip PR (1974). "Enthalpy-Entropy Compensation for Micellization and Other Hydrophobic Interactions in Aqueous Solutions." *Can. J. Chem.*, **52**(10), 1834–1839. ISSN 0008-4042. doi: 10.1139/v74-262. URL https://www.doi.org/10.1139/v74-262.

Kairaliyeva T, Mucic N, Spasojevic L, Bucko S, Katona J, Aksenenko E, Aidarova S, Fainerman V, Makievski A, Tarasevich Y, Miller R (2017). "Surface tension measurements with the drop profile analysis tensiometry-consideration of the surfactant mass balance in a single drop." *Colloids and Interfaces*, **1**(1), 1–11. ISSN 25045377. doi: 10.3390/colloids1010001. URL https://www.doi.org/10.3390/colloids1010001.

USC UNIVERSIDADE DE SANTIAGO DE COMPOSTELA

Kalyanasundaram K (1987). *Photochemistry in Microheterogeneous Systems*. Elsevier. ISBN 9780123949950. doi: 10.1016/B978-0-12-394995-0.X5001-8. URL https://www.doi.org/10.1016/B978-0-12-394995-0.X5001-8.

Kang SJL (2005). "Thermodynamics of the interface." In "Sintering," pp. 9–18. Elsevier. ISBN 9780750663854. doi: 10.1016/B978-075066385-4/50002-9. URL https://www.doi.org/10.1016/B978-075066385-4/50002-9.

Karnes JJ, Benjamin I (2017). "Structure and Dynamics of Host/Guest Complexation at the Liquid/Liquid Interface: Implications for Inverse Phase Transfer Catalysis." *J. Phys. Chem. C*, **121**(9), 4999–5011. ISSN 19327455. doi: 10.1021/acs.jpcc.6b11715. URL https://www.doi.org/10.1021/acs.jpcc.6b11715.

Kellett K, Slochower DR, Schauperl M, Duggan BM, Gilson MK (2021). "Experimental characterization of the association of β-cyclodextrin and eight novel cyclodextrin derivatives with two guest compounds." *J. Comput. Aided. Mol. Des.*, **35**(1), 95–104. ISSN 0920-654X. doi: 10.1007/s10822-020-00350-w. URL https://www.doi.org/10.1007/s10822-020-00350-w.

Kenny GP, Notley SR, Gagnon D (2017). "Direct calorimetry: a brief historical review of its use in the study of human metabolism and thermoregulation." *Eur. J. Appl. Physiol.*, **117**(9), 1765–1785. ISSN 1439-6319. doi: 10.1007/s00421-017-3670-5. URL https://www.doi.org/10.1007/s00421-017-3670-5.

Kerfeld CA, Sawaya MR, Tanaka S, Nguyen CV, Phillips M, Beeby M, Yeates TO (2005). "Microbiology: Protein structures forming the shell of primitive bacterial organelles." *Science (80-.).*, **309**(5736), 936–938. ISSN 00368075. doi: 10.1126/science.1113397. URL https://www.doi.org/10.1126/science.1113397.

Kessler A, Zeeb B, Kranz B, Menéndez-Aguirre O, Fischer L, Hinrichs J, Weiss J (2012). "Isothermal titration calorimetry as a tool to determine the thermodynamics of demicellization processes." *Rev. Sci. Instrum.*, **83**(10), 105104. ISSN 0034-6748. doi: 10.1063/1.4754718. URL https://www.doi.org/10.1063/1.4754718.

Keszei E (2012). *Chemical Thermodynamics*. Springer Berlin Heidelberg, Berlin, Heidelberg. ISBN 978-3-642-19863-2. doi: 10.1007/978-3-642-19864-9. URL https://www.doi.org/10.1007/978-3-642-19864-9.

Khomutov S, Donova MV (2011). "Nanodimer cyclodextrin ligands with high affinity to steroids." *J. Incl. Phenom. Macrocycl. Chem.*, **70**(3-4), 353–357. ISSN 09230750. doi: 10.1007/s10847-010-9896-z. URL https://www.doi.org/10.1007/s10847-010-9896-z.

Kihara F, Arima H, Tsutsumi T, Hirayama F, Uekama K (2002). "Effects of Structure of Polyamidoamine Dendrimer on Gene Transfer Efficiency of the Dendrimer Conjugate with α-Cyclodextrin." *Bioconjug. Chem.*, **13**(6), 1211–1219. ISSN 1043-1802. doi: 10.1021/bc025557d. URL https://www.doi.org/10.1021/bc025557d.

Kim S (2014). "Issues on the choice of a proper time step in molecular dynamics." *Phys. Procedia*, **53**, 60–62. ISSN 18753892. doi: 10.1016/j.phpro.2014.06.027. URL http://doi.org/10.1016/j.phpro.2014.06.027.

Kou Qy, Wu Zl, Hu N (2015). "Thermodynamic adsorption properties of bovine serum albumin and lysozyme on the bubble surface from the binary solution." *Chem. Eng. Res. Des.*, **102**, 26–33. ISSN 02638762. doi: 10.1016/j.cherd.2015.06.013. URL https://www.doi.org/10.1016/j.cherd.2015.06.013.

Kritharides L, Kus M, Brown AJ, Jessup W, Dean RT (1996). "Hydroxypropyl-β-cyclodextrin-mediated Efflux of 7-Ketocholesterol from Macrophage Foam Cells." *J. Biol. Chem.*, **271**(44), 27450–27455. ISSN 00219258. doi: 10.1074/jbc.271.44.27450. URL https://www.doi.org/10.1074/jbc.271.44.27450.

Kronberg B, Holmberg K, Lindman B (2014). *Surface Chemistry of Surfactants and Polymers*. John Wiley & Sons, Ltd, Chichester, UK. ISBN 9781118695968. doi: 10.1002/9781118695968. URL https://www.doi.org/10.1002/9781118695968.

Kurkov SV, Loftsson T (2013). "Cyclodextrins." *Int. J. Pharm.*, **453**(1), 167–180. ISSN 18733476. doi: 10.1016/j.ijpharm.2012.06.055. URL https://www.doi.org/10.1016/j.ijpharm.2012.06.055.

Kushner DJ (1969). "Self-assembly of biological structures." *Bacteriol. Rev.*, **33**(2), 302–345. ISSN 00053678. doi: 10.1128/mmbr.33.2.302-345.1969. URL https://www.doi.org/10.1128/mmbr.33.2.302-345.1969.

Lad MD, Birembaut F, Matthew JM, Frazier RA, Green RJ (2006). "The adsorbed conformation of globular proteins at the air/water interface." *Phys. Chem. Chem. Phys.*, **8**(18), 2179. ISSN 1463-9076. doi: 10.1039/b515934b. URL https://www.doi.org/10.1039/b515934b.

Ladbury J (2010). "Calorimetry as a tool for understanding biomolecular interactions and an aid to drug design." *Biochem. Soc. Trans.*, **38**(4), 888–893. ISSN 0300-5127. doi: 10.1042/BST0380888. URL https://www.doi.org/10.1042/BST0380888.

Ladbury JE (2001). "Isothermal titration calorimetry: application to structure-based drug design." *Thermochim. Acta*, **380**(2), 209–215. ISSN 0040-6031. doi: 10.1016/S0040-6031(01)00674-8. URL https://www.doi.org/10.1016/S0040-6031(01)00674-8.

Ladbury JE (2004). "Application of Isothermal Titration Calorimetry in the Biological Sciences: Things Are Heating Up!" *Biotechniques*, **37**(6), 885–887. ISSN 0736-6205. doi: 10.2144/04376TE01. URL https://www.doi.org/10.2144/04376TE01.

Ladbury JE, Chowdhry BZ (1996). "Sensing the heat: the application of isothermal titration calorimetry to thermodynamic studies of biomolecular interactions." *Chem. Biol.*, **3**(10), 791–801. ISSN 10745521. doi: 10.1016/S1074-5521(96)90063-0. URL https://www.doi.org/10.1016/S1074-5521(96)90063-0.

USC UNIVERSIDADE DE SANTIAGO DE COMPOSTELA

Ladbury JE, Klebe G, Freire E (2009). "Adding calorimetric data to decision making in lead discovery: a hot tip." *Nat. Rev. Drug Discov. 2009 91*, **9**(1), 23–27. ISSN 1474-1784. doi: 10.1038/nrd3054. URL https://www.doi.org/10.1038/nrd3054.

Landau LD, Lifshitz EM (1987). *Fluid Mechanics*, volume 6. Pergamon Press plc, 2 edition. ISBN 978-0-08-033933-7. doi: 10.1016/C2013-0-03799-1. URL https://www.doi.org/10.1016/C2013-0-03799-1.

Langmuir I (1918). "THE ADSORPTION OF GASES ON PLANE SURFACES OF GLASS, MICA AND PLATINUM." *J. Am. Chem. Soc.*, **40**(9), 1361–1403. ISSN 0002-7863. doi: 10.1021/ja02242a004. URL https://www.doi.org/10.1021/ja02242a004.

Larsen KL (2002). "Large cyclodextrins." *J. Incl. Phenom.*, **43**(1-2), 1–13. ISSN 09230750. doi: 10.1023/A:1020494503684. URL https://www.doi.org/10.1023/A:1020494503684.

Lautrup B (2011). *Physics of Continuous Matter*. CRC Press, Boca Raton. ISBN 9780429109508. doi: 10.1201/9781439894200. URL https://www.doi.org/10.1201/9781439894200.

Leclercq L (2016). "Interactions between cyclodextrins and cellular components: Towards greener medical applications?" *Beilstein J. Org. Chem.*, **12**(1), 2644–2662. ISSN 18605397. doi: 10.3762/bjoc.12.261. URL https://www.doi.org/10.3762/bjoc.12.261.

Lee KD (2014). *Python Programming Fundamentals*. Undergraduate Topics in Computer Science. Springer London, London. ISBN 978-1-4471-6641-2. doi: 10.1007/978-1-4471-6642-9. URL https://www.doi.org/10.1007/978-1-4471-6642-9.

Lee KD, Hubbard S (2015). *Data Structures and Algorithms with Python*. Undergraduate Topics in Computer Science. Springer International Publishing, Cham. ISBN 978-3-319-13071-2. doi: 10.1007/978-3-319-13072-9. URL https://www.doi.org/10.1007/978-3-319-13072-9.

Lee W, Lee, Koh (2012). "Development and applications of chip calorimeters as novel biosensors." *Nanobiosensors Dis. Diagnosis*, p. 17. ISSN 2230-6153. doi: 10.2147/ndd.s26438. URL https://www.doi.org/10.2147/ndd.s26438.

Lewis EA, Murphy KP (2005). "Isothermal Titration Calorimetry." In "Protein-Ligand Interact. Methods Mol. Biol.", Humana Press, New Jersey. doi: 10.1385/1-59259-912-5:001. URL https://www.doi.org/10.1385/1-59259-912-5:001.

Li D, Chen L, Wang R, Liu R, Ge G (2017). "Synergetic Determination of Thermodynamic and Kinetic Signatures Using Isothermal Titration Calorimetry: A Full-Curve-Fitting Approach." *Anal. Chem.*, **89**(13), 7130–7138. ISSN 15206882. doi: 10.1021/acs.analchem.7b01091. URL https://www.doi.org/10.1021/acs.analchem.7b01091.

Liu F, Antoniou J, Li Y, Majeed H, Liang R, Ma Y, Ma J, Zhong F (2016). "Chitosan/sulfobutylether-β-cyclodextrin nanoparticles as a potential approach for tea polyphenol encapsulation." *Food Hydrocoll.*, **57**, 291–300. ISSN 0268005X. doi: 10.1016/j.foodhyd.2016.01.024. URL https://www.doi.org/10.1016/j.foodhyd.2016.01.024.

Liu Q, Zhou Y, Lu J, Zhou Y (2020). "Novel cyclodextrin-based adsorbents for removing pollutants from wastewater: A critical review." *Chemosphere*, **241**, 125043. ISSN 00456535. doi: 10.1016/j.chemosphere.2019.125043. URL https://www.doi.org/10.1016/j.chemosphere.2019.125043.

Loftsson T, Másson M, Brewster ME (2004). "Self-Association of Cyclodextrins and Cyclodextrin Complexes." *J. Pharm. Sci.*, **93**(5), 1091–1099. ISSN 00223549. doi: 10.1002/jps.20047. URL https://doi.org/10.1002/jps.20047.

Loftsson T, Saokham P, Sá Couto AR (2019). "Self-association of cyclodextrins and cyclodextrin complexes in aqueous solutions." *Int. J. Pharm.*, **560**, 228–234. ISSN 03785173. doi: 10.1016/j.ijpharm.2019.02.004. URL https://doi.org/10.1016/j.ijpharm.2019.02.004.

Loh W, Brinatti C, Tam KC (2016). "Use of isothermal titration calorimetry to study surfactant aggregation in colloidal systems." *Biochim. Biophys. Acta - Gen. Subj.*, **1860**(5), 999–1016. ISSN 18728006. doi: 10.1016/j.bbagen.2015.10.003. URL https://www.doi.org/10.1016/j.bbagen.2015.10.003.

Lu JR, Su TJ, Thomas RK, Penfold J, Webster J (1998). "Structural conformation of lysozyme layers at the air/water interface studied by neutron reflection." *J. Chem. Soc. - Faraday Trans.*, **94**(21), 3279–3287. ISSN 09565000. doi: 10.1039/a805731a. URL https://www.doi.org/10.1039/a805731a.

Lucio D, Irache JM, Font M, Martínez-Ohárriz MC (2017). "Nanoaggregation of inclusion complexes of glibenclamide with cyclodextrins." *Int. J. Pharm.*, **519**(1-2), 263–271. ISSN 03785173. doi: 10.1016/j.ijpharm.2017.01.028. URL https://doi.org/10.1016/j.ijpharm.2017.01.028.

Luviano AS, Hernández-Pascacio J, Ondo D, Campbell RA, Piñeiro Á, Campos-Terán J, Costas M (2020). "Highly viscoelastic films at the water/air interface: α-Cyclodextrin with anionic surfactants." *J. Colloid Interface Sci.*, **565**, 601–613. ISSN 10957103. doi: 10.1016/j.jcis.2019.12.012. URL https://www.doi.org/10.1016/j.jcis.2019.12.012.

Lyklema H (2000). *Liquid-Fluid Interfaces*, volume 3. Press, Academic, London. ISBN 978-0-12-460523-7.

Lyklema J (1999). "The surface tension of pure liquids: Thermodynamic components and corresponding states." *Colloids Surfaces A Physicochem. Eng. Asp.*, **156**(1-3), 413–421. ISSN 0927-7757. doi: 10.1016/S0927-7757(99)00100-4. URL https://www.doi.org/10.1016/S0927-7757(99)00100-4.

Mahjoubin-Tehran M, Kovanen PT, Xu S, Jamialahmadi T, Sahebkar A (2020). "Cyclodextrins: Potential therapeutics against atherosclerosis." *Pharmacol. Ther.*, **214**, 107620. ISSN 01637258. doi: 10.1016/j.pharmthera.2020.107620. URL https://www.doi.org/10.1016/j.pharmthera.2020.107620.

Majhi PR, Blume A (2001). "Thermodynamic characterization of temperature-induced micellization and demicellization of detergents studied by differential scanning calorimetry." *Langmuir*, **17**(13), 3844–3851. ISSN 07437463. doi: 10.1021/la001660k. URL https://www.doi.org/10.1021/la001660k.

USC UNIVERSIDADE DE SANTIAGO DE COMPOSTELA

Mampallil D, Eral HB (2018). "A review on suppression and utilization of the coffee-ring effect." *Adv. Colloid Interface Sci.*, **252**, 38–54. ISSN 00018686. doi: 10.1016/j.cis.2017.12.008. URL https://www.doi.org/10.1016/j.cis.2017.12.008.

Marchand A, Weijs JH, Snoeijer JH, Andreotti B (2011). "Why is surface tension a force parallel to the interface?" *Am. J. Phys.*, **79**(10), 999. ISSN 0002-9505. doi: 10.1119/1.3619866. URL https://www.doi.org/10.1119/1.3619866.

Marison I, Liu JSS, Ampuero S, Von Stockar U, Schenker B (1998). "Biological reaction calorimetry: Development of high sensitivity bio-calorimeters." *Thermochim. Acta*, **309**(1-2), 157–173. ISSN 00406031. doi: 10.1016/S0040-6031(97)00424-3. URL https://www.doi.org/10.1016/S0040-6031(97)00424-3.

Markovich T, Andelman D, Podgornik R (2014). "Surface tension of electrolyte solutions: A self-consistent theory." *EPL (Europhysics Lett.*, **106**(1), 16002. ISSN 0295-5075. doi: 10.1209/0295-5075/106/16002. URL https://www.doi.org/10.1209/0295-5075/106/16002.

Marques HMC (2010). "A review on cyclodextrin encapsulation of essential oils and volatiles." *Flavour Fragr. J.*, **25**(5), 313–326. ISSN 08825734. doi: 10.1002/ffj.2019. URL https://www.doi.org/10.1002/ffj.2019.

Marsh D (2012). "Thermodynamics of Phospholipid Self-Assembly." *Biophys. J.*, **102**(5), 1079–1087. ISSN 00063495. doi: 10.1016/j.bpj.2012.01.049. URL https://www.doi.org/10.1016/j.bpj.2012.01.049.

Mathapa BG, Paunov VN (2013a). "Cyclodextrin stabilised emulsions and cyclodextrinosomes." *Phys. Chem. Chem. Phys.*, **15**(41), 17903. ISSN 1463-9076. doi: 10.1039/c3cp52116h. URL https://www.doi.org/10.1039/c3cp52116h.

Mathapa BG, Paunov VN (2013b). "Self-assembly of cyclodextrin-oil inclusion complexes at the oil-water interface: a route to surfactant-free emulsions." *J. Mater. Chem. A*, **1**(36), 10836. ISSN 2050-7488. doi: 10.1039/c3ta12108a. URL https://www.doi.org/10.1039/c3ta12108a.

Matilainen L, Larsen KL, Wimmer R, Keski-Rahkonen P, Auriola S, Järvinen T, Jarho P (2008). "The Effect of Cyclodextrins on Chemical and Physical Stability of Glucagon and Characterization of Glucagon/γ-CD Inclusion Complexes." *J. Pharm. Sci.*, **97**(7), 2720–2729. ISSN 00223549. doi: 10.1002/jps.21209. URL https://www.doi.org/10.1002/jps.21209.

McManus JJ, Charbonneau P, Zaccarelli E, Asherie N (2016). "The physics of protein self-assembly." *Curr. Opin. Colloid Interface Sci.*, **22**, 73–79. ISSN 13590294. doi: 10.1016/j.cocis.2016.02.011. URL https://www.doi.org/10.1016/j.cocis.2016.02.011.

McNaught AD, Wilkinson A (eds.) (1997). *IUPAC. Compendium of Chemical Terminology*. Blackwell Scientific Publications, Oxford, 2 edition. ISBN 0-9678550-9-8. doi: 10.1351/goldbook. URL https://www.doi.org/10.1351/goldbook.

Medeiros M, Marcos X, Velasco-Medina AA, Perez-Casas S, Gracia-Fadrique J (2018). "Micellization and adsorption modeling of single and mixed nonionic surfactants." *Colloids Surfaces A Physicochem. Eng. Asp.*, **556**(June), 81–92. ISSN 18734359. doi: 10.1016/j.colsurfa.2018.08.005. URL https://www.doi.org/10.1016/j.colsurfa.2018.08.005.

Medoš Ž, Bešter-Rogač M (2017). "Two-Step Micellization Model: The Case of Long-Chain Carboxylates in Water." *Langmuir*, **33**(31), 7722–7731. ISSN 15205827. doi: 10.1021/acs.langmuir.7b01700. URL https://www.doi.org/10.1021/acs.langmuir.7b01700.

Medoš Ž, Friesen S, Buchner R, Bešter-Rogač M (2020). "Interplay between aggregation number, micelle charge and hydration of catanionic surfactants." *Phys. Chem. Chem. Phys.*, **22**(18), 9998–10009. ISSN 14639076. doi: 10.1039/d0cp00877j. URL https://www.doi.org/10.1039/d0cp00877j.

Meier GH (2014). "Introduction to surface quantities." In "Thermodyn. Surfaces Interfaces," pp. 40–72. Cambridge University Press, Cambridge. ISBN 9781139047029. doi: 10.1017/CBO9781139047029.003. URL https://www.doi.org/10.1017/CBO9781139047029.003.

Meira LH, Soares GA, Bonomini HI, Lopes JF, De Sousa FB (2018). "Thermodynamic compatibility between cyclodextrin supramolecular complexes and surfactant." *Int. J. Pharm.*, **544**(1), 203–212. ISSN 03785173. doi: 10.1016/j.ijpharm.2018.04.036. URL https://www.doi.org/10.1016/j.ijpharm.2018.04.036.

Mendes AC, Baran ET, Reis RL, Azevedo HS (2013). "Self-assembly in nature: Using the principles of nature to create complex nanobiomaterials." *Wiley Interdiscip. Rev. Nanomedicine Nanobiotechnology*, **5**(6), 582–612. doi: 10.1002/WNAN.1238. URL https://www.doi.org/10.1002/WNAN.1238.

Meschel SV (2020). "A brief history of heat measurements by calorimetry with emphasis on the thermochemistry of metallic and metal-nonmetal compounds." *Calphad*, **68**, 101714. ISSN 03645916. doi: 10.1016/j.calphad.2019.101714. URL https://www.doi.org/10.1016/j.calphad.2019.101714.

Messner M, Kurkov SV, Brewster ME, Jansook P, Loftsson T (2011a). "Self-assembly of cyclodextrin complexes: Aggregation of hydrocortisone/cyclodextrin complexes." *Int. J. Pharm.*, **407**(1-2), 174–183. ISSN 03785173. doi: 10.1016/j.ijpharm.2011.01.011. URL https://doi.org/10.1016/j.ijpharm.2011.01.011.

Messner M, Kurkov SV, Jansook P, Loftsson T (2010). "Self-assembled cyclodextrin aggregates and nanoparticles." *Int. J. Pharm.*, **387**(1-2), 199–208. ISSN 03785173. doi: 10.1016/j.ijpharm.2009.11.035. URL https://doi.org/10.1016/j.ijpharm.2009.11.035.

Messner M, Kurkov SV, Palazón MM, Fernández BÁ, Brewster ME, Loftsson T (2011b). "Self-assembly of cyclodextrin complexes: Effect of temperature, agitation and media composition on aggregation." *Int. J. Pharm.*, **419**(1-2), 322–328. ISSN 03785173. doi: 10.1016/j.ijpharm.2011.07.041. URL https://doi.org/10.1016/j.ijpharm.2011.07.041.

USC UNIVERSIDADE DE SANTIAGO DE COMPOSTELA

Meurer A, Smith CP, Paprocki M, Čertík O, Kirpichev SB, Rocklin M, Kumar A, Ivanov S, Moore JK, Singh S, Rathnayake T, Vig S, Granger BE, Muller RP, Bonazzi F, Gupta H, Vats S, Johansson F, Pedregosa F, Curry MJ, Terrel AR, Roučka Š, Saboo A, Fernando I, Kulal S, Cimrman R, Scopatz A (2017). "SymPy: symbolic computing in Python." *PeerJ Comput. Sci.*, **3**(1), e103. ISSN 2376-5992. doi: 10.7717/PEERJ-CS.103. URL https://www.doi.org/10.7717/PEERJ-CS.103.

Michaud-Agrawal N, Denning EJ, Woolf TB, Beckstein O (2011). "MDAnalysis: A toolkit for the analysis of molecular dynamics simulations." *J. Comput. Chem.*, **32**(10), 2319–2327. ISSN 01928651. doi: 10.1002/jcc.21787. URL https://www.doi.org/10.1002/jcc.21787.

Mixcoha E, Campos-Terán J, Piñeiro Á (2014). "Surface Adsorption and Bulk Aggregation of Cyclodextrins by Computational Molecular Dynamics Simulations as a Function of Temperature: α-CD vs β-CD." *J. Phys. Chem. B*, **118**(25), 6999–7011. ISSN 1520-6106. doi: 10.1021/jp412533b. URL https://doi.org/10.1021/jp412533b.

Möbius D, Miller R (eds.) (1998a). *Drops and bubbles in interfacial research*, volume 6. Elsevier Science B.V, Amsterdam. ISBN 9780444828941.

Möbius D, Miller R (eds.) (1998b). *Proteins at liquid interfaces*. Elsevier Science B. V., Amsterdam. ISBN 9780444829443.

Moroi Y (1992). *Micelles*. Springer US, Boston, MA. ISBN 978-1-4899-0702-8. doi: 10.1007/978-1-4899-0700-4. URL https://www.doi.org/10.1007/978-1-4899-0700-4.

Mtaweh H, Tuira L, Floh AA, Parshuram CS (2018). "Indirect Calorimetry: History, Technology, and Application." *Front. Pediatr.*, **6**, 257. ISSN 2296-2360. doi: 10.3389/fped.2018.00257. URL https://www.doi.org/10.3389/fped.2018.00257.

Muankaew C, Saokham P, Jansook P, Loftsson T (2020). "Self-assembly of cyclodextrin complexes: Detection, obstacles and benefits." *Pharmazie*, **75**(7), 307–312. ISSN 00317144. doi: 10.1691/ph.2020.0405. URL https://doi.org/10.1691/ph.2020.0405.

Muller B, Brauns U (1985). "Solubilization of drugs by modified β-cyclodextrins." *Int. J. Pharm.*, **26**(1-2), 77–88. ISSN 03785173. doi: 10.1016/0378-5173(85)90201-7. URL https://doi.org/10.1016/0378-5173(85)90201-7.

Mulligan CN (2005). "Environmental applications for biosurfactants." *Environ. Pollut.*, **133**(2), 183–198. ISSN 02697491. doi: 10.1016/j.envpol.2004.06.009. URL https://www.doi.org/10.1016/j.envpol.2004.06.009.

Muñoz E, Piñeiro A (2018). "AFFINImeter Software: from its Beginnings to Future Trends- A Literature review." *J. Appl. Bioanal.*, **4**(4), 124–139. ISSN 2405710X. doi: 10.17145/jab.18.017. URL https://www.doi.org/10.17145/jab.18.017.

Muñoz E, Sabín J, Rial J, Pérez D, Ennifar E, Dumas P, Piñeiro Á (2019). "Thermodynamic and Kinetic Analysis of Isothermal Titration Calorimetry Experiments by Using KinITC in AFFINImeter." In "Methods Mol. Biol.", volume

1964, pp. 225–239. Methods Mol Biol. doi: 10.1007/978-1-4939-9179-2_16. URL https://www.doi.org/10.1007/978-1-4939-9179-2_16.

Nakagawa T, Ueno K, Kashiwa M, Watanabe J (1994). "The stereoselective synthesis of cyclomaltopentaose. A novel cyclodextrin homologue with D.P. five." *Tetrahedron Lett.*, **35**(12), 1921–1924. ISSN 00404039. doi: 10.1016/S0040-4039(00)73196-0. URL https://www.doi.org/10.1016/S0040-4039(00)73196-0.

Nash T (2017). "The Role of Entropy in Molecular Self-Assembly." *J. Nanomedicine Res.*, **5**(4). doi: 10.15406/jnmr.2017.05.00126. URL https://www.doi.org/10.15406/jnmr.2017.05.00126.

Okhrimenko O, Jelesarov I (2008). "A survey of the year 2006 literature on applications of isothermal titration calorimetry." *J. Mol. Recognit.*, **21**(1), 1–19. ISSN 1099-1352. doi: 10.1002/JMR.859. URL https://www.doi.org/10.1002/JMR.859.

Olesen NE, Holm R, Westh P (2014). "Determination of the aggregation number for micelles by isothermal titration calorimetry." *Thermochim. Acta*, **588**, 28–37. ISSN 00406031. doi: 10.1016/j.tca.2014.04.028. URL https://www.doi.org/10.1016/j.tca.2014.04.028.

Ondo D, Costas M (2017). "Complexation thermodynamics of α-cyclodextrin with ionic surfactants in water." *J. Colloid Interface Sci.*, **505**, 445–453. ISSN 10957103. doi: 10.1016/j.jcis.2017.05.093. URL https://www.doi.org/10.1016/j.jcis.2017.05.093.

Pais JM, Pereira B, Paz FAA, Cardoso SM, Braga SS (2020). "Solid γ-Cyclodextrin Inclusion Compound with Gingerols, a Multi-Component Guest: Preparation, Properties and Application in Yogurt." *Biomolecules*, **10**(2), 344. ISSN 2218-273X. doi: 10.3390/biom10020344. URL https://www.doi.org/10.3390/biom10020344.

Patel M, Hirlekar R (2019). "Multicomponent cyclodextrin system for improvement of solubility and dissolution rate of poorly water soluble drug." *Asian J. Pharm. Sci.*, **14**(1), 104–115. ISSN 18180876. doi: 10.1016/j.ajps.2018.02.007. URL https://www.doi.org/10.1016/j.ajps.2018.02.007.

Pechlaner M, Oostenbrink C, van Gunsteren WF (2021). "On the use of multiple-time-step algorithms to save computing effort in molecular dynamics simulations of proteins." *J. Comput. Chem.*, **42**(18), 1263–1282. ISSN 1096-987X. doi: 10.1002/JCC.26541. URL https://doi.org/10.1002/JCC.26541.

Pellicer J, Manzanares JA, Mafé S (1995). "The physical description of elementary surface phenomena: Thermodynamics versus mechanics." *Am. J. Phys.*, **63**(6), 542–547. ISSN 0002-9505. doi: 10.1119/1.17866. URL https://www.doi.org/10.1119/1.17866.

Perspicace S, Rufer AC, Thoma R, Mueller F, Hennig M, Ceccarelli S, Schulz-Gasch T, Seelig J (2013). "Isothermal titration calorimetry with micelles: Thermodynamics of inhibitor binding to carnitine palmitoyltransferase 2 membrane protein." *FEBS Open Bio*, **3**(1), 204–211. ISSN 22115463. doi: 10.1016/j.fob.2013.04.003. URL https://www.doi.org/10.1016/j.fob.2013.04.003.

USC UNIVERSIDADE DE SANTIAGO DE COMPOSTELA

Piñeiro Á, Muñoz E, Sabín J, Costas M, Bastos M, Velázquez-Campoy A, Garrido PF, Dumas P, Ennifar E, García-Río L, Rial J, Pérez D, Fraga P, Rodríguez A, Cotelo C (2019). "AFFINImeter: A software to analyze molecular recognition processes from experimental data." *Anal. Biochem.*, **577**, 117–134. ISSN 00032697. doi: 10.1016/j.ab.2019.02.031. URL https://www.doi.org/10.1016/j.ab.2019.02.031.

Pitha J, Milecki J, Fales H, Pannell L, Uekama K (1986). "Hydroxypropyl-β-cyclodextrin: preparation and characterization; effects on solubility of drugs." *Int. J. Pharm.*, **29**(1), 73–82. ISSN 03785173. doi: 10.1016/0378-5173(86)90201-2. URL https://doi.org/10.1016/0378-5173(86)90201-2.

Polarz S, Smarsly B, Bronstein L, Antonietti M (2001). "From Cyclodextrin Assemblies to Porous Materials by Silica Templating We thank the Max-Planck society for funding." *Angew. Chemie Int. Ed.*, **40**(23), 4417. ISSN 14337851. doi: 10.1002/1521-3773(20011203)40:23<4417::AID-ANIE4417>3.0.CO;2-P. URL https://doi.org/10.1002/1521-3773(20011203)40:23{%}3C4417::AID-ANIE4417{%}3E3.0.CO;2-P.

Popielec A, Loftsson T (2017). "Effects of cyclodextrins on the chemical stability of drugs." *Int. J. Pharm.*, **531**(2), 532–542. ISSN 03785173. doi: 10.1016/j.ijpharm.2017.06.009. URL https://www.doi.org/10.1016/j.ijpharm.2017.06.009.

Press W, Teukolsky S, Vetterling W, Flannery B (1992). *Numerical recipes in C: The art of scientific computing*. Cambridge University Press, New York.

Probstein RF (1994). *Physicochemical Hydrodynamics*. John Wiley & Sons, Inc., Hoboken, NJ, USA. ISBN 9780471725138. doi: 10.1002/0471725137. URL https://www.doi.org/10.1002/0471725137.

Puskás I, Schrott M, Malanga M, Szente L (2013). "Characterization and control of the aggregation behavior of cyclodextrins." *J. Incl. Phenom. Macrocycl. Chem.*, **75**(3-4), 269–276. ISSN 0923-0750. doi: 10.1007/s10847-012-0127-7. URL http://doi.org/10.1007/s10847-012-0127-7.

Quinn CF, Carpenter MC, Croteau ML, Wilcox DE (2016). "Isothermal Titration Calorimetry Measurements of Metal Ions Binding to Proteins." In "Calorim. (Methods Enzymol.", volume 567, pp. 3–21. Elsevier Inc., 1 edition. doi: 10.1016/bs.mie.2015.08.021. URL https://www.doi.org/10.1016/bs.mie.2015.08.021.

Radke CJ (2015). "Gibbs adsorption equation for planar fluid-fluid interfaces: Invariant formalism." *Adv. Colloid Interface Sci.*, **222**, 600–614. ISSN 0001-8686. doi: 10.1016/J.CIS.2014.01.001. URL https://www.doi.org/10.1016/J.CIS.2014.01.001.

Rapaport DC (2004). *The Art of Molecular Dynamics Simulation*. Cambridge University Press, Cambridge, UK. ISBN 9780521825689. doi: 10.1017/CBO9780511816581. URL https://www.doi.org/10.1017/CBO9780511816581.

Reback J, McKinney W, Jbrockmendel, den Bossche JV, Augspurger T, Cloud P, Gfyoung, Sinhrks, Klein A, Roeschke M, Hawkins S, Tratner J, She C, Ayd

W, Petersen T, Garcia M, Schendel J, Hayden A, MomIsBestFriend, Jancauskas V, Battiston P, Seabold S, Chris-b1, H-vetinari, Hoyer S, Overmeire W, Alimcmaster1, Dong K, Whelan C, Mehyar M (2020). "pandas-dev/pandas: Pandas 1.0.3." *Zenodo*. doi: 10.5281/ZENODO.3715232. URL https://www.doi.org/10.5281/ZENODO.3715232.

Reißer S, Poger D, Stroet M, Mark AE (2017). "Real Cost of Speed: The Effect of a Time-Saving Multiple-Time-Stepping Algorithm on the Accuracy of Molecular Dynamics Simulations." *J. Chem. Theory Comput.*, **13**(6), 2367–2372. doi: 10.1021/ACS.JCTC.7B00178. URL https://doi.org/10.1021/acs.jctc.7b00178.

Rekharsky MV, Inoue Y (1998). "Complexation Thermodynamics of Cyclodextrins." *Chem. Rev.*, **98**(5), 1875–1918. ISSN 0009-2665. doi: 10.1021/cr970015o. URL https://www.doi.org/10.1021/cr970015o.

Rocha BC, Paul S, Vashisth H (2020). "Role of entropy in colloidal self-assembly." *Entropy*, **22**(8). ISSN 10994300. doi: 10.3390/E22080877. URL https://www.doi.org/10.3390/E22080877.

Rodríguez Niño MR, Rodríguez Patino JM (1998). "Surface tension of bovine serum albumin and tween 20 at the air-aqueous interface." *JAOCS, J. Am. Oil Chem. Soc.*, **75**(10), 1241–1248. ISSN 0003021X. doi: 10.1007/s11746-998-0169-6. URL https://www.doi.org/10.1007/s11746-998-0169-6.

Rosen MJ, Kunjappu JT (2012). *Surfactants and Interfacial Phenomena*. John Wiley & Sons, Inc., Hoboken, NJ, USA. ISBN 9781118228920. doi: 10.1002/9781118228920. URL https://www.doi.org/10.1002/9781118228920.

Ruthven DM (2001). "Adsorption, Fundamentals." In "Kirk-Othmer Encycl. Chem. Technol.", volume 1. John Wiley & Sons, Inc., Hoboken, NJ, USA. doi: 10.1002/0471238961.0104191518212008.a01.pub2. URL https://www.doi.org/10.1002/0471238961.0104191518212008.a01.pub2.

Ryzhakov A, Do Thi T, Stappaerts J, Bertoletti L, Kimpe K, Sá Couto AR, Saokham P, Van den Mooter G, Augustijns P, Somsen GW, Kurkov S, Inghelbrecht S, Arien A, Jimidar MI, Schrijnemakers K, Loftsson T (2016). "Self-Assembly of Cyclodextrins and Their Complexes in Aqueous Solutions." *J. Pharm. Sci.*, **105**(9), 2556–2569. ISSN 00223549. doi: 10.1016/j.xphs.2016.01.019. URL https://doi.org/10.1016/j.xphs.2016.01.019.

Sá Couto AR, Ryzhakov A, Loftsson T (2018). "Self-Assembly of α-Cyclodextrin and β-Cyclodextrin: Identification and Development of Analytical Techniques." *J. Pharm. Sci.*, **107**(8), 2208–2215. ISSN 00223549. doi: 10.1016/j.xphs.2018.03.028. URL https://doi.org/10.1016/j.xphs.2018.03.028.

Saha S, Roy A, Roy K, Roy MN (2016). "Study to explore the mechanism to form inclusion complexes of β-cyclodextrin with vitamin molecules." *Sci. Rep.*, **6**(1), 35764. ISSN 2045-2322. doi: 10.1038/srep35764. URL https://www.doi.org/10.1038/srep35764.

Sajomsang W, Gonil P, Ruktanonchai UR, Pimpha N, Sramala I, Nuchuchua O, Saesoo S, Chaleawlert-umpon S, Puttipipatkhachorn S (2011). "Self-aggregates

USC UNIVERSIDADE DE SANTIAGO DE COMPOSTELA

formation and mucoadhesive property of water-soluble β-cyclodextrin grafted with chitosan." *Int. J. Biol. Macromol.*, **48**(4), 589–595. ISSN 01418130. doi: 10.1016/j.ijbiomac.2011.01.028. URL https://doi.org/10.1016/j.ijbiomac.2011.01.028.

Samuelsen L, Holm R, Lathuile A, Schönbeck C (2019). "Correlation between the stability constant and pH for β-cyclodextrin complexes." *Int. J. Pharm.*, **568**, 118523. doi: 10.1016/j.ijpharm.2019.118523. URL https://doi.org/10.1016/j.ijpharm.2019.118523.

Šarac B, Medoš Ž, Cognigni A, Bica K, Chen LJ, Bešter-Rogač M (2017). "Thermodynamic study for micellization of imidazolium based surface active ionic liquids in water: Effect of alkyl chain length and anions." *Colloids Surfaces A Physicochem. Eng. Asp.*, **532**, 609–617. ISSN 09277757. doi: 10.1016/j.colsurfa.2017.01.062. URL https://www.doi.org/10.1016/j.colsurfa.2017.01.062.

Schlossman ML (2002). "Liquid-liquid interfaces: Studied by X-ray and neutron scattering." *Curr. Opin. Colloid Interface Sci.*, **7**(3-4), 235–243. ISSN 13590294. doi: 10.1016/S1359-0294(02)00053-5. URL https://www.doi.org/10.1016/S1359-0294(02)00053-5.

Schönbeck C, Holm R (2019). "Exploring the Origins of Enthalpy-Entropy Compensation by Calorimetric Studies of Cyclodextrin Complexes." *J. Phys. Chem. B*, **123**(31), 6686–6693. ISSN 1520-6106. doi: 10.1021/acs.jpcb.9b03393. URL https://www.doi.org/10.1021/acs.jpcb.9b03393.

Schramm LL, Stasiuk EN, Marangoni DG (2003). "Surfactants and their applications." *Annu. Rep. Prog. Chem., Sect. C Phys. Chem.*, **99**, 3–48. ISSN 0260-1826. doi: 10.1039/B208499F. URL https://www.doi.org/10.1039/B208499F.

Shen Y, Li M, Liu T, Liu J, Xie Y, Zhang J, Xu S, Liu H (2019). "A dual-functional HER2 aptamer-conjugated, pH-activated mesoporous silica nanocarrier-based drug delivery system provides in vitro synergistic cytotoxicity in HER2-positive breast cancer cells." *Int. J. Nanomedicine*, **Volume 14**, 4029–4044. ISSN 1178-2013. doi: 10.2147/IJN.S201688. URL https://www.doi.org/10.2147/IJN.S201688.

Snoeijer JH, Andreotti B (2008). "A microscopic view on contact angle selection." *Phys. Fluids*, **20**(5), 57101. ISSN 1070-6631. doi: 10.1063/1.2913675. URL https://www.doi.org/10.1063/1.2913675.

Spoel DVD, Lindahl E, Hess B, Groenhof G, Mark AE, Berendsen HJC (2005). "GROMACS: Fast, flexible, and free." *J. Comput. Chem.*, **26**(16), 1701–1718. ISSN 1096-987X. doi: 10.1002/JCC.20291. URL https://www.doi.org/10.1002/JCC.20291.

Spyder collective (2021). "Spyder." URL https://www.spyder-ide.org/.

Stensgaard Diget J, Lund R, Nyström B, Wintgens V, Amiel C, Wimmer R, Terndrup Nielsen T (2019). "Self-assembled nanoparticles based on cyclodextrin-modified pullulan: Synthesis, and structural characterization using SAXS." *Carbohydr. Polym.*, **213**, 403–410. ISSN 01448617. doi: 10.1016/j.carbpol.2019.01.106. URL https://www.doi.org/10.1016/j.carbpol.2019.01.106.

Subramani K, Ahmed W (2018). "Self-assembly of proteins and peptides and their applications in bionanotechnology and dentistry." In "Emerg. Nanotechnologies Dent.", pp. 231–249. Elsevier. doi: 10.1016/B978-0-12-812291-4.00012-1. URL https://www.doi.org/10.1016/B978-0-12-812291-4.00012-1.

Suurkuusk J, Suurkuusk M, Vikegard P (2016). "An Odyssey in Calorimetric Development." In M Bastos (ed.), "Biocalorimetry Found. Contemp. Approaches," pp. 62–78. CRC Press, Boca Raton. ISBN 9780429171918.

Sychev VV (1973). *Complex Thermodynamic Systems*. Springer US, Boston, MA. ISBN 978-1-4684-1607-7. doi: 10.1007/978-1-4684-1605-3. URL https://www.doi.org/10.1007/978-1-4684-1605-3.

Szejtli J (1988). *Cyclodextrin Technology*, volume 1 of *Topics in Inclusion Science*. Springer Netherlands, Dordrecht. ISBN 978-90-481-8427-9. doi: 10.1007/978-94-015-7797-7. URL https://www.doi.org/10.1007/978-94-015-7797-7.

Szejtli J (1998). "Introduction and General Overview of Cyclodextrin Chemistry." *Chem. Rev.*, **98**(5), 1743–1754. ISSN 0009-2665. doi: 10.1021/cr970022c. URL https://www.doi.org/10.1021/cr970022c.

Szejtli J (2004). "Past, present, and future of cyclodextrin research." *Pure Appl. Chem.*, **76**(10), 1825–1845. ISSN 00334545. doi: 10.1351/pac200476101825. URL https://www.doi.org/10.1351/pac200476101825.

Szente E, Szejtli J, Kis GL (1998). "Spontaneous opalescence of aqueous γ-cyclodextrin solutions: Complex formation or self-aggregation?" *J. Pharm. Sci.*, **87**(6), 778–781. ISSN 00223549. doi: 10.1021/js9704341.

Takeda Y, Matsuo I (2014). "Isothermal Calorimetric Analysis of Lectin-Sugar Interaction." In J Hirabayashi (ed.), "Lectins. Methods Mol. Biol. (Methods Protoc.", volume 1200 of *Methods in Molecular Biology*, pp. 207–214. Springer New York, New York, NY. ISBN 978-1-4939-1291-9. doi: 10.1007/978-1-4939-1292-6_18. URL https://www.doi.org/10.1007/978-1-4939-1292-6_18.

Tanford C (1978). "The hydrophobic effect and the organization of living matter." *Science*, **200**(4345), 1012–1018. ISSN 00368075. doi: 10.1126/science.653353. URL http://doi.org/10.1126/science.653353.

Tanford C (1980). *The hydrophobic effect : formation of micelles and biological membranes*. John Wiley & Sons, New York, 2 edition.

Thanassoulas A, Nounesis G (2019). "Isothermal Titration Calorimetry: A Powerful Tool for the Characterization of Molecular Interactions." In C Demetzos, N Pippa (eds.), "Thermodyn. Biophys. Biomed. Nanosyst. Ser. Bioeng.", pp. 63–103. Springer, Singapore. doi: 10.1007/978-981-13-0989-2_4. URL https://www.doi.org/10.1007/978-981-13-0989-2_4.

Thomson JA, Ladbury JE (2005). "Isothermal Titration Calorimetry: A Tutorial." In "Biocalorimetry 2 Appl. Calorim. Biol. Sci.", pp. 35–58. John Wiley & Sons, Ltd, Chichester, UK. doi: 10.1002/0470011122.ch2. URL https://www.doi.org/10.1002/0470011122.ch2.

USC UNIVERSIDADE DE SANTIAGO DE COMPOSTELA

Tihonov M, Milyaeva O, Noskov B (2015). "Dynamic surface properties of lysozyme solutions. Impact of urea and guanidine hydrochloride." *Colloids Surfaces B Biointerfaces*, **129**, 114–120. ISSN 09277765. doi: 10.1016/j.colsurfb.2015.03.034. URL https://www.doi.org/10.1016/j.colsurfb.2015.03.034.

Tomeček J, Čablová A, Hromádková A, Novotný J, Marek R, Durník I, Kulhánek P, Prucková Z, Rouchal M, Dastychová L, Vícha R (2021). "Modes of Micromolar Host-Guest Binding of β-Cyclodextrin Complexes Revealed by NMR Spectroscopy in Salt Water." *J. Org. Chem.*, **86**(6), 4483–4496. ISSN 0022-3263. doi: 10.1021/acs.joc.0c02917. URL https://www.doi.org/10.1021/acs.joc.0c02917.

Uchegbu IF, Florence AT (1995). "Non-ionic surfactant vesicles (niosomes): Physical and pharmaceutical chemistry." *Adv. Colloid Interface Sci.*, **58**(1), 1–55. ISSN 00018686. doi: 10.1016/0001-8686(95)00242-I. URL https://www.doi.org/10.1016/0001-8686(95)00242-I.

Uekama K (2004). "Design and Evaluation of Cyclodextrin-Based Drug Formulation." *Chem. Pharm. Bull.*, **52**(8), 900–915. ISSN 0009-2363. doi: 10.1248/cpb.52.900. URL https://www.doi.org/10.1248/cpb.52.900.

Uskoković V (2008). "Isn't self-assembly a misnomer? Multi-disciplinary arguments in favor of co-assembly." *Adv. Colloid Interface Sci.*, **141**(1-2), 37–47. ISSN 0001-8686. doi: 10.1016/J.CIS.2008.02.004. URL https://www.doi.org/10.1016/J.CIS.2008.02.004.

Van Der Walt S, Schönberger JL, Nunez-Iglesias J, Boulogne F, Warner JD, Yager N, Gouillart E, Yu T (2014). "Scikit-image: Image processing in python." *PeerJ*, **2014**(1). ISSN 21678359. doi: 10.7717/peerj.453. arXiv:1407.6245v1, URL https://www.doi.org/10.7717/peerj.453.

Varga M (2016). "Self-assembly of nanobiomaterials." In "Fabr. Self-Assembly Nanobiomaterials," pp. 57–90. Elsevier. doi: 10.1016/B978-0-323-41533-0.00003-9. URL https://www.doi.org/10.1016/B978-0-323-41533-0.00003-9.

Vargas C, Schönbeck C, Heimann I, Keller S (2018). "Extracavity Effect in Cyclodextrin/Surfactant Complexation." *Langmuir*, **34**(20), 5781–5787. ISSN 0743-7463. doi: 10.1021/acs.langmuir.8b00682. URL https://www.doi.org/10.1021/acs.langmuir.8b00682.

Vázquez-Tato MP, Meijide F, Seijas JA, Fraga F, Vázquez Tato J (2018). "Analysis of an old controversy: The compensation temperature for micellization of surfactants." *Adv. Colloid Interface Sci.*, **254**, 94–98. ISSN 00018686. doi: 10.1016/j.cis.2018.03.003. URL https://www.doi.org/10.1016/j.cis.2018.03.003.

Velázquez-Campoy A, Ohtaka H, Nezami A, Muzammil S, Freire E (2004). "Isothermal Titration Calorimetry." *Curr. Protoc. Cell Biol.*, **23**(1), 085201. ISSN 1934-2500. doi: 10.1002/0471143030.cb1708s23. 1011.1669, URL https://www.doi.org/10.1002/0471143030.cb1708s23.

Vella D, Mahadevan L (2005). "The "Cheerios effect "." *Am. J. Phys.*, **73**(9), 817–825. ISSN 0002-9505. doi: 10.1119/1.1898523. URL https://www.doi.org/10.1119/1.1898523.

USC UNIVERSIDADE DE SANTIAGO

Villiers A (1891). "Sur la fermentation de la fécule par láction du ferment butyrique." *Compt. Rend. Acad. Sci*, **112**, 536–538.

Virtanen P, Gommers R, Oliphant TE, Haberland M, Reddy T, Cournapeau D, Burovski E, Peterson P, Weckesser W, Bright J, van der Walt SJ, Brett M, Wilson J, Millman KJ, Mayorov N, Nelson ARJ, Jones E, Kern R, Larson E, Carey CJ, Polat I, Feng Y, Moore EW, VanderPlas J, Laxalde D, Perktold J, Cimrman R, Henriksen I, Quintero EA, Harris CR, Archibald AM, Ribeiro AH, Pedregosa F, van Mulbregt P, Vijaykumar A, Bardelli AP, Rothberg A, Hilboll A, Kloeckner A, Scopatz A, Lee A, Rokem A, Woods CN, Fulton C, Masson C, Häggström C, Fitzgerald C, Nicholson DA, Hagen DR, Pasechnik DV, Olivetti E, Martin E, Wieser E, Silva F, Lenders F, Wilhelm F, Young G, Price GA, Ingold GL, Allen GE, Lee GR, Audren H, Probst I, Dietrich JP, Silterra J, Webber JT, Slavič J, Nothman J, Buchner J, Kulick J, Schönberger JL, de Miranda Cardoso JV, Reimer J, Harrington J, Rodríguez JLC, Nunez-Iglesias J, Kuczynski J, Tritz K, Thoma M, Newville M, Kümmerer M, Bolingbroke M, Tartre M, Pak M, Smith NJ, Nowaczyk N, Shebanov N, Pavlyk O, Brodtkorb PA, Lee P, McGibbon RT, Feldbauer R, Lewis S, Tygier S, Sievert S, Vigna S, Peterson S, More S, Pudlik T, Oshima T, Pingel TJ, Robitaille TP, Spura T, Jones TR, Cera T, Leslie T, Zito T, Krauss T, Upadhyay U, Halchenko YO, Vázquez-Baeza Y (2020). "SciPy 1.0: fundamental algorithms for scientific computing in Python." *Nat. Methods*, **17**(3), 261–272. ISSN 1548-7091. doi: 10.1038/s41592-019-0686-2. 1907.10121, URL https://www.doi.org/10.1038/s41592-019-0686-2.

Wang H, Wagner JC, Chen W, Wang C, Xiong W (2020). "Spatially dependent H-bond dynamics at interfaces of water/biomimetic self-assembled lattice materials." *Proc. Natl. Acad. Sci. U. S. A.*, **117**(38), 23385–23392. ISSN 10916490. doi: 10.1073/pnas.2001861117. URL https://www.doi.org/10.1073/pnas.2001861117.

Wankar J, Kotla NG, Gera S, Rasala S, Pandit A, Rochev YA (2020). "Recent Advances in Host-Guest Self-Assembled Cyclodextrin Carriers: Implications for Responsive Drug Delivery and Biomedical Engineering." *Adv. Funct. Mater.*, **30**(44), 1909049. ISSN 1616-301X. doi: 10.1002/adfm.201909049. URL https://www.doi.org/10.1002/adfm.201909049.

Warrington SB, Höhne GWH (2008). "Thermal Analysis and Calorimetry." In "Ullmann's Encycl. Ind. Chem.", Wiley-VCH Verlag GmbH & Co. KGaA, Weinheim, Germany. doi: 10.1002/14356007.b06_001.pub3. URL https://www.doi.org/10.1002/14356007.b06_001.pub3.

Weijs JH, Snoeijer JH, Andreotti B (2014). "Capillarity of soft amorphous solids: A microscopic model for surface stress." *Phys. Rev. E*, **89**(4), 042408. ISSN 1539-3755. doi: 10.1103/PhysRevE.89.042408. URL https://www.doi.org/10.1103/PhysRevE.89.042408.

Wen X, Franses EI (2001). "Adsorption of bovine serum albumin at the air/water interface and its effect on the formation of DPPC surface film." *Colloids Surfaces A Physicochem. Eng. Asp.*, **190**(3), 319–332. ISSN 09277757. doi: 10.1016/S0927-7757(01)00596-9. URL https://www.doi.org/10.1016/S0927-7757(01)00596-9.

USC UNIVERSIDADE DE SANTIAGO DE COMPOSTELA

Whitesides GM, Boncheva M (2002). "Beyond molecules: Self-assembly of mesoscopic and macroscopic components." *Proc. Natl. Acad. Sci.*, **99**(8), 4769–4774. ISSN 0027-8424. doi: 10.1073/PNAS.082065899. URL https://www.doi.org/10.1073/PNAS.082065899.

Wilhelm E, Letcher T (eds.) (2017). *Enthalpy and Internal Energy*. Royal Society of Chemistry, Cambridge. ISBN 978-1-78262-711-1. doi: 10.1039/9781788010214. URL https://www.doi.org/10.1039/9781788010214.

Wiseman T, Williston S, Brandts JF, Lin LN (1989). "Rapid measurement of binding constants and heats of binding using a new titration calorimeter." *Anal. Biochem.*, **179**(1), 131–137. ISSN 10960309. doi: 10.1016/0003-2697(89)90213-3. URL https://www.doi.org/10.1016/0003-2697(89)90213-3.

Wolkenstein MV (1983). *General Biophysics*, volume I. Elsevier. ISBN 9780127230016. doi: 10.1016/B978-0-12-723001-6.X5001-1. URL https://www.doi.org/10.1016/B978-0-12-723001-6.X5001-1.

Wszelaka-Rylik M, Gierycz P (2015). "Isothermal titration calorimetry (ITC) study of natural cyclodextrins inclusion complexes with tropane alkaloids." *J. Therm. Anal. Calorim.*, **121**(3), 1359–1364. ISSN 1388-6150. doi: 10.1007/s10973-015-4658-1. URL https://www.doi.org/10.1007/s10973-015-4658-1.

Wu A, Shen X, He Y (2006). "Investigation on γ-cyclodextrin nanotube induced by -diphenylbenzidine molecule." *J. Colloid Interface Sci.*, **297**(2), 525–533. ISSN 00219797. doi: 10.1016/j.jcis.2005.11.014. URL https://doi.org/10.1016/J.JCIS.2005.11.014.

Xavier-Júnior F, Tavares C, Rabello M, Hernandes M, Bezerra B, Ayala A, Pessoa O, Ximenes R, Santos-Magalhães N (2019). "Elucidation of the mechanism of complexation between oncocalyxone A and cyclodextrins by isothermal titration calorimetry and molecular modeling." *J. Mol. Liq.*, **274**, 165–172. ISSN 01677322. doi: 10.1016/j.molliq.2018.10.129. URL https://www.doi.org/10.1016/j.molliq.2018.10.129.

Yang LP, Keam SJ (2009). "Sugammadex." *Drugs*, **69**(7), 919–942. ISSN 0012-6667. doi: 10.2165/00003495-200969070-00008. URL https://doi.org/10.2165/00003495-200969070-00008.

Yang S, Yan Y, Huang J, Petukhov AV, Kroon-Batenburg LMJ, Drechsler M, Zhou C, Tu M, Granick S, Jiang L (2017). "Giant capsids from lattice self-assembly of cyclodextrin complexes." *Nat. Commun.*, **8**(1), 15856. ISSN 2041-1723. doi: 10.1038/ncomms15856. URL https://www.doi.org/10.1038/ncomms15856.

Yun M, Park C, Lee J, Kim C (2010). "Self-assembled dendron nanotubes: Surface functionalization with maltosyl units and their reversible complexation with Concanavalin A." *J. Polym. Sci. Part A Polym. Chem.*, **48**(3), 730–734. ISSN 0887624X. doi: 10.1002/pola.23801. URL https://www.doi.org/10.1002/pola.23801.

Zaman H, Bright AG, Adams K, Goodall DM, Forbes RT (2017). "Characterisation of aggregates of cyclodextrin-drug complexes using Taylor Dispersion Analysis."

Int. J. Pharm., **522**(1-2), 98–109. ISSN 03785173. doi: 10.1016/j.ijpharm.2017.02.012. URL https://doi.org/10.1016/j.ijpharm.2017.02.012.

Zhang S (2003). "Fabrication of novel biomaterials through molecular self-assembly." *Nat. Biotechnol.*, **21**(10), 1171–1178. ISSN 10870156. doi: 10.1038/nbt874. URL https://www.doi.org/10.1038/nbt874.

Zhou C, Cheng X, Zhao Q, Yan Y, Wang J, Huang J (2014). "Self-assembly of channel type β-CD dimers induced by dodecane." *Sci. Rep.*, **4**, 1–6. ISSN 20452322. doi: 10.1038/srep07533. URL https://www.doi.org/10.1038/srep07533.

Zhou T, Ao M, Xu G, Liu T, Zhang J (2013). "Interactions of bovine serum albumin with cationic imidazolium and quaternary ammonium gemini surfactants: Effects of surfactant architecture." *J. Colloid Interface Sci.*, **389**(1), 175–181. ISSN 00219797. doi: 10.1016/j.jcis.2012.08.067. URL https://www.doi.org/10.1016/j.jcis.2012.08.067.

Zhou WL, Zhao X, Chen Y, Liu Y (2019). "Construction and heterogeneous photooxidization reactivity of a cyclodextrin/porphyrin polyrotaxane network." *Org. Chem. Front.*, **6**(1), 10–14. ISSN 2052-4129. doi: 10.1039/C8QO00790J. URL https://www.doi.org/10.1039/C8QO00790J.

Zielenkiewicz W (2008). "Towards classification of calorimeters." *J. Therm. Anal. Calorim.*, **91**(2), 663–671. ISSN 13886150. doi: 10.1007/s10973-007-8431-y. URL https://www.doi.org/10.1007/s10973-007-8431-y.

Zihlmann P, Silbermann M, Sharpe T, Jiang X, Mühlethaler T, Jakob RP, Rabbani S, Sager CP, Frei P, Pang L, Maier T, Ernst B (2018). "KinITC-One Method Supports both Thermodynamic and Kinetic SARs as Exemplified on FimH Antagonists." *Chem. - A Eur. J.*, **24**(49), 13049–13057. ISSN 15213765. doi: 10.1002/chem.201802599. URL https://www.doi.org/10.1002/chem.201802599.

USC UNIVERSIDADE DE SANTIAGO DE COMPOSTELA

Part V

Appendix

USC
UNIVERSIDADE
DE SANTIAGO
DE COMPOSTELA

USC
UNIVERSIDADE
DE SANTIAGO
DE COMPOSTELA

Appendix A

List of publications and scientific contributions

A.1. Publications included in this dissertation

According to the PhD requirements, the list of publications with their quality indexes (when corresponding), is here presented. The quality factors have been obtained from InCites - Journal Citation Reports (JCR), and are presented with respect to the year of publication or, if not achievable, the closest one. The presented quality factors are the Journal Impact Factor (JIR), the Journal Impact Factor Percentile in Category (JIR percentile) and the corresponding quartile, and the category (or categories) in which the publication is listed. Additionally, the current number of citations (obtained from Google Scholar on October 14th, 2021) is also provided.

- Paper I

  Garrido PF, Calvelo M, Blanco-González A, Veleiro U, Suárez F, Conde D, Cabezón A, Piñeiro Á, Garcia-Fandino R (2020a). The Lord of the Nano-Rings: Cyclodextrins and the battle against SARS-CoV-2. *Int. J. Pharm.*, **588**, 119689. ISSN 03785173. doi: 10.1016/j.ijpharm.2020.119689. URL https://www.doi.org/10.1016/j.ijpharm.2020.119689

  Cites: 24
  JIR: 5.875

  Category: Pharmacology and Pharmacy
  JIR percentile: 86.73, Q1

  Autorisation of the journal/publisher
  'as the author of this Elsevier article, you retain the right to include it in a thesis or dissertation, provided it is not published commercially. Permission is not required, but please ensure that you reference the journal as the original source '
  https://www.elsevier.com/about/policies/copyright#Author-rights

USC DE SANTIAGO DE COMPOSTELA

- Paper II

  Garrido PF, Bastos M, Velázquez-Campoy A, Dumas P, Piñeiro Á (2021). Fluid interface calorimetry. *J. Colloid Interface Sci.*, **596**, 119–129. ISSN 00219797. doi: 10.1016/j.jcis.2021.03.098. URL https://www.doi.org/10.1016/j.jcis.2021.03.098

  Cites: 2
  JIR: 8.128

  Category: Physical Chemistry
  JIR percentile: 80.56, Q1

  Autorisation of the journal/publisher
  'as the author of this Elsevier article, you retain the right to include it in a thesis or dissertation, provided it is not published commercially. Permission is not required, but please ensure that you reference the journal as the original source '
  https://www.elsevier.com/about/policies/copyright#Author-rights

- Paper III

  Garrido PF, Bastos M, Velázquez-Campoy A, Amigo A, Dumas P, Piñeiro Á (2022). Unsupervised bubble calorimetry analysis: Surface tension from isothermal titration calorimetry. *J. Colloid Interface Sci.*, **606**, 1823–1832. ISSN 00219797. doi: 10.1016/j.jcis.2021.08.115. URL https://www.doi.org/10.1016/j.jcis.2021.08.115

  Cites: 0
  JIR: 8.128

  Category: Physical Chemistry
  JIR percentile: 80.56, Q1

  Autorisation of the journal/publisher
  'as the author of this Elsevier article, you retain the right to include it in a thesis or dissertation, provided it is not published commercially. Permission is not required, but please ensure that you reference the journal as the original source '
  https://www.elsevier.com/about/policies/copyright#Author-rights

- Paper IV

  Piñeiro Á, Muñoz E, Sabín J, Costas M, Bastos M, Velázquez-Campoy A, Garrido PF, Dumas P, Ennifar E, García-Río L, Rial J, Pérez D, Fraga P, Rodríguez A, Cotelo C (2019). AFFINImeter: A software to analyze molecular recognition processes from experimental data. *Anal. Biochem.*, **577**, 117–134. ISSN 00032697. doi: 10.1016/j.ab.2019.02.031. URL https://www.doi.org/10.1016/j.ab.2019.02.031

  Cites: 43
  JIR: 2.877

USC UNIVERSIDADE DE SANTIAGO DE COMPOSTELA

Category: Biochemical Research Methods
JIR percentile: 59.09, Q2

Category: Analytical Chemistry
JIR percentile: 62.21, Q2

Category: Biochemistry and Molecular Biology
JIR percentile: 43.60, Q3

Autorisation of the journal/publisher
'as the author of this Elsevier article, you retain the right to include it in a thesis or dissertation, provided it is not published commercially. Permission is not required, but please ensure that you reference the journal as the original source '
https://www.elsevier.com/about/policies/copyright#Author-rights

- Paper V

  Garrido PF, Rodríguez-Dafonte P, García-Río L, Piñeiro Á (available online: September 27, 2021). Simple approximaTion for Aggregation Number Determination by Isothermal Titration Calorimetry: STAND-ITC. *Langmuir*. ISSN 0743-7463. doi: 10.1021/acs.langmuir.1c01727. URL https://doi.org/10.1021/acs.langmuir.1c01727

  Cites: 0
  JIR: 3.882

  Category: Multidisciplinary Chemistry
  JIR percentile: 60.96, Q2

  Category: Multidisciplinary Materials Science
  JIR percentile: 58.71, Q2

  Category: Physical Chemistry
  JIR percentile: 55.86, Q2

  Autorisation of the journal/publisher
  'Permission for this particular request is granted for print and electronic formats, and translations, at no charge. Figures and tables may be modified. Appropriate credit should be given. Please print this page for your records and provide a copy to your publisher. Requests for up to 4 figures require only this record. Five or more figures will generate a printout of additional terms and conditions. Appropriate credit should read: "Reprinted with permission from COMPLETE REFERENCE CITATION. Copyright YEAR American Chemical Society."Insert appropriate information in place of the capitalized words. '
  https://pubs.acs.org/pb-assets/acspubs/Migrated/dissertation.pdf

- Paper VI

  Castro G, Garrido PF, Amigo A, Brocos P (2018). Boosting the use of thermoacoustimetry in micellization thermodynamics studies by easing an objective determination of the cmc. *Fluid Phase Equilib.*, **478**, 1–13. ISSN 03783812. doi: 10.1016/j.fluid.2018.08.011. URL https://www.doi.org/10.1016/j.fluid.2018.08.011

  Cites: 2
  JIR: 2.514

  Category: Thermodynamics
  JIR percentile: 75.83, Q1

  Category: Physical Chemistry
  JIR percentile: 50.34, Q2

  Category: Chemical Engineering
  JIR percentile: 61.23, Q2

  Autorisation of the journal/publisher
  'as the author of this Elsevier article, you retain the right to include it in a thesis or dissertation, provided it is not published commercially. Permission is not required, but please ensure that you reference the journal as the original source '
  https://www.elsevier.com/about/policies/copyright#Author-rights

- Paper VII

  Garrido PF, Calvelo M, Garcia-Fandiño R, Piñeiro Á (2020b). Rings, Hexagons, Petals, and Dipolar Moment Sink-Sources: The Fanciful Behavior of Water around Cyclodextrin Complexes. *Biomolecules*, **10**(3), 431. ISSN 2218-273X. doi: 10.3390/biom10030431. URL https://www.doi.org/10.3390/biom10030431

  Cites: 6
  JIR: 4.879

  Category: Biochemistry and Molecular Biology
  JIR percentile: 67.85, Q2

  Autorisation of the journal/publisher
  'For all articles published in MDPI journals, copyright is retained by the authors. Articles are licensed under an open access Creative Commons CC BY 4.0 license, meaning that anyone may download and read the paper for free. In addition, the article may be reused and quoted provided that the original published version is cited. These conditions allow for maximum use and exposure of the work, while ensuring that the authors receive proper credit '
  https://www.mdpi.com/authors/rights

USC UNIVERSIDADE DE SANTIAGO DE COMPOSTELA

- Patent registration
- Software registration

A.2. Publications not included in this dissertation

- Garrido PF, Brocos P, Amigo A, García-Río L, Gracia-Fadrique J, Piñeiro Á (2016). STAND: Surface Tension for Aggregation Number Determination. *Langmuir*, **32**(16), 3917–3925. ISSN 0743-7463. doi: 10.1021/acs.langmuir.6b00477. URL https://www.doi.org/10.1021/acs.langmuir.6b00477

- Blanco-González A, Calvelo M, Garrido PF, Amorín M, Granja JR, Piñeiro Á, Garcia-Fandino R (2021). Transmembrane Self-Assembled Cyclic Peptide Nanotubes Based on α-Residues and Cyclic δ-Amino Acids: A Computational Study. *Front. Chem.*, **9**, 530. ISSN 2296-2646. doi: 10.3389/fchem.2021.704160. URL https://www.doi.org/10.3389/fchem.2021.704160

- Conde D, Garrido PF, Calvelo M, Piñeiro Á, Garcia-Fandiño R (submitted). Molecular dynamics simulations of transmembrane cyclic peptide nanotubes using classical force fields, Hydrogen Mass Repartitioning and Hydrogen Isotope Exchange methods: a critical comparison. *Physical Chemistry Chemical Physics*

- Chiodini S, Stoliar P, Garrido PF, Albonetti C (submitted). Differential entropy of self-similar organic islands approached by *in situ* atomic force microscopy. *Materials*

A.3. Conferences

- **Pablo F. Garrido**, Pilar Brocos, Alfredo Amigo, Roberto Rosende, Luis García-Río, Jesús Gracia-Fadrique, Ángel Piñeiro, "STAND: Determinación del Número de Agregación Micelar por Tensión Superficial". *III Reunión de Jóvenes Investigadores en Coloides e Interfases*, Madrid, 13-14 October, 2016.

- **Pablo F. Garrido**, Pilar Brocos, Alfredo Amigo, Roberto Rosende, Luis García-Río, Jesús Gracia-Fadrique, Ángel Piñeiro, "STAND: Determinación do Número de Agregación Micelar por Tensión Superficial". *V Encontro Mocidade Investigadora*, Santiago de Compostela, 12-13 June, 2017.

- **Pablo F. Garrido**, Miguel Ángel Rubio, Pablo Domínguez-García, "Contact angle of spheres floating at an air-water interfaces by solving the Young-Laplace equation". *10th Liquid matter conference*, Ljubljana, 17-21 July, 2017.

- Ángel Piñeiro, Rebeca García-Fandiño, Alejandro Carballosa, Manuel Paz, **Pablo F. Garrido** "Computational molecular dynamics simulations of Cyclodextrin systems: a must". *The 19th International Cyclodextrin Symposium*, Tokyo, 27-30 April, 2018.

- **Pablo F. Garrido**, Margarida Bastos, Adrián Velázquez-Campoy, Philippe Dumas, Ángel Piñeiro, "Novos métodos en ITC: cara unha calorimetría de interfases ". *VII Encontro Mocidade Investigadora*, Santiago de Compostela, 12-13 June, 2017.

- **Pablo F. Garrido**, Martín Calvelo, Rebeca García-Fandiño, Ángel Piñeiro, "Indirect characterization of cyclodextrin inclusion complexes by competitive studies". *6th European Conference on Cyclodextrins - EURO CD 2019*, Santiago de Compostela, 2-4 October, 2019.
- Martín Calvelo, César Porto, **Pablo F. Garrido**, Ángel Piñeiro, Rebeca García-Fandiño, "State-of-the-art computational tools for the simulation and visualization of cyclodextrins". *6th European Conference on Cyclodextrins - EURO CD 2019*, Santiago de Compostela, 2-4 October, 2019.
- Ángel Piñeiro, **Pablo F. Garrido**, Martín Calvelo, Rebeca García-Fandiño, "Tricks for computational simulations of cyclodextrin complexes". *6th European Conference on Cyclodextrins - EURO CD 2019*, Santiago de Compostela, 2-4 October, 2019.
- Rebeca García-Fandiño, César Porto, Martín Calvelo, **Pablo F. Garrido**, Ángel Piñeiro, "Immersive visualization of molecular mechanisms: Seeing is understanding". *6th European Conference on Cyclodextrins - EURO CD 2019*, Santiago de Compostela, 2-4 October, 2019.
- Ángel Piñeiro, **Pablo F. Garrido**, Martín Calvelo, Rebeca García-Fandiño, "From molecular dynamics simulations of cyclodextrin-based molcular machines to macroscopic functional materials". *MM2019 Conference Programme*, Bintan island, Indonesia, 5-8 December, 2019.
- **Pablo F. Garrido**, Martín Calvelo, Rebeca García-Fandiño, Ángel Piñeiro, "The role of solvent molecules in aggregation and adsorption. A MD simulations survey on cyclodextrin complexes". *IX International Conference BIFI 2020*, Zaragoza, 3-5 February, 2020.
- **Pablo F. Garrido**, Margarida Bastos, Adrián Velázquez-Campoy, Philippe Dumas, Ángel Piñeiro, "De la creación de burbujas a la adsorción de proteínas: desarrollo de una calorimetría de interfases fluidas". *V Reunión de Jóvenes Investigadores en Coloides e Interfases*, Zaragoza, 2-4 March, 2020.
- **Pablo F. Garrido**, Margarida Bastos, Adrián Velázquez-Campoy, Philippe Dumas, Ángel Piñeiro, "From bubble formation to protein adsorption: development of fluid interface calorimetry". *10th International Colloids Conference*, Online, 7-9 December, 2020.

USC UNIVERSIDADE DE SANTIAGO DE COMPOSTELA

Appendix B

Complementary information of Papers III and V

The Supplementary Material of Paper III and the Supporting Information of Paper V are included in this appendix chapter as they have been considered to be relevant in the discussion of the papers in this dissertation. Supplementary Material of Paper II was already included in the main text, due to its relevance. On the other hand, complementary information about Paper VI and Paper VII are excluded due to its length, although their respective links to download are provided.

USC
UNIVERSIDADE DE SANTIAGO DE COMPOSTELA

USC
UNIVERSIDADE
DE SANTIAGO
DE COMPOSTELA

Supplementary Material for

Unsupervised Bubble Calorimetry Analysis: Surface Tension from Isothermal Titration Calorimetry

Pablo F. Garrido[1*], Margarida Bastos[2], Adrián Velázquez-Campoy[3,4,5,6,7], Alfredo Amigo[1], Philippe Dumas[8], Ángel Piñeiro[1*]

[1]Departamento de Fisica de Aplicada, Facultade de Fisica, Universidade de Santiago de Compostela, E-15782, Santiago de Compostela, Spain. [2]CIQ-UP, Departamento de Quimica e Bioquimica, Faculdade de Ciencias da Universidade do Porto, R. Campo Alegre 687, P-4169-007, Porto, Portugal. [3]Institute of Biocomputation and Physics of Complex Systems (BIFI), Joint Units IQFR-CSIC-BIFI, and GBsC-CSIC-BIFI, Universidad de Zaragoza, Zaragoza, 50018, Spain. [4]Department of Biochemistry and Molecular and Cell Biology, Universidad de Zaragoza, 50009, Zaragoza, Spain. [5]Aragon Institute for Health Research (IIS Aragon), 50009, Zaragoza, Spain. [6]Biomedical Research Networking Centre for Liver and Digestive Diseases (CIBERehd), 28029, Madrid, Spain. [7]Fundacion ARAID, Government of Aragon, 50018, Zaragoza, Spain. [8]IGBMC, Dept of Integrative Biology, Strasbourg University, F67404, Illkirch CEDEX, France.

E-mail: Pablo.Fernandez@usc.es, Angel.Pineiro@usc.es

Supplementary Material summary:

-Figures S1-S10: Baseline correction and Fourier analysis for 40 selected raw data (Figure S1)

-Figures S11-S12: Period-surface tension relation for all the studied systems.

-Table S1: Surface tension of cyclohexane and water at 283, 298, 310 and 323 K.

USC
UNIVERSIDADE DE SANTIAGO DE COMPOSTELA

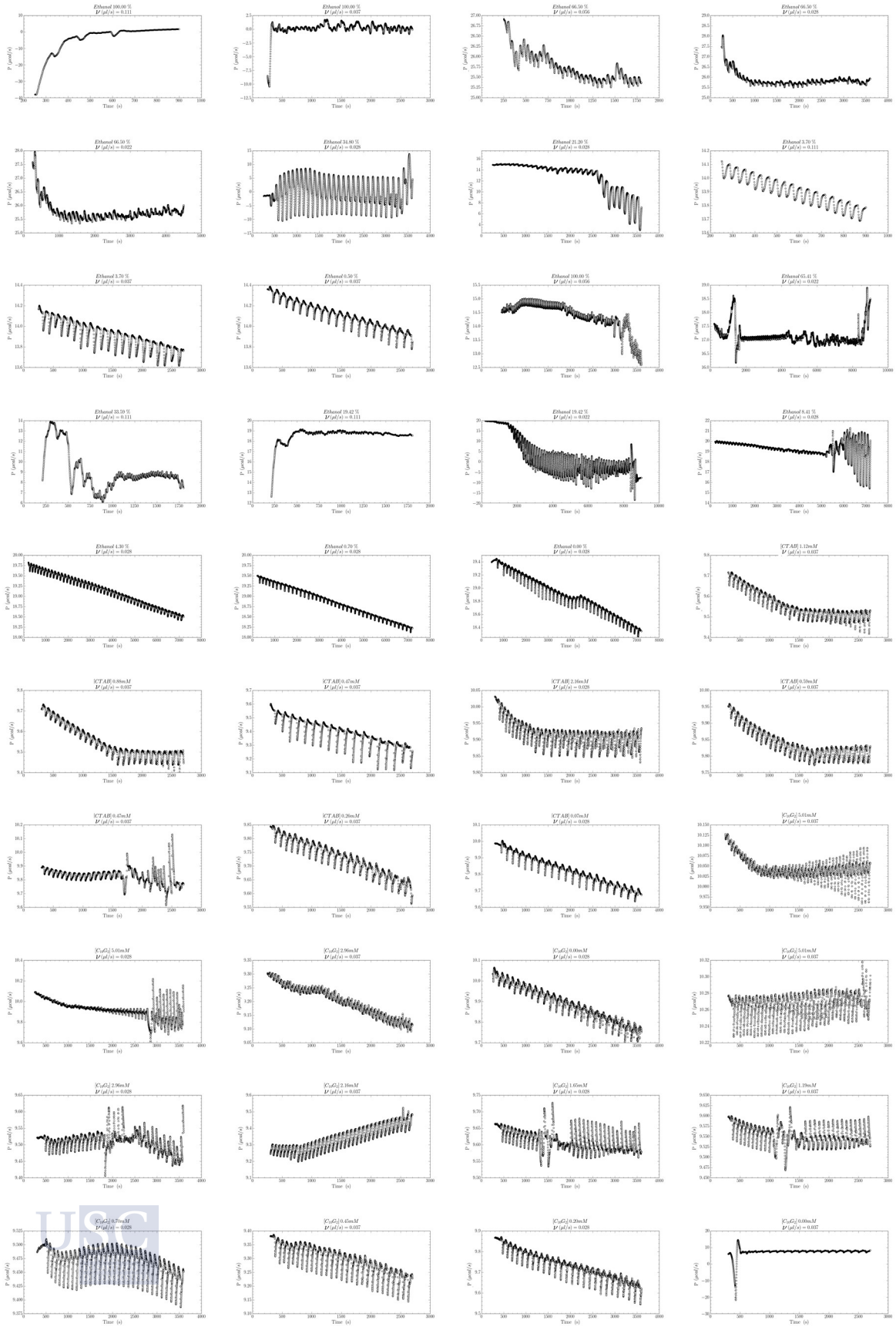


Figure S1: selection of 40 different bubble injection experiments. Raw data.

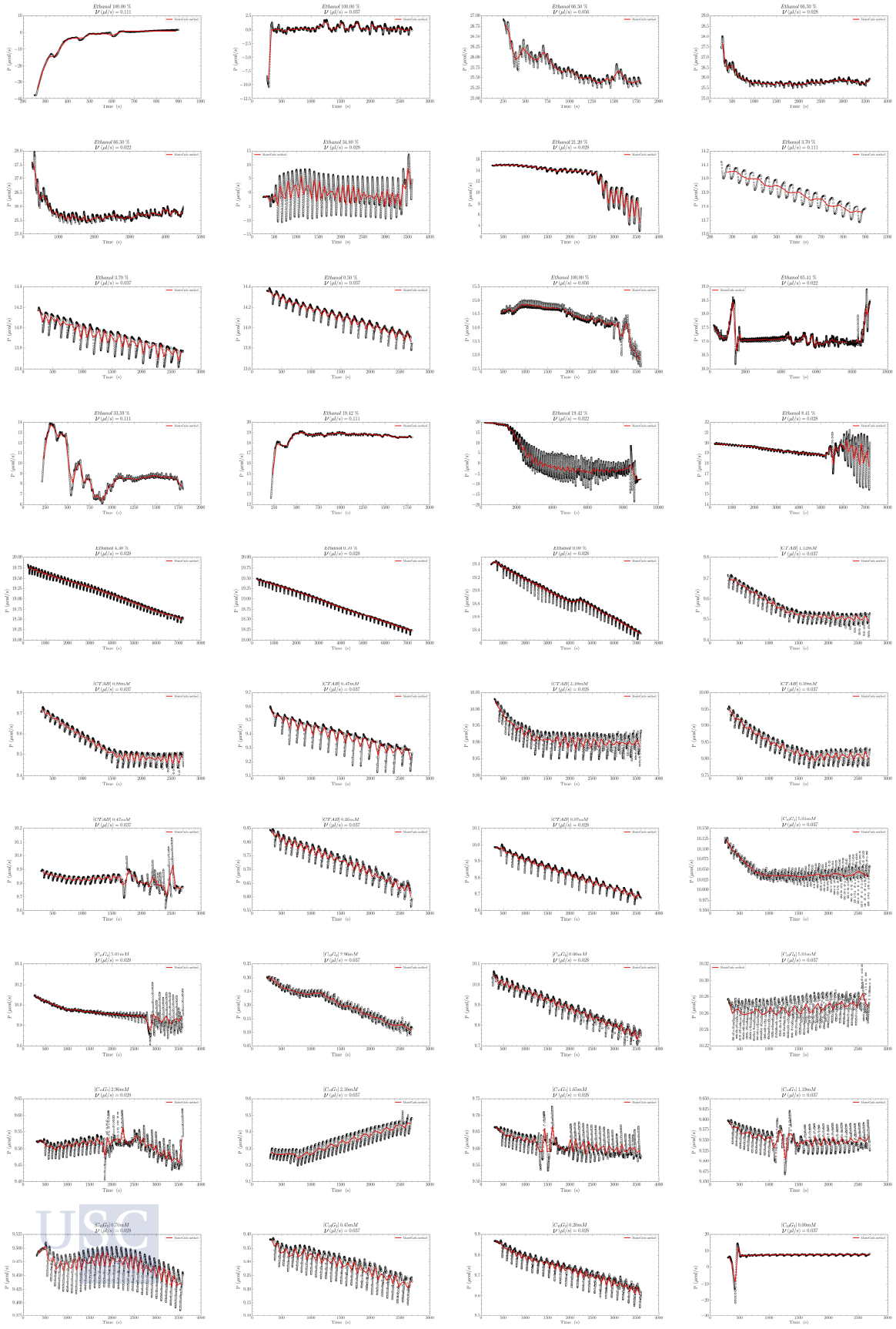


Figure S2: Resolution downgrade (RD) applied on selected data.

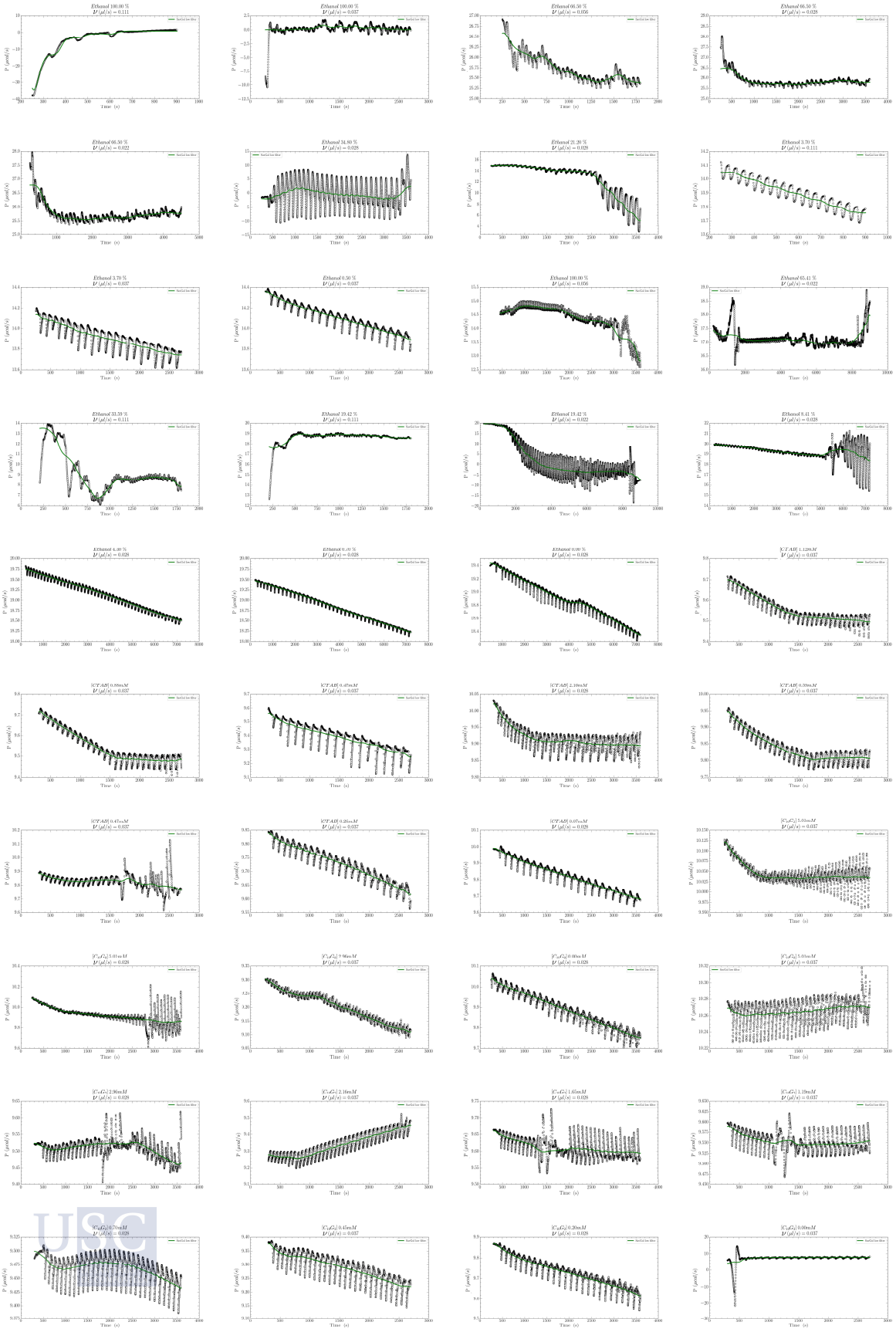


Figure S3: Savitzky-Golay (SG) applied on RD of selected data.

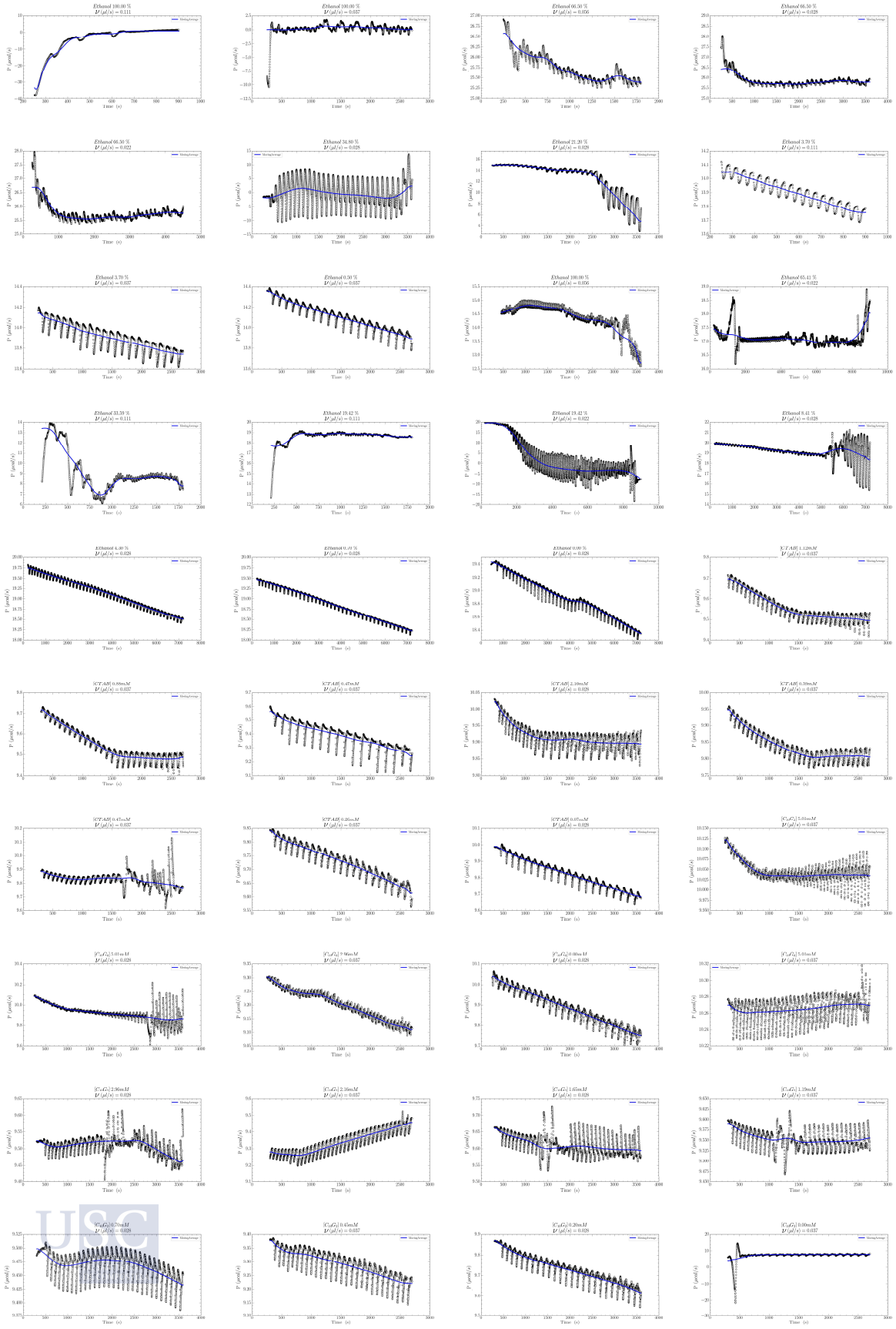


Figure S4: Moving average (MA) applied on SV-RD of selected data.

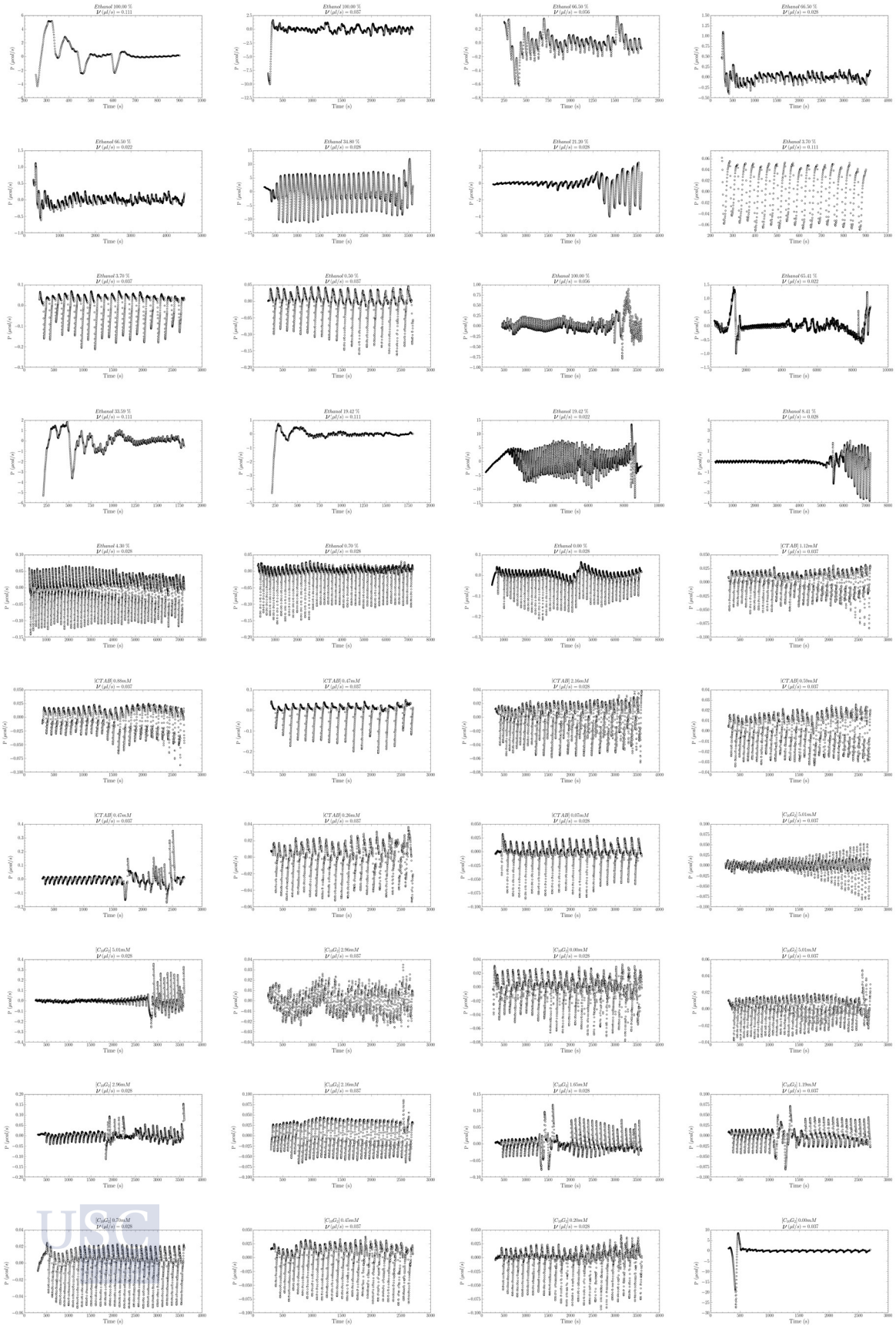


Figure S5: MA-SG-RD baseline subtraction on selected data.

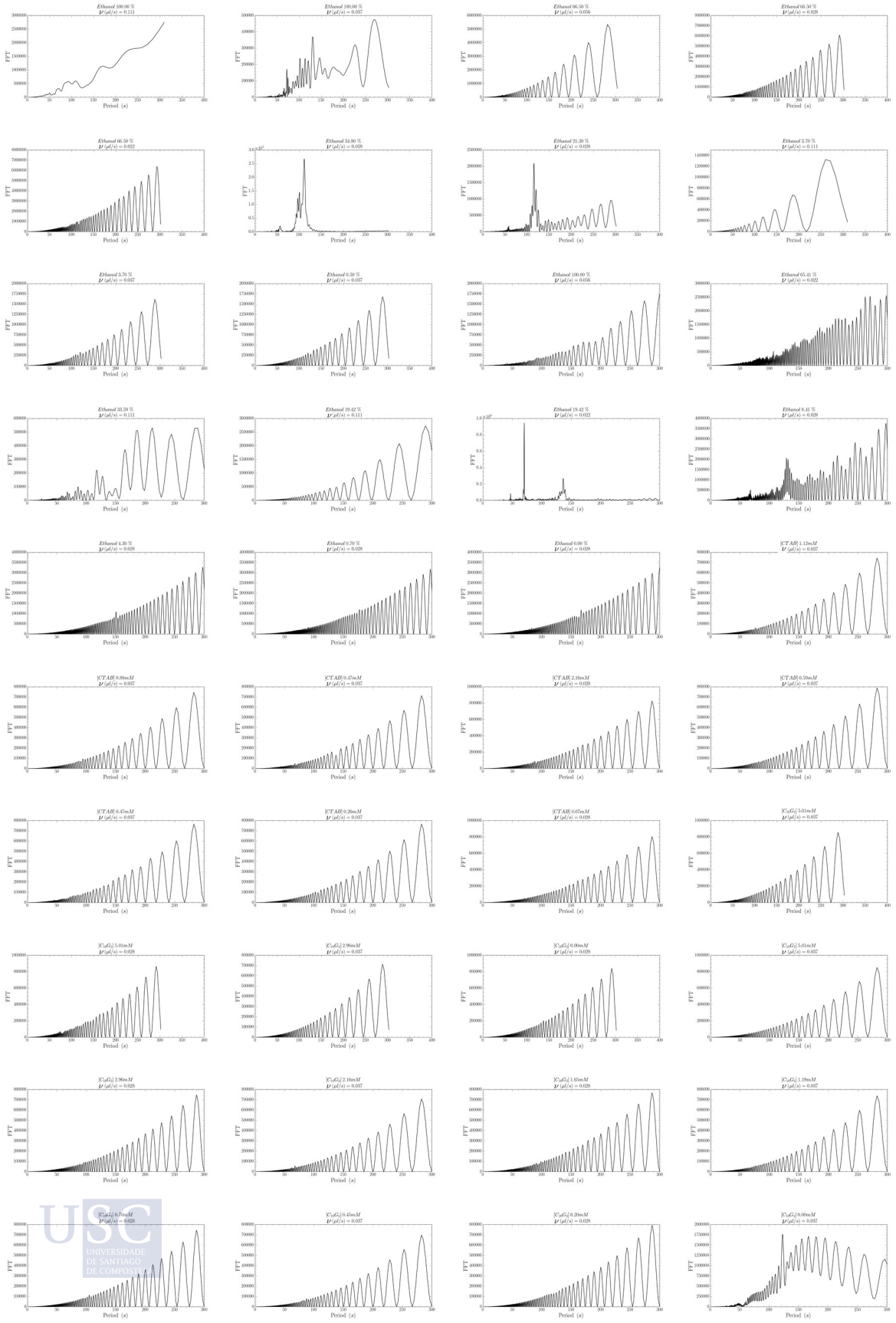


Figure S6: Fast Fourier Transform (FFT) applied on raw selected data.

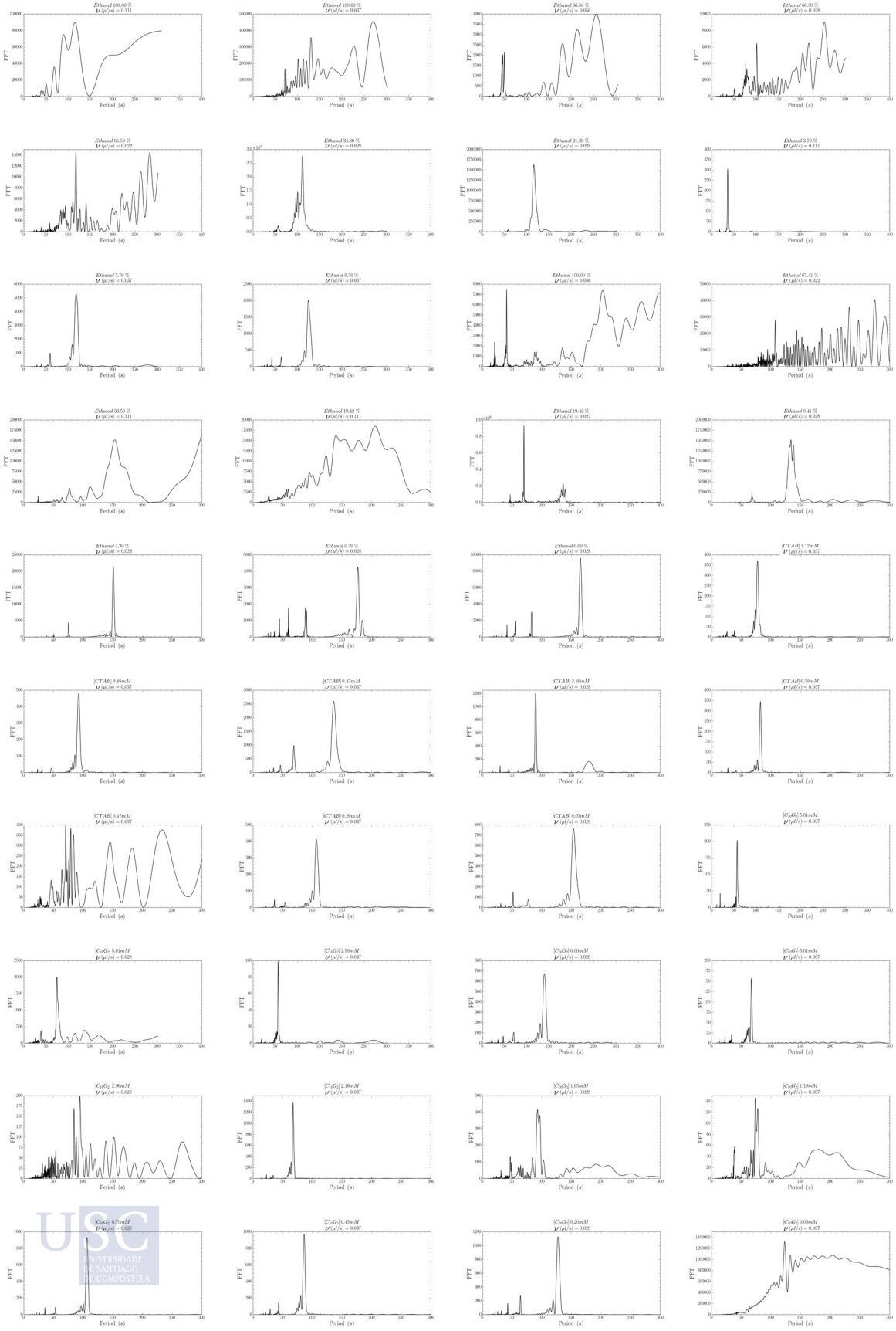


Figure S7: FFT applied on baseline-corrected selected data.

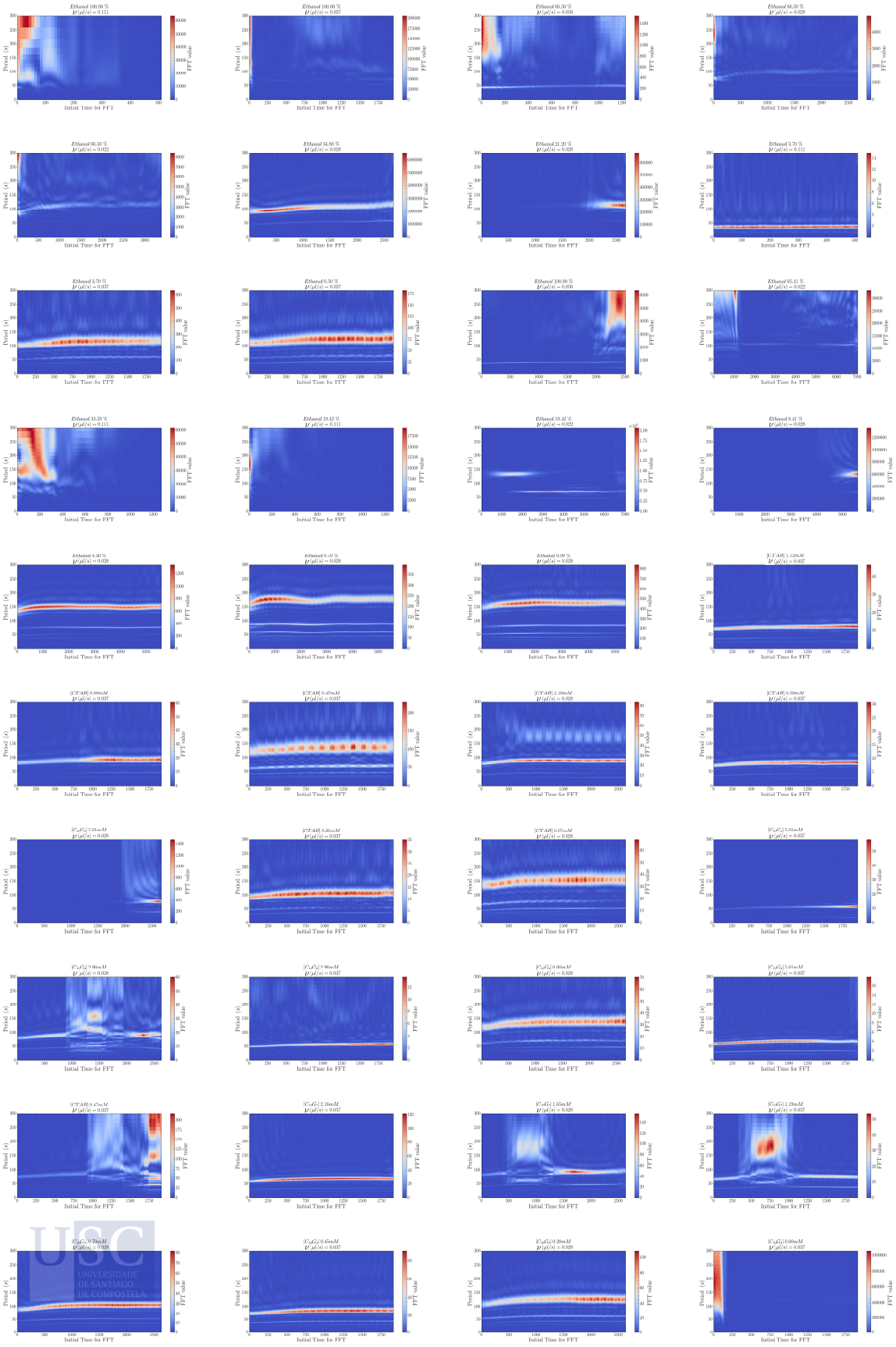


Figure S8: Moving FFT (MFFT) applied on baseline-corrected selected data.

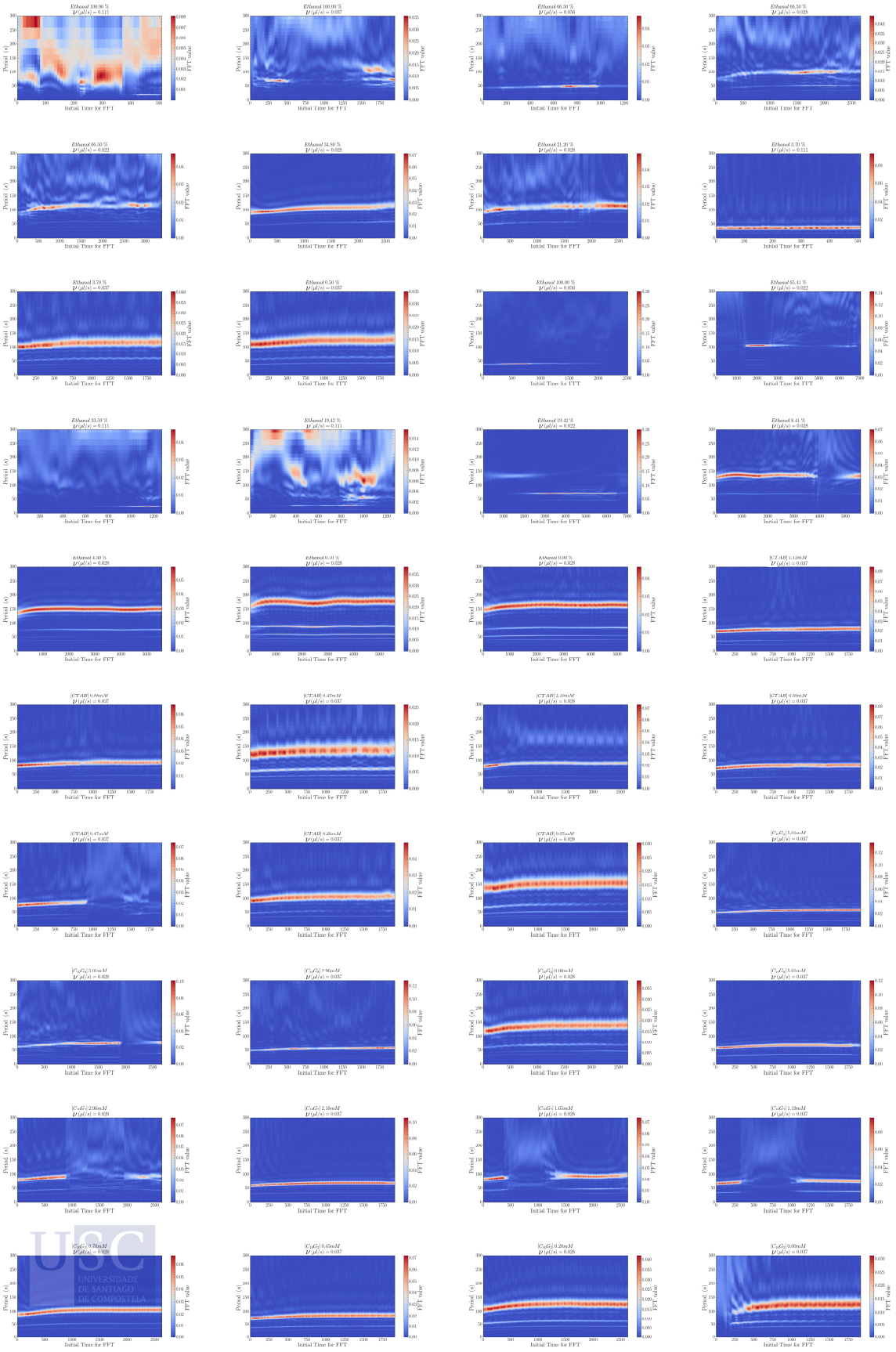


Figure S9: Normalized MFFT applied on baseline-corrected selected data.

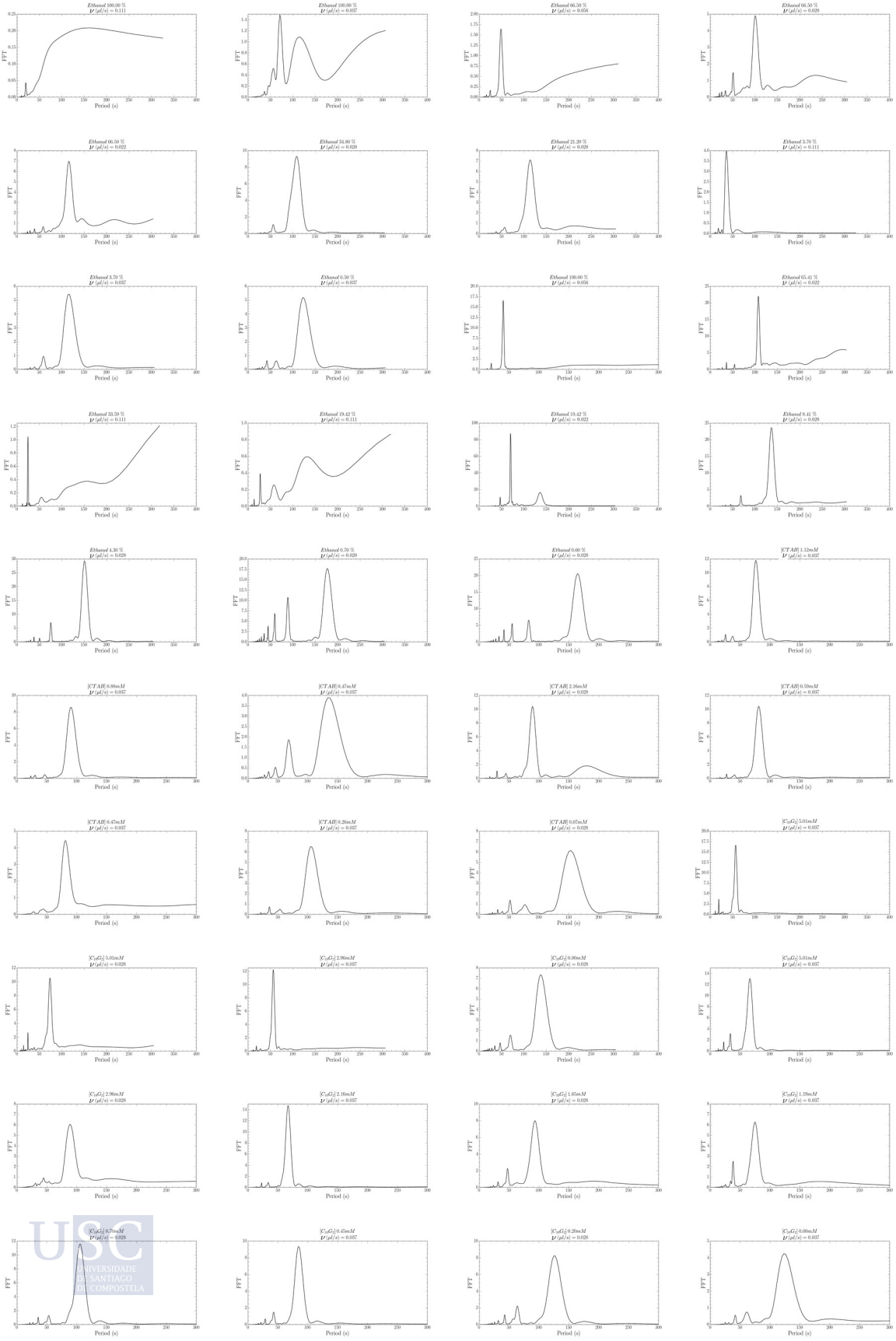


Figure S10: Average Normalized MFFT applied on baseline-corrected selected data.

Table S1: Surface tension values for cyclohexane and water at 4 different temperatures obtained in this work using the drop volume method??

Temperature	Surface tension	
	Cyclohexane	Water
K	mN/m	mN/m
283	26.66 ± 0.05	73.70 ± 0.08
298	24.62 ± 0.05	71.51 ± 0.03
310	23.13 ± 0.07	69.58 ± 0.05
323	21.29 ± 0.06	67.43 ± 0.07

USC
UNIVERSIDADE DE SANTIAGO DE COMPOSTELA

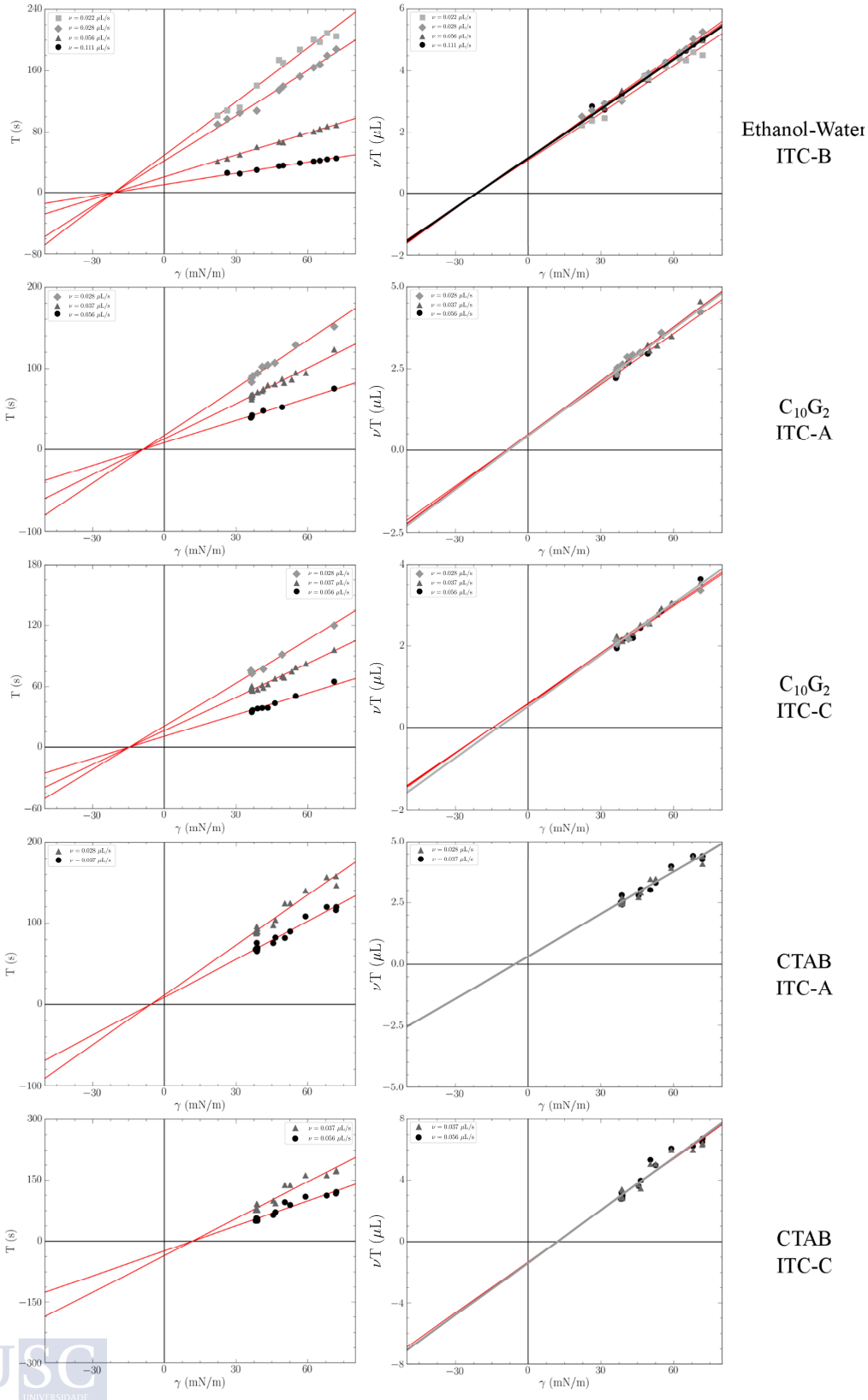


Figure S11: Left: Period obtained from air injection titration experiments by ITC for different injection rates (see legends), as a function of the experimental surface tension. Right: Bubble volume obtained as the product of the period by the injection rate, as a function of the surface tension for the same systems represented in the left plots. The red lines in both plots represent the linear fittings of the experimental points restrained to share a common point at T=0. The grey/black lines represent the master line (see main text).

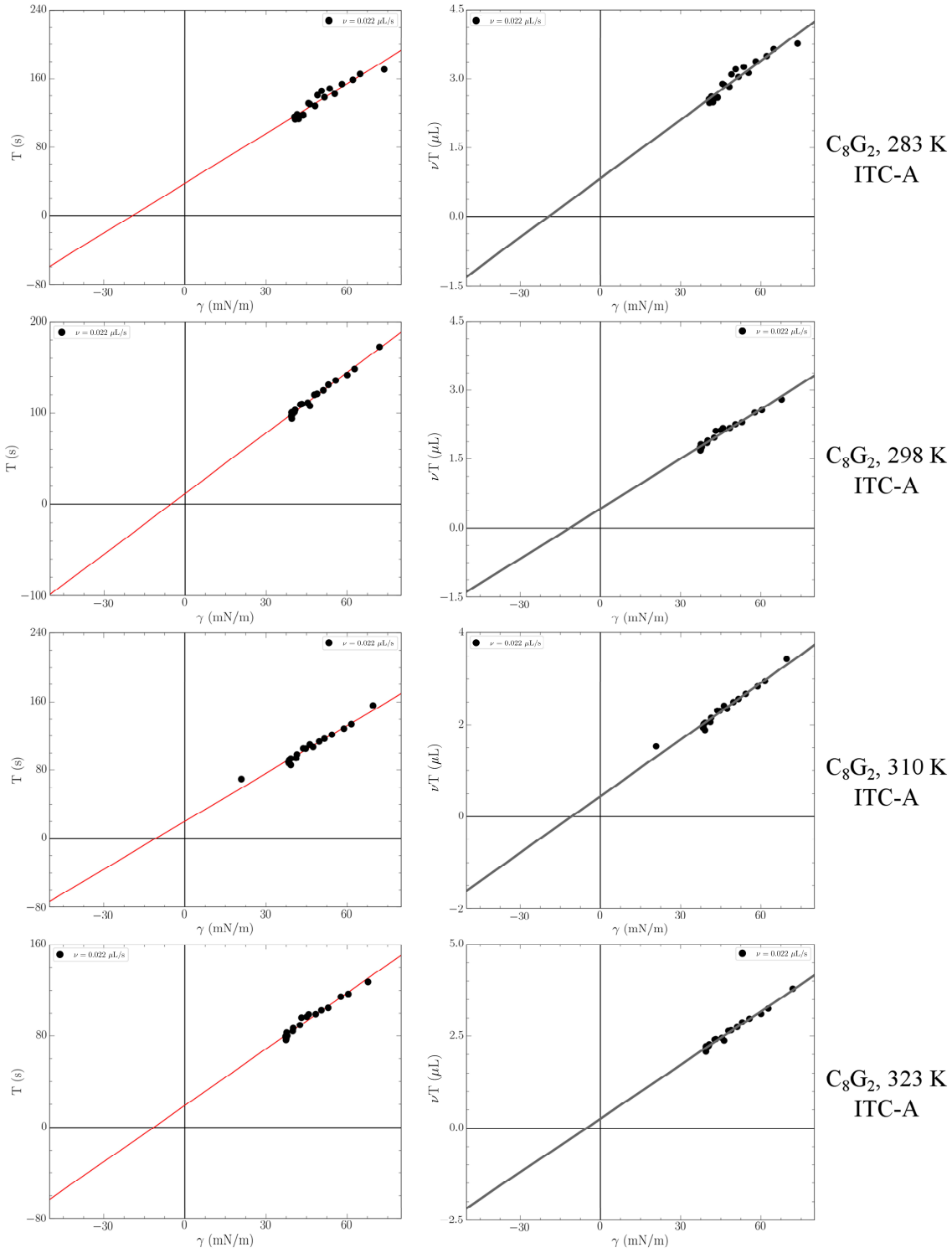


Figure S12: Left: Period obtained from air injection titration experiments by ITC for different injection rates (see legends), as a function of the experimental surface tension. Right: Bubble volume obtained as the product of the period by the injection rate, as a function of the surface tension for the same systems represented in the left plots. The red lines in both plots represent the linear fittings of the experimental points restrained to share a common point at T=0. The grey/black lines represent the master line (see main text).

Supporting Information for

Simple aproximaTion for Aggregation Number Determination by Isothermal Titration Calorimetry: STAND-ITC

Pablo F. Garrido[1], Pedro Rodriguez-Dafonte[2], Luis García-Río[2], Ángel Piñeiro[1*]

[1]Departamento de Fisica de Aplicada, Facultade de Fisica, Universidade de Santiago de Compostela, E-15782, Santiago de Compostela, Spain.
[2]CIQUS, Departamento de Quimica Física, Universidade de Santiago de Compostela, E-15782, Santiago de Compostela, Spain.

E-mail: Angel.Pineiro@usc.es

Table of contents:

Table S1 containing aggregation number values from different fonts

Figure S1 containing the derivative of simulated isotherms with respect to the parameters of the model

List of **references** for Table S1

Table S1: literature comparison of aggregation number values, for all the studied compounds, at different temperatures, concentrations and determined by different techniques.

Compound	T (K)	N_{agg}	$[S_T]$/cmc	Technique	Reference
C_{12}TAB	R. T.	48.4	10	Fluorescence	Tehrani-Bagha et al., 2012 [1]
		51.3	2	Fluorescence	Pisárčik et al., 2015 [2]
		50.8	3	Fluorescence	Pisárčik et al., 2015 [2]
		50.9	4	Fluorescence	Pisárčik et al., 2015 [2]
		51	3	Fluorescence	Kennedy et al., 2001 [3]
		52.1	5	Fluorescence	Pisárčik et al., 2015 [2]
		71.8	10	Fluorescence	Tehrani-Bagha et al., 2012 [1]
	278	44.65	1	ITC	This work
	283	64	1[c]	Fluorescence	Bales & Zana, 2002 [4]
		71.4	7	Fluorescence	Bales & Zana, 2002 [4]
		79.6	13	Fluorescence	Bales & Zana, 2002 [4]
		84.4	23	Fluorescence	Bales & Zana, 2002 [4]
	288	28.40	1	ITC	This work
		28.1	1.3	Fluorescence	This work
		62	<3	Light Scattering	Jones & Piercy, 1972 [5]
	293	58	0.5-2	Conductivity	Mata et al., 2005 [6]
		54	1	Fluorescence	Lianos & Zana, 1981 [7]
		53	3	Fluorescence	Lianos & Zana, 1981 [7]
		57	7	Fluorescence	Lianos & Zana, 1981 [7]
		65	7	Fluorescence	Malliaris et al., 1985 [8]
	298	32	1	Fluorescence	Rodenas et al., 1994 [9]
		36.252	1	ITC	This work
		30	1.3	Fluorescence	This work
		42	3	Fluorescence	Rodenas et al., 1994 [9]
		43	<3	Light Scattering	Jones & Piercy, 1972 [5]
		46	3	Fluorescence	Pal & Pillania, 2015 [10]
		47[a]	3	SANS	Berr et al., 1992 [11]
		48-66	1-2.5	Conductivity	Jalšenjak & Težak, 2004 [12]
		49	3	Fluorescence	Pal & Pillania (2), 2015 [13]
		51	4	Fluorescence	Rodenas et al., 1994 [9]
		51[a]	7	SANS	Berr et al., 1992 [11]
		52-61	<3	Light Scattering	Anacker et al., 1964 [14]
		52-70	<3	Conductivity	Danov et al., 2014 [15]
		54.7	1[c]	Fluorescence	Bales & Zana, 2002 [4]
		55[a]	13	SANS	Berr et al., 1992 [11]
		56	2	Fluorescence	Moyá et al., 2007 [16]
		58	2	Fluorescence	Junquera & Aicart, 2002 [17]
		58	2	Fluorescence	Rodríguez et al., 2004 [18]
		58.2	7	Fluorescence	Bales & Zana, 2002 [4]
		60.8	5	Fluorescence	Bales & Zana, 2002 [4]
		67.7	13	Fluorescence	Bales & Zana, 2002 [4]
		69	7	Fluorescence	Rodenas et al., 1994 [9]
		69.6[a]	3	SANS	Caponetti et al., 1995 [19]
		71.6[a]	4	SANS	Caponetti et al., 1995 [19]
		72.3[a]	6	SANS	Caponetti et al., 1995 [19]
		72.4	23	Fluorescence	Bales & Zana, 2002 [4]
		73.1[a]	9	SANS	Caponetti et al., 1995 [19]
		73.1[a]	12	SANS	Caponetti et al., 1995 [19]
		74	55	Fluorescence	Herrington et al., 1993 [20]
		80.1[a]	12	SANS	Caponetti et al., 1992 [21]

USC UNIVERSIDADE DE SANTIAGO DE COMPOSTELA

		82[b]	13	SANS	Lusvardi et al., 1995 [22]
		86[b]	27	SANS	Lusvardi et al., 1995 [22]
		87.1[a]	55	SANS	Caponetti et al., 1992 [21]
		89	11	Fluorescence	Rodenas et al., 1994 [9]
	303	53	2	Fluorescence	Dar et al., 2006 [23]
		54	0.5-2	Conductivity	Mata et al., 2005 [6]
		56[a]	80	SANS	Mahajan et al., 2008 [24]
		56-62	1-10	Potentiometry	Fafati et al., 2003 [25]
		60[a]	3	SANS	Griffiths et al., 2005 [26]
		61	7	Fluorescence	Malliaris et al., 1985 [8]
		74	9	Fluorescence	Naskar et al., 2003 [27]
	308	34	<3	Light Scattering	Jones & Piercy, 1972 [5]
		34.42	1	ITC	This work
	313	37[a]	1	SANS	Bergström & Pedersen, 1999 [28]
		51[a]	2	SANS	Bergström & Pedersen, 1999 [28]
		51	0.5-2	Conductivity	Mata et al., 2005 [6]
		54	7	Fluorescence	Malliaris et al., 1985 [8]
	318	28	<3	Light Scattering	Jones & Piercy, 1972 [5]
		35.9	1[c]	Fluorescence	Bales & Zana, 2002 [4]
		45	7	Fluorescence	Bales & Zana, 2002 [4]
		50.1	13	Fluorescence	Bales & Zana, 2002 [4]
		58.1	23	Fluorescence	Bales & Zana, 2002 [4]
	323	29.8	1.3	Fluorescence	This work
		49	0.5-2	Conductivity	Mata et al., 2005 [6]
		51	7	Fluorescence	Malliaris et al., 1985 [8]
	328	24	<3	Light Scattering	Jones & Piercy, 1972 [5]
	333	47	0.5-2	Conductivity	Mata et al., 2005 [6]
		65[b]	27	SANS	Lusvardi et al., 1995 [22]
$[C_{12}mim^+][Cl^-]$	Indep. [d]	16.33	<2	ITC	Šarac et al., 2017 [29]
	278	29.54	1	ITC	This work
	288	34.91	1	ITC	This work
		31.5	1.3	Fluorescence	This work
	298	45.2	1	ITC	This work
		29.4	1.3	Fluorescence	This work
		37	>1	Light Scattering	Bai et al., 2008 [30]
		40	<3	Fluorescence	Pal & Yadav., 2020 [31]
		51	---[e]	Fluorescence	Łuczak et al., 2013 [32]
		56	---[e]	Fluorescence	Chabba et al., 2015 [33]
		58	10	Fluorescence	El Seoud et al., 2007 [34]
	303	40-50[a]	3-25	SANS	Sastry et al., 2012 [35]
	323	18.867	1	ITC	This work
$[C_{12}mim^+][CH_3SO_3^-]$	Indep. [d]	21.8	<2	ITC	Šarac et al., 2017 [29]
	278	21.512	1	ITC	This work
	288	24.89	1	ITC	This work
		19.2	1.3	Fluorescence	This work
	298	30.3	1	ITC	This work
		33.1	1.3	Fluorescence	This work
	323	16.003	1	ITC	This work
		19.5	1.3	Fluorescence	This work
$[C_{10}C_{10}mim^+][Cl^-]$	278	19.282	1	ITC	This work
	288	16.08	1	ITC	This work
		7.6	2	Fluorescence	This work
	298	15.62	1	ITC	This work

USC UNIVERSIDADE DE SANTIAGO DE COMPOSTELA

	6.6	2	Fluorescence	This work
303	40[a]	50	SANS	Kaur et al., 2013 [36]
308	14.6	1	ITC	This work
	5.2	2	Fluorescence	This work
318	12.707	1	ITC	This work
	4.1	2	Fluorescence	This work
328	11.93	1	ITC	This work
	6.6	2	Fluorescence	This work

[a] In D_20
[b] Deuterated
[c] Extrapolated
[d] N_{agg} is temperature independent in their model
[e] Concentration cannot be obtained from the paper
*All the concentration ratios are rounded to integers (except for ranges)

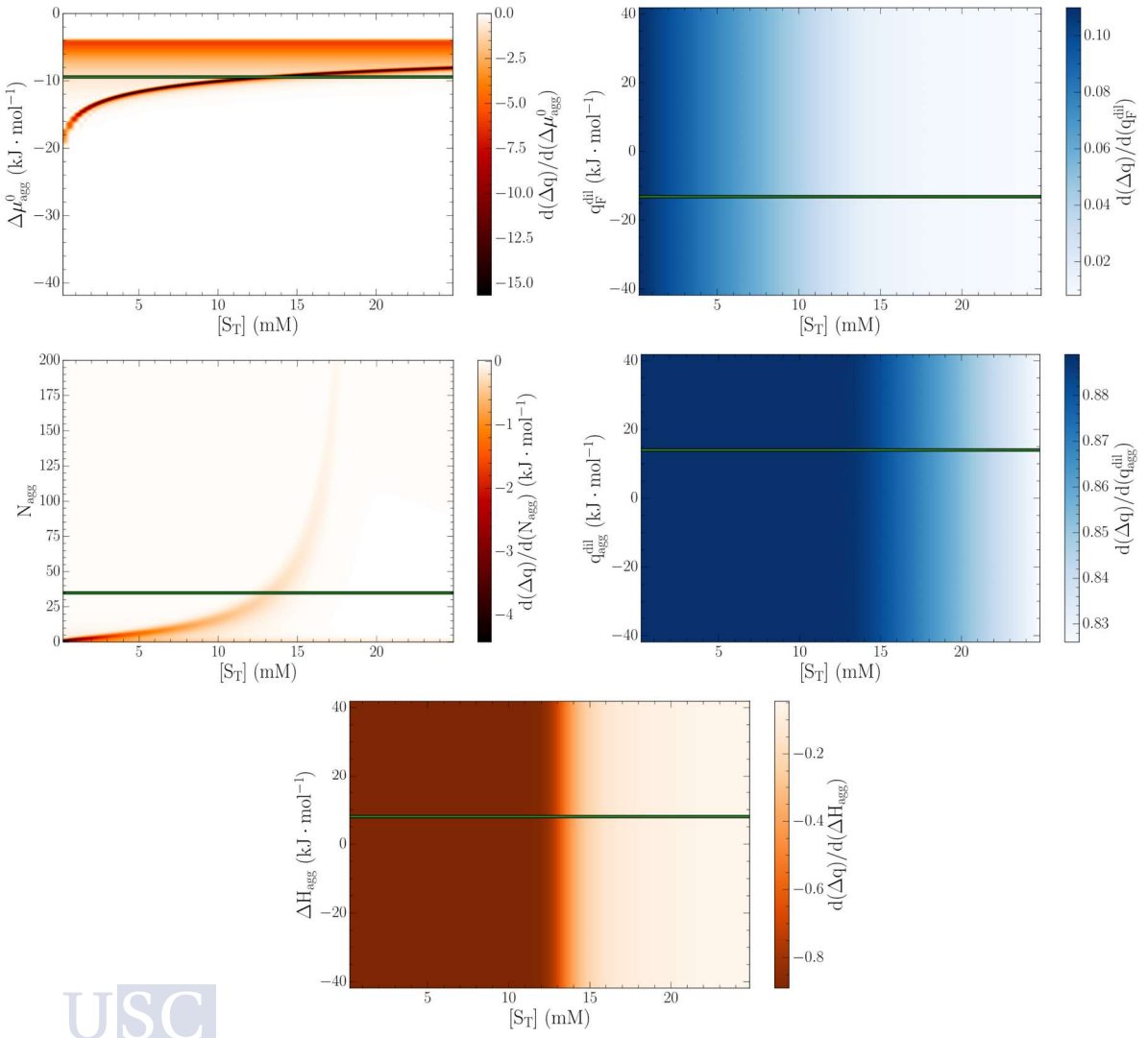


Figure S1: Derivative of the simulated isotherms obtained for dilution experiments using the model described in the theory section. A reference set of parameters given by: N_{agg}=34.91, $\Delta\boldsymbol{\mu}^{\mathbf{0}}_{\mathbf{agg}}$= -9.4183 kJ·mol^{-1}, $\Delta\mathbf{H}_{\mathbf{agg}}$=7.996 kJ·mol^{-1}, $\mathbf{q}_{\mathbf{F}}^{\mathbf{dil}}$ =-13.16 kJ·mol^{-1} , $\mathbf{q}_{\mathbf{agg}}^{\mathbf{dil}}$=14.02 kJ·mol^{-1}, and Q_b=-4.518 mJ, was employed and represented by a green solid line. All the parameters are kept constant except that indicated in each plot, which varies in the range indicated in the corresponding colorbar.

USC
UNIVERSIDADE
DE SANTIAGO
DE COMPOSTELA

References

(1) Tehrani-Bagha, A. R.; Kärnbratt, J.; Löfroth, J. E.; Holmberg, K. Cationic Ester-Containing Gemini Surfactants: Determination of Aggregation Numbers by Time-Resolved Fluorescence Quenching. *J. Colloid Interface Sci.* **2012**, *376* (1), 126–132. https://doi.org/10.1016/j.jcis.2012.02.053.

(2) Pisárčik, M.; Devínsky, F.; Pupák, M. Determination of Micelle Aggregation Numbers of Alkyltrimethylammonium Bromide and Sodium Dodecyl Sulfate Surfactants Using Time-Resolved Fluorescence Quenching. *Open Chem.* **2015**, *13* (1), 922–931. https://doi.org/10.1515/chem-2015-0103.

(3) Kennedy, C. A.; MacMillan, S. N.; McAlduff, M. J.; Marangoni, D. G. The Interaction of Isomeric Hexanediols with Sodium Dodecyl Sulfate and Dodecyltrimethylammonium Bromide Micelles. *Colloid Polym. Sci.* **2001**, *279* (1), 1–7. https://doi.org/10.1007/s003960000392.

(4) Bales, B. L.; Zana, R. Characterization of Micelles of Quaternary Ammonium Surfactants as Reaction Media I: Dodeclytrimethylammonium Bromide and Chloride. *J. Phys. Chem. B* **2002**, *106* (8), 1926–1939. https://doi.org/10.1021/jp013813y.

(5) Jones, M. N.; Piercy, J. Light Scattering Studies on N-Dodecyltrimethylammonium Bromide and n-Dodecylpyridinium Iodide. *J. Chem. Soc. Faraday Trans. 1 Phys. Chem. Condens. Phases* **1972**, *68*, 1839–1848. https://doi.org/10.1039/F19726801839.

(6) Mata, J.; Varade, D.; Bahadur, P. Aggregation Behavior of Quaternary Salt Based Cationic Surfactants. *Thermochim. Acta* **2005**, *428* (1–2), 147–155. https://doi.org/10.1016/j.tca.2004.11.009.

(7) Lianos, P.; Zana, R. Fluorescence Probe Studies of the Effect of Concentration on the State of Aggregation of Surfactants in Aqueous Solution. *J. Colloid Interface Sci.* **1981**, *84* (1), 100–107. https://doi.org/10.1016/0021-9797(81)90263-0.

(8) Malliaris, A.; Le Moigne, J.; Sturm, J.; Zana, R. Temperature Dependence of the Micelle Aggregation Number and Rate of Intramicellar Excimer Formation in Aqueous Surfactant Solutions. *J. Phys. Chem.* **1985**, *89* (12), 2709–2713. https://doi.org/10.1021/j100258a054.

(9) Rodenas, E.; Dolcet, C.; Valiente, M.; Valeron, E. C. Physical Properties of Dodecyltrimethylammonium Bromide (DTAB) Micelles in Aqueous Solution and Their Behavior as the Reaction Medium. *Langmuir* **1994**, *10* (7), 2088–2094. https://doi.org/10.1021/la00019a013.

(10) Pal, A.; Pillania, A. Modulating Effect of Ionic Liquid 1-Butyl-2,3-Dimethylimidazolium Chloride on Micellization Behaviour of Cationic Surfactant Dodecyltrimethylammonium Bromide in Aqueous Media. *Fluid Phase Equilib.* **2015**, *389*, 67–73. https://doi.org/10.1016/j.fluid.2015.01.013.

(11) Berr, S.; Jones, R. R. M.; Johnson, J. S. Effect of Counterion on the Size and Charge of Alkyltrimethylammonium Halide Micelles as a Function of Chain Length and Concentration as Determined by Small-Angle Neutron Scattering. *J. Phys. Chem.* **1992**, *96* (13), 5611–5614. https://doi.org/10.1021/j100192a075.

(12) Jalšenjak, N.; Težak, D. A New Method for Simultaneous Estimation of Micellization Parameters from Conductometric Data. *Chem. - A Eur. J.* **2004**, *10* (20), 5000–5007. https://doi.org/10.1002/chem.200400415.

(13) Pal, A.; Pillania, A. Thermodynamic and Aggregation Properties of Aqueous Dodecyltrimethylammonium Bromide in the Presence of Hydrophilic Ionic Liquid 1,2-Dimethyl-3-Octylimidazolium Chloride. *J. Mol. Liq.* **2015**, *212*, 818–824. https://doi.org/10.1016/j.molliq.2015.10.042.

(14) Anacker, E. W.; Rush, R. M.; Johnson, J. S. Equilibrium Ultracentrifugation and Light Scattering of Sodium Lauryl Sulfate and Dodecyltrimethylammonium Bromide Solutions. *J. Phys. Chem.* **1964**, *68* (1), 81–93. https://doi.org/10.1021/j100783a014.

(15) Danov, K. D.; Kralchevsky, P. A.; Ananthapadmanabhan, K. P. Micelle-Monomer Equilibria in Solutions of Ionic Surfactants and in Ionic-Nonionic Mixtures: A Generalized Phase Separation Model. *Adv. Colloid Interface Sci.* **2014**, *206*, 17–45.

https://doi.org/10.1016/j.cis.2013.02.001.
(16) Moyá, M. L.; Rodríguez, A.; del Mar Graciani, M.; Fernández, G. Role of the Solvophobic Effect on Micellization. *J. Colloid Interface Sci.* **2007**, *316* (2), 787–795. https://doi.org/10.1016/j.jcis.2007.07.035.
(17) Junquera, E.; Aicart, E. Mixed Micellization of Dodecylethyldimethylammonium Bromide and Dodecyltrimethylammonium Bromide in Aqueous Solution. *Langmuir* **2002**, *18* (24), 9250–9258. https://doi.org/10.1021/la026121p.
(18) Rodríguez, A.; Junquera, E.; Del Burgo, P.; Aicart, E. Conductometric and Spectrofluorimetric Characterization of the Mixed Micelles Constituted by Dodecyltrimethylammonium Bromide and a Tricyclic Antidepressant Drug in Aqueous Solution. *J. Colloid Interface Sci.* **2004**, *269* (2), 476–483. https://doi.org/10.1016/j.jcis.2003.09.028.
(19) Caponetti, E.; Martino, D. C.; Floriano, M. A.; Triolo, R.; Wignall, G. D. Effect of Crown Ether 1,4,7,10,13,16-Hexaoxacyclooctadecane on the Structure of Sodium Dodecyl Sulfate and Dodecyltrimethylammonium Bromide Aqueous Micellar Solutions. *Langmuir* **1995**, *11* (7), 2464–2470. https://doi.org/10.1021/la00007a025.
(20) Herrington, K. L.; Kaler, E. W.; Miller, D. D.; Zasadzinski, J. A.; Chiruvolu, S. Phase Behavior of Aqueous Mixtures of Dodecyltrimethylammonium Bromide (DTAB) and Sodium Dodecyl Sulfate (SDS). *J. Phys. Chem.* **1993**, *97* (51), 13792–13802. https://doi.org/10.1021/j100153a058.
(21) Caponetti, E.; Causi, S.; De Lisi, R.; Floriano, M. A.; Milioto, S.; Triolo, R. Dodecyltrimethylammonium Bromide in Water-Urea Mixtures: Structure and Energetics. *J. Phys. Chem.* **1992**, *96* (12), 4950–4960. https://doi.org/10.1021/j100191a042.
(22) Lusvardi, K. M.; Full, A. P.; Kaler, E. W. Mixed Micelles of Dodecyltrimethylammonium Bromide and Didodecyldimethylammonium Bromide. *Langmuir* **1995**, *11* (2), 487–492. https://doi.org/10.1021/la00002a021.
(23) Dar, A. A.; Chatterjee, B.; Rather, G. M.; Das, A. R. Mixed Micellization and Interfacial Properties of Dodecyltrimethylammonium Bromide and Tetraethyleneglycol Mono-n-Dodecyl Ether in Absence and Presence of Sodium Propionate. *J. Colloid Interface Sci.* **2006**, *298* (1), 395–405. https://doi.org/10.1016/j.jcis.2005.12.006.
(24) Mahajan, R. K.; Vohra, K. K.; Aswal, V. K. Small Angle Neutron Scattering Measurements of Aggregation Behaviour of Mixed Micelles of Conventional Surfactants with Triblock Polymer L64. *Colloids Surfaces A Physicochem. Eng. Asp.* **2008**, *326* (1–2), 48–52. https://doi.org/10.1016/j.colsurfa.2008.05.015.
(25) Fafati, A. A.; Gharibi, H.; Iloukhani, H.; Safdari, L. Aggregation Number of Ionic Surfactants and Its Application for Alkyltrimethyl Ammonium Bromides and Sodium Tetradecyl Sulfate by Potentiometric Technique. *Phys. Chem. Liq.* **2003**, *41* (3), 227–238. https://doi.org/10.1080/0031910021000044438.
(26) Griffiths, P. C.; Paul, A.; Khayat, Z.; Heenan, R. K.; Ranganathan, R.; Grillo, I. A Small-Angle Neutron Scattering Study of Biologically Relevant Mixed Surfactant Micelles Comprising 1,2-Diheptanoyl-Sn-Phosphatidylcholine and Sodium Dodecyl Sulfate or Dodecyltrimethylammonium Bromide. *Soft Matter* **2005**, *1* (2), 152–159. https://doi.org/10.1039/b502091c.
(27) Naskar, B.; Dey, A.; Moulik, S. P. Counter-Ion Effect on Micellization of Ionic Surfactants: A Comprehensive Understanding with Two Representatives, Sodium Dodecyl Sulfate (SDS) and Dodecyltrimethylammonium Bromide (DTAB). *J. Surfactants Deterg.* **2013**, *16* (5), 785–794. https://doi.org/10.1007/s11743-013-1449-1.
(28) Bergström, M.; Pedersen, J. S. Structure of Pure SDS and DTAB Micelles in Brine Determined by Small- Angle Neutron Scattering (SANS). *Phys. Chem. Chem. Phys.* **1999**, *1* (18), 4437–4446. https://doi.org/10.1039/a903469b.
(29) Šarac, B.; Medoš, Ž.; Cognigni, A.; Bica, K.; Chen, L.-J.; Bešter-Rogač, M. Thermodynamic Study for Micellization of Imidazolium Based Surface Active Ionic Liquids in Water: Effect of Alkyl Chain Length and Anions. *Colloids Surfaces A Physicochem. Eng. Asp.* **2017**, *532*, 609–617. https://doi.org/10.1016/j.colsurfa.2017.01.062.
(30) Bai, G.; Lopes, A.; Bastos, M. Thermodynamics of Micellization of Alkylimidazolium

Surfactants in Aqueous Solution. *J. Chem. Thermodyn.* **2008**, *40* (10), 1509–1516. https://doi.org/10.1016/j.jct.2008.05.016.
(31) Pal, A.; Yadav, S. Thermodynamic and Surface Properties of Aqueous 1-Dodecyl-3-Methylimidazolium Chloride [C12mim][Cl] Solution in the Presence of a Series of Inorganic Salts. *J. Surfactants Deterg.* **2020**, *23* (1), 53–65. https://doi.org/10.1002/jsde.12347.
(32) Łuczak, J.; Jungnickel, C.; Markiewicz, M.; Hupka, J. Solubilization of Benzene, Toluene, and Xylene (BTX) in Aqueous Micellar Solutions of Amphiphilic Imidazolium Ionic Liquids. *J. Phys. Chem. B* **2013**, *117* (18), 5653–5658. https://doi.org/10.1021/jp3112205.
(33) Chabba, S.; Kumar, S.; Aswal, V. K.; Kang, T. S.; Mahajan, R. K. Interfacial and Aggregation Behavior of Aqueous Mixtures of Imidazolium Based Surface Active Ionic Liquids and Anionic Surfactant Sodium Dodecylbenzenesulfonate. *Colloids Surfaces A Physicochem. Eng. Asp.* **2015**, *472*, 9–20. https://doi.org/10.1016/j.colsurfa.2015.02.032.
(34) El Seoud, O. A.; Pires, P. A. R.; Abdel-Moghny, T.; Bastos, E. L. Synthesis and Micellar Properties of Surface-Active Ionic Liquids: 1-Alkyl-3-Methylimidazolium Chlorides. *J. Colloid Interface Sci.* **2007**, *313* (1), 296–304. https://doi.org/10.1016/j.jcis.2007.04.028.
(35) Sastry, N. V.; Vaghela, N. M.; Aswal, V. K. Effect of Alkyl Chain Length and Head Group on Surface Active and Aggregation Behavior of Ionic Liquids in Water. *Fluid Phase Equilib.* **2012**, *327*, 22–29. https://doi.org/10.1016/j.fluid.2012.04.013.
(36) Kaur, R.; Kumar, S.; Aswal, V. K.; Mahajan, R. K. Influence of Headgroup on the Aggregation and Interactional Behavior of Twin-Tailed Cationic Surfactants with Pluronics. *Langmuir* **2013**, *29* (38), 11821–11833. https://doi.org/10.1021/la401864p.

USC UNIVERSIDADE DE SANTIAGO DE COMPOSTELA

Quedamos así, entón

Ángel Piñeiro Guillén
Supervisor of this thesis

USC
UNIVERSIDADE
DE SANTIAGO
DE COMPOSTELA

USC
UNIVERSIDADE
DE SANTIAGO
DE COMPOSTELA





Many natural phenomena and industrial applications depend directly on molecular aggregation and adsorption processes which, in turn, are intimately connected to each other: molecules with a high affinity for interfaces typically tend to aggregate in the liquid phase. New experimental, theoretical and computational methods are proposed and tested in this thesis to better understand these processes. In particular, the development and first results of what we call Fluid Interface Calorimetry, are presented. Complementary, new semiempirical models for the analysis of experimental measurements from different techniques are proposed. A chapter devoted to the characterization of structure and dynamic behaviour of water molecules around solutes in the liquid bulk and at water/air interfaces is also included.